



AVERTISSEMENT

Ce document est le fruit d'un long travail approuvé par le jury de soutenance et mis à disposition de l'ensemble de la communauté universitaire élargie.

Il est soumis à la propriété intellectuelle de l'auteur. Ceci implique une obligation de citation et de référencement lors de l'utilisation de ce document.

D'autre part, toute contrefaçon, plagiat, reproduction illicite encourt une poursuite pénale.

Contact : ddoc-theses-contact@univ-lorraine.fr

LIENS

Code de la Propriété Intellectuelle. articles L 122. 4

Code de la Propriété Intellectuelle. articles L 335.2- L 335.10

http://www.cfcopies.com/V2/leg/leg_droi.php

<http://www.culture.gouv.fr/culture/infos-pratiques/droits/protection.htm>



UNIVERSITÉ DE LORRAINE

École doctorale RP2E

Centre de Recherches Pétrographiques et Géochimiques

Thèse de doctorat soutenue publiquement pour l'obtention du titre de
Docteur de l'Université de Lorraine (Spécialité : Géosciences)

par

Romain Hemelsdaël

**Evolution spatio-temporelle du couplage entre
système fluvial et rifting :
étude du rift de Corinthe (Grèce)**

Soutenance prévue le 6 octobre 2016 devant le jury composé de

<i>Rapporteurs :</i>	Isabelle COJAN	- MINES ParisTech (France)
	Aurélia HUBERT-FERRARI	- Université de Liège (Belgique)
<i>Examineurs :</i>	Elisabet BEAMUD AMORÓS	- Université de Barcelone (Espagne)
	Sébastien CASTELLTORT	- Université de Genève (Suisse)
	Julien CHARREAU	- CRPG (Nancy, France)
	Jérôme LAVÉ	- CRPG (Nancy, France)
<i>Directeurs :</i>	Mary FORD	- CRPG (Nancy, France)
	Fabrice MALARTRE	- GeoRessources (Nancy, France)

Résumé

Le comportement des rivières au cours du rifting joue un rôle important dans la sédimentation syn-rift et la distribution de la subsidence. Pendant la croissance des failles normales, les rivières répondent aux mouvements verticaux. En réponse au soulèvement tectonique, les rivières peuvent être déviées vers les zones en subsidence ou inversées. Les rivières peuvent aussi inciser les zones en soulèvement. L'évolution à long terme des rivières et leurs enregistrements stratigraphiques restent mal documentés pendant les processus de croissance et de migration des failles normales. Cette thèse analyse les interactions entre les rivières antécédentes et la croissance des réseaux de failles normales. Les implications en termes de distribution des faciès syn-rift sont étudiées à l'échelle du bassin et des blocs de failles.

Les dépôts fluviatiles et deltaïques sont préservés dans plusieurs blocs de failles normales soulevés le long de la marge sud du rift de Corinthe (Grèce). Les logs sédimentaires et la cartographie des faciès syn-rift permettent le découpage lithostratigraphique de la zone d'étude. La série syn-rift est principalement conglomératique et difficile à dater. La magnétostratigraphie et quelques marqueurs biostratigraphiques sont utilisés pour dater et corrélérer les dépôts entre les différents blocs de faille. L'analyse des isotopes cosmogéniques ^{26}Al et ^{10}Be dans les dépôts a permis la détermination d'âge d'enfouissement. L'ensemble des âges obtenus par ces différentes méthodes permet de proposer un modèle de corrélation et de reconstruire l'évolution du rift précoce entre 3,6 et 1,8 Ma environ.

(1) Le système fluviatile étudié évolue à travers plusieurs blocs de failles actives. (2) Le système de drainage antécédent hérité de la chaîne hellénique est caractérisé par un flux sédimentaire important depuis le début du rifting. (3) Le système fluviatile (au moins 30 km de long) remplit le paléorelief et le flux sédimentaire dépasse largement l'accommodation créée par les failles. L'enfouissement des failles par le système fluviatile limite la création de topographie et le développement d'un réseau de drainage conséquent. (4) L'axe fluviatile antécédent reste constant et contrôle la distribution des faciès. (5) Les changements de faciès et les architectures alluviales sont observés à l'échelle du bassin et ne sont pas directement contrôlés par les variations d'accommodation dans les blocs de failles. (6) Les zones d'accommodation maximale sont ici disposées parallèlement à l'axe fluviatile antécédent. La persistance des rivières et le flux sédimentaire pendant plusieurs centaines de milliers d'années ont permis la localisation de la déformation, induisant une rétroaction positive sur la croissance des failles.

Le système distributaire se termine à l'est où des deltas progradent en milieu lacustre peu profond. Les systèmes de dépôts fluviatiles, deltaïques et turbiditiques actifs à l'initiation du rift de Corinthe enregistrent l'approfondissement diachrone du bassin.

Le comportement des rivières antécédentes est aussi étudié à l'échelle d'une zone de relais entre deux failles bordières actuellement actives. Pendant le Pléistocène moyen et supérieur, la zone de relais a capturé la rivière antécédente de Krathis qui a construit une succession de deltas. La connexion entre les deux failles majeures est marquée par (1) des failles obliques dites "de transfert", (2) plusieurs familles de terrasses marines enregistrant le soulèvement diachrone de la rampe de relais, et (3) la migration progressive de l'accommodation vers le bassin. Cette étude permet pour la première fois de reconstruire les processus de connexion de failles sur une période 0,5 Ma. La rivière Krathis persiste au cours du développement de la zone de relais et met en évidence, une fois de plus, l'importance des rivières antécédentes dans la localisation des dépocentres majeurs dans les rifts.

Abstract

Rivers behaviour during early rifting can significantly impact on syn-rift sedimentation and the distribution of subsidence. During normal fault growth, existing rivers can be diverted toward subsiding zones. They can respond to footwall uplift either by reversing their flow or by incising into uplifting zones. Long-lived river systems and their stratigraphic record in rifts are poorly documented, not only during early fault propagation and linkage processes but also during successive migrating phases of fault activity. We investigate the interactions of major antecedent rivers with a growing normal fault system and the implications for facies distributions, both on a basin scale and at the scale of individual normal fault blocks.

Along the southern margin of the western Corinth rift (Greece), the Plio-Pleistocene fluvial and deltaic successions are investigated. Syn-rift deposits are preserved in a series of uplifted normal fault blocks (10–20 km long, 3–7 km wide). Detailed sedimentary logging and high resolution mapping of the syn-rift deposits document variations of alluvial architecture across the basin and enable to define lithostratigraphic units. Magnetostratigraphy and rare biostratigraphic data are used to date and correlate the alluvial succession between fault blocks. Burial ages were tentatively determined using cosmogenic isotopes ^{10}Be and ^{26}Al produced in situ in quartz grains. Based on the correlation model, we reconstruct the evolution of the early western Corinth rift between about 3.6 and 1.8 Ma.

(1) The transverse and antecedent Kalavryta river system flowed and deposited across a series of active normal fault blocks. (2) This river system was inherited from the Hellenide mountain belt and supplied high volumes of coarse sediments from the onset of extension. (3) As depocentres enlarged through time, the fluvial deposits progressively filled palaeorelief. A continuous braided plain developed above active buried faults and no significant consequent drainage system developed between the narrow fault blocks. (4) The main fluvial axis of the antecedent drainage persists through time and controlled facies distribution. (5) The length scale of facies transitions is greater than, and therefore not related to fault spacing. Here, along-strike subsidence variations in individual fault blocks represent a secondary contributor to the alluvial architecture. (6) The zones of maximum subsidence on individual faults are aligned across strike, parallel to the persistent fluvial axis. This implies that long-term sediment supply and loading influenced normal fault growth.

Sediment supply largely outpaced local hangingwall subsidence and overfilled the early rift basin. The river system terminated eastward where small deltas are built into a shallow lake that occupied the central Corinth rift. During this time, another river system built fan deltas along the southern margin, recording diachronous deepening of the basin.

The behaviour of antecedent rivers is also studied at the scale of a relay zone, that developed later in the rift history between two growing fault segments. During the Middle to Late Pleistocene, the relay zone captured the antecedent Krathis River, which deposited prograding Gilbert-type deltas. Transfer faults record progressive linkage and basinward migration of accommodation along the ramp axis, while marine terraces record diachronous uplift in their footwalls. Although early linkage occurred, the main normal faults continued to propagate until final connexion. For the first time a reconstruction of the linkage phase is presented over a period of ca. 0.5 Myr. Throughout this linkage history, the Krathis River continued to flow across the relay zone. Again, this emphasizes the role of antecedent rivers in supplying sediments and controlling the location of the major depocentres along the rift margins.

REMERCIEMENTS

Je tiens à remercier toutes les personnes qui ont été impliquées plus ou moins directement dans l'écriture de ce manuscrit. Je remercie avant tout mes directeurs de thèse, Mary Ford et Fabrice Malartre, qui m'ont tous les deux beaucoup appris pendant ces quatre années de thèse.

Mary, je te remercie pour ta disponibilité, ton impressionnante efficacité, ta rigueur, ta franchise et surtout ta pédagogie. En 2012, pendant mon projet de Master 2, tu m'avais posé la question : "Quel sujet aimerais-tu traiter si à l'avenir tu veux faire une thèse ?" Je t'avais répondu poliment que j'aimerais pourquoi pas étudier les premiers sédiments déposés dans les bassins sédimentaires (je dois avouer que c'était une drôle d'idée). Quatre ans plus tard, j'ai toujours du mal à réaliser que ma thèse porte sur ce sujet ! Fabrice, je te remercie pour ta disponibilité, ta rigueur, ta pédagogie, ton optimisme et ta patience pour essayer de faire de moi un sédimentologue des systèmes fluviaux. C'était très motivant de travailler avec vous deux.

Je remercie la direction du CRPG pour m'avoir permis de travailler dans de très bonnes conditions. Merci au personnel administratif, et notamment Cati pour la préparation des séjours en Grèce. Merci à Isabelle et Bruno pour votre efficacité et votre sympathie. Je tiens à remercier les personnes du CRPG qui ont pu collaborer avec moi au cours de l'acquisition et le traitement des données, et notamment Julien Charreau, Pierre-Henri Blard, Sevket Sen, Emmanuel Davy. Je remercie aussi les scientifiques avec qui j'ai pu longuement discuter pendant les conférences et autres invitations à des séminaires : John Armitage, Laurie Barrier, Rebecca Bell, Robert Gawthorpe, Laurent Husson, Haris Kranis, Charles Poitou, Christopher Jackson, Manolis Skourtsos, Alex Whittaker. On n'a pas idée à quel point c'est encourageant de rencontrer des gens qui s'intéressent à son sujet de thèse.

Merci à mes collègues de bureau, collègues du quatrième étage et tous les autres doctorants rencontrés au CRPG. Merci à toi Léo pour ton aide, ton soutien et les nombreuses séances de footing en forêt après de longues journées passées à rester assis devant l'écran d'ordinateur.

J'ai une pensée particulière (non sans émotion) pour certaines personnes indissociables de cette thèse. Tout d'abord, merci à mes parents qui m'ont toujours fait confiance au cours de mes études sans jamais vraiment comprendre la finalité de mes projets. Merci à mon frère Tomtom pour son soutien continu. Un grand merci à Ju pour les moments incroyables ainsi que pour les relectures, depuis les premiers jets jusqu'à la version définitive. Petit clin d'œil à Hugo, merci pour toutes tes bonnes attentions (émoticône vélo vert). Un grand merci à Anna, Aurélie, Bastien, JB, Louis Alexandre, Rami, Sarah, Tutu pour les nombreux encouragements. Je remercie aussi les amis de ch'nord que j'ai trop peu vu entre les séjours en Grèce, les périodes de labo et de rédaction. On sait tous que ça ne change rien car seuls les meilleurs restent ! Clin d'œil à Ju (Adjovi), Titi, Yoyore, Pavel, Linou, Charlu, Pit et Didi.

Je sais par avance que j'ai oublié de nombreuses personnes. Je suis certain qu'elles sauront se glisser parmi les personnes citées.

Table des matières

Résumé	5
Abstract	7
Introduction générale	19
I Etat des connaissances	23
1 Systèmes fluviaux dans les rifts et enregistrements sédimentaires	25
1.1 Extension lithosphérique	26
1.2 Croissance d'un réseau de failles normales	29
1.2.1 Modèles	29
1.2.2 Réactivation des structures héritées	32
1.2.3 Migration	33
1.3 Soulèvement, flux sédimentaire et sédimentation alluviale	35
1.3.1 Développement des bassins versants	35
1.3.2 Paramètres de contrôle de la sédimentation alluviale	36
1.4 Systèmes fluviaux dans les rifts continentaux	41
1.4.1 Rivières transverses et axiales	41
1.4.2 Réorganisation et adaptation des systèmes de drainage	43
1.5 Architectures fluviales : du terrain aux modèles	46
1.5.1 Echelles d'observation	46
1.5.2 Apport de la stratigraphie séquentielle : modèles et critiques	47
1.5.3 Confinement des systèmes fluviaux	48
1.5.4 Rôle de la subsidence et autres paramètres de contrôle	49
1.6 Evolution tectono-stratigraphique des rifts continentaux	52
1.6.1 Modèles existants	52
1.6.2 Modèle alternatif et contribution de la thèse	54

2	Le rift de Corinthe	59
2.1	Introduction	59
2.2	Contexte tectonique actuel et déformation active	63
2.3	Structuration du rift de Corinthe	65
2.3.1	Histoire des Hellénides externes	65
2.3.2	Histoire tardi-cénozoïque, extension égéenne	68
2.4	Géométrie et modèles d'évolution du rift de Corinthe	73
2.4.1	Modèle de détachement	74
2.4.2	Modèle de rotation des blocs	76
2.5	Stratigraphie syn-rift	79
II	Résultats et discussions	85
3	Multidisciplinary approach to date gravel-dominated syn-rift successions	87
3.1	Introduction	88
3.2	Lithostratigraphy of the Kalavryta river system	92
3.2.1	Southern fault blocks- Coarsening-upward succession	92
3.2.2	Northern fault blocks - Fining-upward succession	92
3.2.3	Lithostratigraphy of the sampled sections	93
3.3	Biostratigraphy	99
3.3.1	Mammal teeth	99
3.3.2	Charophytes	99
3.3.3	Mollusks	99
3.4	Magnetostratigraphy and Rock Magnetism	100
3.4.1	Sampling	100
3.4.2	Magnetic mineralogy	100
3.4.3	Demagnetisation and magnetic directions	102
3.4.4	Magnetic directions and statistical tests	109
3.4.5	Polarity column and robustness	111
3.5	^{26}Al - ^{10}Be burial ages	116
3.6	Age model	116
4	The impact of large antecedent river systems on syn-rift sedimentation	121
4.1	Introduction	124
4.2	The Corinth rift and study area	125

4.2.1	Geological setting	125
4.2.2	Onshore stratigraphy	126
4.2.3	Studied normal fault blocks	126
4.3	Methods	129
4.4	Facies analysis and alluvial architecture of the early rift deposits	130
4.4.1	FA1 : Structureless coarse alluvial conglomerates	130
4.4.2	FA2 : Crudely stratified alluvial conglomerates	130
4.4.3	FA3 : Heterolithic gravel to fine-grained fluvial deposits	135
4.4.4	FA4 : Gravel to fine-grained lacustrine deltas	136
4.4.5	FA5 : Silt and clay lacustrine deposits	137
4.4.6	FA6 : Lagoonal and upper shoreface deposits	138
4.5	Lithostratigraphy of the Lower Group	147
4.5.1	Southern fault blocks	147
4.5.2	Northern fault blocks	148
4.6	Dating and stratigraphic correlation	150
4.7	Evolution of the Kalavryta river system	154
4.7.1	Phase 1 (~3.6–3.5 Ma)	154
4.7.2	Phase 2 (~3.5–3.1 Ma)	155
4.7.3	Phase 3 (~3.1–2.8 Ma)	155
4.7.4	Phase 4 (~2.8–2.3 Ma)	156
4.7.5	Phase 5 (~2.3–1.8 Ma)	157
4.8	Discussion	162
4.8.1	Paucity of footwall-derived sediments	162
4.8.2	Length scale of facies variation and relation with faults	163
4.8.3	Channel belt distribution and subsidence variations	163
4.8.4	Overfill conditions in the early rift basins	164
4.9	Conclusions	167
5	Depositional relay ramp evolution and river behaviour	169
5.1	Introduction	171
5.2	Corinth rift	173
5.3	Coastal normal fault system and relay zone	178
5.4	Offshore faults and seismic stratigraphy : a record of fault propagation and linkage	181
5.5	Length-displacement analysis on controlling faults	184
5.6	Onshore relay zone : a history of migrating sedimentation and uplift	185

TABLE DES MATIÈRES

5.6.1	Geomorphology and marine terraces	185
5.6.2	Middle and Upper groups stratigraphy	186
5.6.3	Age estimates in the Upper group	188
5.7	Relay zone evolution	193
5.8	Discussion	195
5.8.1	Relay ramp geometry and fault growth models	195
5.8.2	Role of structural inheritance in the development of a rift border fault system	195
5.8.3	Sedimentation patterns on relay ramps	196
5.8.4	Role of antecedent drainage	196
5.9	Conclusions	197
5.10	Appendix : Technical details on U–Th dating of <i>Cladocora caespitosa</i> from Kryoneri location	198
6	Regional stratigraphy and general discussion	201
6.1	Introduction	202
6.2	Regional syn-rift stratigraphy	202
6.2.1	C5 : Westernmost rift	203
6.2.2	C4 and C3 : central and western rift, and correlation to the eastern rift (C2)	206
6.2.3	C1 : Corinth isthmus	208
6.2.4	MB : Megara Basin	208
6.3	Corinth rift evolution	211
6.3.1	Phase 1 : Late Pliocene–Early Pleistocene (4–3.6 to 1.5 Ma)	211
6.3.2	Phase 2 : Early–Middle Pleistocene (1.5 to -0.7 Ma)	213
6.3.3	Phase 3 : Calabrian–Middle Ionian (0.7 to 0.4 Ma)	216
6.3.4	Phase 4 : Middle Ionian–present day (0.4–Present Ma)	218
6.4	Significance for rift basin deepening	221
6.5	Compilation of rivers behaviour	221
6.5.1	Response to footwall uplift	221
6.5.2	Response to fault migration	222
6.6	Significance of through-going river systems	223
	Conclusions et perspectives	228
III	Annexes	233
A	Mesures et traitement des données de paléocourants	235

B	Sédimentologie et paléontologie	243
B.1	Analyse sédimentologique détaillée des faciès syn-rift du <i>Lower group</i>	243
B.2	Logs sédimentaires	252
B.3	Algues vertes calcaires : détermination et distribution stratigraphique	261
C	Isotopes cosmogéniques : âges d'enfouissement ^{26}Al et ^{10}Be	263
C.1	Origine des isotopes cosmogéniques	263
C.2	Production <i>in situ</i> des isotopes cosmogéniques	264
C.3	Décroissance radioactive et production de ^{26}Al et ^{10}Be	265
C.4	Détermination d'âge d'enfouissement à partir de ^{10}Be et ^{26}Al	268
C.5	Taux de dénudation et de taux de production initial à partir des rivières actuelles	271
D	^{26}Al-^{10}Be burial ages and interpretations	273
D.1	Theory of cosmogenic burial dating	273
D.2	Sample collection and analysis	274
D.3	Local production rate and determination of burial ages	275
D.4	Burial age results	282
D.5	Significance to date the Gilbert deltas of the Killini river system	285
E	Palaeomagnetic rotations	289
F	Publication en second auteur	293
IV	Bibliographie	339

Liste des acronymes

A	Accommodation/subsidence rate	MIS	Marine isotope stage
AF	Alternating field	MNN	Marine nanno-fossil zonation
AVA	Aegean volcanic Arc	PDF	Present day field
ChRM	Characteristic remanent magnetisation	PG	Patras Gulf
DF	Derveni Fault	PMF	Pirgaki Mamoussia Fault
DFS	Distributive fluvial system	Q1	Quality-1
EHF	East Helike Fault	Q2	Quality-2
Fm	Formation	Q3	Quality-3
GAD	Geomagnetic axial dipole	KrF	Krathis Fault
GD	Gilbert-type delta	NAF	North anatolian Fault
Gp	Group	S	Sediment supply
IS	<i>in situ</i> (coordonnées géographiques)	SPR	Sediment preservation rate
IRM	Isothermal remanent magnetization	SU	Seismic unit
MAD	Maximum angular deviation	TC	Tilt-corrected
Mb	Member	TG	Terrace group
MB	Megara Basin	TWTT	Two way travel time (s, ms)
MCC	Metamorphic core complex		

Introduction générale

Couplage entre rivières et rifting

Les rivières modulent l'évolution des paysages dans les chaînes de montagnes et au cours de la tectonique active. Dans les rifts continentaux, les rivières reflètent la complexité des processus dynamiques de surface depuis les zones en érosion jusqu'au bassin sédimentaire. Pendant la croissance des failles normales, les rivières répondent aux mouvements tectoniques que sont la subsidence et le soulèvement. Ainsi, les rivières peuvent être déviées, capturées par les zones de relais entre les failles, ou encore être inversées. L'évolution du couplage entre les systèmes de rivières et le phénomène tectonique de rifting est étudiée selon différentes échelles de temps et d'espace. On s'intéresse ici à l'évolution stratigraphique des systèmes alluviaux afin de reconstruire l'histoire du rift de Corinthe (Grèce) durant la période Pliocène-Pléistocène.

Les modèles tectono-stratigraphiques existants dans les rifts continentaux sont généralement établis dans les demi-grabens ou les grabens, sur plusieurs dizaines voire centaines de kilomètres. Les dépocentres dans les blocs de failles normales peuvent être alimentés par des rivières conséquentes en réponse à la création de topographie. La sédimentation syn-rift est couramment interprétée comme la réponse plus ou moins directe à l'activité tectonique. Cette simple relation de cause à effet est discutée ici en considérant un flux sédimentaire antécédent au rifting.

Le rift de Corinthe est un lieu privilégié pour l'étude de l'interaction entre tectonique et sédimentation. Il s'agit d'un rift jeune (moins de 5 Ma) présentant la sismicité est la plus active en Europe. Le golfe actuel correspond approximativement aux bordures du rift actif. Le soulèvement des blocs de failles inactifs et l'incision consécutive par les rivières actuelles ont permis de mettre à l'affleurement les dépôts du syn-rift suivant des conditions d'observation optimales. La zone d'étude se situe le long de la marge sud du golfe, dans la partie ouest du rift de Corinthe, principalement entre les villes de Diakopto, Akrata et Kalavryta.

La vitesse des processus tectoniques actuels est rapide (taux d'extension 5–16 mm/an, vitesse de soulèvement ~ 1 mm/an) et permet de documenter les interactions tectono-sédimentaires sur quelques 100 ka. De plus, les blocs de failles normales sont étroits dans le rift de Corinthe, généralement inférieurs à 10 km de large. La résolution spatio-temporelle des objets géologiques étudiés est donc une des originalités principales de cette thèse.

Ici, la "marge" du rift ne se résume pas à une faille majeure contrôlant à la fois la subsidence et le soulèvement en bordure de bassin, mais à un système de failles en cours de développement. Cette "marge" peut s'étendre sur plusieurs dizaines de kilomètres, depuis l'entrée des sédiments jusqu'à l'embouchure des rivières. La préservation des dépôts syn-rift à travers plusieurs blocs de failles étroites constitue un cas particulier parmi les rifts continentaux.

Le rifting continental intra-montagneux suppose la présence d'une paléotopographie plus ou moins importante, dessinée par l'incision des rivières pré-rift. La subsidence à l'initiation du

rifting permet à ces rivières de passer d'un contexte en dégradation/érosion à un contexte en aggradation/sédimentation. Dans le cas où le paysage pré-rift est marqué par d'importants reliefs (plusieurs centaines de mètres de hauteur), **comment les rivières antécédentes remplissent-elles les paléoreliefs à l'initiation du rifting ? Comment se comportent les rivières antécédentes au cours de la croissance des failles normales ?** Les implications en termes de distribution des faciès dans l'enregistrement sédimentaire sont étudiées à l'échelle de la marge du rift continental (échelle régionale) et des blocs de failles normales (échelle locale).

On ne s'intéresse pas uniquement au rôle des rivières antécédentes pendant la phase d'initiation du rift, mais également pendant les phases successives de migration de l'activité des failles. **Les rivières antécédentes persistent-elles depuis l'initiation du rift ou sont-elles réorganisées aux cours du développement du rift ?**

Un autre point important est la quantification du couplage entre rivière et rifting. **A quelle échelle spatio-temporelle se produisent les différents comportements des rivières ?** La quantification de ce couplage implique la datation des séries syn-rift. Les travaux sur la stratigraphie syn-rift sont intégrés à l'échelle de toute la marge du rift et contribuent à mieux comprendre la dynamique des marges de rift, depuis la source des sédiments jusqu'au bassin. **Comment évoluent les environnements de dépôt le long de la marge du rift ? Le bassin de Corinthe était-il alimenté par un ou plusieurs systèmes alluviaux ? En quoi les spécificités du rift de Corinthe peuvent-elles être généralisées à d'autres rifts continentaux ?**

Objectifs

En utilisant la marge sud du rift de Corinthe comme laboratoire naturel, ces travaux sur la stratigraphie syn-rift permettent de reconstruire l'histoire du rift. Les corrélations stratigraphiques sont nécessaires et révèlent la complexité de la sédimentation alluviale syn-tectonique (variations latérales de faciès, discordances, etc). Les objectifs majeurs de la thèse sont de :

- Documenter la sédimentation d'un système fluvial antécédent à l'initiation du rift, à l'échelle d'un système de failles normales.
- Définir un nouveau modèle tectono-stratigraphique à l'initiation du rift en considérant le rôle d'un système fluvial antécédent.
- Documenter l'enregistrement sédimentaire deltaïque et la déviation des rivières au cours du développement d'une zone de relais.
- Dater la série syn-rift à partir d'une approche pluridisciplinaire (lithostratigraphie, magnétostratigraphie, géochimie des isotopes cosmogéniques, biostratigraphie).
- Définir les incertitudes liées à la détermination des âges et les implications sur les corrélations stratigraphiques.
- Etablir la chronostratigraphie pour les phases précoces du rift.
- Essayer de quantifier plus précisément les taux de processus sédimentaires dans les rifts, aussi bien la sédimentation fluvio-deltaïque que la croissance des systèmes de failles

normales.

- Proposer un modèle de corrélation stratigraphique à l'échelle régionale afin de documenter l'ensemble des systèmes de rivières et les environnements de dépôt au cours d'ouverture du rift.

Démarche et approche pluridisciplinaire

La thèse s'inscrit dans la continuité d'études précédentes portant sur la stratigraphie du rift de Corinthe. Elle fait suite aux travaux de thèse de Sébastien Rohais (2007) dans la partie centrale du rift, et à ceux de Nicolas Backert (2009) dans la partie ouest. Ces travaux de thèse sont en partie intégrés au projet de l'ANR SISCOR qui a pour objectif d'apporter de nouvelles observations de terrain et des méthodologies avancées pour affiner les lois de prédiction des séismes et les modèles de l'activité des failles.

En 2009, une étude paléomagnétique préliminaire a été réalisée dans les séries fluviales, deltaïque et lacustres dans la partie ouest du rift de Corinthe. Les résultats encourageants en magnétostratigraphie ont été à l'origine de ce projet de thèse (octobre 2012). Cependant, la magnétostratigraphie ne peut pas être utilisée comme seul outil, et d'autres contraintes temporelles sont nécessaires pour définir des âges absolus. En effet, les inversions de polarité dans ces sédiments sont rares en raison de l'âge plio-quadernaire et de la courte période de temps étudiée (quelques millions d'années). L'idée est donc de coupler les datations magnétostratigraphiques "semi-absolues" avec d'autres méthodes telles que les âges d'enfouissement à partir des isotopes cosmogéniques ^{26}Al - ^{10}Be (travail en collaboration avec Pierre-Henri Blard, CRPG).

Cette thèse regroupe des travaux de terrain (six mois cumulés sur le terrain) couplé aux travaux en laboratoire consacrés à la datation des séries syn-rift. Il s'agit avant tout de caractériser les faciès dans différents blocs de failles normales à partir des logs sédimentaires, des mesures de paléocourants et de la cartographie du remplissage syn-rift. La série syn-rift est subdivisée en différents groupes, formations et membres lithostratigraphiques qui sont corrélés avec les travaux antérieurs.

L'ensemble des observations de terrain permet, dans un premier temps, d'effectuer des corrélations lithostratigraphiques. Bien que les marqueurs biostatigraphiques dans les dépôts fluviaux soient rares, ils ne sont pas totalement inexistantes. La découverte de fossiles (os de mammifères, dents de micromammifères, etc) offre la possibilité d'estimer l'âge des dépôts étudiés. Ce travail a été effectué en collaboration avec Sevket Sen (Muséum d'Histoire Naturelle, Paris).

Organisation du mémoire

Le manuscrit est subdivisé en trois parties. La première partie correspond à l'état des connaissances des notions abordées dans cette thèse. Cette partie rédigée en français est constituée de

deux chapitres.

- Le chapitre 1 présente une synthèse relative à la tectono-stratigraphie des rifts continentaux. Ce chapitre s'intéresse particulièrement au couplage entre rivières et rifting
- Le chapitre 2 est consacré à la présentation du contexte géologique du rift de Corinthe.

La seconde partie est dédiée aux résultats et interprétations. Elle est articulée en quatre chapitres qui sont rédigés en anglais sous forme d'articles publiés, acceptés pour publication ou encore en préparation.

- Le chapitre 3 présente les résultats de datation des dépôts syn-rift à partir des différentes techniques utilisées. Le modèle de corrélation stratigraphique est détaillé et exploité dans le chapitre 4.
- Le chapitre 4 présente la sédimentologie d'un système fluvial à l'initiation du rift de Corinthe (partie ouest). Ce chapitre met l'accent sur le rôle des systèmes de rivières antécédentes dans la distribution des faciès au cours de la croissance d'un réseau de failles normales. L'architecture stratigraphique est étudiée à l'échelle du bassin et à celle des blocs de failles normales.
- Le chapitre 5 décrit le comportement d'une rivière antécédente à l'échelle d'une zone de relais, au cours des processus de croissance et de connexion entre deux failles bordières majeures.
- Enfin, le chapitre 6 est une compilation de la stratigraphie issues de nos travaux et des données existantes afin de construire un modèle d'évolution du rift de Corinthe. Ce chapitre présente une synthèse des différents comportements des rivières dans les rifts, ainsi que les particularités de l'enregistrement sédimentaire par les rivières antécédentes.

La troisième partie de cette thèse correspond aux annexes incluant des données complémentaires de terrain (annexes A et B). La méthode de datation à partir des isotopes cosmogéniques est expliquée dans l'annexe C. Le détail des analyses en géochimie isotopique, le traitement des résultats et les interprétations sont détaillés dans l'annexe D. Ces données non présentées dans la deuxième partie sont susceptibles d'être soumises pour publication dans le futur. Les résultats et les interprétations des rotations paléomagnétiques sont détaillés dans l'annexe E. Enfin l'annexe F comprend à un article publié dans la revue *Geological Society, London, Special Publications*. La contribution à la préparation de cet article m'a permis d'être second auteur. Certains éléments de cette publication sont ré-utilisés dans le chapitre 6.

Première partie

Etat des connaissances

Chapitre 1

Systemes fluviaux dans les rifts et enregistrements sédimentaires

L'étirement de la lithosphère au cours de la divergence des plaques est à l'origine de nombreux processus dynamiques de surface depuis les zones en soulèvement jusqu'au bassin sédimentaire de type "rift". En réponse à la tectonique active, les rivières modulent le paysage pendant plusieurs millions d'années. Le transport de sédiments par les rivières permet ensuite de remplir les dépressions créées par la distension. Ainsi, les rivières dans les rifts continentaux sont des laboratoires naturels pour étudier les interactions tectono-sédimentaires. De façon générale, l'étude des rivières dans les rifts actifs peut être effectuée par la caractérisation du système hydrographique, la quantification des processus de surface dans les bassins versants (flux sédimentaires, taux d'érosion, etc) et l'enregistrement sédimentaire. On s'intéresse surtout à l'enregistrement sédimentaire et à l'évolution stratigraphique des systèmes fluviaux au cours du développement des rifts. Les séries fluviales sont typiquement déposées pendant les phases précoces de la distension et peuvent être à l'origine de la formation des réservoirs porteurs d'hydrocarbures ou encore des aquifères. Au delà des enjeux liés à l'exploration des ressources et à la compréhension des systèmes pétroliers, l'étude de la sédimentation fluviale dans les rifts est importante en recherche fondamentale pour déchiffrer les mécanismes de contrôle et leurs rétroactions au cours du temps.

Ce chapitre examine l'état des connaissances sur le couplage entre rivières et rifting. Une première partie est consacrée à la structuration des rifts continentaux et au développement des failles normales. La suite du chapitre se focalise sur l'étude de la sédimentation alluviale, les systèmes fluviaux dans les rifts et l'architecture des séries fluviales. Les dernières parties introduisent les modèles tectono-stratigraphiques existants dans les rifts continentaux ainsi que les améliorations apportées par cette thèse.

Sommaire

1.1	Extension lithosphérique	26
1.2	Croissance d'un réseau de failles normales	29
1.2.1	Modèles	29
1.2.2	Réactivation des structures héritées	32
1.2.3	Migration	33
1.3	Soulèvement, flux sédimentaire et sédimentation alluviale	35
1.3.1	Développement des bassins versants	35
1.3.2	Paramètres de contrôle de la sédimentation alluviale	36
1.4	Systèmes fluviaux dans les rifts continentaux	41
1.4.1	Rivières transverses et axiales	41
1.4.2	Réorganisation et adaptation des systèmes de drainage	43
1.5	Architectures fluviales : du terrain aux modèles	46
1.5.1	Echelles d'observation	46
1.5.2	Apport de la stratigraphie séquentielle : modèles et critiques	47
1.5.3	Confinement des systèmes fluviaux	48
1.5.4	Rôle de la subsidence et autres paramètres de contrôle	49
1.6	Evolution tectono-stratigraphique des rifts continentaux	52
1.6.1	Modèles existants	52
1.6.2	Modèle alternatif et contribution de la thèse	54

1.1 Extension lithosphérique

Le rifting est le processus tectonique qui étire et amincit la lithosphère (Figure 1.1). L'étiement lithosphérique implique la déformation cassante de la croûte supérieure limitée par la profondeur de la zone sismogénique, à 10–15 km environ (Figure 1.2 ; Scholz, 1988; Burov & Diament, 1995; Burov *et al.*, 2014). L'échelle de déformation dans les rifts dépend principalement du taux d'extension, de la dimension des failles normales et du bassin sédimentaire qui sont eux-mêmes fonctions des propriétés mécaniques de la lithosphère et de l'épaisseur de la croûte élastique (Figure 1.2 ; Hayward & Ebinger, 1996; Foster & Jackson, 1998; Ebinger *et al.*, 1999).

Les rifts continentaux se forment au cours de la divergence des plaques continentales, en contexte de distension arrière arc, dans les zones orogéniques de croûte surépaissie (effondrement post-orogénique). La subsidence peut être d'origine tectonique et/ou thermique, ou encore liée à la charge sédimentaire. L'amincissement lithosphérique dépend principalement du taux d'extension, de la rhéologie, du gradient thermique (Hopper & Buck, 1996; Kruse *et al.*, 1997) et aussi de l'anisotropie crustale en lien avec les structures pré-rift. En réponse à cet amincissement

lithosphérique, la remontée asthénosphérique et la compensation isostatique sont à l'origine des mouvements verticaux (McKenzie, 1978b; Weissel & Karner, 1989). Le soulèvement des épaules du rift peuvent être notamment amplifié par le flux ductile de la croûte inférieure vers l'extérieur du rift (Burov & Cloetingh, 1997) ou encore la charge sédimentaire (Lavie & Steckler, 1997). Ces mouvements verticaux à grande échelle (lithosphérique) sont superposés aux mouvements verticaux créés par les des failles normales.

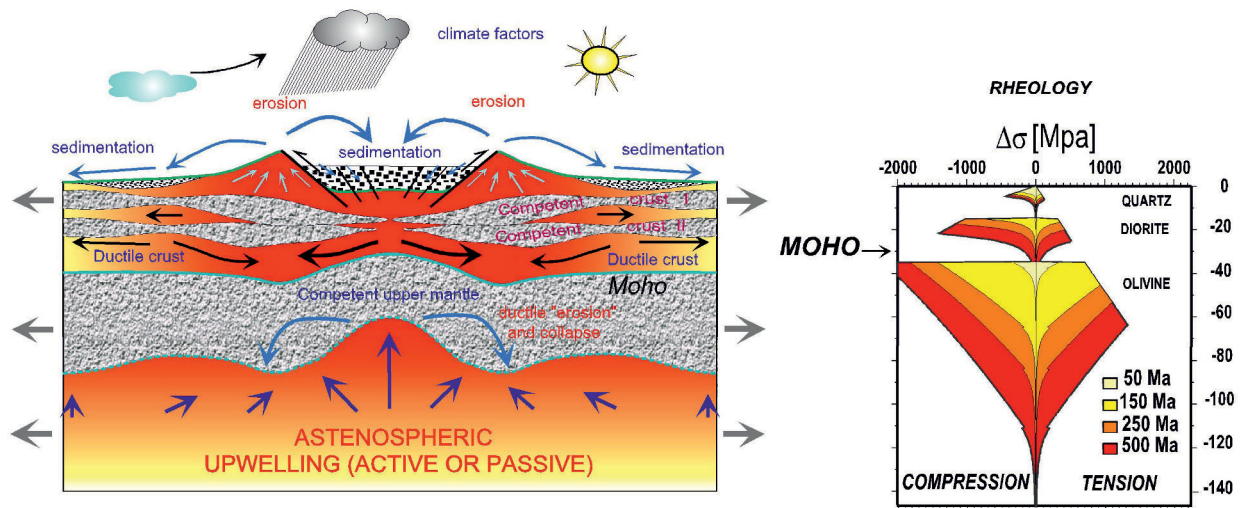


FIGURE 1.1 – Modèle d'extension lithosphérique en considérant les comportements rhéologiques fragile de la croûte supérieure et ductile dans le manteau supérieur, ainsi que les processus de surface (érosion et sédimentation). L'enveloppe de résistance (MPa) de la lithosphère continentale est subdivisée en trois couches représentées par les comportements rhéologiques du quartz, de la diorite et de l'olivine. L'enveloppe de résistance est représentée pour différents âges thermiques depuis le dernier événement tectonique. Une lithosphère plus jeune est susceptible d'être plus faible qu'une lithosphère vieille et froide. (d'après Burov *et al.*, 2014).

En fonction du gradient thermique et du stade de développement, les rifts peuvent être magmatiques ou amagmatiques. On s'intéresse ici au cas des rifts continentaux amagmatiques (cas du rift de Corinthe). De nombreux modèles thermo-mécaniques (Morgan *et al.*, 1986; Allemand *et al.*, 1989; Weissel & Karner, 1989; Cloetingh *et al.*, 1995; Burov & Cloetingh, 1997; Brun, 1999) tentent de reproduire la localisation de la déformation et l'amplitude des mouvements verticaux observés en surface en paramétrant la rhéologie de la lithosphère et la limite fragile/ductile. Ce chapitre se concentre uniquement sur la déformation dans la croûte supérieure au cours du développement des systèmes de failles normales. Les marges soulevées en érosion sont à l'origine du flux sédimentaire et du remplissage du rift (Figure 1.1)

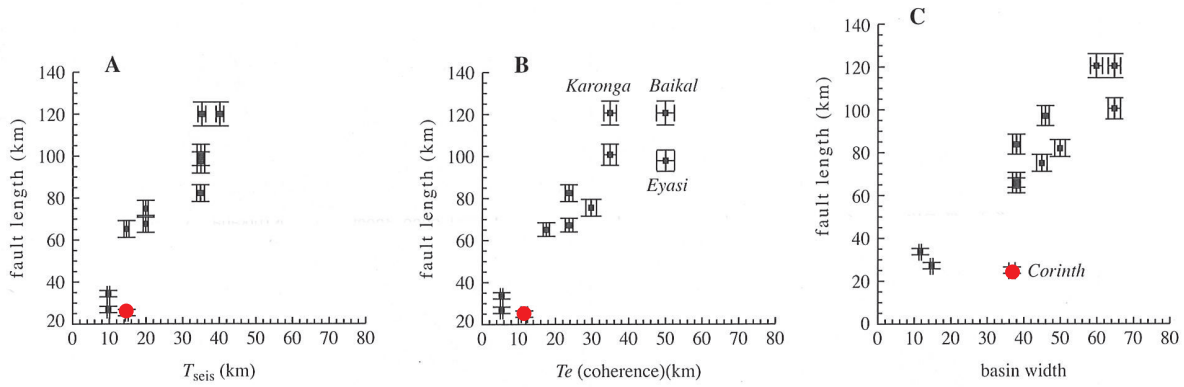


FIGURE 1.2 – Variations de la longueur des failles bordières dans différents rifts continentaux (principalement dans les rift Est africain) en fonction de (A) l'épaisseur de la croûte sismogénique T_{seis} , (B) l'épaisseur élastique efficace T_e et (C) la largeur du bassin. Les points rouges correspondent aux valeurs pour le rift de Corinth, Grèce (modifié d'après [Ebinger et al., 1999](#)).

Les rifts continentaux sont dominés par des systèmes de failles bordières planaires à pendage compris entre 45 et 70° ([Jackson & McKenzie, 1983, 1988](#)) et qui peuvent accumuler plusieurs kilomètres de déplacement. Des systèmes de failles à pendage faibles (moins de 30°) et des failles à géométries listriques sont aussi documentés dans les rifts continentaux ([Wernicke & Burchfiel, 1982](#); [Rosendahl, 1987](#); [Lister & Davis, 1989](#); [Friedmann & Burbank, 1995](#)). Ces failles peuvent suivre les discontinuités lithologiques en profondeur et ces dernières peuvent être à l'origine d'importants niveaux de décollement ([Wernicke & Burchfiel, 1982](#)). Dans certains cas ("Basin and Range" par exemple), l'extension est contrôlée par des détachements majeurs le long desquels peuvent s'enraciner des failles mineures à pendage plus fort ([Wernicke & Burchfiel, 1982](#); [Gans & Miller, 1983](#); [Brun & Choukroune, 1983](#)).

Les failles recoupant la croûte sismogénique ont généralement une longueur d'au moins 20–30 km (Figure 1.2). La longueur des failles est plus importante (60 à 130 km) quand la croûte sismogénique est plus épaisse (20 à 50 km de profondeur), comme dans le Rift Est Africain ([Jackson & White, 1989](#)), et quand l'âge thermique de la lithosphère augmente (voir Figure 1.1).

L'extension crustale est exprimée par le coefficient d'étirement β ¹ qui varie entre <1,5 (initiation du rifting et rifts avortés ; [Roberts et al., 1993](#); [Morley, 1994](#); [Banks et al., 1995](#)) et 3–3,5 (marges passives ; [Brun & Beslier, 1996](#)). En fonction de la rhéologie de la lithosphère et du taux d'extension, les rifts peuvent être étroits (50 à quelques centaines de km de large) comme dans le rift Est africain, le graben du Rhin (France) ou encore le rift du Rio Grande (Etats-Unis). Les rifts peuvent aussi se former sur des zones plus larges (>1000 km), comme dans la région du "Basin and Range" (Etats-Unis) qui est caractérisée par un ensemble de grabens et de horsts larges de 30–40 km et qui répètent périodiquement ([Brun & Choukroune, 1983](#)).

Les principaux contrôles structuraux de la sédimentation syn-rift sont (i) la longueur et la

1. $\beta = 1 + (L_f - L_0)/L_0$, avec L_0 la longueur initiale et L_f la longueur finale.

géométrie des failles normales, (ii) la distance entre les blocs de faille, (iii) les mouvements verticaux au cours des processus de propagation et l'histoire de connexion et de migration des failles normales, et (iv) la réactivation de structures pré-rift héritées plus ou moins obliques. Tous ces contrôles influent sur le développement des bassins versants et indirectement sur le flux sédimentaire. Ces différents contrôles sont détaillés ci-dessous.

1.2 Croissance d'un réseau de failles normales

1.2.1 Modèles

La croissance d'une faille normale n'implique pas seulement sa trace en surface, mais aussi sa géométrie 3D en profondeur au cours de l'accumulation du déplacement. La compréhension de la croissance des failles est basée sur les observations de terrain et les données sismiques. Les modèles analogiques et numériques permettent aussi de reproduire le développement 3D des systèmes de failles normales. Il existe deux modèles de croissance d'un réseau de failles normales : (1) le modèle de failles isolée ("isolated fault model") et (2) le modèle des failles à longueur constante ("constant length/coherent fault model").

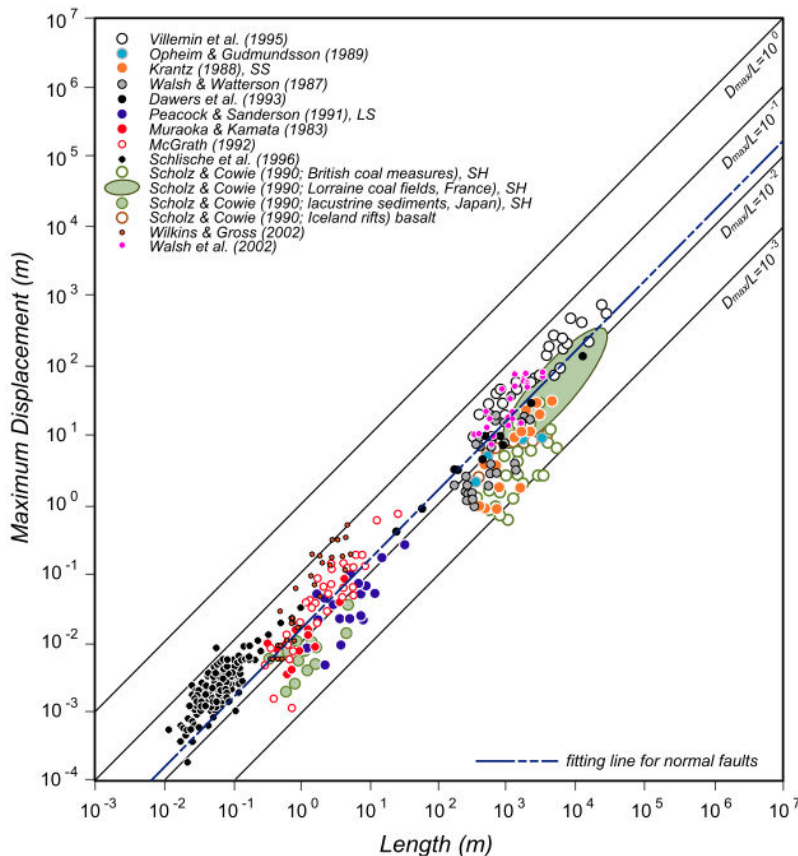


FIGURE 1.3 – Déplacement maximal en fonction de la longueur des failles (Kim & Sanderson, 2005)

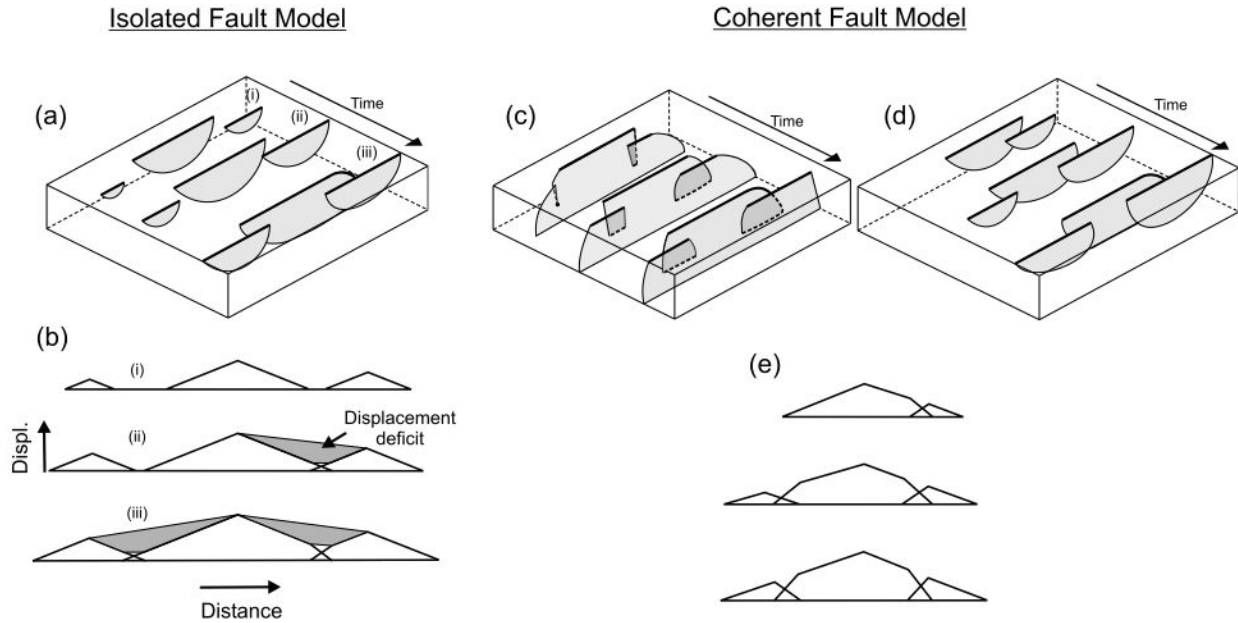


FIGURE 1.4 – Schéma simplifié illustrant le modèle de croissance des failles isolées (a-b) et le modèle de failles à longueur constante (c-e). Les blocs diagrammes (a, c, d) montrent trois stades de développement du système de failles (i, ii, iii). (i) Stade d'initiation, (ii) interaction et connexion entre les failles, (iii) formation d'une seule faille à partir de la connexion des trois segments initialement isolés. Les zones de déficit de déplacement en gris correspondent aux zones de relais. Les lignes en pointillés correspondent aux lignes de branchement des failles en profondeur. Displ., déplacement (d'après Walsh *et al.*, 2002).

(1) Dans le cas du modèle des failles isolées, la croissance d'une faille normale se fait par propagation latérale (Figure 1.4a-b ; Cowie & Scholz, 1992; Cartwright *et al.*, 1995; Huggins *et al.*, 1995; Schlische & Anders, 1996; Morley & Wonganan, 2000). Le déplacement est maximal au centre de la faille et diminue vers ses extrémités. La compilation des mesures de déplacement D et de longueur L des failles dans différents cas naturelles (Figure 1.3) ont permis d'établir la relation suivante : $D = c.L^n$, avec c une constante fonction des propriétés mécaniques de la roche et n compris entre 1 et 2 (Dawers *et al.*, 1993; Dawers & Anders, 1995; Cartwright *et al.*, 1995; Schlische & Anders, 1996; Kim & Sanderson, 2005).

Les traces de failles actives en surface sont divisées en plusieurs segments (Figure 1.4) entre lesquels se forment des zones de transfert aussi appelées "zones de relais" (Griffiths, 1980; Crossley, 1984; Morley *et al.*, 1990). Ces zones de relais forment des zones accès préférentielles pour les rivières drainant les marges en soulèvement (Cohen, 1991). L'analyse du déplacement le long des failles (ou de leur rejet vertical) permet de comprendre la formation des dépocentres au cours du temps. Les courbes de déplacement (profil convexe, Figure 1.4) peuvent être asymétriques ou symétriques, et mettent en évidence les zones de subsidence maximale. Les zones en déficit de déplacement correspondent aux zones de relais entre les segments où une partie du déplacement est accommodée par la rotation de la rampe (de relais). Même si les failles paraissent discontinues en surface, elles peuvent être connectés en profondeur et se comportent comme une seule faille

dont le profil de déplacement est semblable à celui d'une faille isolée (Figure 1.4a-b).

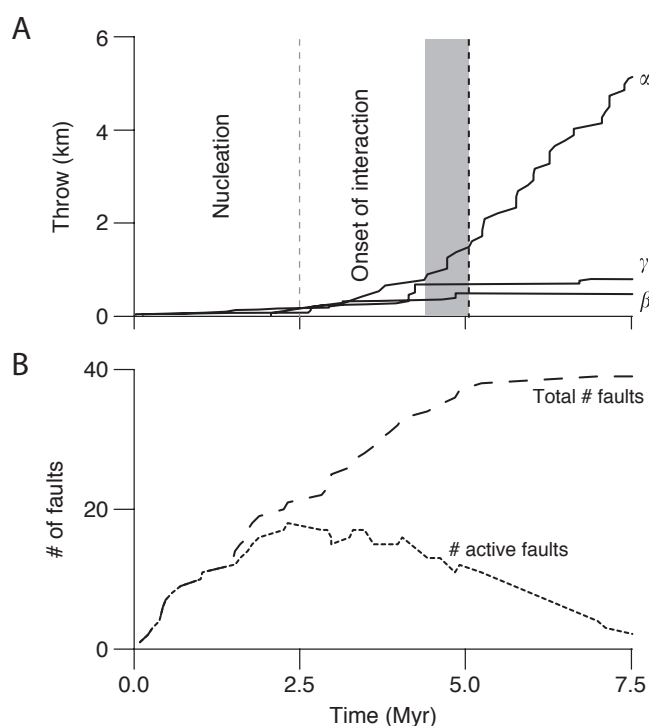


FIGURE 1.5 – Résultat de simulations numériques montrant le rejet vertical des failles α , β et γ (A) et le nombre de failles actives (B) au cours de l'évolution d'un réseau de failles. La bande grise correspond à la période pendant laquelle un réseau de failles connectées se forme. Alors que la faille α est toujours active après 5 Ma, les failles β et γ deviennent inactives (d'après Cowie *et al.*, 2006).

(2) Le modèle alternatif de la croissance des failles normales est caractérisé par l'établissement rapide de la longueur des failles (en quelques centaines de milliers d'années). La longueur des failles reste constante au cours de l'accumulation du déplacement (Figure 1.4c-e; Walsh & Watterson, 1991; Childs *et al.*, 1995; Walsh *et al.*, 2002; Giba *et al.*, 2012), et contrairement au modèle classique ("isolated fault growth model"), le déplacement ne s'accumule pas par propagation radiale (Figure 1.4c-e). Même si les segments de failles à longueur constante peuvent paraître isolés en surface, ils peuvent être connectés en profondeur ("soft linkage"). Ce mode de croissance a été initialement documenté en lien avec la réactivation de structures fortement obliques, sub-perpendiculaire à la direction d'extension (Figure 1.8). Cependant, il est de plus en plus utilisé comme un modèle alternatif de croissance des failles normales, même en l'absence de structures réactivées (Morley, 2002; Walsh *et al.*, 2003; Schlagenhauf *et al.*, 2008).

Ces différents modes de croissance des failles normales sont particulièrement discriminants dans les processus de propagation et de connexion, et ils génèrent des géométries différentes dans les dépocentres. Tous deux sont considérés au cours du développement d'une zone de relais qui fait l'objet du chapitre 5).

Les processus de propagation et de connexion entre les failles sont rapides à l'échelle géologique et se produisent en moins de 10^6 ans (Cowie *et al.*, 2007). Ils se produisent durant les différents stades de développement des rifts mais sont surtout caractéristiques de la phase précoce de rifting; période durant laquelle les failles normales nucléent et délimitent des dépocentres isolés (Gupta *et al.*, 1998; Cowie *et al.*, 2000, 2006). Les failles croissent et interagissent entre elles

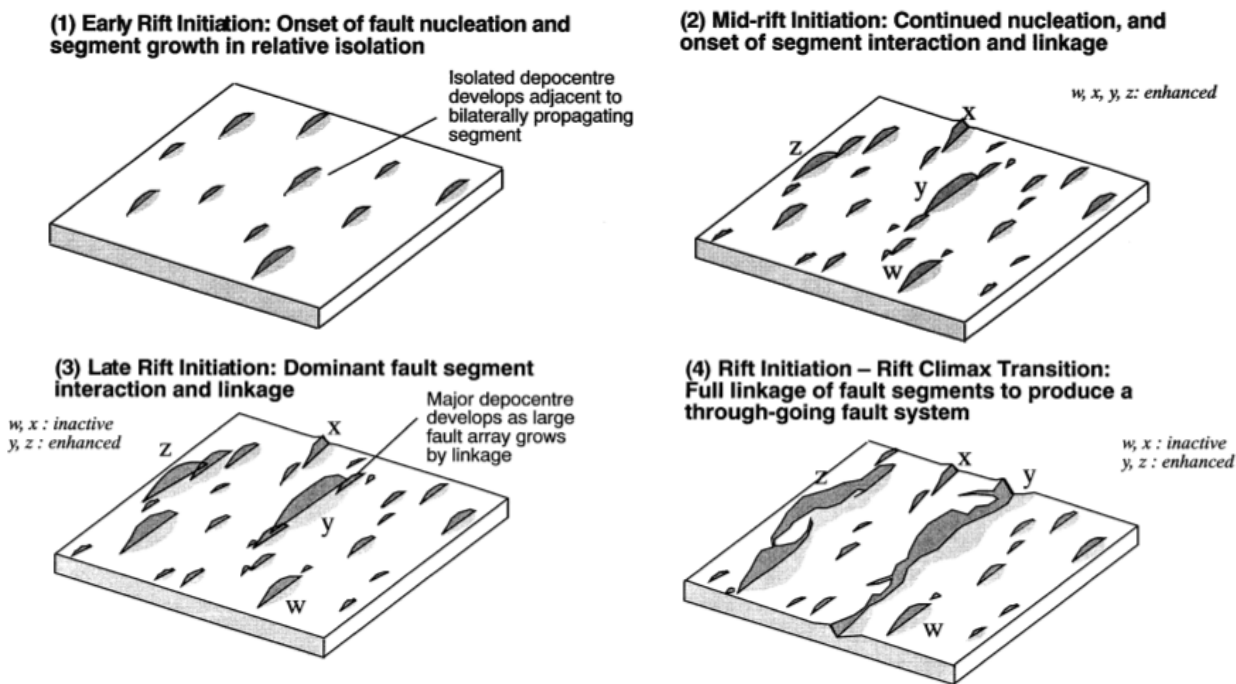


FIGURE 1.6 – Modèle d'évolution d'un réseau failles normales en surface issu des résultats de simulations numériques (d'après Cowie, 1998).

pour former un réseau connecté de failles. En supposant une croûte supérieure initiale homogène, les modèles numériques de Cowie *et al.* (1993, 1995, 2000) décrivent une nucléation aléatoire des failles normales (Figure 1.6). La zone en extension s'étend sur une large zone comprenant de nombreuses failles actives à faible déplacement (Figure 1.5). Ensuite, l'interaction et la connexion de certaines failles permet ensuite de focaliser la déformation sur un nombre restreint de failles. La plupart des failles précoces deviennent inactives au profit des failles majeures qui accommodent ainsi une plus grande part de l'extension (Figures 1.5 et 1.6). L'ensemble de ces études et modèles suggèrent que cette phase d'initiation peut durer plusieurs millions d'années (5 Ma sur la Figure 1.6), et cette durée est largement supérieure aux processus de connexion des failles ($<10^6$ ans). Les mécanismes contrôlant la durée de la phase d'initiation et l'établissement d'un réseau connecté de failles restent peu documentés. La durée de la phase d'initiation est-elle dépendante des dimensions de la zone en extension, de la distribution des contraintes, du taux d'extension ?

1.2.2 Réactivation des structures héritées

Les structures héritées (failles, contrastes lithologiques et rhéologiques dans la croûte supérieure) correspondent à des zones de faiblesse ou de résistance et jouent un rôle important dans la localisation et la géométrie des failles. En théorie, l'extension par cisaillement pur génère une population de failles perpendiculaires à la direction d'extension (Figure 1.7A). L'obliquité d'un

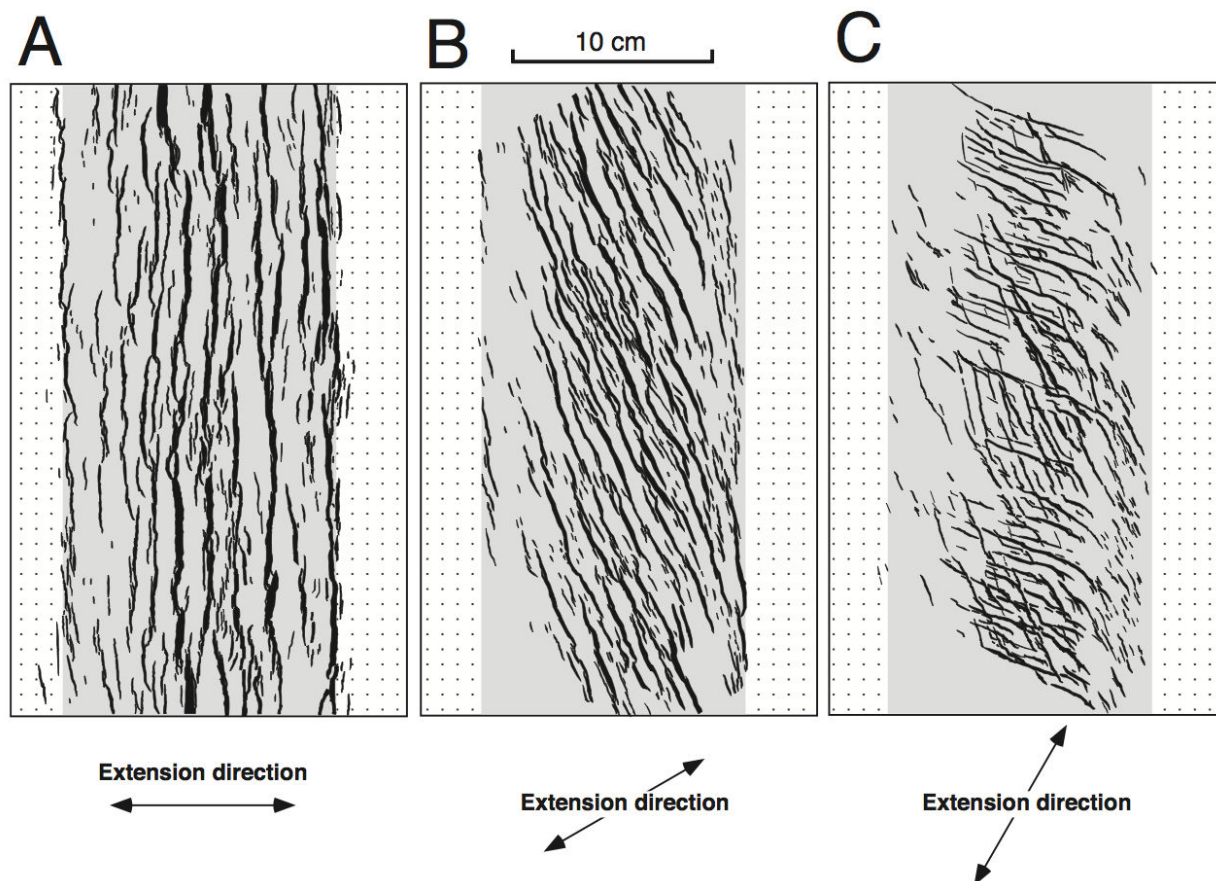


FIGURE 1.7 – Résultats des modèles analogiques (argiles) reproduisant la direction des structures rifts en lien avec l’obliquité des structures héritées. (A) : Direction d’extension perpendiculaire à l’axe du rift. (B) et (C) : Direction d’extension oblique par rapport à l’axe du rift ($\alpha = 60$ et 30°) (d’après Clifton *et al.*, 2000).

rift est définie par l’angle α , entre la direction d’extension et l’axe du rift (Withjack & Jamison, 1986). Les valeurs de α (entre 0 et 90°) sont faibles dans le cas d’une forte obliquité du rift (Figure 1.7). La réactivation des structures héritées peut générer des failles obliques par rapport à la direction d’extension (Clifton *et al.*, 2000), et ainsi peut être à l’origine de la formation des systèmes de failles en échelon (Figure 1.8). L’obliquité des structures par rapport à la direction d’extension peut favoriser la formation des zones de relais (Morley, 1999), mais dans de nombreux contextes extensifs, ces dernières peuvent se développer sans la présence de structures héritées (Schlische & Withjack, 2009; Fossen & Rotevatn, 2016). La réactivation des structures héritées joue un rôle majeur non seulement dans la géométrie 3D du système de failles, mais aussi sur le mode de propagation des failles normales. En effet, la réactivation des structures peut faciliter la nucléation des failles et leurs connexions en profondeur (croissance des failles à longueur constante).

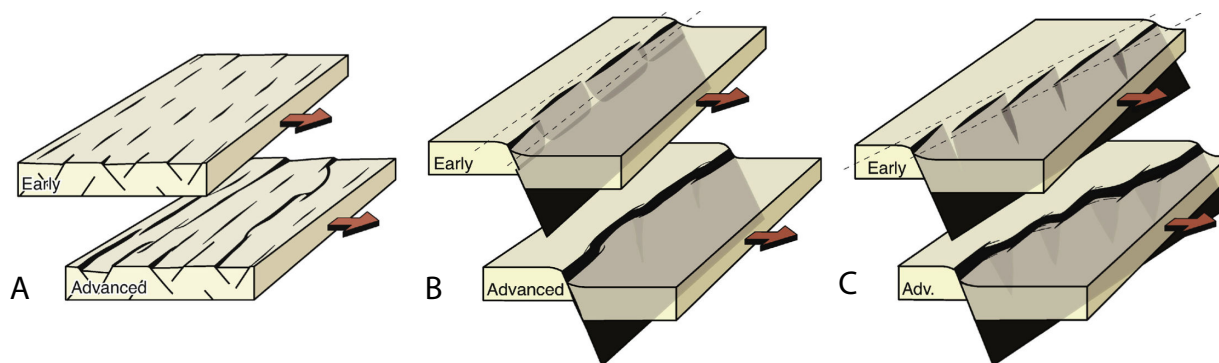


FIGURE 1.8 – **A** : Nucléation aléatoire et croissance d’un réseau de failles dont la direction est perpendiculaire à la direction d’extension. **B** et **C** : Initiation et croissance d’un réseau de failles normales contrôlé par la présence d’une structures héritée parallèle (**B**) ou oblique (**C**) à la direction d’extension (d’après [Fossen & Rotevatn, 2016](#)).

1.2.3 Migration

La migration de l’activité des failles correspond au déplacement du champ de contraintes au cours du développement du rift. Une faille est abandonnée quand la force requise pour la maintenir active est insuffisante. La migration des failles permet la localisation de la déformation et se produit généralement en direction de l’axe du rift, formant ainsi un rift de plus en plus étroit. La migration des failles peut être contrôlée par plusieurs mécanismes décrits ci-dessous.

Le **mécanisme 1** de la migration des failles est l’accélération du taux d’extension en lien avec la connexion des failles et la formation de failles majeures ([Schlische & Anders, 1996](#); [Cowie, 1998](#); [Gupta *et al.*, 1998](#); [Morley & Wonganan, 2000](#); [Cowie *et al.*, 2000](#)). Ce mécanisme de migration des failles a notamment été mise en évidence le long de la marge sud du rift de Corinthe ([Goldsworthy & Jackson, 2001](#)), dans la partie est du rift de Suez ([Gawthorpe *et al.*, 2003](#)) ou en Mer du Nord ([Cowie *et al.*, 2005](#)). Des observations similaires sont documentées le long de la marge ibérique ([Ranero & Pérez-Gussinyé, 2010](#)) et namibienne ([Mohammed *et al.*, 2016](#)). La migration des failles induit la migration des dépocentres syn-rift et la présence de discordances angulaires entre les blocs de failles (Figure 2.9). Ces relations géométriques caractéristiques peuvent être observées dans les blocs basculés (sur le terrain ou sur les profils sismiques) et permettent d’interpréter la chronologie relative ou absolue des failles ([Ter Voorde & Cloetingh, 1996](#)).

La migration des failles peut aussi être contrôlée par des mécanismes externes au système de failles, à l’échelle lithosphérique (**mécanisme 2**). Les modèles numériques de [Behn *et al.* \(2002\)](#); [Huisman \(2003\)](#); [Huisman & Beaumont \(2007\)](#) proposent que la migration des failles est causée par une augmentation du gradient thermique en lien avec l’amincissement de la lithosphère et/ou à la relaxation des contraintes ("frictional-plastic strain softening") en lien avec des zones de faiblesses héritées. En plus de ces processus, les modèles thermo-mécaniques de [Brune *et al.* \(2014\)](#) montrent que cette migration peut être accentuée par le fluage de la croûte inférieure.

A une plus petite échelle, la migration des failles peut être aussi expliquée par la perturba-

tion locale du champ de contraintes en lien avec la charge sédimentaire (**mécanisme 3**). [Bialas & Buck \(2009\)](#) reproduisent la migration des failles vers l'axe du rift en prenant en compte la charge sédimentaire. L'érosion des marges en soulèvement et le flux sédimentaire permettent ainsi de transférer les contraintes vers le centre du bassin. Les modèles numériques de [Olive *et al.* \(2014\)](#) s'intéressent au déplacement et à la durée d'activité des failles en intégrant le bilan de matériel érodé et déposé. Ces travaux montrent que le transfert de masse vers les dépocentres accélère le glissement sur les failles (dans le cas d'une croûte supérieure d'environ 15 km). De plus, le déplacement total et la durée d'activité des failles diminuent avec l'épaisseur de la croûte supérieure et il est plus facile de générer de nouvelles failles en présence d'une croûte supérieure épaisse (>15 km). La rétroaction entre la sédimentation syn-rift et la déformation à long terme est mal connue et reste à explorer pour mieux comprendre les causes de la migration des failles ainsi que les autres processus associé au rifting.

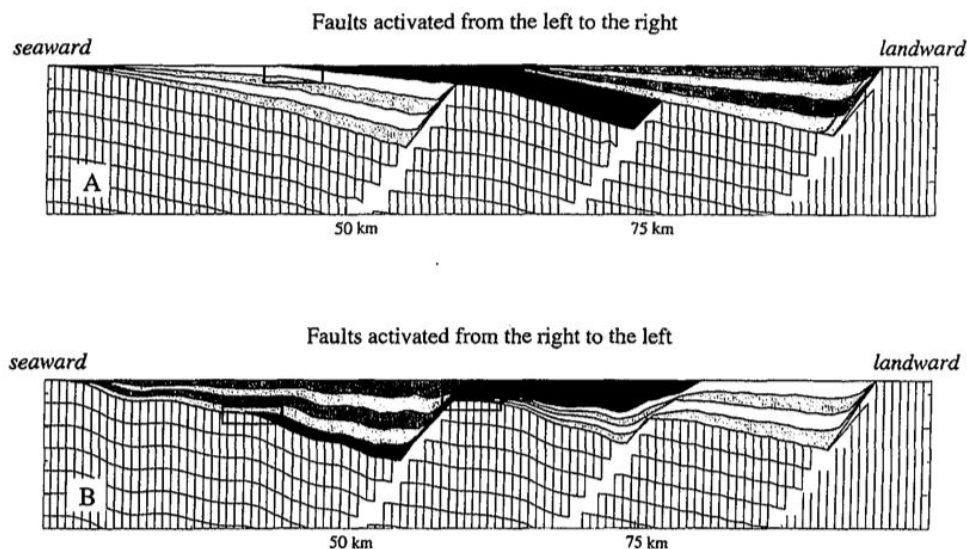


FIGURE 1.9 – Résultat de simulations numériques de l'étirement crustal à partir de trois failles normales activés simultanément de gauche à droite (**A**) et de droite à gauche (**B**). La migration de l'activité tectonique vers les toits (axe du rift) (**A**) et vers les murs de failles normales (**B**) génère des relations stratigraphiques différentes entre les blocs de failles normales (d'après [Ter Voorde & Cloetingh, 1996](#)).

1.3 Soulèvement, flux sédimentaire et sédimentation alluviale

1.3.1 Développement des bassins versants

L'activité des failles et le développement des bassins versants modulent la morphologie des marges de rift ([Tucker & Slingerland, 1994](#); [Kooi & Beaumont, 1994](#); [Densmore *et al.*, 1998](#); [Ellis *et al.*, 1999](#)). Dans les rifts actifs, le développement des bassins versants conséquents et an-

técédents dans les zones en soulèvement sont à l'origine du flux sédimentaire dans le bassin. On s'intéresse ici principalement au développement des bassins versants consécutifs en lien avec le soulèvement dans les murs de failles normales. La composante de soulèvement (0,1 à 1 mm/an) intègre le soulèvement local associé à l'activité des failles ("footwall uplift" ; Figure 1.10) généralement plus élevé que le soulèvement régional (compensation isostatique et flexure à l'échelle lithosphérique). Ces deux "types" de soulèvement ne sont pas séparés pour étudier la morphologie des bassins versants dans les murs de failles normales en réponse à l'activité tectonique.

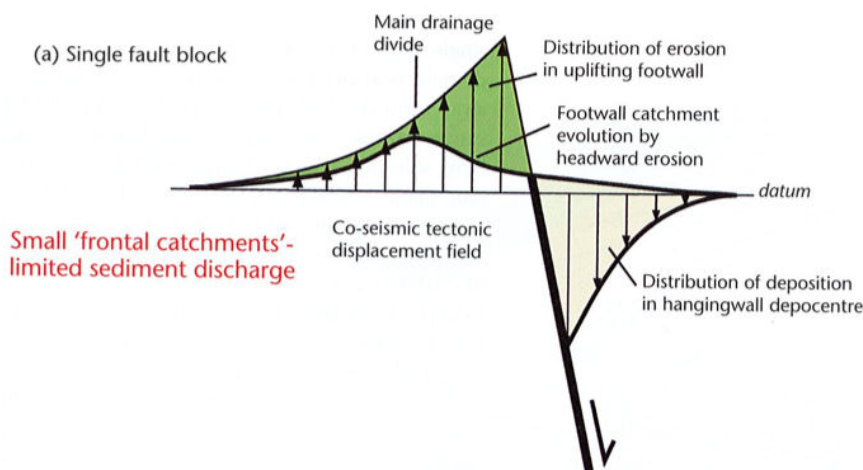


FIGURE 1.10 – Flexure et déplacement associés à l'activité d'une faille normale (coupe transverse) montrant la distribution du soulèvement dans le mur et de la subsidence dans le toit (d'après Allen & Allen, 2013).

La création de topographie (Figure 1.10) dépend principalement de la quantité de déplacement sur la faille, de son pendage et de l'espacement entre les failles (Densmore *et al.*, 2005). Le flux sédimentaire issu des rivières consécutives et transverses contrôle la construction des cônes alluviaux au pied des failles actives (Leeder *et al.*, 1991; Leeder, 1993; Whipple & Trayler, 1996; Allen, 1998). Une des caractéristiques majeures des bassins versants dans les murs de failles est l'espacement régulier des rivières (Talling *et al.*, 1997; Hovius, 1996; Castelltort & Simpson, 2006) suivant la loi de Hack² (Hack, 1957) (Figure 1.11). La longueur des bassins versants est limitée par la surrection des murs de failles et les paramètres la contrôlant (voir ci-dessus). L'aire des bassins versants augmente vers le centre des failles où le déplacement est maximal (Figure 1.11). Dans les murs de failles actives, les bassins versants sont relativement courts (~10 km de long) et sont caractérisés par un fort gradient de pente. Les travaux de (Duffy *et al.*, 2015) montrent que la faible distance entre les blocs (<10 km) joue un rôle important dans la taille des bassins versants et favorise la formation de bassins versants courts et fortement pentés. Les zones de relais entre les segments de failles sont souvent caractérisées par le développement de bassins versants plus étendus (Densmore *et al.*, 2003) et forment un accès principal pour le transport de sédiments.

De nombreux systèmes actifs de failles ont permis d'étudier la morphologie des bassins

2. La longueur des rivières (L) augmente en fonction de l'aire des bassins versants (A) en suivant la relation exponentielle : $L = c.A^b$, avec b et c des constantes dépendant des paramètres liés au développement des bassins versants (climat, lithologie, érosion, flux sédimentaire, etc.)

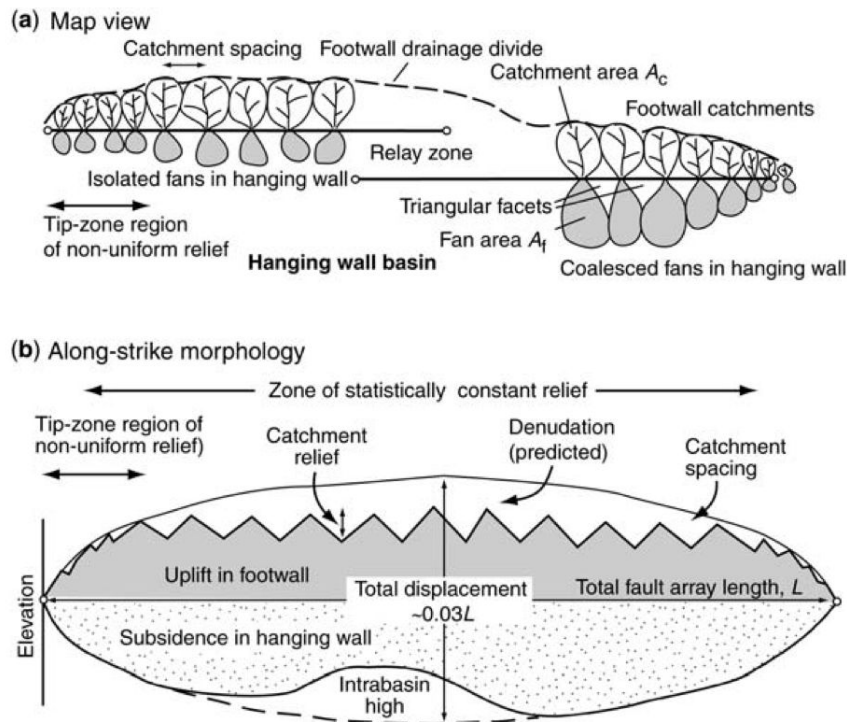


FIGURE 1.11 – (a) Système de drainage transverse et cônes alluviaux au pied de deux segments de failles normales. (b) Schéma simplifié de la topographie se développant le long de ces mêmes segments de failles. Le déficit de déplacement au niveau de la zone de relais génère un haut morphologique ("intrabasin high") dans le bassin (d'après Allen, 2008).

versants dans les murs de failles normales. On peut notamment citer les travaux de Cowie *et al.* (2006); Whittaker *et al.* (2010) dans le massif des Apennins ou encore ceux de Allen & Densmore (2000) dans la "Vallée de la mort" (sud-ouest des Etats-Unis). Ces travaux ont permis d'élaborer des modèles numériques de l'évolution des paysages en bordure de rifts actifs, à partir des calculs de bilans de matériel exportés depuis les bassins versants jusqu'au bassin sédimentaire. On peut notamment citer le modèle Zcape développé par Densmore *et al.* (1998) ou encore CASCADE initialement développé par Braun & Sambridge (1997). Ces modèles tentent de reproduire réalistement les soulèvements des murs de failles et de quantifier le flux sédimentaire (Q_s ; Figure 1.12), au cours du développement des bassins versants et en réponse aux forçages tectoniques et climatiques (Cowie *et al.*, 2006; Allen *et al.*, 2013).

1.3.2 Paramètres de contrôle de la sédimentation alluviale

Une coupe transverse d'un bassin alluvial est schématiquement représentée par un éventail syn-sédimentaire (Blair & Bilodeau, 1988). Sur le plan sédimentologique, les bassins alluviaux dans les zones tectoniquement actives sont généralement caractérisés par (i) le développement des cônes alluviaux en partie proximale, (ii) le système fluvial en tresse ou plus sinueux (sys-

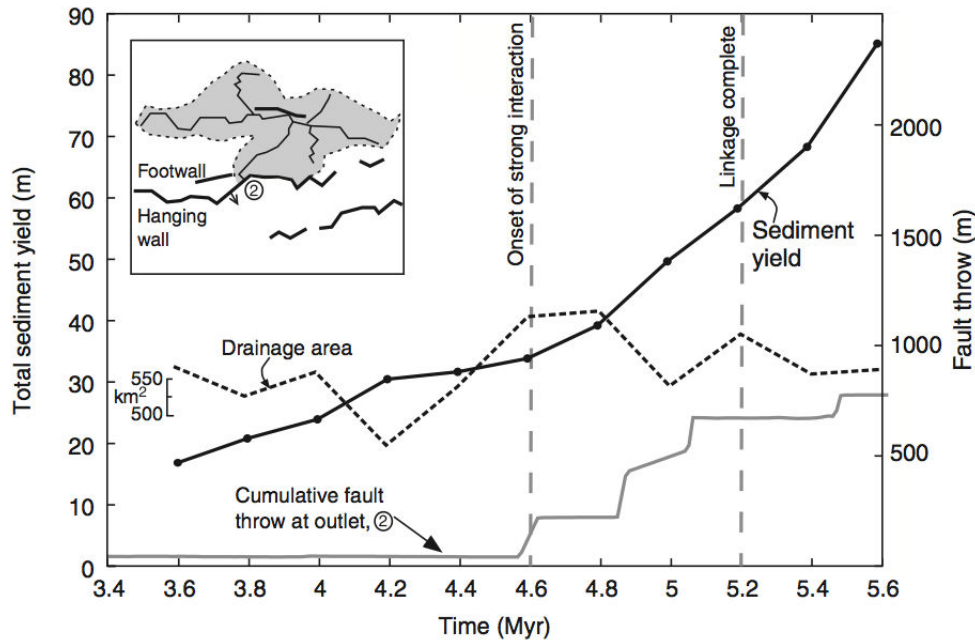


FIGURE 1.12 – Résultats du modèle tectonique couplée au modèle d'évolution des reliefs CASCADE montrant l'évolution du taux de productivité du bassin versant (volume de sédiments/aire du bassin versant), du flux sédimentaire (Q_s) et du rejet vertical des failles en fonction du temps (d'après Cowie *et al.*, 2006).

tèmes transverse ou axial) en partie médiane, et (iii) le transport des sédiments jusqu'aux marges d'un bassin (lacustre ou marin) via un système deltaïque ou estuarien. La distribution des sédiments dans le bassin alluvial dépend à la fois des mécanismes internes de transport et de dépôt, ainsi que des forçages externes que sont la tectonique et le climat (Figure 1.13). Ces paramètres de contrôle sont variables au cours du temps et affectent individuellement le système de dépôt à différentes échelles de temps et d'espace. Prendre en compte l'ensemble des paramètres de contrôles permet de déterminer les conditions limites à l'origine des changements majeurs de l'architecture stratigraphique (Allen & Densmore, 2000; Densmore *et al.*, 2007; Armitage *et al.*, 2011; Allen *et al.*, 2013; Ballato & Strecker, 2014).

Dans les rifts, l'évolution du remplissage sédimentaire est expliquée qualitativement par le rapport entre le taux d'accommodation (A) et le flux sédimentaire (S). L'accommodation est définie comme l'espace disponible pour l'accumulation des sédiments (Jervey, 1988). Plus récemment, Mutto & Steel (2000) définissent l'accommodation comme étant l'espace rempli par des sédiments pendant un intervalle de temps considéré. Les différents cas $A > S$, $A < S$ et $A = S$ permettent d'expliquer les architectures stratigraphiques observées et notamment les conditions de remplissage dans le bassin : sous-alimenté ("underfilled/starved"), suralimenté ("overfilled"), équilibré ("balanced") (Carroll & Bohacs, 1999; Bohacs *et al.*, 2000).

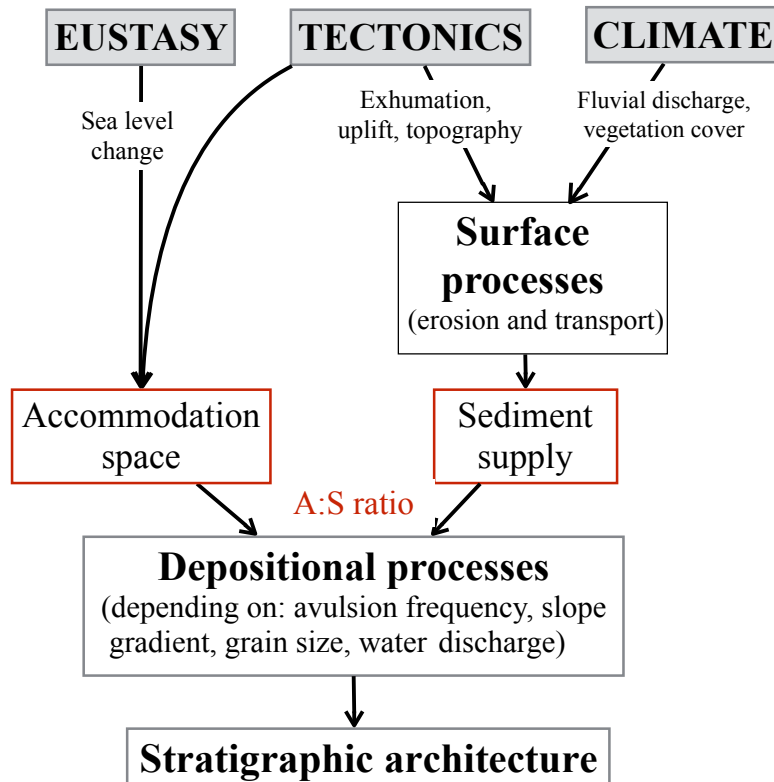


FIGURE 1.13 – Principaux paramètres de contrôle de l’architecture stratigraphique des systèmes alluviaux et fluviaux. Les forçages externes (allogéniques) que sont la tectonique, le climat et l’eustatisme contrôlent l’accommodation disponible (A) et le flux sédimentaire (S)

Le temps de réponse aux forçages externes est influencé par la granulométrie, la longueur du système fluvial, la largeur des plaines d’inondation ou encore la proximité de la source des sédiments (Allen, 2008). Le temps de résidence des sédiments fins des plaines d’inondation est plus long que les sédiments grossiers transportés potentiellement dans les chenaux. (Paola, 2000) suggère que le stockage des sédiments dans la plaine d’inondation tamponne les variations du niveau de base et du flux sédimentaire. Les modèles de la sédimentation alluviale applicables aux contextes extensif ou compressif (Paola *et al.*, 1992; Allen & Densmore, 2000; Densmore *et al.*, 2007; Allen, 2008; Allen & Heller, 2012) estiment le temps de réponse entre les processus d’érosion et de dépôt suite aux perturbations tectoniques et climatiques. Ce temps de réponse est généralement compris entre 10^5 et 10^6 ans (Paola *et al.*, 1992; Whipple & Meade, 2006).

L’apport de matériel grossier dans le bassin est classiquement interprété par l’augmentation du flux sédimentaire en lien avec une accélération de l’activité tectonique (Burbank *et al.*, 1988; Newell *et al.*, 1999; Fang *et al.*, 2005), des changements climatiques majeurs (Zheng *et al.*, 2000; Peizhen *et al.*, 2001), ou l’expansion des bassins versants (Whittaker *et al.*, 2010). Par exemple, une augmentation de taux de soulèvement conduit à un apport de matériel grossier en générant des géométries progradantes. Au contraire, une baisse du taux de soulèvement peut conduire à un

granoclasement positif dans la succession alluviale, voire même une augmentation de l'espace disponible (rétrogradation) si $A > S$ (Densmore *et al.*, 2007). Bien que la tectonique représente un contrôle prépondérant, les variations climatiques peuvent aussi affecter le flux sédimentaire et perturber l'enregistrement stratigraphique (Figure 1.14). En effet, la température, les précipitations, la saisonnalité et la végétation contrôlent les processus d'altération, le flux sédimentaire et les environnements de dépôt. L'augmentation des précipitations annuelles peut notamment conduire à la progradation des faciès grossiers (Armitage *et al.*, 2011, 2013). Le type de lithologie soumis à érosion influe aussi sur la taille des bassins versants et le remplissage sédimentaire (Gupta *et al.*, 1999; Densmore *et al.*, 2003).

Les modèles expérimentaux des cônes alluviaux de Rohais *et al.* (2012) montrent que les variations du taux de précipitation ou de soulèvement des bassins versants peuvent produire les mêmes effets sur la pente et les géométries sédimentaires ("onlap" et "downlap"). La réduction de la pente du cône (induite par l'augmentation des précipitations) favorise les géométries d'"onlap" lors de la rétrogradation des dépôts. Au contraire, une augmentation de la pente (induite par la diminution des précipitations et l'augmentation du taux de soulèvement) génère des géométries de "downlap" au cours de la progradation du cône.

Le transport des sédiments produit une diminution de la granulométrie des sédiments qui deviennent de plus en plus fins vers l'aval ("downstream fining"). Cette granodécroissance au cours du transport des sédiments est contrôlée par le transport et la sédimentation différentielle de la charge de fond ("bedload"), ainsi que l'abrasion des particules (Parker, 1991; Hoey & Bluck, 1999; Attal & Lavé, 2009). Ce granoclasement induit le stockage des faciès grossiers au pied des reliefs et l'évacuation des faciès fins vers l'aval. La quantification de ce granoclasement et les modèles d'écoulement dans les systèmes de rivières actuels a permis d'établir des modèles quantitatifs de la sédimentation alluviale. Ces derniers documentent notamment la transition entre les faciès conglomératiques et sableux ("gravel front") (Paola *et al.*, 1992; Paola, 2000; Marr *et al.*, 2000; Fedele & Paola, 2007; Duller *et al.*, 2010; Whittaker *et al.*, 2011). La position du front conglomératique au niveau des piémonts et la terminaison du front sableux en partie plus distale dépendent (i) de la pente, (ii) du flux sédimentaire, (iii) de la subsidence et (iv) des variations du niveau de base (Heller *et al.*, 1988; Paola *et al.*, 1992). Les travaux de Strong *et al.* (2005), Fedele & Paola (2007), Paola & Martin (2012) établissent des équations d'extraction de masse sédimentaire afin de supprimer les effets des variations granulométriques vers l'aval ("downstream mass extraction") et de faire ressortir les perturbations stratigraphiques générées par les forçages externes.

Cependant, les modèles quantitatifs de la stratigraphie alluviale considèrent une entrée fixe des sédiments au cours du remplissage du bassin. A partir des quantifications des variations granulométriques et la distribution du diamètre moyen D_{50} en front de chaîne, les travaux de Dubille & Lavé (2015) expliquent les transitions abruptes des faciès conglomératiques (exemple des Siwaliks, Himalaya) par la migration des chevauchements actifs, sans nécessairement modifier

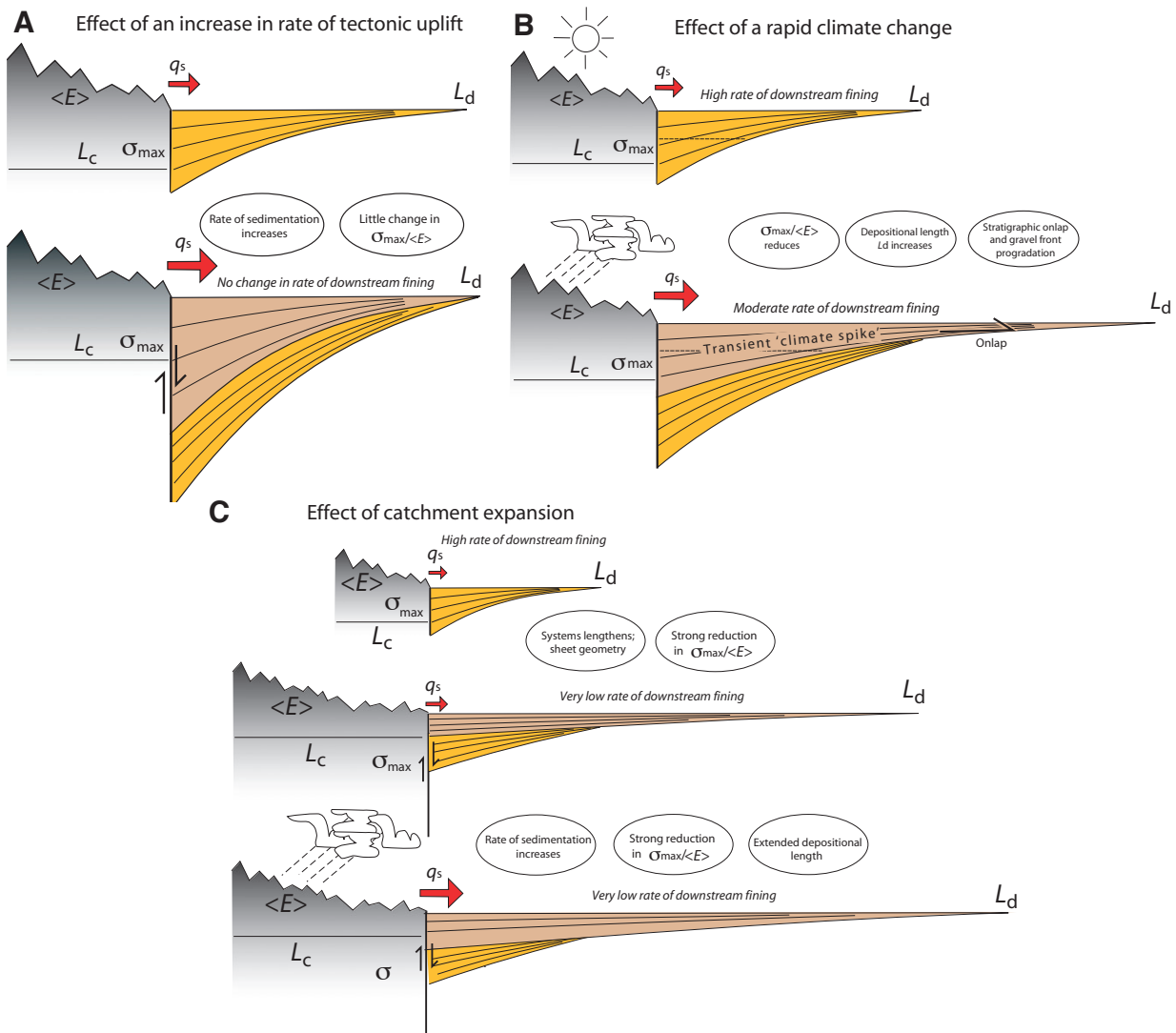


FIGURE 1.14 – Représentation schématique du flux sédimentaire depuis les zones en soulèvement et du remplissage syn-rift dans le bassin pour trois cas différents. **A** : Effet de l'augmentation rapide de la surrection. **B** : Effet du changement climatique rapide. **C** : Effet de l'augmentation de l'aire du bassin versant. $\sigma_{max} / \langle E \rangle$ correspond au rapport entre le taux de subsidence maximale et le taux d'érosion. La diminution de ce rapport engendre des géométries en "onlaps" dans la partie distale et une migration du front conglomératique vers le bassin. Q_s , sediment discharge ; L_c , catchment length ; L_d , depositional length (d'après Allen *et al.*, 2013).

les forçages externes. Cela montre l'importance du forçage tectonique et la proximité de la source de sédiments dans l'architecture stratigraphique.

1.4 Systèmes fluviaux dans les rifts continentaux

Le **système alluvial** est défini par l'ensemble des écoulements des cours d'eau pérennes et éphémères en milieu continental. La sédimentation alluviale regroupe les dépôts clastiques depuis les conglomérats grossiers jusqu'aux argiles. Le **système fluvial** correspond à l'ensemble des rivières (lit majeurs) qui évoluent au sein d'une plaine d'inondation (zone inondable, lit mineur). On ne travaille pas à l'échelle du chenal, mais à l'échelle de l'ensemble des chenaux drainant un bassin versant ou une plaine alluviale. La notion de "système" est ici rattachée à un certain degré de complexité interne des processus de transport et de dépôt par les rivières.

1.4.1 Rivières transverses et axiales

Les cônes alluviaux au pied des failles actives ne sont pas nécessairement alimentés par des rivières transverses pérennes. L'instabilité des pentes dans le mur des failles est notamment à l'origine de nombreux glissements de terrain et permet l'accumulation de dépôts gravitaires (Yarnold & Lombard, 1989; Bentham *et al.*, 1991). En milieu proximal du cône, les dépôts fluviaux grossiers alternent avec les dépôts gravitaires (de type "debris flow" ; Blair & McPherson, 1994).

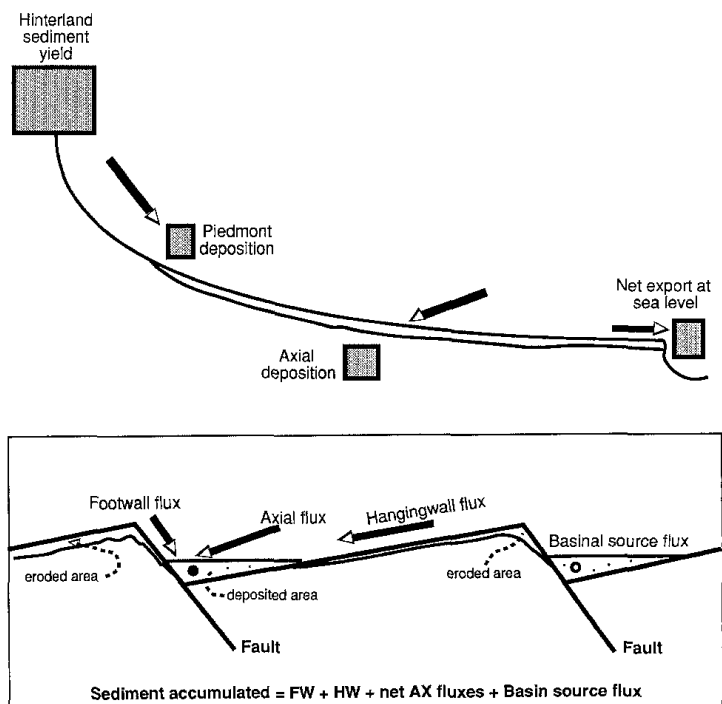


FIGURE 1.15 – Flux sédimentaire et préservation des dépôts dans les bassins. Les aires des rectangles représentent les volumes de sédiments distribués depuis la source jusqu'aux différents dépocentres. FW : "foot-wall" ; HW : "hangingwall" ; AX : "axial" (d'après Leeder *et al.*, 1991).

Les rivières distributaires divergent de l'apex et restent séparés du cours d'eau principal

(Weissmann *et al.*, 2010; Hartley *et al.*, 2010a,b; Nichols & Fisher, 2007; Fisher *et al.*, 2008; Cain & Mountney, 2009). Les rivières distributaires transverses se développent dans la partie distale du cône, formant ainsi un "megafan" dont les cours se terminent au niveau des rivières axiales, parallèles aux failles actives (Figure 1.15 et 1.16). En réponse à l'activité des failles, le flux sédimentaire peut provenir non seulement des murs de failles mais aussi des toits de failles ("nez de bloc") où les bassins versants sont plus étendus et se développent sur des pentes plus faibles (Figure 1.15).

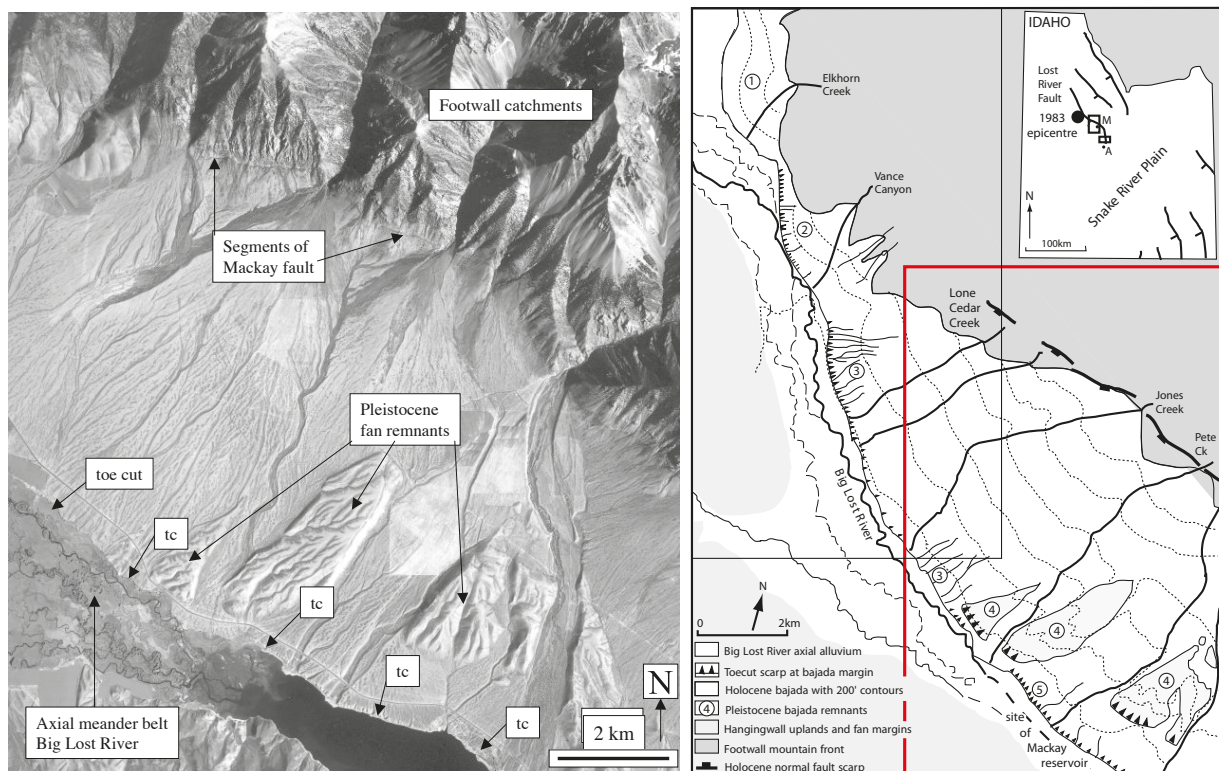


FIGURE 1.16 – Vue aérienne d'un système axial de rivières ("Big Lost River", Idaho, Etats-Unis) recoupant les rivières distributaires des cônes alluviaux transverse aux failles normales actives (d'après Leeder & Mack, 2001).

L'ensemble des systèmes de rivières transverse peut interagir avec un système de drainage axial à l'intérieur d'un même bloc ou demi-graben (Figures 1.15 et 1.16). Les rivières axiales en tresses ou méandrique peuvent se développer sur plusieurs kilomètres, voire plusieurs dizaines de kilomètres de large. Elles prennent leurs sources à l'extérieur du bassin et peuvent être antécédentes au rifting (Cohen, 1991; Tiercelin *et al.*, 1992). Le système fluvial axial peut alimenter un bassin lacustre/marin où la création d'accommodation est plus importante au centre du rift ("longitudinal supply axial drainage"; Figures 1.17 et 1.18). De nombreux analogues actuels sont documentés dans les lacs du rift est africain tels que le lac Turkana (Figure 1.17), le lac

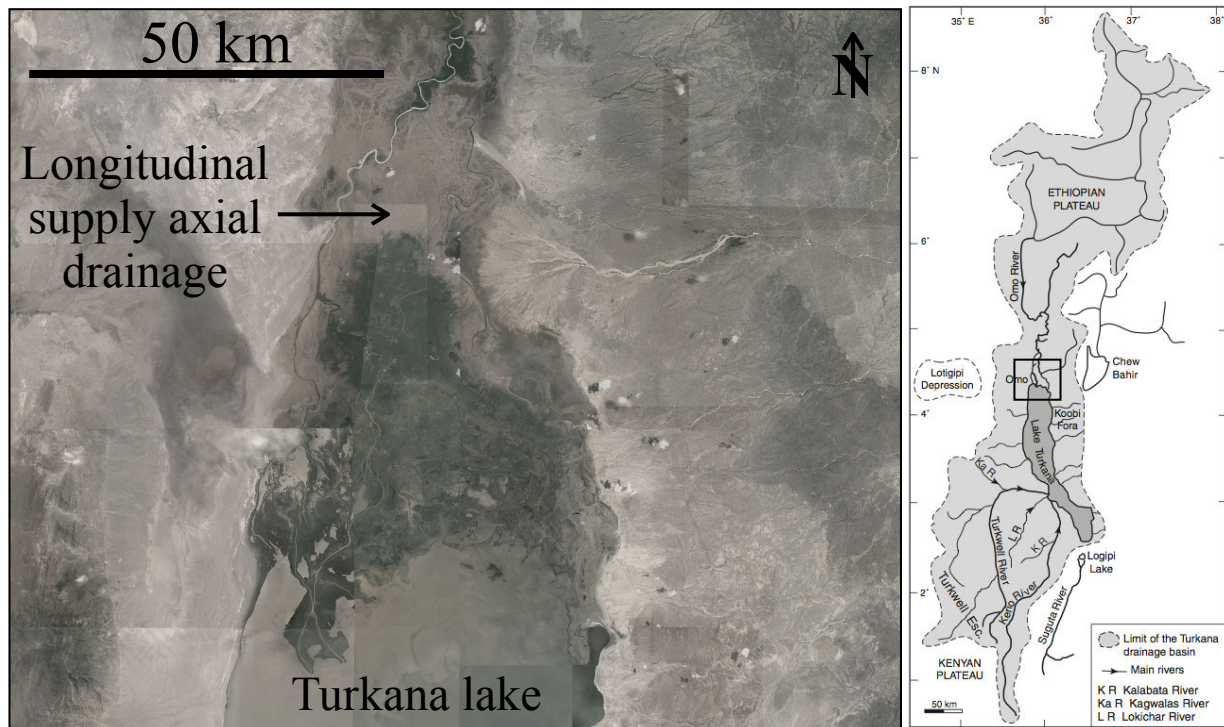


FIGURE 1.17 – Vue aérienne (Google Earth) de l'extrémité nord du lac Turkana (Kenya) alimenté par un système fluvial axial (carte extraite de [Vétel et al., 2005](#)).

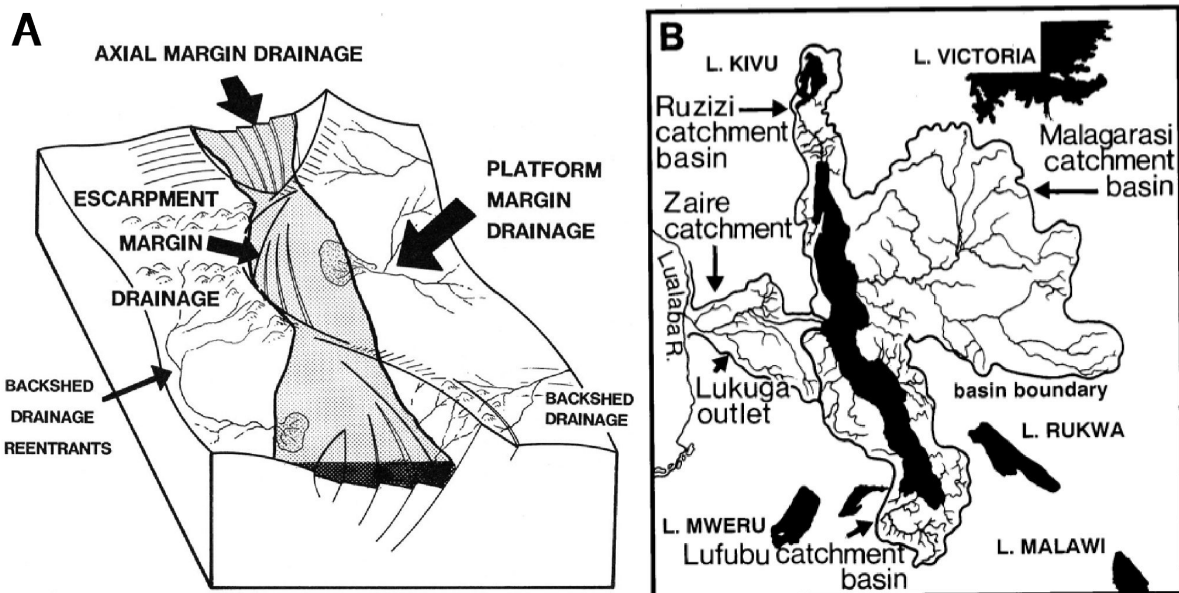


FIGURE 1.18 – (A) Bloc diagramme illustrant les systèmes de rivières transverse ("platform margin drainage") et axiales ("axial margin drainage") dans les différents demi-grabens du lac Tanganyika. (B) Réseau hydrographique du lac Tanganyika montrant les principales sources de sédiments entrants dans le bassin (d'après [Tiercelin et al., 1992](#); [Cohen, 1991](#)).

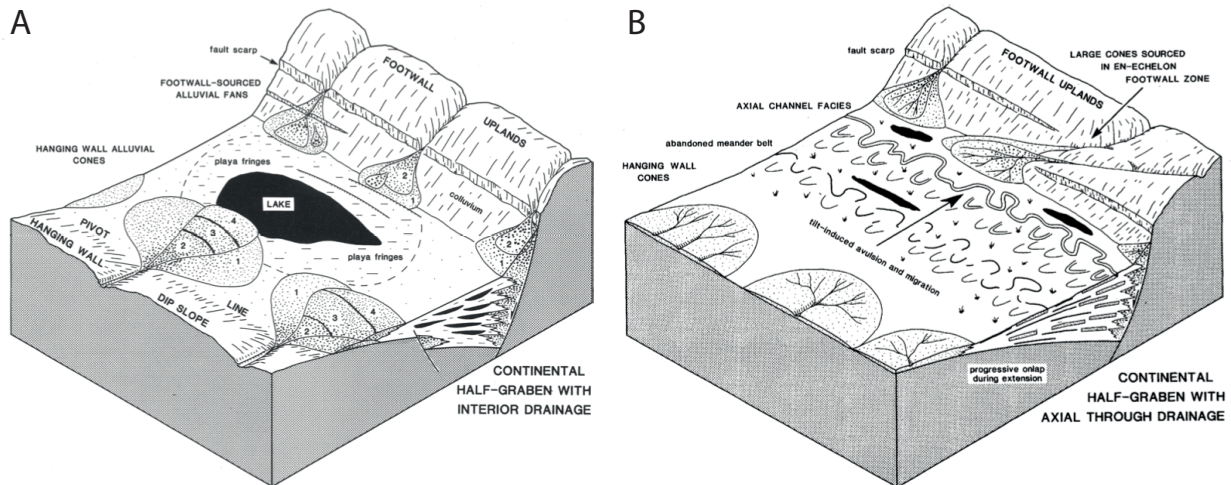


FIGURE 1.19 – Modèle conceptuel de demi-graben illustrant (A) un système de drainage interne, transverse et (B) un système de drainage axial/longitudinal (d'après Leeder & Gawthorpe, 1987).

Tanganyika (Figure 1.18), ou encore le lac Baïkal en Russie.

Les interactions entre rivières axiales et transverses ont notamment été étudiées dans le rift du Rio Grande (Nouveau Mexique ; Leeder *et al.*, 1996), dans le bassin "Big Lost River" (Idaho) (Leeder *et al.*, 1996; Mack & Leeder, 1999; Peakall *et al.*, 2000; Leeder & Mack, 2001), ou encore grâce au modèle analogique établi par Kim *et al.* (2011). Les phases de progradation des cônes alluviaux vers le bassin peuvent être déviées par les rivières axiales (Giles *et al.*, 2016). L'érosion des cônes alluviaux par les rivières axiales sont à l'origine de surfaces majeures ("toe-cutting" ; Leeder & Mack, 2001). Les dépôts de cônes alluviaux peuvent être remaniés par les rivières axiales et ils sont ainsi peu préservés dans l'enregistrement sédimentaire (Paim, 1995).

La position et la migration des rivières axiales sont contrôlées par les phénomènes d'avulsion, eux-mêmes gouvernées par le basculement tectonique (paramètre allogénique) et par le flux sédimentaire et hydraulique des rivières transverses (paramètre autogénique) (Leeder & Gawthorpe, 1987; Cohen *et al.*, 1995; Kim *et al.*, 2011). Par exemple, la proximité des rivières axiales avec les failles actives est liée à un plus fort taux d'accommodation. La forte progradation des cônes alluviaux transverses et la migration des rivières axiales vers le bassin sont plutôt associées à des zones où la subsidence est limitée par rapport au flux sédimentaire (Cohen *et al.*, 1995; Santos *et al.*, 2014). La diminution du taux de subsidence favorise le développement des systèmes fluviaux distributaires (transverses) et la progradation des faciès vers le bassin (Nichols & Fisher, 2007). L'enregistrement stratigraphique des systèmes fluviaux transverses et axiaux dans les rifts sont marqués par des architectures bien distinctes qui peuvent être utilisées pour retracer l'évolution des grabens (Leeder & Gawthorpe, 1987; Santos *et al.*, 2014).

1.4.2 Réorganisation et adaptation des systèmes de drainage

Le soulèvement dans le mur des failles normales et la baisse du niveau de base perturbent le profil d'équilibre des rivières permettant l'incision des vallées en amont. L'**adaptation** ou l'**inadaptation** des cours d'eau face à la tectonique active et aux variations lithologiques peut être expliquée par différents phénomènes. La **surimposition** (Figure 1.20) correspond à l'ajustement du réseau hydrographique en lien avec les variations lithologiques. La rivière s'installe sur une surface d'aplanissement généralisée, nivelant les roches tendres et dures. La surimposition peut aussi se produire à partir d'une couverture discordance ou des structures héritées (zones broyées de failles, plissement, etc).

L'adaptation des rivières aux mouvements verticaux induits par la tectonique dépend de l'équilibre entre le taux de soulèvement et le pouvoir érosif des rivières. Dans certains cas, le soulèvement généré par les failles peut conduire à l'**inversion** ou la **dévi**ation des rivières vers les zones en subsidence ("backshed drainage reentrants" ; Figure 1.18). Le phénomène de **capture** correspond à l'incision rapide d'une rivière (A) vers un autre cours d'eau (B) dont le gradient est différent. Le cours d'eau (B) a donc capturé la rivière (A). La capture est associée à une réduction, voire à un abandon de la rivière (A) alors que la rivière (B) ajuste son profil d'équilibre.

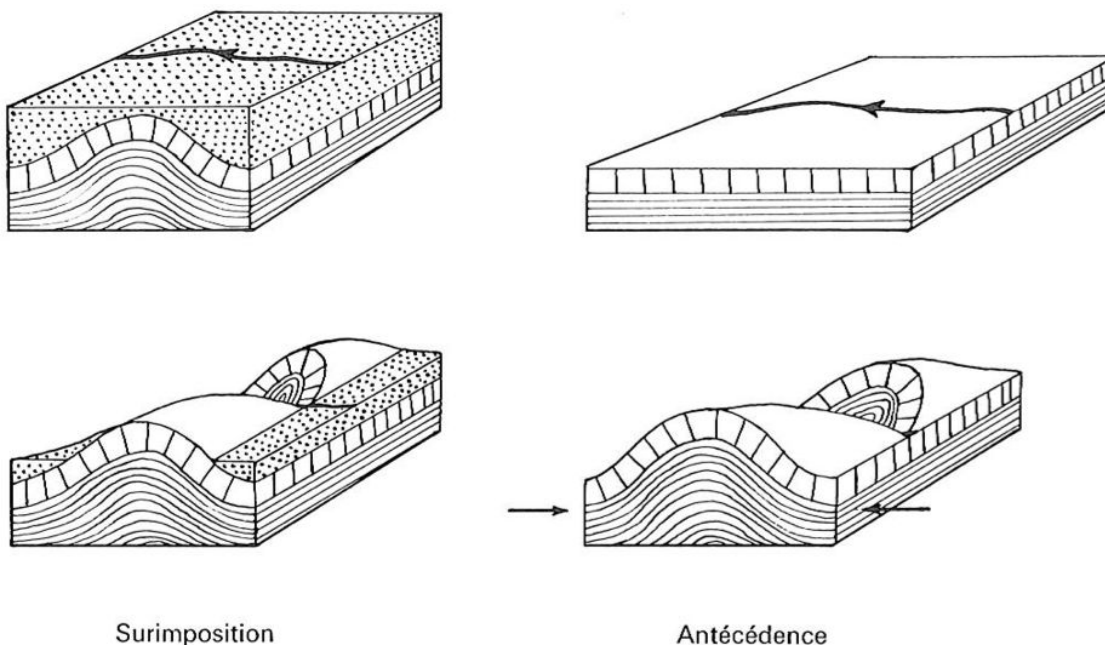


FIGURE 1.20 – Surimposition et antécédence en contexte compressif (d'après Coque, 1977).

L'**antécédence** (Figure 1.20) correspond au phénomène de persistance d'une rivière en réponse à la tectonique active (Hayden, 1862; Powell, 1875; Dutton, 1882; Medlicott, 1864; Derruau, 1965; Schumm *et al.*, 2000; Twidale, 2004; Derruau, 2010). L'antécédence est souvent considérée comme une anomalie ou une inadaptation du système hydrographiques où les rivières ont donc un pouvoir érosif suffisamment important pour inciser les zones en soulèvement. Sur-

imposition et antécédence peuvent être documentées pour une même rivière. La rivière peut être surimposée à une surface d'aplanissement et antécédente par rapport à une phase tectonique active (Alvarez, 1999).

Les rivières antécédentes peuvent être transverses ou obliques aux structures actives. Dans les rifts continentaux, les rivières antécédentes recoupent les failles normales et les zones en soulèvement, et peuvent être à l'origine de la création d'un relief important et de gorges. Le lac George (Nouvelles Galles du Sud, Australie) est un exemple de rift montrant la persistance des rivières antécédentes en réponse au développement des failles normales depuis le Miocène supérieur jusqu'à l'actuel (Ollier & Pain, 2000). On peut aussi citer l'exemple de la rivière Turkwell sur la marge ouest du lac Turkana au Kenya (Vétel *et al.*, 2004, 2005).

L'antécédence des rivières est très largement documentée dans les systèmes compressifs (Figure 1.20), recoupant les anticlinaux en surrection, perpendiculairement aux fronts de chevauchements actifs (Strahler, 1945; Mazzanti & Trevisan, 1978; Oberlander, 1985; Jackson *et al.*, 1996). Peu de travaux sont consacrés à la notion d'antécédence en domaine extensif. Dans certains cas, l'abandon des terrasses fluviales par ces rivières permet de contraindre l'histoire du soulèvement du pli (Hubert-Ferrari *et al.*, 2007; Charreau *et al.*, 2008; Saint-Carlier *et al.*, 2016). Cependant, peu de travaux s'attachent à comprendre comment les rivières sont capables de persister dans un état d'"inadaptation" pendant plusieurs centaines de milliers d'années, voire plusieurs millions d'années. Les modèles numériques développés par Simpson (2004) montrent que l'incision continue par les rivières antécédentes engendre l'accélération de la déformation des plis en front de chaîne. Cette rétroaction positive entre la persistance des rivières antécédentes et la tectonique active n'a jamais été mise en évidence dans les rifts continentaux et encore moins à partir de l'enregistrement sédimentaire.

1.5 Architectures fluviales : du terrain aux modèles

1.5.1 Echelles d'observation

Pour appréhender la dynamique d'un système sédimentaire, il convient tout d'abord de définir l'échelle d'observation des objets élémentaires ou des groupes d'objets étudiés dans le système naturel. L'**architecture fluviale** (Allen, 1978) correspond à la géométrie, l'organisation interne, la densité et l'interconnectivité des chenaux (conglomératiques ou sableux) parmi les dépôts de plaine d'inondation (à dominance de silts et argiles). La stratigraphie fluviale (Figure 1.21) se compose d'éléments à l'échelle (i) du chenal et de son remplissage (micro-échelle, 0,01 à 10 m), (ii) de la ceinture de chenaux (méso-échelle, 1 à 100 m), et (iii) du bassin sédimentaire (macro-échelle, 10 à 1000 m). L'échelle temporelle des séquences de dépôts observées (méso-échelle) est de l'ordre de 10^6 ans. Les unités tectono-stratigraphiques et les "méga-séquences" se développent à un ordre de grandeur supérieur ($10^6 - 10^7$ et $10^7 - 10^8$ ans respectivement). On

s'intéresse ici à la variabilité des faciès dans les rifts continentaux à l'échelle locale et régionale (dans les blocs de faille normale et le long de la marge du rift respectivement), et des successions alluviales/fluviatiles pour des intervalles de temps de l'ordre de 10^6 à 10^7 ans.

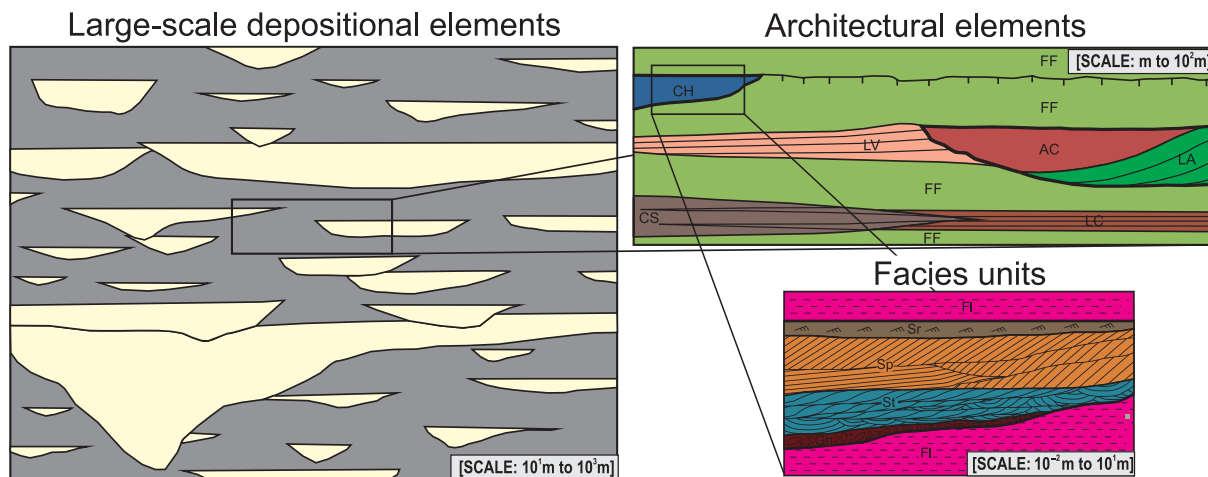


FIGURE 1.21 – Représentation des différentes échelles spatiales et des types d'unités sédimentaires observées dans l'enregistrement sédimentaire des systèmes fluviatiles. Architecture elements : FF, "overbank fines" ; CH, "crevasse channel" ; AC, "abandoned channel fill" ; LV, "levée" ; CS, "crevasse splay". Exemples of facies units : *Fi*, interlaminated very fine sand, silt and clay ; *Sr*, current ripple cross-laminated sand ; *Sp*, planar cross-stratified sand ; *St*, trough cross-stratified sand (d'après Colombera *et al.*, 2013).

1.5.2 Apport de la stratigraphie séquentielle : modèles et critiques

En stratigraphie séquentielle, la géométrie des séquences de dépôts est classiquement interprétée en termes de variations du niveau marin relatif. Ces dernières intègrent les variations absolues du niveau marin (eustatisme) et les mouvements tectoniques (dont la subsidence), et les variations des apports sédimentaires (Posamentier *et al.*, 1988; Posamentier & Vail, 1988; Van Wagoner *et al.*, 1988, 1990). Ainsi les séquences de dépôts sont définies sur la base des variations relatives du niveau marin (Martins-Neto & Catuneanu, 2010). Cette approche est difficile pour interpréter les architectures stratigraphiques alluviales dans les rifts continentaux isolés, déconnectés du niveau marin. Néanmoins, on a très vite substitué au niveau marin un référentiel correspondant au niveau de base, surface d'équilibre au dessous de laquelle les sédiments se déposent, et au dessus de laquelle il y a érosion (Wheeler, 1964).

L'abondante littérature et les critiques associées ont surtout porté sur les différents modèles architecturaux proposés et la terminologie pour rendre compte de l'extraordinaire variabilité rencontrée dans les processus et les faciès en domaine continental (Wright & Marriott, 1993; Shanley & McCabe, 1994; Emery & Myers, 1996; Miall, 1996, 2010, 2013; Posamentier & Allen, 1999; Catuneanu, 2006; Blum & Törnqvist, 2000; Ethridge *et al.*, 1998; Dalrymple *et al.*, 1998; Le-

garreta, 1998). Dans l'enregistrement sédimentaire, l'accommodation est décrite qualitativement pour définir l'"aggradation" et la "dégradation" en environnement fluviale (Olsen *et al.*, 1995; Currie, 1997). La densité des chenaux et les éléments architecturaux sont interprétés par les variations d'accommodation (Figure 1.22). En contexte de fort taux d'accommodation, les chenaux actifs sont moins susceptibles d'occuper la même place en raison d'une subsidence rapide. En contexte de faible taux d'accommodation, il est plus probable de remobiliser les dépôts et de générer une succession de chenaux amalgamés.

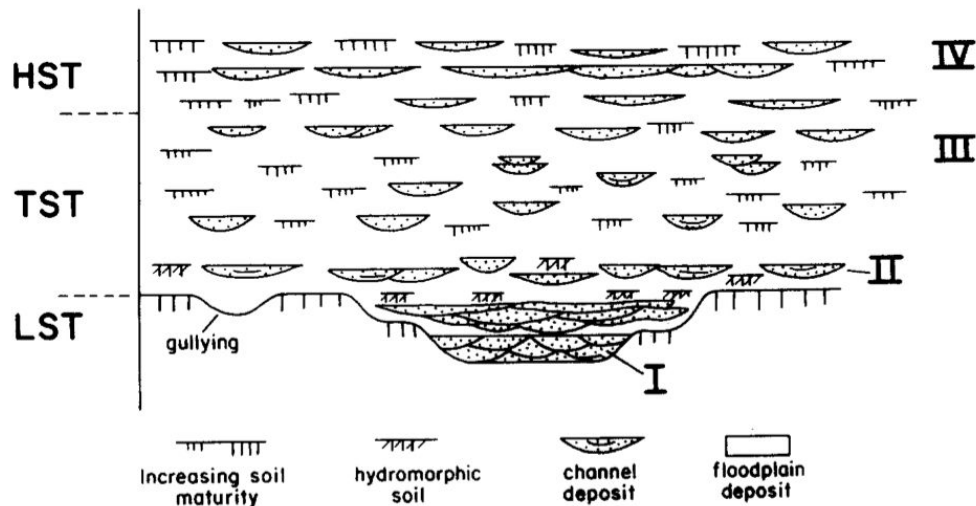


FIGURE 1.22 – Modèle architectural d'une succession fluviale enregistrent un cycle de variation du niveau de base de troisième ordre (séquence de type 1 *sensu*; Posamentier *et al.*, 1988). LST : "lowstand systems tract"; TST : "transgressive systems tract"; HST : "highstand systems tract". I : Remplissage des paléovallées par des dépôts de rivières en tresses dans un espace confiné pendant le LST. La forte connectivité des chenaux induit la faible préservation des faciès fins de plaines d'inondation II : Faible création d'accommodation en début de transgression avec le remplissage polyphasé des chenaux. La hausse du niveau de base favorise le développement des paléosols hydromorphes (eaux stagnantes). III : Hausse du niveau de base en fin de transgression conduisant à la formation de chenaux isolés, qui se développent verticalement en aggradation. Les sols sont peu différenciés mais bien drainés. IV : Réduction de la création d'accommodation conduisant à l'accrétion latérale des chenaux, à une plus forte interconnectivité latérale et à une forte plus faible préservation des faciès de plaine d'inondation. Les sols sont matures mais leur potentiel de préservation diminue en lien avec la migration des chenaux (Wright & Marriott, 1993).

1.5.3 Confinement des systèmes fluviales

Un paramètre important dans l'architecture stratigraphique est la notion de confinement du système fluvial. Les travaux de Pisel (2015) comparent les mécanismes à l'origine des architectures stratigraphiques dans les environnements fluviaux "confinés et "non confinés"(Dakota Sandstone et Lower Wasatch Formation dans le bassin de Uinta).

Les systèmes fluviaux actuels dits "confinés" sont caractérisés par une faible extension latérale des plaines d'inondation (quelques kilomètres de large). Le système fluvial est délimité par des paléoreliefs et des flancs de vallées incisées (Van Wagoner *et al.*, 1990; Dalrymple & Zaitlin, 1994; Posamentier, 2001; Strong & Paola, 2008; Bhattacharya, 2011; Blum *et al.*, 2013; Li *et al.*, 2013). Les systèmes confinés sont caractérisés par une forte interconnexion verticale et latérale des chenaux (Figures 1.22 et 1.23B).

Les systèmes fluviaux dits "non confinés" présentent une géométrie radiale et se développent sur une large zone (plus de 10 km). La migration des chenaux sur de plus larges plaines d'inondation favorise l'accrétion latérale des chenaux (Figure 1.23A). Ces systèmes "non confinés" forment des mégafans, des systèmes fluviaux distributaires (DFS) ou des "terminal fans" (Geddes, 1960; Kumar, 1993; Hartley *et al.*, 2010b; Kelly & Olsen, 1993; Singh *et al.*, 1993; Stanistreet & McCarthy, 1993; Sinha & Friend, 1994; Gupta, 1997; Nichols & Watchorn, 1998; DeCelles & Cavazza, 1999; Horton & DeCelles, 2001; Leier *et al.*, 2005; Weissmann *et al.*, 2010; Buehler *et al.*, 2011; Davidson *et al.*, 2013). Le fan Okavango (Botswana) est un exemple de DFS qui se développe en bordure de rift (Figure 1.24).

Le chapitre 4 documente l'architecture stratigraphique d'un système fluvial qui remplit un paléorelief important hérité de l'orogène hellénique (Oligo-Miocène) pendant les stades précoces de rifting. **Quelle est la morphologie de ce système fluvial qui se développe a priori dans un environnement "confiné" ?**

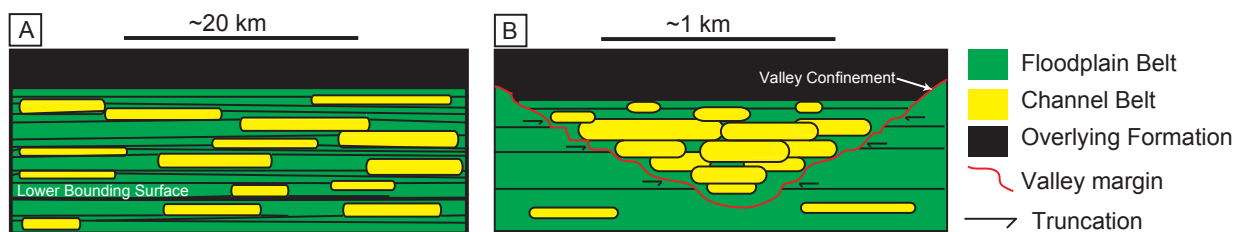
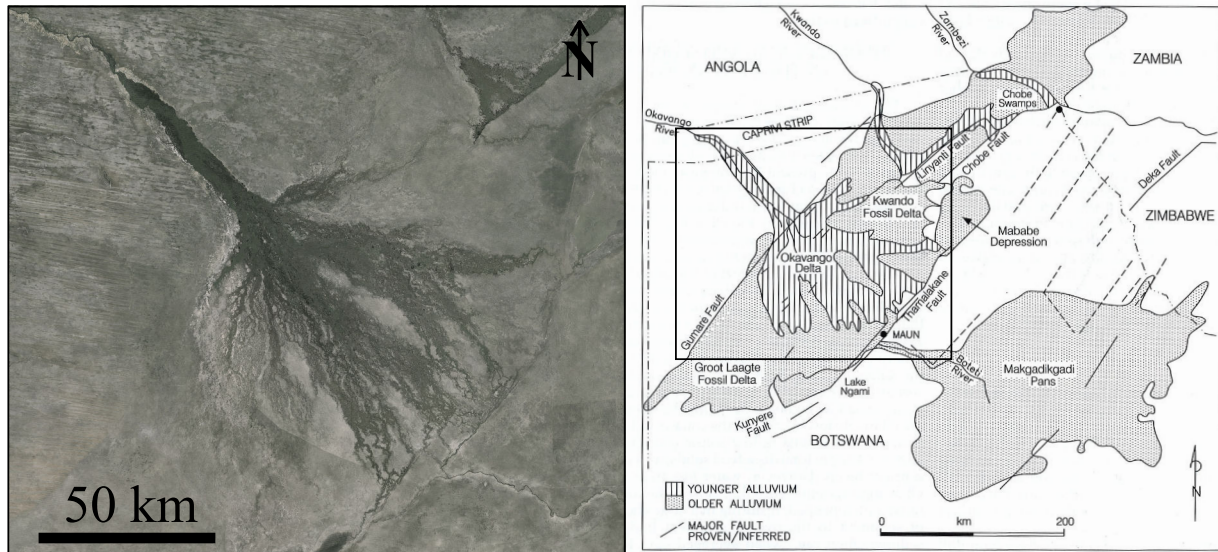


FIGURE 1.23 – Coupe transverse à l'axe fluvial illustrant schématiquement l'architecture stratigraphique dans le cas d'un système distributaire non confiné (A) et d'un système confiné (Pisiel, 2015).

1.5.4 Rôle de la subsidence et autres paramètres de contrôle

La tendance des chenaux à préférentiellement occuper les zones de subsidence maximale dans les rifts a été pour la première fois décrites par Leeder (1978), Bridge & Leeder (1979), Alexander & Leeder (1987) et Leeder & Alexander (1987). Le rôle de la tectonique sur l'architecture fluviale est particulièrement important pour comprendre et caractériser la formation de ces corps sableux, les potentiels réservoirs d'hydrocarbures ou aquifères. Les zones en subsidence (contexte extensif ou compressif) concentrent les faciès grossiers et peuvent générer différentes



LOW SINUOSITY/MEANDERING FLUVIAL FAN

INNER FAN :
Active meander belts run through permanent swamps with vegetated levees

MID FAN :
Low Sinuosity/Anastomosing river with vegetated levees

OUTER FAN :
Low sinuosity/Anastomosing rivers incised with little channel confinement

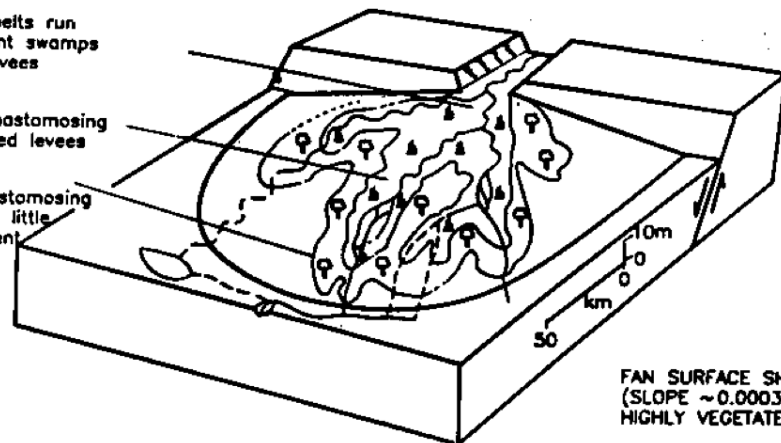


FIGURE 1.24 – Vue aérienne (Google Earth) du fan Okavango (Botswana) (carte d’après McCarthy, 2002). Le bloc diagramme est issu de la classification des cônes alluviaux de Stanistreet & McCarthy (1993). D’après cette classification, le fan Okavango est l’archétype du cône alluvial faiblement penté, caractérisé par un système de rivières faiblement sinueux voire méandriforme.

architectures fluviales (Bridge & Leeder, 1979; Alexander & Leeder, 1987; Peakall *et al.*, 2000; Kim & Sanderson, 2010).

Les modèles quantitatifs LAB (Leeder, Allen, Bridge) envisagent le comportement des rivières en réponse au basculement tectonique et au gradient de déplacement le long des failles (Figure 1.25). Ces modèles ont été développés à partir des processus connus dans les rivières actuelles (équations d’écoulements de fluides et de transport des sédiments, cyclicité des phénomènes d’avulsion, etc) et des enregistrements fluviaux à l’Holocène. Ils simulent la migration des rivières axiales dans un demi-graben en subsidence (Figure 1.25).

Les modèles LAB mettent en évidence la migration des chenaux et leur faible interconnectivité dans les zones de subsidence maximale (**architecture 1**, Figure 1.25) (Allen, 1978;

Leeder, 1978; Bridge & Leeder, 1979; Bridge, 1993; Bridge & Mackey, 1993; Mackey & Bridge, 1995). Ces premiers modèles LAB (Bridge & Leeder, 1979) supposent une fréquence des avulsions constante. Les améliorations apportées aux modèles (Bridge, 1993; Bridge & Mackey, 1993; Mackey & Bridge, 1995) permettent de contraindre la localisation et la fréquence des avulsions. Ces modèles montrent que les éléments architecturaux sont, de façon plus complexe, contrôlés par : (i) la largeur des chenaux et de la plaine d'inondation, (ii) la profondeur des chenaux, (iii) le taux de sédimentation, (iv) le taux d'aggradation des plaines d'inondation, (v) la fréquence des avulsions, (vi) la profondeur d'enfouissement (effet de compaction) et (vii) le basculement tectonique. Néanmoins, ces modèles ne prennent pas en compte les variations du flux sédimentaire.

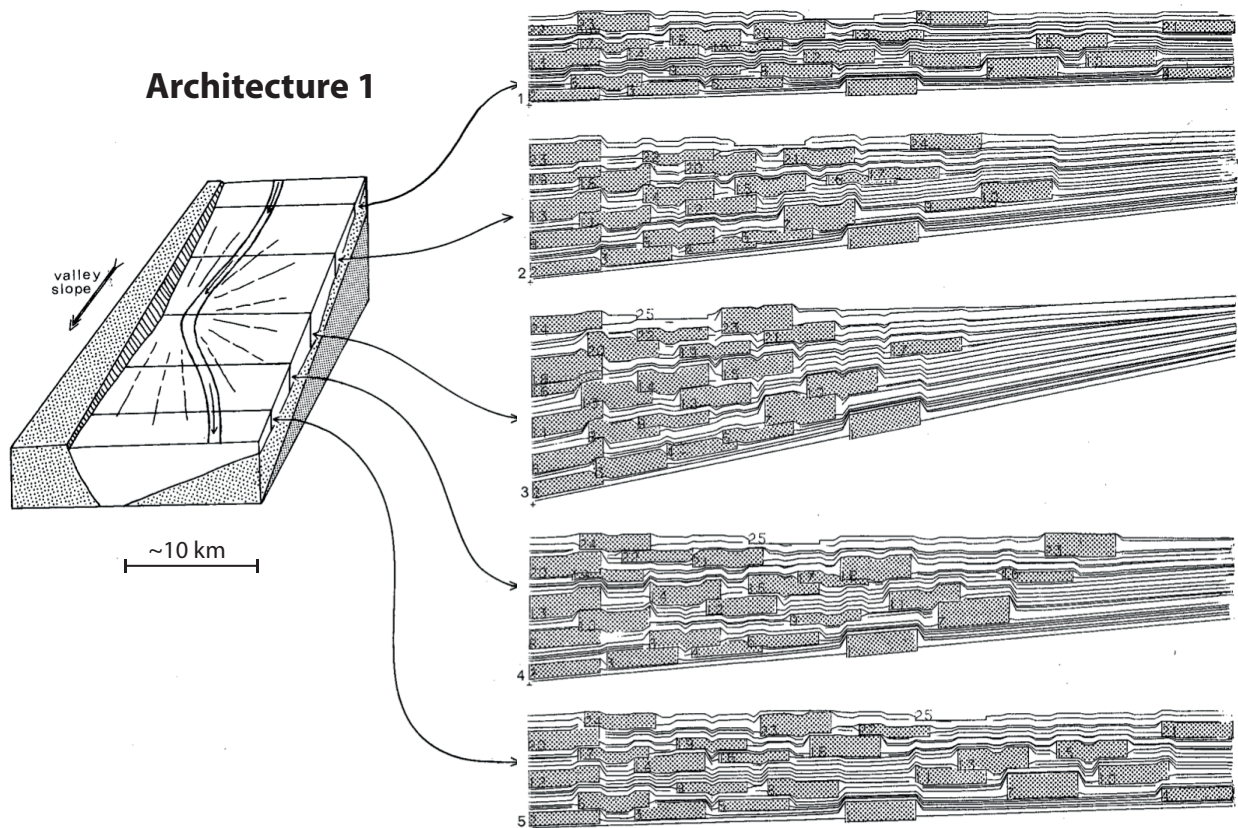


FIGURE 1.25 – Modèle 2D de la stratigraphie alluviale d'une rivière axiale (modèle LAB) dans un demi-graben (modifié d'après Alexander & Leeder, 1987).

La plupart des enregistrements sédimentaires montrent que la préservation maximale des faciès fins de plaines d'inondation et la faible interconnectivité des chenaux sont associées aux zones de subsidence maximale (**architecture 1**). Cette architecture alluviale a notamment bien été documentée dans le bassin de Neuquén (Argentine, Legarreta, 1998), dans le bassin Almazan (Espagne, Huerta *et al.*, 2011), dans la Formation de Castissent (Espagne, Marzo *et al.*, 1988), le Groupe Mesaverde (*Price Canyon*, Utah, Shanley & McCabe, 1993; Olsen *et al.*, 1995), ou encore dans le *Triassic Sheerwood Sandstone Group* (*Eastern England Shelf*, Royaume-Uni, Medici *et al.*, 2015).

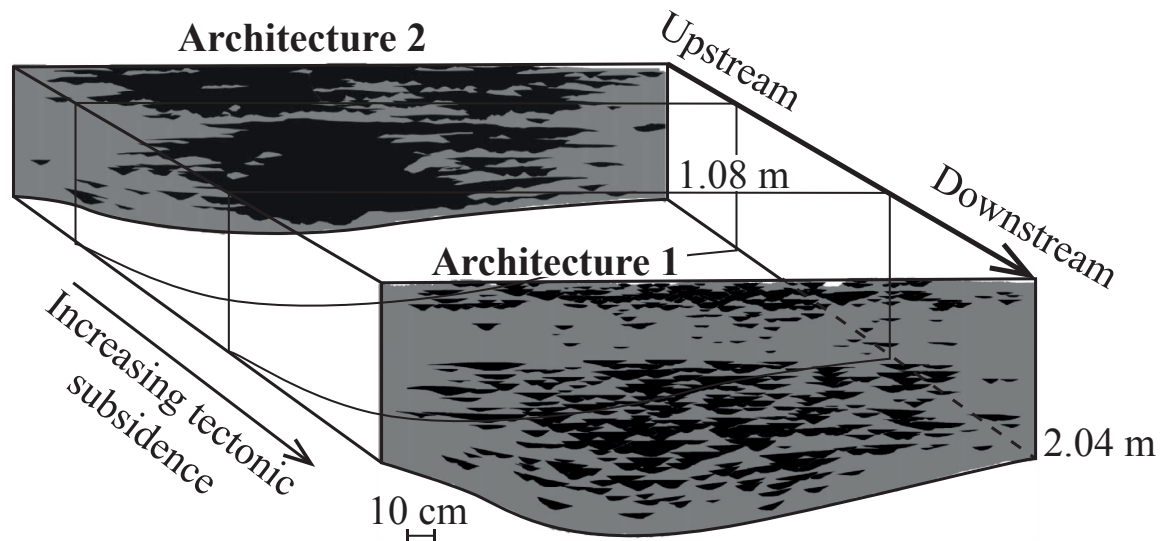


FIGURE 1.26 – Résultat des modélisations expérimentales de l'architecture fluviale d'amont en aval. Un gradient de subsidence est appliqué parallèlement et perpendiculairement à la direction du flux sédimentaire. Les chenaux isolés ou amalgamés sont représentés en noir. Les faciès fins (plaines d'inondation) sont indiqués en gris. La distance en mètres correspond à la distance depuis l'entrée "virtuelle" des sédiments dans le bassin expérimental (modifié d'après [Hickson et al., 2005](#)).

En utilisant les modèles LAB, [Heller & Paola \(1996\)](#) montrent que le basculement tectonique et l'augmentation de la fréquence des avulsions dans les zones de subsidence maximale favorisent l'amalgamation des chenaux (**architecture 2**). La fréquence des avulsions reste un paramètre difficilement quantifiable à partir des enregistrements sédimentaires car elle est proportionnelle au flux sédimentaire ([Bryant et al., 1995](#)).

En plus des modèles numériques, les modèles expérimentaux XES (*Experimental Earthscape* aussi appelés "Jurassic tank") s'attachent à caractériser les architectures alluviales et à quantifier les paramètres de contrôle ([Sheets et al., 2002](#); [Hickson et al., 2005](#); [Hajek et al., 2010](#); [Kim et al., 2011](#); [Straub et al., 2013, 2014](#); [Kopp & Kim, 2015](#)). Les modèles XES reproduisent les différentes architectures alluviales en lien avec les variations de subsidence (Figure 1.26). L'augmentation de subsidence dans la partie distale du système transverse permet de générer une architecture de chenaux isolés alors que les chenaux connectés sont localisés vers les zones de plus faible subsidence (**architecture 1**, Figure 1.26). Un gradient de subsidence perpendiculaire à l'axe de drainage fluviale permet de concentrer préférentiellement les faciès grossiers dans les zones de subsidence maximale (**architecture 2**, Figure 1.26). Les **architectures 1 et 2** observées dépendent de la direction du basculement tectonique par rapport à la direction de l'axe fluviale. Cela met en évidence l'importance du flux sédimentaire dans le contrôle de l'architecture stratigraphique.

Un fort taux de sédimentation ($A < S$) peut surpasser l'influence de la subsidence tectonique sur l'architecture alluviale ([Hickson et al., 2005](#)). Les modèles expérimentaux de [Strong et al.](#)

(2005) démontrent qu'une réduction du taux de subsidence associée à une réduction du flux sédimentaire et hydraulique, conduit à une rétrogradation et une diminution de la connectivité des chenaux. Les variations du flux sédimentaires sont cruciales pour déchiffrer les architectures alluviales et fluviales mais restent difficiles à quantifier directement à partir des enregistrements sédimentaires (Allen *et al.*, 2013). L'architecture alluviale et fluviale en lien avec le gradient de subsidence est développée dans le chapitre 4, dans les blocs de failles normales et à l'échelle du système fluvial considéré.

1.6 Evolution tectono-stratigraphique des rifts continentaux

1.6.1 Modèles existants

Les principaux environnements de dépôt documentés dans les rifts continentaux sont : (i) les cônes alluviaux, (ii) les plaines fluviales et (iii) les deltas qui se développent en milieu lacustre/marin plus ou moins profond. Tous ces environnements de dépôt peuvent être enregistrés dans une même succession syn-rift et permettent de reconstruire l'évolution du bassin (Surlyk, 1978; Frostick & Reid, 1987; Leeder & Gawthorpe, 1987; Morley, 1989; Mack & Seager, 1990; Schlische & Olsen, 1990; Lambiase, 1990; Leeder *et al.*, 1991).

Le remplissage syn-rift sédimentaire dans les rifts continentaux est typiquement caractérisé par (i) une série fluviale inférieure au cours de l'initiation du rift, (ii) une série intermédiaire lacustre/marin plus ou moins profonde enregistrant l'approfondissement du bassin ("rift climax"), et enfin (iii) une série supérieure fluvio-lacustre progradante (post-rift) marquant l'arrêt de l'activité des failles et/ou le comblement du bassin associé à la surrection et l'érosion de la marge du rift. (Schlische & Olsen, 1990; Schlische, 1991; Lambiase, 1990; Prosser, 1993). Les relations stratigraphiques entre les séries pré-rift/syn-rift ou à l'intérieur des séries syn-rift dans les grabens (géométries en "onlap" principalement) mettent en évidence la propagation latérale des failles et la connexion entre les dépocentres (e.g. Leeder & Gawthorpe, 1987; Gibson *et al.*, 1989; Schlische & Olsen, 1990).

Des modèles de sédimentation alluviales dans les rifts continentaux ont notamment été proposés par Alexander & Leeder (1987); Leeder & Gawthorpe (1987); Leeder (1993); Cohen *et al.* (1995); Gawthorpe & Leeder (2000). Le modèle de Gawthorpe & Leeder (2000) décrit l'évolution du remplissage sédimentaire en lien avec les processus de surface et la croissance des failles normales (Figure 1.27). La phase d'initiation du rifting est caractérisée par un faible taux d'accommodation au cours de la nucléation des failles. La création de topographie en lien avec l'activité des failles est à l'origine des systèmes de rivières transverses conséquentes (Figure 1.27B).

Dans un stade précoce, les dépocentres sont isolés les uns des autres et la sédimentation est

contrôlée par des systèmes hydrographiques internes aux blocs de failles. La compartimentalisation des dépocentres suggère des niveaux de base différents dans le rift. De même, la stratigraphie peut être gouvernée par des taux d'accommodation et de subsidence distincts dans chacun des blocs. Les géométries syn-rift sont fortement progradantes et sont expliquées par le faible taux d'accommodation à l'initiation du rift par rapport au flux sédimentaire ($A < S$). Les dépocentres sont donc suralimentés pendant la phase d'initiation du rift (Lambiase, 1990; Prosser, 1993; Wirthjack *et al.*, 2002; Melchor, 2007; Holz *et al.*, 2014).

Les systèmes de drainage plus importants qui se développent à travers plusieurs blocs de failles sont hérités du paysage pré-rift (Figure 1.27A). A l'initiation du rifting, les rivières antécédentes ont la capacité de recouper les zones en soulèvement et peuvent être aussi localement modifiées par la propagation latérale des failles (Figure 1.27A, B). La migration de l'activité des failles implique la réorganisation du système de drainage et peut être marqué par des discontinuités majeures dans la succession syn-rift. Le modèle conceptuel de Gawthorpe & Leeder (2000) montre l'inversion des rivières antécédentes au cours des stades plus avancés du rifting (Figure 1.27C). **La persistance des rivières antécédentes pendant les différentes phases de rifting n'est pas documentée dans ces modèles.**

L'interaction et la connexion entre les failles permet d'agrandir et de connecter les dépocentres qui étaient initialement isolés. La déformation devient progressivement localisée sur un nombre restreint de failles qui accommodent une plus grande part de la déformation (Gupta *et al.*, 1998; Ravnås & Steel, 1998; Cowie, 1998; Cowie *et al.*, 2000; Gawthorpe & Leeder, 2000). La connexion des segments de failles est associée à une accélération de la subsidence et du taux d'extension ($A > S$). Ce stade de connexion des failles marque le début du "rift climax" qui peut être enregistré dans la stratigraphie syn-rift par un approfondissement du bassin et une transition entre les faciès fluviatiles et lacustres/marins. Cependant, cette transition des faciès fluviatiles aux faciès lacustres/marins peut aussi être associée à une baisse du flux sédimentaire ou une augmentation du niveau de base alors que le taux d'accommodation reste constant (Schlische & Olsen, 1990; Kreuser *et al.*, 1990).

Il est aussi possible que le "rift climax" ne soit pas toujours associé à un approfondissement généralisé du bassin (Santos *et al.*, 2014). Une augmentation de l'accommodation (A) et de la surrection le long des failles peuvent être associées à une augmentation du flux sédimentaire (S), tel que le flux sédimentaire égale la capacité du bassin. Les rivières axiales sont bien établies et interagissent avec les systèmes de rivières transverses le long des demi-grabens (Figures 1.28 et 1.27). Les rivières axiales peuvent aussi alimenter un bassin lacustre/marin où la subsidence est plus importante. L'approfondissement du bassin est alors uniquement enregistré au centre du bassin alors que les systèmes fluviatiles drainent les bordures du rift. Le diachonisme lié à l'approfondissement du bassin est développé dans les chapitres 4 et 6.

1.6.2 Modèle alternatif et contribution de la thèse

La complexité des processus engagés dans le couplage entre rivières et rifting ne permet pas de comprendre facilement l'ensemble du système depuis la source des sédiments jusqu'au bassin. La vision schématique des rifts où la subsidence dans les grabens ou demi-grabens (plusieurs dizaines voire centaines de kilomètres) est contrôlée par quelques failles majeures, n'est pas directement applicable à notre cas d'étude (Leeder & Gawthorpe, 1987; Cohen *et al.*, 1995; Nichols & Watchorn, 1998; Gawthorpe & Leeder, 2000). En effet, on s'intéresse ici aux relations tectono-sédimentaires dans des dépo-centres de plus petites dimensions (<20 km de long, <10 km de large). **La résolution spatiale des structures étudiées dans le rift de Corinthe permet donc d'améliorer et de préciser les modèles tectono-stratigraphiques existants.**

Dans le contexte de blocs de failles relativement étroits, la notion de "marge de rift" est confuse. Celle-ci ne se résume pas à UNE structure majeure contrôlant à la fois la subsidence et le soulèvement en bordure de bassin, mais à un système de failles en cours de développement. La marge de rift peut alors s'étendre sur plusieurs dizaines de kilomètres de large. La faible distance entre les blocs et la complexité des mouvements verticaux à travers les différents blocs de faille jouent un rôle important dans le développement des bassins versants et le remplissage syn-rift (Densmore *et al.*, 2005). Les dépo-centres peuvent aussi évoluer indépendamment et selon différentes altitudes (Duffy *et al.*, 2015). Les implications sur la distribution des faciès restent peu documentées dans un tel contexte et sont étudiées ici .

Le flux sédimentaire est couramment interprété comme la réponse à l'activité tectonique. Le flux sédimentaire est quasiment nul à l'initiation des rifts et augmente au cours de la croissance du système de failles normales (Figure 1.12 ; Cowie *et al.*, 2006). Cette simple relation de cause à effet est discutée ici en considérant la présence de rivières antécédentes. De plus, les modèles classiques à l'initiation du rifting continental supposent l'absence de relief significatif. Néanmoins, la distension en contexte intra-montagneux suppose la présence d'une paléotopographie plus ou moins importante, dessinée par l'incision des rivières pré-rift. Dans le cas où le paysage pré-rift est marqué par d'importants reliefs (plusieurs centaines de mètres de hauteur), la présence d'un réseau de rivières antécédentes bien établies peut être caractérisé par un flux sédimentaire significatif dès l'initiation du rifting. Cette hypothèse permet de soulever les questions suivantes :

- **Quelles sont les arguments en faveur d'un flux sédimentaire antécédent dans l'enregistrement stratigraphique syn-rift ?**
- **Comment se comporte le système fluvial antécédent en réponse à la nucléation et à la croissance des failles normales ?**
- **Comment les rivières antécédentes remplissent-elles les paléoreliefs à l'initiation du rifting ?**
- **Quelles sont les implications sur la stratigraphie syn-rift ?**

On ne s'intéresse pas uniquement au comportement des rivières pendant la phase d'initiation du rift, mais aussi à leur adaptation et inadaptation pendant les phases successives de migration

de l'activité des failles.

- **Les rivières antécédentes persistent-elles ou sont-elles ré-organisées aux cours du développement du rift ?**
- **Comment la ré-organisation des rivières antécédentes est-elle enregistrée dans la stratigraphie syn-rift ?**

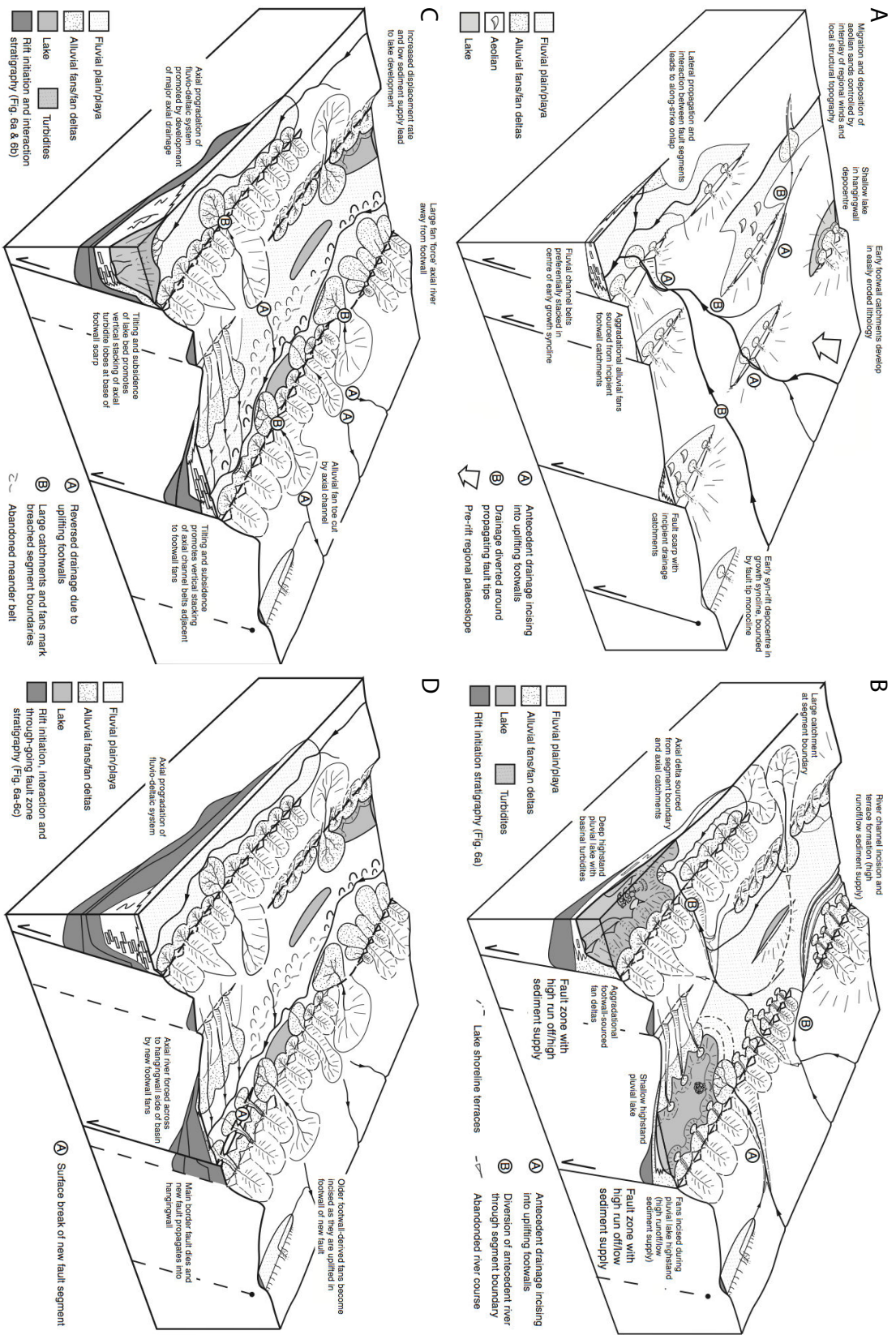


FIGURE 1.27 – Modèle conceptuel de l'évolution tectono-sédimentaire des rifts en milieu continental. **A** Phase d'initiation du rift ; **B** et **C** Phase d'interaction et de connexion entre les segments de failles ; **D** Formation d'un système de failles connectées (Gawthorpe & Leeder, 2000).

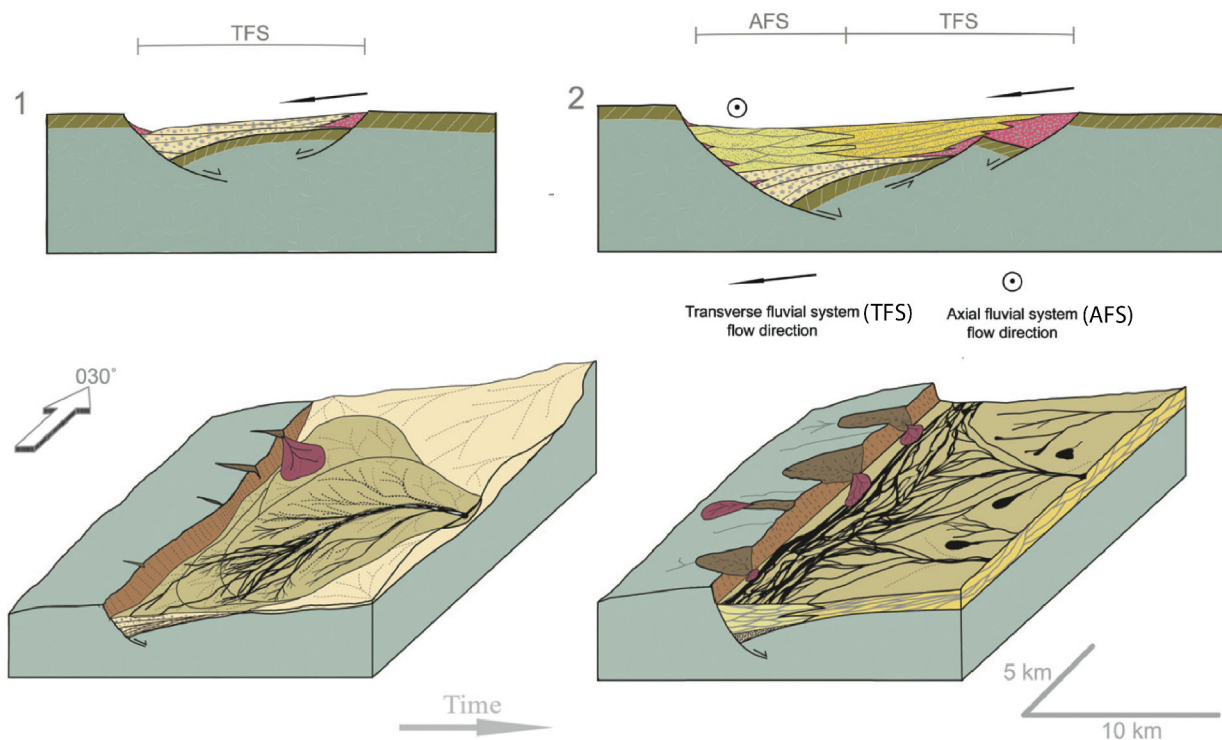


FIGURE 1.28 – Reconstitution paléogéographique du système fluviale "Guarda Velta", bassin cambrien de Camaqua au sud du Brésil. (1) La phase d'initiation du rift est caractérisée par le développement des systèmes fluviales transverse distributaires. Contrairement au modèle classique, les sédiments proviennent du côté antithétique du graben ("hangingwall sediment flux"). (2) Pendant la phase "climax" du rift ("Guaritas rifting event"), un système fluviale axial se développe en interaction avec les systèmes transverse (modifié d'après Santos *et al.*, 2014).

Chapitre 2

Le rift de Corinthe

Ce chapitre présente le contexte géologique du rift de Corinthe et l'état des connaissances sur les modèles d'évolution existants. Le contexte géodynamique actuel de la région égéenne permet de mieux comprendre les mécanismes à l'origine de sa formation.

Sommaire

2.1	Introduction	59
2.2	Contexte tectonique actuel et déformation active	63
2.3	Structuration du rift de Corinthe	65
2.3.1	Histoire des Hellénides externes	65
2.3.2	Histoire tardi-cénozoïque, extension égéenne	68
2.4	Géométrie et modèles d'évolution du rift de Corinthe	73
2.4.1	Modèle de détachement	74
2.4.2	Modèle de rotation des blocs	76
2.5	Stratigraphie syn-rift	79

2.1 Introduction

Le golfe de Corinthe (Grèce) est une des expressions récentes de l'extension en région égéenne. Le rift de Corinthe sépare le Péloponnèse de la Grèce Centrale (Figure 2.1) et se situe en arrière de l'arc de subduction hellénique. Il est localisé au nord-est de la faille de Céphalonie et au sud-ouest de la faille nord anatolienne qui sont des structures actives majeures dans la région. Il s'agit d'un rift non magmatique, étroit et qui s'étend sur 120 km de long. L'axe du rift présente une orientation N110°, et la direction d'extension est N005°. Le golfe de Corinthe se prolonge à l'est en deux branches que forment les golfes des Alcyonides et de Lechaion (Figure 2.1). Dans sa partie orientale, la largeur maximale du golfe est de 30 km et la bathymétrie est de 900 m.

Vers l'ouest, le golfe devient plus étroit, peu profond (moins de 100 m) et se connecte avec la mer Ionienne via le détroit de Patras (Figure 2.1).

Le rift de Corinthe est la zone la plus sismiquement active en Europe. L'initiation du rift est d'âge Pliocène, il y a environ 4–5 Ma. La déformation récente (Pléistocène à actuel) est principalement localisée dans la partie ouest du rift, dans une zone étroite de quelques dizaines de kilomètres où se produisent la plupart des séismes. D'après les données GPS, le taux d'extension varie entre 15 et 5 mm/an d'ouest en est respectivement (Davies *et al.*, 1997; Billiris *et al.*, 1991; Briole *et al.*, 2000; Avallone *et al.*, 2004). Depuis les quarante dernières années, plusieurs séismes de magnitudes supérieures à 6 ont été enregistrés dans l'ensemble du rift (Figure 2.2; Rigo *et al.*, 1996; Jackson *et al.*, 1982; Hatzfeld *et al.*, 2000) ainsi qu'une forte activité microsismique (Pacchiani & Lyon-Caen, 2010; Bernard *et al.*, 2006). Depuis les années 1990, l'analyse des mécanismes au foyer des séismes et les vitesses GPS permettent de comprendre les mouvements des blocs continentaux dans la région égéenne ainsi que les mécanismes responsables de la distension.

Le rift recoupe obliquement la chaîne hellénique (mise en place de l'Oligocène au Miocène) dont les grandes structures sont principalement orientées NNO-SSE. Cette chaîne de montagne est à l'origine d'importantes variations lithologiques et rhéologiques de la croûte continentale. La géologie de la région égéenne a été initialement entreprise dans le but de comprendre l'évolution de la chaîne hellénique (Aubouin & Dercourt, 1965; Dercourt, 1964). Pendant les années 1970–80, des études se sont focalisées sur l'évolution des bassins téthysiens mésozoïques et le nord du Péloponnèse est considéré comme un bassin "néo-tectonique" peu étudié (Dufaure, 1975; Jacobshagen *et al.*, 1978; Dufaure *et al.*, 1979; Le Pichon & Angelier, 1979; Fleury, 1980). À partir des années 1980, les travaux de recherche sur la marge sud du golfe de Corinthe permettent de documenter la structuration du rift et les interactions tectono-sédimentaires dans les blocs de failles normales (Jackson *et al.*, 1982; Ori, 1989; Collier, 1988; Doutsos *et al.*, 1988; Doutsos & Piper, 1990; Poulimenos *et al.*, 1993). Le rift de Corinthe devient un lieu privilégié pour l'étude de la sismicité, la cinématique des failles normales (Armijo *et al.*, 1996; Roberts, 1996; Morewood & Roberts, 1999; Cowie *et al.*, 2000) et les interactions tectono-sédimentaires. Le laboratoire du rift de Corinthe (CRL), initié en 1989, est un site pilote européen pour les recherches sur la mécanique des failles et des séismes. Ce laboratoire de terrain est aussi intégré dans l'infrastructure de recherche européenne EPOS.

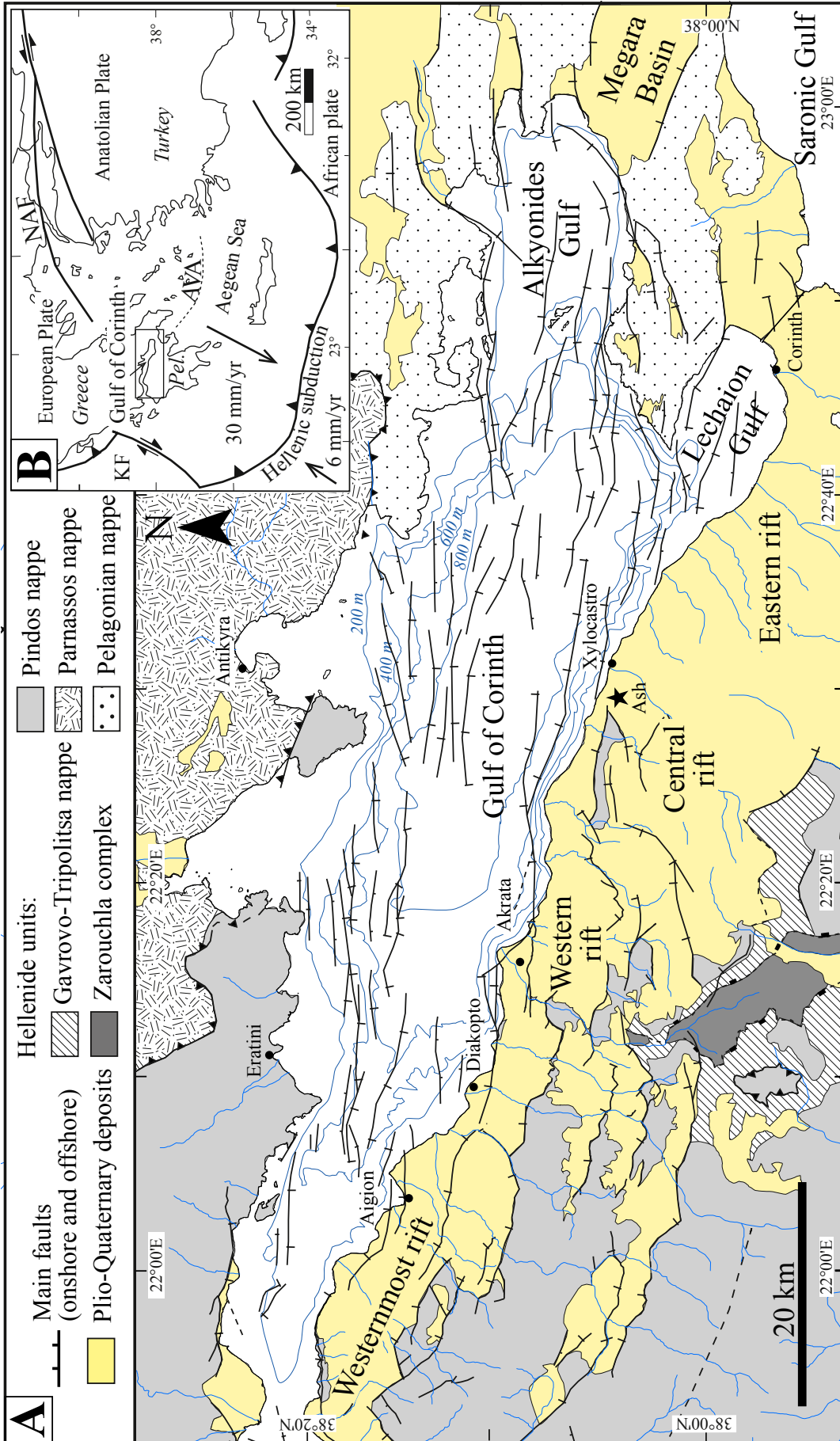


FIGURE 2.1 – **A** : Contexte géodynamique de la région égéenne (KF : faille de Céphalonie ; NAF : faille nord anatolienne ; AVA : Arc volcanique égéen ; Pel. : Péloponnèse). **B** : Carte géologique du rift de Corinthe et des structures helléniques majeures. Tracé des failles *offshore* d'après [Beckers et al. \(2015\)](#), [Hemelsdaël & Ford \(2016\)](#) et [Nixon et al. \(2016\)](#). Tracé des failles *onshore* d'après [Rohais et al. \(2007a\)](#); [Ford et al. \(2013\)](#); [Leeder et al. \(2012\)](#). L'étoile noire indique la position des cendres volcaniques datées à 2,55 Ma ([Leeder et al., 2012](#)).

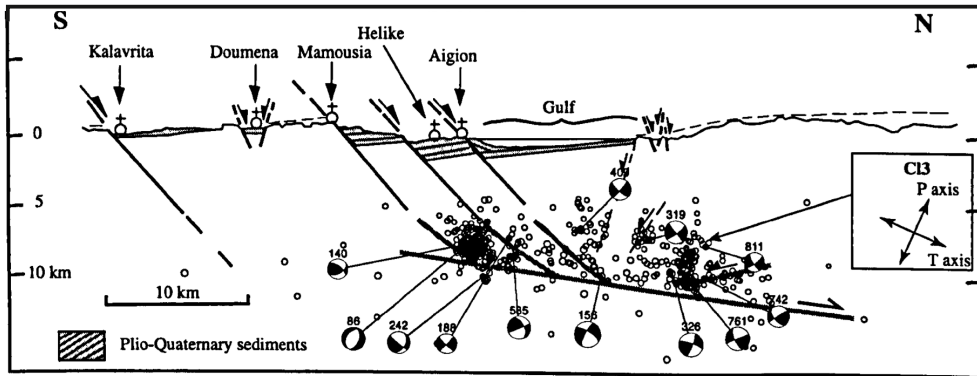


FIGURE 2.2 – Coupe N-S à l’ouest du rift de Corinthe passant par Aigion (Figure 2.1). L’ensemble de la microsismicité et les séismes majeurs définissent la zone sismogénique (5 et 12 km de profondeur) le long de laquelle un détachement est interprété (d’après Rigo *et al.*, 1996).

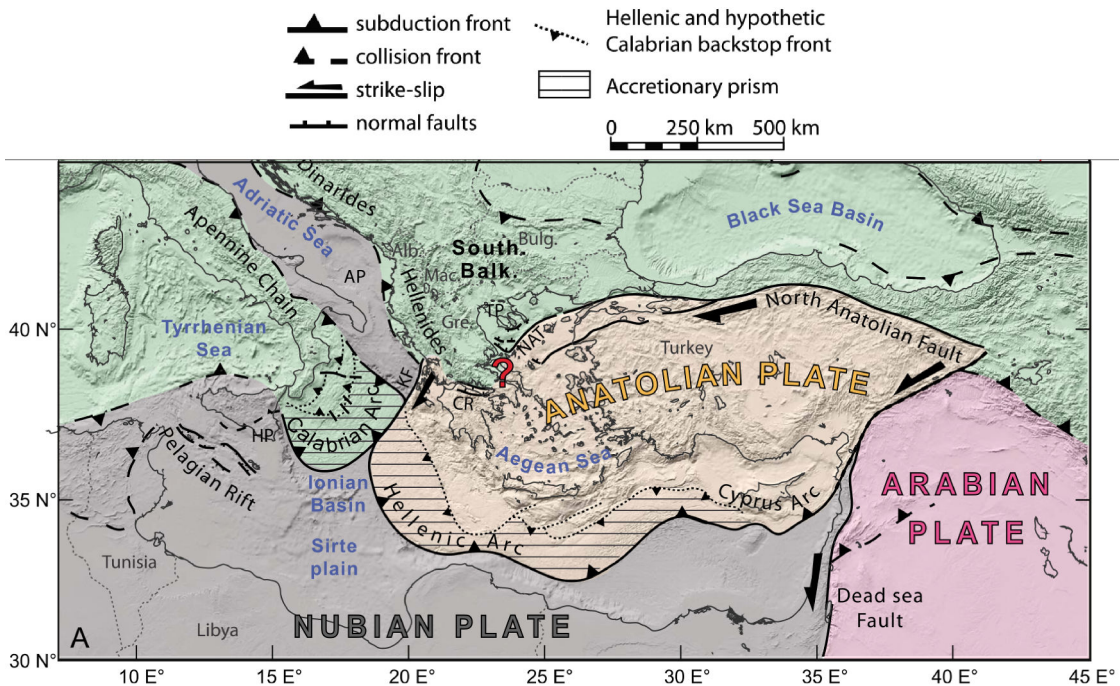


FIGURE 2.3 – Carte tectonique de la région méditerranéenne (centrale et Est). Southern Balk : partie méridionale des Balkans ; Alb : Albanie ; Mac : Macédoine ; Bulg : Bulgarie ; Gr : Grèce ; AP : plateforme apulienne ; HP : plateau hybléen ; KF : faille de Céphalonie ; CR : rift de Corinthe ; TP : péninsule de Thessalonique ; NAT : fosse égéenne (‘North Aegean Trough’). D’après Pérouse *et al.* (2012).

2.2 Contexte tectonique actuel et déformation active

Le domaine égéen comprend la mer Egée avec les Cyclades, les zones côtières de la Grèce et de la Turquie (Anatolie). Cette région est limitée au sud par le front de subduction hellénique (subduction active depuis la fin du Crétacé) et au nord par la faille décrochante dextre nord anatolienne (Figure 2.3). Le contexte tectonique actuel de la région égéenne est le résultat du couplage entre subduction et extension arrière-arc depuis l'Eocène moyen (Le Pichon & Angelier, 1979; Jolivet *et al.*, 1994; Armijo *et al.*, 1996, 1999, 2002). Actuellement, la plaque africaine est subduite sous la plaque européenne (Argus *et al.*, 1989). La convergence nord-sud de la plaque nubienne (Afrique) sous l'Europe est estimée à 6 mm/an alors que le front de subduction se retire vers le sud-ouest à une vitesse de 25 mm/an (McClusky *et al.*, 2000). La croûte océanique mésozoïque de la plaque africaine a presque complètement été subduite et elle est localement préservée dans le prisme de subduction. L'arc de subduction hellénique devient une zone de collision entre l'Afrique et l'Europe. Il contourne la chaîne des Hellénides (au sud de la Crète), où la croûte continentale est épaissie et réactivée au cours de l'extension post-orogénique (Miocène). A l'ouest du domaine égéen, la faille majeure de Céphalonie (KF, Figure 2.3) recoupe le panneau plongeant et participe à la collision continentale, toujours active au nord de la Grèce. Cette faille décrochante dextre, active depuis 6–8 Ma, présente un déplacement en surface de 100–120 km (Royden & Papanikolaou, 2011).

La région égéenne est subdivisée en plusieurs micro-plaques dont le nombre et les limites varient selon les auteurs et les données GPS disponibles (McKenzie, 1972; McKenzie & Jackson, 1983; Taymaz *et al.*, 1991; Le Pichon *et al.*, 1995; Armijo *et al.*, 1996; McClusky *et al.*, 2000; Goldsworthy *et al.*, 2002; Nyst & Thatcher, 2004). D'après Nyst & Thatcher (2004), la région égéenne est subdivisée en quatre micro-plaques (Figure 2.4) que sont :

- le bloc anatolien à l'est,
- le sud de Marmara limité au nord par la faille nord-anatolienne (NAF),
- la Grèce centrale et le bloc égéen incluant le Péloponnèse,
- la mer Egée.

La collision de la plaque arabique avec l'Eurasie à une vitesse de 20 mm/an cause l'extrusion de l'Anatolie vers l'ouest (Figure 2.3). Le mouvement du bloc anatolien de 15 mm/an vers l'ouest est principalement accommodé par la faille décrochante dextre nord-anatolienne. Cette dernière est active dans la région depuis environ 10–13 Ma (Dewey *et al.*, 1979; Le Pichon *et al.*, 1995, 2003). Les mesures GPS montrent que la vitesse actuelle le long de cette faille est de 23–30 mm/an (McClusky *et al.*, 2000; Reilinger *et al.*, 2006, 2010). L'Anatolie se découple de l'Europe par une rotation anti-horaire et se déplace vers l'ouest. Le bloc anatolien pousse le bloc égéen au dessus de la plaque africaine à une vitesse de 35 mm/an. Ce phénomène entraîne le retrait du front de subduction hellénique et de l'arc volcanique vers le sud.

Le Pichon *et al.* (1995) ont suggéré une ouverture du rift de Corinthe par le mouvement

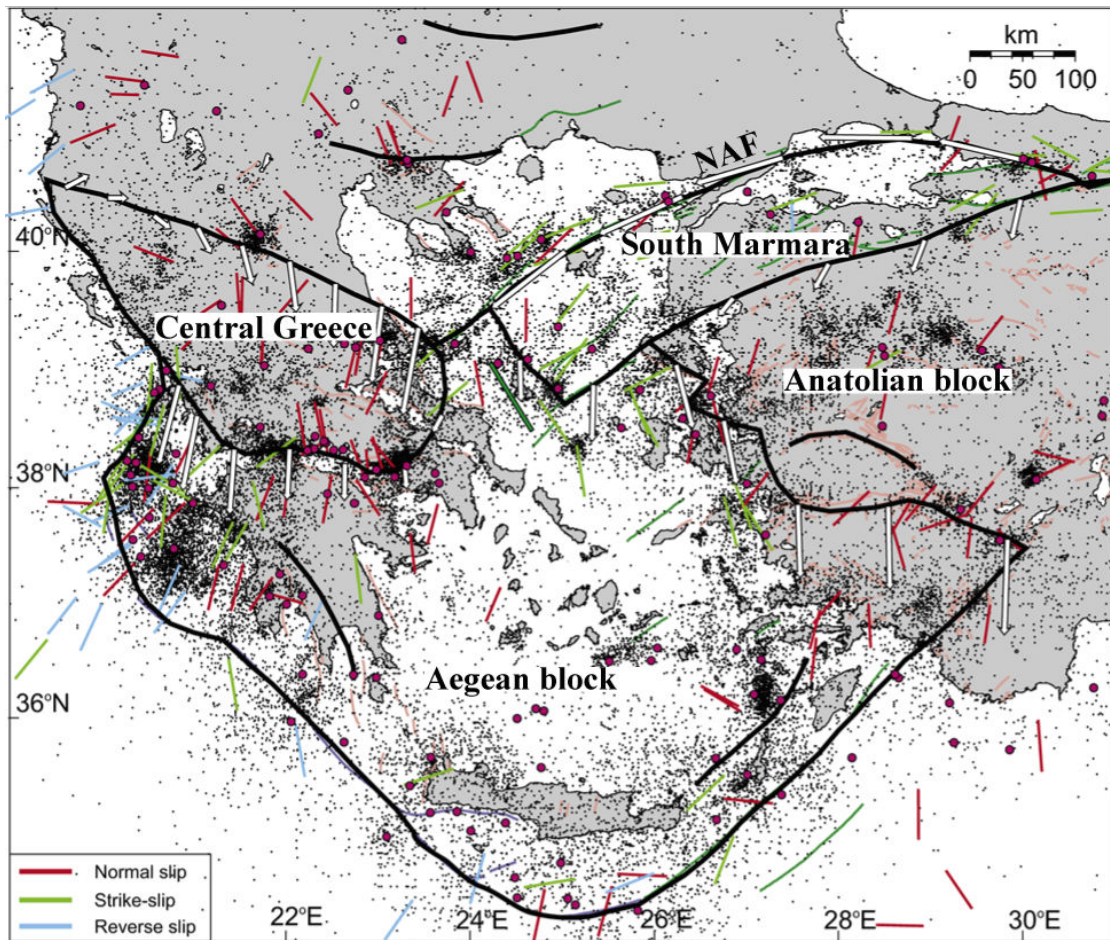


FIGURE 2.4 – Carte de la région égéenne montrant les limites des microplaques interprétées à partir des données GPS, la distribution des failles actives majeures et la localisation des séismes $M > 6$ (entre 1900 et 2000) (Nyst & Thatcher, 2004).

de blocs rigides entre le Péloponnèse et la Grèce centrale (rotation anti-horaire du bloc du Péloponnèse par rapport à la rotation horaire de la Grèce Centrale). Les mesures GPS montrent une rotation anti-horaire du bloc du Péloponnèse par rapport à la Grèce Centrale mais horaire par rapport à l'Europe fixe.

Certains auteurs suggèrent que le rift de Corinthe est l'expression récente de l'extension arrière-arc en mer Egée (Doutsos & Kokkalas, 2001; Nyst & Thatcher, 2004; Jolivet *et al.*, 1994; Jolivet, 2001; van Hinsbergen & Schmid, 2012). D'autres auteurs (Dewey *et al.*, 1979; Armijo *et al.*, 1996, 1999; Le Pichon *et al.*, 2003) proposent d'intégrer le rift de Corinthe à une zone diffuse de cisaillement (*Central Hellenic shear zone*) entre la faille nord-anatolienne et la faille de Céphalonie (Papanikolaou & Royden, 2007). La combinaison des différents modèles est possible pour expliquer l'ouverture du rift de Corinthe. Cependant, les mécanismes d'ouverture sont complexes et sont encore largement débattus actuellement. La faille Nord-Anatolienne disparaît-elle en Mer Egée ou se connecte-elle jusqu'à la faille de Céphalonie ? Cette possible connexion forme-t-elle une structure aveugle en surface et active en profondeur ?

Récemment, les travaux de restauration de van Hinsbergen & Schmid (2012) proposent la jonction de la faille de Céphalonie avec la faille Nord-Anatolienne via le système de failles décrochantes dextres au nord du rift de Corinthe et traversant la Grèce Centrale. La déformation associée à l'ouverture du bassin de Corinthe correspondrait alors à la continuité de l'extension égéenne plutôt qu'à une zone de transfert entre la faille Nord-Anatolienne et la faille de Céphalonie.

2.3 Structuration du rift de Corinthe

2.3.1 Histoire des Hellenides externes

La chaîne hellénique résulte de la convergence entre l'Apulie¹ et l'Eurasie. Au début du Jurassique, l'océan Vardar et le bassin de Pinde sont séparés par le micro-continent pélagonien. Depuis le Jurassique, la subduction continentale de la plaque apulienne a donné lieu à une série de chevauchements à vergence sud ouest (Aubouin *et al.*, 1963; Jacobshagen *et al.*, 1978; Papanikolaou, 1993) et à un empilement de nappes (d'une dizaine de kilomètres d'épaisseur) depuis l'Eocène jusqu'au Miocène inférieur. Cinq domaines paléogéographiques structurent les Hellenides externes (Figure 2.5). D'ouest en est, les nappes sont stratigraphiquement plus jeunes. (Figure 2.6A).

Dans le nord du Péloponnèse, le long de la marge sud du golfe de Corinthe, trois unités

1. Microcontinent rattaché à l'Afrique au début du Mésozoïque, limité au nord par la Téthys, et qui est venu se souder à l'Europe en formant les Alpes pendant le Cénozoïque. Aujourd'hui la plaque apulienne (aussi appelée plaque hellénique ou adriatique) comprend la péninsule italienne (sauf la Sicile et la Sardaigne), la mer Adriatique, l'ex-Yougoslavie, la Grèce et le sud-ouest de la Turquie. La limite nord de la plaque apulienne est marquée par la faille active nord-anatolienne Marthaler (2001).

tectono-stratigraphiques sont principalement exposées (dans l'ordre stratigraphique) : la nappe Phyllite-Quartzite, la nappe Gavro-Tripolitsa et la nappe du Pinde. L'épaisseur de ces unités pré-rift est de 8–11 km à l'Est et de 2–5 km à l'ouest du Péloponnèse (Ghisetti & Vezzani, 2005) (Figure 2.5C).

La **nappe ionnienne** ou "**Plattenkalk**" correspond à l'unité tectonique inférieure parmi les unités reconnues dans le Péloponnèse. Cette nappe affleure principalement à l'ouest de la Grèce continentale et au sud du Péloponnèse. Elle comprend des dépôts triasiques évaporitiques, une succession carbonatée jurassique-crétacée et une série turbiditique d'âge Oligocène-Miocène au sommet (Seidel *et al.*, 1982).

La **nappe des Phyllades** est reconnue principalement en Crète et au sud du Péloponnèse (*Phyllite-quartzite nappe* ; 2.5). Cette nappe affleure localement au sud du rift de Corinthe, dans la fenêtre de Zarouchla (Figures 2.1 et 2.5). Cette nappe est le résultat de l'exhumation le long d'un détachement à la base de la nappe de Gavrovo-Tripolitsa (Trotet *et al.*, 2006; Jolivet *et al.*, 2010). La nappe des Phyllades (1500 à 2000 m d'épaisseur) est composée de quartzites et de phyllites enregistrant un métamorphisme de haute pression et basse température affectant des roches évaporitiques, détritiques, volcaniques et carbonatées (Doutsos & Poulimenes, 1992). Le protolithe de cette série est considéré d'âge Carbonifère à Trias moyen (Thiébault & Triboulet, 1984). L'âge du métamorphisme est daté entre la fin de l'Oligocène et le début du Miocène en Crète, en lien avec l'extension post-orogénique. Le découplage de cette nappe marque un contraste rhéologique majeur et joue un rôle important dans la réactivation des structures (issues de l'extension en région égéenne à l'Oligocène-Miocène).

La **nappe Gavrovo-Tripolitsa** est exposée à l'ouest de la Grèce continentale, dans l'ensemble du Péloponnèse et en Crète. Cette nappe est chevauchée par la nappe de Pinde et se découple de la nappe des Phyllades par une zone de détachement. La base de la nappe contient des séries clastiques et volcaniques d'âge Permien à Trias supérieur (*Tyros Beds*) (Fytrolakis, 1971; Lallemand, 1984). La nappe Gavrovo-Tripolitsa comprend des dépôts de plateformes carbonatées du Trias supérieur à l'Eocène supérieur (1000 à 1500 mètres d'épaisseur) et des turbidites de bassin d'avant pays datées de l'Oligocène au Miocène (100 mètres environ) (De Wever, 1975; Fleury, 1980; Jacobshagen, 1987). La nappe Gavrovo-Tripolitsa passe latéralement à la zone ionienne (plateforme proximale d'une marge de rift) et à d'autres unités continentales au nord-ouest.

La **nappe du Pinde** (ou Pinde-Olonos dans le Péloponnèse) s'étend du Péloponnèse à la Grèce continentale et l'Albanie. Cette nappe chevauche la nappe de Gavrovo-Tripolitsa. La zone paléogéographique du Pinde correspondait à un bassin profond non océanisé de 500 km de large environ, en contexte de marge passive entre les microcontinents de l'Apulie et la Péloganie. La succession sédimentaire est datée du Trias supérieur à l'Eocène (Fleury, 1980; Pe-Piper & Piper, 1984). Elle peut localement atteindre 2000 mètres d'épaisseur (Pe-Piper & Piper, 1984; Degan & Robertson, 1998). La succession stratigraphique de la nappe du Pinde dans le nord du Péloponnèse est résumée sur la figure 2.6B. Cette unité est principalement composée de calcaires

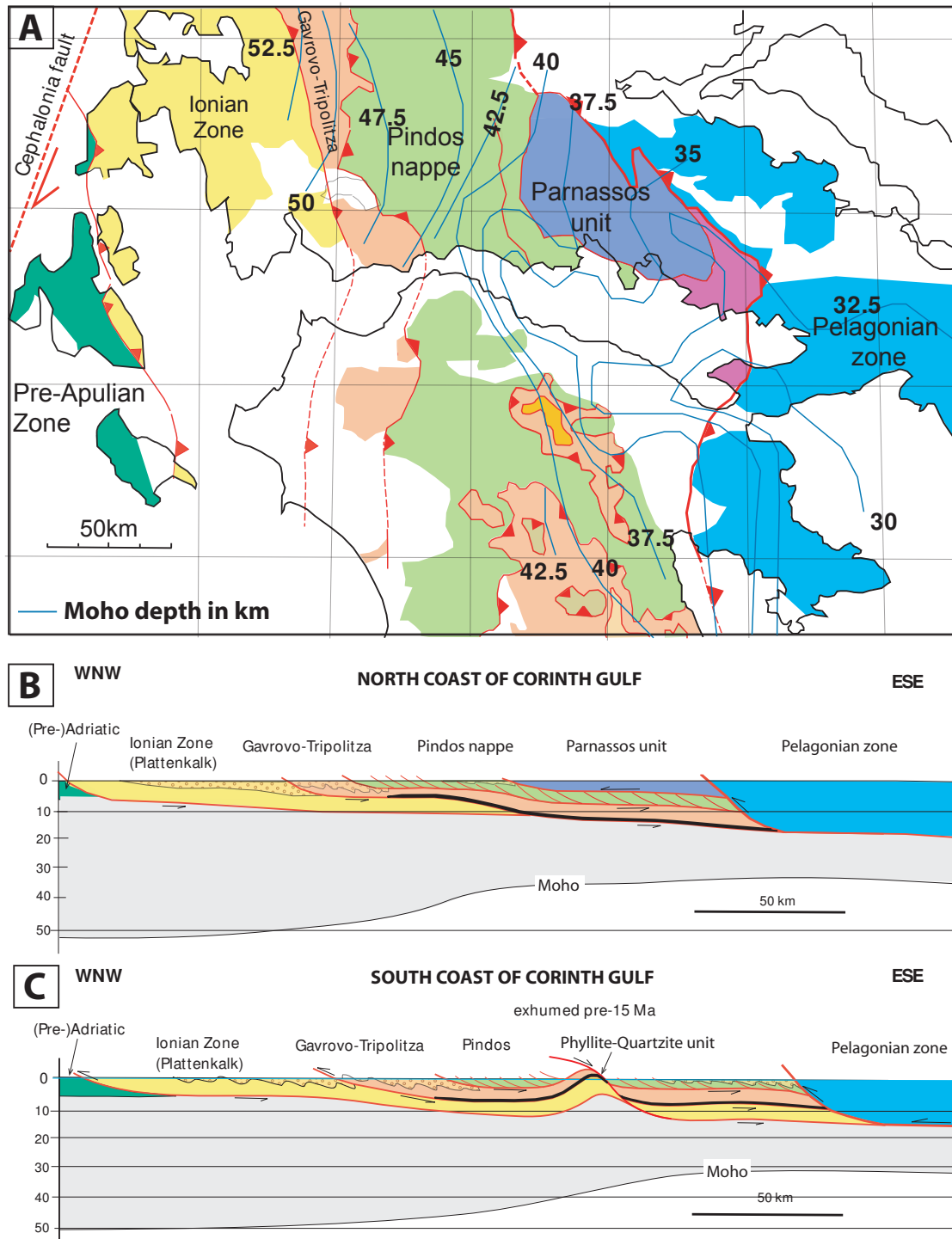


FIGURE 2.5 – **A** : Carte simplifiée des nappes helléniques dans la région du golfe de Corinthe. Les isopaques en bleu représentent la profondeur du Moho (d'après Sachpazi *et al.*, 2007). **B** et **C** : Coupes crustales orientées ONO-ESE le long de la marge nord et sud du rift de Corinthe. Les nappes des Phyllades (Phyllite-Quartzite) et Gavrovo-Tripolitza sont exhumées au nord du Péloponnèse dans la fenêtre tectonique de Feneos (**C**)

hémipélagiques déposés en milieu marin profond, de cherts et des radiolarites (Aalénien à Tithonien). Au Crétacé supérieur, le dépôt de carbonates pélagiques (calcaires "en plaquettes") se

généralise. Ces derniers peuvent localement atteindre une épaisseur de 1500 mètres.

A partir de la fin du Crétacé supérieur (Maastrichien à Eocène), la sédimentation turbiditique (de type *flysch*) provient du microcontinent pélagonien (nappe ophiolitique à vergence ouest) chevauchant la nappe du Pinde (Aubouin *et al.*, 1963; Fleury, 1980; Piper, 2006). Ces dépôts turbiditiques enregistrent la phase terminale de fermeture du bassin du Pinde à la fin de l'Eocène, il y a 34–37 Ma (Stampfli & Borel, 2004). Les turbidites furent incorporées dans un prisme d'accrétion d'âge Eocène (Lutétien à Priabonien) dans le Péloponnèse central mais elles furent principalement déposées dans un bassin d'avant-pays au nord de la Grèce (fin Paléocène à Oligocène) (Zelilidis *et al.*, 2002).

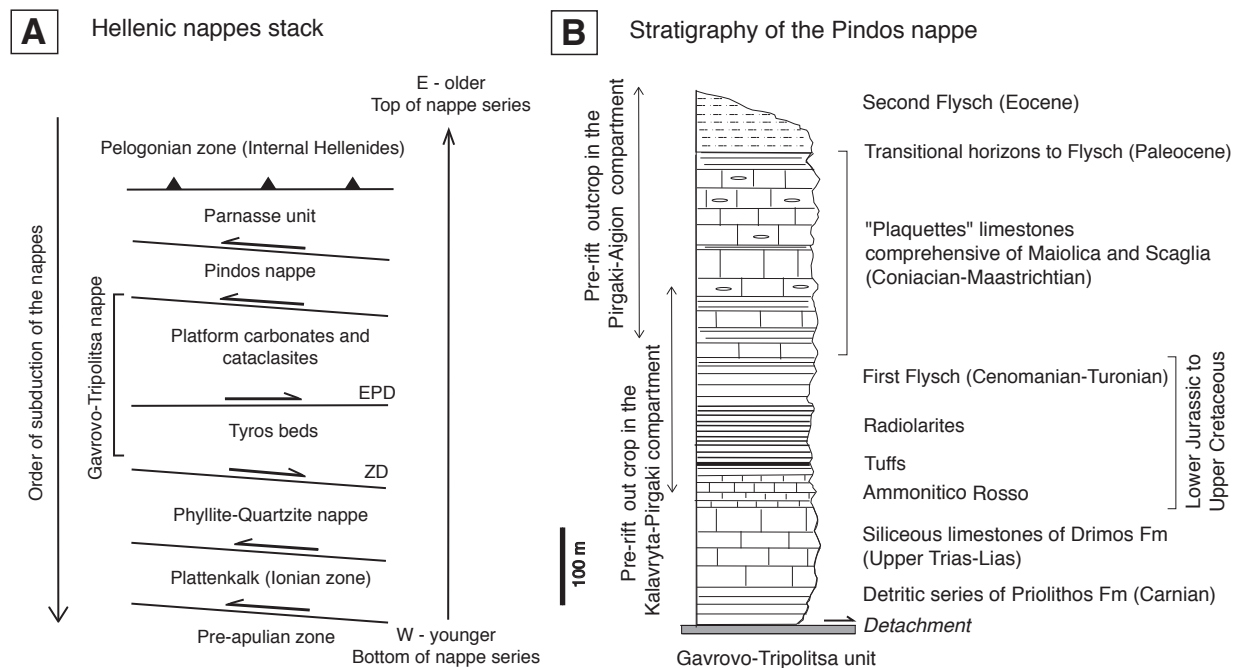


FIGURE 2.6 – (A) Schéma simplifié de l'empilement des nappes helléniques externes. ZD : Zarouchla detachment ; EPD : East Peloponnese detachment. (B) Litho-stratigraphie de la nappe de Pinde-Olonos observée le long de la marge sud du rift de Corinthe (d'après Degnan & Robertson, 1998; Aubouin, 1959; Dercourt *et al.*, 1973; Fleury, 1980). Fm : Formation (dessiné à partir de la synthèse bibliographique).

La nappe du Pinde est recoupée obliquement par les failles orientées ouest-est structurant le rift de Corinthe. La caractérisation des différentes lithologies de la nappe du Pinde est essentielle car cette nappe correspond à la source principale des sédiments syn-rift étudiés. Les clasts de grès issus des turbidites contiennent des grains de quartz, minéral cible pour la détermination des âges d'enfouissement ^{26}Al et ^{10}Be .

La **nappe du Parnasse** affleure en Grèce continentale et au nord-ouest du Péloponnèse. Cette nappe chevauchant la nappe du Pinde correspond à l'unité supérieure des nappes helléniques externes. Elle comprend des calcaires néritiques (Trias à Crétacé supérieur) recouverts par des marnes paléogènes et des turbidites clastiques éocènes.

Un chevauchement majeur sépare les Hellénides externes et internes. Plus à l'est, la **zone Pélagonienne** affleure en Grèce continentale et à l'est du Péloponnèse (région de l'Attique). Cette zone complexe correspond au socle hercynien recouvert par les roches paléozoïques et mésozoïques, ainsi que des nappes ophiolitiques du Jurassique supérieur. La zone pélagonienne est interprétée comme un micro-continent au sein de la Néotéthys (Robertson *et al.*, 1996).

2.3.2 Histoire tardi-cénozoïque, extension égéenne

Dans la région égéenne (Cyclades notamment), l'extension arrière-arc Nord-Sud a débuté entre 45 et 35 Ma (fin Eocène-début Miocène) (Le Pichon & Angelier, 1979). La direction de l'extension est globalement orienté N030–N050. Le début de l'extension est synchrone des derniers chevauchements actifs dans le Péloponnèse et de la fermeture du bassin du Pinde à l'Eocène moyen. L'équivalence stratigraphique du domaine du Pinde dans les Cyclades correspond aux Schistes Bleus qui ont été exhumés à l'Eocène supérieur par les "*Metamorphic Cores Complexes*" (MCC) dans la région de Rhodes (Figure 2.7). Pendant cette période, la compétition entre compression et extension au cours de l'empilement des nappes helléniques induit leurs découplages et leurs exhumations.

L'extension égéenne est expliquée par (1) le retrait du panneau plongeant vers le sud-ouest et le ralentissement de la subduction de la lithosphère africaine (Papazachos & Comninakis, 1971; McKenzie, 1978a; Jackson & McKenzie, 1984; Le Pichon & Angelier, 1979, 1981; Doutsos *et al.*, 1988; Meulenkamp *et al.*, 1988, 1994), (2) l'effondrement gravitaire post-orogénique de la croûte continentale épaissie (entre 30 et 50 km) et (3) l'exhumation des roches de hautes pressions-basses températures issu du chenal de subduction (Jolivet *et al.*, 1994; Jolivet & Patriat, 1999; Jolivet *et al.*, 2004). Les modèles tomographiques mettent en évidence une lithosphère peu épaisse sous la région égéenne et une influence du flux asthénosphérique dans la déformation crustale (Jolivet *et al.*, 2013; Piromallo & Morelli, 2003).

Depuis le Miocène, le retrait du panneau plongeant sous la région égéenne a été mis en évidence par la migration de la distension vers le sud (Figure 2.9). Les travaux de Royden & Papanikolaou (2011) mettent en évidence un ralentissement de la subduction à partir de -50 Ma environ jusqu'à la fin de l'Eocène (40–60 mm.a⁻¹ à 25–35 mm.a⁻¹). Un ralentissement majeur (5–12 mm.a⁻¹) est documenté au Miocène (~15 Ma) en lien avec le retrait du panneau plongeant. Depuis 35 Ma, le front de subduction hellénique a migré vers le sud-ouest d'une distance de 550–600 km au nord des Hellénides et de 750–800 km au sud des Hellénides (Crète) (Jolivet, 2001; Faccenna *et al.*, 2003). La migration de l'arc volcanique vers le sud en lien avec le retrait du panneau plongeant est estimée à ~100 km et à 300–350 km au nord et au sud des Hellénides respectivement (Papanikolaou, 1993). La segmentation du panneau plongeant par la faille de Céphalonie (décrochement dextre) apparaît fin Miocène-début Pliocène (il y a 5–7 Ma) et sé-

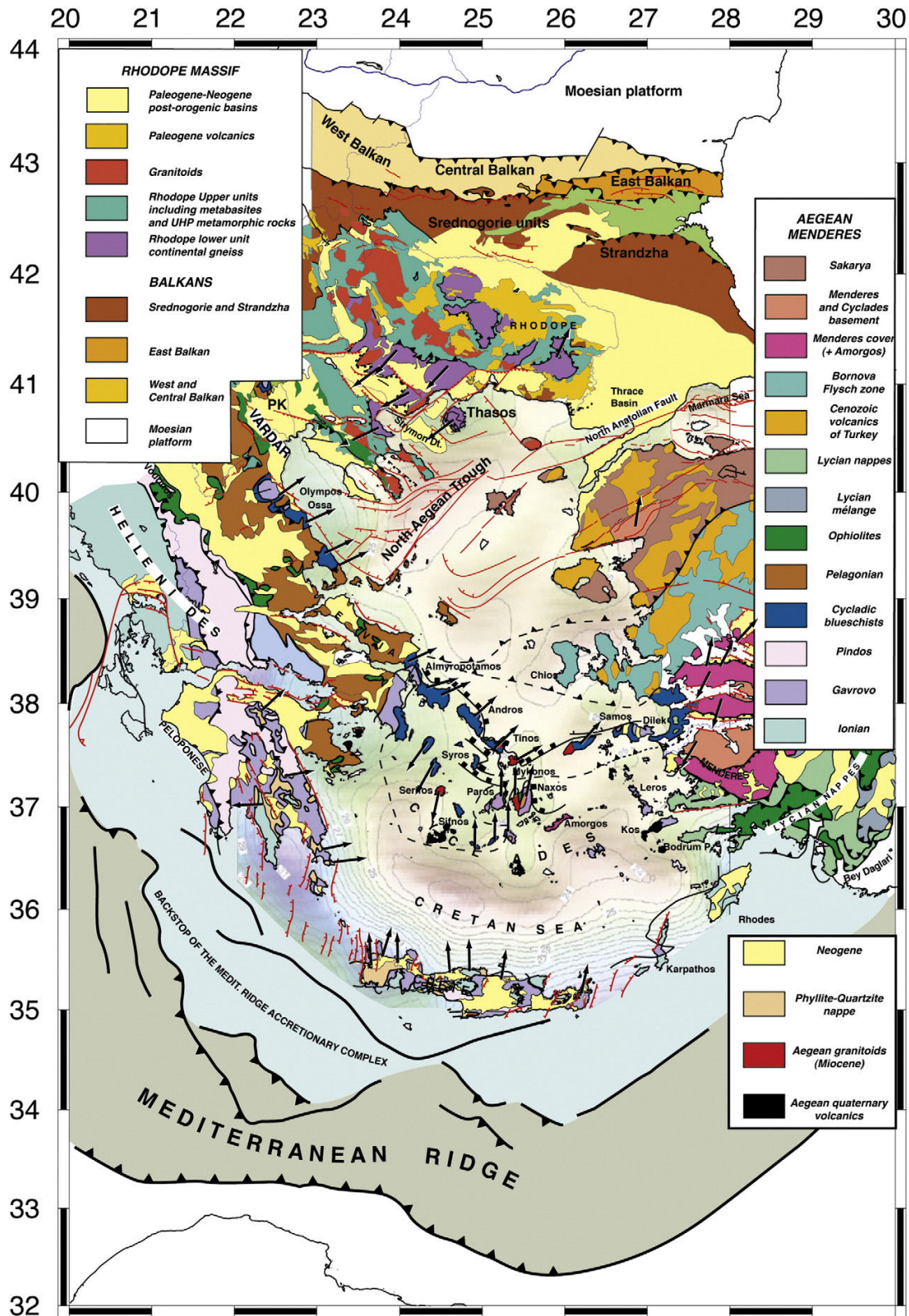


FIGURE 2.7 – Carte tectonique générale de la Méditerranée orientale incluant la région égéenne, le massif Rhodope, les Menderes et les Balkans (d’après Jolivet *et al.*, 2013).

pare la partie septentrionale et méridionale des Hellénides : subduction active au sud et collision

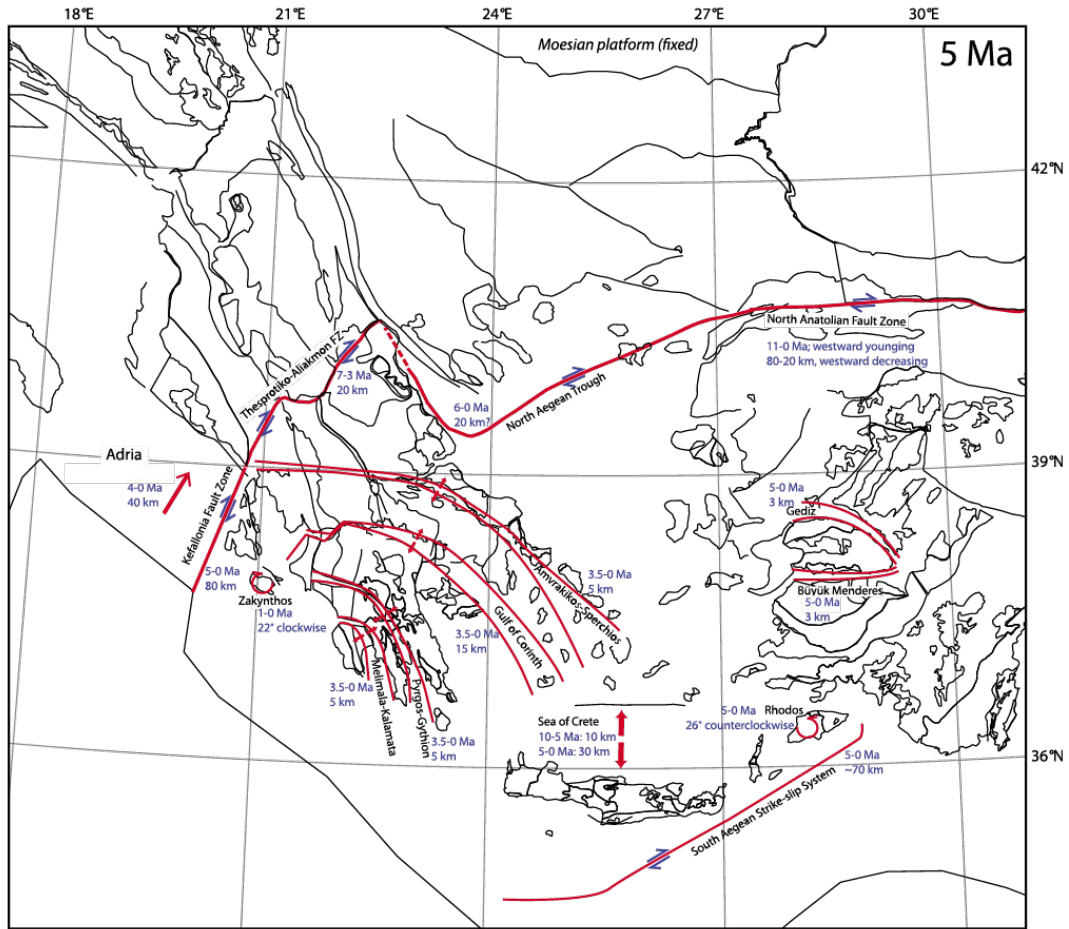


FIGURE 2.8 – Reconstruction paléogéographique de la région égéenne à -5 Ma. Les valeurs en km correspondent au déplacement accommodé par les structures actives depuis 5 Ma (van Hinsbergen & Schmid, 2012).

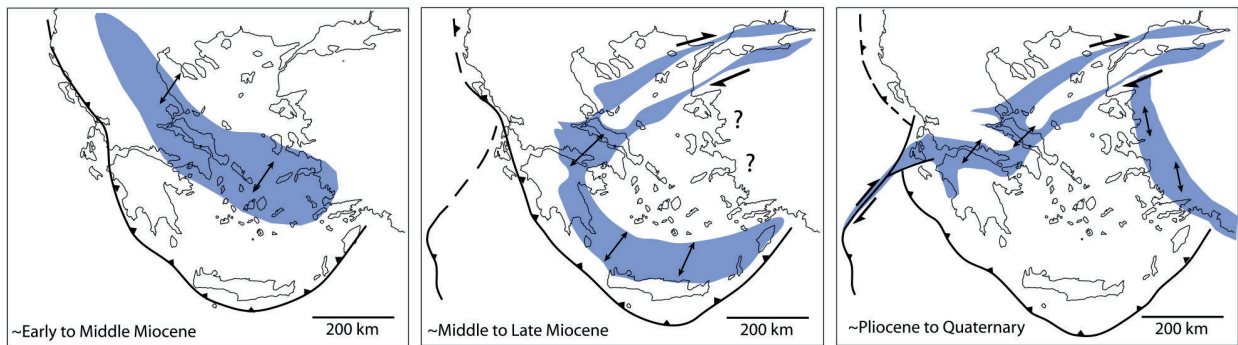


FIGURE 2.9 – Migration de la déformation au cours de l’extension égéenne depuis le Miocène. La propagation de la faille nord anatolienne et la segmentation du front de subduction par la faille de Céphalonie permet de concentrer la déformation au niveau du rift de Corinthe (*Central Hellenic Shear Zone*) (d’après Royden & Papanikolaou, 2011).

continentale au nord (Figure 2.9).

Les structures helléniques sont réactivées au cours de l’extension égéenne. Dans les Cy-

clades, l'exhumation des MCC est localisée le long d'une zone de cisaillement ductile. La nappe des Phyllades est exhumée le long du détachement crétois (Fin Oligocène - début Miocène) qui se prolonge jusqu'au sud du Péloponnèse et en Crète (Jolivet & Faccenna, 2000). L'exhumation de cette nappe enregistre une direction d'extension N030. Au sud du rift de Corinthe, l'exhumation de la nappe des Phyllades dans la fenêtre tectonique de Zarouchla (Figure 2.1) correspond au même détachement réactivé entre le Miocène moyen et le Pliocène inférieur (*East Peloponnesus Detachment* défini par Papanikolaou & Royden (2007). D'après Jolivet *et al.* (2010), la fenêtre de Zarouchla est associée à l'exhumation d'un MCC. Ce détachement est ensuite recoupé par les failles associées à l'ouverture du rift de Corinthe (Figure 2.10). La continuité de ce détachement est documentée par Papanikolaou *et al.* (2009) sur la marge nord du rift avec le détachement de Itea-Amfissa (Figure 2.10). Les structures extensives majeures à la fin du Miocène sont orientées NNO-SSE et sont recoupées obliquement par les structures du rift de Corinthe (ouest-est). En faisant l'hypothèse que cette structure traverse le Péloponnèse et le golfe de Corinthe, ce système de détachement majeur a pu jouer un rôle important au cours de l'initiation du rift de Corinthe. L'influence d'une telle structure héritée sur les processus de propagation et de connexion des failles sera discutée dans le chapitre 5.

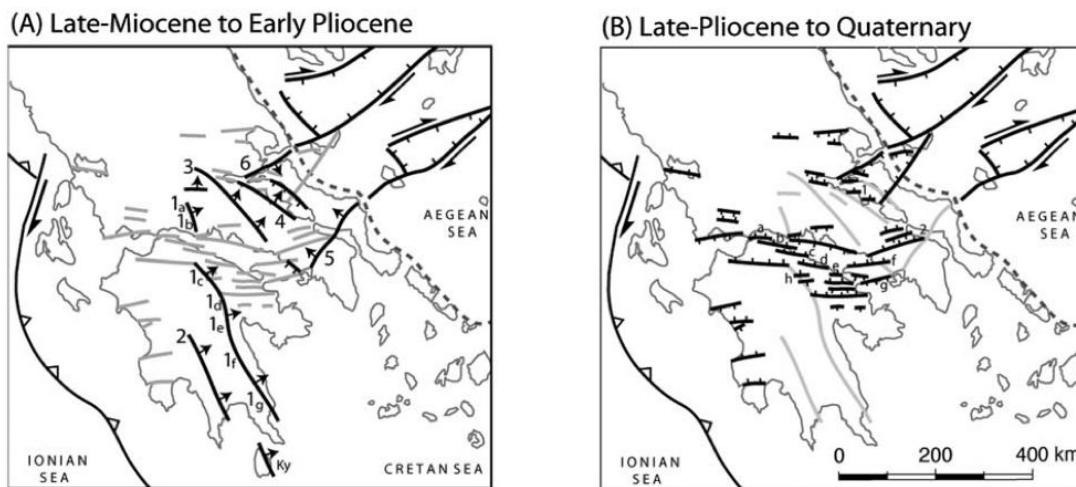


FIGURE 2.10 – Carte simplifiée du domaine égéen et des structures extensives majeures à la fin du Miocène (A) et depuis la fin du Pliocène (B). Les flèches indiquent la direction de pendage des détachements. Les structures actives sont tracées en noir. 1 : *East Peloponnesus detachment*, 2 : (d'après Papanikolaou & Royden, 2007).

2.4 Géométrie et modèles d'évolution du rift de Corinthe

Les blocs inactifs et soulevés le long de la marge sud du golfe de Corinthe représentent un véritable laboratoire naturel pour reconstituer l'évolution du rift. Les structures et la géométrie des dépôts syn-rift le long de la marge sud ont permis de proposer plusieurs modèles d'évolution.

Même si ces modèles sont encore largement débattus, il est communément admis que la déformation a migré vers le nord au cours du rifting. Les travaux les plus notables s'intéressent aux causes de l'asymétrie du rift, à la migration de l'activité des failles, au soulèvement le long de la marge sud, à la variabilité spatio-temporelle du taux d'extension et au couplage entre tectonique et sédimentation.

La marge sud est en soulèvement alors que la marge nord subside (Lykousis *et al.*, 1998). La bordure sud du rift est marquée par un saut topographique important entre le littoral et l'arrière pays, créé par l'activité des failles bordières. La limite du rift de Corinthe ne correspond pas uniquement à la morphologie actuelle du golfe mais s'étend plus au sud sur une trentaine de kilomètres, où les blocs de failles sont inactifs et soulevés. Au cours de l'évolution du rift, le système de failles a migré vers l'axe du rift et les différentes phases de migration des failles sont enregistrées par les séries sédimentaires syn-rift (Goldsworthy & Jackson, 2001; Ford *et al.*, 2013). Au contraire, la marge nord n'enregistre presque pas de dépôts syn-rift et la migration de l'activité tectonique est enregistrée par quelques failles antithétiques à pendage sud.

Le rift de Corinthe est considéré comme asymétrique. La déformation est principalement localisée le long de la marge sud du golfe, par un système de failles "en échelon" d'orientation N090–N100, et à pendage vers le nord (Figure 2.1B). Les profils sismiques *offshore* montrent que les dépocentres majeurs se situent le long de ces failles bordières sud (Papatheodorou & Ferentinos, 1993; Stefatos *et al.*, 2002; Moretti *et al.*, 2003; Bell *et al.*, 2008, 2009; Taylor *et al.*, 2011; Nixon *et al.*, 2016). À l'extrémité ouest du rift, entre le détroit de Patras et Diakopto, le rift devient plus étroit, plus jeune, et les failles majeures à pendage nord et sud forment un graben symétrique (McNeill *et al.*, 2005; Bell *et al.*, 2008; Beckers *et al.*, 2015; Nixon *et al.*, 2016). Les travaux de restauration à partir de l'interprétation des profils sismiques indiquent aussi la présence d'un rift symétrique pendant les premiers stades du rifting (Stefatos *et al.*, 2002; Moretti *et al.*, 2003; Bell *et al.*, 2008, 2009; Taylor *et al.*, 2011; Nixon *et al.*, 2016).

À l'échelle régionale et crustale, les modèles d'évolution du rift de Corinthe cherchent à comprendre (i) la cinématique des failles et les mécanismes d'extension en lien avec la géométrie du panneau plongeant, (ii) la propagation de la faille nord-anatolienne vers le sud-ouest ou encore (iii) l'héritage structural de la chaîne Hellénique. Les données gravimétriques permettent d'estimer la profondeur du Moho dans la région de Corinthe (Makris, 1978; Tiberi *et al.*, 2001; Sachpazi *et al.*, 2007). Les anomalies gravitaires de la croûte continentale sont le résultat de la compression hellénique et de la distension égéenne depuis le Miocène. La profondeur du Moho passe progressivement de 30 à 40 km, depuis la partie ouest vers la partie est du golfe de Corinthe (Figure 2.5). Cette diminution vers l'est est cohérente avec le réajustement isostatique de la croûte épaissie (empilement des nappes qui a donné lieu à un épaississement crustal de 10 km environ; Tiberi *et al.*, 2001; Sachpazi *et al.*, 2007) et avec la diminution de la topographie moyenne dans la région (Makris, 1978). Un amincissement crustal de 4–6 km est observé au nord du golfe de Corinthe, en Grèce centrale.

D’après [Tiberi *et al.* \(2000\)](#), une zone crustale amincie est localisée au nord du rift (Figure 2.11). D’après les auteurs, ce décalage de la zone amincie par rapport à l’axe du rift mettrait en évidence une extension en cisaillement simple dans la partie est du rift. Cela permettrait aussi d’expliquer l’asymétrie du rift de Corinthe et la présence d’une structure à pendage faible vers le nord traversant la zone sismogénique. [Tiberi *et al.* \(2001\)](#) interprètent les zones d’amincissement crustal comme étant issues de la réactivation des structures héritées pendant l’extension égéenne qui auraient favorisé de l’ouverture du rift de Corinthe. De nombreux autres travaux se sont attachés à comprendre les structures profondes du rift et à faire le lien avec la géométrie des failles et la déformation observée en surface.

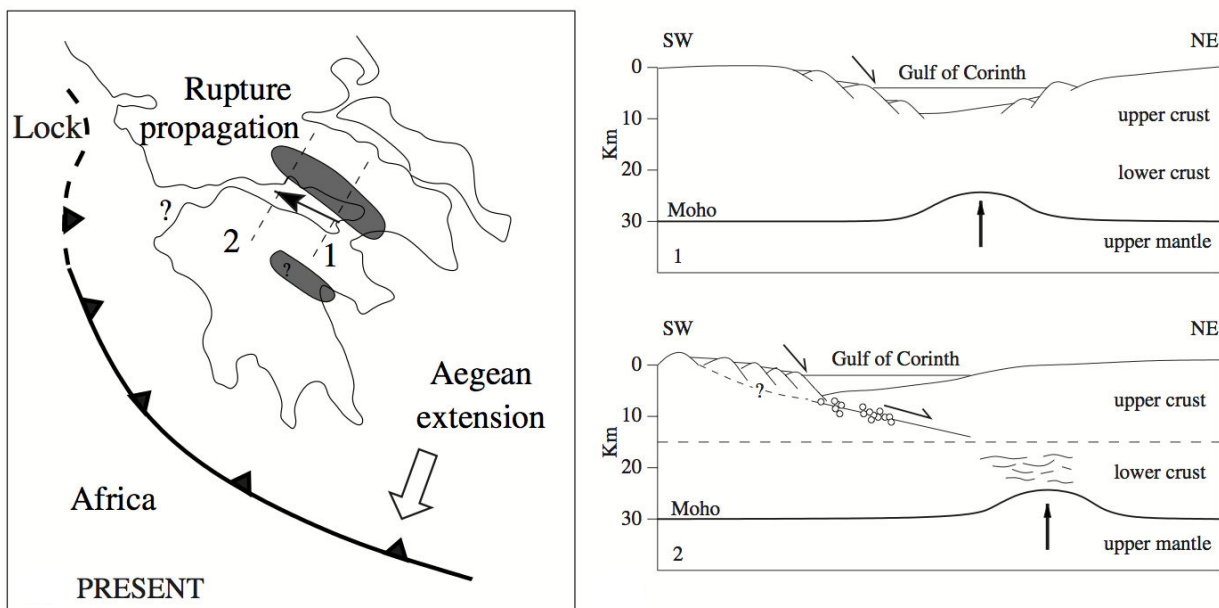


FIGURE 2.11 – Location de la zone d’amincissement crustale maximale à l’est du rift de Corinthe. Le décalage de cette zone crustale amincie par rapport à l’axe du rift est cohérent avec l’idée d’une faille majeure à pendage faible à 12–15 km de profondeur (d’après [Tiberi *et al.*, 2001](#))

2.4.1 Modèle de détachement

[Melis *et al.* \(1989\)](#) proposent pour la première fois que les failles bordières des golfes de Patras et de Corinthe (partie ouest) présentent une géométrie listriques et s’horizontalisent en profondeur jusqu’à la base de la croûte supérieure. Sur la base de ce modèle, certains auteurs suggèrent la présence d’un détachement majeur le long duquel s’enracinent les failles majeures observées en surface ([Rigo *et al.*, 1996](#); [Sorel, 2000](#); [Flotté *et al.*, 2005](#); [Jolivet *et al.*, 2010](#)) (Figure 2.12A). Ce détachement est prolongé sous le golfe de Corinthe avec un pendage de 15–20°. A l’affleurement, la présence de ce détachement est mise en évidence par une zone de cataclasites (20 mètres d’épaisseur) et par des plans striés à faible pendage (N124–24°N) dans la partie nord du massif de Khelmos (Figure 2.12).

La localisation des mécanismes au foyer des séismes et les essaims de microsismicité (entre 5 et 12 km de profondeur) sont organisés selon une surface à pendage faible (Rigo *et al.*, 1996; Lyon-Caen *et al.*, 2004; Bernard *et al.*, 2006; Lambotte *et al.*, 2014) (Figures 2.2 et 2.14). Par projection sous le golfe, ce détachement reste trop peu profond pour atteindre la base de la zone sismogénique située entre 8 et 12 km (Figure 2.14). Bien que le modèle de détachement soit très critiqué, le détachement de Khelmos met en évidence l'importance d'une structure à pendage faible qui ont pu jouer un rôle important au cours du développement précoce du rift de Corinthe.

Les profils sismiques mettent aussi en évidence la présence de failles actives dont la géométrie est biplanaire (Figure 2.13; Clément *et al.*, 2004; Sachpazi *et al.*, 2003; Taylor *et al.*, 2011). Cependant, il n'est pas non plus possible de prolonger ces failles jusqu'à la base de la zone sismogénique (Figure 2.14). Les travaux récents de Lambotte *et al.* (2014) rejettent l'interprétation d'un détachement majeur à l'ouest du rift de Corinthe. D'après Lambotte *et al.* (2014), les variations spatio-temporelles de la sismicité dans la partie ouest du rift (Figures 2.14 et 2.15) sont expliquées par la migration et les variations de pression de fluides. La zone sismogénique à faible pendage vers le nord résulterait plutôt de la genèse d'un détachement non connecté à la croûte ductile. Ce détachement est considéré comme étant "en cours d'activation" et n'aurait pas (encore ?) d'effet sur l'ouverture du rift de Corinthe.

L'exhumation des Phyllades au sud du rift le long du détachement de Zarouchla met en évidence l'importance de l'héritage et de l'hétérogénéité crustale (Figures 2.1 et 2.5). Le faciès métamorphique à schistes bleus de la nappe des Phyllades marque un contraste rhéologique important et une zone de faiblesse dans les nappes helléniques externes. Les changements de contraintes différentielles en lien avec la forte pression de pores peut notamment être à l'origine d'une zone de cisaillement ductile en profondeur. Cette zone de détachement potentielle a même été interprétée comme étant un MCC en cours d'initiation, analogue à ceux observés dans les Cyclades (Chéry, 2001; Jolivet *et al.*, 2010; Jolivet, 2001).

D'après les modèles thermo-mécaniques 2D de Le Pourhiet *et al.* (2003, 2004, 2006), la nappe des Phyllades correspond à une zone de faiblesse à l'origine de la formation de détachements. Néanmoins, la corrélation de ces modèles avec la sismicité à l'ouest du rift n'est pas cohérente avec les données en surface (Le Pourhiet *et al.*, 2004). Le détachement de Zarouchla présente une direction de N120° et un pendage vers le nord-est. Si le découplage de la nappe des Phyllades est à l'origine d'un détachement en profondeur, ce dernier doit être localisé dans la partie centrale et est du rift, ce qui n'est pas documenté d'après les travaux actuels.

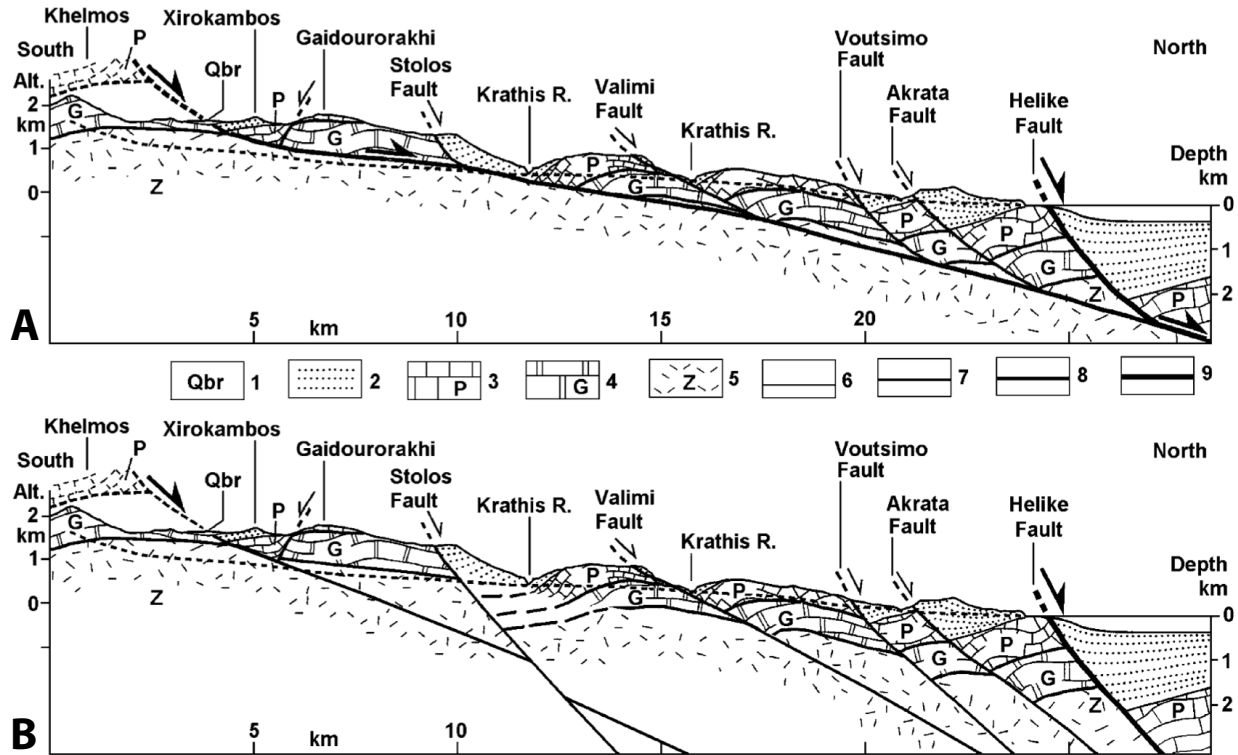


FIGURE 2.12 – Coupes N-S de la marge sud du rift de Corinthe, le long de la vallée de Krathis illustrant deux modèles géométriques des failles (d’après [Westaway, 2002](#)). (A) Modèle de détachement d’après [Sorel \(2000\)](#). (B) Modèle sans détachement proposé par [Westaway \(2002\)](#). 1 : Brèches cimentées ; 2 : Succession syn-rift ; 3 : Nappe du Pinde ; 4 : Nappe de Gavrovo-Tropolitsa ; 5 : Complexe de Zarouchla ; 6 : Contact stratigraphique ; 7 et 8 : Faille inactive ; 9 : Faille active.

2.4.2 Modèle de rotation des blocs

En réponse au modèle de détachement proposé, [Westaway \(2002, 2007\)](#) propose un modèle numérique de rift asymétrique caractérisé par le développement de failles planaires à fort pendage ($45\text{--}60^\circ\text{N}$) traversant la croûte supérieure (Figure 2.12B). Ce modèle tente de reproduire le soulèvement de la marge sud du rift, la structure des blocs de failles et l’asymétrie du rift sans la présence de détachement (Figure E.2). D’après l’auteur, l’ouverture du rift de Corinthe et la rotation des blocs de failles actives sont associées à un flux de matériel ductile sous la croûte fragile depuis le bassin vers le sud du rift. La réponse isostatique en lien avec ce flux crustal serait responsable du soulèvement de la marge du rift et du flux sédimentaire important vers le bassin. (Figure E.2). Le champ de contraintes est alors modifié par la rotation des blocs et ensuite rétabli par le développement de nouvelles failles à fort pendage.

De plus, il n’existe pas de modèle impliquant ce détachement en accord avec la cinématique des failles en surface et la sédimentation syn-rift. Par conséquent, la présence d’un détachement actif est toujours controversée. D’autres auteurs suggèrent aussi que la présence d’un détachement actif sous le golfe n’est pas nécessaire pour expliquer la distribution de la déformation ([Moretti](#)

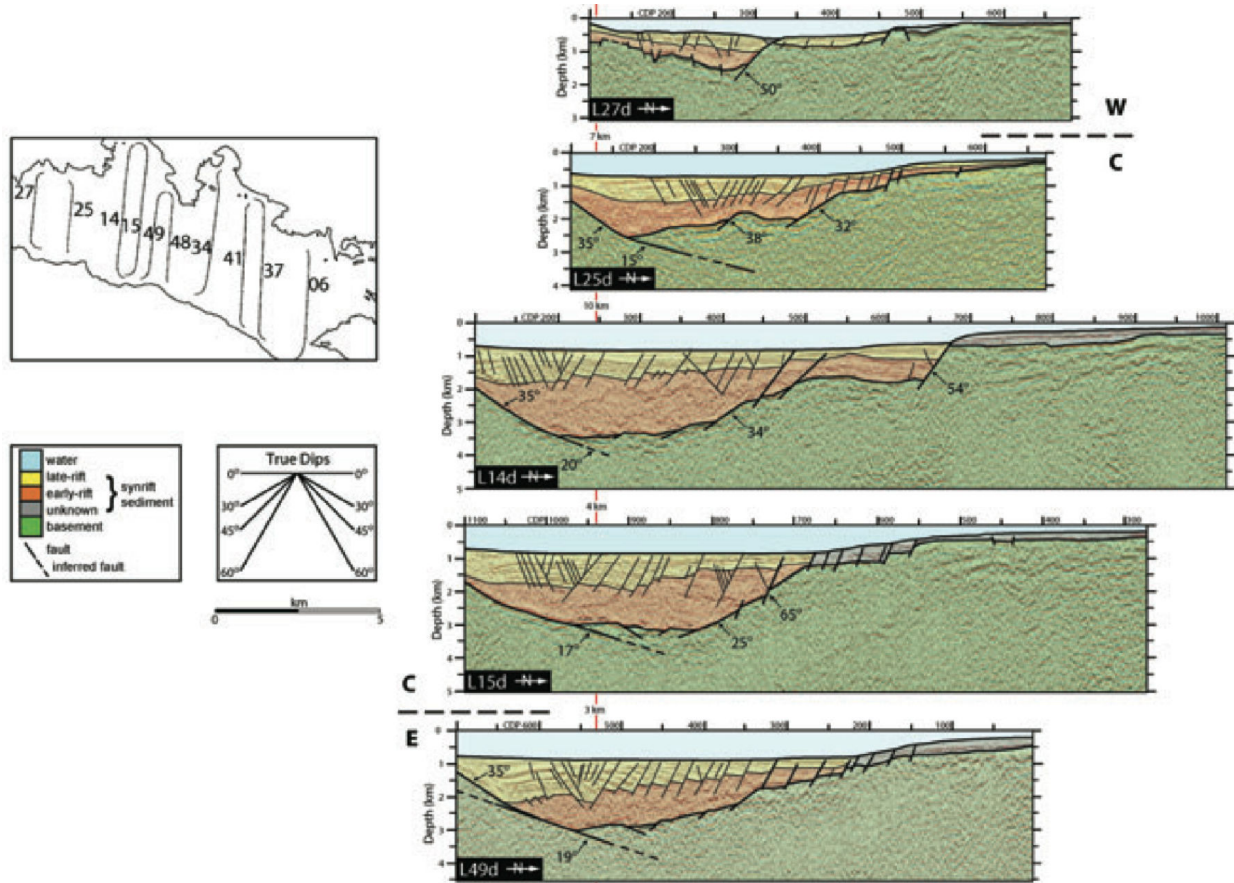


FIGURE 2.13 – Exemples de profils sismiques (EW0108 *Multichannel seismic*, campagne géophysique Maurice Ewing 2001) convertis en profondeur. Du haut vers le bas, les profils sismiques sont localisés d'ouest en est. Les failles majeures le long de la bordure sud du golfe de Corinthe présentent une géométrie biplanaire (d'après Taylor *et al.*, 2011).

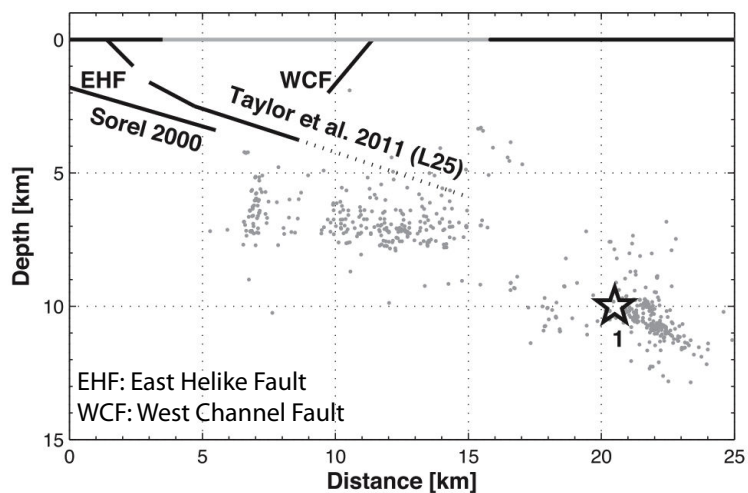


FIGURE 2.14 – Coupe schématique N-S présentant la sismicité et la géométrie des failles proposée par Sorel (2000) et Taylor *et al.* (2011). L'étoile correspond à l'épicentre du séisme d'Aigion en 1995 $M_s = 6.2$ (Bernard *et al.*, 1997) (d'après une compilation de Lambotte *et al.*, 2014).

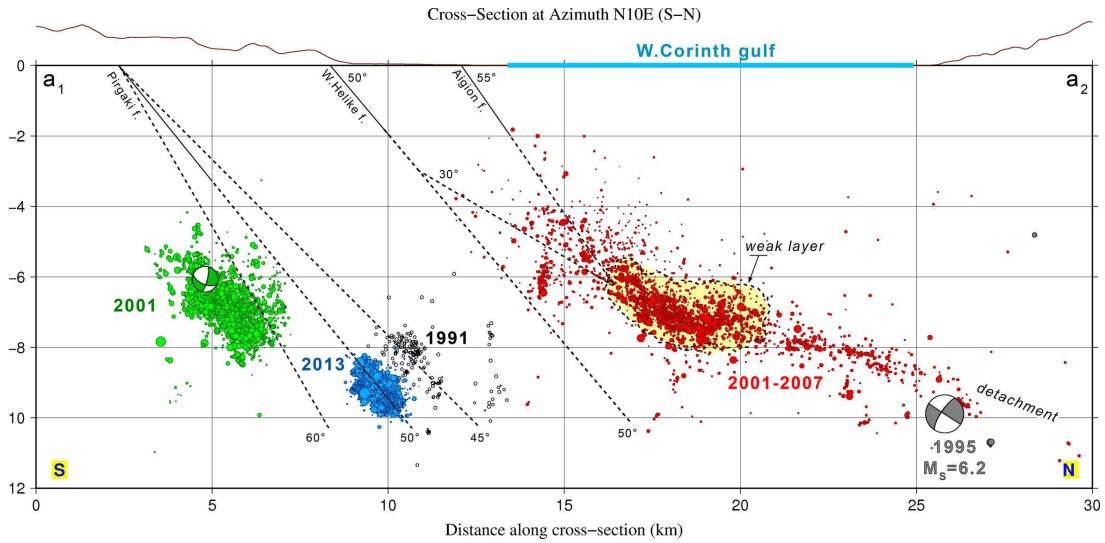


FIGURE 2.15 – Coupe N-S de la partie ouest du rift de Corinthe et illustrant les essais de sismicité récents de 1991, 2001, 2007 et 2013. Ces différents événements sont corrélés avec les structures actives en surface (d’après une compilation de [Kapetanidis et al., 2015](#))

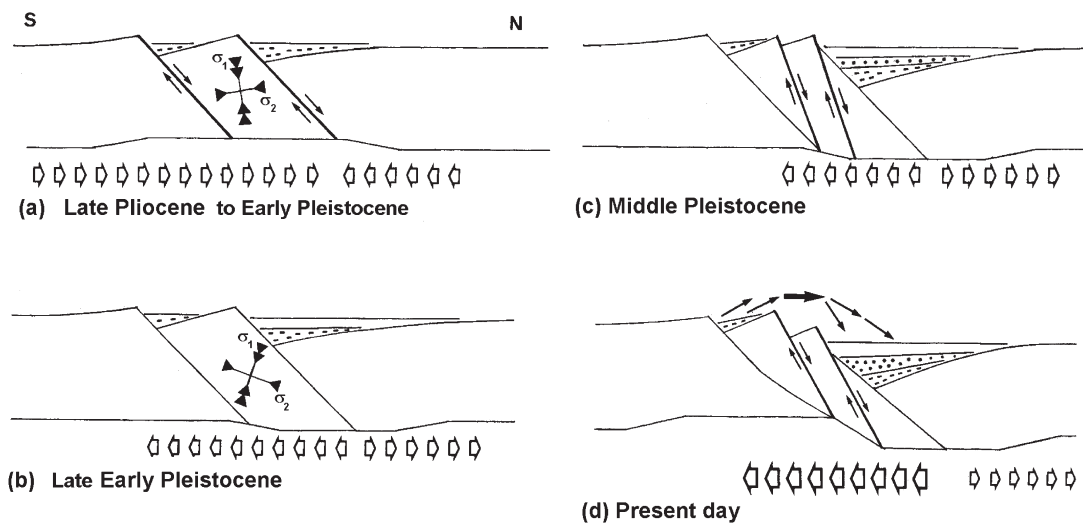


FIGURE 2.16 – Coupe simplifiée issue d’un modèle numérique et mettant en évidence un flux de matériel crustal vers le sud, sous le Péloponnèse (flèches blanches). La rotation des failles à fort pendage en lien avec ce flux entraîne le soulèvement de la marge, la migration de l’activité tectonique et le développement du bassin vers le nord ([Westaway, 2002](#)).

[et al., 2003](#); [McNeill & Collier, 2004](#); [McNeill et al., 2005](#); [Bell et al., 2008, 2009, 2011](#); [Taylor et al., 2011](#)). L’interprétation de failles actives à pendage 45–60° en surface atteignant la zone sismogénique (8–12 km) sous le golfe occidental est largement utilisée dans les études récentes et dans le cadre de cette thèse. Un des arguments en faveur des failles à pendage fort est notamment le soulèvement important de la marge sud du rift. Le rapport entre le soulèvement et la subsidence ($U : S$ ratio) est compris est estimé à 1 : 1.2–3.2 pour la faille Helike (EHF) ([McNeill & Collier, 2004](#); [McNeill et al., 2005](#)). Les systèmes de détachement ne produisent pas de soulèvement aussi

important. Ce modèle est cohérent avec l'histoire de propagation latérale du système de failles et les phases de migrations tectoniques enregistrées par les séries syn-rift (Goldsworthy & Jackson, 2001; Ghisetti & Vezzani, 2004; Ford *et al.*, 2007, 2013).

2.5 Stratigraphie syn-rift

Le soulèvement des blocs inactifs a permis l'exposition des séries syn-rift le long de la marge sud. Elles ont été déposées dans des environnements sédimentaires fluviaux, lacustres ou deltaïques. L'épaisseur de la série syn-rift peut atteindre près de 3000 m *onshore* dans la partie est du rift, et près de 3500 m en domaine *offshore*. L'épaisseur de la série diminue significativement (moins de 800 mètres) dans la partie ouest du rift. La lithostratigraphie syn-rift *onshore* et les subdivisions des unités *offshore* seront développées dans les chapitres suivants. L'état des connaissances sur la stratigraphie syn-rift n'est donc pas exhaustif ici.

A partir de l'interprétation des données sismiques 2D, de nombreuses études dans la partie *offshore* du rift se sont attachées à (i) cartographier la structure du rift, (ii) caractériser la géométrie du système de failles et (iii) définir des successions stratigraphiques (Stefatos *et al.*, 2002; McNeill *et al.*, 2005; Lykousis *et al.*, 2007; Sakellariou *et al.*, 2007; Bell *et al.*, 2008, 2009; Taylor *et al.*, 2011; Charalampakis *et al.*, 2014; Nixon *et al.*, 2016). Ces données sismiques comprennent des profils haute résolution-basse profondeur (~ 400 ms) (Stefatos *et al.*, 2002; Lykousis *et al.*, 2007; Bell *et al.*, 2008, 2009; Beckers *et al.*, 2015) et des profils profonds de plus basse résolution (~ 3 s TWTT) (Zelt *et al.*, 2004; Taylor *et al.*, 2011). Les profils sismiques profonds disponibles n'ont pas la résolution suffisante pour imager en détail l'ensemble de la série syn-rift. De plus, il n'existe pas encore de forage sous le golfe permettant de dater les dépôts syn-rift (Figure 2.13). Ces derniers sont estimés d'âge Pléistocène à actuel, et la présence de dépôts Pliocène n'est pas prouvée *offshore*. En raison du manque de contrainte temporelle de la série syn-rift, les corrélations stratigraphiques entre les domaines *offshore* et *onshore* sont rares. Le chapitre 5 présente plusieurs coupes de corrélations *onshore-offshore* dans la partie ouest du rift de Corinthe.

Onshore, la série syn-rift reste aussi assez mal datée et il n'existe pas d'âge précis pour l'initiation du rift. Les âges varient du Pliocène au Pléistocène inférieur selon les auteurs et la position le long de l'axe du rift (Doutsos & Piper, 1990; Rohais *et al.*, 2007a; Ford *et al.*, 2013). La datation des séries syn-rift correspond à une des thématiques principales de cette thèse et l'ensemble des travaux de datation existants seront présentés dans le chapitre 3.

Le début du rifting correspond à la formation d'un bassin fluvio-lacustre (*Lower Group*) occupant la majeure partie de la marge actuelle. Durant cette période, le taux d'extension est estimé à moins de 1 mm/an (Ford *et al.*, 2013). Alors que des séries alluviales conglomératiques sont principalement enregistrées dans la partie ouest du rift, des successions lacustres (siltosableuses) sont documentées à l'est du rift pendant les premières phases du remplissage.

L'histoire du rift est notamment caractérisée par la migration successive de l'activité des failles vers le nord ainsi que plusieurs événements d'approfondissement du bassin. Dans la partie centrale du rift (région de Xylocastro ; Figure 2.1), un approfondissement majeur est estimé à 3.2–3.0 Ma à la base d'une série turbiditique (Leeder *et al.*, 2012). Les travaux de datation et de corrélations stratigraphiques permettent ici de reconstruire la "phase d'initiation" du rift (chapitres 3 et 4). La corrélation stratigraphique de cet approfondissement du bassin dans la partie ouest du rift est discutée dans le chapitre 4.

A partir de 1.8–1.5 Ma, un approfondissement majeur du bassin est associé à la migration de l'activité des failles vers le nord (~15 km) et la construction de deltas de type Gilbert dans la partie ouest du rift (*Middle Group*). (Rohais *et al.*, 2008; Backert *et al.*, 2010; Ford *et al.*, 2013). A partir de cette période, le taux d'extension augmente est estimé à 2–2.5 mm/an. Les rivières antécédentes ont incisé les blocs en soulèvement pour construire une série de deltas alignés le long de la marge sud. La préservation exceptionnelle de ces deltas a fait l'objet de nombreuses études (Ori, 1989; Poulimenos *et al.*, 1993; Dart *et al.*, 1994; Malartre *et al.*, 2004; Ford *et al.*, 2007; Rohais *et al.*, 2007a, 2008; Backert *et al.*, 2010; Ford *et al.*, 2013; Gobo *et al.*, 2014). La migration des failles vers le nord pendant cette période est aussi marquée par (i) la ré-organisation du système de drainage, à l'origine d'une discontinuité majeure dans la stratigraphie syn-rift et (ii) une période de non dépôt pendant probablement plusieurs dizaines voire centaines de milliers d'années.

A partir de 0.7–0.4 Ma (*Upper Group*), une seconde phase de migration de l'activité des failles vers le nord (~5 km) est documentée dans la partie ouest et centrale du bassin. L'incision des rivières au cours du soulèvement de la marge sud permet la construction d'une nouvelle génération de deltas dont la plupart sont encore actifs actuellement. Cette dernière migration de l'activité des failles donne lieu à la configuration actuelle du golfe de Corinthe.

L'interprétation des profils sismiques 2D *offshore* montrent une discordance majeure à l'ouest du golfe. La corrélation de l'amplitude des réflecteurs sismiques avec les variations du niveau marin permet d'estimer l'âge de cette discordance à environ 620 ka (Nixon *et al.*, 2016). Cette discordance est expliquée par le changement de polarité des failles. Alors que les failles majeures à pendage sud deviennent inactives, le système de failles à pendage nord migre et devient prédominant à partir de ~620 ka (Figure 2.17).

L'extension totale est calculée à partir de rejet horizontal cumulé sur l'ensemble des failles. Elle est plus importante dans la partie centrale du rift (11–21 km) que dans la partie ouest du rift (5–13 km) (Bell *et al.*, 2011). Cependant, les données géodésiques montrent des taux d'extension actuels plus importants dans la partie ouest (>10–15 mm/an) que dans la partie est du rift (<5 mm/an) (Davies *et al.*, 1997; Billiris *et al.*, 1991; Briole *et al.*, 2000; Avallone *et al.*, 2004). Le taux d'extension au Plio-Pléistocène dans la partie ouest du rift est estimé à 0,6–4,8 mm/an (Ford *et al.*, 2013). La compilation de ces travaux suggère une migration récente de la déformation vers l'ouest du rift, associée à une accélération du taux d'extension. Certains auteurs expliquent cette

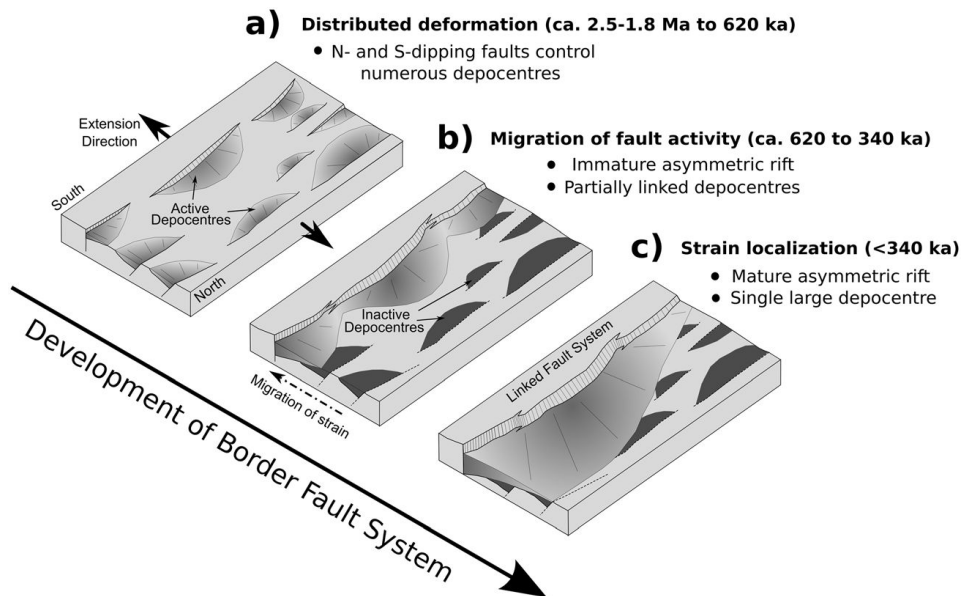


FIGURE 2.17 – Bloc diagramme 3D illustrant le développement de la marge sud du rift de Corinthe et des dépocentres associés (d'après Nixon *et al.*, 2016).

migration de la déformation en lien avec la dynamique du panneau plongeant (Tiberi *et al.*, 2000; Le Pourhiet *et al.*, 2003; Leeder *et al.*, 2003).

La migration des failles vers le nord a permis le soulèvement progressif de la marge sud du rift de Corinthe. L'évolution de la marge sud et les travaux existants sont largement développés dans le chapitre 5. L'incision continue des rivières dans la partie ouest de la marge sud forme des vallées étroites et profondes (gorges de 500 à 800 m de profondeur dans la vallée du Vouraikos). Les rivières s'écoulent vers le nord et sont régulièrement espacées d'une distance de 6 à 8 km. La longueur des principaux bassins versants varient entre 10 et 50 km environ (Figure 2.18). Le bassin versant le plus large dans le nord du Péloponnèse est celui de Sélinous qui s'étend sur une superficie de 366 km² et sur 49 km de long (Demoulin *et al.*, 2015). Le soulèvement de la marge a localement inversé le sens d'écoulement des rivières et est à l'origine des bassins endorhéiques au sud du rift de Corinthe. Ces bassins endorhéiques forment notamment les plaines de Feneos et le lac de Stymfalia (Figure 2.18).

De nombreux travaux de recherche ont permis de caractériser le rift de Corinthe à partir d'objets variés et sur différentes échelles de temps. Une des difficultés majeures de ce contexte géologique est d'expliquer la différence entre la cinétique des processus actuels et l'enregistrement des processus passés. Par exemple, les vitesses GPS actuellement mesurées sont significativement plus importantes par rapport aux estimations du taux d'extension. Cette différence est ici expliquée par une accélération de l'activité tectonique et par la localisation récente de la déformation en lien avec les structures actives. Cependant, il est possible qu'une partie de la déformation passée ne soit pas enregistrée. Dans ce cas, l'interprétation des processus passés sont "sous contraints" et ne peuvent pas être directement comparés aux processus actuellement mesurés

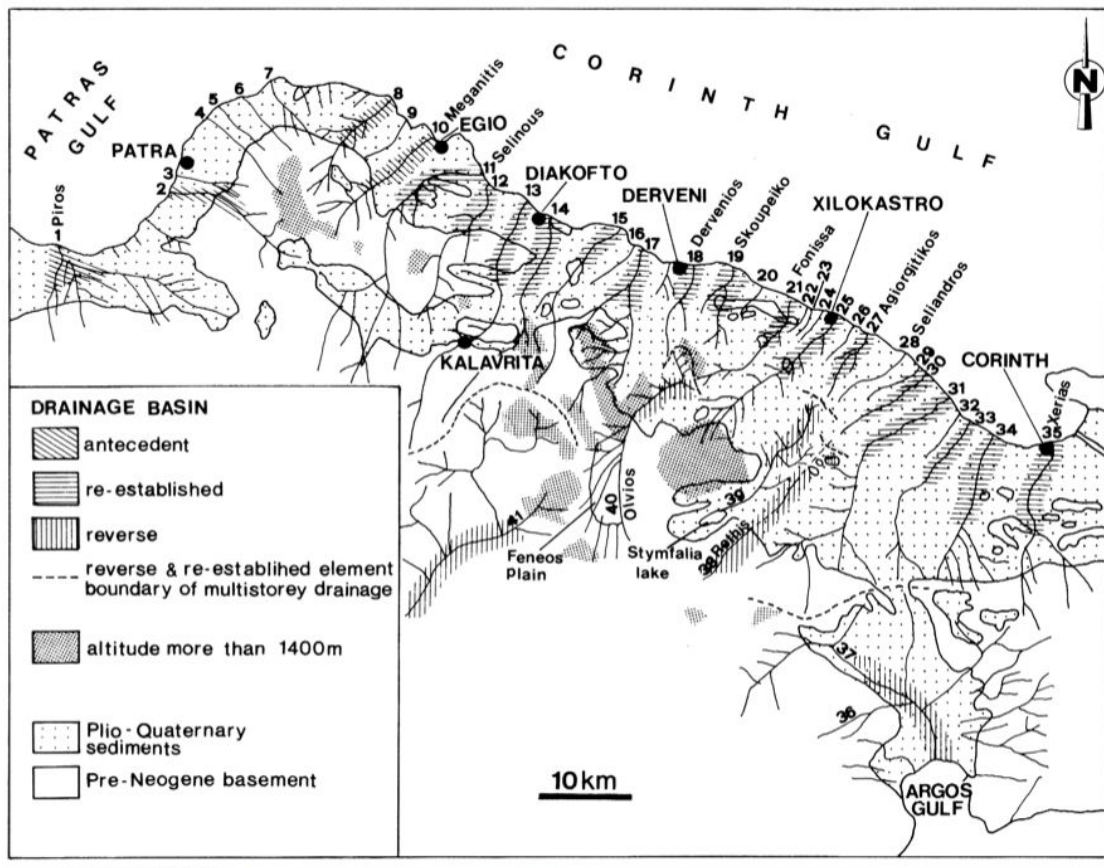


FIGURE 2.18 – Carte géologique simplifiée de la marge sud du golfe de Corinthe illustrant les différentes rivières. 1 : Patras, 2 : Glaukos, 3 : Diakoniaris, 4 : Charadros, 5 : Selemnos, 6 : Xilokeras, 7 : Volineos, 8 : Finix, 9 : Tholopotami, 10 : Meganitis, 11 : Selinous, 12 : Kerinitis, 13 : Vouraikos, 14 : Ladopotamos, 15 : Krathis, 16 : Tholopotamos, 17 : Krios, 18 : Dervenios, 19 : SKoupeiko, 20 : Agriolagado, 21 : Fonissa, 22 : Arachovitikos, 23 : Spartila, 24 : Kolones, 25 : Trikalilikos, 26 : Katharoneri, 27 : Agiorgitikos, 28 : Seliandros, 29 : Kyrillou, 30 : Elisson, 31 : Asopos, 32 : Gourgouroti, 33 : Nemeas, 34 : Rachiani, 35 : Xerias, 36 : Xirias, 37 : Inachos, 38 : Souteni, 39 : Rethis, 40 : Olvios, 41 : Ladonas. (d'après [Zelilidis, 2000](#)).

En lien avec la problématique du couplage rivières/rifting, l'étude de l'enregistrement des systèmes fluviaux syn-rift permet de mettre en avant les questions suivantes :

- Les rivières actuelles drainant la marge sud du rift de Corinthe sont-elles analogues aux rivières passées ?
- Comment reconstruire l'histoire des rivières passées à partir de leurs enregistrements sédimentaires ?
- Quelles sont les incertitudes associées aux reconstructions paléogéographiques ?

Deuxième partie

Résultats et discussions

Chapitre 3

Multidisciplinary approach to date gravel-dominated syn-rift successions

Ce chapitre est consacré à la présentation des résultats de datations dans les successions sédimentaires enregistrant l'initiation du rift de Corinthe (*Lower Group*). La cartographie et la sédimentologie des faciès syn-rift ont permis d'établir la lithostratigraphie dans plusieurs blocs de failles normales. La cartographie des unités lithostratigraphiques met en évidence des variations de faciès internes aux blocs de failles, mais aussi, et surtout, des variations de faciès progressives d'un bloc à l'autre. Les dépôts syn-rift deviennent de plus en plus fins depuis un pôle fluvial proximal au sud du secteur vers un pôle plus distal fluvio-lacustre et deltaïque au nord-est. L'initiation de la partie ouest du rift de Corinthe est caractérisée par le développement d'un système fluvial à travers une série de failles normales actives au cours du Plio-Pléistocène. La stratigraphie syn-rift peut donc être corrélée entre les blocs de failles. Les données de terrain sont couplées à des travaux de datations afin de contraindre en temps l'activité des failles en lien avec le développement de ce système fluvial. Le défi majeur est d'obtenir des âges précis dans les dépôts alluviaux grossiers plio-quadernaires pour quantifier les processus tectono-sédimentaires à l'initiation du rift.

Plusieurs successions sédimentaires du *Lower Group* sont documentées dans les différents blocs de failles normales. L'analyse des faciès est présentée dans le chapitre 4 et des données complémentaires sont disponibles en annexe B. Ces mêmes séries sédimentaires sont échantillonnées pour les analyses paléomagnétiques, la détermination de marqueurs biostratigraphiques (dents de micromammifères, charophytes, gastéropodes) et la détermination d'âges d'enfouissement à partir des isotopes cosmogéniques ^{26}Al et ^{10}Be . Les différents âges obtenus permettent de construire un modèle de corrélation stratigraphique.

Sommaire

3.1 Introduction	88
3.2 Lithostratigraphy of the Kalavryta river system	92
3.2.1 Southern fault blocks- Coarsening-upward succession	92
3.2.2 Northern fault blocks - Fining-upward succession	92
3.2.3 Lithostratigraphy of the sampled sections	93
3.3 Biostratigraphy	99
3.3.1 Mammal teeth	99
3.3.2 Charophytes	99
3.3.3 Mollusks	99
3.4 Magnetostratigraphy and Rock Magnetism	100
3.4.1 Sampling	100
3.4.2 Magnetic mineralogy	100
Curie point analysis	100
IRM and hysteresis parameters	100
3.4.3 Demagnetisation and magnetic directions	102
Demagnetisation techniques	102
Principal component analysis	104
3.4.4 Magnetic directions and statistical tests	109
3.4.5 Polarity column and robustness	111
3.5 ^{26}Al-^{10}Be burial ages	116
3.6 Age model	116

3.1 Introduction

Stratigraphic correlation between fault blocks is the main challenge encountered when facies change laterally over short distances. Typically, few reliable time constraints are available in the fluvial sedimentary archive ; especially in the gravel-dominated successions as high stream power fluvial environments have low preservation potential of biota of any kind. For Mesozoic and particularly Cenozoic fluvial successions, magnetostratigraphy is known as a powerful dating tool, when rocks are suitably magnetised and when independent calibration is available (e.g. [Johnson *et al.*, 1975](#); [Barndt *et al.*, 1978](#); [Lindsay *et al.*, 1981](#); [Mack *et al.*, 1993](#)). This chapter presents results of a multidisciplinary approach to date this gravel-dominated fluvial succession.

Along the southern margin of the western Corinth rift, the inactive normal fault blocks are uplifted to over 1000 m above sea level. Average uplift rate is estimated between 0.9 and 2.2 mm/yr ([Stewart & Vita-Finzi, 1996](#); [Stewart, 1996](#); [Pirazzoli *et al.*, 2004](#); [McNeill & Collier,](#)

2004). Incision by present day rivers has generated excellent exposures of syn-rift deposits. The study area is delimited to the south by the Khelmos massif (2200 m alt.), and to the north by the present day coastline (Figure 3.1). The major north-dipping faults are the Kalavryta, Prinos, Kerpini, Tsivlos, Doumena and Valimi faults. Fault blocks are 10 to 15 km long (strike length) and 4 to 7 km wide (Figure 3.2). The strike of major faults is N086 to N110 and their average dip varies between 42°N and 64°N (Ford *et al.*, 2013). Pure dip-slip displacement is recorded on the majority of faults with stretching directions oriented N–S to SSW–NNE (Rohais *et al.*, 2007a; Ford *et al.*, 2013). Maximum sediment thickness within the major hangingwall depocentres varies from 400 to 1600 m. Dip fans and stratal wedging are observed in many fault blocks. Syn-rift strata can also describe growth synclines.

We focus here on the early rift succession of the Late Pliocene to Early Pleistocene western Corinth rift known as the Lower Group (Rohais *et al.*, 2007a). The transition between the Lower and Middle Groups at about 1.8 Ma is marked by northward migration of fault activity (Ford *et al.*, 2007, 2013). Middle Group Gilbert deltas record progressive basin deepening (Rohais *et al.*, 2008; Backert *et al.*, 2010; Ford *et al.*, 2013). The northward migration of fault activity at the beginning of the Upper group at 0.7 Ma, transferred the deformation onto present day coastal faults system (in the study area). Syn-rift stratigraphy records the persistence of rivers systems and their reorganisation during the successive migrating phases of fault activity. The Lower Group succession that thickens and fines toward the east and north from coarse alluvial conglomerates to fine-grained lacustrine turbidites across a series of E-W normal faults blocks (Rohais *et al.*, 2007a,b; Ford *et al.*, 2013). Facies analysis and detailed mapping of the syn-rift facies are presented in Chapter 4. The Lower Group stratigraphy shows that facies change laterally gradually from one fault block to another. The fault blocks were traversed by a single fluvial system, allowing us to correlate stratigraphic units.

We carried out magnetostratigraphic analyses in four logged sections located in four different fault blocks. Additional absolute ages are necessary as any magnetostratigraphic sequence may include long hiatuses of deposition in fluvial conglomerates, leading to error and misinterpretation. $^{26}\text{Al}/^{10}\text{Be}$ cosmogenic nuclide burial dating technique (Granger *et al.*, 1997; Granger & Muzikar, 2001) and biostratigraphic data (mammal teeth, charophytes) were used to provide additional age constraints. The age model presented at the end of this chapter is then used to reconstruct the early rift phase and the palaeogeography of the Corinth rift basin.

The description and recognition of the mammal teeth were provided by Sevket Sen (*Muséum National d'Histoire Naturelle*, Paris, France).

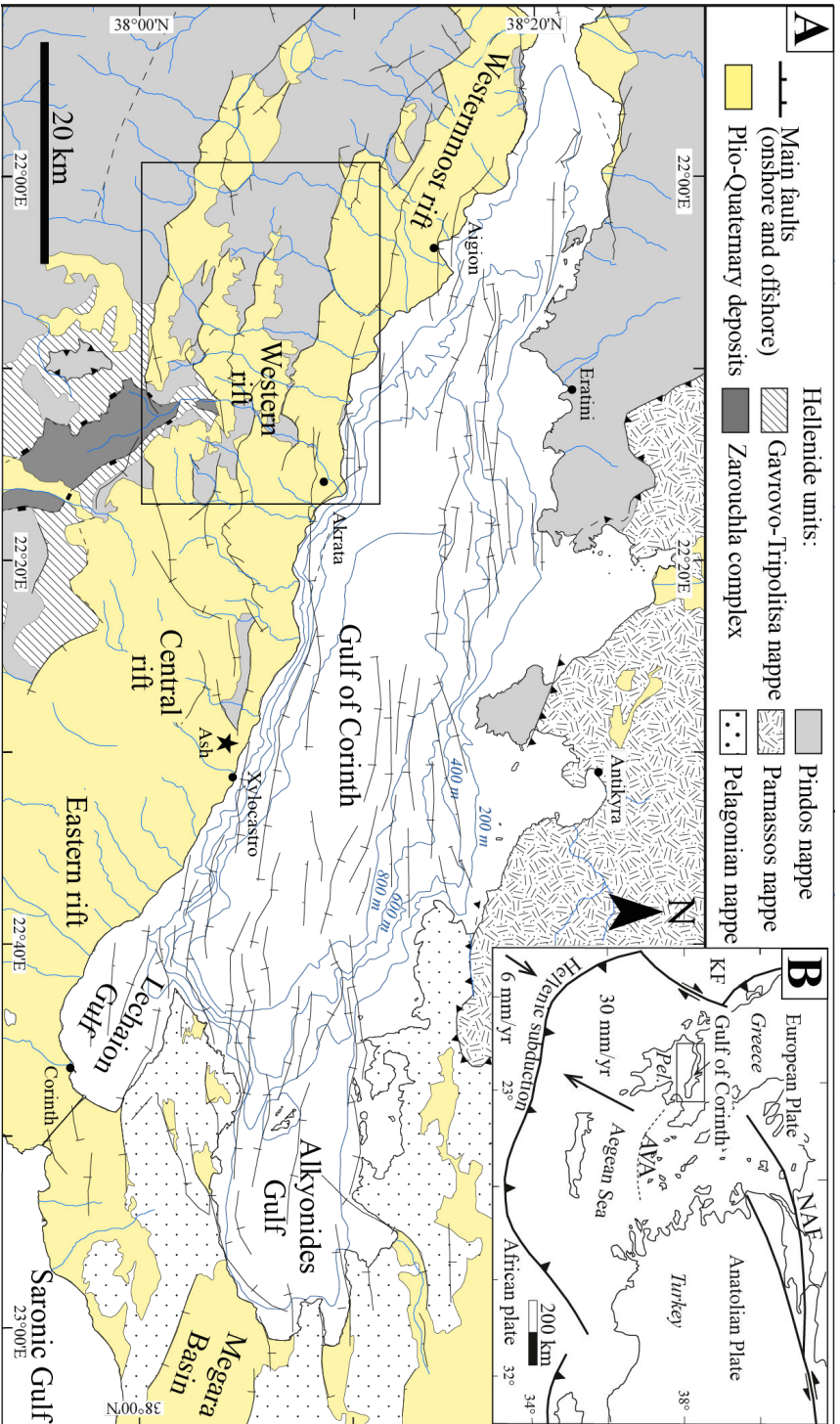


FIGURE 3.1 – **A** : Geological map of the Corinth rift. The black box corresponds to the study area shown in the Figure 3.2. Offshore fault traces [Beckers et al. \(2015\)](#); [Hemelsdaël & Ford \(2016\)](#); [Nixon et al. \(2016\)](#), onshore fault traces from [Rohais et al. \(2007a\)](#); [Leeder et al. \(2012\)](#). **B** Regional context of the Corinth above the active Hellenic subduction zone and lying between the Cephalonia Fault (KF) and the North Anatolian Fault (NAF). Subduction of the African plate generated the Aegean Volcanic Arc (AVA). The rift separates mainland Greece from the Peloponnese peninsula (Pel.). Tilted-corrected mean palaeomagnetic declinations in the four studied sections are compared with the values of [Mattei et al., 2004](#)) along the Corinth and Megara basins. All declination values in each sections are transferred to normal polarity. **1** : Kerpini section ; **2** : Doumena section ; **3** : Voutsimos section ; **4** : Valimi section.

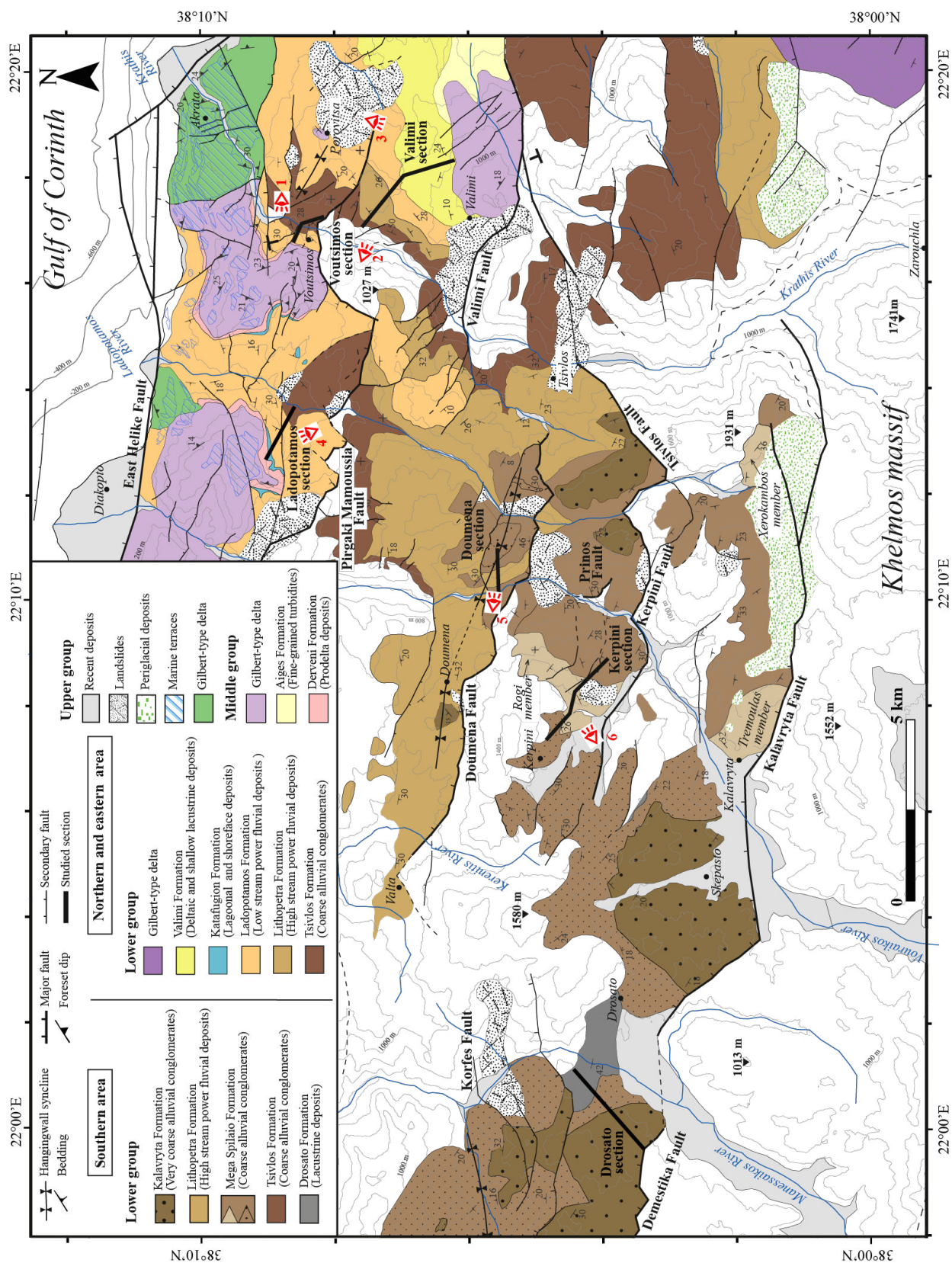


FIGURE 3.2 – Geological map of the study area. The onshore syn-rift stratigraphy is defined for the southern and northeastern areas. Palaeomagetic sections and other logged sections are indicated. The red eyes (1 to 6) are directed toward the photos in Figure 3.5D (1) ; Figure 3.5A (2) ; Figure 3.5C (3) ; Figure 3.6(4) ; Figure 3.3 (5) ; Figure 3.4 (6).

3.2 Lithostratigraphy of the Kalavryta river system

The lithostratigraphy of the Lower Group is summarised in two main stratigraphic columns (Figure 3.2). The first column covers the Demestika, Kalavryta, Kerpini, Tsivlos and Doumena fault blocks in the southwestern area where coarse alluvial conglomerates record a coarsening upward succession with rare lacustrine deposits at the base. The second column represents the northern and eastern areas characterised by a fining upward trend in the Pirgaki-Mamoussia and Valimi fault blocks. Sedimentology of the facies characterising the lithostratigraphic units are presented in details in the Chapter 4 and the appendix B. A brief summary of the lithostratigraphic unit is presented here.

3.2.1 Southern fault blocks- Coarsening-upward succession

The **Drosato Formation** (Figure 3.2) comprises silt and clay deposits with variable proportions of terrestrial organic matter including lignite beds (up to 1.5 m thick). This formation is exposed in the western/central Kalavryta fault block where it can reach up to 100 meters, however its continuity across the block is uncertain.

The overlying **Mega Spilaio Formation** consists of coarse conglomerates to fine-grained fluvial deposits. In the central Doumena fault block (Figure 3.2), in the vicinity of the Mega Spilaio monastery, massive coarse alluvial conglomerates form distinctive cliffs up to 20 m high (Figure 3.3). This formation is dominant in the Doumena, Kerpini and Kalavryta fault blocks where its thickness varies from 300 to 1100 m. Laterally, at the fault tips, "fine-grained members" comprise conglomerates interbedded with variable silt and clay deposits. Those members are : the Tremoulas Member in the Kalavryta area, the Xerokambos Member in the eastern Kalavryta block, and the Rogi Member in the western Kerpini fault block (Figures 3.2 and 3.4).

The **Kalavryta Formation** is 100 to 500 m thick and consists of structureless to crudely stratified clast supported conglomerates with abundant boulder clasts and presents no significant lateral facies change. This formation lies conformably above the Mega Spilaio Formation and forms the uppermost part of the southern syn-rift succession in the Kalavryta, Kerpini and Tsivlos blocks (Figure 3.4). It also marks the coarsening up trend of the syn-rift succession.

3.2.2 Northern fault blocks - Fining-upward succession

At the base of the syn-rift succession the **Tsivlos Formation** mainly consists of massive and crudely stratified alluvial conglomerates : Exochi Formation of Rohais *et al.* (2007a) and Basal Conglomerates of Ford *et al.* (2013). These strata onlap and fill palaeorelief (up to 700 m high). An abrupt facies change defines the upper limit of the formation. The best outcrops are exposed

along the Krathis and Vouraikos valleys where thicknesses range from 100 to 300 m (Figure 3.5).

The overlying **Lithopetra Formation** is composed of coarse conglomerates, predominantly massive but interbedded in places with cross-bedded sandstones and siltstones in variable proportions. The thickness of this formation ranges from 200 to 700 meters. It lies conformably above the Tsivlos Formation in the Doumena, Tsivlos, Valimi fault blocks or directly on the basal syn-rift unconformity in the western Doumena fault block where it is laterally equivalent to the Mega Spilaio Formation (Figures 3.2 3.3 and 3.5).

The **Ladopotamos Formation** consists of massive conglomerate bodies (up to 10 m thick) interbedded with red siltstone/sandstone intervals (Ford *et al.*, 2007). In the Pirgaki-Mamoussia fault block, the succession is about 500 m thick and gradually fines upward. The Ladopotamos Formation thins eastward to 200 m along the Krathis valley where fluvio-lacustrine deposits contain abundant oligohaline to freshwater fauna, recording the lateral transition of the Valimi Formation (see below).

The **Valimi Formation** is a 700 m thick succession lying above the Ladopotamos Formation in the Valimi fault block. It consists of CU sequences (20 to 50 m thick) of fine grained lacustrine deposits overlain by prograding packages of sandstones and conglomerates (up to 15 m thick). Between the Valimi and Pirgaki-Mamoussia fault blocks (Porovitsa village ; Figure 3.2), the Valimi Formation lies unconformably above the Ladopotamos Formation.

In the Pirgaki-Mamoussia block, the **Katafugion Formation** (up to 30 m thick) consists of lagoonal calcisiltites and upper shoreface conglomerates and sandstones (Malartre *et al.*, 2004; Ford *et al.*, 2007, 2013) lying conformably above the fluvial deposits of the Ladopotamos Formation in the Ladopotamos valley. The Katafugion Formation marks the beginning of the transgression in the northern area at the end of the Lower Group (Figure 3.6).

3.2.3 Lithostratigraphy of the sampled sections

Four sections were sampled for palaeomagnetic analyses. They are located in the Kerpini, Doumena, Pirgaki-Mamoussia and Valimi fault blocks (Figure 3.2). Few complete and unfaulted successions were accessible in the study area. The targeted facies for palaeomagnetic analysis comprise red to brown siltstone and clay (overbank deposits), and fine-grained to medium sandstones, likely to have been deposited in a calm, non-turbulent environment. Suitable facies are preserved in variable proportions in coarse conglomeratic formations.

- The **Valimi section** (Figure 3.5) is 1300 m thick and displays a general fining upward trend. The base of the Lower Group succession comprises coarse alluvial conglomerates (Tsivlos Formation, 220 m) and evolves vertically to fine-grained fluvial deposits (Lithopetra and Ladopotamos Formations ; both about 180 m thick). The upper part of the

section comprises the finer-grained Valimi Formation (700 m thick).

- The **Voutsimos section** is located in the eastern Pirgaki-Mamoussia fault block, in the Krathis River valley (Figure 3.5). The Lower group succession is considerably thinner than the Valimi section. The sampled section is about 450 m thick, characterised by a general fining-upward trend. It consists of coarse alluvial conglomerates at the base (Tsivlos Formation ; 100 m thick) overlain by fluvio-lacustrine deposits (Ladopotamos Formation ; 230 m thick) comprising reddish sandstones to pebbly fluvial conglomerates alternating with yellow to beige well-laminated siltstones lacustrine deposits in the upper part of the section.
- The **Doumena section** is located in the central Doumena fault block, along the Vou-raikos River valley (Figure 3.2) where syn-rift strata form a large hangingwall syncline (Figure 3.3). The basal part of the syn-rift succession is not exposed here. This section is 900 m thick and consists of coarse conglomerates of the Mega Spilaio and Lithopetra Formations. The succession displays a coarsening-upward trend. Sample sites correspond to rare siltstone and sandstone intervals.
- The **Kerpini section** is located in the westernmost Kerpini fault block where syn-rift strata onlap onto the pre-rift relief (Figure 3.4). The 600 m section is tilted toward the south against the Kerpini Fault. The succession consists of coarse conglomerates at the base (Mega Spilaio Formation) overlain by fine-grained fluvial succession predominated by red sandstones and siltstones (Rogi Member) which are particularly suitable for palaeomagnetic analysis.

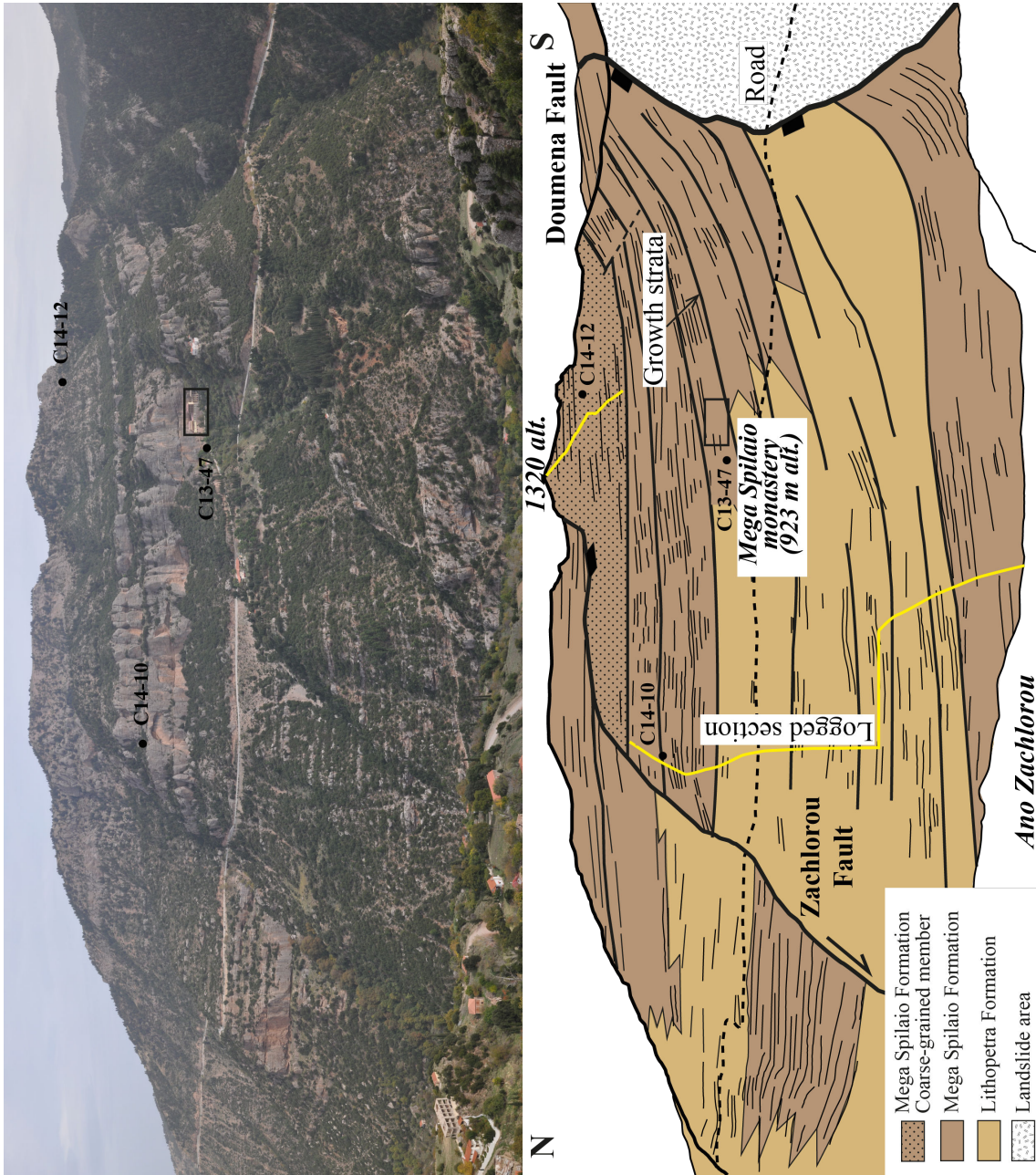


FIGURE 3.3 – Interpretation of syn-rift succession in the central Doumena fault block. The yellow line corresponds to the trace of the Doumena logged section. This log is presented in Figures 3.11 and 3.13. the samples C13-37, C14-10 and C14-12 in the Mega Spilaio Formation were collected for the determination of ^{26}Al – ^{10}Be burial ages.

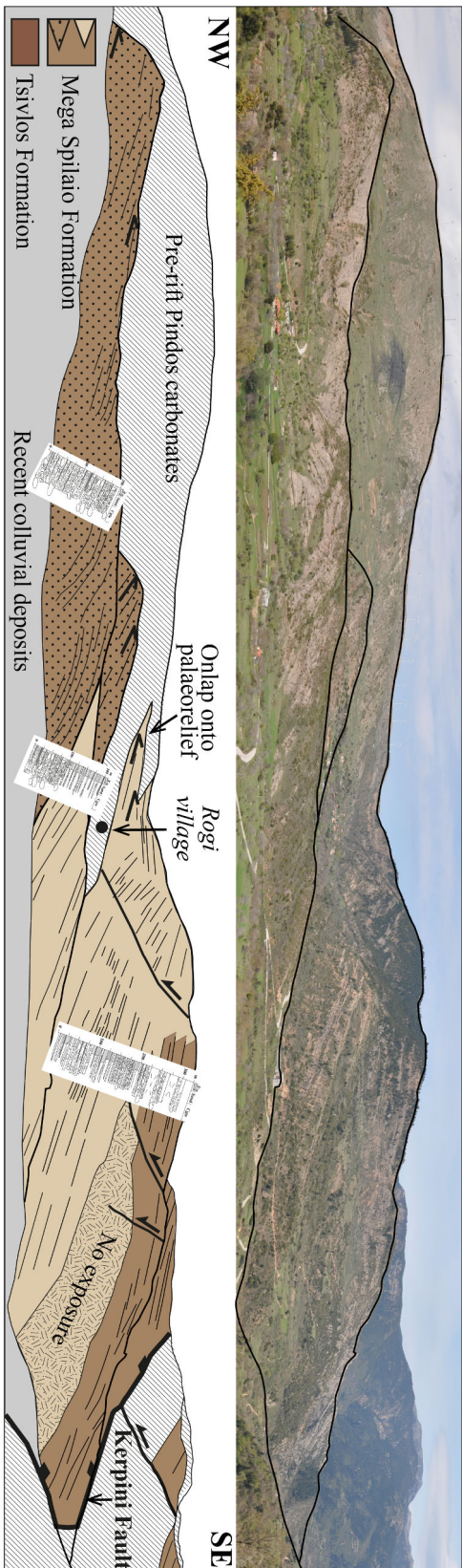


FIGURE 3.4 – Interpretation of syn-rift succession in the western Kerpiní fault block where the Kerpiní section were sampled for palaeomagnetic analysis. This log is presented in more details in Figures 3.11 et 3.13.

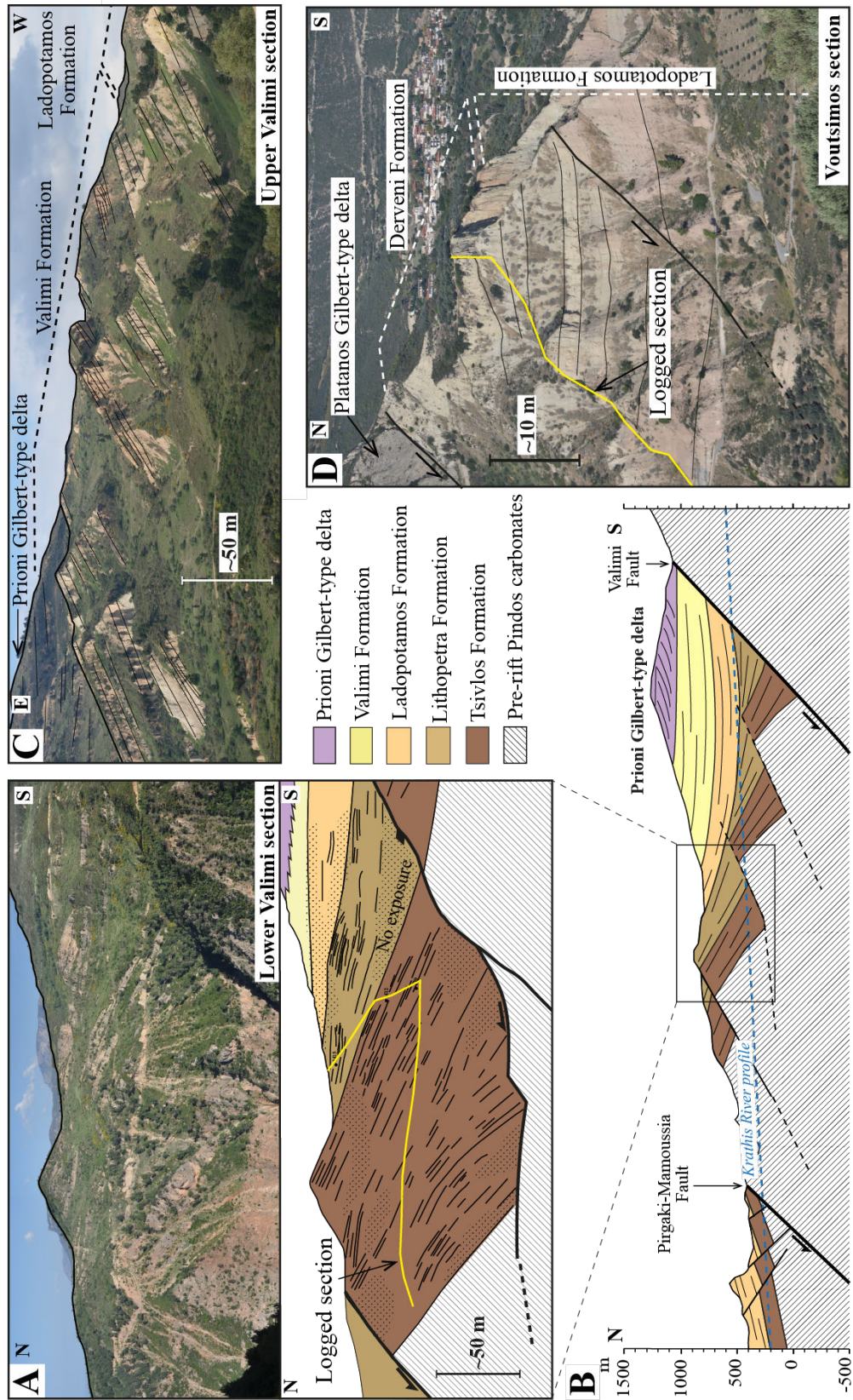


FIGURE 3.5 – **A** : Interpretation of syn-rift succession in the northern Valimi fault block along the Krathis River valley. The yellow line corresponds to the trace of the lower Valimi section. **B** : N-S oriented cross section of the Valimi fault block. The early rift blocks were rotated by the activation of the Valimi Fault to the south. The Valimi Fault was active during both the Lower and Upper Groups. The black box delimits the interpreted photo (A). **C** : Upper part of the Valimi section. **D** : Upper part of the Voutsimos logged section exposed along the Krathis River valley. The corresponding sedimentary logs are presented in Figures 3.11 et 3.13.

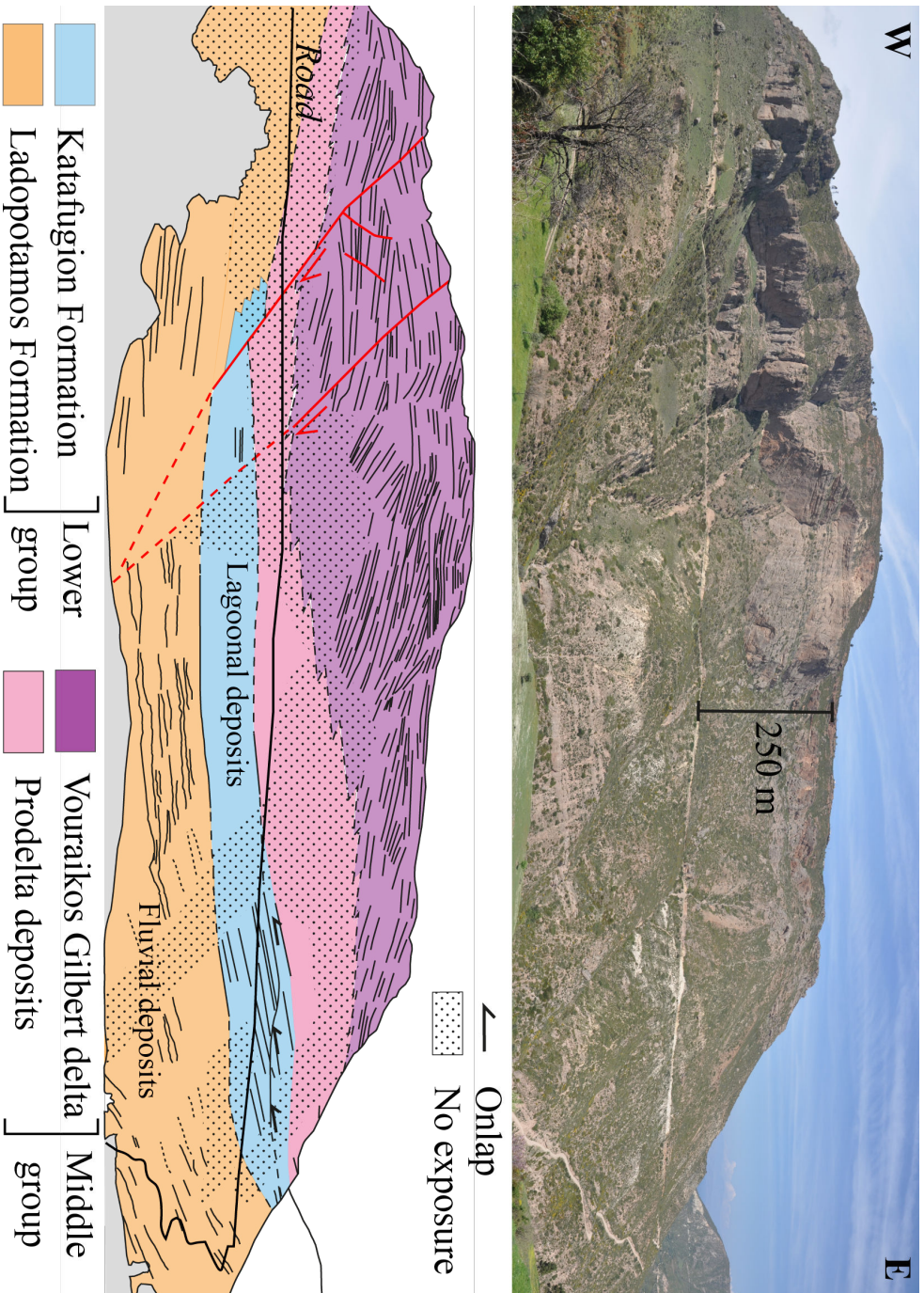


FIGURE 3.6 – Interpretation of syn-rift succession in the Pirgaki-Mamoussia fault block exposed along the Ladopotamos River valley. The Ladopotamos and Katafugion formations (Lower Group) are preserved below the Middle Youraikos Gilbert-type delta (see Ladopotamos log; Figure 3.13).

3.3 Biostratigraphy

3.3.1 Mammal teeth

Teeth of voles (Arvicolidae, Rodentia) are found within a palaeosol bed at the base of the Ladopotamos Formation (38.148747°N ; 22.229661°E – Figure 3.2). The fragmentary state of the specimens and the lack of characteristic elements do not allow genus and species identification. These teeth are hypsodont, rooted, lack cement in the re-entrant angles, and the enamel is thicker on the posterior sides of triangles. Such a character combination rather indicates late Pliocene voles, such as *Mimomys* or some late Pliocene-earliest Pleistocene voles like *Borsodia* (Popov, 2001; Sala & Masini, 2007). This biomarker gives an age ranging from 2.6 to 3.6 Ma.

3.3.2 Charophytes

Screen-washing of samples in the upper part of the Drosato Formation (38.072890°N ; 22.016513°E – Figure 3.2) show the presence of many gyrogonites of charophytes identified as *Nitellopsis megarensis*, *Nitellopsis group merianii*, *Chara sp.* and *Lychnothamnus sp.*. These charophytes indicate shallow freshwater environments, although they are not characteristic enough for a precise age determination (Riveline *et al.*, 1996). However, the species *Nitellopsis megarensis* was initially described in the Megara basin in Greece (Soulié-Märsche, 1979) and is assigned to the Upper Pliocene. This is consistent with the overlying Pagea Ash dated at 2.82 Ma (Leeder *et al.*, 2008) found in the topmost Megara basin sedimentary succession (Alepochori Group). The Drosato Formation is therefore assigned as Upper Pliocene age.

3.3.3 Mollusks

Well preserved mollus are scarce in the sedimentary facies. However, fine-grained dominated formations show locally entire shells of gastropods. The gastropod *Adelinella elegans* is locally abundant in the fluvial Ladopotamos Formation, mainly in the Voutsimos area. Within fine-grained lacustrine deltas facies association, silt and clay deposits present variable organic matter content with plant remains, coal fragments, and gastropods (*Melanopsis aff. mizopouloisi*, *Adelinella elegans*), and other undetermined bioclasts.

Lagoonal deposits are represented by calcareous silts with abundant broken bivalves and gastropod shells. Determination of the gastropods shows high abundance of *Theodoxus micans* (Marco Mancini, personal communication). This gastropod fauna is relatively well known in Central Greece in the Atlanti basin (Koskeridou & Ioakin, 2009). In the eastern Mediterranean, the biostratigraphic range of this species is comprised from Upper Pliocene to Early Pleistocene (Bandel, 2001; Gillet, 1963; Keraudren, 1975, 1979; Koskeridou & Ioakin, 2009; Stevanovic, 1963).

3.4 Magnetostratigraphy and Rock Magnetism

3.4.1 Sampling

Samples were collected using a gasoline-powered drill and were oriented using magnetic and, whenever possible, sun compasses. The average magnetic declination anomaly is of $3.4 \pm 2.2^\circ$ ($N = 347$). When drilling was impossible in the poorly consolidated facies, oriented samples were housed in plastic boxes (8 cm^3). For each sampling site, two or three cores were drilled. All cores are prepared into standard specimens of 2.5 cm in diameter and 2.2 cm in length with a volume of 10–11 cm^3 . Samples were collected at 69, 62, 61 and 71 sites in the Kerpini, Doumena, Voutsimos and Valimi sections respectively. Because of the low preservation of fine beds, the sampling interval may reach up to 36 to 74 m. However, the average stratigraphic distance between two sites remains low and varies from 6 to 13 m for the four sections.

3.4.2 Magnetic mineralogy

To identify the magnetic carriers, the magnetic mineralogy was investigated using thermomagnetic curves to determine the Curie points, isothermal remanent magnetisation (IRM) and hysteresis acquisitions.

Curie point analysis

The thermomagnetic curves were measured on 34 porphyrised sediments at the 'Institut de Physique du Globe' of Paris (IPGP), using an AGICO KLY2 KapaBridge susceptibility meter coupled with a CS5 furnace and CSL cryostat under argon atmosphere to avoid alteration (oxidation) of magnetic minerals during heating. Most of the samples show irreversible curves. Cooling curves present higher susceptibility values than those of the heating curves. The large difference between heating and cooling of the sample suggests that the magnetic iron oxides were initially altered and oxidised (Figure 3.7). Maximum increase in magnetic susceptibility occurs between 400 and 550°C, and corresponds to the crystallisation of new magnetic minerals during heating. The major fall is observed at 580°C indicating the presence of Ti-poor magnetite. Stable values in susceptibility above 600°C suggest the presence of hematite.

IRM and hysteresis parameters

Isothermal remanent magnetisation (IRM) acquisition curves were obtained for 63 samples in order to determine the magnetic mineral carriers. We present 6 representative samples here (Figure 3.8). Few IRM acquisition experiments indicated that saturation magnetisation occurs

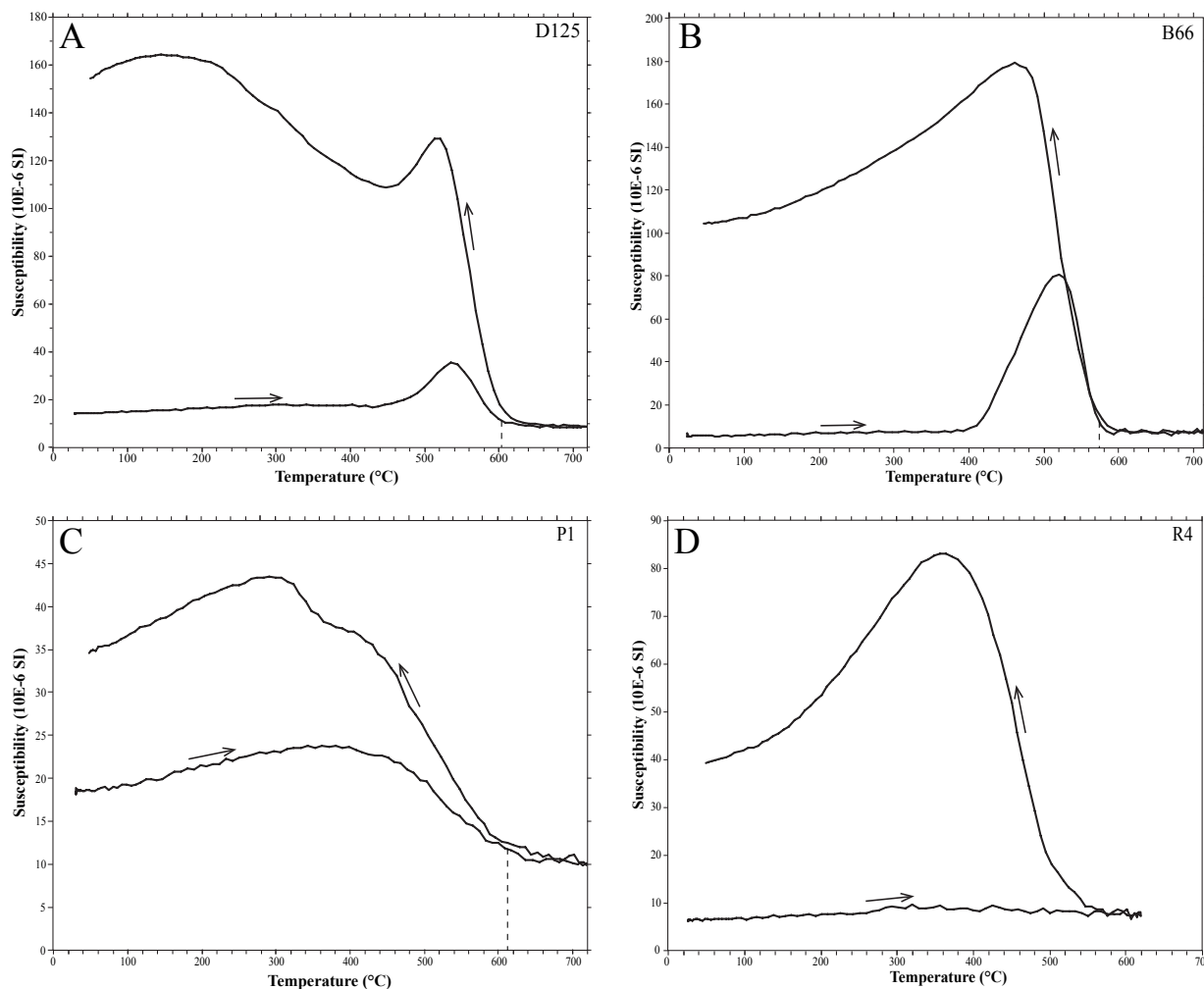


FIGURE 3.7 – Thermomagnetic curves (temperature v. magnetic susceptibility) in four representative samples (A to D). Heating and cooling were proceeded in Argon atmosphere to avoid alteration processes. The directions of arrows indicate heating and cooling curves. The curves are not reversible upon cooling, indicating significant magnetic alteration of the magnetic carriers prior the experiment (secondary iron oxides). During the heating, maximum decrease of magnetic susceptibility occurred between from 570 to 610°C, marking the presence of magnetite (A to C).

between 70 and 90 mT, which typifies low coercivity (<100 mT) remanence carriers such as a magnetite and/or titanomagnetite (e.g. Ti-poor magnetite; Dunlop & Özdemir, 2001). However, most of the samples do not reach saturation magnetisation after 100 mT, indicating the presence of higher coercivities minerals such as hematite (hundreds of mT to 1T) or even goetite, when saturation is achieved between 1 and >1.5 T. A mixture of magnetic carriers are interpreted in the samples. A mixture of magnetic carrier can be interpreted of the studied samples, although hematite is predominant and magnetite is not always present. This interpretation is in good agreement with the unblocking temperatures determined in Figure 3.7.

Hysteresis loops were measured on the same samples to estimate the domain structure of magnetic minerals. Hysteresis loop experiments and IRM were acquired on a vibrating sampler

magnetometer (VSM Micromag 3900) at the IPGP. The hysteresis curves are corrected from the paramagnetism to interpret the ferrimagnetic component of the minerals. The samples (half of them) show a wasp-waisted loop (Figure 3.9), indicating a combination of magnetic minerals with strongly contrasting coercivities such as magnetite and hematite or a mixture of single-domain and superparamagnetic grains in the samples. Some samples present a narrow hysteresis loop indicating the presence of a single low coercivity ferromagnetic mineral population, probably in the pseudo-single domain grain size range. This also suggests a range of magnetic particle sizes in the submicron range (Tauxe *et al.*, 1996; Dunlop & Özdemir, 2001). Because of this mixture, the mineralogical interpretation of the classical Day plot used to characterize the magnetic grain size (Day *et al.*, 1977) can be misleading, and is therefore worthless.

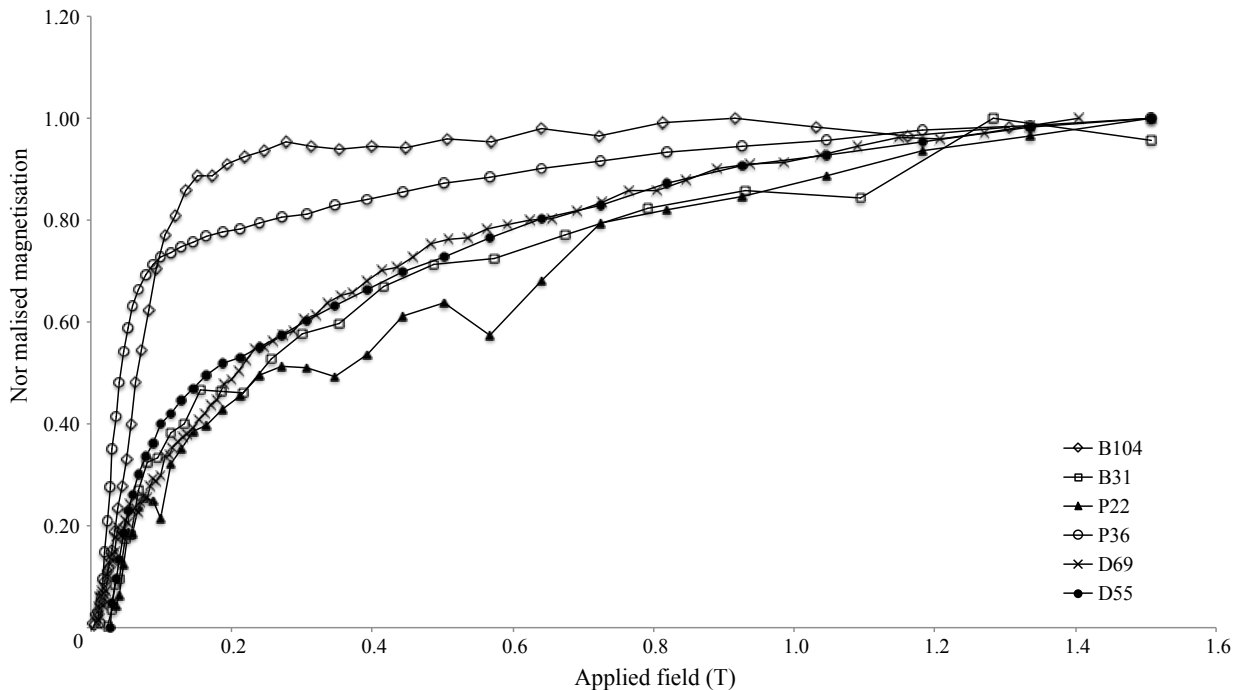


FIGURE 3.8 – Isothermal remanent acquisition curves for six representative samples. Normalised intensities v. applied magnetic field. Maximum magnetisation values for the selected samples are : $3.45 \times 10^{-4} \text{Am}^2 \text{kg}^{-1}$ (B104); $6.96 \times 10^{-5} \text{Am}^2 \text{kg}^{-1}$ (B31); $5.64 \times 10^{-4} \text{Am}^2 \text{kg}^{-1}$ (P22); $1.16 \times 10^{-3} \text{Am}^2 \text{kg}^{-1}$ (P36); $6.12 \times 10^{-4} \text{Am}^2 \text{kg}^{-1}$ (D69); $5.54 \times 10^{-4} \text{Am}^2 \text{kg}^{-1}$ (D55).

3.4.3 Demagnetisation and magnetic directions

Demagnetisation techniques

A total of 398 specimens were submitted to progressive thermal (99 specimens) and alternating field (AF) stepwise demagnetization (299 specimens) to clean the magnetic remanence. Thermal demagnetisation was applied using a furnace housed in a shielded room at the IPGP. AF

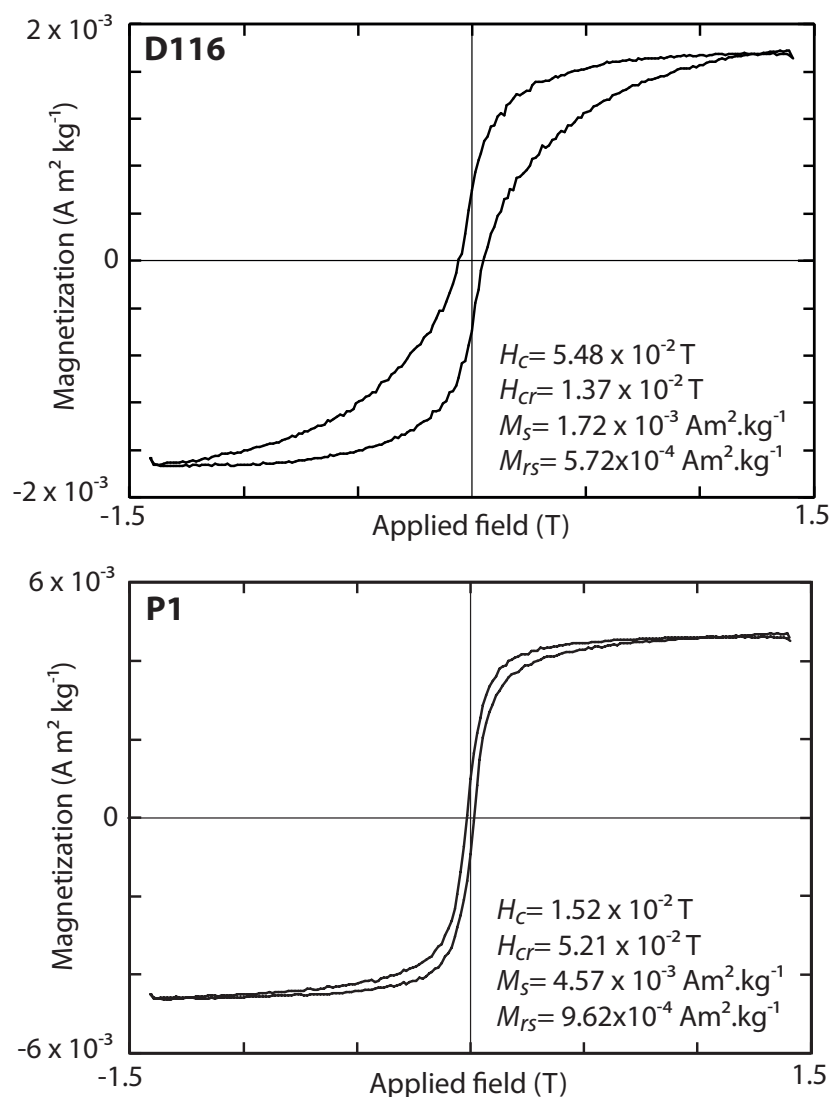


FIGURE 3.9 – Hysteresis curves of two representative samples (D116) with the diamagnetic component removed. Hysteresis curves show a typical « wasp-waisted » loop. The narrow hysteresis loop (P1 sample) indicates pseudo-single domain grains.

demagnetisation was applied in the same shielded laboratory using 2G in-line three-axis and was preferentially used for poorly consolidated samples. Both methods were applied on two specimens of the same site in both the Kerpini and Doumena sections. The samples were subjected to 10–12 steps of demagnetisation. Alternating fields of 2, 4, 8, 15, 30, 50, 70, 90, 110, 130, 150 mT were applied for the samples of Voutsimos, Doumena and Kerpini sections. For the samples of the Valimi section, stepwise alternating fields of 1, 2, 3, 5, 8, 13, 21, 34, 55, 75, 100 mT were applied. Thermal demagnetisation was performed at temperatures of 100, 200, 250, 300, 350, 400, 450, 500, 525, 550, 575 and 600 °C for samples from the Doumena and Kerpini sections. The remanent magnetisations were measured at each step on a 2G Enterprises horizontal DC SQUID cryogenic magnetometer in the same laboratory. Natural Remanent Magnetization (NRM) intensities are generally low and do not display significant variations throughout the sections. The intensity

of the NRM is low and ranges from 7.00×10^{-5} to 5.58×10^{-2} A/m, with an average value of $2.14 \pm 5.64 \times 10^{-3}$ A/m.

Principal component analysis

Magnetic components were identified using stereographic projections and orthogonal vector diagrams (Zijderveld, 1967). The principal component (Kirschvink, 1980) and the mean directions were computed using Fisher statistics (Fisher, 1953) with Paleomac software (Cogné, 2003). Both demagnetization techniques usually isolated two magnetic components with one at low temperature (100–350°) and low field (2–30 mT) that did not decay toward the origin and another at higher temperature (>250–350°) and higher field (>20–30 mT) (Figure 3.10). In the Doumena section, it was easier to isolate the ChRM (characteristic remanent magnetisation) with AF demagnetisation than thermally. Demagnetisation curves show a particular soft resistance to alternative field as NRM drops after 4 mT.

In good quality samples, the second component usually passes through the origin and can be interpreted as the characteristic remanent magnetization (ChRM). However, because the NRM is relatively low in most of the samples the demagnetization techniques failed to remove the second component and the remanence is unstable at higher field and temperature (Figure 3.7). Hence, based on the overall quality of the demagnetization diagrams and the stability of the remanence, we defined three different quality groups named Q1, Q2 and Q3.

- In Quality-1 (Q1) samples, the low temperature and weak field component was successfully removed. Projected directions on the Zijderveld plot form a linear and stable demagnetisation path at high temperature and strong field that decays through or close to the origin (Figure 3.10A–D). The magnetic direction of the ChRM can be easily calculated and usually show maximum angular deviation (MAD) of the magnetic components less than 20°.
- Quality-2 (Q2) samples were identified when the best-fit line does not pass through the origin, suggesting that the secondary magnetic component was only partially removed during the demagnetization. The ChRM direction is thus uncertain and presents high MAD values (higher than 30°). This quality group also includes samples with their remanent direction trajectories following a great circle (Figure 3.10E, F).
- Quality-3 (Q3) samples often present unstable magnetic behaviour. In several samples no clear demagnetisation path was identified and the signal was too unstable to determine the ChRM (Figure 3.10G). Some Q3 samples are systematically located at the top of sections. In these samples, the demagnetization isolated one single clear component that decays to the origin (Figure 3.10H) but with intermediate E-W magnetic direction and very low inclination, which may suggest a secondary magnetisation especially during lightning impact.

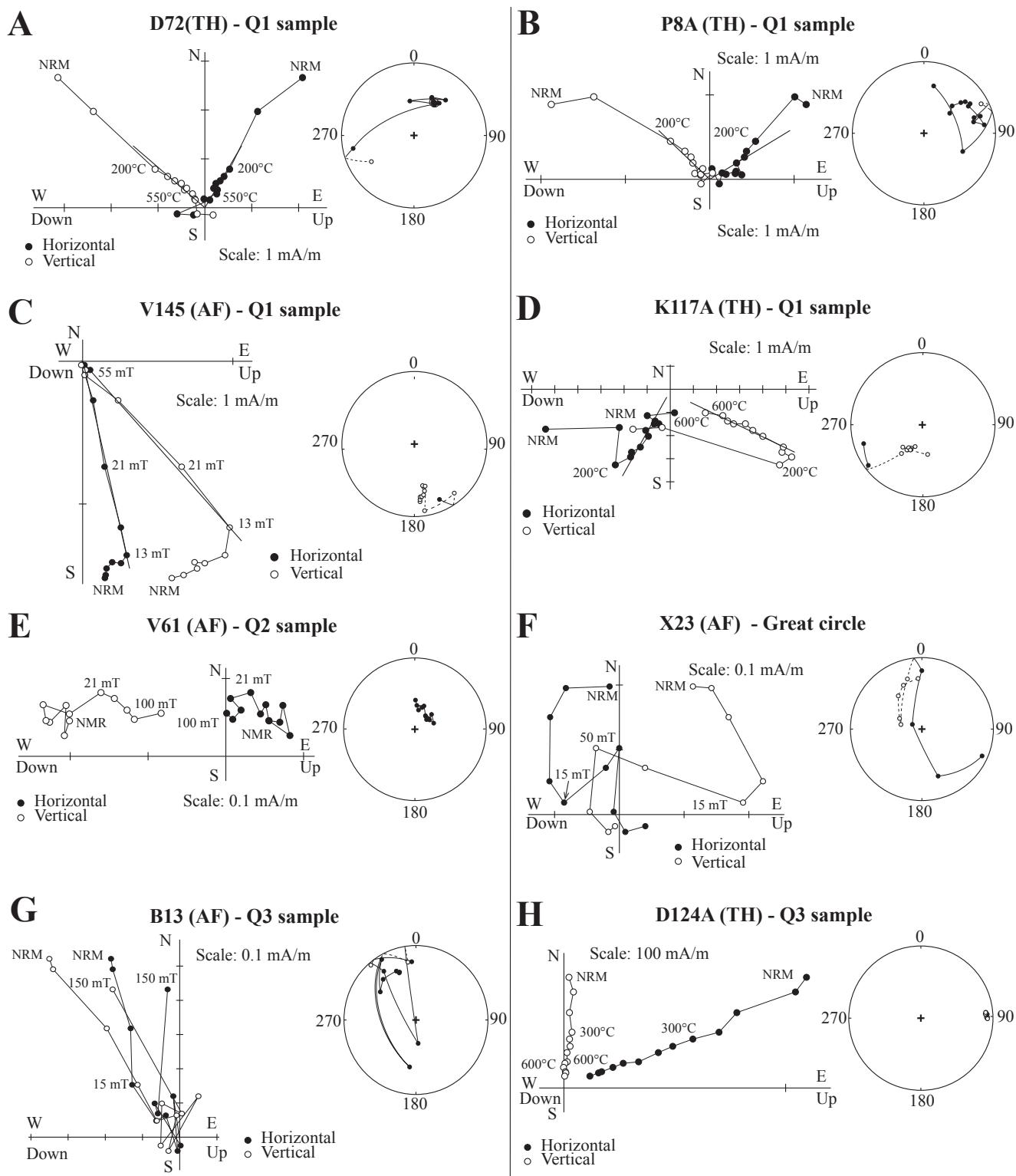


FIGURE 3.10 – Representative demagnetization diagrams and stereographic projections (tilt corrected). **A** and **B** : Q1 samples showing normal polarity. **C** and **D** : Q1 samples showing a reversed polarity. **E** Q2 sample. **F** Stereographic projection showing a typical great circle. **G** and **H** Q3 samples excluded from the palaeomagnetic analysis. Full symbol are projections on the horizontal plane and open symbols on the vertical plane.

TABLE 3.1 – Palaeomagnetic data of the Valimi section. (c) : samples housed in plastic boxes. * Broken cores that may lead to erroneous orientation of the sample on the field.

Specimen	Thickness (m)	Bedding	AF/TH	Min–Max	Dg (°)	Ig (°)	Ds (°)	Is (°)	MAD (°)	Quality	Polarity
M1	5	065-20	AF	NRM–100 mT	52.6	54.6	81.0	53.9	5.0	Q1	N
M3B	23	065-20	AF	NRM–100 mT	14.8	9.0	18.8	24.0	3.6	Q1	N
M4B	29	013-26	AF	3–100 mT	25.1	-3.7	22.3	-8.6	8.7	Q1	N
M5A	40	013-26	AF	13–100 mT	343.6	52.3	21.2	57.4	8.1	Q1	N
M6	50	060-47	AF	NRM–100 mT	14.5	52.3	93.3	59.2	4.8	Q1	N
M9	124	060-42	AF	NRM–100 mT	32.3	74.5	126.9	53.1	4.5	Q1	N
M10	177	058-41	AF	13–100 mT	36.7	81.7	135.5	51.4	10.3	Q1	N
M12	197	058-41	AF	13–100 mT	348.6	64.2	13.8	83.3	14.0	Q2	-
M13	228	058-41	AF	13–100 mT	31.8	74.4	109.4	74.2	7.7	Q1	N
M15	305	058-41	AF	5–100 mT	10.7	57.5	80.9	64.0	4.6	Q1	N
M16	355	058-41	AF	13–100 mT	206.9	74.0	181.7	57.0	3.4	Q2	-
M17A	387	054-36	AF	8–100 mT	168.6	62.2	156.7	27.8	4.0	Q2	-
V5(c)	429	065-32	AF	13–100 mT	177.3	75.1	162.8	43.9	6.3	Q2	-
V8(c)	435	065-32	AF	3–100 mT	288.4	41.5	261	54.1	9.9	Q2	-
V17*	510	065-32	AF	13–100 mT	1.8	51.9	54.7	73.5	2.5	Q1	N
V18(c)	510	065-32	AF	13–100 mT	355.1	41.4	21.2	69.1	2.3	Q1	N
V19	523	065-32	AF	5–100 mT	19.6	73.6	124.5	67.0	4.8	Q2	-
V22	523	065-32	AF	8–100 mT	19.8	62.8	96.2	67.8	5.1	Q1	N
V24	545	065-32	AF	8–100 mT	359.2	51.1	48.9	74.5	3.1	Q1	N
V25	550	065-32	AF	8–100 mT	331.9	38.6	327.8	70.5	2.0	Q1	N
V27	567	065-32	AF	8–100 mT	353.2	29.6	1.5	55.2	3.8	Q1	N
V29(c)	575	065-32	AF	8–100 mT	293.6	40.2	260.9	58.3	3.6	Q1	N
V32	580	060-25	AF	8–100 mT	3.2	39.2	23.0	57.9	2.7	Q1	N
V33	585	060-25	AF	8–100 mT	1.1	54.9	44.2	75.7	4.2	Q1	N
V35	595	060-25	AF	2–100 mT	359.2	51.4	31.8	69.8	3.2	Q1	N
V36*	590	060-25	AF	2–100 mT	45.3	56.3	82.6	54.5	6.9	Q2	-
V38*	630	060-25	AF	13–100 mT	115.5	-50.3	82.9	-66.9	5.4	Q2	-
V40	642	060-25	AF	8–100 mT	356.7	40.8	15.3	61.4	5.6	Q1	N
V41	649	060-25	AF	NRM–100 mT	0.2	51.4	33.1	69.4	3.1	Q1	N
V43	662	058-30	AF	2–100 mT	9.5	54.8	63.2	67.5	2.9	Q1	N
V52(c)	685	058-30	AF	5–100 mT	291.4	-23.6	294.9	1.2	4.0	Q2	-
V55	693	058-30	AF	13–100 mT	329.9	50.3	335.1	80.2	13.8	Q1	N
V58	698	058-30	AF	8–100 mT	1.1	54.9	44.2	75.7	4.2	Q1	N
V59(c)	728	058-30	AF	NRM–100 mT	349.1	33	4.7	59.6	2.3	Q2	-
V64	733	058-30	AF	21–100 mT	354.2	2.0	358.2	28.6	5.6	Q1	N
V66	740	058-30	AF	8–100 mT	338.7	36.9	349.3	65.9	3.0	Q1	N
V68	745	058-30	AF	8–100 mT	344.2	38.9	10.8	71.3	2.1	Q1	N
V69	768	058-30	AF	13–100 mT	20.2	30.6	41.4	44.8	1.9	Q1	N
V74(c)	805	058-30	AF	13–100 mT	36.9	60.1	88.8	57.2	6.4	Q1	N
V75	815	058-30	AF	8–100 mT	351.0	44.2	19.5	69.0	4.6	Q1	N
V127	830	058-30	AF	8–100 mT	350.0	54.6	69.4	77.2	3.9	Q1	N
V129(c)	835	058-30	AF	8–100 mT	331.1	46.7	337.3	76.6	5.3	Q1	N
V132	840	058-30	AF	NRM–55 mT	350.8	52.5	37.0	75.4	5.8	Q1	N
V136	850	058-30	AF	5–100 mT	353.8	54.9	49.1	75.3	4.1	Q1	N
V139	885	058-30	AF	13–75 mT	324.1	35.3	318.1	71.1	4.5	Q1	N
V143(c)	912	058-30	AF	5–100 mT	164.5	-22.2	172.3	-50.5	4.4	Q1	R
V145(c)	917	058-30	AF	8–100 mT	163.9	-8.7	167.9	-37.4	3.3	Q1	R
V151	933	058-30	AF	21–100 mT	143.4	35.1	144.2	5.2	5.1	Q2	-
V156*	962	058-30	AF	8–55 mT	154.8	-25.3	158.8	-54.9	2.5	Q1	R
V162	982	058-30	AF	21–100 mT	191.6	-24.6	208.0	-43.7	10.9	Q1	R
V163*	1020	058-30	AF	13–100 mT	169.2	-34.0	185.6	-60.5	6.0	Q1	R
V169	1050	058-30	AF	13–75 mT	162.3	-24.5	173.5	-58.6	9.3	Q1	R
V177	1085	058-30	AF	21–100 mT	165.0	-33.3	178.4	-61.0	3.2	Q1	R
V189(c)	1137	074-20	AF	8–100 mT	171.0	-43.1	175.3	-62.9	2.6	Q1	R
V191	1142	074-20	AF	21–100 mT	160.9	-46.6	158.7	-66.5	5.5	Q1	R
V193(c)	1153	074-20	AF	13–100 mT	198.9	-34.3	210.8	-49.6	14.5	Q1	R
V195	1157	074-20	AF	5–100 mT	158.0	-20.0	156.6	-39.9	7.6	Q1	R
V218(c)	1218	066-36	AF	1–100 mT	10.6	69.9	44.3	87.4	5.2	Q2	-
V223	1235	066-36	AF	5–100 mT	249.4	32.5	218.2	60.2	3.7	Q2	-
V225	1260	066-36	AF	8–100 mT	16.6	57.5	26.9	74.9	4.9	Q2	-
R7	1266	082-36	AF	8–150 mT	43.9	69.3	130.3	65.4	10	Q2	-
R15	1275	082-36	AF	2–150 mT	316.0	27.7	296.7	50.7	5.3	Q1	N
R18	1279	082-36	AF	30–150 mT	36.2	55.7	95.7	66.2	9.7	Q1	N
V230	1298	066-36	AF	NRM–100 mT	297.6	62.3	208.1	68.5	3.7	Q1	N

3.4 Magnetostratigraphy and Rock Magnetism

TABLE 3.2 – Palaeomagnetic data of the Voutsimos section. * Broken cores that may lead to erroneous orientation of the sample on the field.

Specimen	Thickness (m)	Bedding	AF/TH	Min–Max	Dg (°)	Ig (°)	Ds (°)	Is (°)	MAD (°)	Quality	Polarity
B1	20	240-20	AF	NRM–150	351.2	54.4	344.9	35.3	5.3	Q1	N
B17	71	220-18	AF	NRM–150	355.6	46.2	345.8	32.4	3.9	Q1	N
B20*	79	240-20	AF	NRM–150	356.9	42.7	351.4	24.4	3.4	Q1	N
B22	81	240-20	AF	2–150 mT	7.1	38.0	.7	21.4	5.5	Q1	N
B25	95	240-20	AF	NRM–150	5.3	35.8	359.7	18.9	3.7	Q1	N
B28	98	227-20	AF	NRM–150	9.6	44.8	358.1	31.0	5.9	Q1	N
B32A*	105	227-20	AF	4–150 mT	346.1	47.7	339.1	29.6	7.2	Q1	N
B34	110	227-20	AF	2–150 mT	0.7	46.8	350.5	31.0	2.5	Q1	N
B39	124	198-36	AF	NRM–150	3.1	57.6	328.4	37.0	6.3	Q1	N
B42	127	198-36	AF	NRM–150	10.2	45.0	342.9	31.0	2.0	Q1	N
B48*	138	198-36	AF	NRM–150	354.1	57.5	45.0	63.2	4.4	Q1	N
B50A	150	210-28	AF	4–150 mT	347.7	51.3	29.4	62.5	4.9	Q1	N
B50F	160	210-28	AF	NRM–13	343.9	50.6	24.8	63.8	1.2	Q1	N
B51	177	210-28	AF	4–150 mT	293.2	20.5	290.5	48.3	8.2	Q1	N
X4	178	215-36	AF	2–150 mT	334.4	71.8	316.1	37.5	3.3	Q1	N
X5	179	215-36	AF	M15–150 mT	23.5	37.9	2.7	23.9	6.5	Q1	N
X7	181	215-36	AF	2–150 mT	38.7	30.8	18.4	26.5	4.7	Q1	N
X9	182	215-36	AF	30–150 mT	325.8	19.7	325.2	-14.2	5.1	Q2	-
B54	182	215-36	AF	M15–150 mT	341.7	25.6	352.4	17.2	5.6	Q1	N
B56	185	215-36	AF	NRM–150	344.3	30.7	338.0	1.3	4.9	Q1	N
X11*	187	215-36	AF	8–150 mT	341.4	39.4	332.6	8.6	1.1	Q2	-
X13	188	215-36	AF	2–130 mT	356.8	53.3	336.4	25.5	7.2	Q1	N
X15	189	215-36	AF	2–150 mT	325.5	53.3	317.7	18.7	3.2	Q1	N
B58	197	215-36	AF	2–150 mT	179.7	-49.0	160.5	-22.8	9.6	Q1	R
X22	198	215-36	AF	-	-	-	-	-	-	Q2	R? (GC)
X23	199	215-36	AF	-	-	-	-	-	-	Q2	R? (GC)
X29*	201	224-32	AF	15–150 mT	4.3	14.4	2.6	-6.7	13.3	Q1	N
B62	212	224-32	AF	NRM–150	6.0	40.2	349.6	17.7	4.8	Q1	N
X31	221	224-32	AF	NRM–150	12.4	48.8	353.0	27.1	2.6	Q1	N
X33	223	224-32	AF	NRM–150	2.4	52.3	344.9	27.2	2.3	Q1	N
B64	223	215-36	AF	NRM–150	11.3	47.7	348.3	26.1	3.4	Q1	N
B66	228	215-36	AF	NRM–150	11.2	62.4	337.2	37.4	3.6	Q1	N
B68	229	240-32	AF	NRM–150	0.2	49.0	350.7	20.7	4.6	Q1	N
B74	289	240-32	AF	NRM–150	344.3	63.1	337.6	31.6	4.2	Q1	N
B75	290	245-18	AF	-	-	-	-	-	-	Q2	N? (GC)
B79	296	245-18	AF	8–150 mT	321.3	47.3	324.4	29.7	10.8	Q1	N
B89	300	245-18	AF	15–150 mT	334.5	34.5	334.6	16.5	14.5	Q1	N
B93	335	210-20	AF	15–150 mT	318.5	26.2	316.7	7.1	13.8	Q1	N
B96	337	210-20	AF	-	-	-	-	-	-	Q2	R? (GC)
B97	338	210-20	AF	-	-	-	-	-	-	Q2	R? (GC)
B100	339	210-20	AF	-	-	-	-	-	-	Q2	R? (GC)
B101	342	210-20	AF	-	-	-	-	-	-	Q2	R? (GC)
B103	359	260-26	AF	-	-	-	-	-	-	Q2	R? (GC)
B106	362	260-26	AF	-	-	-	-	-	-	Q2	R? (GC)
B108	364	260-26	AF	8–110 mT	342.5	31.7	343.6	5.9	14.3	Q1	N
B109	366	260-26	AF	NRM–110	341.0	46.7	343.4	20.9	4.6	Q1	N

TABLE 3.3 – Palaeomagnetic data of the Doumena section. * Broken cores that may lead to erroneous orientation of the sample on the field.

Specimen	Thickness (m)	Bedding	AF/TH	Min-Max	Dg (°)	Ig (°)	Ds (°)	Is (°)	MAD (°)	Quality	Polarity
D1	1	305-30	AF	2-110 mT	349.0	63.9	11.1	38.7	2.6	Q1	N
D2	1	305-30	TH	100-600°C	223.7	18.2	227.4	47.7	8.1	Q1	R
D4	11	310-20	TH	200-600°C	180.5	-56.9	193.1	-40.0	7.6	Q1	R
D8	15	310-24	AF	2-110 mT	18.4	49.5	24.5	26.7	6.2	Q1	N
D8	15	310-24	TH	100-550°C	25.6	22.1	26.6	-1.3	12.7	Q1	N
D9	37	310-24	AF	NRM-50 mT	54.4	64.5	48.1	40.9	7.1	Q1	N
D11	47	310-34	AF	2-110 mT	26.4	44.0	29.6	20.5	5.2	Q1	N
D12	47	310-24	TH	200-500°C	25.4	33.7	27.7	10.3	5.6	Q1	N
D17	60	325-35	AF	2-110 mT	34.3	42.3	39.6	8.9	11.8	Q1	N
D22	138	290-26	AF	2-110 mT	4.8	34.9	7.4	9.7	11.2	Q1	N
D25	148	290-26	AF	2-110 mT	3.9	51.1	8.8	25.8	4.7	Q1	N
D33	189	310-30	AF	2-110 mT	353.4	54.4	10.7	30.2	8.7	Q1	N
D35	233	310-30	AF	2-110 mT	35.2	62.6	37.4	32.6	8.6	Q1	N
D37	251	315-20	AF	2-110 mT	340.6	38.4	351.9	27.9	6.6	Q1	N
D39	258	315-20	AF	2-90 mT	18.8	50.6	25.7	32.1	7.5	Q1	N
D41	264	310-22	AF	NRM-100 mT	19.2	50.9	25.0	29.9	4.2	Q1	N
D43	280	310-22	AF	4-110 mT	4.0	39.1	10.9	20.5	8.2	Q1	N
D46	281	310-22	AF	NRM-110 mT	351.2	62.1	10.3	44.8	6.1	Q1	N
D46	281	310-22	TH	100-600°C	342.3	53.3	359.7	38.6	5.7	Q1	N
D47	287	330-20	AF	NRM-110 mT	22.2	61.1	35.8	43.8	6.5	Q1	N
D48	287	330-20	TH	200-600°C	357.4	33.2	5.0	19.9	7.5	Q1	N
D49	320	330-20	AF	2-90 mT	4.1	53.4	20.0	39.8	5.9	Q1	N
D52	333	330-20	AF	2-110 mT	339.5	64.9	11.9	55.8	11.2	Q1	N
D56	356	330-20	TH	100-600°C	7.4	46.5	21.8	34.9	6.1	Q1	N
D56	356	330-20	AF	NRM-50 mT	35.5	57.2	46.6	39.6	3.1	Q1	N
D60	384	290-22	AF	NRM-110 mT	8.8	59.3	12.8	37.6	8.8	Q1	N
D62	426	290-22	AF	2-110 mT	17.9	47.3	18.4	25.3	7.1	Q1	N
D63	444	340-23	AF	2-110 mT	203.2	53.3	168.2	63.9	6.5	Q1	N?
D64*	450	340-23	TH	200-575°C	187.3	39.7	166.2	46.6	7.1	Q1	N?
D66A	461	340-23	TH	200-600°C	20.0	18.8	23.4	3.4	8.8	Q1	N
D68	477	340-23	AF	2-110 mT	22.6	48.5	35.4	30.9	8.1	Q1	N
D70	490	310-22	AF	2-110 mT	24.2	51.2	28.7	29.7	6.8	Q1	N
D71	502	310-22	AF	NRM-50 mT	15.8	53.4	23.1	32.7	5.4	Q1	N
D72	502	310-22	TH	100-600°C	22.7	67.6	30.6	46.1	3.6	Q1	N
D75*	534	310-22	AF	2-90 mT	8.7	53.5	18.2	33.7	7.6	Q1	N
D77	545	310-22	AF	NRM-110 mT	6.8	58.7	18.5	39.0	9.0	Q1	N
D78	545	310-22	TH	250-550°C	7.8	56.8	18.6	37.1	4.6	Q1	N
D80*	573	310-22	AF	M2	15.9	52.5	23.0	31.8	4.6	Q1	N
D84	599	330-16	TH	100-550°C	353.5	53.9	5.1	41.7	5.3	Q1	N
D88	611	330-16	AF	NRM-110 mT	330.5	59.4	355.4	55.7	14.1	Q1	N
D90*	613	312-20	AF	2-110 mT	17.4	63.5	26.9	44.6	9.0	Q1	N
D104	711	350-12	AF	2-110 mT	7.3	66.8	29.1	61.0	5.8	Q1	N
D106*	728	350-12	AF	2-110 mT	345.7	58.2	4.7	57.1	8.8	Q1	N
D107	731	350-12	AF	2-110 mT	354.8	74.5	29.8	69.7	13	Q2	-
D113	804	290-15	AF	NRM-110 mT	1.2	47.1	4.9	32.7	4.7	Q1	N
D114	804	290-15	AF	NRM-550°C	24.8	61.5	23.3	46.5	7.0	Q1	N
D115	810	290-15	AF	2-110 mT	61.4	-4.7	63.3	-15.8	1.3	Q1	N
D120*	825	290-15	TH	200-550°C	150.2	48.5	133.4	56.5	9.0	Q1	N
D124	856	290-15	TH	-	-	-	-	-	-	Q2	N? (GC)
D126*	868	254-10	AF	-	-	-	-	-	-	Q2	N? (GC)
D128	907	245-10	TH	200-550°C	146.1	44.6	144.1	54.5	11.9	Q1	N

TABLE 3.4 – Palaeomagnetic data of the Kerpini section. (c) : samples housed in plastic boxes. * Broken cores that may lead to erroneous orientation of the sample on the field.

Specimen	Thickness (m)	Bedding	AF/TH	Min/Max	Dg (°)	Ig (°)	Ds (°)	Is (°)	MAD (°)	Quality	Polarity
P2	18	N040-22S	AF	8–150 mT	351.6	46.1	15.4	59.6	12.8	Q1	N
P3	42	N030-20S	AF	NRM–110	19.0	68.4	64.9	63.9	8.1	Q1	N
P7	55	N030-20S	AF	2–150 mT	38.7	45.9	56.6	39.7	5.8	Q1	N
P8A	55	N030-20S	TH	200–600°C	46.8	36.4	58.7	28.5	13.0	Q1	N
P9	70	N030-20S	AF	NRM–150	12.6	52.1	36.8	66.8	5.3	Q1	N
P13*	109	N040-20S	AF	15–50 mT	209.0	0.0	209.6	-3.7	1.9	Q1	R
P14	109	N040-20S	TH	-	-	-	-	-	-	Q2	R? (GC)
P16	118	N060-18S	TH	200–600°C	165.2	-22.3	168.3	-39.6	7.4	Q1	R
P18*	118	N060-18S	AF	2–150 mT	27.0	55.9	55.8	61.9	11.0	Q1	N
P22	132	N060-22S	TH	250–600°C	52.8	42.7	73.0	41.6	9.7	Q1	N
P25	142	N060-22S	TH	100–600°C	27.3	29.4	41.0	39.2	12.5	Q1	N
P27	147	N060-22S	TH	200–550°C	183.4	-37.5	198.5	-54.4	6.2	Q1	R
P29	160	N060-22S	TH	350–600°C	298.8	61.0	252.7	75.1	6.8	Q2	N
P32	174	N080-20S	TH	100–550°C	190.8	-10.1	193.5	-28.6	26.2	Q1	R
P35*	174	N080-20S	TH	100–550°C	163.2	-21.1	161.6	-40.9	15.4	Q1	R
P41	196	N060-20S	TH	100–550°C	183.1	-40.5	197.8	-55.9	6.1	Q1	R
P43	200	N060-30S	TH	200–550°C	193.5	-22.1	208.3	-41.4	1.9	Q1	R
P45	207	N060-30S	AF	8–90 mT	185.3	8.0	186.7	-16.5	7.1	Q1	R
P48	211	N060-30S	TH	200–550°C	201.6	-4.1	207.4	-21.9	8.4	Q1	R
P55(c)	240	N060-30S	AF	8–150 mT	191.6	-191.6	-2.4	196.7	-24.2	Q1	R
P56(c)	240	N060-30S	AF	15–150 mT	209.3	-8.9	217.1	-22.7	10.2	Q1	R
P57	250	N060-30S	AF	-	-	-	-	-	-	Q2	R? (GC)
P58	250	N060-30S	TH	200–550°C	227.1	-49.2	261.6	-46.8	8.8	Q1	R
P59	258	N040-30S	AF	30–90 mT	198.4	6.0	204.1	-15.9	23.8	Q1	R
P60	258	N040-30S	TH	200–450°C	191.9	-20.2	205.8	-31.3	2.2	Q1	R
P64	263	N040-30S	TH	200–450°C	195.6	-34.1	218.7	-41.0	3.7	Q1	R
K91*	300	N090-18S	AF	8–150 mT	177.9	-29.5	177.3	-47.5	5.0	Q1	R
K91*	300	N090-18S	TH	200–600°C	165.7	-37.5	160.1	-54.7	9.6	Q1	R
K93	300	N090-18S	TH	200–600°C	181.1	-25.6	181.3	-43.6	7.1	Q1	R
K97	317	N090-18S	AF	8–150 mT	179.8	-24.2	179.8	-42.2	6.2	Q1	R
K97	317	N090-18S	TH	200–600°C	169.4	-36.0	165.5	-53.6	6.4	Q1	R
K106	338	N060-20S	TH	200–600°C	175.4	-24.6	181.8	-42.2	27.6	Q1	R
K114	369	N060-20S	TH	100–550°C	30.2	68.3	84.2	69.4	6.6	Q1	N
K115	397	N060-20S	AF	2–150 mT	19.4	36.1	34.5	47.2	3.7	Q1	N
K116	397	N060-20S	TH	200–600°C	20.4	31.4	33.2	42.5	9.4	Q1	N
K117A	404	N042-20S	TH	200–600°C	185.1	-48.8	209.8	-57.4	5.5	Q1	R
K121*	412	N042-20S	TH	200–600°C	182.9	-43.6	203.0	-53.5	3.9	Q1	R
K133*	439	N057-18S	AF	2–150 mT	278.9	69.2	223.5	74.2	5.7	Q1	N
K135	441	N057-18S	AF	2–150 mT	352.3	52.2	9.8	67.4	7.1	Q1	N
K137	452	N057-18S	AF	2–150 mT	343.9	64.1	13.5	79.9	3.5	Q1	N

3.4.4 Magnetic directions and statistical tests

Among the 398 specimens, samples 168, 54 and 176 were interpreted as Q1, Q2 and Q3 samples respectively. Details of the palaeomagnetic directions of Q1 and Q2 samples are presented in Tables 3.1, 3.2, 3.3 and 3.4. The sections are subdivided into different thickness intervals taking into account lithostratigraphic boundaries, magnetic polarity and the data available. The mean palaeomagnetic direction for each thickness interval is calculated and presented in Table 3.5.

- In the **Valimi section**, ChRM directions were found for 45% of the samples (48 Q1 samples) with both normal and reversed polarities. Assuming a fisherian distribution, the mean direction in stratigraphic coordinates for normal polarity is $D_s = +34.8^\circ$, $I_s = +71.3^\circ$, $\alpha_{95} = 8.4^\circ$ where D is declination, I the inclination and α_{95} is the radius of 95% confidence cone. The mean direction for reversed polarity is $D_s = +177.2^\circ$, $I_s = -54.7^\circ$, $\alpha_{95} = 8.5^\circ$ (Figure 3.12A).
- In the **Voutsimos section**, ChRM directions were determined in 57% of the samples (35 Q1 samples), mainly normal polarity. Fisher statistics yields in stratigraphic coordinate a mean declination $D_s = +345.5^\circ$, $I_s = +28.9^\circ$, $\alpha_{95} = 7.2^\circ$. A small reversed polarity at 197 m is recorded in three samples (one Q1 sample) over a short thickness interval (2 m) within the Ladopotamos Formation ($D_s = +160.7^\circ$, $I_s = -22.8^\circ$, $\alpha_{95} = 9.6^\circ$, Figure 3.12A).
- In the **Doumena section**, ChRM direction was found for 43% of the samples (48 Q1 samples) with mainly normal polarity. The mean sampling interval of 12 m. The mean normal polarity direction is $D_s = +24.2^\circ$, $I_s = +37.9^\circ$, $\alpha_{95} = 8.0^\circ$ (Figure 3.12A).
- Lastly, in the **Kerpini section**, ChRM directions were determined in 29% of the samples (37 Q1 samples) with both polarities. Accordingly, the mean thickness interval between two Q1 samples is 10 m. The normal polarity samples have a mean direction of $D_s = +46.0^\circ$, $I_s = +62.3^\circ$, $\alpha_{95} = 12.1^\circ$. Conversely, the reversed polarity samples have a mean direction of $D_s = 195.8^\circ$, $I_s = -40.3^\circ$, $\alpha_{95} = 8.6^\circ$ (Figure 3.12A).

The ChRM directions of 168 Q1 samples were used for Fisherian statistics and to demonstrate that the magnetisation is stable since the time of the rock formation (McFadden, 1990). To calculate the mean direction, the samples were all transferred to normal polarity. The overall mean direction in geographic coordinates is $D_g = +2.6^\circ$, $I_g = +45.6^\circ$, $\alpha_{95} = 3.7^\circ$, while in stratigraphic coordinates (tilt-corrected), the mean direction is $D_s = +12.5^\circ$, $I_s = +47.4^\circ$, $\alpha_{95} = 4.7^\circ$. The mean of the normal polarities in stratigraphic coordinates ($D_s = +13.3^\circ$, $I_s = +49.0^\circ$, $\alpha_{95} = 5.6^\circ$) are statistically the same (at 95%) as the present day field. Accordingly, the reversal test on these Q1 samples is positive at 95%.

To perform a reliable fold test, we have used the mean values for normal and reversed sites in all sections (Table 3.5 and Figure 3.12A). Maximum clustering of the directions is given by the k value (precision parameter) and occurs at 23% unfolding (Figure 3.12D). Directions before bedding correction is $D_g = 1.4^\circ$; $I_g = 43.9^\circ$; $\alpha_{95} = 15.8^\circ$ and change to $D_s = 11.0^\circ$; $I_s = 50.9^\circ$; $\alpha_{95} = 20.1^\circ$ after bedding corrections. Maximum clustering after partial unfolding suggests that magnetisation was acquired during the deformation of the different normal fault blocks. This interpretation is consistent with the observation of syn-rift growth strata. However, the dips in the different blocks are not sufficiently different to accurately apply the fold test.

Despite the non-conclusive result of the fold test, the reversal test was positive. A positive reversal test indicates that ChRM directions are free of secondary NRM components, and thus the paleomagnetic data can be used to average the geomagnetic secular variations. The measured directions were acquired during or soon after deposition at least in the Valimi and Kerpini sections where both polarities are recorded. The similarity between the present day field (PDF) and the overall mean direction is explained by the young age of the measured sections. Consequently, in those two sections we assume that primary magnetisation is recorded. As no clear reversal were identified in the Voutsimos and Doumena sections, we cannot fully demonstrate the absence of recent remagnetisation in these two sections. However, the sampled facies, magnetic mineralogy and demagnetization diagrams were similar. Primary magnetisation is also probable in these sections.

3.4.5 Polarity column and robustness

The magnetozones were determined mainly using Q1 samples (Tables 3.11). Q2 samples can be used when demagnetisation paths of several successive samples follow a great circle on the stereographic projections that evolve toward normal or reversed polarity directions (Figure 3.10F). Similarly, Quality-3 samples (Q3) were also ruled out. Each magnetozone was defined from a minimum of two successive horizons with Q1 samples possessing the same polarity. When polarity change is supported by only one Q1 sample, the magnetozone is interpreted as uncertain.

- In the **Valimi section** two main polarity magnetozones were identified. Most of the section records a normal polarity over 900 m (Figure 3.11). Then, one main polarity reversal is recorded within the Valimi Formation over 300 m. Two small uncertain reversed magnetozones (at 30 m and 580 m) and one uncertain normal magnetozone (from 1220 m to 1300) are tentatively identified. The mean thickness interval between two Q1 samples is 23 m. However, this average thickness interval decreases in the upper part of the section (from 500 to 1300 m) but increases in the lower part (from 0 to 500 m). In the lower part of the Valimi section, maximum thickness interval can reach 205 m and only nine Q1 samples were found (Figure 3.11). The interpretation for the base of the Valimi section is therefore uncertain.
- In the **Voutsimos section**, normal polarity is mainly recorded. The mean thickness between Q1 samples is 9 m but can reach 44 m in the upper part of the section. A small reversed polarity at 197 m may be recorded in one Q1 sample and two Q2 samples over a short thickness interval (2 m) within the Ladopotamos Formation (Figure 3.11). This reversed magnetozone is interpreted as uncertain.
- In the **Doumena section** one normal magnetozone was identified. However, three uncertain reversed intervals are interpreted, located at the base, in the middle part (at 450 m over few metres) and at the top of the section (830–910 m). The mean thickness between

two Q1 samples is 21 m but with gaps that can reach up to 98 m.

- Three complete reversed magnetozone were identified along the **Kerpini section**, within the Mega Spilaio Formation. The main reversed magnetozone is recorded from 150 to 340 m. Two other reversed magnetozone are recorded over shorter thickness intervals (110–120 m and 400–410 m). The mean thickness interval between Q1 samples is 10 m without significant gap (>50 m).

Very few polarities intervals were recognised in the four studied sections. We may question the robustness of these columns and whether other magnetic reversals may have been missed or not. The average number of Q1 samples per magnetozone (1 to 44) is largely greater than the number of magnetic reversals per section (1 to 7). The high density of good quality samples along the sections ensures that all the main magnetic reversals have been identified. The main uncertainty in the interpretation of the palaeomagnetic sections is related to the main gap intervals between the Q1 samples. Gaps larger than 50 m are reported in the palaeomagnetic logs (Figure 3.11). The largest gaps lie at the base of the Valimi section and in the Doumena section, systematically within the coarse conglomeratic fluvial formations (Tsivlos, Lithopetra and Mega Spilaio Formations) where fine-grained sediments are poorly preserved and mostly eroded. The intervals of lower density of data or complete gaps should be treated with caution as magnetozone may have been missed.

TABLE 3.5 – D and I are the magnetic declination and inclination, respectively at the corresponding site with α_{95} being the radius of the cone in which the mean direction lies within 95% confidence; n represents the number of samples at each site. The paleomagnetic pole were calculated using Paleomac software and then were compared to the apparent polar wander path (APWP) reference poles to calculate rotations, with λ_p the latitude and φ_p the longitude, while dp/dm are the corresponding confidence angles. Relative rotations were calculated using the APWP reference for Europe from (Besse & Courtillot, 2002). Magnetostratigraphic sections are treated as a single site. We compare the observed average directions with the 5 Ma reference pole ($\lambda_p = 86.3^\circ$; $\varphi_p = 172.0^\circ$; $\alpha_{95} = 2.6^\circ$).

Serie	Polarity	Thickness	Q1 specimen	n	Formation (fm)	Observed direction				Paleopole				Rotation	
						Dg (°)	Ig (°)	α_{95} (°)	Ds (°)	Is (°)	α_{95}	λ_p (°)	φ_p (°)		dp/dm
Valimi section (38.11°N; 22.32°E)															
V1	N	0–225	M1 to M10	7	Tsivlos Fm	19.8	48.2	27.6	61.9	53.1	35.6	40.6	97.5	0.69	59.6 ± 3.2
	-	300–500	No data	-	-	-	-	-	-	-	-	-	-	-	±
V2	N	500–575	V17 to V29	7	Lithopetra fm	346.1	47.6	16.8	10.1	77.2	17.3	61.9	31.2	0.93	7.9 ± 3.2
V3	N	575–700	V32 to V58	8	Valimi Fm	356.1	48.8	7.3	31.1	70.6	8.7	63.2	63.6	0.87	28.8 ± 3.2
V4	N	700–900	V59 to V139	11	Valimi Fm	350.9	42.9	12.5	22.1	69.4	12.6	68.6	60.7	0.86	19.9 ± 3.2
V5	R	900–1275	V143 to V195	11	Valimi Fm	168.8	-29.4	9.2	177.2	-54.7	8.5	-86.4	61.2	0.71	175.0 ± 3.2
V6	N	1275–1310	R15 to V230	3	Valimi Fm	n/a	n/a	n/a	n/a	n/a	n/a	-	-	-	-
Mean normal	N	-	-	37	-	355.3	48.2	7.3	34.8	71.3	8.4	60.8	63.3	0.87	32.6 ± 3.2
Mean	-	0–1310	M1 to V230	48	All section	353.4	43.8	6.3	21.0	68.5	7.1	35.3	38.1	0.84	19.2 ± 2.6
Voutsimos section (38.14°N; 22.28°E)															
B1	N	0–100	B1 to B28	6	Tsivlos Fm	1.4	43.8	7.0	353.7	27.4	7.5	65.7	217.3	0.55	-8.6 ± 3.2
B2	N	100–200	B32A to B50A	6	Ladopotamos Fm	357.1	51.3	6.8	351.6	44.9	21.4	76.4	236.0	0.63	-10.7 ± 3.2
B3	N	200–240	B50F to B68	16	Ladopotamos Fm	356.3	46.0	11.4	345.4	27.2	11.8	63.0	234.9	0.55	-16.9 ± 3.2
B4	N	240–300	B74 to B89	3	Ladopotamos Fm	332.2	48.6	24.8	332.2	26.1	15.7	55.4	255.2	0.54	-30.1 ± 3.2
B5	N	300–370	B93 to B109	3	Derveni Fm	333.3	35.4	23.9	334.5	11.6	26.9	50.3	244.4	0.51	-27.8 ± 3.2
Mean normal	N	-	B1 to B109	35	All section	353.0	46.3	6.1	345.5	28.9	7.2	64.0	235.6	0.56	-16.7 ± 3.2
Doumena section (38.09°N; 22.18°E)															
D1	N	0–200	D1 to D33	12	Mega Spilaio Fm	18.1	47.3	11.0	23.3	21.5	11.3	55.9	158.3	0.53	21.1 ± 3.2
D2	N	200–300	D35 to D48	9	Mega Spilaio Fm	3.8	51.5	10.4	15.3	33.1	10.4	65.9	164.2	0.57	13.1 ± 3.2
D3	N	300–400	D49 to D60	5	Mega Spilaio Fm	8.2	57.2	11.7	23	42.2	12.7	66.1	140.6	0.62	20.8 ± 3.2
D4	N	400–620	D62 to D90	15	Mega Spilaio Fm	12.0	53.6	7.4	21.1	35.2	7.6	63.9	151.8	0.58	18.8 ± 3.2
	-	620–700	No data	-	-	-	-	-	-	-	-	-	-	-	-
D5	N	700–910	D104-D128	7	Kalavryta Fm	n/a	n/a	n/a	n/a	n/a	n/a	n/a	n/a	n/a	n/a
Mean	N	-	D1 to D128	46	All section	16.0	55.8	8.0	24.7	36.5	8.5	63.2	144.2	0.60	22.0 ± 3.2
Kerpini section (38.07°N; 22.12°E)															
K1	N	0–100	P2 to P9	5	Mega Spilaio Fm	23.3	51.6	18.3	49.1	53	19.6	50.4	103.2	0.69	46.8 ± 3.2
K2	N	100–150	P13 to P43	4	Mega Spilaio Fm	22.7	53.6	37.7	54	61.7	37.7	49.4	87.6	0.77	51.7 ± 3.2
K3	R	150–350	P45 to K97	20	Mega Spilaio Fm	188.1	-21.9	8.8	195.7	-38.5	9.6	-68.8	338.2	0.60	-166.5 ± 3.2
K4	N	350–450	K114 to K137	6	Mega Spilaio Fm	3.8	57.5	21.5	34.1	70.1	21.1	61.9	66.3	0.86	31.8 ± 3.2
K5	N	450–570	No data	-	-	-	-	-	-	-	-	-	-	-	-
Mean normal	N	-	-	15	-	16.0	54.8	11.7	46	62.3	12.1	55.2	88.1	0.78	43.8 ± 3.2
Mean reversed	R	-	-	23	-	187.3	-24.2	8.1	195.8	-40.3	8.6	-69.7	335.8	0.61	-166.5 ± 3.2
Mean	-	0–570	P2 to K137	38	All section	9.8	36.2	8.0	24.2	49.7	8.0	51.8	56.9	0.66	46.9 ± 3.5

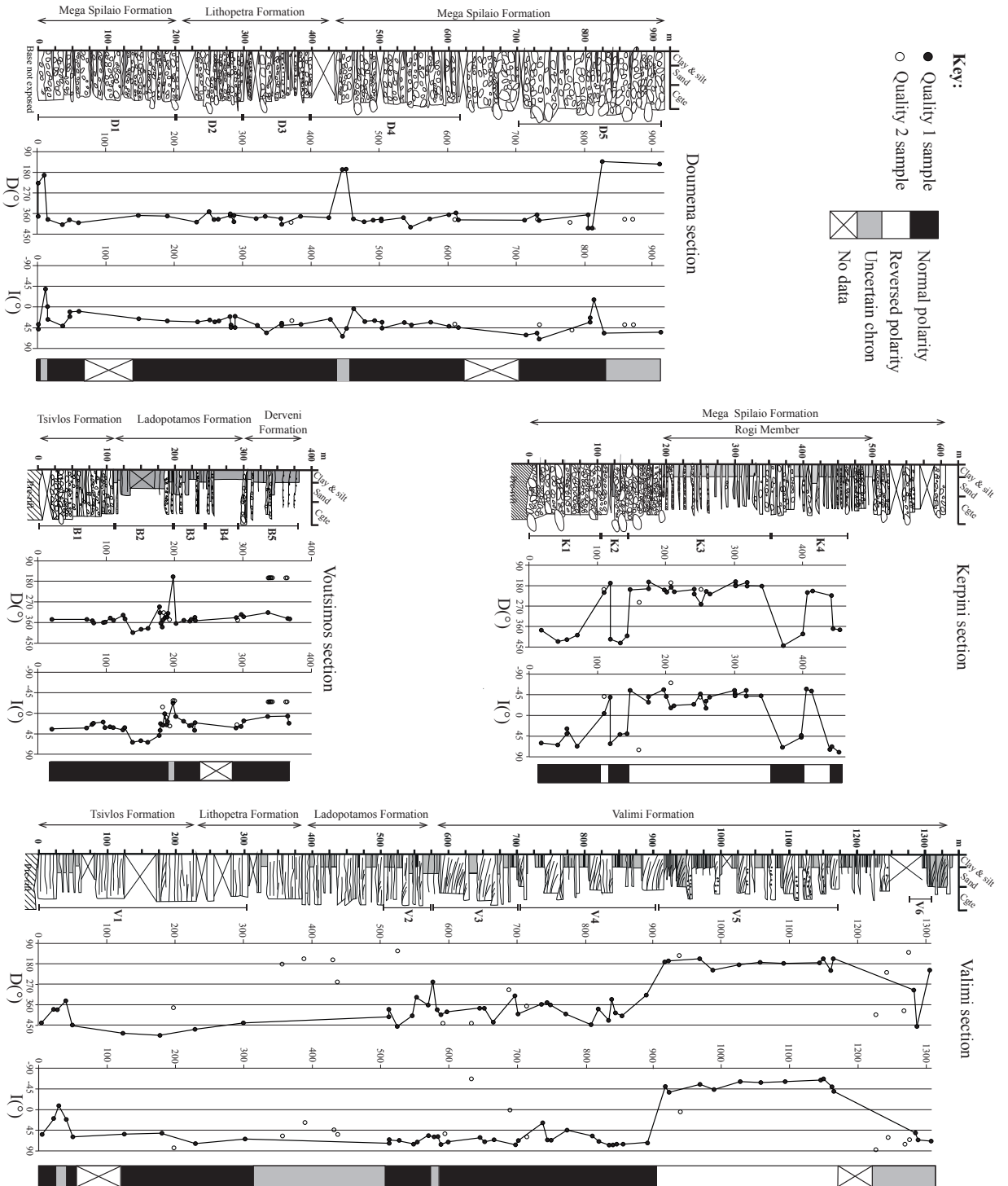


FIGURE 3.11 – Magnetostratigraphic columns for the four studied section. The declination and inclination curves are traced using the Q1 samples (blacks dots). The Q2 samples are also represented (white dots). The polarity columns show normal, reversed and uncertain magnetozones, as well as the thickness interval with no good quality data available.

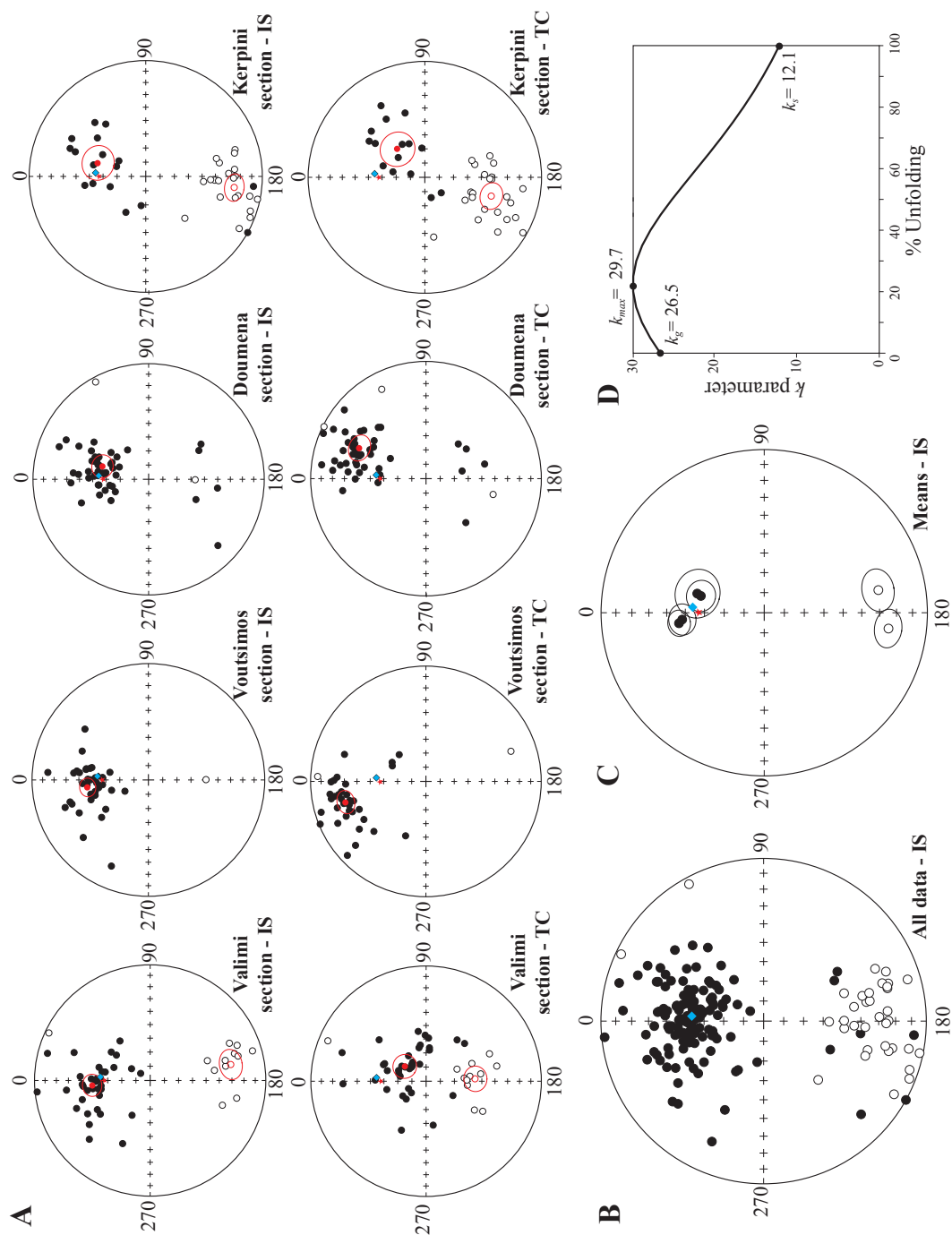


FIGURE 3.12 – (A) Equal-area projections of the principal component directions (Q1 samples) for the Valimi, Voutsimos, Doumena and Kerpini sections. In situ non corrected (IS) and tilt-corrected (TC) coordinates are plotted separately. (B) Equal-area projections of the principal component directions from all sections (IS) and tilt-corrected (TC). (C) Means of normal and reversed polarities found in each palaeomagnetic section and used to perform the fold test. Blue diamond represents the present-day earth's magnetic field (PDF) and red star is the geomagnetic axial dipole directions (GAD). (D) Fold test of Fisher-averaged for 6 direction means (McElhinny, 1964). k parameter is inversely proportional to the dispersion of the data.

3.5 ^{26}Al - ^{10}Be burial ages

Given the rarity of the biostratigraphic data available in the syn-rift deposits, additional age constraints were sought to correlate our polarity columns with the polarity reference scale. We present ^{26}Al - ^{10}Be burial ages obtained in two samples within the Mega Spilaio Formation of the Doumena fault block (see locations on Figure 3.3). The analytical procedure and the details of the cosmogenic data are presented in the appendix D. The determination of burial ages is based on the concentration of cosmogenic isotopes ^{10}Be and ^{26}Al produced *in situ* in quartz grains. The radionuclides were produced before they were shielded from cosmic radiation. After production has stopped, each radionuclide will decay with respect to its half-life : 0.708 Ma for ^{26}Al (Nishiizumi, 2004) and 1.387 Ma for ^{10}Be (Korschinek *et al.*, 2010; Chmeleff *et al.*, 2010). In our study we sampled the deepest and freshest outcrops with at least 10 m of rock overburden to minimize post-burial production. Rare quartz grains were found in clasts of the turbiditic sandstones of the Pindos nappe (Upper Cretaceous to Eocene).

Measured $^{26}\text{Al}/^{27}\text{Al}$ and $^{10}\text{Be}/^9\text{Be}$ ratio are expressed with 1σ analytical uncertainties. ^{10}Be concentrations of all samples are on the order of 10^4 atoms g^{-1} of quartz . ^{26}Al concentrations range from 10^4 – 10^5 atoms g^{-1} of quartz and present much larger uncertainties than in ^{10}Be concentrations due to insufficient counts of AMS measurement. Both samples C13-47 and C14-12 were used to give burial ages of 1.29 ± 0.89 Myr and 1.51 ± 0.98 Myr respectively (1σ uncertainties). Initially, more samples were analysed across the study area but only those with less than 100% analytical uncertainties were used to calculate burial age. The syn-rift deposits where stands the Mega Spilaio monastery are here younger than 2.5 Ma. The significance of this maximum age for the magnetostratigraphic correlations is discussed below.

3.6 Age model

A correlation model is presented for the Lower Group across the study area, striking SW–NE and E–W linking the four studied sections. We first correlated the normal and reversed polarities of the Valimi section to the magnetic reference scale (Lourens *et al.*, 2004).

The syn-rift succession of the eastern Corinth rift was dated at 3.62 ± 0.18 Ma and 4.00 ± 0.40 Ma based on a radiometric age in andesites overlying the early rift deposits (Collier & Dart, 1991). To be consistent with this constraint, the main polarity reversal at 900 m cannot be older than 3.6 Ma and we propose a correlation of the polarity reversal in the Valimi section with the polarity reversal at 2.58 Ma between the Gauss long normal chron and the Matuyama long reversed chron. The short possible reversed magnetozones between 0 and 900 m could therefore correspond to the Gauss polarity sequence C2An (2.58–3.60 Ma), which includes three long normal and two short reversed chrons. The possible reversal in the uppermost Valimi section is then dated at 2.15 Ma. This correlation would date the whole Valimi section from about 3.5 Ma to 2.1

Ma. The age estimate at the top of the section at 2.15 Ma is consistent with the previous ages of 1.8 Ma (with high uncertainty) for the top of the Lower Group succession in the western and central rift in the area (Symeonidis *et al.*, 1987; Malartre *et al.*, 2004; Rohais *et al.*, 2007b) based on palynological data, forams and fossils of vertebrates. The age determination for the base of the section is more uncertain and could be older than 3.5 Ma.

The Kerpini column also presents several clear reversals but with no independent age controls. Nevertheless, the Kerpini and Valimi columns are similar. The long reversal interval 150–350 m is therefore correlated with the C2r.2r Matuyama reference chron (2.15–2.58 Ma). Accordingly, the three normal intervals at 0–100 m, 120–150 m and 350–400 m correspond to the C2n Olduvai, the C2r.1n Reunion and the Gauss polarity sequence C2An, respectively. These correlations date the Kerpini section and the upper part of the Mega Spilaio Formation between about 1.8 and 3.0 Ma. This correlation is consistent with the Upper Pliocene charophytes (3.6 and 2.6 Ma) found at the base of the syn-rift succession in the Drosato Formation (Figure 3.13).

An alternative correlation with an older age for the main polarity reversal (e.g. C2Ar ; 4.19–3.59 Ma) is not possible here. Mapping of the syn-rift succession across the fault blocks shows that the Kerpini section lies in the upper part of the Lower group succession and is equivalent to the upper part of the Doumena and Valimi sections. Thus, the main polarity reversal recorded in the Kerpini section cannot be older than the one recorded in the Valimi section. We suggest that these two reversed magnetozones have the same age. The base of the polarity reversal at 2.58 Ma between the Gauss and Matuyama reference chrons is the key timeline of our correlation model.

The large normal magnetozone recorded throughout the Voutsimos section is correlated with long normal intervals found in the Kerpini and Valimi sections and thus also corresponds to the Gauss polarity sequence. If true, the Voutsimos section ranges between >2.6 and <3.6Ma. Accordingly, the small polarity reversal recorded between 197 m and 199 m could be tentatively correlated with the reversed chron C2An.1r (3.12–3.03 Ma) and therefore would be equivalent to the uncertain reversed interval interpreted in the Valimi section, at the base of the Valimi Formation. The base of the Valimi Formation in the Voutsimos section therefore correlates to the Ladopotamos Formation, which agrees with the age of the Arvicollidae teeth found at the base of the Ladopotamos Formation (Figure 3.13).

Similarly, the long normal interval observed in the Doumena section is correlated to the Gauss polarity sequence (>2.6 and <3.6 Ma). However, such a correlation may conflict with the cosmogenic burial ages found in the upper part of the section, which suggest depositional ages younger than ~2.5 Ma at the 1 σ confidence limit. If the mean burial ages (~1.3 and ~1.5 Ma) represent the true depositional ages, the dated sediments should lie within the long reversed Matuyama chron (C1r), which is missing here. This implies the presence of a long hiatus of deposition of about 0.4 Myrs, which is difficult to explain. Alternatively, if we consider the whole probabilistic distribution of the burial ages (or at least 2 σ confidence limit), they could be older than and thus lie in the Gauss polarity sequence (Figure 3.13). Since we have not observed any

strong erosional surface or unconformity that would support the presence of such a significant hiatus, we accept the low confidence limits of ^{26}Al - ^{10}Be burial ages and that they may lie within the Gauss chron. Thus, the Doumena section was deposited between >2.6 and <3.6 Ma. The base of the syn-rift succession was not exposed in this section and can therefore be older than 3.6 Ma.

The base of the Lower group succession in the Voutsimos, Valimi and Kerpini sections is characterised by magnetic direction of normal polarity. The long C2Ar reversed Gilbert chron below the Gauss normal succession was not detected in those three sections suggesting an age of 3.6 Ma for the lower limit of the syn-rift succession. Nevertheless, the Kerpini section lies in the upper part of the Lower Group succession and the base of the Valimi section is poorly constrained. Therefore, the base of the syn-rift succession could be locally older than 3.6 Ma. Our age model is used to reconstruct the early rift history and the behaviour of the Kalavryta river system over less than 2 Ma, between about 3.6 to 1.8 Ma.

This age model enables estimations of average sedimentation rates. The term "sediment preservation rate" (SPR) is preferentially used here as the sedimentation rate is minimal in a gravel-dominated succession. In the Kerpini section, several polarity reversals are clearly identified and one reversal is complete. Hence, the SPR value is robust and ranges from 0.3 to 0.5 mm/yr (Figure 3.14). In the Kerpini, Doumena, Voutsimos and Valimi sections, the uncertain polarity intervals are tentatively correlated with the magnetostratigraphic columns but the base and top of the main polarity intervals remain unknown in most cases. The correlation lines are poorly constrained and cannot provide detailed evolution of the sedimentation rates through the records. In those sections, the overall SPR value is estimated at 0.5 mm/yr. These values are first order averages and must be considered as minimum values. These values were not corrected for compaction as the series were buried at depths less than 2 km and since compaction rate within gravel-dominated succession are considered negligible.

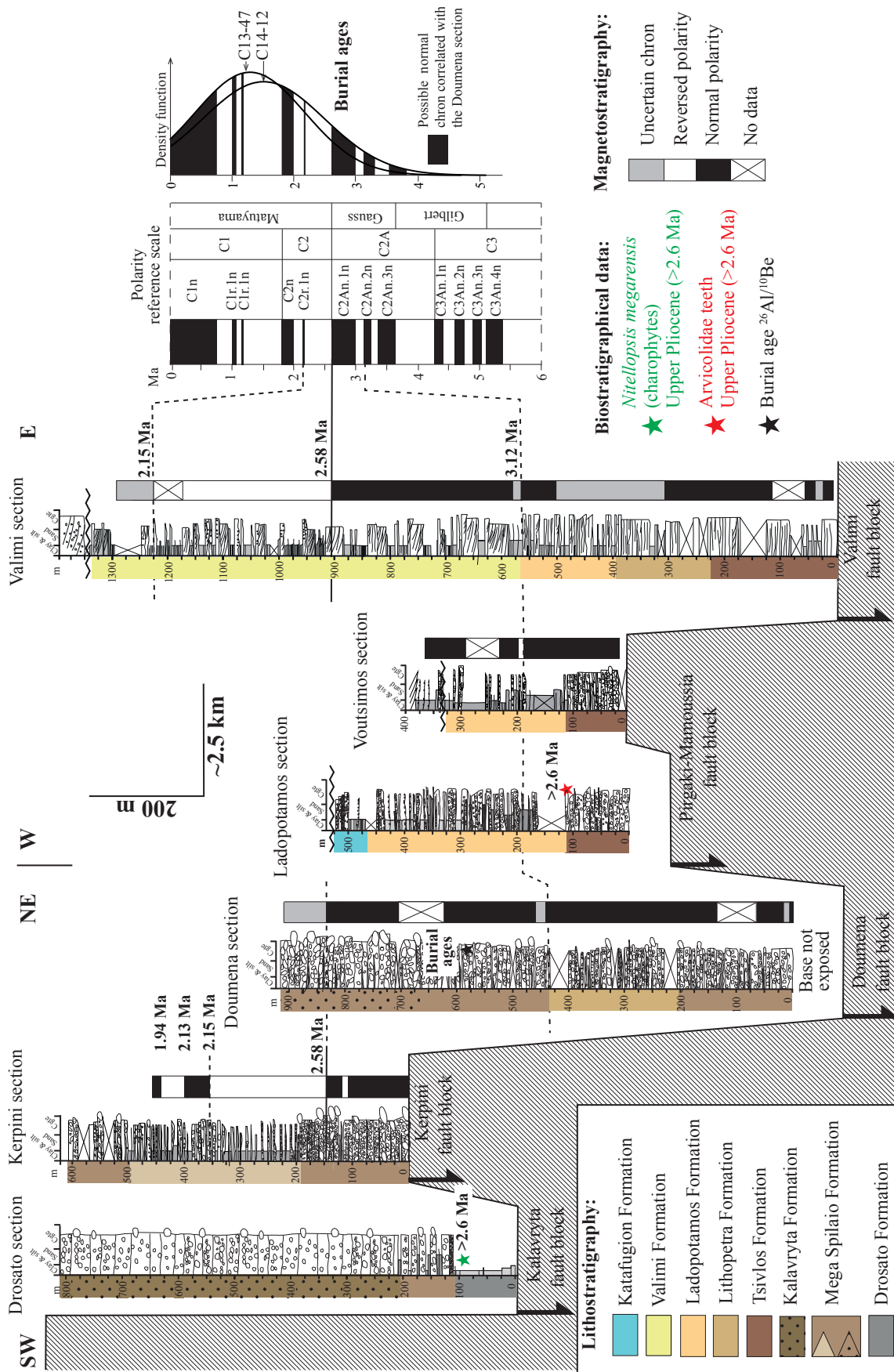


FIGURE 3.13 – Correlation models of the Kalavryta river system across a series of normal faults combining magnetostratigraphy results, biomarkers (charophytes and mammal teeth) and $^{26}\text{Al}/^{10}\text{Be}$ burial ages. The best time constraint is the polarity reversal at 2.58 Ma between C2A and C2 (Gauss and Matuyama chrons). The implications of the correlations is developed in the text.

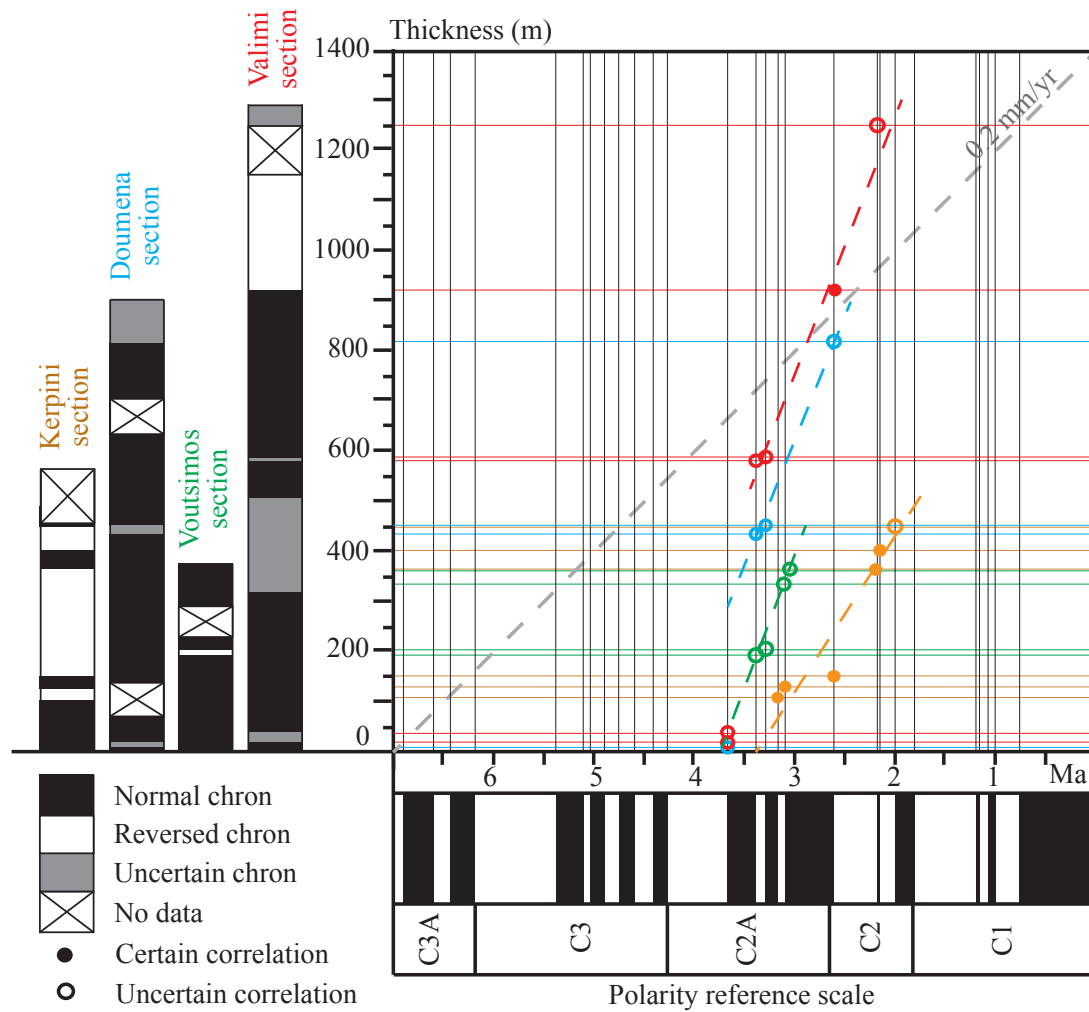


FIGURE 3.14 – Correlation between thickness of the paleomagnetic sections and the polarity reference scale (Lourens *et al.*, 2004). The best fit line is tentatively traced for each sections. Two solution are proposed for the Doumena section. The slope of the best fit line gives the sedimentation rate in m/Myr. The sediment grey dotted indicates a sedimentation rate of 200 m/Myr or 0.2 mm/yr.

Chapitre 4

The impact of large antecedent river systems on syn-rift sedimentation

Peu de rifts présentent l'opportunité d'étudier en détail l'initiation de l'étirement de la croûte continentale grâce à l'enregistrement sédimentaire. Les interactions tectono-sédimentaires à l'initiation du rift sont peu étudiées. Dans le rift de Corinthe, les premiers dépôts syn-rift sont préservés dans différents blocs de failles normales. De nombreuses études sont consacrées au remplissage du rift par un système de drainage conséquent (transverses et axiaux) en réponse à la croissance des failles. La présence de rivières antécédentes est souvent documentée au cours du développement des rifts continentaux mais leurs rôles dans la distribution des faciès restent mal connus. Dans le cas d'un rift continental superposé à une chaîne de montagne, la présence d'un système de drainage antécédent implique un flux sédimentaire important à l'initiation du rift. Ce chapitre présente l'impact d'un système de drainage antécédent majeur dans la stratigraphie syn-rift à partir du cas d'étude du rift de Corinthe

Les dépôts syn-rift étudiés sont principalement conglomératiques. L'analyse des faciès dans les blocs de failles normales et les directions de paléocourants sont présentées dans ce chapitre. A partir des modèles de corrélations stratigraphiques établis dans le chapitre précédent, l'évolution du système fluvial antécédent est présentée entre $\sim 3,6$ et $\sim 1,8$ Ma. Outre les contraintes temporelles obtenues, la cartographie détaillée dans les blocs de failles permet de subdiviser la succession syn-rift en plusieurs stades d'évolution.

Dans le rift de Corinthe, le système de drainage antécédent, hérité de la chaîne hellénique, remplit progressivement le paléorelief et s'étend sur plusieurs blocs de failles actifs. L'absence de création de topographie entre les blocs de failles inhibe le développement d'un système de drainage conséquent. L'axe fluvial antécédent principal est resté constant et a contrôlé la distribution des faciès au cours des stades précoces du rifting. Les variations de faciès sont principalement observées le long de cet axe et à l'échelle du bassin. Les variations d'accommodation dans les blocs de failles ne contrôlent pas directement la distribution des faciès et correspondent donc

à un paramètre de contrôle secondaire dans l'architecture alluviale.

La capacité du bassin à accommoder les dépôts syn-rift est limitée par rapport au flux sédimentaire considérable. La progradation des faciès est ici expliquée par un flux sédimentaire important et continu, plutôt que par la création d'accommodation à l'initiation du rift. Les dépocentres principaux sont alignés parallèlement à l'axe de drainage antécédent. La persistance du flux sédimentaire le long de cet axe crée une surcharge sédimentaire et favorise la croissance des failles. La constance du système de drainage antécédent contrôle donc la localisation des dépocentres et des faciès syn-rift. Ces travaux sont acceptés avec révisions à la revue *Sedimentology* (*International Association of Sedimentologists, Wiley Ed.*)

Sommaire

4.1	Introduction	124
4.2	The Corinth rift and study area	125
4.2.1	Geological setting	125
4.2.2	Onshore stratigraphy	126
4.2.3	Studied normal fault blocks	126
4.3	Methods	129
4.4	Facies analysis and alluvial architecture of the early rift deposits	130
4.4.1	FA1 : Structureless coarse alluvial conglomerates	130
4.4.2	FA2 : Crudely stratified alluvial conglomerates	130
4.4.3	FA3 : Heterolithic gravel to fine-grained fluvial deposits	135
4.4.4	FA4 : Gravel to fine-grained lacustrine deltas	136
4.4.5	FA5 : Silt and clay lacustrine deposits	137
4.4.6	FA6 : Lagoonal and upper shoreface deposits	138
4.5	Lithostratigraphy of the Lower Group	147
4.5.1	Southern fault blocks	147
4.5.2	Northern fault blocks	148
4.6	Dating and stratigraphic correlation	150
4.7	Evolution of the Kalavryta river system	154
4.7.1	Phase 1 (~3.6–3.5 Ma)	154
4.7.2	Phase 2 (~3.5–3.1 Ma)	155
4.7.3	Phase 3 (~3.1–2.8 Ma)	155
4.7.4	Phase 4 (~2.8–2.3 Ma)	156
4.7.5	Phase 5 (~2.3–1.8 Ma)	157
4.8	Discussion	162
4.8.1	Paucity of footwall-derived sediments	162
4.8.2	Length scale of facies variation and relation with faults	163

4.8.3	Channel belt distribution and subsidence variations	163
4.8.4	Overfill conditions in the early rift basins	164
4.9	Conclusions	167

Abstract

Early rift basins are conventionally explained as overfilled basins due to low rate of creation of accommodation compared with sediment supply. Alternatively, overfilled conditions can be explained by the presence of antecedent drainage that provides high volumes of sediments. The impact of antecedent drainage on facies distribution and their interactions with a growing normal fault system are investigated in the Plio-Pleistocene alluvial succession of the western Corinth rift.

Detailed sedimentary logging and mapping of the preserved syn-rift succession document the alluvial architecture. Magnetostratigraphy and biostratigraphic markers are used to date and correlate the alluvial succession across normal fault blocks. During the early rift phase, the transverse depositional system evolved downstream from coarse alluvial conglomerates to fine-grained lacustrine deposits across E-W faults blocks. A low sinuosity braided river system flowed over 15 to 30 km. The termination of the distributive river system consisted of stacked deltas prograding into a shallow lake.

The presence of a major antecedent drainage is evidenced by : (1) burial of the active faults, preventing footwall topography, (2) one major entry point of sediments, (3) persistence of the main channel axis, (4) downstream fining at the scale of the rift basin. The length scale of facies transitions is greater than and not directly related to fault spacing. However, the zones of maximum subsidence on individual faults are aligned parallel to the persistent fluvial axis. This emphasizes the role of long-term sediment loading on normal fault growth.

Syn-rift deposits first infilled palaeorelief inherited from the Hellenide mountain belt. Increasing subsidence within the basin led to retrogradation and the establishment of the facies belts across the fluvial system. Then, most of the early rift history records facies progradation from ~ 3.2 to ~ 1.8 Ma, which can be explained by increasing sediment supply associated with footwall migration of fault activity and/or climate degradation.

Keywords : fluvial, conglomerate facies, rift basin setting, antecedent rivers.

4.1 Introduction

In standard models of early rift phase, fluvial deposits fill the depocentres that are controlled by numerous small-displacement faults (Gawthorpe & Leeder, 2000; Cowie *et al.*, 2006). Over several Myr, these faults enlarge and link to form larger depocentres that are tens of kilometers long (Ravnås & Steel, 1998; Gupta *et al.*, 1999; Cowie *et al.*, 2000). Models of single half-graben depocentres (e.g. Alexander & Leeder, 1987; Leeder & Gawthorpe, 1987; Leeder *et al.*, 1991; Leeder, 1993; Gawthorpe & Leeder, 2000), where strain is localised on 10–30 km spaced normal faults, include both transverse and axial drainage systems and predict distinctive syn-rift

stratigraphy and facies distributions.

Sediments deposited in the early rift basin originate from transverse footwall drainage and axial drainage systems. Consequent drainage systems develop in response to footwall uplift and footwall catchments progressively feed the growing hangingwall depocentres (e.g. Blair & Bilo-deau, 1988; Schlische & Olsen, 1990; Schlische, 1991; Leeder, 1993; Eliet & Gawthorpe, 1995; Lambiase & Bosworth, 1995; Schlische & Anders, 1996; Allen & Densmore, 2000). Drainage systems are deflected by uplifting footwalls to conduct sediments to the basin through topographic lows between fault segments. Developing relay ramps can capture drainage systems and control the location of the main rift depocentres (e.g. Leeder & Gawthorpe, 1987; Leeder & Alexander, 1987; Morley *et al.*, 1990; Gawthorpe & Hurst, 1993; Childs *et al.*, 1995; Lambiase & Bosworth, 1995; Leeder, 1993; Gupta *et al.*, 1999; Athmer *et al.*, 2010; Athmer & Luthi, 2011; Hemelsdaël & Ford, 2016).

Antecedent, pre-rift drainage networks are integrated in models of the early syn-rift phase but only small antecedent rivers are considered (Gawthorpe & Leeder, 2000; Cowie *et al.*, 2006). They are often modified by the growing fault network (e.g. Leeder, 1993; Davies *et al.*, 2000) and can be deflected into depocentres (e.g. Crossley, 1984; Jackson *et al.*, 2006). However, antecedent rivers are not always deflected by vertical motion during faults growth. When sufficiently powerful, rivers can also incise through uplifting footwalls (Trudgill, 2002). The case of large antecedent rivers and their implications in syn-rift stratigraphic architecture have not yet been investigated. The aim of this paper is to redress this omission by studying the fluvial succession of the early Plio-Pleistocene Corinth rift (Greece). We address the following questions : how do large antecedent rivers respond to the development of normal fault systems ? What is the impact of drainage antecedence on early syn-rift facies distribution ?

Along the southern margin of the Corinth rift, inactive and uplifted normal fault blocks preserve an early alluvial system (referred to as the Lower Group). Facies analysis and stratigraphic correlation show that the succession evolved laterally from coarse alluvial to a fluvio-deltaic system across a series of normal faults blocks. We present a chronostratigraphy of the early rift constrained by magnetostratigraphic and biostratigraphic data. The new tectono-stratigraphic model of the early rift phase incorporates an antecedent drainage system capable of high sediment supply.

4.2 The Corinth rift and study area

4.2.1 Geological setting

The east-west-trending Gulf of Corinth (105 km long, 30 km wide) separates the Peloponnese peninsula from mainland Greece (Figure 4.1A). Geodetically measured N–S extension rates over the last 20 years show an increase from *ca.* 6–11 mm/yr in the east to 15 mm/yr the west

(Clarke *et al.*, 1998; Briole *et al.*, 2000; Bernard *et al.*, 2006). On a regional scale, the NNE-directed subduction of the African plate into the Hellenic trench since the Oligocene generated orogenic crustal thickening, collapse and back-arc extension through slab roll-back (Le Pichon *et al.*, 2002; Jolivet & Brun, 2008). The N–S extension in the Corinth rift is located between the southwest-propagating North Anatolian Fault and the Cephalonia Fault in the Central Hellenic Shear Zone (Nyst & Thatcher, 2004; Papanikolaou & Royden, 2007). The rift is superimposed at a high angle onto the north-northwest- to northwest-trending Hellenide external fold and thrust belt, which was emplaced towards the west-southwest from Late Eocene to Late Miocene (van Hinsbergen *et al.*, 2005; Reilinger *et al.*, 2006; Jolivet & Brun, 2008; van Hinsbergen & Schmid, 2012). In the study area, the pre-rift basement corresponds to the Pindos nappe.

4.2.2 Onshore stratigraphy

The Corinth rift initiated sometime during the early Pliocene (Doutsos & Piper, 1990; Collier & Dart, 1991). The western rift is believed to be younger but no absolute age for the onset of rifting is currently known. The only absolute age, found in an ash layer in the central rift (Xylocastro area; Figure 4.1B), has been dated at 2.55 ± 0.007 Ma (Leeder *et al.*, 2012). This age has been used to estimate a basin deepening event at 3.0–3.2 Ma in the central and eastern rift. In the western rift, the syn-rift succession is divided into three informal lithostratigraphic groups: Lower, Middle and Upper Groups, first defined by Rohais *et al.* (2007a,b). Formation boundaries within these groups are laterally diachronous recording eastward deepening of the rift.

The Lower Group (Pliocene to Lower Pleistocene) consists of an alluvial succession that thickens and fines toward the east from coarse conglomerates to fine grained lacustrine turbidites (Rohais *et al.* (2007a)). These deposits are preserved in a series of fault blocks. Ford *et al.* (2013) argue that these early rift sediments were supplied from the SW by a well-established antecedent drainage system. The temporal and spatial relationships between alluvial sedimentation and fault activity are the main focus of this paper. The Lower Group is absent in the westernmost part of the onshore rift. The continuity of the Lower Group offshore is uncertain but is likely to correspond to the lower SU1 seismic unit locally as suggested by Hemelsdaël & Ford (2016) and Nixon *et al.* (2016).

The Middle group is characterised by giant conglomeratic Gilbert-type fan deltas and their finer prodelta deposits (Figure 4.1B). Deltas were supplied by footwall-derived point sources feeding into the hangingwalls of the rift border faults. These deltas record rapid basin deepening related to an increase in normal fault connectivity, migration of tectonic activity and rift acceleration in the Early Pleistocene (Rohais *et al.*, 2008; Ford *et al.*, 2007, 2013; Backert *et al.*, 2010).

Onshore, the Upper group is represented by small Gilbert-type fan deltas, marine terraces, red palaeosols, all recording progressive uplift of the southern margin and northward migration of tectonic activity. Uplift along the southern rift border began at 0.4–0.7 Ma and since then, most

north flowing rivers have continued to incise and feed deltas along the present day margin.

4.2.3 Studied normal fault blocks

Along the western southern rift margin, the inactive normal fault blocks have been uplifted to over 1000 m above sea level. Incision by the present-day rivers has created excellent exposures of the syn-rift deposits. The study area is delimited by the Khelmos massif to the south (2200 m alt.), and by the present day coastline to the north (Figure 4.1B). We focus on the major north-dipping faults (Demestika, Kalavryta, Prinos, Kerpini, Tsivlos, Doumena and Valimi faults) that are 10 to 15 km long (strike length). Fault blocks are 4 to 7 km wide. The strike of major faults is N086 to N110 and their average dip varies between 42°N and 64°N. Low-angle faults dipping 20° to 40° (e.g. Prinos Fault; Figure 4.9) result from block rotation during the development of later major faults (footwall migration of fault activity). Maximum throw for the major faults varies between 400 and 1500 m. Pure dip-slip displacement is recorded on the majority of faults with stretching directions oriented N–S to SSW–NNE (Rohais *et al.*, 2007a; Ford *et al.*, 2013). Pre-rift and syn-rift sediments are often juxtaposed along major faults and fault planes are well exposed in places (Bastesen *et al.*, 2009; Ford *et al.*, 2013; Bussolotto *et al.*, 2015). Maximum sediment thickness within the major hangingwall depocentres varies from 400 to 1600 m. Growth strata and tilted block geometries thickening toward faults are observed in the study area (Figure 4.1C). Syn-rift strata can also form growth synclines in the hangingwall depocentres.

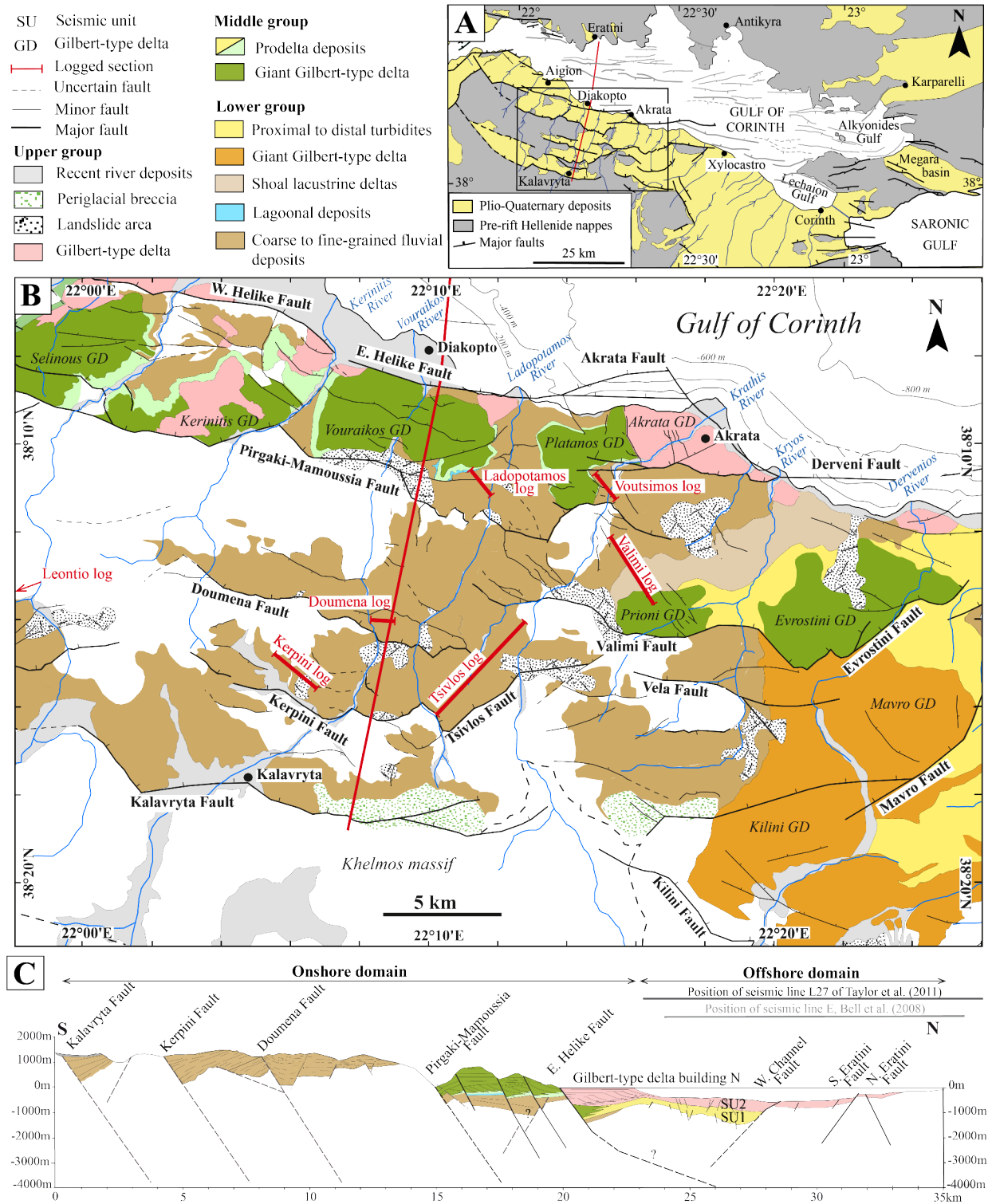


FIGURE 4.1 – (A) Geological map of the Plio-Pleistocene Corinth rift that was superimposed on the alpine Hellenide nappes. The rift separates mainland Greece (northern margin) from the Peloponnese peninsula (southern margin). The black box delimits the detailed geological map. (B) Geological map of syn-rift stratigraphy in the central northern Peloponnese. The syn-rift succession is divided into three groups : Lower, Middle and Upper Groups. (C) N-S cross-section of the western Corinth, including both onshore and offshore domains by Ford *et al.* (2013).

4.3 Methods

This study of the Lower Group in the western Corinth rift integrates regional stratigraphic mapping, detailed logging (vertical scale 1 :200) and palaeocurrent analysis. The recognition of lithofacies (F1 to F20) is mainly based on grain size, texture, colour and sedimentary structures. Description and interpretation of each lithofacies (referred in brackets in the text) are presented in Tables 4.1, 4.2, 4.3 and illustrated in Figures 4.4, 4.5, 4.6. The facies associations (FA) are described below and summarized in Table 4.4. The Lower Group syn-rift succession is subdivided into lithostratigraphic units, characterised by one or more facies associations. Here the adjective "alluvial" is used as a general term for both alluvial fan *sensu stricto* and low-gradient braided river deposits.

In the conglomeratic facies examined, the clast lithologies consists overwhelmingly of micritic carbonates. Black chert nodules, radiolarites (Upper Triassic to Jurassic) and turbiditic sandstones (Upper Cretaceous) form secondary populations originating from the pre-rift Pindos nappe. The proportions of clast lithologies do not vary significantly and cannot be used to trace sediment provenance in the Lower Group. Palaeocurrent data define the main sediment transport pathways. Palaeocurrents were measured from imbricated clasts, trough cross-bedding, planar cross-bedding, channel flanks and scour surfaces. These data were restored to horizontal depositional bedding. Rose diagrams are presented where a large number of data is available in the same stratigraphic unit, otherwise a vector mean is used (Figures 4.2, 4.3).

Age constraints are difficult to acquire in conglomeratic alluvial successions. Four key logged sections were analysed to establish a magnetostratigraphy. They are located in the Kerpini, Doumena, Valimi and PMF blocks (Figure 4.8) where syn-rift sediment thickness varies from 400 m to 1300 m. The targeted facies are red and brown siltstones to medium-grained sandstones. The spacing of the sampling sites is variable and depends on the preservation of the fine-grained deposits. The average spacing between sampling sites is 6 to 13 m. The maximum sampling interval per site ranges from 36 to 74 m. Thermal and alternating field demagnetisation showed good quality results for 29% to 57% of the samples and thus enabled the construction of local stratigraphic reversals (Figure 4.10). Details of the palaeomagnetic methods and results for all sections are presented in chapter 3.

Very few biostratigraphic ages have been found to calibrate the polarity reversals with the reference polarity scale (Lourens *et al.*, 2004). Based on high-resolution mapping, additional pseudo-timelines have been identified at major lithological boundaries, and were traced within and across the fault blocks. These pseudo-timelines enable the calibration of our correlation model.

4.4 Facies analysis and alluvial architecture of the early rift deposits

4.4.1 FA1 : Structureless coarse alluvial conglomerates

Description

FA1 consists predominantly of massive coarse conglomerate beds (pebble to boulder clasts) with weakly developed internal sedimentary structures (F2) that represent more than 85% of the vertical succession. FA1 forms a stacked successions up to 50 m thick that are laterally uniform. The coarseness of the facies is a distinctive feature of FA1. Conglomerate beds containing pebble to boulder clasts are poorly to moderately sorted and present a sub-rounded to rounded shape (F2). Boulders are locally aligned parallel to the bedding. They can also be randomly distributed, isolated within clast-supported pebble and cobble conglomerates. Beds are highly erosive and present a crude discontinuous stratification, locally defined by clast alignment (Figure 4.4B). Crudely stratified clast-supported conglomerates (F3) can locally present internal structures such as clast imbrication, horizontal bedding, scour pockets and groove casts. Matrix-supported breccia (F1) is rare but very distinctive in FA1 comprising isolated angular boulders (Figure 4.4A). These beds are metric to plurimetric and present a chaotic fabric with sharp non-erosive bases (Leontio log, Figure 4.2).

Interpretation

Massive structureless clast-supported conglomerates (F2) are likely to be a consequence of rapid to instantaneous deposition in turbulent stream flows with tractional bedload transport (Harvey, 1984; Nemeč & Steel, 1984). Given the disorganised fabric and the presence of isolated boulder clasts, it is probable that these conglomerates were deposited under highly flashy flow conditions. However, clast-supported conglomerates record tractional bedload transport processes likely to take place in shallow braided streams. The chaotic fabric of matrix-supported breccia is interpreted as due to subaerial debris flows. The coexistence of bed load and debris-flows in FA1 suggests an overall alluvial fan depositional environment (Gloppen & Steel, 1981; Nemeč & Steel, 1984; Blair & McPherson, 1994; Mack, 2002).

TABLE 4.1 – Conglomeratic lithofacies (cs : clast size; mcs : Maximum clast size; mbt : mean bed thickness)

Facies	Lithology and stratification	cs (cm)	mcs (cm)	mbt (m)	Sedimentary structures	Interpretation
F1 Matrix-supported breccia	-Massive matrix-supported pebble to boulder breccia -Very poorly sorted -Metric-scale boulders localised in the middle part of bed -Poorly consolidated matrix composed of brown silt and clay -Planar bed surfaces (bottom an top) -Sharp non-erosive unchannelised base	n/a	80	0.5–3.0	-A few isolated vertical clasts -Planar and sharp base of beds	-Debris flow Harvey (1984); Nemec & Steel (1984); Nemec & Postma (1993); Blair & McPherson (1994); Leeder & Mack (2007)
F2 Poorly-sorted conglomerate	-Clast-supported pebbles to boulders -Poorly sorted conglomerates -Mainly rounded clasts sometimes angular -Massive metric to plurimetric beds -Highly erosive beds -Very crudely stratified	4–5	20–30	>1.0	-Mostly structureless	Rapid deposition as bars within large channels -Bed load transport in high flow regime Hein (1984); Nemec & Postma (1993)
F3 Crudely stratified conglomerate	-Massive clast-supported pebbles to large cobbles -Poorly to moderately sorted conglomerate pebbles to large cobbles -Various basal channelized contact with metre-scale incision -Channel amalgamation	4–6	10–20	>1.0	- $\alpha(t)b(t)$ imbrications -Crude horizontal stratification -Frequent deep scour pockets	-Gravel sheet transport processes; -Gravel bars and bed forms Harms <i>et al.</i> (1975); Brayshaw (1984); Hein (1984); Miall (1996)
F4 Cross-stratified pebbles conglomerate	-Clast-supported pebble conglomerate -Poorly to moderately sorted -Subangular to well rounded clasts -Poor lateral extension	3–7	10–15	0.1–1.0	-Normal grading -Clast imbrication locally Cross stratification -Tabular to tangential strata	Downstream accretion of low relief gravel bar - Low sinuosity river Church (1983); Billi <i>et al.</i> (1987); Miall (1996); Bridge & Lunt (2006)
F5 Clast-supported pebble conglomerate	-Clast-supported pebble conglomerate -Moderately well sorted -Subangular to rounded pebbles -Crudely stratified -Highly erosive beds with lenticular shape	3–4	6–8	0.1–1.0	-Crude horizontal stratification -Scour and fill structure - <i>Per descensum</i> clastic dykes	Sediment injection due to overpressurization Rust (1972); Rust & Koster (1984); ; Jolly & Loneragan (2002); -Deep channelized flow, braided channels Van Rensbergen <i>et al.</i> (2003); Vandromme (2007)
F6 Bedded pebble conglomerate	-Clast-supported pebbles conglomerate -Moderately to well-sorted -Well rounded, spherical clasts -Regularly bedded -Erosive and sharp base of beds	2–3	6	0.1–0.4	Horizontal and parallel stratification	Low velocity flow within gravel bedforms Harms <i>et al.</i> (1975)

TABLE 4.2 – Sandy lithofacies (mbt : mean bed thickness)

Facies	Lithology and stratification	mbt (m)	Sedimentary structures	Interpretation
F7	-Granule conglomerate and coarse-grained sandstone -Rounded grains and clasts -Pebbles locally present (matrix supported) -Tabular beds	0.2-1.0	-Low angle planar thinly bedded strata	High wave energy shoreface-barrier, beach system <i>Nemec & Steel (1984)</i> ; <i>Walker & James (1992)</i> ; <i>Ford et al. (2007)</i>
F8	-Coarse to medium sandstone -Lenticular beds -Poorly consolidated -Poorly-preserved facies within erosive conglomeratic beds	0.1-0.3	-Planar parallel or undulating lamination -Tangential lamination, trough cross-bedding	Flash flood event Weakly developed megaripples <i>Williams (1971)</i> ; <i>Harms et al. (1975)</i> <i>Allen (1983)</i> ; <i>Collinson et al. (2006)</i>
F9	-Medium to fine grained sandstone with interbedded pebble clasts -Well-sorted rounded clasts -Metre-scale cliniform geometry with internal erosive base	0.05-0.4	-Plumetric cliniform -Horizontal and parallel lamination underlined by pebble lag	Small-scale prograding foresets Gilbert-type fan deltas <i>Nemec & Steel (1984)</i> ; <i>Postma (1990)</i>
F10	-Coarse to fine-grained -Poorly-consolidated well-sorted sandstone	0.1-1.0	-Tangential foresets	Migrating 3D bedforms (dunes) <i>Miall (1996)</i>
F11	-Medium to fine-grained, well-sorted sandstone -Poorly-consolidated -Yellow to beige and reddish colours -Crudely stratified -Not well-exposed, beds succession of several meters thick	0.2-1.0	-Horizontal parallel lamination -Top of bed highly bioturbated by 3D burrow systems produced by <i>Camborygma ichnogemus</i>	-Subaqueous deposition at high flow velocity -Discontinuous sedimentation of sandy beds -Biogenic structures <i>Bromley (1996)</i> ; <i>Buatois & Mángano (2011)</i> ; <i>Knaust & Bromley (2012)</i>
F12	-Fine grained sandstone to silt -Granules and pebbles locally -Beige to reddish colour sandstone and silt	<1.0	-Mostly structureless -Rare carbonates glaebules -Weak horizontal lamination disrupted by water-escape structure -Bioturbation (vertical to low inclined centimetre scale burrows) -Teeth and bone fragments	-Floodplain overbank facies -Few developed palaeosol <i>Behrensmeyer (1987, 1988)</i> ; <i>Koster (1987)</i> <i>Wood et al. (1988)</i> <i>Retallack (1988, 2001)</i> ; <i>Bridge (2003)</i> ; <i>Hasiotis et al. (2006)</i>

TABLE 4.3 – Fine-grained lithofacies

Facies	Lithology and stratification	Colour	Biota	Sedimentary structures	Interpretation
F13 Laminated calcareous silt	-Finely laminated calcareous silt -Shell laminae -Rare isolated and aligned clasts or sandy beds interstratified	White, beige to orange	-Abundant oligohaline to freshwater fauna (<i>Theodoxus</i>), ostracods and undetermined shell clasts	-Flat and parallel lamination	-Protected subtidal lagoon -Brackish coastal environment Flemming (1988); Anthony <i>et al.</i> (1996); Ford <i>et al.</i> (2007, 2013)
F14 Laminated sand and silt	-Finely and regularly laminated sand and silt (few mm to cm) -Thin iron-rich laminae	Grey, beige to orange		-Planar and parallel lamination -Convolute laminations, symmetric ripples	-Oscillation processes with periods of quiescence Lawrence & Williams (1987); Ford & Pyles (2014)
F15 Well laminated silt	-Regularly bedded (mm to cm) silt -Well consolidated -Organic rich laminae	Beige to grey color		-Horizontal and undulating laminations	-Deposition from suspension and weak traction current Miall (1996)
F16 Red clayey silt	-Poorly-consolidated clayey silt -Variegated colour, drab-haloed spots and discontinuous layers	Red to brown	-Locally freshwater gastropods (<i>Planorbis</i>) and undetermined shell debris	-Carbonates glaebules	-Pedogenic overprinting, immature palaeosol -Flooding margins Retallack (1988, 2001)
F17 Alternating silt and clay	-Alternating silt and clay -Few cm bed thickness -Shell beds (few mm) -Iron rich laminae -Poorly consolidated -Coal fragments or laminae	Greenish to beige	-Trace of plant foliage -Variable content of oligohaline to freshwater fauna (<i>Melanopsis aff.</i> <i>mitzopotulsi</i> , <i>Adelinella elegans</i>)	-Horizontal and parallel lamination -Soft sediment deformation	-Shallow lacustrine and prodelta deposits
F18 Poorly and plastic clay consolidated silt	-Poorly consolidated silt and plastic clay -Decimetre bed thickness Locally isolated small gravels -Variable content in organic matter	Brown to dark grey	-Wood debris and root remnants -Freshwater gastropod shells -Rare ostracod shells -Bones and teeth fragments -Charophyta: <i>Nitellopsis megarensis</i> , <i>Lychnothamrus sp.</i>	-No clear lamination	-Floodplain -Shallow lacustrine McCabe (1984)
F19 Silty clay with variable organic content	-Silty clay, poorly consolidated -Variable proportion of organic matter, rare coarse grains -Dispersed coal fragments	Grey		-No internal structure -Minor bioturbation at bed base	-Low velocity flow -Suspension fall-out Oligotrophic freshwater Grambast (1974); Wray (1977)
F20 Lignite	-Lignite beds (soft brown coal) -Few centimetres to 1 m -Non consolidated, often inter stratified with lenticular silty beds	Dark brown to black	-Undetermined wood and leaf fragments	-Horizontal parallel lamination -Soft sediment deformation	-Humic organic deposits -Low-lying swamp or planar mire McCabe (1984); Papanicolaou <i>et al.</i> (2000, 2004)

TABLE 4.4 – Summary of the facies associations

Facies association	<i>Characteristic facies</i> Predominant facies (Minor occurrence)	Main features	Depositional environment	Corresponding units
FA1 Structureless coarse alluvial conglomerates	(F1) - F2 - F3	Boulder clasts in structureless beds >85% of conglomeratic facies <5% of preserved silt and clay facies <10% of preserved sandy facies No specific vertical organisation	-Alluvial fan	Kalavryta Fm Mega Spilaio Fm
FA2 Crudely stratified alluvial conglomerates	F2 - F3 - (F4) - (F5) - F8 - (F12)	<15% of preserved silt and clay facies <15% of preserved sandy facies	-Gravel-dominated, braided river	Tsivlos Fm Kalavryta Fm Mega Spilaio Fm Lithopetra Fm Ladopotamos Fm
FA3 Gravel to fine-grained fluvial deposits	F3 - F4 - F5 - F8 - - F12 - F16 - (F18)	25–50% of preserved silt and clay facies 15–30% of preserved sandy facies Possible lateral accretion bars	-Gravel- to fine-grained, -Braided river -Floodplain deposits and immature palaeosols	Mega Spilaio Fm Lithopetra Fm Ladopotamos Fm
FA4 Gravel to fine-grained lacustrine deltas	F3 - F5 - F6 - <i>F9</i> - F10 - F11 - F14 - F17	<20% of conglomeratic facies 30–60% of preserved silt and clay facies 30–40% of preserved sandy facies Few evidence of pedogenic overprinting Variable organic content	-Lacustrine delta	Valimi Fm
FA5 Silt and clay lacustrine deposits	F15 - F18 - F19 - <i>F20</i>	>90% of preserved silt and clay facies	-Lacustrine <i>s.s.</i>	Drosato Fm
FA6 Lagoonal and shoreface deposits	F7 - F13	<i>n/a</i>	-Finely laminated silt with brackish fauna -Coastal plain, lagoon	Katafugion Fm

4.4.2 FA2 : Crudely stratified alluvial conglomerates

Description

FA2 forms very distinctive bed succession over several tens of metres thick (Figure 4.7) with poor preservation of silty facies. FA2 mostly consists of massive metric to plurimetric clast-supported conglomerates with less than 30% of preserved sandstones and siltstones (F8, F12). Conglomerates beds clasts are poorly to moderately sorted and pebble to cobble clasts are sub-angular to rounded. Clast-supported conglomerates can present crude stratification (F3, F5) and metre-scale oblique tabular to tangential and sigmoidal cross-stratification (F4; Figure 4.4C). Clast are imbricated with their long axes aligned transverse to the inferred direction of palaeoflow – *a(t)b(i)* (Figure 4.4D). Interbedded sandstones and siltstones display weak parallel planar to undulating lamination and cross lamination in places. Erosional features in clast-supported conglomerates (mostly in F3) include (i) deep scour pockets (up to 1 m); (ii) continuous elongate ridges with a sharp relief, developed on the base of beds; (iii) deep incisions (up to 5 m) on the base of channels. Individual channels and scour pockets mostly correspond. Width and thickness of individual channel bodies are 2–15 and 0.5–3 m respectively. Amalgamated channels record multistory infill (Figure 4.4E).

Interpretation

The conglomerates described in FA2 were deposited in a high stream power braided river environment. The structureless clast-supported conglomerates (F2) result from rapid deposition by bedload transport in a high flow regime (see FA1). Better sorting of the clasts associated with crude planar parallel stratification is interpreted as due to longitudinal bars (Miall, 1996). Migrating bedforms and downstream accretion are poorly developed. Conglomeratic bodies were accreted laterally and mostly vertically with present high interconnection. Highly erosive features (e.g. channel incisions, deep scour pockets) mostly represent single scour-and-fill events. Stacking of coarse conglomeratic bodies forms highly interconnected channel-belts where fine-grained overbank deposits represent less than 30% of the vertical succession (Figure 4.7A, B, C).

4.4.3 FA3 : Heterolithic gravel to fine-grained fluvial deposits

Description

FA3 forms thick conglomeratic bodies of 3 to 15 m thick that are sometime characterised by fining-upward trends. Conglomeratic beds consist of clast-supported pebble to cobble conglomerates. (F3, F4, F5) alternating with fine sand, silts and claystone facies preserved in variable proportions (F12, F16, F18). Clast-supported conglomerates are highly erosive beds represent 20 to 60% of the FA. Sandy and finer-grained facies (F12, F16, F18) respectively represent 15–30% and 25–50% of the vertical succession. Wedge-shaped conglomeratic beds show lateral transition to siltstone.

Compared with FA2, a wide variety of lithofacies are present in FA3. Massive clast-supported

conglomerates can display subtle normal grading (F5). They are interbedded with moderately to well-sorted conglomerates displaying tangential and sigmoidal cross-stratification (F4; Figure 4.4F). Low-dipping inclined strata sets not exceeding 2 m in height were observed. Imbricated clasts are often observed in structureless or crudely stratified clast-supported conglomerates. Conglomeratic beds generally display similar erosional features as those of FA2. Deep channel incision and scour-and-fill structures can be associated with *per descencum* clastic dykes (Figure 4.4G).

Coarse to medium sandstones with oblique tabular and trough cross-stratification are locally preserved between erosive conglomerates (F8). Most silty beds display poor internal structures and contain isolated granules and pebbles in variable proportions. Crude planar parallel lamination can be disrupted by water-escape structures. Locally, variegated orange to pale green clayey silts form discontinuous layers. Pedogenic overprinting is uncommon and rare carbonate glaeubules show no internal fabric (F12; Figure 4.5G). Remnants of organic matter and wood debris are locally preserved in siltstones and silty clay. When not totally fragmented, rare gastropod shells, ostracods, fish bones, mammal bone and teeth can be recognised (F18).

Interpretation

This lithofacies association represents a low sinuosity braided river environment. The variety and organisation of facies reflect the variability of the fluvial processes. Crudely stratified clast-supported conglomerates (F3) are interpreted as longitudinal gravel bar deposits (as in FA2). Metre-scale cross-stratification (in F4) suggests downstream to lateral accretion of clasts during deposition within conglomeratic channels (F4). Trough cross-bedding observed in conglomerates indicates deposition by migrating 3D bedforms (Williams, 1971; Harms *et al.*, 1975; Allen, 1983; Bridge & Mackey, 1993; Collinson *et al.*, 2006). Fine-grained sandstone and red clayey silt with poorly developed palaeosols correspond to overbank deposits (Retallack, 1988, 1997; Bridge, 2003; Hasiotis *et al.*, 2006). Organic rich silty clays mixed with detrital grains were deposited in small swamps of the floodplain margin (F18; Figure 4.5H).

The multiple erosion surfaces reflect the combined effect of both entrenching and lateral shifting of braided channels (Rust, 1972; Rust & Koster, 1984). Deep erosion of conglomeratic beds often obscures the continuity of lateral accretion surfaces. The bars were mainly accreted downstream with a slightly oblique direction and are thus probably deposited in low sinuosity (i.e. braided pattern) to more sinuous river (i.e., classic meandering river). Nevertheless, it is not possible to clearly distinguish between sediment transported over well-developed braid bars and true point bars. Inclined strata sets may record diversely orientated components of downstream accretion.

FA3 represents the predominant fluvial succession in the area. It can form successions of several 10s to 100 m in thickness (Figure 4.2, 4.3). The alluvial architecture of FA3 is one of disconnected conglomeratic channels within overbank deposits.

4.4.4 FA4 : Gravel to fine-grained lacustrine deltas

Description

FA4 is organised in about twelve coarsening upward (CU) successions of 30–70 m thickness that comprise a large variety of facies. FA4 is dominated by well-laminated sand and silt with variable organic content. Sandstones and siltstones represent respectively 30–40% and 40–60% of the vertical succession (F11, F14, F17). Conglomeratic facies (F3, F5, F6) represents less than 20%.

The lower part of the CU succession is characterised by alternating sandstones and siltstones with planar parallel to undulating lamination associated with symmetrical ripples and climbing ripples (F14; Figure 4.6B). Well-sorted, medium to fine-grained sandstones (F11; Figure 4.6F) can be highly bioturbated with 3D burrow systems related to the *Camborygma ichnogenus* (Hasiotis *et al.*, 2006; Knaust & Bromley, 2012). Silt and clay deposits contain variable organic matter content with plant debris, coal fragments and laminae, gastropods (*Melanopsis aff. mitzopouloisi*, *Adelinella elegans*) and other undetermined bioclasts (F17; Figure 4.6D, E).

The most characteristic feature in FA4 is the presence clinoforms that are 2 to 10 m-structures high consisting of well-sorted, medium to fine-grained (poorly consolidated) sandstones (F9) and also pebbles conglomerates (F3, F5). Sandy clinoforms can downclimbing or descending cross strata (F10; Figure 4.5D). Clinoforms display a depositional dip of 5° to 10°. Up dip, they pass to horizontal, crudely stratified pebble conglomerates. Down-dip, they pass to near horizontal fine-grained strata (F14, F17). In the uppermost CU succession, clinoforms are overlain by well-sorted and near-spherical pebble conglomerates, which present planar and sharp erosive bases (F6; Figure 4.4I).

Interpretation

The clinoform packages are interpreted as foresets of small Gilbert-type deltas (Postma, 1990). Clast-supported pebble conglomerates (F3, F5) correspond to fluvial topsets. Good sorting of F6 facies with near-spherical pebbles in the upper levels of FA4 packages suggests deposition under wave action and thus in a shoreface environment. Foreset beds become sandier down dip. The horizontal well-laminated silt and clay deposits (F14, F17) correspond to the distally equivalent bottomsets. The fauna in these deposits are interpreted as a freshwater to oligohaline lacustrine assemblage. Symmetrical ripples in F14 are also encountered in bottomsets. They suggest wave-related processes within shallow water depth. The CU successions evolve from lacustrine deposits to delta foresets, and finally to fluvial topsets (Figure 4.3). Foreset height suggests that deltas prograded into a shallow lake (5 to 15 m).

4.4.5 FA5 : Silt and clay lacustrine deposits

Description

FA5 mainly consists of grey to brown, poorly consolidated silt and clay with variable content of organic matter such as wood debris, lignite fragments, undetermined bioclasts, ostracod shells,

mammal teeth, fish bones and remnants of charophytes algae (group of macrophytic green algae) (F18, F19). Beds are also locally highly bioturbated (Planolites-like burrows). Distinctive levels of metre-scale lignite (F20 ; Figure 4.6H) are interstratified with decimetric lenticular silty. FA5 also comprises white well-consolidated silts with well-developed, planar parallel to undulating laminations. This facies corresponds to an intermixing of carbonaceous with coal laminae and minor clastic material (F15).

Interpretation

Well-developed horizontal to undulated laminations in silt and clay suggest steady deposition by suspension fallout with weak traction currents in a lacustrine environment. The charophytes found in the poorly consolidated silt and plastic clay show that the calcified part of the oogonium (called gyrogonite) can be well preserved. *Nitellopsis megarensis* (Soulié-Märsche, 1979), *Lychnothamnus sp.* were identified. Charophytes live in shallow (up to 15 m) oligotrophic freshwater environments such as lakes (Grambast, 1974; Wray, 1977; Platt & Wright, 1991). The biomarker distributions (Cameron *et al.*, 1984; Papanicolaou *et al.*, 2000, 2004) of the lignite suggest a large contribution from gymnosperms plants (mainly dominated by *Glyptostrobus*) that is accustomed to high water-table levels within subaerial wetland environments (Velitzelos & Gregor, 1990; Velitzelos *et al.*, 2014; Vassio *et al.*, 2008). Organic rich sediments are deposited and temporarily preserved under anoxic conditions. Lignite beds probably formed in autochthonous peat at the margin of the shallow lake, up to 15 m deep (McCabe, 1984; Diessel, 1992). This depositional setting is coherent with the intercalated well-laminated silts.

4.4.6 FA6 : Lagoonal and upper shoreface deposits

Description

FA6 consists predominantly of a distinctive white-weathering parallel-laminated shelly calcareous siltstone to marly limestone and sandier beds of beige colour (F13 ; Figure 4.6A). Detailed facies analysis is presented in Ford *et al.* (2007). Broken bivalves and gastropod shells lie mostly parallel to bedding. The gastropod shells of *Theodoxus micans* (Neritidae) are abundant. The calcareous silts are unconformably overlain and partly truncated by coarse sands and conglomerates composed of well-sorted, nearly rounded granules (F7) that are well-stratified and with well-developed low angle planar to tangential stratification (Figure 4.5A).

Interpretation

The calcareous silts are interpreted by Ford *et al.* (2007) as being deposited in subtidal lagoon in a microtidal regime (cf. Flemming, 1988; Anthony *et al.*, 1996). The occurrence of *Theodoxus micans* attests an oligohaline freshwater coastal environment. This mixed fine-grained clastic-carbonate system is capped by coarser upper shoreface deposits (F7).

4.4 Facies analysis and alluvial architecture of the early rift deposits

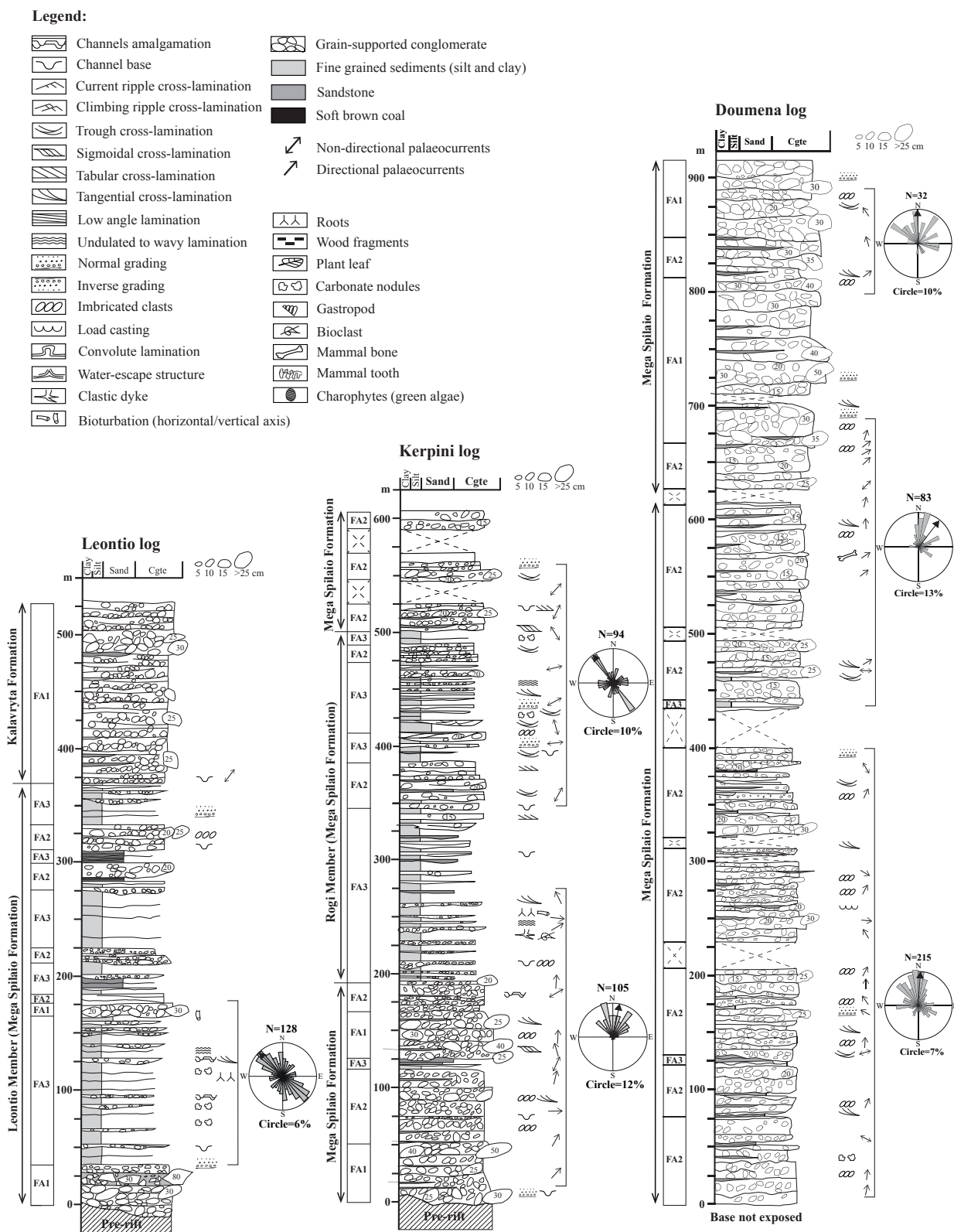


FIGURE 4.2 – Logged sections in the southern fault blocks of the study area. The logs are indicated on the geological map (Figures 4.1B and 4.8). Leontio, Kerpini and Doumena logs are respectively located in the north-western Demestika, western Kerpini and central part of the Doumena fault blocks. Facies associations are indicated along the logs (see details in the text).

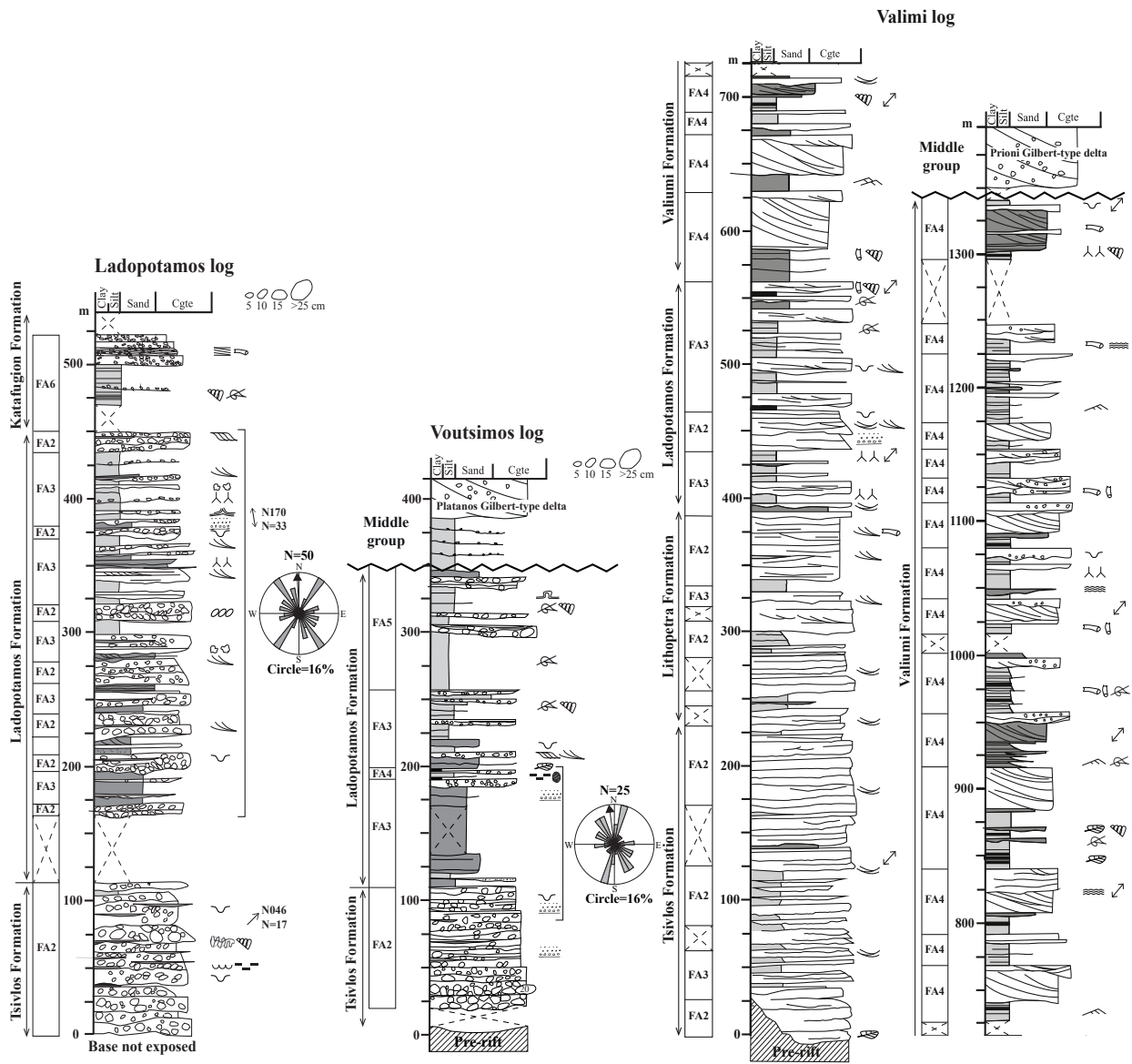


FIGURE 4.3 – Logged sections in the northern study area. The logs are indicated on the geological map (Figures 4.1B and 4.8). Ladopotamos and Voutsimos logs are both located in the PMF block. Facies associations are annotated along the logs (see details in the text).

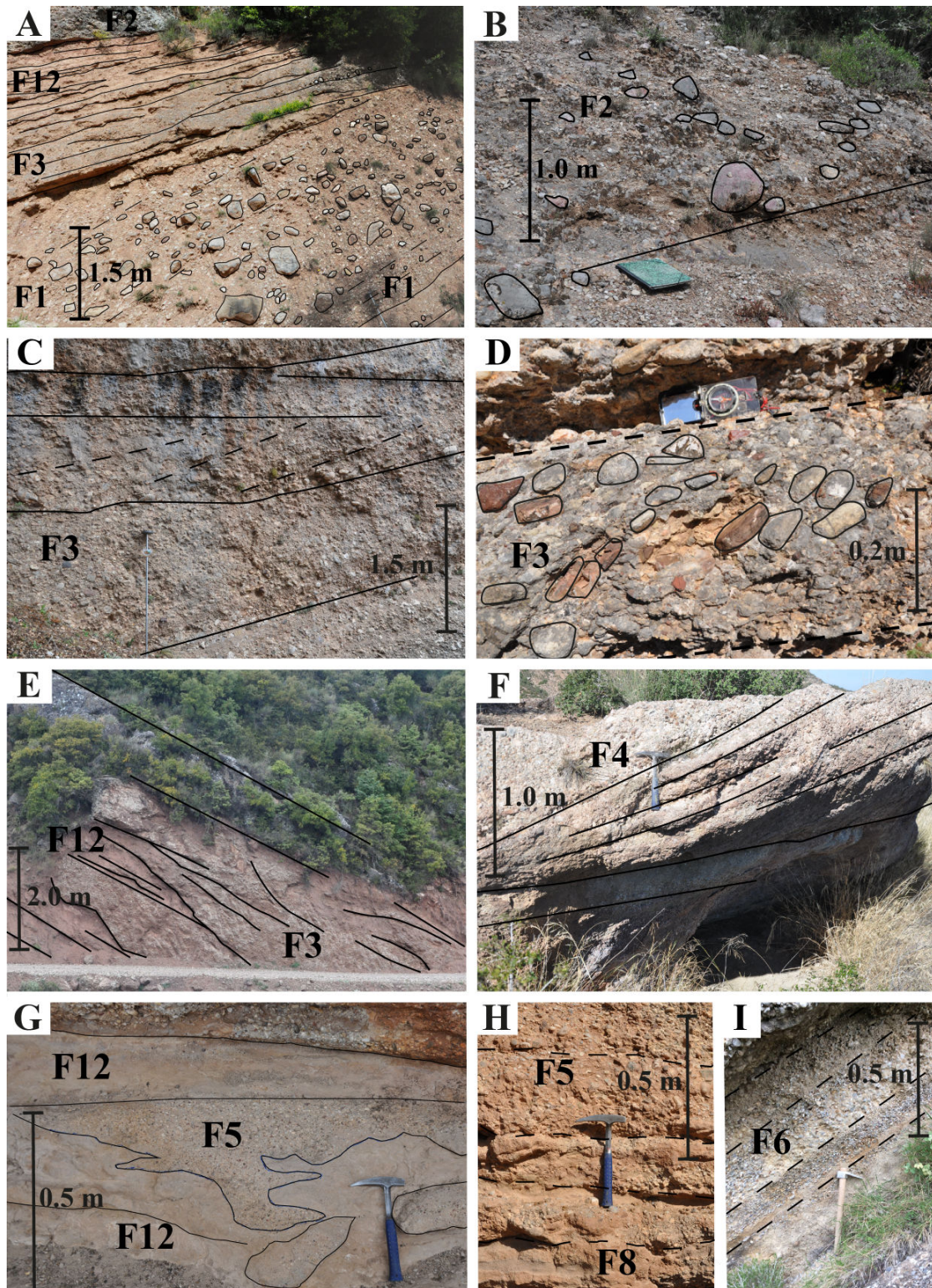


FIGURE 4.4 – Conglomeratic lithofacies (A) Very poorly sorted debris flow conglomerate bed (F1), Mega Spilaio Fm, Demestika fault block. (B) Massive poorly sorted and clast-supported conglomerates (F2), Kalavryta Fm, Kalavryta fault block. (C) Crudely stratified clast-supported conglomerates (F3), Mega Spilaio Fm, Doumena fault block. (D) Imbricated clasts (F3), Mega Spilaio Fm, Doumena fault block. (E) Channels clustering (F3 facies), Mega Spilaio Fm, Doumena fault block. (F) Foresets in clast-supported pebble conglomerate (F4), Ladopotamos Fm, PMF block. (G) *Per descensum* "wing shape" clastic dykes of clast-supported pebble conglomerates (F5), Mega Spilaio Fm, Doumena fault block. (H) Lenticular shape, crudely stratified, highly erosive beds (F5), Mega Spialio Fm, Doumena fault block. (I) Regularly bedded, well-sorted, clast-supported, conglomerates (structural dip of about 30°, F6), Valimi Fm, Valimi fault block. Detailed descriptions and interpretations of the lithofacies are given in Table 4.1. Fm : Formation. 143

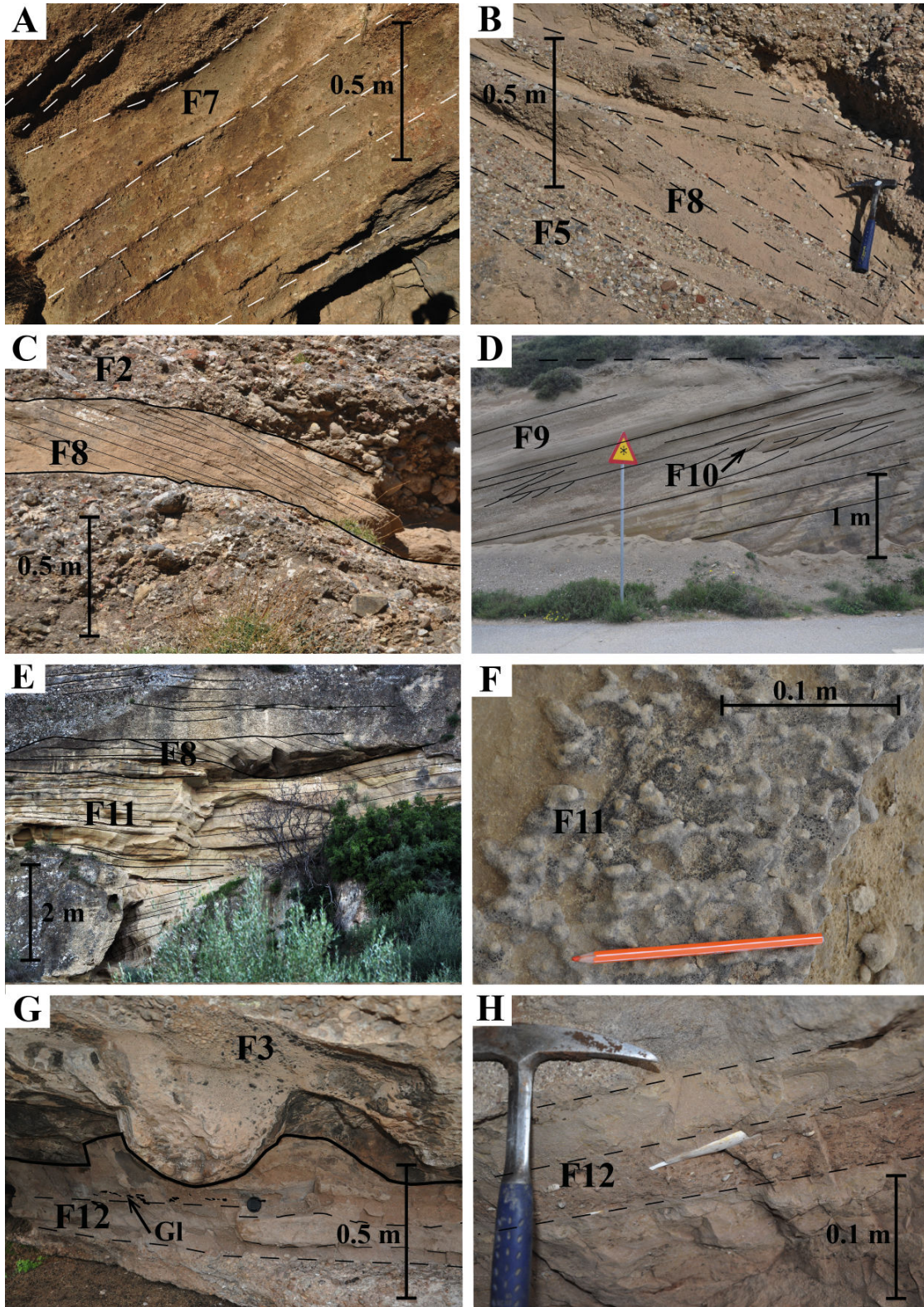


FIGURE 4.5 – Sandy lithofacies. (A) Low-angle, granule conglomerates with coarse-grained sandstones, nearshore high-energy environment (F7), Katafugion Fm, PMF block. (B) Cross-stratified, coarse to medium sandstones (F8), Lithopetra Fm, Valimi fault block. (C) F8 facies preserved between F2 conglomerate beds, Mega Spilaio Fm, Kerpini fault block. (D) Well-sorted sandstones, metre-scale clinoform (F9) and internal oblique laminations (F10), Valimi Fm, Valimi fault block. (E) Medium to fine-grained sandstones, horizontal lamination (F11), Ladopotamos Fm, Valimi fault block. (F) Top of highly bioturbated (Camborygma) sandstone bed (F11), Valimi Fm, Valimi fault block. (G) Well-bedded fine-grained sandstone to siltstone, carbonate glaeboles (G1) (F12), overlain by a massive scour-pocket (F3), Mega Spilaio Fm, Doumena fault block. (H) Fine-grained sandstones to siltstones interstratified by a white-marked bone bed (F12), Mega Spilaio Fm, Doumena fault block. Detailed descriptions and interpretations of the lithofacies are given in Table 4.2. Fm : Formation.

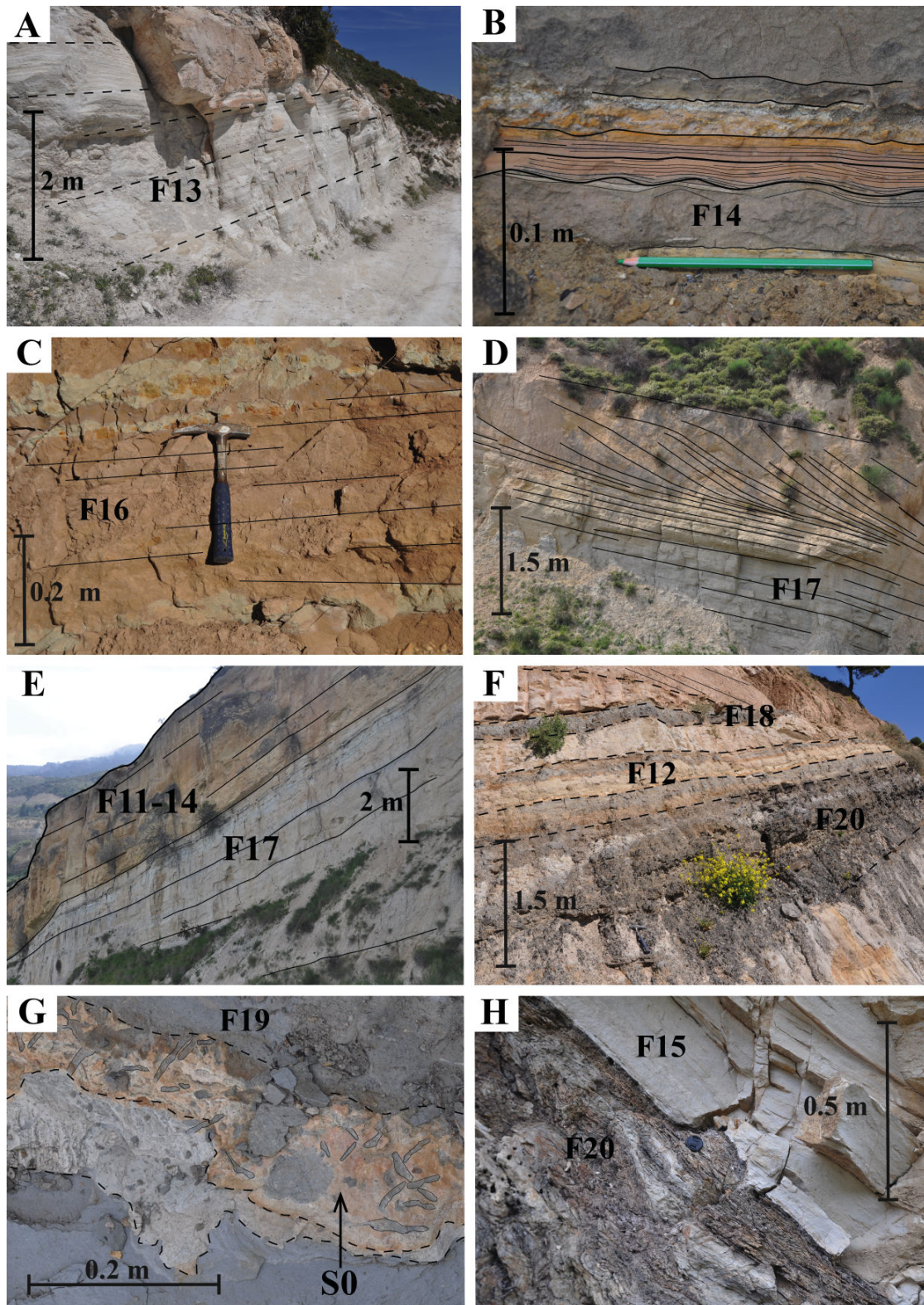


FIGURE 4.6 – Fine-grained (silt to clay) lithofacies. (A) Regularly laminated clayey silt, subtidal lagoon (F13), Katafugion Fm, PMF block. (B) Symmetric ripples to horizontal lamination within sand and silt (F14), Valimi Fm, Valimi fault block. (C) Variegated pedogenic clayey silt (F16), Ladopotamos Fm, PMF block. (D) Transition from bottomset to foreset progradation of silty Gilbert-type delta (F17), Valimi Fm, Valimi fault block. (E) Regularly, horizontally, well-bedded, silt (F17) sharply overlain by coarse facies (F8 and F14), Valimi Fm, Valimi fault block. (F) Massive soft brown coal (F20) interstratified with fine-grained sandstone (F12) and silt (F18) containing organic rich remnants (wood, fresh water shells, Rodentia teeth), Ladopotamos Fm, Voutsimos area. (G) Top of highly bioturbated silty bed (F19), Drosato Fm, (H) Lignite bed (F20) overlain by horizontal laminated silt (F15), Drosato Fm. The descriptions and interpretations of the lithofacies are given in Table 4.3. Fm : Formation. 145

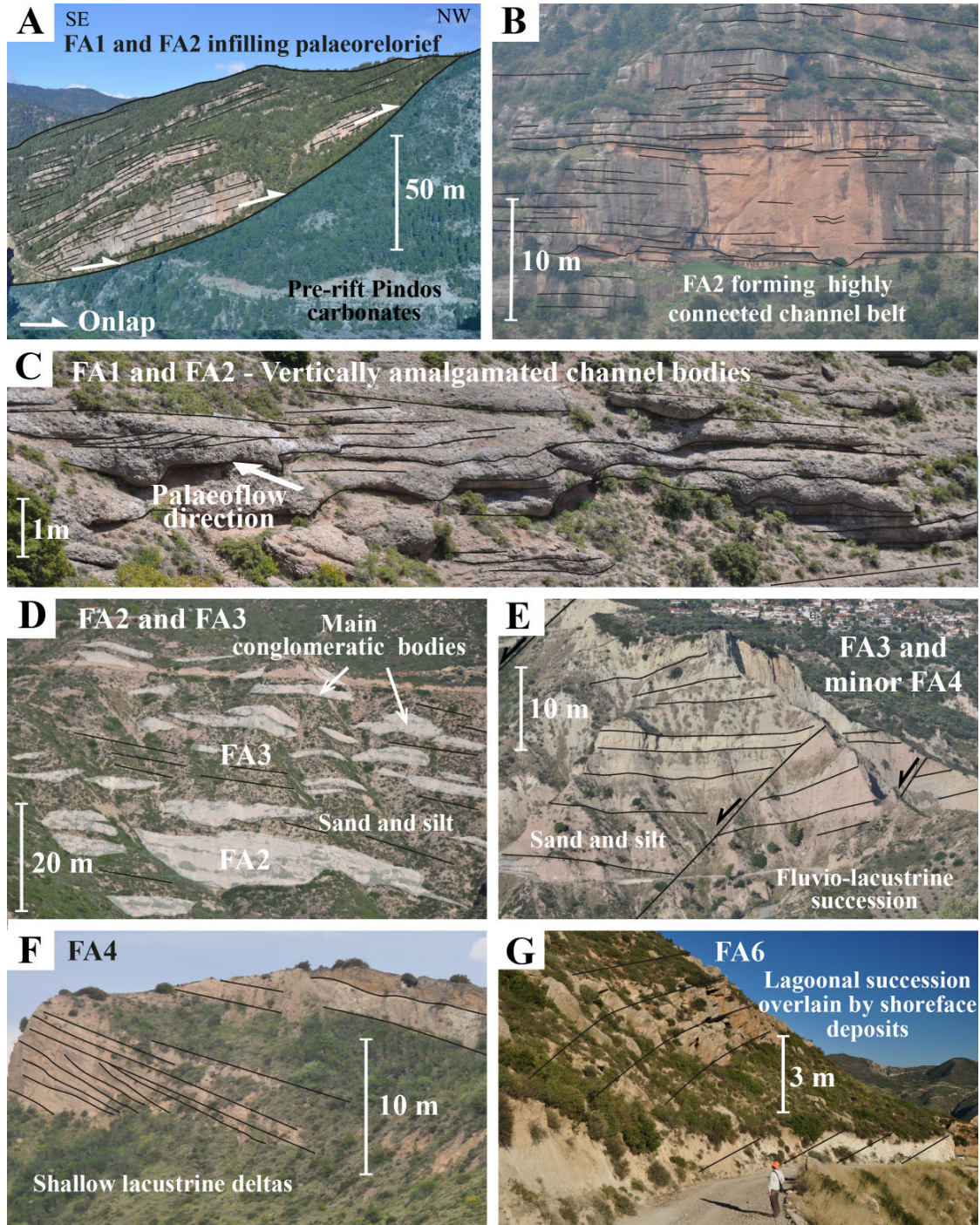


FIGURE 4.7 – Main alluvial-fluvial architectures observed in the main facies associations. **(A)** Coarse conglomeratic deposits onlap onto pre-rift Pindos carbonates (here FA2) and infill the palaeoreliefs, Tsivlos Fm, northern Tsivlos fault block. **(B)** Coarse conglomeratic channel belt deposits (FA2) with rare preservation of fine-grained deposits, Mega Spilaio Fm, central Doumena fault block. **(C)** Clustering of elementary vertical stacked channels (FA1 and FA2), Mega Spilaio Fm, Kerpini fault block. **(D)** Large-scale architecture displaying disconnected conglomeratic channels (FA2) alternating with sand and silt (FA3), Ladopotamos Fm, PMF block. **(E)** Fluvio-lacustrine succession, predominantly sand and silt (FA3 and minor occurrence of FA4), Ladopotamos Fm, PMF block. **(F)** Small Gilbert-type deltas (5 to 10 m thick) alternating with shallow lacustrine deposits (FA4), Valimi Fm, Valimi fault block. **(G)** Lagoonal succession overlain by shoreface deposits (FA6) and recording transgression at the end of the Lower group succession, Katafugion Fm, PMF. FM : Formation

4.4 Facies analysis and alluvial architecture of the early rift deposits

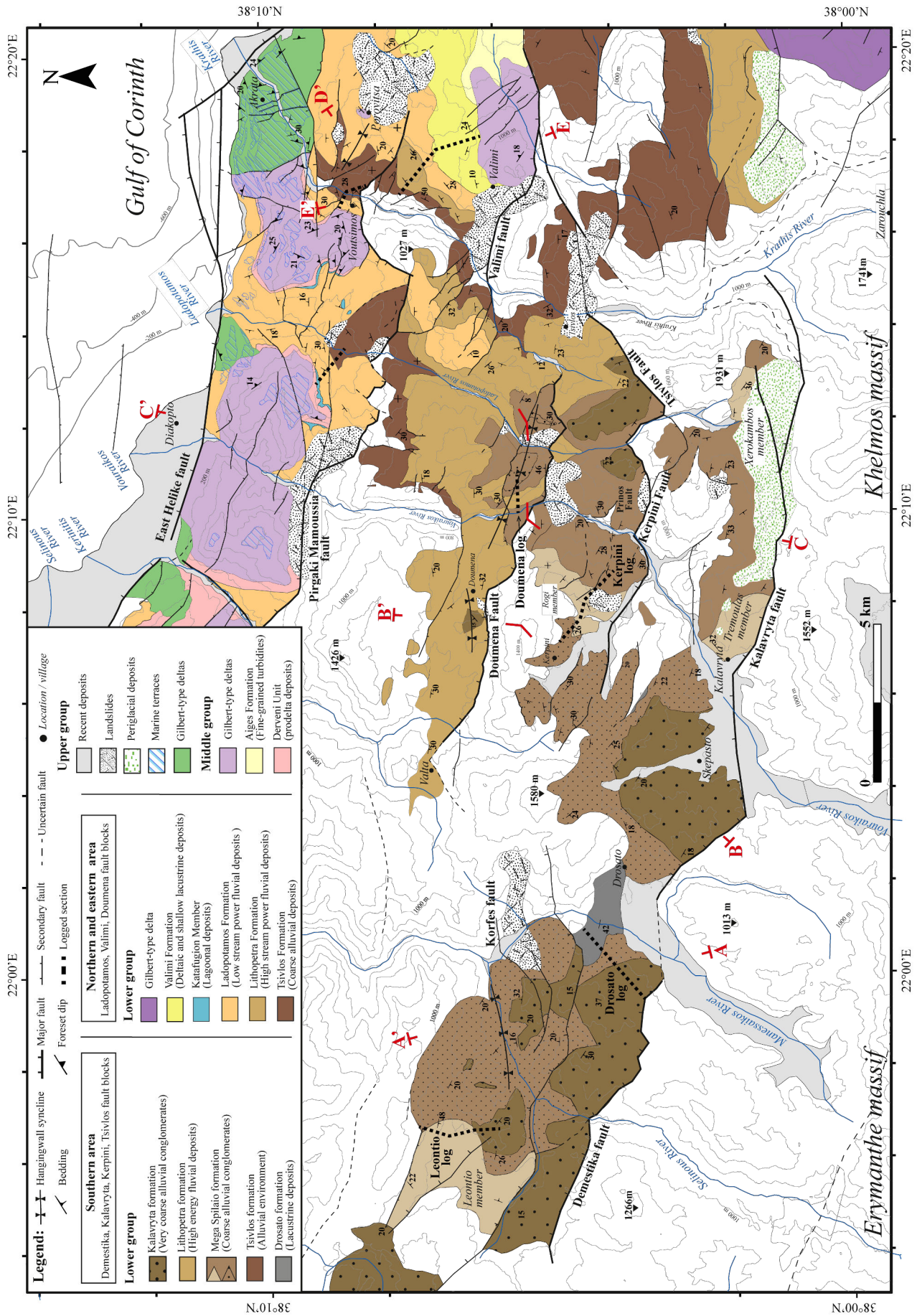


FIGURE 4.8 – Geological map of the study area. The onshore syn-rift stratigraphy is defined for the southern and northern area. Coarsening upward and fining upward successions are observed in the southern and northern study area respectively. Cross sections of Figure 4.9 are located on the map, as well as the logged sections (dashed black lines).

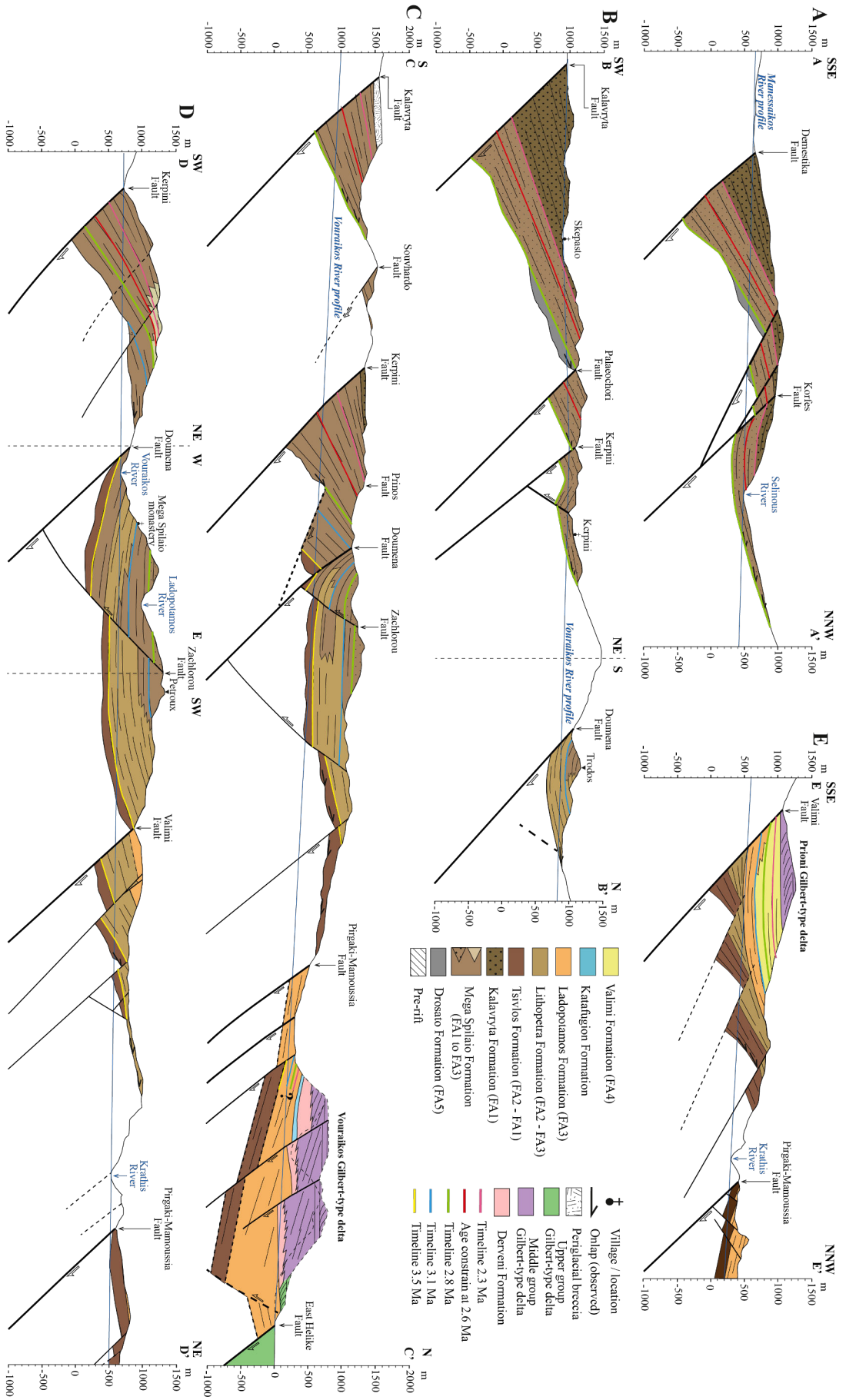


FIGURE 4.9 – (A) to (E) Cross-sections showing the details of the Lower Group stratigraphy across the different fault blocks. Location of the cross sections is indicated in Figure 4.8. Syn-sedimentary tilted faults and growth synclines are observed. Early syn-rift sediment can form dip fans along low-dipping faults (20–40°). Low dip of these faults is explained by block rotation during the development of later major faults (E).

4.5 Lithostratigraphy of the Lower Group

Two successions are presented for the Lower Group stratigraphy in the western Corinth rift (Figure 4.8), one for the southern area and the others for the northern and eastern. Syn-rift facies vary significantly over short distances and some of the defined lithostratigraphic units are laterally equivalent. Large-scale facies variations and progressive fining occur from SW to NE across the different fault blocks. More specifically, the Mega Spilaio Formation (FA1 and FA2) passes to the Lithopetra Formation (FA2 and FA3), to the Ladopotamos Formation (mainly FA3) and then to the Valimi Formation (FA4) at the eastern termination of the alluvial system.

4.5.1 Southern fault blocks

The southern area covers Demestika, Kalavryta, Kerpini, Tsivlos and Doumena fault blocks (Figure 4.8). Coarse alluvial conglomerates record a CU succession with locally preserved lacustrine units at the base. From base to top, the syn-succession comprises the Drosato, Tsivlos, Mega Spilaio, Lithopetra and Kalavryta Formations. These units are described below.

Drosato Formation

The Drosato Formation comprises silt and clay deposits with a variable proportion of terrestrial organic matter (FA5). Lignite beds are preserved at the base of the syn-rift succession. These deposits were first described by Koukouzias (1978) in the Kalavryta fault block. The best outcrops are located in the vicinity of Drosato village, along the Manessaikos River (Figure 4.8), where a 100 m thick succession is exposed. The continuity of this formation in the Kalavryta fault block is uncertain. The occurrence, distribution and quality of the lignite have been the subject of various studies (Cameron *et al.*, 1984; Papanicolaou *et al.*, 2000, 2004) to determine (i) their potential economic value, (ii) coal rank, calorific parameters and (iii) nature of plant contribution. The different biomarkers suggest that organic matter accumulated in subaquatic swamp conditions (McCabe, 1984; Diessel, 1992).

Mega Spilaio Formation

The Mega Spilaio Formation comprises coarse to fine-grained fluvial deposits. This formation is defined in the central Doumena fault blocks, in the vicinity of the Mega Spilaio monastery (Figure 4.8) and is equivalent to D2, D3, K2 and K3 units of Ford *et al.* (2013). It largely occurs in the Doumena, Kerpini, Kalavryta and Demestika fault blocks where the exposed thickness varies from 300 to 1100 m. It comprises mainly massive coarse alluvial conglomerates (FA2 and minor FA1) that form distinctive tabular bed successions in cliffs up to 20 m high. Conglomerates are coarser in the Kalavryta and Demestika fault blocks where cobble and boulder clasts are abundant

(FA1). Laterally, "fine-grained members" within the Mega Spilaio Formation correspond to alternating conglomerates, silt and clay deposits (FA3 and minor FA2). Those members are : (i) the Leontio Member in the western Demestika block, (ii) Tremoulas Member in the central Kalavryta block, (iii) Xerokambos Member in the eastern Kalavryta block, and (iv) Rogi Member in the western Kerpini fault block (Figure 4.8).

Lithopetra Formation

The Lithopetra Formation is composed of massive coarse conglomerates interbedded with cross-bedded sandstone and siltstone deposits in variable proportions (FA2 and FA3). The thickness of this formation ranges from 200 to 700 m. It lies conformably above the Tsivlos Formation (Doumena, Tsivlos, Valimi fault blocks) or directly on the basal syn-rift unconformity (western Doumena fault block). This formation is laterally equivalent to the Mega Spilaio Formation in the Doumena fault block and is also mapped in the Tsivlos and Valimi blocks (Figures 4.8 and 4.9).

Kalavryta Formation

The Kalavryta Formation comprises structureless to crudely stratified conglomerates with abundant boulder clasts (FA1 and minor FA2) with no significant lateral facies change. This formation lies conformably above the Mega Spilaio Formation and forms the uppermost part of the southern syn-rift succession in the Demestika, Kalavryta, Kerpini and Tsivlos blocks (Figures 4.8 and 4.9) marking a CU trend of the syn-rift succession. The preserved (minimum) thickness is 500 to 800 m in the Kalavryta and Demestika fault blocks, up to 100 m thick in the Kerpini and Tsivlos blocks (Figure 4.9A, B).

4.5.2 Northern fault blocks

In the northern and eastern study area, the syn-rift succession presents a fining upward trend. The original Lower Group stratigraphy defined by (Rohais *et al.*, 2007a) for the Valimi fault block is revised. From base to top, the Lower group succession here comprises the Tsivlos, Lithopetra, Ladopotamos, Katafugion and Valimi Formations. The Exochi Formation is here subdivided into the Tsivlos and Lithopetra Formations. The Valimi Formation of Rohais *et al.* (2007a) comprises the fluvial deposits of the Ladopotamos Formation overlain by the Valimi Formation (*sensu stricto*) in the upper part.

Tsivlos Formation

The Tsivlos Formation mainly consists of massive and crudely stratified alluvial conglomerates (FA2) at the base of the syn-rift succession (D1 and K1 units ; Ford *et al.*, 2013). These

conglomerates overlapped and filled palaeoreliefs. The formation is identified in hangingwall depocentres controlled by small displacement faults. An abrupt facies change defines the upper limit of the formation. The best outcrops are exposed along the Krathis and Vouraikos valleys where the thickness of the formation ranges from 100 to 300 m (Figure 4.7A).

Ladopotamos Formation

The Ladopotamos Formation consists of interbedded conglomerate bodies and red siltstone/sandstone intervals (FA3) with minor occurrences of massive crudely stratified conglomerates (FA2). This formation was first described in Ford *et al.* (2007) in the PM block where the succession is about 500 m thick above the Tsivlos Formation. The succession gradually fines upward (see Ladopotamos log ; Figure 4.3). In the westernmost PMF block, the laterally equivalent Melisia Formation (Backert *et al.*, 2010) comprises 250 to 500 m thick of fluvio-lacustrine facies (Figure 4.13). The Ladopotamos Formation thins eastward to 200 m along the Krathis valley (Voutsimos log, Figure 4.3) and contains fluvio-lacustrine deposits with abundant oligohaline to freshwater fauna recording a lateral facies transition to the Valimi Formation (FA4).

Katafugion Formation

The Katafugion Formation consists of lagoonal and upper shoreface deposits (FA6) described in detail in Malartre *et al.* (2004) and Ford *et al.* (2007, 2013). It locally outcrops in the Ladopotamos valley (Figure 4.8) and lies conformably above the fluvial deposits of the Ladopotamos Formation. The Katafugion Formation records the marine transgression in the northern area at the end of the Lower Group.

Valimi Formation

In the Valimi fault block, the Valimi Formation (FA4) is 700 m thick and lies above the Ladopotamos Formation in the Valimi fault block (Figures 4.3 and 4.8). It consists of CU sequences (20 to 50 m thick) of lacustrine deposits overlain by small Gilbert-type deltas (up to 15 m thick) that prograded into a shallow lacustrine environment.

4.6 Dating and stratigraphic correlation

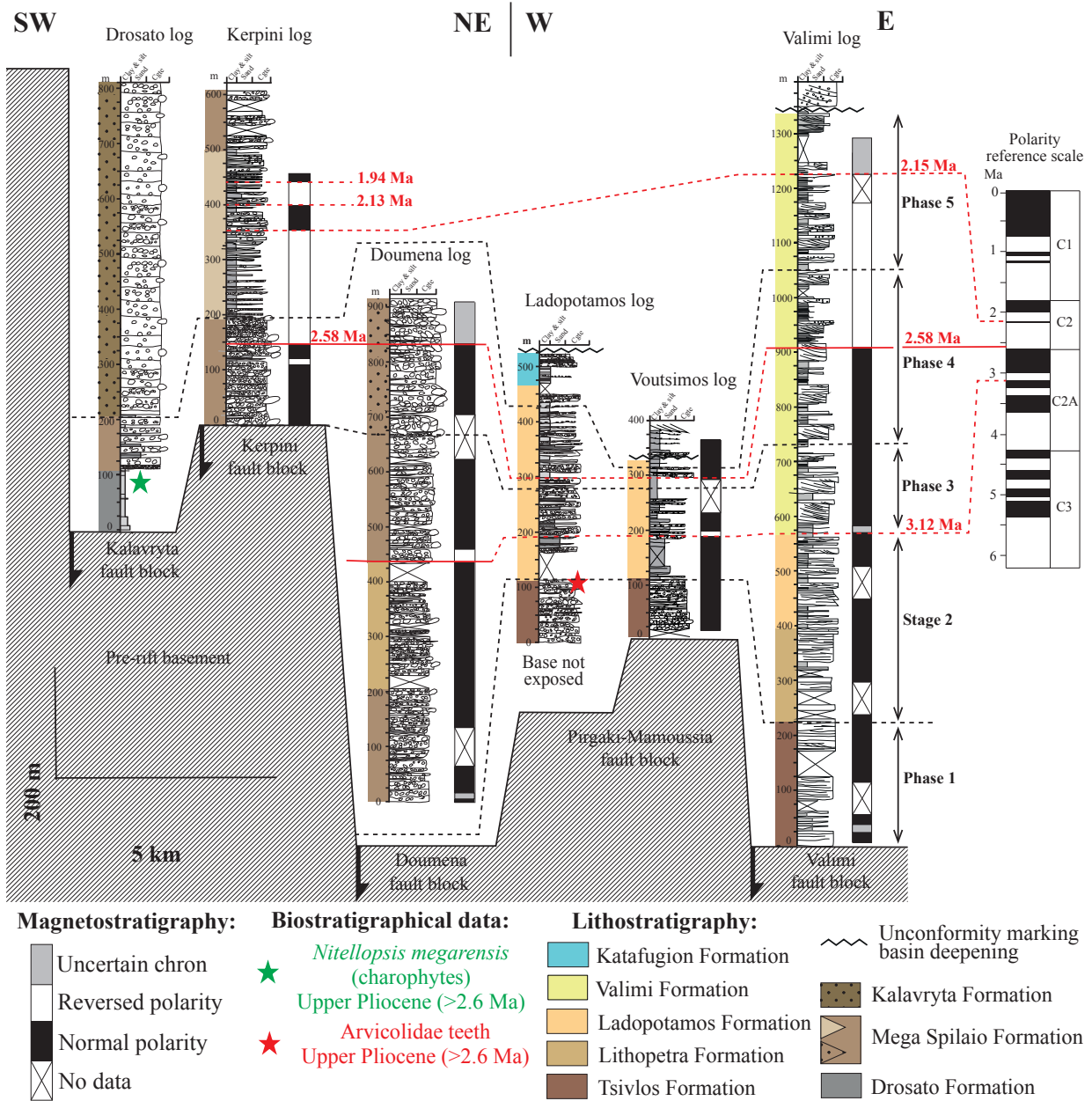


FIGURE 4.10 – Correlation model of the Lower Group across a series of normal fault by combining magnetostratigraphy results and biostratigraphic ages. The location of the sedimentary logs is indicated on Figure 4.1B. The polarity reversal at 2.58 Ma (C2r.2r) is the most robust age constraint, identified in the Valimi log (in the Valimi Formation) and the Kerpini log (in the Mega Spilaio Formation). The polarity reversal at 3.12 Ma (C2An.1r) is identified but with more uncertainty in the Doumena, Voutsimos and Valimi logs. Additional pseudo-timelines (black dotted lines) enable the subdivision of the Lower Group history in five phases. Geomagnetic polarity time scale is from Lourens *et al.* (2004).

Age constraints are challenging to acquire in conglomeratic alluvial successions due to the rarity of reliable biostratigraphic indices. We report two new biostratigraphic dates from the

Lower group. Arvicolidae rat teeth were found at the base of the Ladopotamos Formation and the species of charophytes *Nitellopsis megarensis* were found within the Drosato Formation (Figure 4.9). These biostratigraphic markers give an age of Upper Pliocene ranging from 3.6 to 2.6 Ma. Moreover, we report the presence of *Adelinella elegans* found in the Ladopotamos Formation, which, in the eastern Mediterranean, gives an age range from Upper Pliocene to Early Pleistocene (Gillet, 1963; Keraudren, 1975, 1979).

Based on the magnetostratigraphic study (Chapter 3), the polarity reversal at 2.58 Ma between the Gauss and Matuyama chrons (C2r.2r) is the most robust age constraint (Figure 4.10). It was identified in the Valimi log (in the Valimi Formation), in the Kerpini log (in the Mega Spilaio Formation) and with more uncertainty in the Doumena log (in the Mega Spilaio Formation). This polarity reversal is a key time-line for the chronostratigraphic correlation across the study area (Figure 4.10). The polarity reversal at 3.12 Ma (C2An.1r) is identified but with more uncertainty in the Doumena, Voutsimos and Valimi logs. The polarity reversal at 2.15 Ma (C2r.1n) is also tentatively identified in the upper part of the Valimi and Kerpini logs. The younger reversals at 2.13 Ma (C2r.1r) and 1.94 Ma (C2n) are identified in the Kerpini log but cannot be correlated elsewhere. These age constraints provide an average SPR of 0.5 mm/yr, which is extrapolated across the Lower Group to provide an estimate of the full age range from base to top of the succession. The base of the Lower Group is thus estimated at 3.6 Ma and the upper boundary at around 2.0–1.8 Ma. These estimates are consistent with the previous ages proposed by Rohais *et al.* (2007b) and Ford *et al.* (2013).

These age constraints do not necessarily date the main events of the early rift sedimentation. Based on high-resolution mapping, additional pseudo timelines were interpreted following syn-rift strata at the main lithological boundaries. This is possible because the lithostratigraphic formations and facies belts traverse several fault blocks. These pseudo-timelines were identified at major lithological boundaries as close to the magnetozone boundaries as possible and then were traced across and between normal fault blocks (Figure 4.11C). They provide the temporal framework for the distributed facies necessary to reconstruct an evolutionary model. The Lower Group history is subdivided into five phases (Figure 4.12). The time markers defining the limits between the phases are explained below.

- Between Phases 1 and 2, the timeline at 3.5 Ma is defined in the Valimi log at the top of the Tsvilos Formation. This lithological boundary is assumed to have the same age throughout the area and is the most uncertain of our timelines. This timeline is consistent with the biostratigraphic age (Arvicolidae teeth) of >2.6 Ma on the Ladopotamos log (Figure 4.13).
- Between Phases 2 and 3, the timeline at 3.1 Ma is defined at the base of the chron C2An.1r and corresponds to the base of the Valimi Formation on the Valimi log (Figure 4.13). On the Voutsimos log, this timeline lies within the Ladopotamos Formation. On the Doumena log, the timeline is mapped within the Mega Spilaio Formation, at the base of the prograding unit.

- Between Phases 3 and 4, the timeline at 2.8 Ma is defined at the top of the series in the Prinos fault block (Figures 4.9 and 4.11). On the Kerpini log, this timeline is traced at the base of the syn-rift succession and lies within the Mega Spilaio Formation on the Doumena log. The timeline lies in the Lithopetra Formation in the Tsivlos block (Figure 4.11C), and in the Valimi Formation in the Valimi log (Figure 4.10).
- Between Phases 4 and 5, the timeline at 2.3 Ma is defined at the base of the Rogi Member (Mega Spilaio Formation) in the western Kerpini fault block (Figures 4.11A). On the Kerpini log, it lies 40 m above the polarity reversal at 2.58 Ma (Figure 4.10). This timeline also corresponds to the boundary between the Mega Spilaio and Kalavryta Formations in both the Demestika and Kalavryta fault blocks (Figure 4.13).

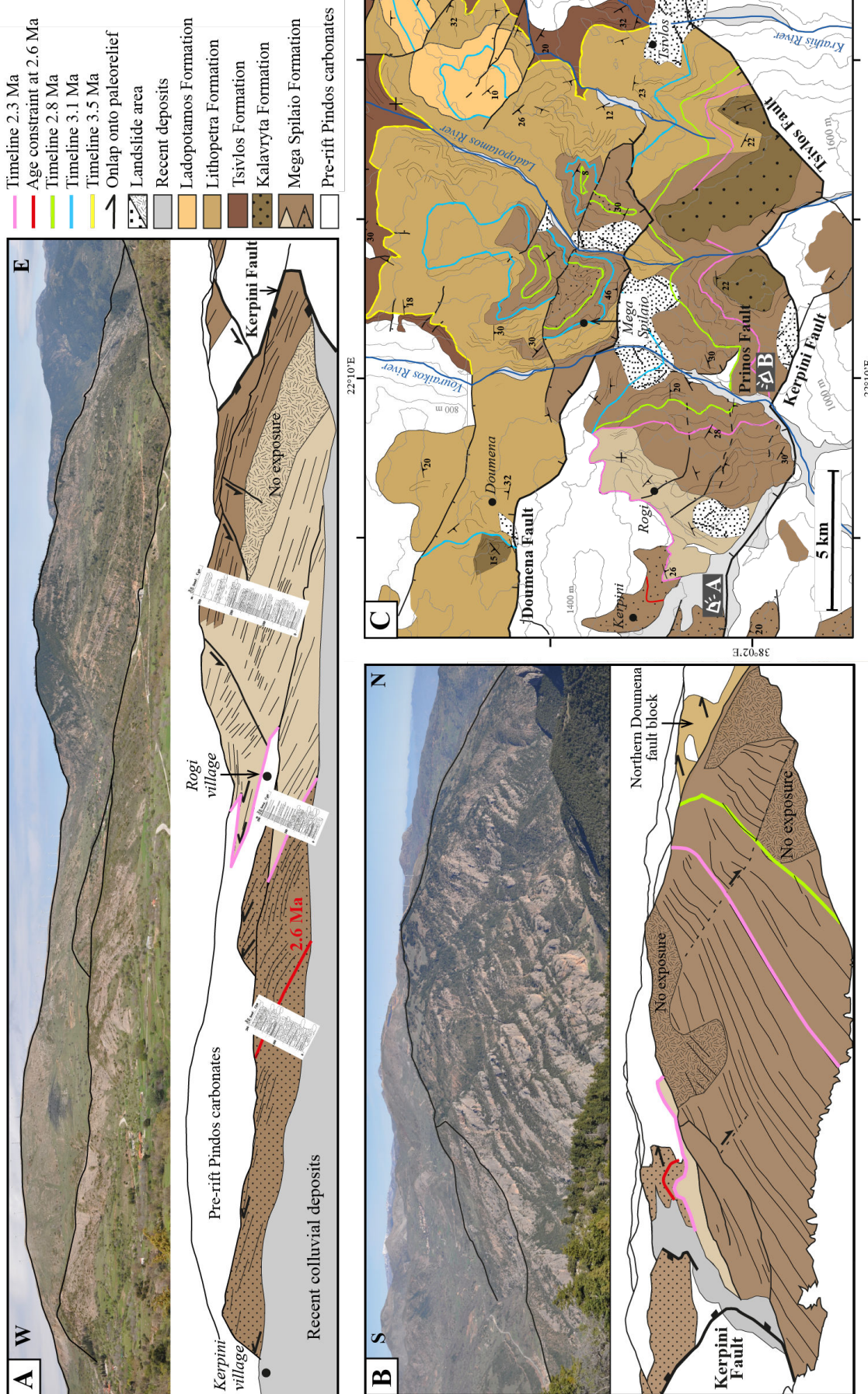


FIGURE 4.11 – Interpretation of pseudo-timelines with respect to the main lithostratigraphic markers and age constraints. (A) Kerpini fault block viewed from the western tip of the Kerpini Fault. (B) Central Kerpini fault block viewed from the eastern Vouraikos valley. (C) Close-up of the geological map including the timelines interpreted along strike of the Kerpini, Tsiavlos and Doumena fault blocks.

4.7 Evolution of the Kalavryta river system

Based on the timelines defined above, we reconstruct the rift geometry and palaeogeography of the drainage pattern for each phase.

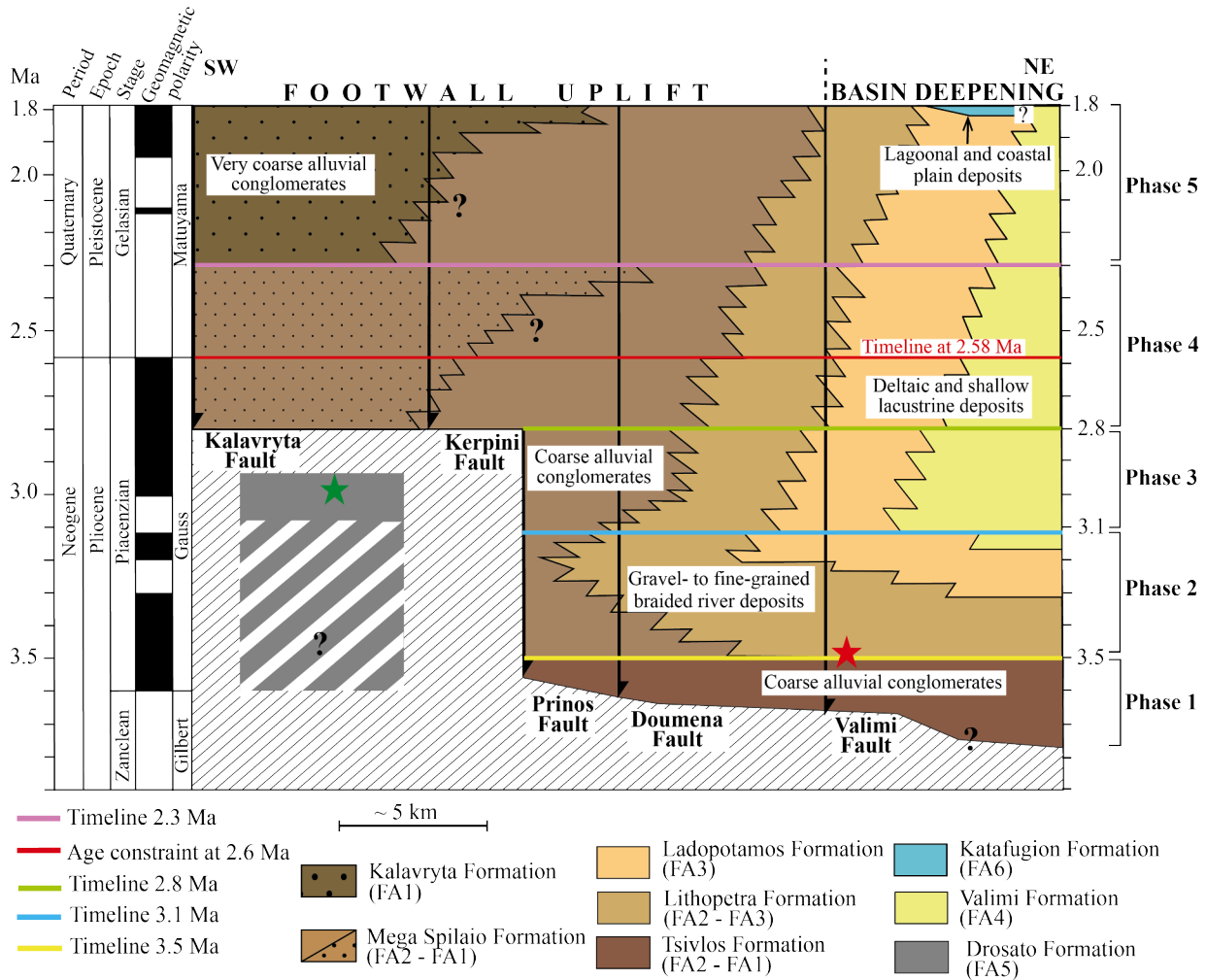


FIGURE 4.12 – Chronostratigraphic scheme of Lower Group depositional fluvial system. The stratigraphic elements are projected along a SW-NE transect that correspond to the main axis of the depositional system. Red star : Arvicolidae teeth ; green star : charophytes. Chronostratigraphic scale from [Gradstein et al. \(2012\)](#).

4.7.1 Phase 1 (~3.6–3.5 Ma)

During incipient rifting, the basin was 15 to 20 km wide and was characterised by small faults (throws up to 200 m) controlling isolated depocentres. The southern margin was defined by the Prinos and Tzivlos Faults. Poorly constrained south-dipping fault(s) defined the northern rift margin in the vicinity of the modern coast. The basin closed to the west and to the south against

significant palaeorelief (Figure 4.14A).

Coarse basal alluvial conglomerates (100–300 m thick) filled the inherited palaeorelief. During this phase, the river system developed in a confined area. Conglomeratic facies do not significantly change across and between fault blocks. Palaeocurrent directions record an overall flow to the north and northeast. Clasts are well rounded throughout, recording significant sediment transport. The absence of finer facies indicates that they were evacuated to the east by a through-going river system. There is no evidence of locally-derived sediments or reworking of older deposits. These observations suggest that high-energy rivers flowed across the young rift system depositing coarse conglomerates form broad alluvial plain below which active blind normal faults accommodated subsidence. Although data are not sufficient to reconstruct the river pattern at this time, we suggest that these coarse sediments were supplied by an antecedent river system, inherited from the drainage of the mountain belt.

During this phase, isolated lacustrine and swamp environments (Drosato Formation), typical of floodplains, developed to the south. The sediments were supplied by local drainage originating from the palaeorelief. Age control of lacustrine sedimentation is poorly constrained in time (Figure 4.12) and is likely to predate the onset of rifting.

4.7.2 Phase 2 (~3.5–3.1 Ma)

The southern rift border defined by the Prinos, Tsvilos and Doumena Faults became larger (at least 20 km) as faults grew laterally (Figure 4.14B). The active structures defining the northern margin are poorly constrained during this phase. While the rift remained closed to the southwest it propagated to the northwest with the activation of the Mamoussia Fault.

Palaeoflow directions are better constrained than in Phase 1 and plot mainly in the north- and northeast-quadrants. Phase 2 is characterised by general fining of deposits and landward retreat of facies belts (retrogradation) (Figures 4.12 and 4.13). Coarse alluvial conglomerates (Mega Spilaio Formation) were restricted to the southern blocks close to the sediment entry points (downstream distance up to 5 km). Facies became finer toward the NE where coarse conglomerates alternated with fine-grained overbank deposits.

The eastern termination of the Kalavryta river system is not recorded during this phase and lies to the east beyond the study area. Another river system developed outside of the study area and fed the Killini deltaic system to the east. The drainage pattern of the Killini river system is not considered here.

4.7.3 Phase 3 (~3.1–2.8 Ma)

The southern and northern rift margins remained similar to that in Phase 2. As hangingwall depocentres grew laterally, syn-rift deposits progressively onlapped and filled palaeorelief. Phase

3 is marked by deltaic and lacustrine sedimentation at the eastern end of the alluvial basin (Valimi Formation). Small Gilbert-type deltas prograded eastward into a shallow lake (Rohais *et al.*, 2007a). Fluvio-lacustrine environments also probably prevailed in the northwestern part of the rift with the deposition of the Melisia Formation (Backert *et al.*, 2010). In the Valimi fault block, the transition from fluvial to lacustrine environment is recorded at around 3.1 Ma between the Ladopotamos and the Valimi Formations. A similar transition between the fluvial Amfithea and turbiditic Rethio-Dendro Formations in the eastern Corinth rift was estimated at around 3.0–3.2 Ma by Leeder *et al.* (2012). This emphasizes the synchronous record of the shallow lacustrine conditions developing along the early rift margin. However, correlation between the central and eastern rift is not straightforward as different river systems (Kalavryta and Killini river systems) supplied the rift basin during the Lower Group.

During this phase, coarse conglomeratic facies belt prograded toward the north and east (Figures 4.12 and 4.13) and thus covered a larger area (about 7 km in length). Palaeoflow directions became more dispersive in the distal part of the Kalavryta river system, suggesting that a distributive pattern developed downstream and across the subsiding fault blocks. Locally, a small consequent drainage system developed in the western Doumena fault block (Figure 4.14C) and flowed to the NE. Otherwise the single sediment entry point from the antecedent drainage system persisted and controlled the facies distribution across the alluvial basin.

4.7.4 Phase 4 (~2.8–2.3 Ma)

This phase is characterised by the migration of the rift margin to the south and west and the opening of the rift to the west. The Kerpini, Kalavryta and Demestika Faults were activated while the Prinos Fault became inactive (Figure 4.14D). The newly-formed hangingwall depocentres were filled by coarse alluvial conglomerates (Mega Spilaio Formation, FA1 and FA2) that onlapped onto palaeorelief. Coarse alluvial conglomerates were locally coarser than those of Phase 3 and extended 12–15 km downstream.

The main NE-flowing channel axis of the Kalavryta river system remained stable. At the edges of fault-controlled depocentres, away from the main channel axis, fine-grained overbank deposits are preserved. Footwall migration of fault activity was not associated with facies retreat but with progradation indicating significant input of coarse-grained material into the fluvial system.

In the SW, the Demestika fault block formed an isolated depocentre delimited by palaeorelief and filled with coarse conglomerates. Conglomerates in this depocentre contain a higher proportion of radiolarite clasts than in the rest of the fluvial system (30–60%, compared with 10–25% elsewhere). This suggests sediment supply by another river system that sourced from the south and flowed towards the NW.

4.7.5 Phase 5 (~2.3–1.8 Ma)

During phase 5, fault segments linked together to form major active faults that were 15 to 30 km long (Figure 4.14D). The linked Kalavryta and Demestika fault segments formed the southwestern rift margin. The linked Kerpini, Tsivlos and Valimi fault segments formed the second major controlling fault. The active faults along the northern margin remain unknown.

Coarse alluvial conglomerates of the Kalavryta Formation were mainly deposited in the southern blocks in the Kalavryta and Demestika fault blocks. These coarse alluvial conglomerates are coarser than those deposited during the former phases and mark a CU trend in the southern fault blocks. Again, the Demestika hangingwall depocentre was encompassed by palaeorelief but was possibly connected to the Kalavryta river system at this time. Palaeocurrent data for this phase are rare, but we assume that the rivers persisted and flowed in the same direction.

Phase 5 is also preserved in the Valimi and Pirgaki-Mamoussia fault block (Figure 4.13A, B). In the PMF block, the lagoonal sediments (Katafugion Formation) lying above the fluvial deposits (Ladopotamos Formation) mark the end of Phase 5. The overlying upper shoreface deposits document shoreline retreat during a transgressive phase.

At 1.8 Ma, the subsequent northward migration of fault activity marks the transition between the Lower and Middle Groups (Ford *et al.*, 2013). During the Middle Group, the southern rift margin was defined by the Pirgaki-Mamoussia and Valimi Faults. Inactive fault blocks were progressively uplifted along the southern margin.

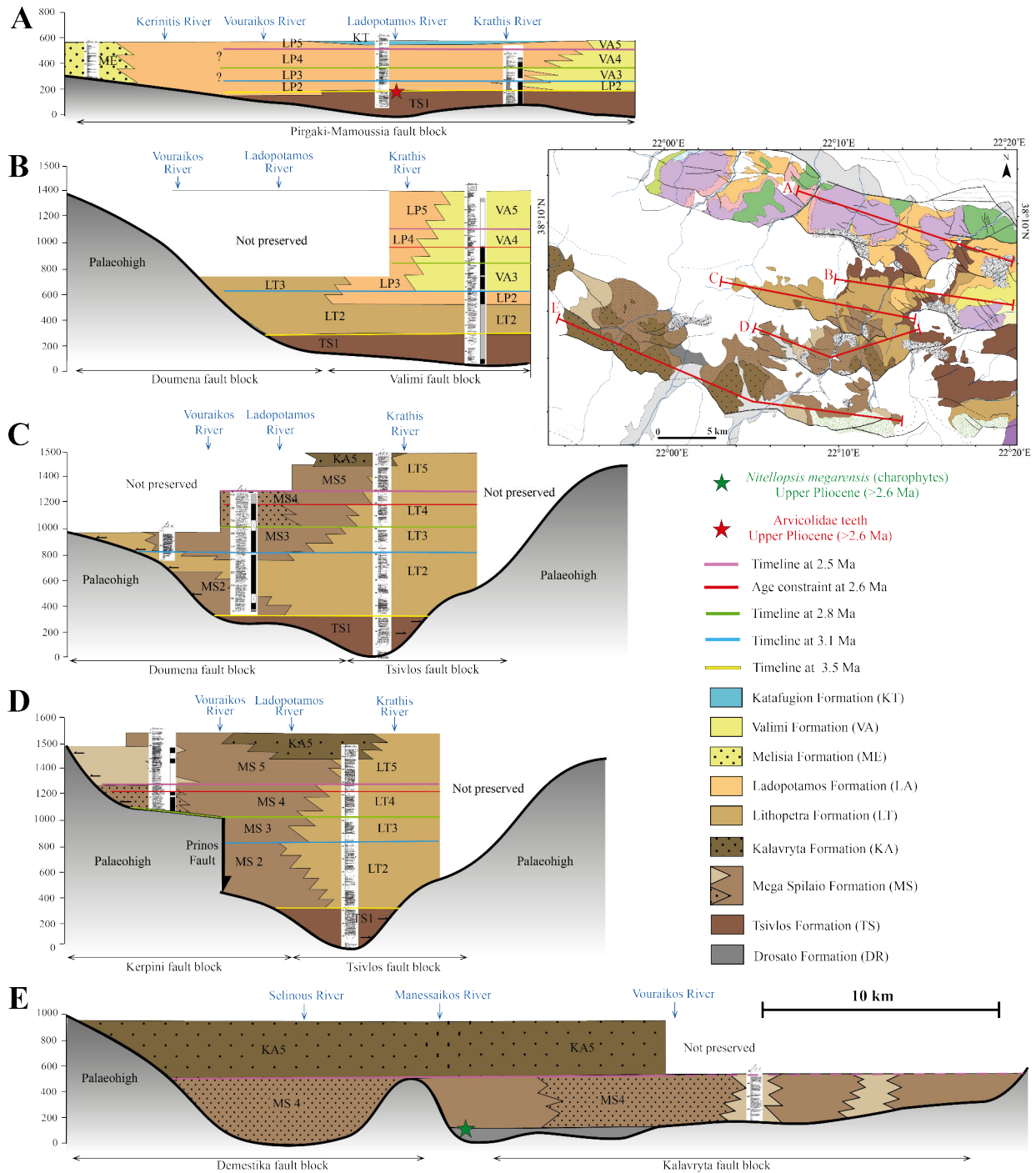
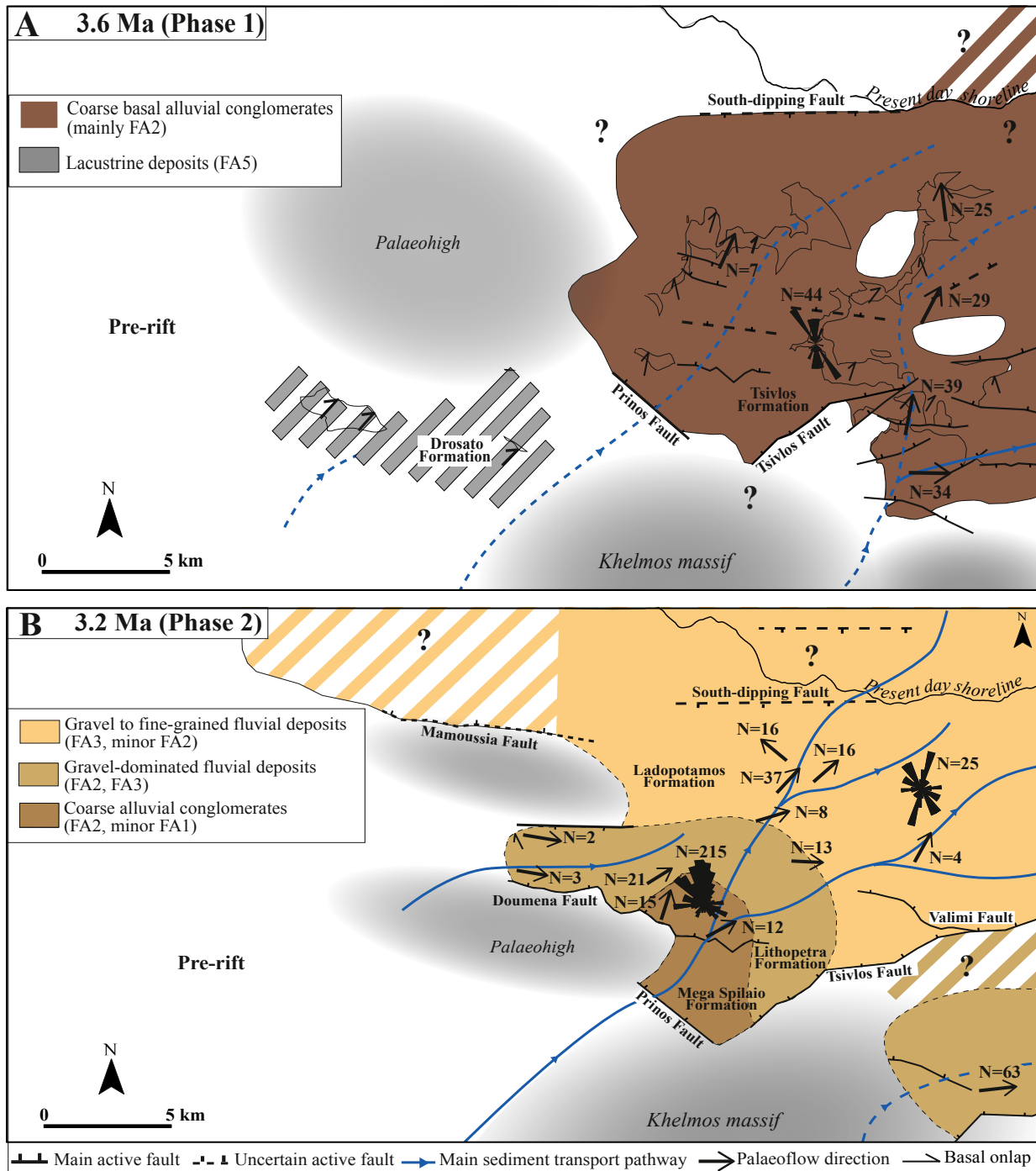
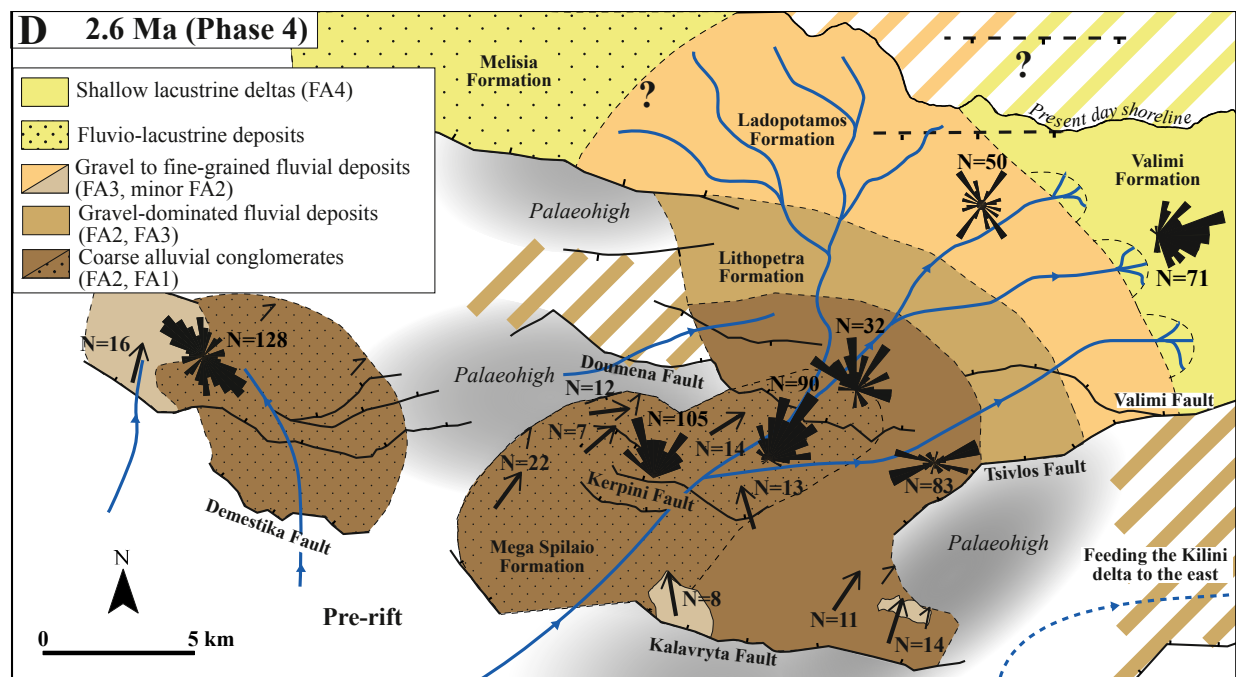
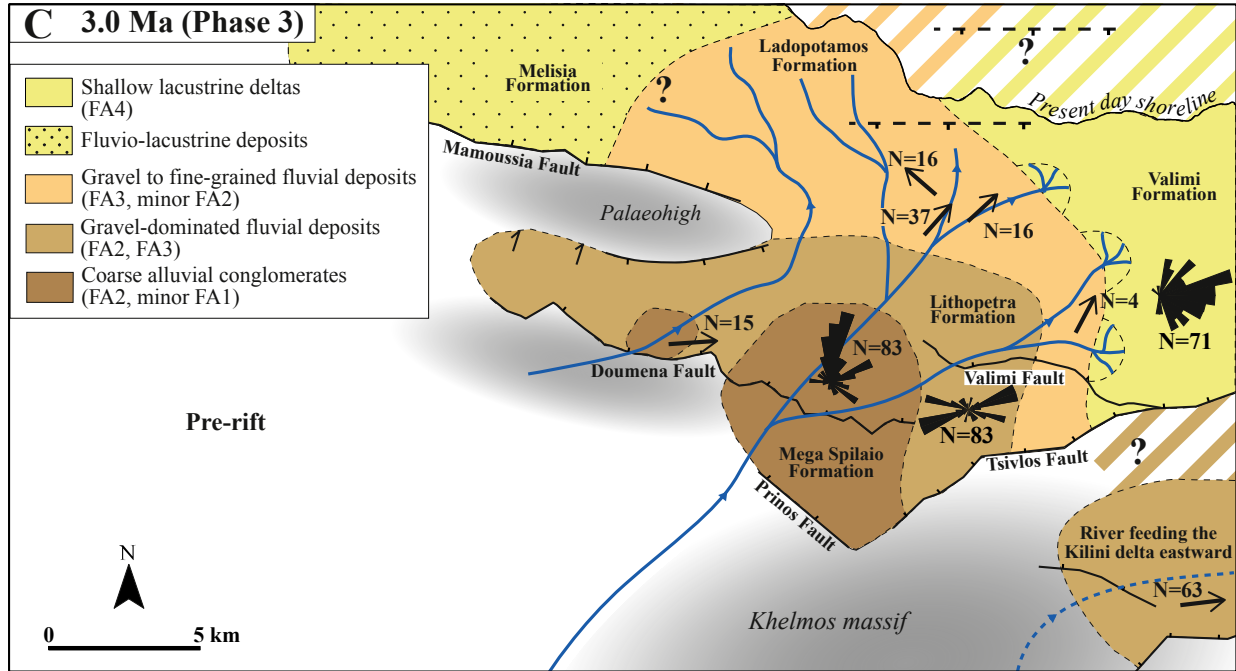


FIGURE 4.13 – Fence diagrams along strike of the hangingwall depocentres showing the different timelines. (A) Pirgaki-Mamoussia and Valimi fault blocks. (B) Northern Doumena and Valimi fault blocks. (C) Southern Doumena and Tsvilos fault blocks. (D) Kerpini and Tsvilos fault blocks. (E) Demestika and Kalavryta fault blocks. The thickness of the preserved syn-rift succession varies significantly along strike. Central and western parts of the Kerpini, Doumena and Valimi hangingwall depocentres are preserved. Syn-rift deposits in the eastern Tsvilos block are not preserved due to later footwall uplift and erosion on the Valimi Fault.





— Main active fault - - - Uncertain active fault → Main sediment transport pathway ↗ Palaeoflow direction ↘ Basal onlap

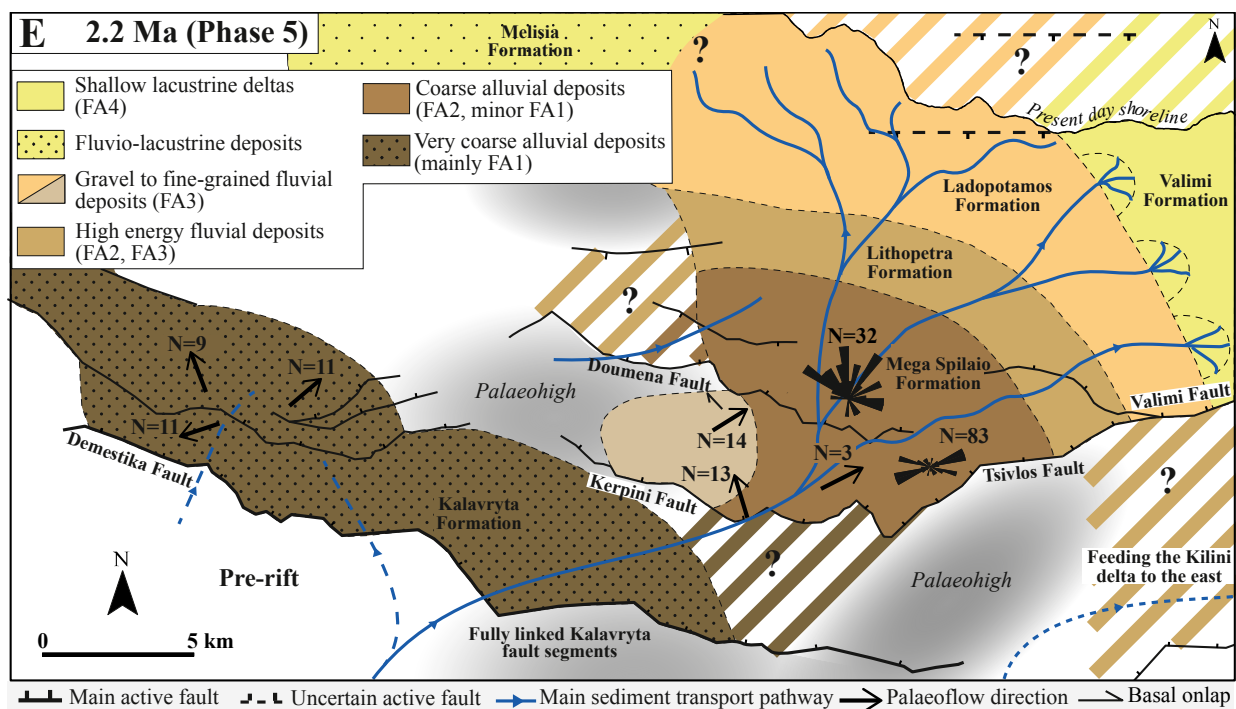


FIGURE 4.14 – (A) to (E) Palaeogeographic reconstructions describing the main tectono-sedimentary features for the five evolutionary phases. The maps are not corrected from the N-S extension. The drainage pattern was reconstructed using the palaeoflow directions.

4.8 Discussion

4.8.1 Paucity of footwall-derived sediments

No footwall topography was created between the fault blocks during the development of the early western Corinth rift basin. The rare consequent drainage documented originated from palaeorelief (Figure 4.15B). We demonstrate that the antecedent Kalavryta river system smothered the uplifting zones from the onset of rifting and high sediment supply largely exceeded subsidence ($A < S$). This observation differs considerably from classic models of the early rift phase (e.g. Gawthorpe & Leeder, 2000; Cowie *et al.*, 2006).

Studies from the North Sea document the covering of the fault network by the depositional system such as in the Middle to Late Jurassic shoreface sandstones reservoir in the northern part of the Danish Central Trough and the fluvial to shallow marine Middle Jurassic Tarbert Formation of the East Shetland Basin. However, drowning of the active fault blocks is explained by sea level rise, leading to the development of a more open depositional setting and then retreat of the syn-rift facies. As footwall-derived sedimentation ceased, the antecedent drainage system in the pre-rift hinterland predominantly fed the depositional system (e.g. Johannessen & Andsbjerg, 1993; Johannessen *et al.*, 1996; Davies *et al.*, 2000). The Upper Devonian Old Red Sandstone in the Munster basin (SW Ireland) show that a large fluvial system (radius of 120 km) developed across the rift basin, burying the active faults (Williams, 2000).

The absence of created footwall topography between the fault blocks during the development of the depositional system basin is poorly understood. To enable the burial of active faults from the onset of rifting, sediment supply must predate fault activity. This is consistent with the presence of the antecedent Kalavryta river system supplying the early rift basin. Moreover, sediment loading from the antecedent river system probably influenced the overall isostatic response of footwall uplift and flexure of the hangingwall.

Assuming a domino-like rotation of the active faults blocks (e.g. Gans & Miller, 1983) footwall exposure mainly depends on fault dip, thickness of the brittle upper crust, the possible presence of a décollement layer in the upper crust and normal fault spacing (Anders *et al.*, 1993; Scholz & Contreras, 1998). The zone of footwall uplift is particularly limited when faults are closely-spaced (Densmore *et al.*, 2005). One of the main characteristics of the early Corinth rift phase is the presence of narrow fault blocks (4–7 km wide). Limited footwall uplift could partly contribute to burial of the faults by the depositional system. We suggest that the combination of high sediment supply from the antecedent drainage and closely-spaced faults explains the absence of footwall topography between the active faults. This hypothesis needs further investigation, especially regarding the coupling between long-term sediment supply and normal fault growth, and the boundary conditions leading to burial of normal fault systems in general.

4.8.2 Length scale of facies variation and relation with faults

The antecedent Kalavryta river system was inherited from the Hellenide thrust and fold belt (Figure 4.15) and persisted to control facies distribution throughout the early rift evolution. Facies transitions between lithostratigraphic formations document an overall downstream fining. Therefore length of the coarse conglomeratic facies belt (defined by the Mega Spilaio and Kalavryta Formations) varies from 7 to 12 km through time (Figure 4.12) while fault spacing is lower. Facies belt transitions were therefore not controlled by faults but occurred at the scale of the full alluvial system.

Longitudinal cross sections along the Kerpini and Doumena fault blocks (Figure 4.13C, D) shows that coarse facies are skewed to the west of the zone of maximum subsidence giving an unexpected asymmetry in facies distribution. Again, this shows that facies distribution was not governed by fault displacement alone and was related to the position of the main fluvial channel.

The zones of maximum subsidence on individual fault blocks are aligned parallel to the persistent fluvial system (Figure 4.13). Continuous high sediment supply was superimposed on the growing normal fault system, differentially loading the hangingwall depocentres and thus localising maximum displacement. This demonstrates that long-term sedimentation can influence normal fault growth and thus the location of the main rift depocentres.

4.8.3 Channel belt distribution and subsidence variations

A large number of studies on the role of subsidence in controlling alluvial architecture, have focussed on where and when highly interconnected channel-belts occur (e.g. Bridge & Leeder, 1979; Bridge, 1993; Mackey & Bridge, 1995; Sheets *et al.*, 2002; Hickson *et al.*, 2005). Field examples, experimental models and numerical models such as LAB models (Leeder-Allen-Bridge) show that it is possible to record highly interconnected channel belts in both low and high accommodation settings. However, most studies show that low channel interconnectivity and high preservation of floodplain deposits are found in areas of high subsidence (e.g. Bridge & Leeder, 1979; Alexander & Leeder, 1987; Santos *et al.*, 2014; Colombera *et al.*, 2015; Medici *et al.*, 2015). These studies are based on axial river and consequence transverse drainage systems along strike of the main bounding faults (e.g. Alexander & Leeder, 1987; Leeder & Mack, 2001; Kim *et al.*, 2011). The role of subsidence in the case of a major transverse antecedent drainage system superimposed on a growing rift has not been investigated.

Coarse alluvial conglomerate facies were preferentially stacked along the persistent fluvial axis, while fine-grained overbank deposits are more locally preserved in the zones of low subsidence, toward fault tips (e.g. western Doumena and Kerpini blocks; Figures 4.8 and 4.13). The observation of stacked channel bodies in areas of high subsidence is consistent with the prediction of alluvial architecture proposed by Sheets *et al.* (2002), Hickson *et al.* (2005), Strong *et al.*

(2005) and Kim & Paola (2007).

In contrast, in the early Corinth rift basins, stratigraphic architecture was governed by sediment and water supplies from the antecedent river system. Subsidence variation along strike in the hangingwall depocentres was secondary in the control. This finding emphasizes the role of autogenic control on alluvial stratigraphy as supported by Hajek *et al.* (2012). Results of experimental models by Hickson *et al.* (2005) demonstrate that downstream and across stream changes in subsidence have little effect on alluvial architecture when sediment supply is high. The downstream facies belt transitions recorded in the early Corinth rift basin is a good field example to test existing models of downstream sediment loss and fining (e.g. Fedele & Paola, 2007; Paola & Martin, 2012).

4.8.4 Overfill conditions in the early rift basins

Allogenic and autogenic drivers control accommodation, sediment supply and sediment mass-balance of alluvial basins (e.g. Allen, 1978; Bridge & Leeder, 1979; Heller & Paola, 1996; Kraus, 2002; Leeder, 1978, 1993; Sheets *et al.*, 2002; Strong *et al.*, 2005; Hajek *et al.*, 2012; Paola & Martin, 2012; Allen *et al.*, 2013). The stratigraphic organisation of facies belts through time can therefore be used to interpret the controlling parameters of the early-rift sedimentation.

During the early evolutionary phases of closed continental rift basins, accommodation changes cannot be related to eustatic cycles but only to subsidence on normal faults. Classical concepts of sequence stratigraphy cannot be directly applied to interpret progradational and retrogradational geometries within the syn-rift succession. A general prograding stratigraphic pattern generally characterises the early rift basins due to overfilled conditions ($A < S$). These conditions are usually explained by low created accommodation on the young fault system (e.g. Lambiase & Bosworth, 1995; Prosser, 1993; Withjack *et al.*, 2002; Holz *et al.*, 2014). The Corinth rift case demonstrates that another factor, the presence of a major antecedent alluvial system, can generate high sediment supply and thus contribute to overfilled conditions, whether accommodation is low or high.

Our evolutionary model shows a first phase of infill of palaeorelief during incipient rifting (Phase 1; Figure 4.14A). As supported by the first preserved sediment packages (i.e. Tsivlos Formation), the sedimentation is confined into alluvial valleys and dominated by crudely stratified alluvial conglomerates. As the main palaeorelief is infilled, the overall alluvial architecture evolves to a more classical organised fluvial depositional system but still delimited by paleohighs (Phase 2; Figure 4.14B). The alluvial plain extended over a broader area allowing facies belts to develop. The main axial stream river was dominated by coarse-grained material but displayed lateral fine-grained facies changes (i.e. Mega Spilaio to Lithopetra Formations). Fining and sudden facies retreat from 3.5 to 3.2–3.1 Ma (Figure 4.12) can be explained by the increase in basin subsidence assuming constant sediment supply. Subsequent early rift history records a general

progradational trend (Phases 3 to 5 ; Figure 4.14C–E). This progradation can be explained by a decrease in accommodation rate and/or an increasing sediment supply induced either by tectonic uplift in the drainage basin and/or climate change (discussed below).

Fault kinematics and the order of fault activation (landward or basinward) can generate distinct stratigraphic patterns across and between the fault blocks (e.g. Ter Voorde & Cloetingh, 1996). In a rift with transverse drainage, footwall migration of faulting should lead to facies retreat and fining of the stratigraphic succession. In the Corinth rift however, footwall migration of fault activity at ~ 2.8 Ma (Phase 4 ; Figure 4.14D) did not perturb the continuous progradational trend observed since 3.2–3.1 Ma (Figure 4.12). The coarse conglomeratic facies belt enlarged and the downstream length of the other facies belts remained constant. Footwall migration of fault activity was associated with an increased input of coarse material and sediment supply, which may have been due to uplift in the drainage basin or to climate change. As accommodation was in deficit, sediments were bypassed downstream to more distal areas, generating continuous progradation of the facies belts.

The onset of progradation at 3.2–3.1 Ma occurred before the footwall migration of fault activity at ~ 2.8 Ma (Figure 4.12). There is no argument to support a decrease in accommodation space between ~ 2.8 and ~ 3.2 Ma causing lower A/S ratio and facies progradation. Instead, the beginning of progradation may be explained by increasing sediment supply due to climate change. Reconstruction of past climates in the Central and Eastern Mediterranean show that more humid and colder conditions were established from 3.2 to 2.8 Ma due to glaciation at higher latitudes (Bertini, 2010; Herbert *et al.*, 2015). Expansion of open vegetation may have led to increased sediment supply to the alluvial system.

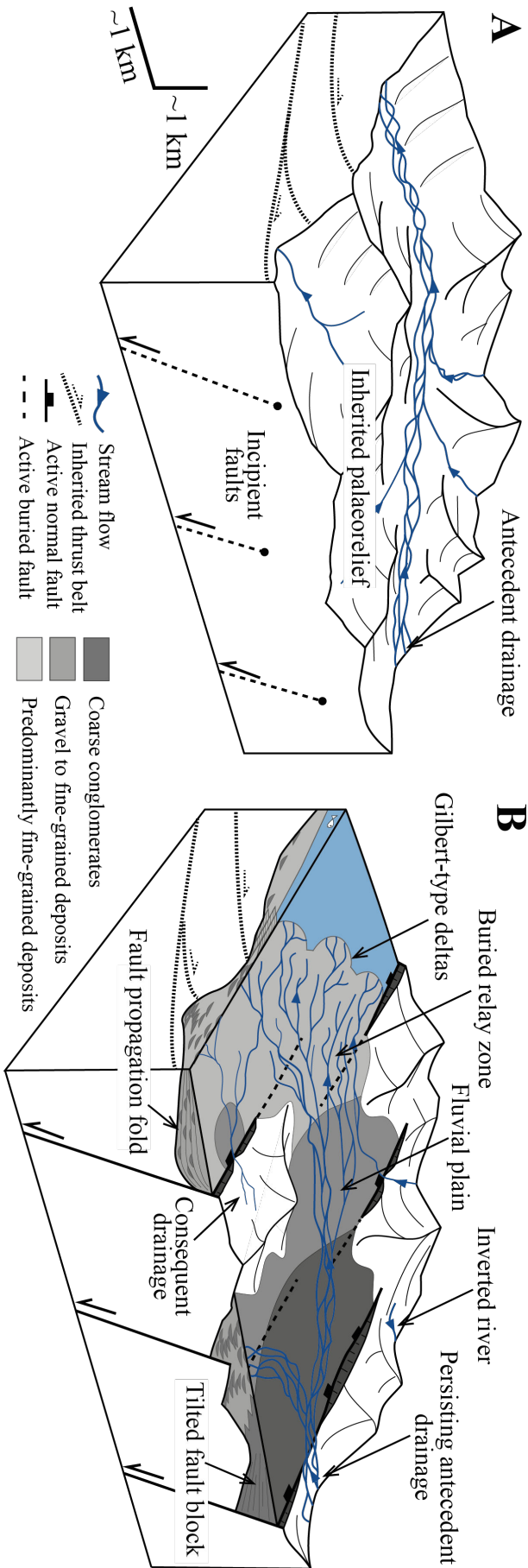


FIGURE 4.15 – Conceptual block diagrams of the early rift phase incorporating an antecedent drainage. (A) Pre-rift relief was inherited and drainage system from the Hellenide fold and thrust belt. Sediments were transported out the system to an unknown pre-existing sedimentary basin. (B) The early rift phase is characterised by nucleation and growth of normal faults. The antecedent drainage system preserved its main course and developed across the normal fault system.

4.9 Conclusions

1. The long-lived Kalavryta river system was superimposed on a growing normal fault system. Along the southern margin of the western Corinth basin, the early rift alluvial succession (Lower Group) is dated as between ~ 4.0 and ~ 1.8 Ma using magnetostratigraphy and biostratigraphic dating. As age constraints are rare in gravel-dominated alluvial successions, we propose an alternative method to define additional timelines. Based on high-resolution mapping, pseudo-timelines identified at major lithological boundaries close to dated logs, and were traced within and across fault block. Chronostratigraphic correlations across the different fault blocks enable reconstruction of the early rift basin in five main phases. The depositional system (Kalavryta river system) evolved downstream from coarse conglomerates to fine-grained lacustrine deposits. A low sinuosity braided river system developed over 15 to 30 km to the NE across a series of narrow normal fault blocks. The distributive river pattern terminated eastward where it built stacked small deltas into a shallow lake that occupied the central Corinth rift.
2. The early rift stratigraphic record shows very rare evidence of footwall-derived sedimentation. Instead, the alluvial system buried the active faults, preventing creation of footwall topography between the fault blocks. The Kalavryta river system was supplied from one major sediment entry point throughout the early rift history. The main channel axis remained constant through time and controlled downstream facies distributions. Facies belt transitions were not controlled by faults but occurred at the scale of the full alluvial system. All these observations suggest the presence of a major and well-established antecedent drainage system.
3. The active faults during the early rift phase were particularly closely-spaced. Burial of the active faults by the depositional system can be explained by limited footwall uplift due to small fault block size and high sediment supply from the antecedent river system. Furthermore, the zones of maximum subsidence on individual normal fault are aligned parallel to the persistent fluvial channel axis. This suggests that long-term localised sediment supply from an antecedent drainage can influence normal fault growth.
4. During the earliest phase of faulting, the major antecedent river system filled the main palaeorelief (Phase 1). Then, the alluvial plain extended over a broader area where facies belts developed over at least 20 km. The main axial stream drainage carried mainly coarse-grained material but displayed lateral fine-grained facies changes. Fining and sudden facies retrogradation from 3.5 to 3.2 Ma can be explained by an increase in basin subsidence (Phase 2). Subsequent early rift history records a general progradational trend from 3.2 to 1.8 Ma (Phases 3 to 5) probably caused by increasing sediment supply in response to the footwall migration of fault activity at ~ 2.8 Ma and/or climate change at ~ 3.2 Ma. These observations demonstrate that antecedent drainage systems and high sediment supply can be important in the tectono-sedimentary evolution of rift basins.

The main limit of this study is the qualitative approach used to define the facies belts and their lateral transitions. Quantitative study of downstream fining from source to sink is required to decipher the role of variable sediment supply and accommodation in the long-term stratigraphic record.

Acknowledgments

This project was financed by a bursary from the French Ministry of Research and Higher Education and SISCOR ANR project. Fieldwork was funded by a OTELO grant (local geoscience research consortium for the Université de Lorraine, France) obtained in 2013. We thank Laurie Barrier (IPGP, France) for helpful discussions related to the correlation model presented in this paper.

Chapitre 5

Relay zone evolution and river behaviour : a history of repeated fault propagation and linkage

On s'intéresse ici au comportement des rivières durant le développement d'une zone de relais. Il s'agit de la zone de relais entre les failles East Helike (EHF) et Derveni (DF) le long de la marge sud du rift de Corinthe, dans la région d'Akrata. Ces deux failles majeures sont à présent connectées via une série de failles de "transfert" permettant ainsi le soulèvement de cette zone. L'incision par la rivière Krathis permet d'accéder à des affleurements de grande qualité dans cette vallée. Le système de failles et la stratigraphie syn-rift sont étudiés 'onshore' et 'offshore'. La cartographie de la zone de relais d'Akrata inclut : (i) les différentes familles de failles normales, (ii) la stratigraphie syn-rift, (iii) les surfaces d'incision majeures et (iv) les terrasses marines enregistrant différents épisodes de soulèvement. Les interprétations des profils sismiques 2D offshore permettent de contraindre la localisation des failles majeures en profondeur (2 s TWTT) ainsi que la succession syn-rift. Un modèle 3D du réseau de la zone de relais est présenté. Les corrélations onshore-offshore permettent de reconstruire l'histoire de propagation et de connexion entre les failles normales pendant une période de 500 ka. L'enregistrement haute résolution des processus de connexion de failles et la qualité des données présentées ici forment l'originalité de cette étude.

Au cours du Pléistocène moyen à supérieur, la zone de relais a capturé la rivière antécédente de Krathis qui a permis la construction de Gilbert-deltas entre les failles EHF et DF. Les failles de transfert obliques à ces deux failles majeures documentent la migration de (i) l'activité tectonique et, (ii) la succession deltaïque vers le bassin. L'âge de formation des terrasses marines enregistre le soulèvement diachrone dans la zone de relais. Cette étude met en évidence une connexion précoce des failles bordières EHF et DF, il y a environ 600 ka. Cependant ces failles restent actives après 600 ka et continuent à se propager jusqu'à un stade final de connexion il y a environ 200 ka. La rivière de Krathis persiste et nourrit un dépocentre majeur au pied de la zone de relais. On souligne ici l'interaction entre les rivières antécédentes, la formation des zones de relais et les

dépocentres en bordure de rift actif. La connexion des segments de failles en plusieurs étapes (*multiple breaching*) est ici probablement contrôlée par la présence d’une structure héritée de la chaîne hellénique. Enfin, ce cas d’étude permet de discuter le mode de propagation des failles normales dans le rift de Corinthe. Ces travaux sont publiés dans la revue *Basin Research* (Wiley Ed.).

Romain Hemelsdaël, Mary Ford, Relay zone evolution : a history of repeated fault propagation and linkage, central Corinth rift, Greece. *Basin Research*, 2016, 28 (1), 34–56, doi : 10.1111/bre.12101

Sommaire

5.1	Introduction	171
5.2	Corinth rift	173
5.3	Coastal normal fault system and relay zone	178
5.4	Offshore faults and seismic stratigraphy : a record of fault propagation and linkage	181
5.5	Length-displacement analysis on controlling faults	184
5.6	Onshore relay zone : a history of migrating sedimentation and uplift	185
5.6.1	Geomorphology and marine terraces	185
5.6.2	Middle and Upper groups stratigraphy	186
5.6.3	Age estimates in the Upper group	188
5.7	Relay zone evolution	193
5.8	Discussion	195
5.8.1	Relay ramp geometry and fault growth models	195
5.8.2	Role of structural inheritance in the development of a rift border fault system	195
5.8.3	Sedimentation patterns on relay ramps	196
5.8.4	Role of antecedent drainage	196
5.9	Conclusions	197
5.10	Appendix : Technical details on U–Th dating of <i>Cladocora caespitosa</i> from Kryoneri location	198

Abstract

Established models indicate that, before being breached, relay zones along rift borders can evolve either by lengthening and rotating during progressive overlap of growing fault segments (isolated fault model), or, by simply rotating without lengthening before breaching (coherent fault model). The spatio-temporal distribution of vertical motions in a relay zone can thus be used to distinguish fault growth mechanisms. Depositional relay zones that develop at sea level and accommodate both deposition on the ramp itself as well as transfer of sediment from the uplifting footwall into the hangingwall depocentres provide the most complete record of vertical motions. We examine the development of a depositional relay ramp on the border of the active Corinth rift, Greece in order to reconstruct fault interaction in time and space using both onshore and offshore (2D seismic lines) data. The Akrata relay zone developed over a period of ca. 0.5 Myr since the Middle Pleistocene between the newly forming East Helike Fault (EHF) that propagated toward the older, more established Derveni Fault (DF). The relay zone captured the Krathis River, which deposited prograding Gilbert-type deltas on the sub-horizontal ramp. Successive oblique faults record progressive linkage and basinward migration of accommodation along the ramp axis while marine terraces record diachronous uplift in their footwalls. Although early linkage of the relay zone occurs, continuous propagation and linkage of the EHF onto the static DF is recorded before final beaching. Rotation on forced folds above the upward and laterally propagating normal faults at the borders of the relay zone represent the ramp hinges. The Akrata relay zone cannot be compared directly to a simple fault growth model because (1) the relay zone connects two fault segments of different generations ; (2) multiple linkage during propagation was facilitated by the presence of pre-existing crustal structures, inherited from the Hellenide fold and thrust belt. The linkage of the EHF to the DF contributed to the westward and northward propagation of the southern rift border.

Keywords : Relay zone, breaching, Corinth rift, Gilbert-type fan delta, fault propagation, inherited structure.

5.1 Introduction

Few geological datasets have the temporal or spatial resolution necessary to track progressive fault interaction and linkage (Figure 5.1). Those that do can provide important new insight into fault behaviour (e.g. Giba *et al.*, 2012). In this paper, a high resolution fault linkage history, which took place over a period of 0.5 Myr, is reconstructed. The relay zone forms part of the active normal fault system along the southern margin of the Corinth Gulf that separates the subsiding offshore depocentres from the uplifting Peloponnese peninsula (Figure 5.2a). The Akrata relay zone developed since the Middle Pleistocene between the older, more established Derveni Fault (DF) and the newly forming East Helike Fault (EHF) that propagated toward the older fault. The

relay ramp is breached and exposed onshore while offshore seismic data constrains depocentre and fault geometries. This relay zone evolved at around sea level, thus subsidence is recorded by fluvio-deltaic sedimentation on the ramp, while marine terraces and river incision record diachronous uplift of the breaching ramp.

Relay zones accommodate displacement between adjacent synthetic segments of a fault array that will eventually become linked to form a through-going fault as displacement increases (Peacock, 1991; Peacock & Sanderson, 1994; Walsh & Watterson, 1991; Trudgill & Cartwright, 1994; Walsh *et al.*, 1999; Peacock & Par, 2002; Acocella *et al.*, 2005; Conneally *et al.*, 2014). Growth and linkage of fault segments and the development of relay zones can significantly control sediment supply into rift basins (Gupta *et al.*, 1999). Footwall drainage systems commonly exploit topographic lows between fault segments to concentrate sediments in hangingwall depocentres along rift borders (Leeder & Gawthorpe, 1987; Leeder, 1993; Athmer *et al.*, 2010; Athmer & Luthi, 2011). Fault interaction in relay zones gradually modifies the drainage pattern as a tilted ramp evolves (Densmore *et al.*, 2003). In the case of depositional relay ramps, these changes are recorded in sedimentary facies and thickness distributions (Morley *et al.*, 1990; Gawthorpe & Hurst, 1993; Young *et al.*, 2001; Giba *et al.*, 2012).

The geometry of relay zones and the way they develop differs in the two end-member kinematic models for the growth of normal fault systems.

1. In the 'coherent fault' model (Childs *et al.*, 1995; Walsh *et al.*, 2002, 2003) fault segments initiate and grow as kinematically-related components of a fault array (Figure 5.1a). Fault segment lengths and the position of relay zones are established rapidly so that most fault growth is characterised by increasing displacement on fault segments of constant length, thus giving steep fault growth paths on displacement-length graphs. Relay zones are established quickly and evolve simply by rotating without lengthening before being breached.
2. The 'isolated fault' model (Cowie & Scholz, 1992; Cartwright *et al.*, 1995; Huggins *et al.*, 1995; Schlische & Anders, 1996; Morley & Wonganan, 2000) proposes that extension is initially accommodated by a dispersed array of isolated and independent fault segments that grow by lateral propagation until some coincidentally overlap (Figure 5.1). Fault linkage leads to the development of fewer but larger fault zones (Morley *et al.*, 1990; Trudgill & Cartwright, 1994; Cartwright *et al.*, 1995; Dawers & Anders, 1995). The systematic increase in displacement with increasing fault length is predicted by a power-law relationship (Walsh & Watterson, 1988). In this model, the geometry of a relay ramp changes gradually as the length of the overlapping zone increases and displacement accumulates. Strain accumulation causes the progressive rotation of the ramp. Eventually, the ramp is breached when strain compatibility can no longer be maintained (Long & Imber, 2012).

Relay ramp evolution in natural fault systems should therefore reflect these fault growth

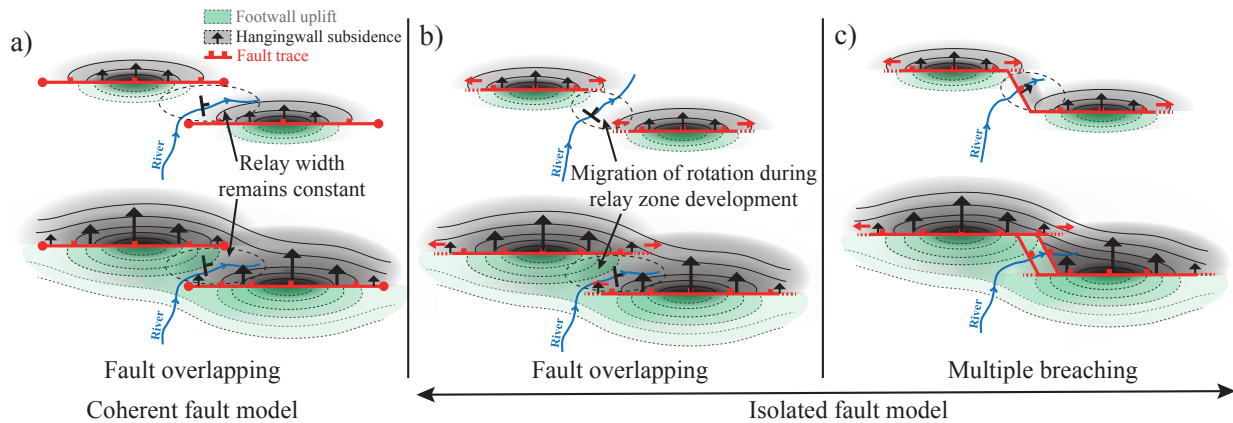


FIGURE 5.1 – (a) Schematic map view of the development of a relay ramp according to the coherent fault model (a) and the isolated fault model (b-c). Both overlapping faults lengthen synchronously with increasing displacement. Since the early stage of relay ramp development the footwall drainage system exploits topographic lows between fault segments, modifying sediment routing. There is high competition between hangingwall subsidence in the footwall fault and footwall uplift in the hangingwall fault (dashed ellipse). A tilted ramp develops during fault interaction in the overlapping zone (a-b). The case of early fault linkage (c) and thus the absence of fault overlap changes significantly vertical motions in a relay zone. Contours and colour density indicate gradual changes in subsidence and footwall uplift.

mechanisms. But natural systems are complex and other factors may play a role in fault linkage histories. For example, while these standard models consider linkage of the same generation of faults with similar dimensions, little has been published on how new faults link to older established faults. In addition, the influence of structural inheritance on the location and behaviour of linkage zone in fault systems is not considered in these models, but can be important in natural systems (e.g. Childs *et al.*, 1995; Paton & Underhill, 2004; Bellahsen & Daniel, 2005; Giba *et al.*, 2012). The aim of the paper is to investigate the factors controlling the linkage history between an established fault and a newly growing fault, and to examine the applicability of fault growth models. Using onshore sedimentary, structural and geomorphological data and offshore seismic reflection data in the Akrata area of the Corinth rift, the objectives of this paper are (1) to present a detailed description of both the onshore and offshore characteristics of the Akrata relay zone; (2) to reconstruct the progressive evolution of the relay zone. The presented data improves our understanding of sediment supply across relay ramps into the main basin and provides insight into the evolution of the normal fault network of the active Corinth rift.

5.2 Corinth rift

The east-trending Gulf of Corinth (105 km long, 30 km wide) separates the Peloponnese peninsula from mainland Greece (Fig. 2). Over the last 20 years, geodetically measured N-S extension rates show an increase from $\sim 6\text{--}11\text{ mm yr}^{-1}$ in the east to 15 mm yr^{-1} in the west (Clarke

et al., 1998; Briole *et al.*, 2000; Bernard *et al.*, 2006). On a regional scale, the NNE-directed subduction of the African plate into the Hellenic trench since the Oligocene has generated orogenic crustal thickening, collapse and back-arc extension through slab rollback (Figure 5.2b ; (Le Pichon *et al.*, 2002; Jolivet & Brun, 2008). The N-S extension in the Corinth rift was generated within a diffuse zone between the southwest-propagating North Anatolian Fault and the Cephalonia Fault (Central Hellenic Shear Zone of Nyst & Thatcher, 2004; Papanikolaou & Royden, 2007) (Figure 5.2b). The rift is superimposed at a high angle to the north-northwest- to northwest-trending Hellenide external fold and thrust belt, which was itself emplaced toward the west-southwest from late Eocene to late Miocene (van Hinsbergen *et al.*, 2005; Reilinger *et al.*, 2006; Jolivet & Brun, 2008; van Hinsbergen & Schmid, 2012).

The thickness of the Hellenide nappe stack is estimated to be 10 km (Papanikolaou & Royden, 2007). The southern central rift is principally underlain by the Pindos thrust sheet (Figure 5.2a ; Upper Triassic to Jurassic cherty limestones with red and green radiolarites and Upper Cretaceous sandy turbidites), which is in turn underlain by the Gavrovo-Tripolitsa nappe (Triassic to upper Eocene platform carbonates and Upper Eocene deep water turbidites). The underlying Phyllite-Quartzite nappe (Zarouchla complex) records HP-LT metamorphism (Theye *et al.*, 1992; Trotet *et al.*, 2006; Jolivet *et al.*, 2010). These workers suggest that Miocene NE-directed extension was responsible for exhumation of these high-pressure rocks, directly south of the study area (in the Zarouchla-Feneos tectonic window). Ghisetti & Vezzani (2004, 2005) and Papanikolaou & Royden (2007) propose that this major crustal structure may continue northward to underlie the central Gulf and thus may have played an important role in the evolution of the Corinth rift.

Timing of rift initiation is uncertain but was probably sometime in the early Pliocene, around 5 Ma (Doutsos & Piper, 1990; Collier & Dart, 1991). Depocentres were controlled by a 090-100° trending north-dipping normal fault system that migrated north with time (Goldsworthy & Jackson, 2001; Ford *et al.*, 2013). The uplifted fault blocks of the northern Peloponnese are incised by north-flowing rivers providing excellent cliff exposures.

The onshore syn-rift stratigraphy has been well documented along the southern margin of the Gulf (Ghisetti & Vezzani, 2004; Rohais *et al.*, 2007a; Backert *et al.*, 2010; Ford *et al.*, 2013). The succession is divided into three informal lithostratigraphic groups : the Lower, Middle and Upper groups, first defined by (Rohais *et al.*, 2007a). Despite the lack of absolute ages in the study area, correlation with adjacent dated successions provides reasonable age constraints (Figure 5.3). Here, the Lower group (Pliocene to Lower Pleistocene) consists of an upward fining continental succession that also thickens and fines from west to east. In the Akrata area, the Lower group is relatively thin (up to 400 m), comprising 90–100 m of basal coarse alluvial conglomerates (Exochi formation) overlain by 200–220 m of reddish fluvial sandstones and pebbly conglomerates (Figures 5.3 and 5.4). Lignite beds (<0.5 m) are locally preserved in the Voutsimos area (Figure 5.4). The upper part of the Lower group comprises poorly consolidated, well-laminated siltstones with alternating iron-rich laminae and minor pebble conglomerate beds. It also contains an abun-

dant oligohaline-freshwater fauna (e.g. *Melanopsis aff. mitzopoulosi* and *Adelinella elegans*). This fluvio-lacustrine system is equivalent to the Ladopotamos formation to the west (Ford *et al.*, 2007, 2013). East of the Krathis valley, the Lower group thickens considerably (>1 km) and passes into the fluvio-deltaic Valimi formation dominated by fine siltstones to sandstones with small deltas (up to 5 m) building eastward (Rohais *et al.*, 2007a, 2008). Basin deepening is locally recorded in the western rift at the top of the Lower group by lagoonal calcisiltite and upper shoreface fine gravel deposits observed in the Ladopotamos valley (Figure 5.4; Katafugion formation; Ford *et al.* (2007)).

The Middle group (Lower to Middle Pleistocene) is mostly characterised by large conglomeratic Gilbert-type deltas (3–4 km in radius, 400–800m thick) that built mainly northward into a lacustrine or marine basin. In the Akrata area itself, the Middle group is represented by the Platanos Gilbert-type delta in the hangingwall of the easternmost Pirgaki-Mamoussia fault and the equivalent prodelta deposits of the Derveni formation (Figures 5.3 and 5.4). In the Middle Pleistocene (Upper group), fault activity migrated north again in the western rift to the fault system that defines the current southern border of the gulf (Ford *et al.*, 2013). Uplift of the Pirgaki-Mamoussia fault block is recorded by strongly-prograding Gilbert-type deltas, depositional marine terraces (De Martini *et al.*, 2004; McNeill & Collier, 2004) and notch sequences along the exhumed range front of the East and West Helike faults (Stewart, 1996; Stewart & Vita-Finzi, 1996; Pirazzoli *et al.*, 2004). The Akrata relay zone developed from around 0.7 Ma onwards while Upper group deltas were deposited on the evolving ramp (McMurray & Gawthorpe, 2000; Gobo *et al.*, 2014). The following sections present a detailed description of the Akrata relay zone based on fieldwork and offshore seismic interpretations.

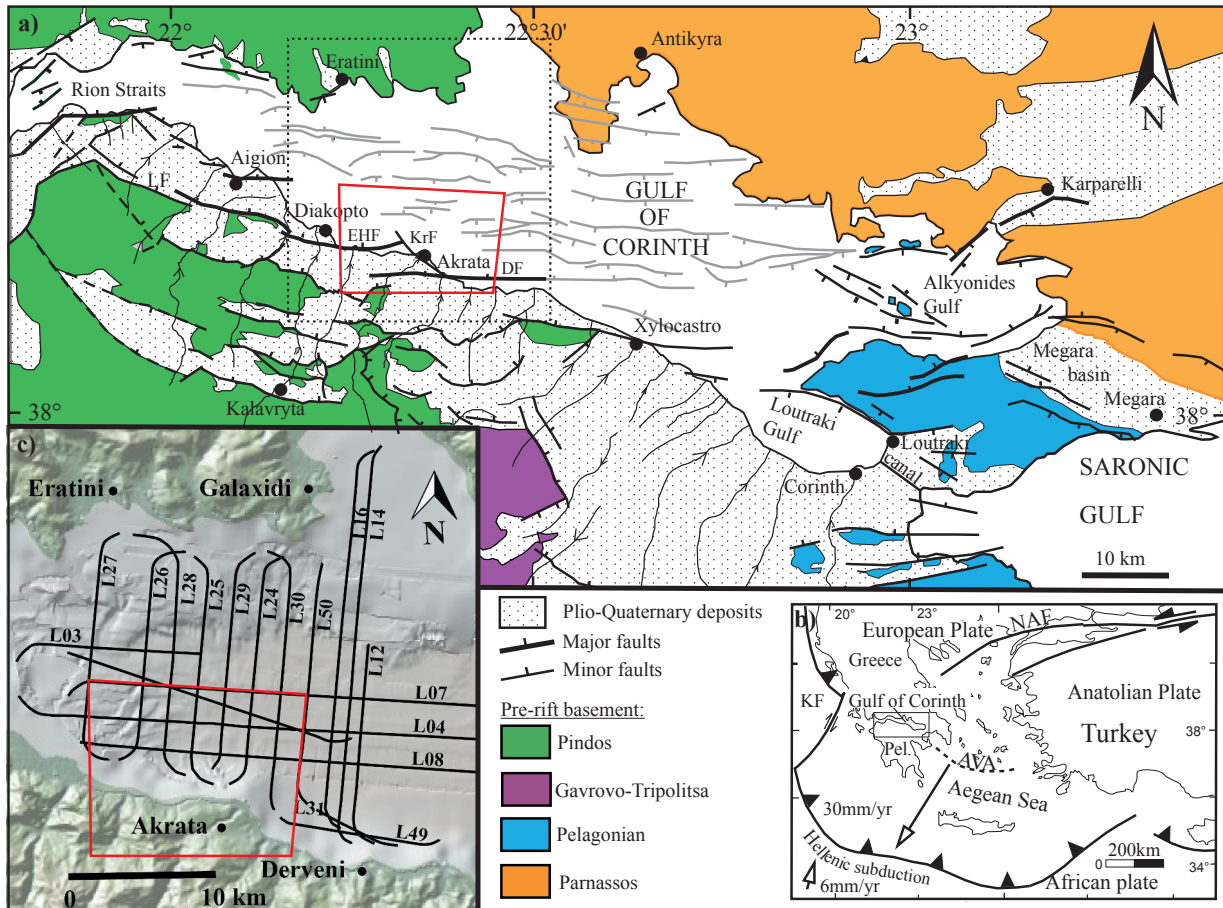


FIGURE 5.2 – (a) Geological map of the Gulf of Corinth rift (EHF : East Helike Fault ; KrF : Krathis Fault ; DF : Derveni Fault) also showing the NW-SE oriented Hellenide nappes (pre-rift basement) on which the rift is superimposed ; (b) Regional context of the Corinth rift above the active Hellenic subduction zone and lying between the Kefelonia Fault (KF) and the North Anatolian Fault (NAF). Subduction of the African plate generated the Aegean volcanic Arc (AVA). The rift separates mainland Greece from the Peloponnese peninsula (Pel.) The dotted black box delimits the inset map (c) with selected seismic profiles used in this study. The red box delimits the onshore study area of the geological map (Figure 5.4) and the onshore-offshore correlations (Figure 5.7) (modified from Ford *et al.*, 2013; Taylor *et al.*, 2011).

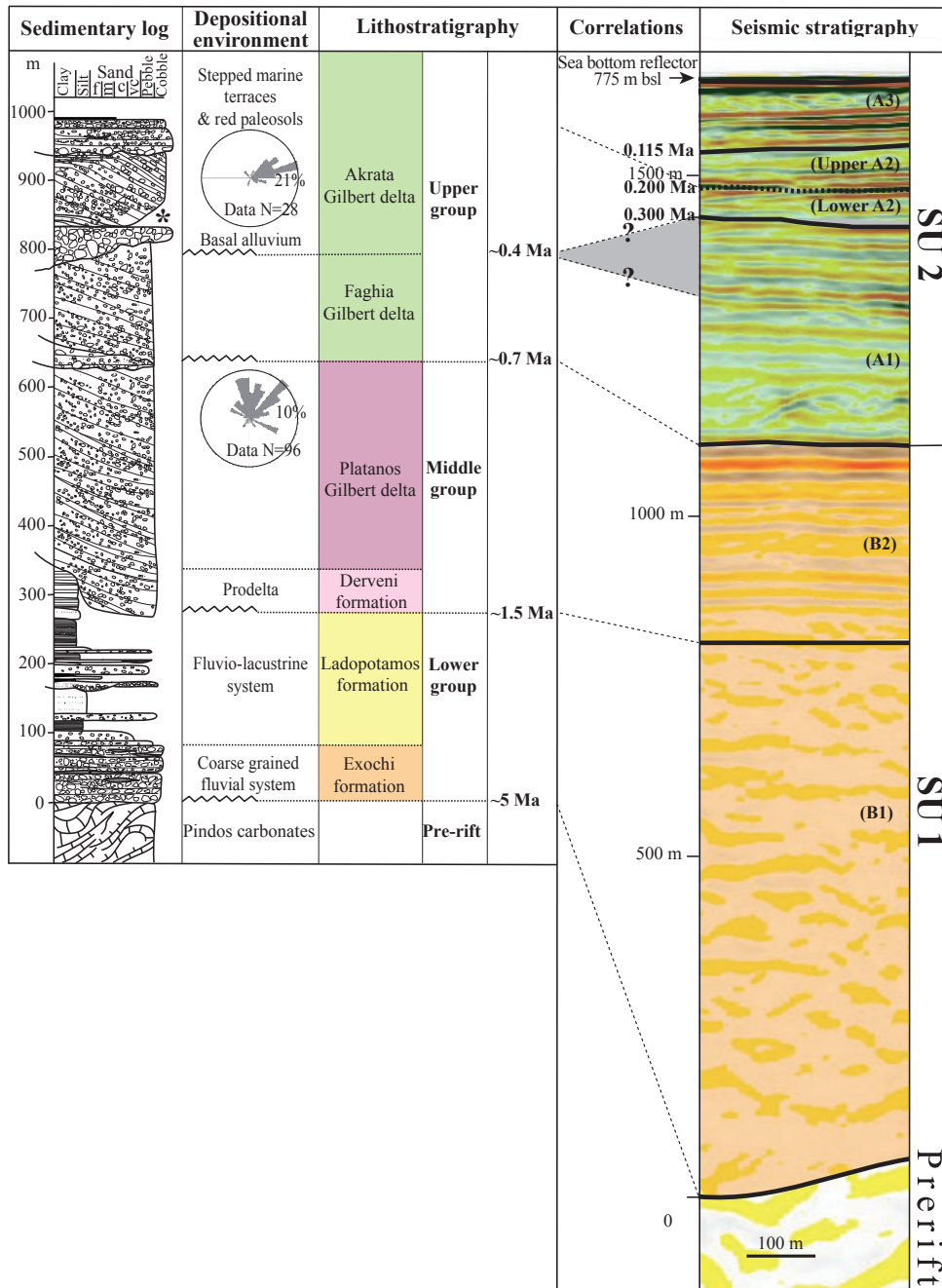


FIGURE 5.3 – Stratigraphic correlation between offshore and onshore domains in the Central rift basin (both logs are represented at the same vertical scale). On the right : offshore syn-rift succession interpreted from seismic profile L07 after time-depth conversion to indicate sediment thickness. Angular unconformity between reflectors of seismic units (SU) SU1 and SU2 is not observed on the east-west profiles. SU1 is divided in two sub-packages SU1a and SU1b. Three main sub-packages SU2a, SU2b and SU2c are distinguished in SU2. Ages of reflector boundaries within SU2 are taken from [Taylor *et al.* \(2011\)](#) and were determined by correlation with 100 kyr glacio-eustatic cycles. Note that SU2b is subdivided in two other sub-packages separated by a basin-wide seismic reflector dated at about 200 ka. Colours are those used in cross sections. On the left : synthetic sedimentary and lithostratigraphic log of the onshore syn-rift stratigraphy in the Akrata area, following nomenclature of [Ford *et al.* \(2013\)](#) and [Rohais *et al.* \(2007a\)](#). Rose diagrams represent foreset dip directions of the Middle group (Platanos) and Upper group (Faghia and Akrata) Gilbert-type deltas. Colours are those used in the Figure 5.4. The grey zone in the correlation column is the lack of sedimentation between 0.4 and 0.3 Ma (development of palaeovalley). Question marks correspond to uncertain correlations.

5.3 Coastal normal fault system and relay zone

The right-stepping Akrata relay ramp developed between the EHF and the DF. The overlap zone has a strike length of about 6.5 km and with N-S spacing between the two faults of 4.0 km. West of the Ladopotamos River, the EHF (15 km long; striking 098°–105°) comes onshore and defines a range front over 800 m high (Figures 5.4 and 5.5). The position of the easternmost tip of the EHF has been variably identified offshore as it is composed of two north-dipping splay faults. The northern splay, known as the Akrata fault, was first recognised by [Stefatos *et al.* \(2002\)](#) and [Bell *et al.* \(2008\)](#) on shallow seismic profiles. The southern splay, identified by [Stefatos *et al.* \(2002\)](#) lies just offshore closely paralleling the coast. This southern splay has been illustrated in previous publications as the EHF ([McNeill & Collier, 2004](#); [Bell *et al.*, 2008, 2009](#)). The more deeply penetrating seismic lines do not reach far enough south to image the southern splay at surface, however [Taylor *et al.* \(2011\)](#) identify this fault (their Helike fault) at depth further north but do not recognise the Akrata fault. Between the Ladopotamos River and Akrata village, the Akrata fault trace is here identified on several seismic lines (Figure 5.6a, b) with a dip of 45°–50° down to 2500 m bsl, below which the dip is 30°N. Contrary to the northern splay, no data are available to constrain fault displacement along the southern splay. Onshore-offshore correlations (Figures 5.7b, 5.7c) indicate that the splays branch at 2000–2500 m depth. In the rest of this paper we will refer to both splays as the EHF-north splay (formerly the Akrata fault) and the EHF-south splay. The hypocentres of the 1981 and 1995 (Aigion) earthquakes (Ms 6.6 and respectively, 10 km depth) may be associated with rupture of the EHF or of a blind fault at depth ([Bernard *et al.*, 2006](#)).

The DF is a significantly larger fault than the EHF with a trace length of 40 km, lying principally offshore but continuing onshore westward from Akrata village for a distance of about 8 km to delimit the southern boundary of the relay zone. On seismic lines, the DF is biplanar (~40° down to 1500 m decreasing to 25°N below this to 3 km ([Taylor *et al.*, 2011](#))). [Hatzfeld *et al.* \(1996\)](#) related the 1992 Galaxidi earthquake (Ms= 5.9) to an asperity zone at 10 km depth between the EHF and the Xylocastro fault, which is likely to represent the DF plane at depth.

The newly named Krathis Fault (KrF), northwest-striking and dipping northeast, is here identified as the youngest and principal breaching fault of the Akrata relay zone (Figure 5.4). Onshore, the KrF separates the area of active subsidence (Krathis delta) from the area of active uplift. Maximum displacement on this fault is estimated at about 1000 m (Figure 5.7d). It is subparallel to other transverse faults and fractures that cut the uplifted ramp (Kalamias, Platanos and Faghia Faults; Figure 5.4). The area outside the relay zone is also cut by a family of northwest-striking normal faults dipping both northeast and southwest (Figure 5.4). Despite the complex trace of the fault system at the surface, our 3D modelling predicts that this fault system is connected at depth (at around 4000 m; Figure 5.5a).

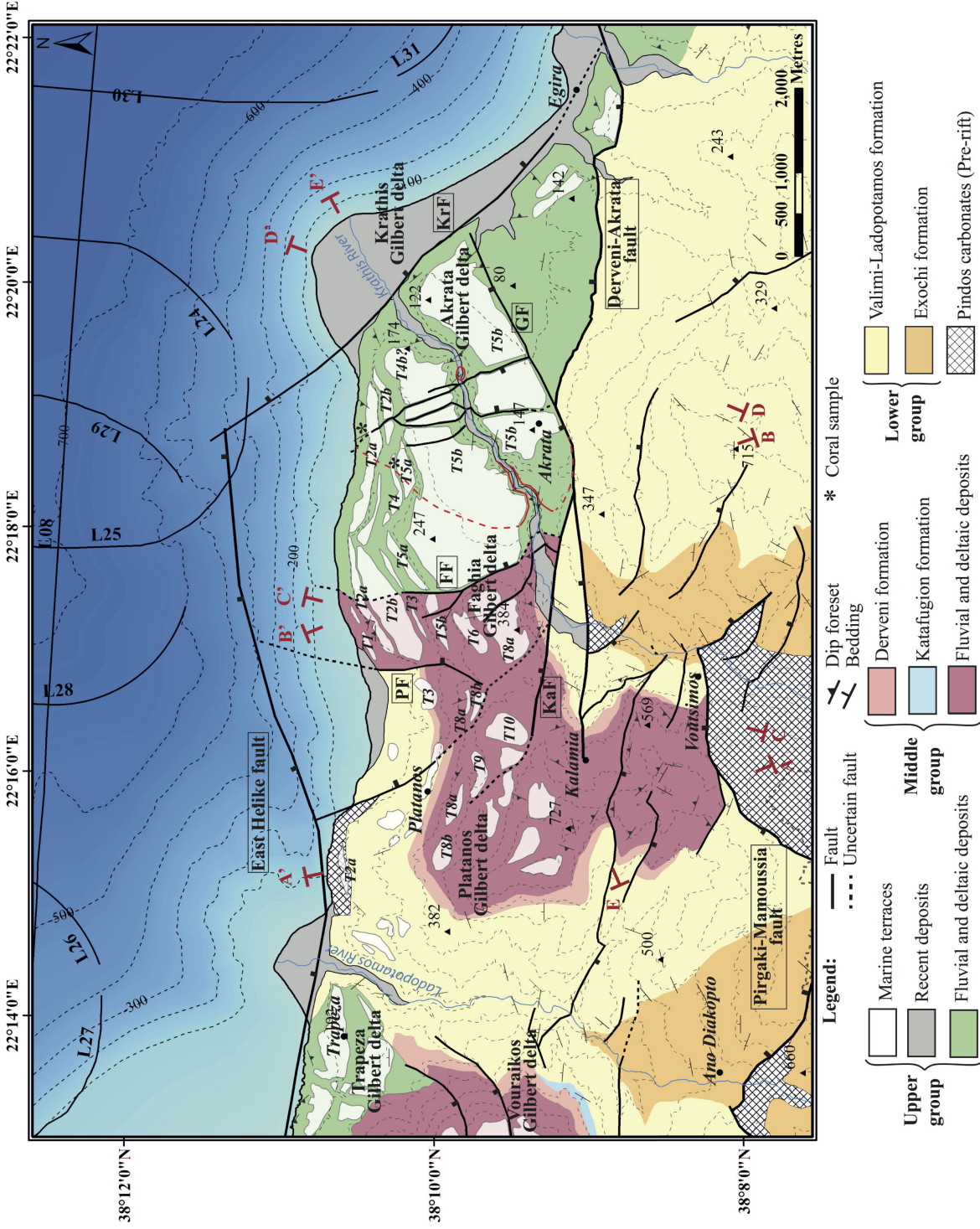


FIGURE 5.4 – Map of the Akrata area including onshore and offshore domains. Location of the cross-sections are indicated and illustrated in Figures 5.7 and 5.9. Abbreviations KaF, PF, FF, GF and KrF represent the major faults within the relay zone : Kalamias, Platanos, Faghia, Goumeika and Krathis faults respectively. Red line indicates the limit of the Akraia incised valley of Gobo *et al.* (2014). The inlier (red circle) northeast of the Akraia graben exposes foreset of the Faghia delta at the valley bottom. The numbering of marine terraces is adapted from McNeill & Collier (2004).

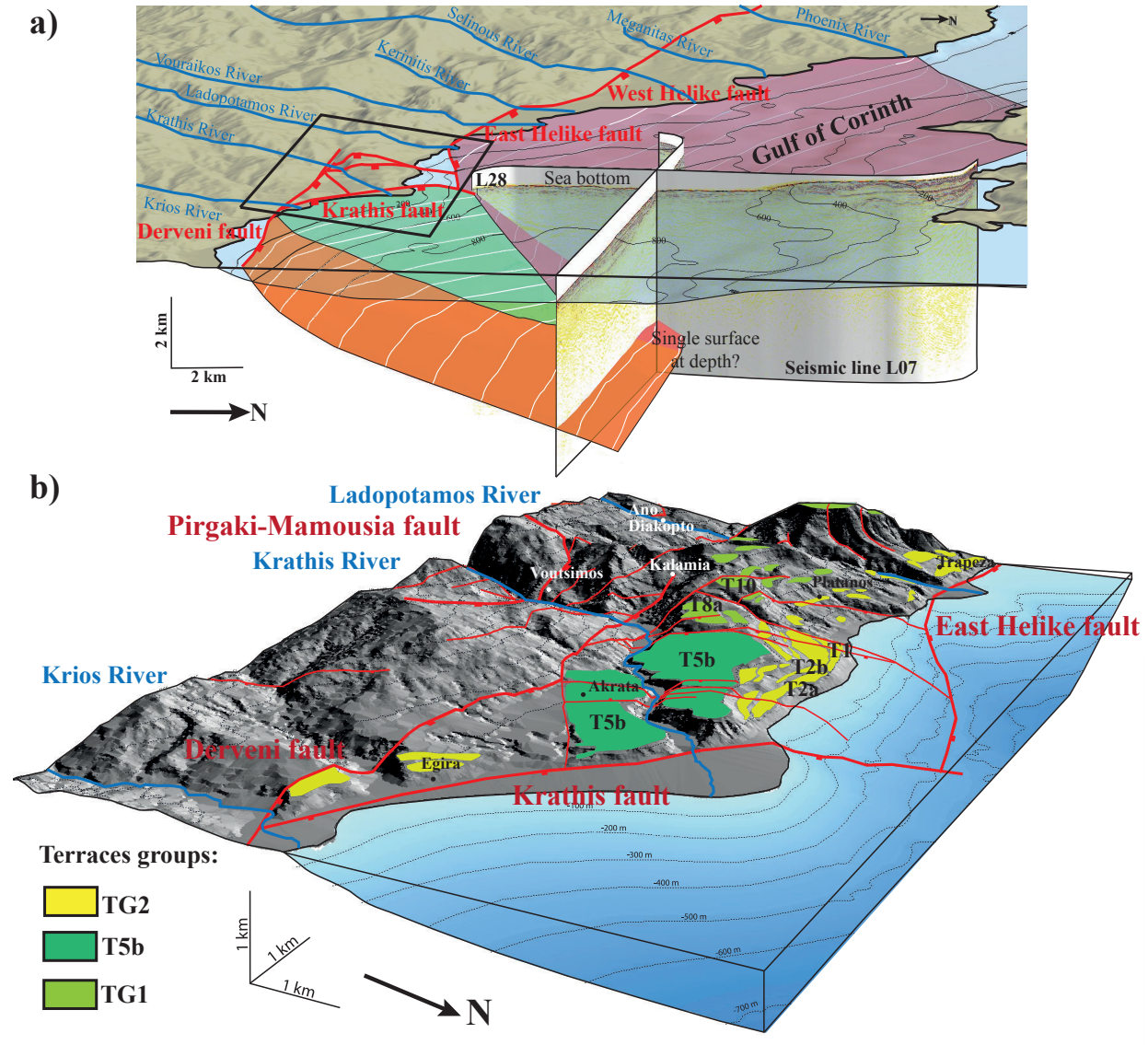


FIGURE 5.5 – (a) Gocad view (from NE) of the Derveni-Krathis-East Helike fault system along the southern rift border. East Helike and West Helike faults are simplified to a single fault surface. Other faults are not represented here. The DF surface can be traced to about 25 km offshore. Contour interval on fault surfaces (white contour lines) is 500 m. Bathymetry is illustrated by the blue transparent surface and the black contour lines. Two seismic lines L07 and L28 are illustrated here. The black block delimits the area of the 3D DEM represented below ; (b) 3D DEM of the present-day onshore geomorphology. Uplifted terraces defined by McNeill & Collier (2004) are shown and re-interpreted in the context of the relay zone uplift history. They are divided into three groups named TG1, T5b and TG2 (see text for explanations). Note the deflection of the Krathis River (blue line) on crossing the DF (also see Figure 5.4) to flow NE. The river strongly incises the uplifting onshore relay zone before crossing the breaching KrF (pale green surface) to deposit the Krathis Gilbert-type delta in its hangingwall.

5.4 Offshore faults and seismic stratigraphy : a record of fault propagation and linkage

The study area extends offshore for about 8 km (Figure 5.2c) where bathymetry can reach up to 800 m. Multichannel 2D seismic profiles (MCS) down to 3 s TWTT collected during the Maurice Ewing (EW0108) 2001 geophysical survey (Taylor *et al.*, 2011) and high resolution 2D seismic data (Greek SEIS-GREECE 1997 ; Sachpazi *et al.* (2003)) constrain the geometry of the main faults and the offshore syn-rift succession down to approximately 2500 m bsl. This study integrates the southern part of N-S seismic lines from L27 in the west to L12 in the east and east-west lines, being limited to the north by the E-W seismic line L07 (Figure 5.2c). These N-S and E-W seismic profiles are separated by a distance of approximately 1900 m and 2200 m respectively and have been used to construct a 3D model of faults and principal stratigraphic horizons in GOCAD modelling software (Paradigm). Time-depth conversion was carried out using the velocity model of Weiss (2004) and Zelt *et al.* (2004). A linear velocity gradient was applied for the water column (1500 m s^{-1}), the syn-rift sediments ($1500 \text{ m s}^{-1} [1+\delta T]$) and the pre-rift carbonates ($5000 \text{ m s}^{-1} [1+0.25\delta T]$).

The offshore syn-rift deposits are divided into two major stratigraphic units : Seismic Unit 1 (SU1) and Seismic Unit 2 (SU2) separated by an unconformity, which is locally angular (Stefatos *et al.*, 2002; Sachpazi *et al.*, 2003; Clément *et al.*, 2004; Lykousis *et al.*, 2007; Sakellariou *et al.*, 2007; Bell *et al.*, 2008, 2009; Taylor *et al.*, 2011). SU1 and SU2 are equivalent to the "early rift" and "late rift" units defined by Taylor *et al.* (2011). Despite the lack of clear seismic impedance contrasts in SU1, it can be subdivided into two packages on the studied lines (SU1a and SU1b ; Figure 5.3), while SU2 can be clearly subdivided into three packages, SU2a, SU2b and SU2c (Figures 5.3, 5.6 and 5.7). Piston cores up to 30 m long (Lykousis *et al.*, 2007; Moretti *et al.*, 2003) show that the uppermost strata of SU2c comprise hemipelagic, fine-grained turbidites and debris flow sediments deposited under alternating lacustrine and marine conditions. Subdivisions of SU2 have therefore been correlated with Pleistocene 100 kyr glacio-eustatic cycles by Bell *et al.* (2008), Sachpazi *et al.* (2003) and Taylor *et al.* (2011), although the number of packages varies depending on the study area of each paper. The base of SU2 is assigned to an age varying between 0.4 Ma (unit A in the western Gulf ; Bell *et al.*, 2009) and 0.7 Ma (central and eastern Gulf ; Taylor *et al.*, 2011). In the study area, the deposition of the entire SU2 was tectonically controlled by the coastal fault system, since the Middle Pleistocene (McNeill & Collier, 2004; Ford *et al.*, 2013). As the onshore Middle and Upper groups comprise large conglomeratic Gilbert-type deltas building northward into the deep basin (Figure 5.4) it is reasonable to assume that the alternating, highly contrasting reflectors of SU2 and at least the upper part of SU1 comprise equivalent fine-grained prodelta facies. SU2 can therefore be correlated with the onshore Upper group and SU1b with the onshore Middle group deltas. A series of N-S cross sections across the EHF-DF fault zone (Figure 5.7) integrate offshore seismic lines with onshore cross sections (Figure 5.4 for locations), providing a model for estimation of fault displacement variations and hangingwall geometry. The gap

between onshore and offshore datasets (~2 km) is completed through extrapolation, including the representation of EHF-north splay and EHF-south splay (Figures 5.7b and 5.7c). The representation of SU2 in this zone and particularly between those splays is uncertain. Here we assume that only the northern splay controls the deposition of the Upper group sediments.

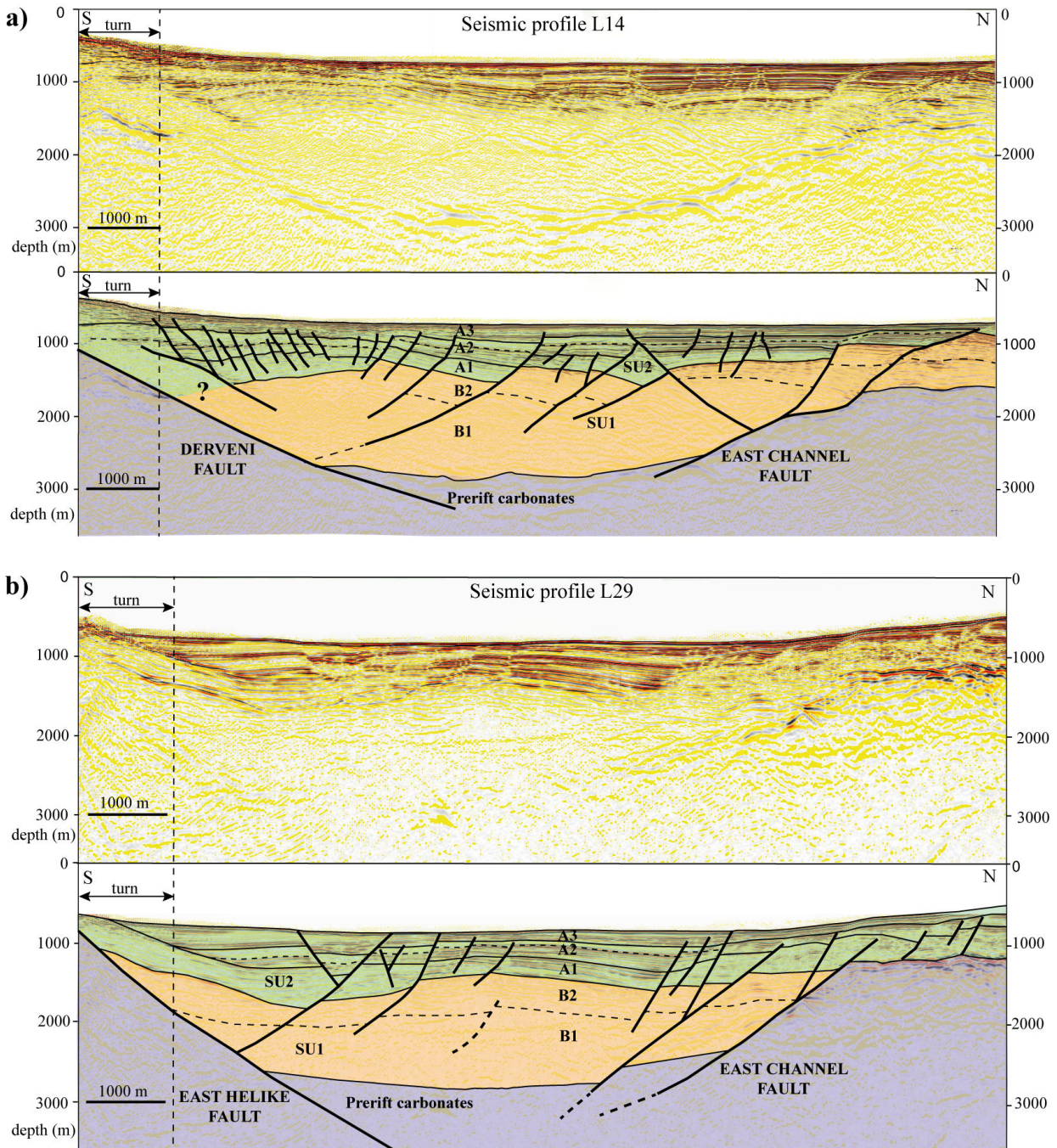


FIGURE 5.6 – Un-interpreted and interpreted complete seismic lines L14 (a) and L29 (b) . Both DF and EHF display contrasting hangingwall geometries described below in the text. Black arrows indicate onlaps of reflectors. Interpretations near the turns of the seismic lines (about 1.2 km) must be treated with caution. Colours are those used in the seismic log (Figure 5.3).

5.4 Offshore faults and seismic stratigraphy : a record of fault propagation and linkage

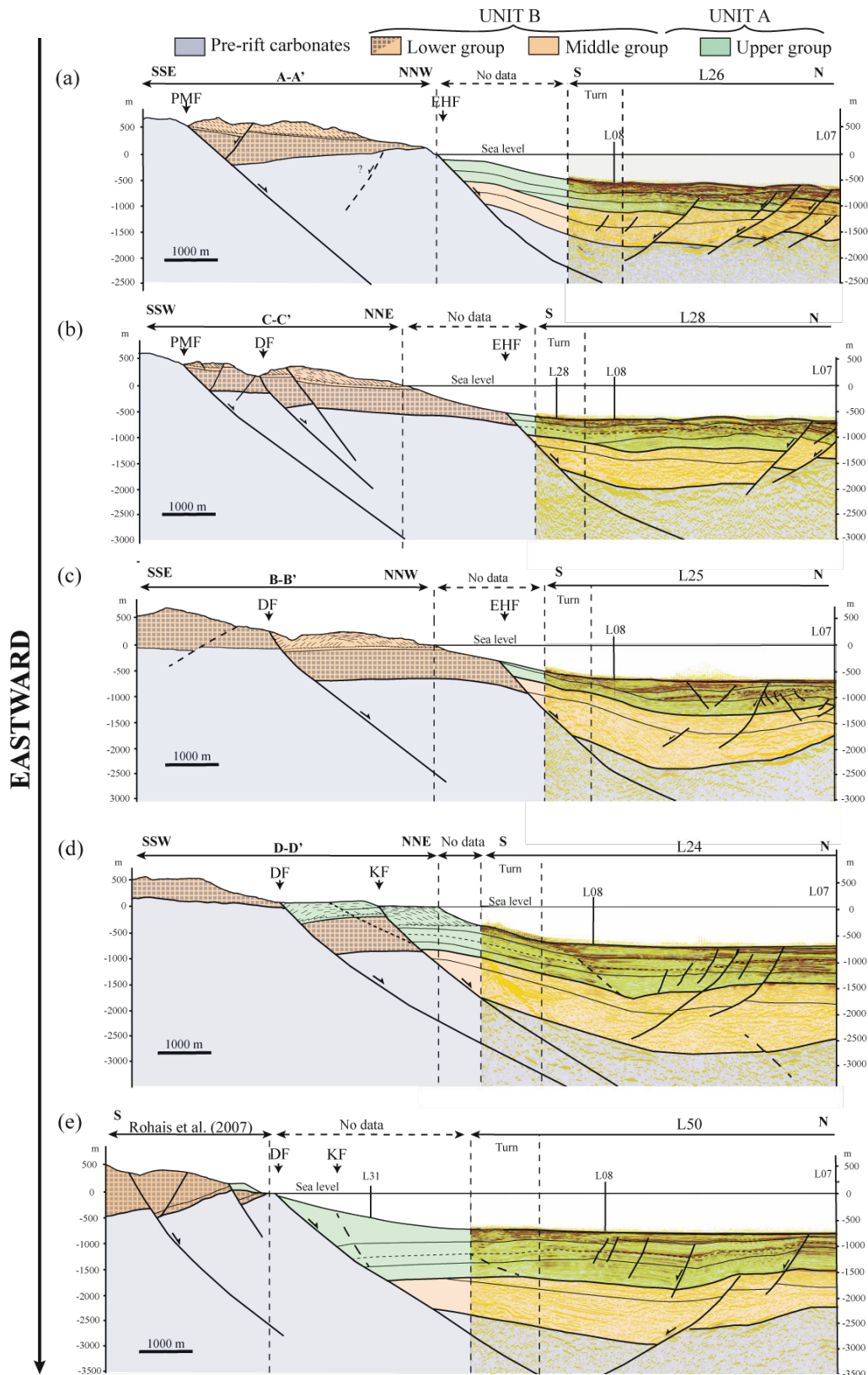


FIGURE 5.7 – Onshore-offshore cross-sections transverse to the relay zone. Cross-sections (a), (b), (c), (d) and (e) are presented from west to east. Here interpretations of seismic profiles are limited by the E-W seismic line L07. Onshore cross-sections A-A', B-B', C-C', D-D' and E-E' are shown in Figure 5.4. Black arrows are stratigraphic onlaps.

5.5 Length-displacement analysis on controlling faults

Fig. 8a represents the displacement-length profiles for the base of the Upper group/SU2 along the EHF (fault displacement is only constrained along the EHF-north splay), KrF and DF fault segments based on onshore-offshore cross section construction and stratigraphic correlation. Displacement was measured on a series of N-S cross sections (Figure 5.7) projected onto a 40 km long WNW-ESE transect located 4 km offshore and parallel to the main rift border. For the oblique KrF apparent displacement was measured parallel to the section lines. The displacement profile for each fault segment is typically bell-shaped (Muraoka & Kamata, 1983; Nicol *et al.*, 1996; Manighetti *et al.*, 2001). Displacement on the EHF and the KrF segments incorporate rotation of strata caused by syn-sedimentary folding, which increases displacement by 30 to 40% (Figure 5.8a). A similar correction is made by Giba *et al.* (2012). The 40 km long DF has a maximum displacement (L50, Figure 5.7e) skewed to the west giving an asymmetrical form to the curve. The asymmetrical profile of the DF indicates kinematic interaction with the EHF (e.g. Peacock & Sanderson, 1996; Nicol *et al.*, 2010). Maximum displacement on the DF is considerably greater (maximum 3400 m) than that of the corrected EHF (maximum 2200 m), indicating that this is the principal fault. Displacement across the onshore western DF is poorly constrained as there are no Upper group strata preserved in its footwall. As we assumed that the onshore segment of the DF propagated during the development of the relay ramp, total displacement along the western DF occurred during the Upper group. Cumulative displacement was derived by summing displacement of fault segments on each cross section (including the growth fold component). The resulting profile is bell-shaped and symmetrical, centred on the Krathis breaching fault. This suggests that the EHF-KrF-DF fault system accommodated extension as a single fault zone since final breaching. The timing of hard linkage is recorded by onshore Upper group stratigraphy and geomorphology.

5.6 Onshore relay zone : a history of migrating sedimentation and uplift

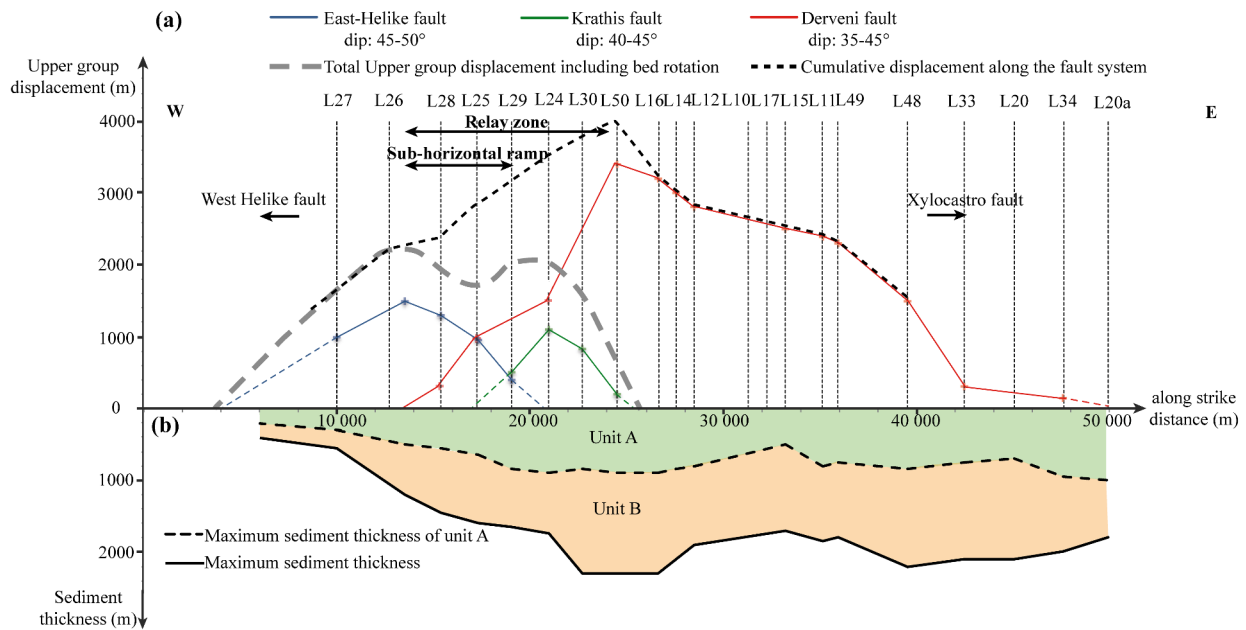


FIGURE 5.8 – (a) Upper group displacement profile plotted along the East Helike-Derveni fault system. Displacement of EHF and KrF were corrected from syn-sedimentary folding and used to estimate the total Upper group displacement along the southern margin. (b) Maximum syn-rift sediment thickness and maximum thickness of SU2 measured along the same transect, in the direct wall of the fault system.

5.6 Onshore relay zone : a history of migrating sedimentation and uplift

A large part of the Akrata relay zone lies onshore (Figure 5.4), where the uplift history is recorded in flights of well documented erosional and depositional marine terraces (De Martini *et al.*, 2004; McNeill & Collier, 2004). Upper group sedimentation history that preceded uplift is characterised by a series of fluvio-deltaic successions deposited by the antecedent Krathis River on the evolving relay ramp. McMurray & Gawthorpe (2000) describe these deposits as a forced regressive wedge. More recently, Gobo *et al.* (2014) describe the youngest succession as an incised valley fill. We first analyse and interpret the marine terraces covering the uplifted relay zone, followed by a description and interpretation of Middle to Upper group deposits. Age estimates for the Upper group are reviewed and a new geochronological date is presented here.

5.6.1 Geomorphology and marine terraces

Pleistocene-Holocene marine terraces have been mapped on the uplifted footwall of the EHF (Figure 5.4) by many authors and used to evaluate displacement and deformation rate on controlling faults (Stewart, 1996; Stewart & Vita-Finzi, 1996; McNeill & Collier, 2004; McNeill

et al., 2005). Marine deposits including coral bioherms, oyster-bearing beds, small (<20 m high) Gilbert-type deltas, beach and lagoonal facies are preserved in and on many of these terraces.

The highest flight of stepped marine terraces TG1 (including T10-T8a; Figure 5.5b) is located on the Platanos Gilbert-type delta at altitudes of 700 to 360 m. These terraces are west-northwest-trending and are confined to the footwall of the Faghia Fault. They are cut by several transverse faults, complicating the identification of true terraces. We propose here that the TG1 terraces record early uplift of the Platanos delta in the footwall of the Faghia fault zone.

A second flight of marine terraces TG2 (Figure 5.5b; including T1 to T5a on Figure 5.4) is oriented parallel to the coast in the footwalls of the EHF and KrF between sea level and 247 m. These terraces record footwall uplift on these faults, the timing of which is discussed below. The T5b terrace is the uppermost of the TG2 terrace group. This broad terrace (1.5–2.0 km wide) forms the top of the Faghia delta and Akrata palaeovalley fill and has been incised by the Krathis River. It is tilted gently SSE (3–6°) and terminates southward against the Goumeika fault (Figures 5.4 and 5.5b).

The T5b terrace terminates to the WSW against a prominent NNW-SSE oriented scarp with a slope of 22° (100 m high, 250 m wide). Following McMurray & Gawthorpe (2000) (their figure 9), this scarp slope is interpreted as an incision surface, which has been displaced by the Faghia Fault. In the hangingwall an equivalent erosional surface, exposed in the Krathis river valley, is overlain by Faghia delta conglomerates (Figures 5.4 and 5.10). Conjugate normal faults also cut the T5b terrace at the upper village of Akrata (Figures 5.4, 5.5 and 5.10) to form a small graben with a structural relief of 30–40 m. McNeill & Collier (2004) tentatively distinguish the T4 terrace to the east of this graben, however this is more likely to be a continuation of the T5b terrace. At the eastern termination of the T5b terrace a major topographic scarp (>180 m) marks the active KrF (Figure 5.4).

It is worth noting that the distribution of footwall uplift does not correspond to the distribution of cumulative hangingwall subsidence along the relay zone (Figure 5.8). This is because the coastal uplift described here reflects only the eastward propagation of the EHF and the progressive breaching of the relay zone. Footwall uplift on the older DF would affect areas to the south. The footwall of the DF certainly lies at higher altitudes, however no markers, such as marine terraces, which could constrain the timing of this uplift, have so far been detected.

5.6.2 Middle and Upper groups stratigraphy

The Krathis River flows northward for over 25 km across the northern Peloponnese incising into the syn-rift strata and pre-rift Hellenide nappe stack. On crossing the westernmost trace of the DF, the river turns abruptly to flow NE, incising into the uplifting relay ramp, exposing syn-rift sediments in cliffs ranging in height from 300 m in the west to 40 m to the east (Figure 5.4). The river is currently building the Krathis Gilbert-type delta in the hangingwall of the active

KrF. The geometry and building directions of Middle and Upper group deposits show that they were successively deposited by the same antecedent Krathis River thus recording fault migration, growth and linkage.

The Platanos Gilbert-type delta (Middle group) is one of four major point source deltas deposited in the hangingwall of the PMF (Figure 5.4) during the Lower to Middle Pleistocene (1.8–0.7 Ma). The delta top has been uplifted to an altitude of over 700 m (Figure 5.4). The delta base incises locally into the Derveni and Ladopotamos formations (Figure 5.3). Topset beds are thin and poorly preserved (marine terraces blanket much of the delta top and flanks) and foreset beds strongly prograde toward the north and north-east (rose diagram, Figure 5.3). Foreset height varied between 100 and 300 m with an average dip of 20°. Foreset and topset beds are mostly composed of pebble grade clast-supported conglomerates with variable proportions of coarse sandy matrix. Clast lithology is similar to other Middle group deltas, comprising mainly limestone, sandstones (Oligocene 'flysch') and radiolarites of the Pindos nappe, but also containing some low grade green metamorphic rocks of the phyllite-quartzite nappe and, more rarely, basaltic clasts. Foreset deposits are well-bedded, locally erosive and are characterised by 'open-framework' texture in places (Longhitano, 2008; Backert *et al.*, 2010). Thin layers (0.1 to 0.2 m) of interbedded siltstone and sandstone drape the tops of individual foreset beds. The underlying and laterally equivalent Derveni formation consists of fine sandstones and well-laminated silts-tones (with possible convolute lamination), representing distal turbidites and suspension fallout deposits (Backert *et al.*, 2010) in the prodelta environment.

In the westernmost hangingwall of the onshore DF, the Platanos Gilbert-type delta has been downthrown to the east by <50 m on a fault zone comprising the Kalamias Fault and the Platanos Fault (Figures 5.4, 5.5 and 5.10). In the immediate hangingwall of the Kalamias Fault, northeast dipping fine-grained strata of the Derveni formation underlie Platanos delta foresets building to the northeast (rose diagram, Figure 5.3). The overlying marine terrace T8 (McNeill & Collier, 2004) lies at 343 m altitude and is underlain by a small (~5 m high) north-building delta (Figure 5.10).

Lithologically, Middle and Upper groups deltas are very similar (sand-rich pebble conglomerates); they are distinguished by their stratal architecture (foreset height, foreset dip direction), their mean elevation and relationship to terraces and incision surfaces. Upper group deposits are exposed along a 3.8 km-long transect in the lower Krathis river valley east of the Faghia fault. Highly fractured foreset beds of the eastern Platanos Gilbert-type delta can be traced along the river for less than 1 km to where they are delimited by an incision surface at the base of the Faghia Gibert-type delta (Figure 5.10). For cross section construction we used a maximum thickness of 200 m for the Faghia delta foreset beds.

The Akrata palaeovalley infill (Gobo *et al.*, 2014) is exposed in the lower Krathis valley (Figure 5.4). The palaeovalley fill comprises an upstream basal alluvial succession (~25 m) overlain by two stacked shoal water deltas (~18 m) and finally, the prograding Akrata Gilbert-type

delta (~140 m thick) (Figures 5.4 and 5.11). The erosive base of the palaeovalley and the underlying foreset beds (here assigned to the Faghia delta) are well-exposed in the river valley (Figures 5.4 and 5.9). Gobo *et al.* (2014) propose that a relay ramp hinge marks the transition from the upstream alluvial succession to the downstream fluvio-deltaic succession. However, we have not been able to detect evidence for this ridge in the field. As reported above, we have identified the hinge of the relay zone offshore (Figure 5.9). Delta foresets dip on average 30° NE. The fluvial topset beds are up to 20 m thick. Foreset clasts are derived mainly from the Pindos thrust sheet but also include an abundance of phyllite clasts from the exhumed Zarouchla-Feneos tectonic window and various clast types from other unknown sources (e.g. unmetamorphosed oncolitic limestone). The foreset-topset transition is a composite surface comprising thin packages of topsets passing to foresets separated by toplapping or truncated foreset packages (Figure 5.11). This pattern records strong progradation superimposed by high frequency eustatic variations.

5.6.3 Age estimates in the Upper group

Biostratigraphic ages in delta conglomerates are difficult to establish. However, Gobo *et al.* (2014) report the presence of calcareous nannofossils *Gephyrocapsa* sp. (green algae) and the absence of *Pseudoemiliana lacunosa* in the fine-grained lower shoreface deposits and interbeds in the prodelta facies of the Akrata palaeovalley fill. The presence of *Gephyrocapsa* and absence of *P. lacunosa* marks the MNN 20 nannozone. While Gobo *et al.* (2014) citing Sprovieri *et al.* (1998) place the *P. lacunosa* last occurrence at 0.40 Ma, more recent publications place its last occurrence at 0.46 Ma (Raffi *et al.*, 2006) and at 0.44 Ma (for full references see Palyvos *et al.*, 2010). The end of MNN 20 nannozone is dated at either 0.265 Ma (Raffi *et al.*, 2006) or 0.27 Ma (Lourens *et al.*, 2004), corresponding to the first occurrence of *Emiliana huxley*, which was not found in the study area. Therefore, the Akrata palaeovalley fill is younger than 0.46 Ma. The major sea-level fall from 0.40 to 0.33 Ma (MIS 11; Figure 5.12e) is a good candidate for the period of incision of the Akrata palaeovalley followed by its infill.

Elevation profiles through stepped depositional terraces and limestone notches on the south coast of the Corinth Gulf have been correlated with Pleistocene eustatic variations to give an age range of 0.40 Ma to Recent (Tselentis & Makropoulos, 1986; Keraudren & Sorel, 1987; Billiris *et al.*, 1991; Collier *et al.*, 1992; Mouyaris *et al.*, 1992; Armijo *et al.*, 1996; Davies *et al.*, 1997; Houghton *et al.*, 2003). More specifically, using the TG2 terraces, De Martini *et al.* (2004) and McNeill & Collier (2004) estimate an average uplift rate for the EHF footwall of 0.9 to 1.1 mm yr⁻¹ since at least 0.5 Ma that increases to 1.3–2.2 mm y⁻¹ in the Holocene (Stewart, 1996; Stewart & Vita-Finzi, 1996; Pirazzoli *et al.*, 2004). The broad T5b terrace is the oldest of the TG2 terraces (5.4) and represents the composite top of the Faghia and Akrata deltas just before final fault linkage. Based on the work of De Martini *et al.* (2004) and McNeill & Collier (2004), the age of this terrace can be estimated at around 0.2 Ma. This dates the end of the Akrata palaeovalley

fill.

Two coral bioherms (*Cladocora caespitosa*) were dated using the U-series by (McNeill & Collier, 2004) (located in Figure 5.4). The upper site lies on the T4 terrace at c. 190 m. Two samples gave ages of 0.271–0.313 Ma and 0.291–0.324 Ma. However, McNeill & Collier (2004) reject these dates, considering them as minimum ages due to later alteration. Their U-series dating of corals from the lower site (at 30 m above sea level, 500 m west of Kryoneri port) gave an age of 0.228–0.266 Ma, which is again rejected as anomalously old despite good preservation of the corals. More recently, the same coral level has been dated again by Gobo *et al.* (2014) using thermal ionization mass spectrometry to yield a U-series isotopic age of 0.275–0.315 Ma, which is slightly older than that of McNeill & Collier (2004). Their specimen was characterized by a high $^{230}\text{Th}/^{232}\text{Th}$ ratio, so that possible detrital contamination cannot be excluded (see Appendix 5.10). Gobo *et al.* (2014) correctly point out that, at the Kryoneri site, the *Cladocora caespitosa* bioherm is preserved *in situ* in a cliff section overlain by deltaic conglomerates. It does not therefore represent a young terrace in the TG2 series.

At the Kryoneri site, a 70 m long roadside (NR8) exposure presents a 2.8 m thick bioherm comprising several well-preserved layers of corals in growth position. It is underlain by 2 m of gravels with *Lithophaga* sp. bored pebbles and sands, which are interpreted by Gobo *et al.* (2014) as a transgressive lag. The top of the bioherm is an erosive surface cutting down to the west. Overlying sandy and conglomeratic foresets downlap onto the erosion surface building to the west. The foreset package is 70–80 m thick and is overlain by the T2 marine terrace. Given their position and altitude, these Gilbert-type delta foresets are interpreted as part of the Akrata palaeovalley fill. The *Cladocora caespitosa* corals and underlying transgressive lag may therefore represent a transgression into the incised valley. These corals require clear water with low suspended sediment content, implying that, while the corals must have been deposited at the seaward exit of the palaeovalley, they were somehow protected from the sediment that was continuously supplied by the Krathis River. We surmise that the corals were deposited in a protected marine inlet.

A *Cladocora caespitosa* specimen with aragonite walls and septa was collected at the Kryoneri site. The pure aragonite composition implies that no calcite recrystallization has occurred, thus providing a high quality specimen for U-series dating. Dating was carried out at the U/Th dating laboratory of the CNR-IGAG (Monterotondo Scalo, Rome, Italy) using the α -particles spectrometry method. The ratios of $^{234}\text{U}/^{238}\text{U}$ and $^{230}\text{Th}/^{238}\text{U}$ are close to 1 (see Table ??) implying that the age of the Kryoneri corals (>0.380 Ma) exceed the limit of resolution of the U/Th method. Compared with Gobo *et al.* (2014), this sample has a low concentration of ^{232}Th , which indicates minor detrital contamination. Activity ratios $^{230}\text{Th}/^{234}\text{U}$ and $^{234}\text{U}/^{238}\text{U}$ were corrected by comparing values of $^{230}\text{Th}/^{232}\text{Th}$ and $^{234}\text{U}/^{232}\text{Th}$ activity ratios with those of Gobo *et al.* (2014). The corrected age of the Kryoneri corals is 0.241–0.319 Ma which is not significantly different from the age estimates of McNeill & Collier (2004) and Gobo *et al.* (2014). This age lies within the age estimate for the palaeovalley fill (0.34–0.20 Ma) and is tentatively correlated to the sea level high MIS 9 (Figure 5.12e).

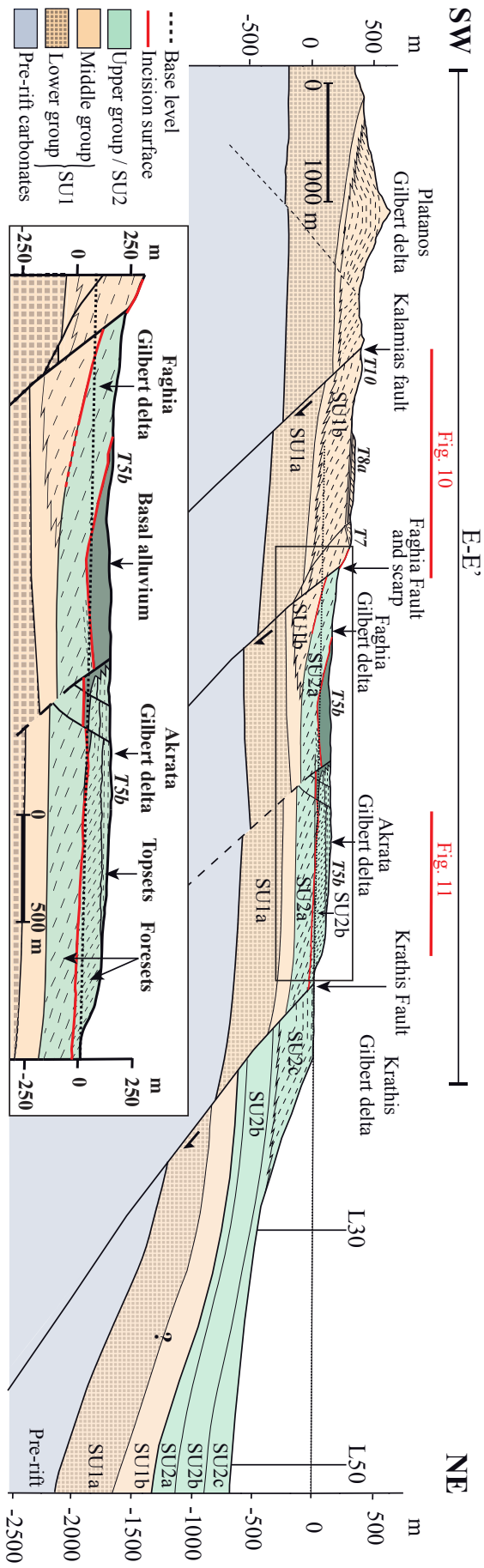


FIGURE 5.9 – Cross-section of the Akkrata relay zone constructed by correlation between the cross-section E-E' (Figure 5.4) and offshore data. SU1 and SU2 are here tentatively correlated with onshore stratigraphic units. Deltaic sedimentation on the relay zone records the deviation of the Krathis River during the construction of Platanos and Faghia Gilbert-type deltas, propagating northward and then progressively eastward respectively. Bed rotation mainly occurs offshore whereas the onshore ramp is particularly flat and cut by a series of transverse faults. Marine terraces initially defined by McNeill & Collier (2004) are indicated here and in Figures 5.4, 5.10, 5.11 and 5.12. Details of sedimentation on the ramp and the Akkrata palaeovalley fill are represented in the inset below. The incised valley identified and described by Gobo *et al.* (2014) is shown by the red line.

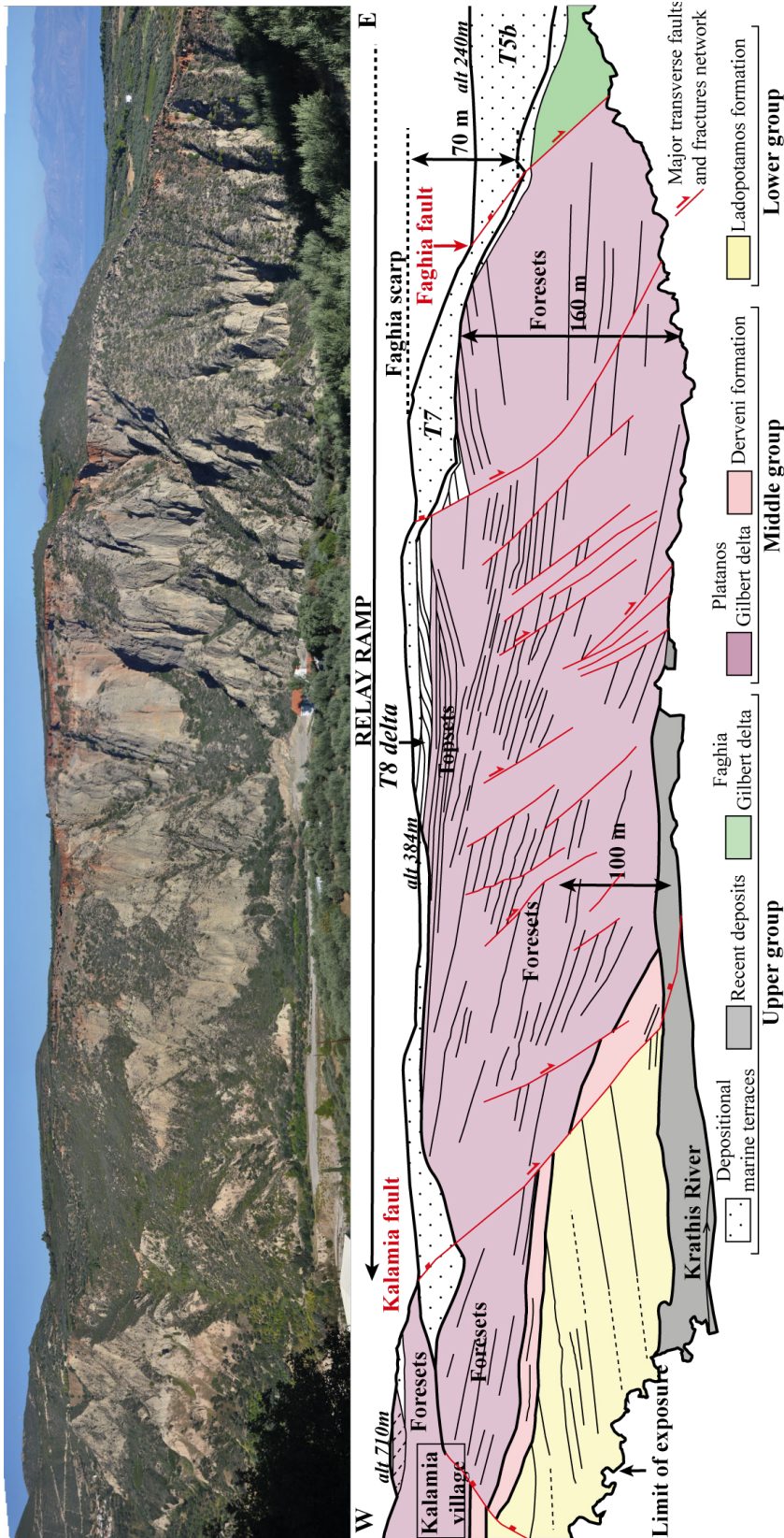


FIGURE 5.10 – Krathis valley between Kalamias and Akrata looking N. The location of the photo is indicated in Figure 5.9. The sketch highlights the deformation and faulting at the entry of the relay zone. Foreset dip directions progressively change from north to northeast (Faghia Gilbert-type delta). Platanos and Faghia Gilbert-type deltas are separated by a significant fault scarp (Faghia fault) marked by the topography. This geomorphological feature delimits the western limit of the Faghia Gilbert-type delta and the T5b marine terrace.

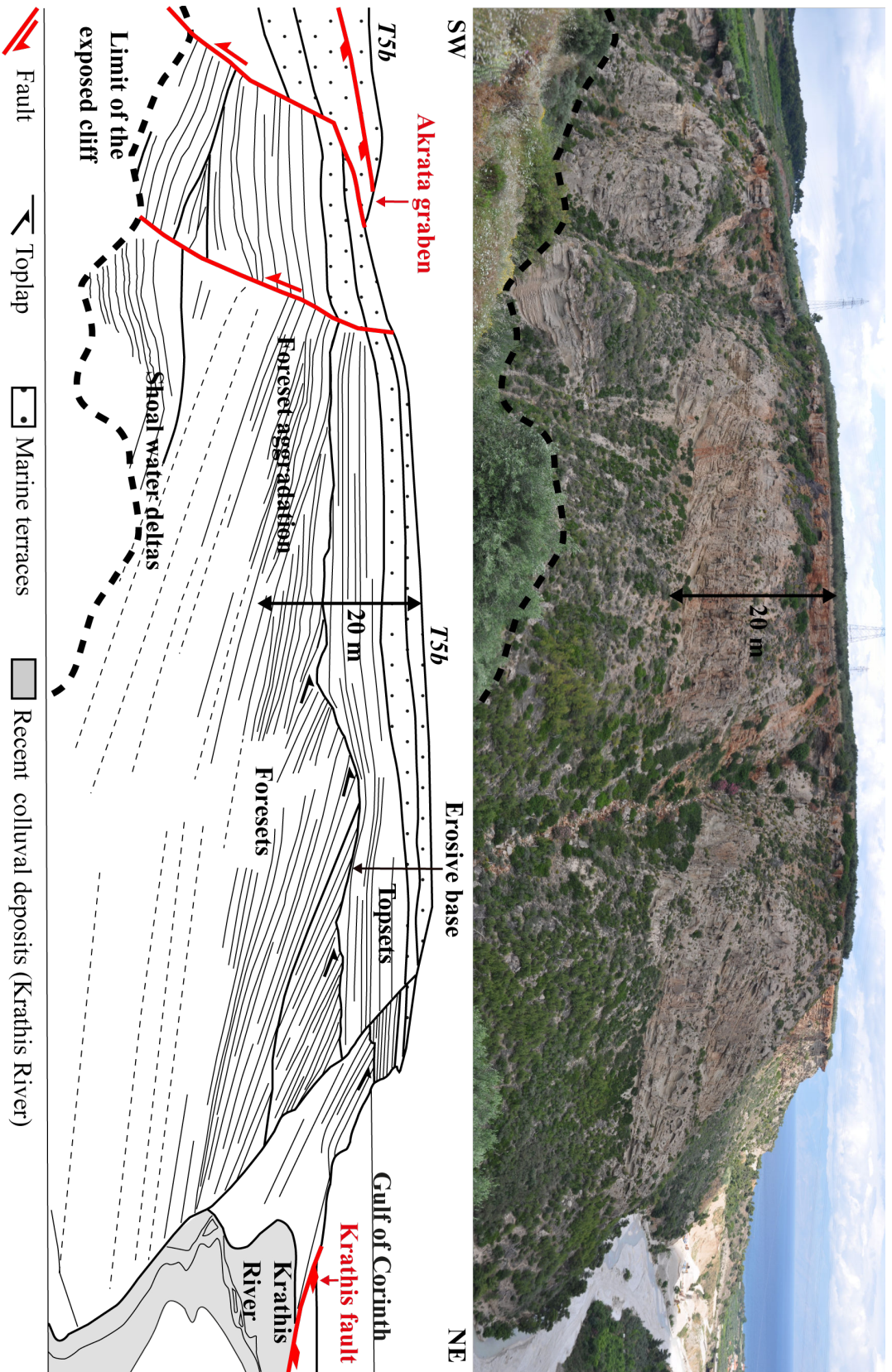


FIGURE 5.11 – Akrata Gilbert-type delta seen from the Akrata village, along the Krathis River. The location of the picture is indicated in Figure 5.9. Foreset aggradation is observed just east of the Akrata graben. The detailed drawing shows that the topset-foreset transition comprises packages of truncated foresets separated by packages of topsets passing into foresets. The stratal architecture records strong progradation superimposed by high frequency eustatic variations.

5.7 Relay zone evolution

Here we combine published data with our own observations to reconstruct the history of vertical motions, sedimentation and erosion across the relay zone and thus to propose a complete model of fault propagation, growth and linkage (Figure 5.12). Timing of phases is represented on the eustatic sea level curve (Figure 5.12e), using the scheme of Siddall *et al.* (2003). The relay zone developed over a period of around 0.5 Myr (phases 2 and 3). The reconstruction of the Akrata palaeovalley incision and fill as proposed by Gobo *et al.* (2014) represents only one of the last phases of relay zone history (phase 3).

During the period 1.8–0.7 Ma (phase 1, Figure 5.12a), the Platanos Gilbert-type delta (Middle group) was deposited by the Krathis River in the hangingwall of the eastern segment of the PMF and prograded northward (Figure 5.12a). Platanos prodelta facies are identified both onshore (Derveni formation) and offshore (SU1b; Figures 5.3, 5.7 and 5.9). The DF was active further east since at least 2.0 Ma while the East Channel Fault defined the northern margin of the rift at this time (Figure 5.6).

The period 0.7–0.4 Ma (Phase 2, Figure 5.12b, e) marks the early growth of the EHF system (Figure 5.12b, e). The EHF propagated eastward preceded by a forced fold as recorded on offshore seismic data, whereas the DF propagated westward. The young relay zone formed a flat shelf delimited by growth folds to the north (EHF) and to the east (relay ramp hinge at the future KrF). Before fault overlapping, the EHF and DF became connected through a zone of transverse faults (including the Platanos, Kalamias and Faghia Faults). Despite this early linkage, the EHF continued to propagate eastward but the DF ceased to lengthen. The PMF block started to uplift in the footwall of the Platanos, Kalamias and Faghia Faults as recorded by the TG1 marine terraces (T8 to T10 on Figure 5.4). The Krathis River deviated to the northeast, to build the strongly prograding Faghia Gilbert-type delta onto the subsiding relay ramp. The Faghia delta is correlated with the SU2a sub-package offshore. The incision surface at the base of the Faghia delta was probably due to a sea level fall during MIS 17 and 16, before initiation of the Kalamias, Platanos and Faghia faults.

During the period 0.4–0.2 Ma (Phase 3, Figure 5.12c, e), the EHF continued to propagate eastward (3 to 4 mm yr⁻¹ as a maximum value). The relay ramp hinge was still growing as the KrF progressively propagated upward. This phase is distinguished by the incision and infill of a large palaeovalley (up to 140 m deep, 3 km across) on the relay ramp. Using the dating presented above, we estimate that incision occurred from 0.40 to 0.34 Ma while the valley was infilled from 0.34 to 0.20 Ma. The construction of the Kryoneri bioherm may represent the maximum transgression of MIS 9a. The palaeovalley was progressively filled by two shoal water deltas Gobo *et al.* (2014) followed by the strongly prograding Akrata Gilbert-type delta (Figure 5.11). Using the dating of seismic stratigraphic boundaries, the valley fill succession is correlated with the lower SU2b sub-package offshore.

At about 0.2 Ma (onset of phase 4, Figure 5.12d, e) final breaching occurred when KrF linked the EHF and DF, and marks the onset of the post-linkage phase. There is no evidence that the EHF continued to propagate eastward. The uplifting relay zone is cut by a series of young transverse normal faults. The north-northwest trending graben (40 m maximum downthrow) developed during this phase (cuts T5b terrace) and thus cannot be ascribed to a relay ramp hinge as suggested by Gobo *et al.* (2014). Since final breaching, footwall uplift has been homogenous along the coastal fault system creating the flight of TG2 terraces. The Krathis River did not change its course during the last 0.2 Myr during which time it has been incising into its own deposits, while building the Krathis Gilbert-type delta in the hangingwall of the Krathis fault. Stratigraphically equivalent offshore deposits are the units SU2b and SU2c.

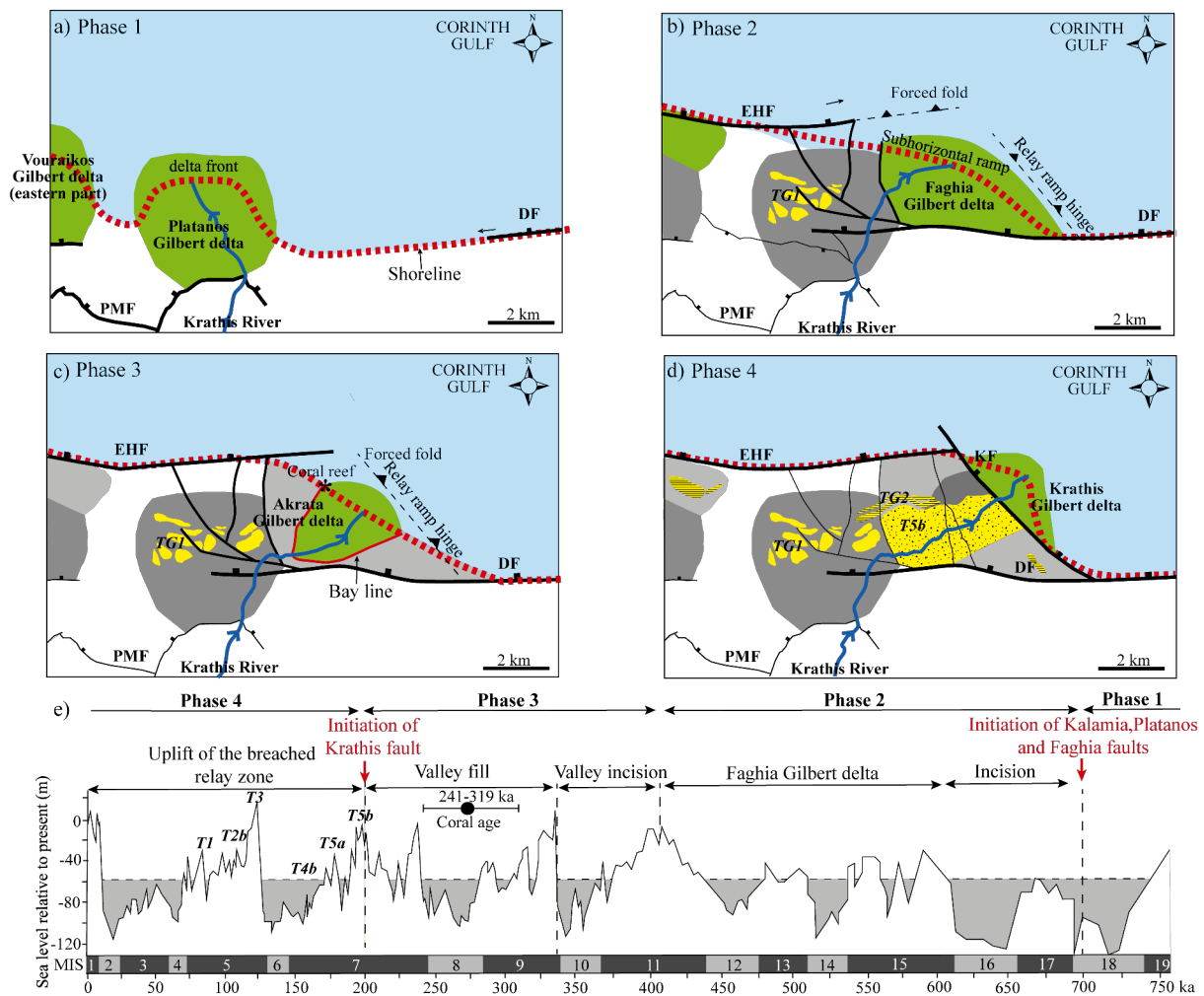


FIGURE 5.12 – Palaeogeographic maps of the Akrata relay zone evolution. The cartoons (a), (b), (c) and (d) correspond with the four major phases of sedimentation in the relay zone. For a detailed explanation see the text. These phases were constrained by eustatic sea level variations (Siddall *et al.*, 2003) and by combining tectonic, sedimentological and geomorphological data. Active Gilbert-type deltas (topset and foreset) are shown in green whereas grey Gilbert-type deltas are uplifted and incised. Thick fault traces correspond to active faults.

5.8 Discussion

5.8.1 Relay ramp geometry and fault growth models

Numerous studies of fault growth evolution describe a relay zone as an area of displacement deficit compensated by the rotation of the ramp in the overlapping zone (Peacock & Sanderson, 1994; Trudgill & Cartwright, 1994; Crider & Pollard, 1998; Ferrill & Morris, 2001; Young *et al.*, 2001; Peacock & Par, 2002; Crider & Peacock, 2004). These models are based on data that document pre-linkage and post-linkage phases but not the syn-linkage phase (Trudgill & Cartwright, 1994; Young *et al.*, 2001; Morley, 2002; Hus *et al.*, 2005; Soliva *et al.*, 2008). The stratigraphic succession in the Akrata relay zone is well constrained at a timescale of 10^5 to 10^6 years and permits, for the first time, a detailed reconstruction of the syn-linkage phase that lasted around 0.5 Myr. This corroborates previous evidence that fault linkage is a rapid process lasting less than 2–3 Myr (McLeod *et al.*, 2000).

Here the development of the relay zone is the result of two episodes of fault propagation and linkage. The Akrata relay zone is therefore a doubly-breached relay zone (e.g. Walsh *et al.*, 1999; Mansfield & Cartwright, 2001). Before the fault segments could overlap they were linked via a zone of oblique transverse faults. Evidence of rotation is only observed in forced folds and the relay ramp itself seems to have remained sub-horizontal. Differential vertical motion along the relay zone was instead accommodated by a series of oblique breaching faults that became younger basinward.

Both the coherent and isolated fault models (Figure 5.1) consider two new fault segments that initiate and grow synchronously toward one another (e.g. Childs *et al.*, 1995; Gupta & Cowie, 2000; Meyer *et al.*, 2002; Childs *et al.*, 2003). These models do not consider the case of interacting faults with different dimensions and displacements, which is the case in the Akrata relay zone. The displacement profiles along the EHF-DF system (Figure 5.9) clearly demonstrate the greater importance of the DF compared with the EHF. Initiation and growth of the EHF contributed to the propagation of the rift toward the west. Tip propagation of the EHF clearly agrees with the isolated fault model. On a larger scale, it can also be argued that the lateral propagation of the rift border fault system is more compatible with the isolated fault model than with the coherent fault model. However, in the case of the Akrata relay zone, the changes in ramp geometry during the syn-linkage phase cannot be used to discriminate between these kinematic models, which are limited (illustrated in Figure 5.1a, b) to the case of fault segments of the same size and generation. The repeated history of fault propagation and linkage of segments can be explained by other controlling factors developed below.

5.8.2 Role of structural inheritance in the development of a rift border fault system

Early and multiple linkage is probably facilitated by inherited basement faults. The Akrata area lies within a zone of structural complexity that affected the Corinth rift and older Hellenide tectonic units. About 20 km south of the study area, the Zarouchla culmination (Flotté *et al.*, 2005; Trotet *et al.*, 2006) records a NE-verging extensional detachment cutting the Hellenide nappe stack. This detachment was active from Late Oligocene to Middle Miocene in Crete and in the southern Peloponnese. Ghisetti & Vezzani (2005) propose that this crustal culmination continues northward at depth below the western part of the Akrata area and below the Corinth Gulf. More recently, Papanikolaou *et al.* (2009) identify the same structure as part of their East Peloponnese Detachment. Moreover, a broad corridor of NW-SE trending faults is present south of the relay zone along the Krathis valley (Figure 5.2). This suggests that an inherited structural trend may have strongly influenced rift evolution in this area, in particular palaeodrainage patterns, sediment distribution, the location of the Akrata relay zone and the style of linkage during fault growth.

The Akrata relay zone represents a broad damage zone that developed as a result of the westward propagation of the southern margin border fault system. During the Middle Pleistocene, it appears to have been more efficient to nucleate a new fault segment (EHF) rather than to enlarge the existing fault (DF) by lateral propagation. Contributing factors may have been (1) the migration of the focus of deformation to the north and west in the western rift associated with an increasing extension rate (Ford *et al.*, 2013) and (2) the presence of oblique mechanical crustal layering in the Akrata area that focussed the transfer zone. It is therefore not possible to directly compare the Akrata relay zone with simple kinematic models.

5.8.3 Sedimentation patterns on relay ramps

Relay zones along rift border fault systems are zones of transfer of sediment from the uplifting footwall into hangingwall depocentres. Present knowledge focuses on the modifications of drainage patterns and sediment pathways across relay zones leading to deposition in the hanging-wall depocentre. Typically, due to bed rotation, the slope of a ramp (2° to 10°) is too high for stable deposition and sediments are transported directly into the basin (e.g. Athmer *et al.*, 2010; Athmer & Luthi, 2011). However, this and other case studies (e.g. Giba *et al.*, 2012) show that relay ramps can also behave as areas of deposition under certain circumstances. We show that, in the case of a doubly-breached relay zone, coarse-grained sediments can be trapped on the sub-horizontal ramp. The continuous supply of sediment by a well established antecedent river allowed the construction of a series of conglomeratic Gilbert-type deltas sensitive to sea level variations and vertical motions related to fault linkage history. As linkage evolved, deposition migrated laterally on the ramp toward the main basin. Finer fractions were transported basinward and deposited as turbidites and suspension fallout deposits. The distinct facies distributions and ramp geometry of

doubly–breached relay zones have potentially important implications for the characterisation of fluid flow and distribution of hydrocarbon reservoirs along rift margins.

5.8.4 Role of antecedent drainage

Conceptual and numerical models of interactions between surface and tectonic processes at relay ramps generally consider only consequent drainage systems (e.g. [Densmore *et al.*, 2003](#)). However, throughout much of the Corinth rift evolution, the antecedent Krathis River continued to flow northward, cutting across active and inactive normal fault blocks. Its incision rate always exceeded footwall uplift making it particularly efficient in transmitting sediments into the basin (e.g. [Leeder & Mack, 2007](#)). The river was captured by the developing Akrata relay zone, turning it NE to build strongly prograding deltas across the ramp. All major rivers in the Corinth rift west of Akrata demonstrate the same high erosion power allowing them to continue to flow northward despite high rates of footwall uplift on new faults. While the Krathis and Kerinitis rivers have exploited relay zones to access rift depocentres, other rivers have cut across faults at their point of maximum displacement and maximum footwall uplift (Vouraikos River ; [Ford *et al.*, 2007](#)). The exceptional erosive power of these rivers is probably related to the coarseness of their bedloads as suggested by models of [Cowie *et al.* \(2006\)](#).

5.9 Conclusions

1. Along the southern rift margin of the Gulf of Corinth, the doubly-breached Akrata relay zone developed between an older, principal footwall fault (DF) and a younger and smaller hangingwall fault (EHF). This study, which includes a detailed onshore-offshore stratigraphic correlation and new dating, permits for the first time, a high resolution reconstruction of the syn-linkage phase over a period of approximately 0.5 Myr.
2. The Akrata relay zone developed as a depositional ramp throughout fault linkage history. The antecedent Krathis River was captured by, and deflected into, the relay zone to provide a high volume of coarse sediment. Because it was sub-horizontal rather than tilted, coarse sediment did not bypass the ramp. Instead, prograding Gilbert-type deltas were deposited on the ramp while finer fractions were transferred out into the basin. These Gilbert-type deltas record a series of forced regressions along the relay ramp due to basinward migration of the ramp depocentre combined with eustatic variations. Diachronous uplift of the onshore relay ramp records complimentary migration of footwall uplift.
3. The pre-linkage phase is characterised by the development of forced folds offshore that propagated laterally and upward ahead of the EHF and the breaching KrF (from 0.7 to 0.4 Ma), while a tilted fault block developed in the hangingwall of the more established

DF. The young EHF propagated toward the older DF but did not initially overlap with it because early linkage occurred (around 0.6 Ma), probably due to reactivation of existing oblique structures. A subhorizontal ramp subsequently developed due to multiple breaching during the continued lateral propagation of the hangingwall fault. Transverse faults progressively accommodated fault displacement deficit in the transfer zone until final breaching at around 0.2 Ma. The Akrata relay zone therefore forms a broad damage zone composed of small fault blocks that down-step toward the basin.

4. Several aspects of the lateral fault growth history of the Akrata relay ramp are more indicative of the isolated fault model than the coherent fault model. However, neither model can adequately explain the early and multiple breaching of the relay zone. Such a pattern of deformation is here interpreted as being due to the reactivation oblique basement faults.
5. The linkage of the EHF to the DF accommodated the westward propagation of the rift system. The initiation of the EHF and its connection with the existing DF was more efficient than simple lateral propagation of the DF. The presence of inherited oblique crustal layering (probably Hellenide) in the Akrata area may have acted as a mechanical barrier to simple fault propagation and to have thus controlled the location of the relay zone. This illustrates that crustal structures played an important role in evolution of the Corinth rift, and deserve further investigation, particularly along the Krathis valley.
6. On the scale of the rift border fault system, the migration of deformation to the north and west in the western Corinth rift is responsible for the en échelon right-stepping geometry of the active southern margin. The migration and acceleration of rifting since the Middle Pleistocene has focussed strain below the westernmost Gulf, which may be due to the SW propagation of the North Anatolian Fault and/or the anticlockwise rotation of the Peloponnese peninsula (Goldsworthy *et al.*, 2002; Mattei *et al.*, 2004).

5.10 Appendix : Technical details on U–Th dating of *Cladocora caespitosa* from Kryoneri location

The aragonitic nature of the sample of *Cladocora coespitosa* from the Kryoneri exposure (Figure 5.4) was tested by a staining method using Meigen's solution of cobalt nitrate. Five grams of the tested sample were treated with concentrated H₂O₂ for 24 hours and then dissolved in 1 mol l⁻¹ HNO₃, spiked with a ²³²U/²²⁸Th tracer (²²⁸Th/²³²U activity ratio = 1.027) and charged with few drops of pure FeCl₃. U and Th were co-precipitated with iron hydroxide by adding NH₄ OH up to pH ~3.5–5.0. The precipitate was washed with distilled water, dissolved in 10 mol l⁻¹ HCl and passed through columns of anionic Dowex 1×8 resin (10 mol l⁻¹ HCl conditioned) for separating U from Th. U and Th fractions were then dissolved in 7 mol l⁻¹ HNO₃ and further purified by passing through Dowex 1×8 resin columns (7 mol l⁻¹ HNO₃ conditioned). After

5.10 Appendix : Technical details on U–Th dating of *Cladocora caespitosa* from Kryoneri location

selective extraction with TTA (thenoyltrifluoroacetone), U and Th fractions were deposited on U and Th-free steel planchets and their activity determined by α -spectrometry (Table ??).

The data obtained are just to the limit of the potentiality of the dating method giving only a rough indication of an age >380 ka ; however, comparing the $^{230}\text{Th}/^{232}\text{Th}$ and $^{234}\text{U}/^{232}\text{Th}$ activity ratios of our sample with the sample of *Cladocora coespitosa* studied by [Gobo *et al.* \(2014\)](#) (Table ??) it appears clearly that the former is more contaminated than the latter and can be therefore used for correcting the age of both the samples and to eliminate any influence of detrital contamination. The assumptions of the correction are that the two samples, contaminated by detrital component at a different extent, are coeval and have the same initial $^{230}\text{Th}/^{232}\text{Th}$ activity ratio. The correction scheme is analogous to that used for correcting impure carbonates by different leachates ([Ku & Liang, 1984](#); [Schwarcz & Latham, 1989](#)) and where the corrected $^{230}\text{Th}/^{234}\text{U}$ and $^{234}\text{U}/^{238}\text{U}$ activity ratios are given by the slopes of the straight line between the two leachates in each of the two diagrams ($^{234}\text{U}/^{232}\text{Th}$ vs. $^{238}\text{U}/^{232}\text{Th}$; $^{230}\text{Th}/^{232}\text{Th}$ vs. $^{234}\text{U}/^{232}\text{Th}$) shown in Figure 5.1 . The ^{230}Th -age of the corrected pure carbonate was finally calculated iteratively using the following equation 5.1 where t is the age in years (a), and $\lambda_{234} = 2.826 \times 10^{-6} \text{ a}^{-1}$ and $\lambda_{230} = 9.157 \times 10^{-6} \text{ a}^{-1}$ are the most recent decay constants given by [Cheng *et al.* \(2000\)](#). The corrected age is $275 +44/-34 \text{ ka}$ and is consistent with the age of one of the corals analysed by [McNeill & Collier \(2004\)](#). Activity ratios in pure carbonate corrected for detrital contamination according to the scheme of [Ku & Liang \(1984\)](#); [Schwarcz & Latham \(1989\)](#) : $^{230}\text{Th}/^{234}\text{U} = 0.943 \pm 0.018$ (1σ); $^{234}\text{U}/^{238}\text{U} = 1.089 \pm 0.018$ (1σ).

$$^{230}\text{Th}/^{234}\text{U} = 1 - \frac{e^{-\lambda_{230}t}}{^{234}\text{U}/^{238}\text{U}} + \left(1 - \frac{1}{^{234}\text{U}/^{238}\text{U}}\right) \times \frac{\lambda_{230}}{\lambda_{230} - \lambda_{234}} \times (1 - e^{\lambda_{230}t - \lambda_{234}t}) \quad (5.1)$$

TABLE 5.1 – Results of U series in the sample of *Cladocora coespitosa* (Kryoneri coral site) in this study and compared with [Gobo *et al.* \(2014\)](#).

	U (ppm)	Th (ppm)	$^{234}\text{U}/^{238}\text{U}$	$^{230}\text{Th}/^{234}\text{U}$	$^{230}\text{Th}/^{232}\text{Th}$	$^{234}\text{U}/^{232}\text{Th}$	$^{238}\text{U}/^{232}\text{Th}$
This study	2.78 ± 0.04	0.37 ± 0.02	1.03 ± 0.02 (1-sigma)	1.01 ± 0.02 (1-sigma)	24.0 ± 1.0	23.8 ± 1.0	23.1 ± 1.0
Gobo <i>et al.</i> (2014)	2.59	0.07	1.081 ± 0.009 (2-sigma)	0.956 ± 0.01 (2-sigma)	119.9 ± 1.0	125.4 ± 1.0	116.0 ± 1.0

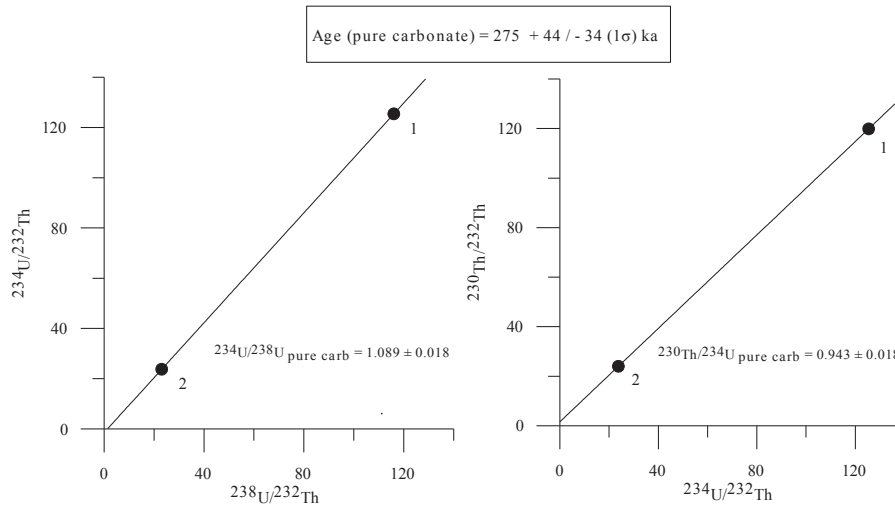


FIGURE 5.13 – Correction schemes for *Cladocora coespitosa* samples : 1, Gobo *et al.* (2014) ; 2, this study. The slopes of the curves are $^{234}\text{U}/^{238}\text{U}$ and $^{230}\text{Th}/^{234}\text{U}$ activity ratios of the pure carbonate. Uncertainties were less than the diameter of points and final uncertainty of each activity ratio was calculated by conventional error propagation procedures.

Acknowledgment

Fieldwork was funded by the SISCOR ANR project. We thank Paradigm for access to and use of GOCAD software. The authors thank Nicolas Meyer for his help with this software. We are also grateful to Edward Williams for fruitful observations and discussions in the field. Mario Voltaggio and Marco Mancini of the CNR-IGAG (Monterotondo Scalo, Rome, Italy) provided the U-series isotopic dating and assisted in its interpretation. We thank Nicholas Christie-Blick and Casey Nixon for their constructive reviews to make the paper more appealing to the continental rift community.

Chapitre 6

Regional stratigraphy and general discussion

Sommaire

6.1	Introduction	202
6.2	Regional syn-rift stratigraphy	202
6.2.1	C5 : Westernmost rift	203
6.2.2	C4 and C3 : central and western rift, and correlation to the eastern rift (C2)	206
6.2.3	C1 : Corinth isthmus	208
6.2.4	MB : Megara Basin	208
6.3	Corinth rift evolution	211
6.3.1	Phase 1 : Late Pliocene–Early Pleistocene (4–3.6 to 1.5 Ma)	211
6.3.2	Phase 2 : Early–Middle Pleistocene (1.5 to -0.7 Ma)	213
6.3.3	Phase 3 : Calabrian–Middle Ionian (0.7 to 0.4 Ma)	216
6.3.4	Phase 4 : Middle Ionian–present day (0.4–Present Ma)	218
6.4	Significance for rift basin deepening	221
6.5	Compilation of rivers behaviour	221
6.5.1	Response to footwall uplift	221
6.5.2	Response to fault migration	222
6.6	Significance of through-going river systems	223

6.1 Introduction

Rifting evolves by initiation and slow growth of isolated normal faults that rapidly link to form master faults onto which extension focuses. Assuming no inherited bathymetry, the early phase of slow subsidence with continental conditions (rift initiation) is followed by acceleration in subsidence and abrupt deepening of the basin, known as the 'rift climax' (Lambiase, 1990; Schlische & Olsen, 1990; Prosser, 1993; Patton *et al.*, 1994; Lambiase & Bosworth, 1995; Gupta *et al.*, 1998). The transition from rift initiation to 'rift climax' is an integral part of the standard model for single phase 'static' rifting (e.g. Prosser, 1993; Cowie *et al.*, 2000; Withjack *et al.*, 2002). However, the migration and lateral propagation of the fault systems can produce a more complex evolution of the rift, involving the connexion and shift between depocentres as well as multiple deepening events. This study provides new insights into major events recorded in the stratigraphic record of rifts. We discuss in particular the evolution of sediment routing systems, the relevance of deepening events across a rift, and the importance of rates of rifting and related surface processes.

What is the stratigraphic pattern in a rift that migrates across strike and/or propagates along strike? How should we interpret deepening events and define the 'climax' in a rift where faults and depocentres shift with time?

We address these questions by establishing a regional syn-rift stratigraphy of the Corinth rift. The preserved fluvial, deltaic and lacustrine successions are used to reconstruct the palaeogeography of the southern rift margin. We identify several major long-lived sediment routing systems (antecedent rivers) that supplied coarse sediments into the basin. The Kalavryta, Killini and Rodini River systems distributed sediments across the active margins feeding the deeper parts of the basin from Late Pliocene to Late Pleistocene. Different depositional environments can co-exist during the evolution of the rift margin. They mainly record overflow of the subsiding basin, a fluvial to lacustrine transition through time and diachronous basin deepening along the margin. These river systems persisted but were reorganised during the successive phases of northward fault migration. We show that they record a range of interactions with faulting at different time intervals and scales. In particular, different orders of fault activations (hangingwall v. footwall fault migrations) will generate different characteristic stratigraphic signatures by through-going rivers. The implications for the geometry of depocentres and syn-rift facies distributions are also discussed.

6.2 Regional syn-rift stratigraphy

The compilation of our work presented in the previous chapters is integrated at the regional scale and correlated with other existing studies in order to build the syn-rift stratigraphy along the entire southern Corinth rift margin (Figures 6.1 and 6.2). Following Ford *et al.* (2016), the

Corinth rift is divided into six zones (C1 to C5) oriented NNE-SSW with respect the previous works (Figures 6.1 and 6.2). We add the Megara Basin (MB) to the east of C1. The stratigraphy within the different zones is summarised in Figure 6.3, which are from west to east :

- and the westernmost rift which includes the Lakka fault block and the offshore basin south to the Marathias Fault (C5). The Patras Gulf (PG) lies further to the west.
- the western rift, between Aegion and Akrata (C4),
- the central rift, east of Akrata (C3),
- the Xylocastro area (C2)
- the Corinth Isthmus, the Alkyonides and the Lechaion Gulfs (C1),
- the Megara Basin (MB)

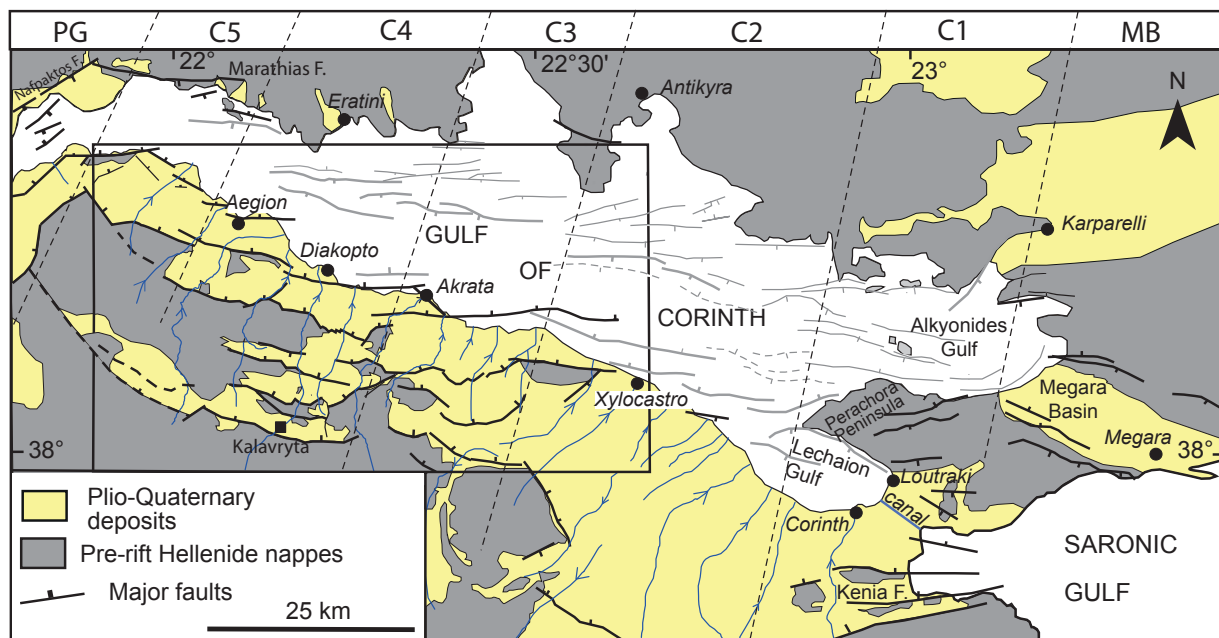


FIGURE 6.1 – Tectonic map of the Corinth rift showing principal faults and the onshore distribution. Rivers of the northern Peloponnese are shown with an arrow in the direction of flow. The location of Figure 6.2 is boxed. The Corinth rift (onshore and offshore) is subdivided into five areas, C1 to C5 (top of figure). PG is the Patras rift to the west. MB is the Megara Basin to the east.

6.2.1 C5 : Westernmost rift

Between the Rion Straits in the west and the Selinous river, syn-rift strata are preserved on the 7–8 km wide Lakka fault block (Figure 6.2). The syn-rift succession is estimated to have a maximum thickness of 1400 m. It is divided into two informal groups, the Profitis Elias Group and

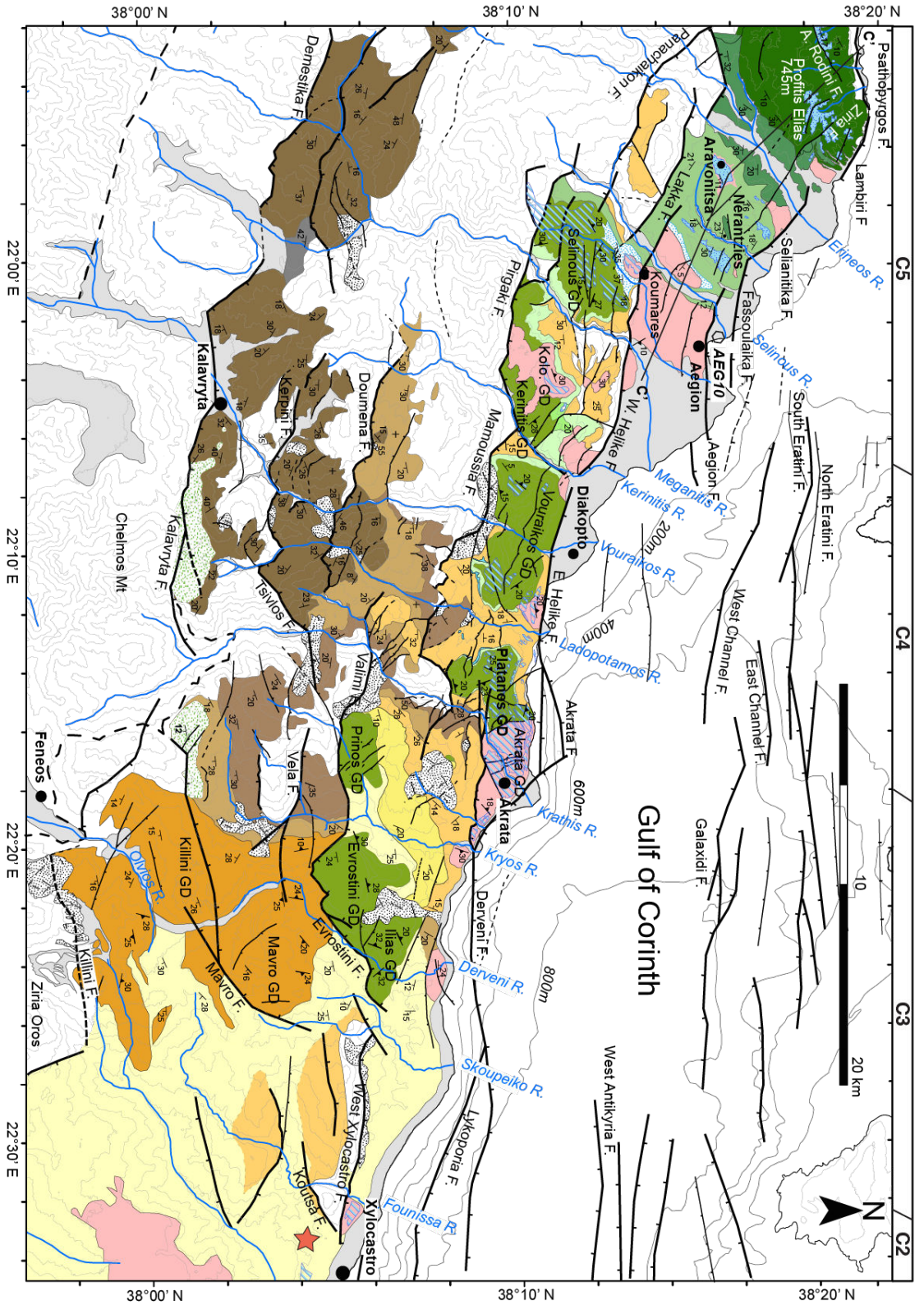
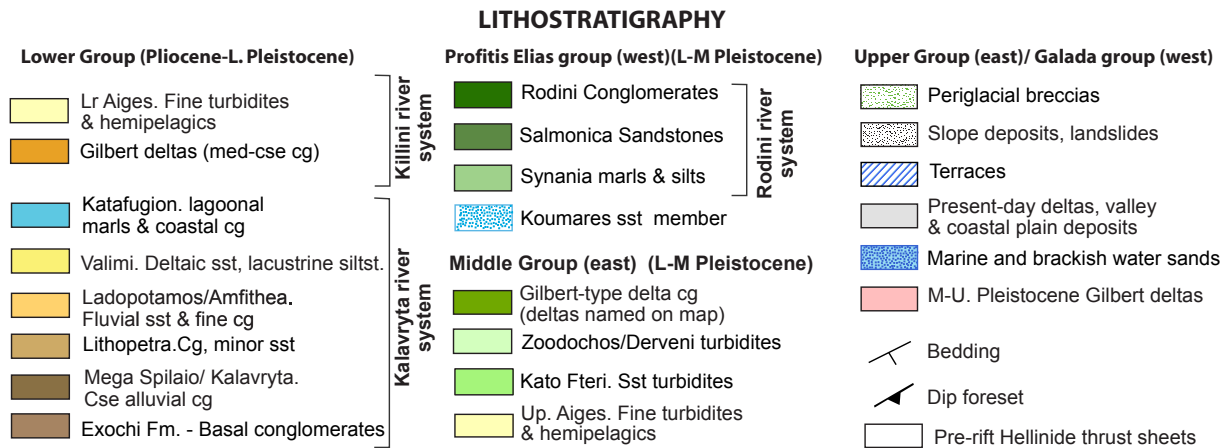


FIGURE 6.2 – Geological map of the Plio-Pleistocene Corinth rift of the northern Peloponnese from Xylocastro to Psathopyrgos. The map of the central and eastern areas (C2, C3, C4) is compiled from [Rohais et al. \(2007a,b\)](#), [Leeder et al. \(2012\)](#) and [Ford et al. \(2013\)](#). The western area integrates the work of [Palyvos et al. \(2005\)](#); [Vasilatos et al. \(2010\)](#). Bathymetric and topographical contours are spaced every 200 m. The red star shows the location of the dated ash layer of [Leeder et al. \(2012\)](#). Abbreviations on map and legend : A, Ano; cg, conglomerate; cse, coarse; F, fault; Fm, Formation; E, east; GD, Gilbert Delta; Lr, Lower; med, medium; M, Middle; Mt, Mountain; R, River; silst, siltstone; Up., Upper; W, West.



the younger Galada Group (Figure 6.3; Palyvos *et al.*, 2010). Further explanations and figures are provided in appendix F.

The Profitis Elias Group (Early to Middle Pleistocene) consists of the laterally equivalent Rodini Conglomerate Formation, the Salmoniko Sandstone Formation and the Synania Siltstone Formation, which record an overall fining to the east across the Lakka fault block. The Rodini Conglomerate Formation (<600 m) was deposited by a braided river system, most probably sourced from the north (**Rodini river system**). It passes laterally to the east into the Salmoniko Formation (<250 m), also interpreted as being deposited in a fluvial environment and passing eastward to a deltaic environment. The Synania Formation (<400 m) comprises lacustrine to brackish water deposits and is laterally equivalent to the Zoodochos Formation to the east (Figure 6.3; Backert *et al.*, 2010).

The Galada Group unconformably overlies all formations of the Profitis Elias Group, often with angular discordance. It comprises variable lithologies including cool water carbonate marine terraces, Gilbert-type delta conglomerates, and shallow marine to brackish water sands and silts. As a whole, the Galada Group records discontinuous marine-brackish-lacustrine sedimentation due to the interplay of eustatic sea-level fluctuations and tectonics during the progressive uplift of the Lakka fault block since around 400 ka (Palyvos *et al.*, 2010). Its depositional history is intimately linked to the tectonic evolution of the coastal fault system (Ford *et al.*, 2016).

The Lakka fault block contains no strata equivalent to the Lower Group. However a fine-grained fluvial succession is preserved further south in the hangingwall of the eastern Panachai-kon Fault block. This unit correlates laterally to the Melisia Formation (Lower Group) of the PMF block (Figure 6.3; Backert *et al.*, 2010). With its upper boundary at 400 ka, the Early to Middle Pleistocene Profitis Elias Group is laterally equivalent to the Middle Group and to part of the Upper Group further east. However, direct correlation is obscured by the presence of a palaeohigh oriented roughly N-S extending at the eastern part of the Selinous valley (Figure 6.2). This feature extends northward across the gulf to the Psaromita Peninsula on the north shore

(Psaromita-Aegion High).

The Lakka Fault was active during deposition of the Profitis Elias Group although no sediment appears to have been supplied from its footwall during this time. Instead, its footwall area appears to have drained eastward across the relay zone between the Panachaikon and Pirgaki faults to feed the Selinous delta complex building to the E and NE (Figure 6.3). The small north building Aravonitsa Gilbert delta dated at as 400–300 ka (Palyvos *et al.*, 2010) records the first coarse sediment supplied from the Lakka footwall (possibly by the proto-Erineos river). The Lakka and Panachaikon faults were active until about this time when the new coastal fault system initiated to the NW (Pspathopyrgos Fault) and propagated eastward.

The **Rodini river system** interacted with a footwall migrating fault system. Due to northward footwall migration of the fault system the river abandoned its older deposits to accumulate sediments in the footwall of the abandoned fault. This river system supplied the Profitis Elias Group across a south-dipping faults at the western end of the rift.

6.2.2 C4 and C3 : central and western rift, and correlation to the eastern rift (C2)

Ghisetti & Vezzani (2004) were the first recognise two sub-basins along the southern margin, which they propose separated by a N-S paleo-topographic high located along the Krathis valley (Figure 6.2). To the west, their Aigion sub-basin corresponds to zone C4. East of the Krathis River, their Derveni sub-basin corresponds to zone C3. In the field, there is no clear structure that separates the sub-basins as envisaged by Ghisetti & Vezzani (2004, 2005). However, we agree that the morphology of the rift basin geometry changes across the Krathis valley. To the east, spacing between major fault is greater and the syn-rift succession is significantly thicker and finer. We suggest that the real variation in stratigraphy, identified by Ghisetti & Vezzani (2004) as different sub-basins, is related to different river systems supplying sediment into the Corinth Gulf (from Late Pliocene to Early Pleistocene); the **Kalavryta river system** fed the western basin (chapter 4), the **Killini river system** fed the central rift (chapter F).

In the western rift, the Lower Group **Kalavryta river system** (C4) mainly consists of an alluvial succession that fines toward the east from coarse alluvial conglomerates to fine grained lacustrine turbidites (Figure 6.2). These deposits (400 to 1400 m thick) are preserved in a series of fault blocks, which were active during the early rift phase. The antecedent Kalavryta river system was sourced from the SW and flowed toward the NE. Fluvial facies transitions occurred at a larger scale than the spacing of the growing faults. This distributive river system was oblique to transverse to the fault system in the proximal part (in the SW), and become axial in the NE, building small deltas into a shallow lacustrine basin (see chapter 4 for more details on the sedimentology and the lithostratigraphy of the Kalavryta river system).

To the east of the Krathis valley (C3), in the central part of the southern rift margin, four

large Gilbert-type delta complexes are aligned N-S over some 15 km (Figure 6.2). Their stratigraphic development records the northward migration of fault activity and depocentres (Rohais *et al.*, 2008). The stable coarse sediment input from the south as supplied by the **Killini river system**, which built the Killini, the Mavro and the Evrostini deltas. The same river system successively incised and cannibalised its own deltas during the northward migration of fault activity. These three main deltas record increasing palaeobathymetry (up to ca. 500 m for the Evrostini delta) and thus progressive deepening of the rift basin. The Killini and Mavro Gilbert-type deltas comprise stacked, small conglomeratic deltas (10 to some 10's meters) (Rohais *et al.*, 2007a,b).

In the eastern Corinth rift, the 'Xylocastro Ash' (C2, Figure 6.2) was found within fine-grained turbidites and hemipelagites (Rethio-Dendro Formation, Figure 6.3) and dated at 2.550 ± 0.007 Ma (by $^{40}\text{Ar}/^{39}\text{Ar}$ dating using single-crystal CO_2 laser fusion; Leeder *et al.*, 2012). Leeder *et al.* (2012) correlate this ash westward with the lower Aiges Formation and to either the Killini or Mavro Gilbert-type deltas, which are assigned to the Middle Group (Rohais *et al.*, 2007a,b). While we agree with the correlation of the ash with the Killini or Mavro Gilbert deltas, we propose that both the Killini and Mavro deltas are older and thus assigned to the Lower Group (Ford *et al.*, 2016). This correlation model enables to date the main first "basin deepening event" at around 3.0–3.2 Ma (Leeder *et al.*, 2012). This correlation also suggests that both Kalavryta and Killini river systems were active during the Lower Group, and thus diachronous deepening of the basin occurred during the early rift phase.

In the Early Pleistocene, at around 1.8 Ma, the southern rift margin migrated northward by 10–15 km. The Middle Group and the construction of giant conglomeratic Gilbert-type deltas (in C4) marked the onset of basin deepening in the western rift (Ori, 1989; Dart *et al.*, 1994; Ford *et al.*, 2007, 2013; Rohais *et al.*, 2007a; Backert *et al.*, 2010). Lower fluvial deposits and Middle Group Gilbert deltas are separated by a major unconformity and several 100's ka are possibly missed in C4 (Figure 6.3). Stratal architectures of the Gilbert-type deltas present stacked aggradation-progradation stratal packages recording multiple episodes of base-level fall. Foreset height representing palaeowater depth, can reach up to 360 m for the Kerinitis delta (Backert *et al.*, 2010). North-flowing rivers supplied the Gilbert-type deltas across the PMF along the southern rift margin. From west to east, the preserved Gilbert-type deltas are named Paleo-Meganitis, Kerinitis, Vouraikos and Platanos (Figure 6.2). Equivalent prodelta facies are preserved in the Derveni and Zoodochos Formations.

To the east of the Krathis valley (C3), the same basin deepening is recorded by the Evrostini and Ilias Gilbert-type deltas in the hangingwall of the Evrostini Fault. This delta lies physically below the Evrostini fan delta (Rohais *et al.*, 2008). Equivalent prodelta facies correspond to the upper Aiges Formation. These deltas were supplied by the Killini river system that continued to flow northward without major interruption throughout the Middle Group but was turned southward at around 0.7 Ma (Rohais *et al.*, 2007a).

The Upper Group deposits onshore corresponds to small Gilbert-type fan deltas, marine

terraces, slope deposits and red palaeosols. Upper Group deposits are mostly preserved offshore (e.g. [Bell *et al.*, 2009](#); [Taylor *et al.*, 2011](#); [Hemelsdaël & Ford, 2016](#); [Nixon *et al.*, 2016](#)). The Upper Group records the phase when tectonic activity migrated northward to form the present-day 'en-échelon' right-stepping fault system, which defines the central southern Gulf margin (Figure 6.2). Since then, the inactive normal fault blocks have been uplifted to over 1000 m above sea level. The north flowing rivers have continued to incise and feed Gilbert-type deltas offshore. The best-preserved Upper group succession onshore corresponds to the Akrata relay zone (Chapter 5). The average total uplift rate along the southern shore of the Gulf is estimated between 0.9 and 2.2 mm/yr using Holocene coastal markers and Upper Quaternary marine terraces ([Stewart, 1996](#); [Stewart & Vita-Finzi, 1996](#); [Pirazzoli *et al.*, 2004](#); [McNeill & Collier, 2004](#)).

6.2.3 C1 : Corinth isthmus

The C1 area includes the Alkyonides Gulf, the Perachora Peninsula, the Lechaion Gulf and the mainland rift bounded to the south by the Kenia Fault (Figure 6.1). The Corinth isthmus is located at the easternmost end of the Corinth rift basin. It is delimited to the north by the major bounding Loutraki Fault, and to the south along the coast of the Saronic Gulf (Figure 6.1). The syn-rift stratigraphy in this area has been mainly studied by [Collier \(1990\)](#); [Collier & Dart \(1991\)](#); [McMurray & Gawthorpe \(2000\)](#). The Lower Pliocene Group (early rift succession) is exposed east of the Isthmus (the Charalampos fault block, Figure 6.4). This east-west asymmetric graben characterised by an axial dispersal system separated from the main Gulf of Corinth to the west by a horst. The Lower Pliocene age of this succession is derived from the overlying andesites that are typical of the calc-alkaline volcanics of the south Aegean volcanic arc ([Fytikas *et al.*, 1984](#)). Biotite and hornblende phenocrysts of these andesites are K–Ar dated at 3.62 ± 0.18 and 4.0 ± 0.4 Ma ([Collier & Dart, 1991](#)). Subsequent sedimentation occurred to the south of the Charalampos fault block with deposition of the Trapeza-Isthmos Group (Figure 6.3). Subsidence continues today south of the Trapeza-Isthmos block (where stands the Corinth Canal), as part of the development of the Saronic Gulf (Figure 6.1). The absence of Upper Pliocene to Early Pleistocene sediments (Figure 6.3) implies a period of emergence and erosion during the Late Pliocene to mid-Pleistocene ([Collier & Dart, 1991](#)).

The section of the Corinth canal (Figure 6.1) shows a central horst block with the Isthmia graben to the south. The sediments exposed in the canal consists of marls, sandstones and conglomerates that reflect deposition in shallow marine, shoreface, foreshore and alluvial environments ([Collier, 1990](#)). They correspond to a coastal facies belt that prograded westward from the central horst while responding to eustatic sea-level variations during the last 430 kyr. The different depositional sequences have been dated by using the U-series in corals ([Collier, 1990](#)). The Corinthian Marls ([von Freyberg, 1973](#)) contain evidence for the first truly marine transgression in the Corinth basin over at least the last 400 kyr. According to [Collier \(1990\)](#), continuous offlapping marine sequences above the the complex rising horst of the Corinth Isthmus requires broad and

steady uplift. It suggests that regional uplift rates exceeded hangingwall subsidence rate to create this broad uplift in an area segmented by many faults of minor displacements (throws of 5 to 20 m; Collier, 1990).

6.2.4 MB : Megara Basin

The Megara Basin is located in east of the Gulf of Corinth, between the Lechiaon Gulf and the Saronic Gulf (Figure 6.1). This half graben trends NW-SE, is 10 km wide, about 20 km long, and is bounded to the north by the Pateras fault system. The sedimentology of the syn-rift succession in the Megara Basin (Figure 6.3) is described by Theodoropoulos (1968); Bentham *et al.* (1991).

- The base of the syn-rift succession is estimated to have an age of Miocene to earliest Pliocene. The Pliocene Paliochori Group contains two formations : the Mylou Vrachia (200 m) and Pigaddi Dourakis formations (50 m). The Mylou Vrachia Formation comprises angular breccias and conglomerates overlain by sandstone of the Pigaddi Dourakis Formation. This Group consists of footwall-derived alluvial fans restricted built along the northern margin of the basin.
- A basinwide lacustrine transgression is recorded by the deposition of thick marls (Rema Mazi Formation) followed by coarse fluvio-deltaic deposits marking the beginning of a basinwide overfilled phase (Kremida Formation). The Ayio Ioannou Group contains the Rema Mazi Formation (75 to 300 m) with marls, passing transitionally from the Pigaddi Dourakis Formation below. The lake includes the construction of Gilbert-type deltas of the Kremida Formation along the main antithetic faults. These were sourced from the SW.
- The overlying (unconformable ?) Tombse Koukies Group consists of the Toumpaniari (30–150 m), the Pistarda (2–5 meters) and the Harbour Ridges Formations (75–150 meters). The Toumpaniari Formation consists of fluvial pebbly sandstones and conglomerates. The overlying Harbour Ridges Formation is made up of pebbly sandstones, calcareous sandstones, marls and lignites. The frequency of paleosol and lignite horizons increases toward the top. This group is interpreted as the continued overfilling of the basin by mainly braided stream deposits.
- Deposition of the Aleochori Group was largely controlled by the northern bounding faults. The conglomerates and sands of the Louba Formation (90–320 m) were deposited by a NE to N flowing axial fluvial system that was sourced from drainage catchments to the SE. This formation is interfingered with debris flow facies marking catastrophic event(s) from the basin margin (Ayia Sofia Formation ; 0–40 m). An ash layer found in the topmost Louba Formation has been dated (using ^{40}Ar – ^{39}Ar analyses by laser fusion) at 2.82 ± 0.06 Ma (Leeder *et al.*, 2008). Fluvial incision due to footwall uplift along the South Alkyonides coastal faults was recorded by calcretes, which unconformably cap

the abandoned Megara basin fill. The U–Pb age of these calcretes is 0.77 ± 0.08 Ma (Leeder *et al.*, 2008). With magnetostratigraphy results, both age constraints date the abandonment of the Megara Basin and the activation of the active South Alkyonides coastal faults (Figure 6.5) that presently bound the southern rift-margin at ~ 2.2 Ma.

6.2 Regional syn-rift stratigraphy

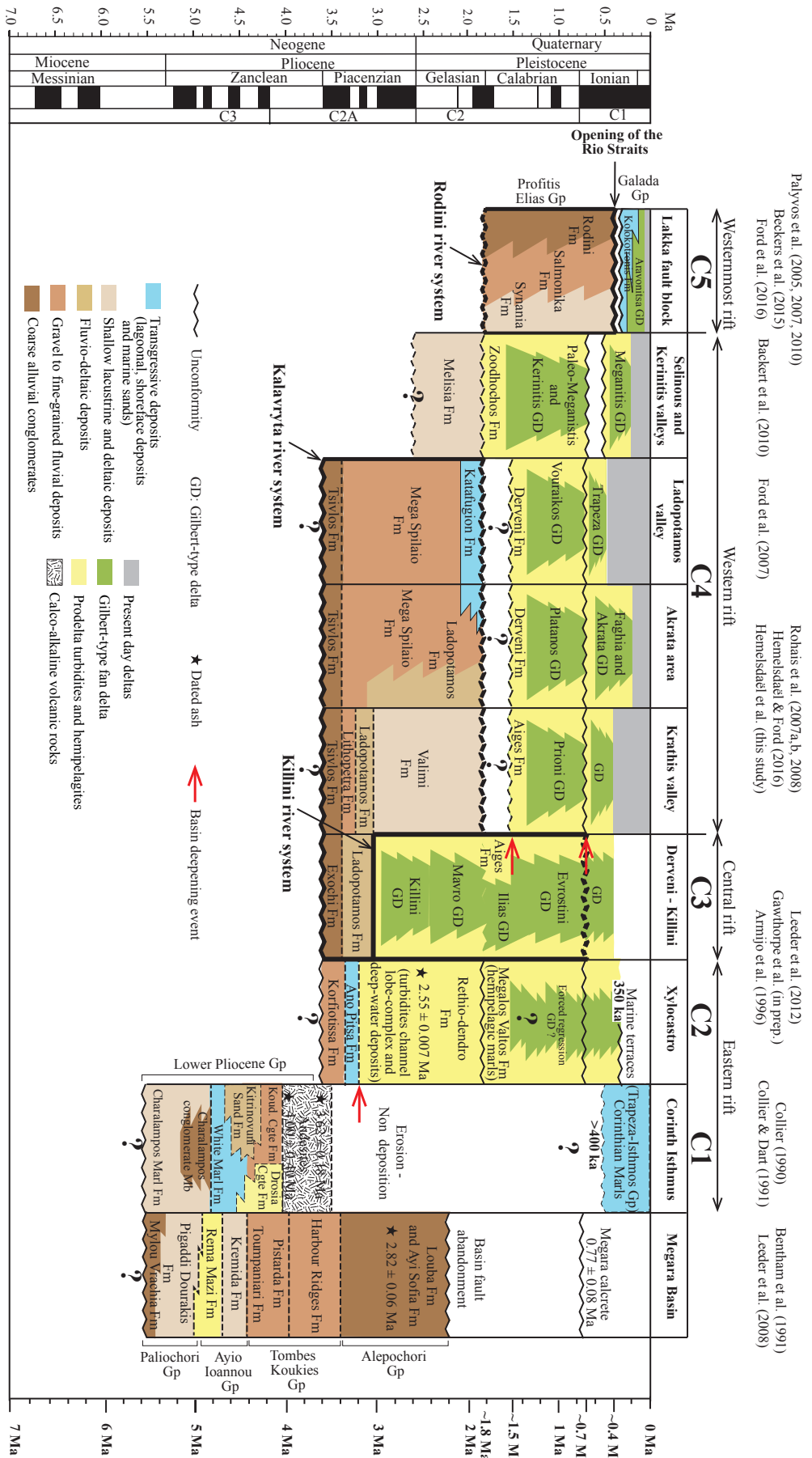


FIGURE 6.3 – Synthetic regional chronostratigraphy along the southern Corinth rift margin. Black stars indicate radiogenic ages. Dotted lines and question marks correspond to uncertain age of the stratigraphic units. Fm, Formation; Gp, Group; GD, Gilbert delta; Koud, Koudounista; Cgte, conglomerate. Used references are indicated above each column.

6.3 Corinth rift evolution

Facies defining the lithostratigraphic units in the different zones of the southern margin vary significantly. The subdivisions Lower, Middle and Upper Groups in C3 and C4 previously used are thus not adequate to establish a comprehensive regional syn-rift stratigraphy. Here, the regional stratigraphy is summarised using the overall depositional environments, as listed below :

- Coarse alluvial conglomerates
- Gravel to fine-grained fluvial deposits
- Fluvio-deltaic deposits
- Transgressive deposits and marine incursions (corals, lagoonal, shoreface deposits and marine sands)
- Shallow lacustrine and deltaic deposits
- Gilbert-type fan deltas
- Prodelta turbidites and hemipelagites

The representation of these depositional environments on the figures 6.2 and 6.3 show that they can coexist during the evolution of the rift margin. They mainly record the (i) infill of the subsiding basin by several river systems, (ii) fluvial to lacustrine transition through time, (iii) diachronous basin deepening along the margin, and (iv) persistence of palaeohighs.

We present the Corinth evolution over the last *ca.* 4 Myr in four phases that are explained below. Our paleogeographic maps combined the offshore fault traces of Nixon *et al.* (2016) and Beckers *et al.* (2015), with the onshore fault traces from our work and the recent compilation of Ford *et al.* (2016).

6.3.1 Phase 1 : Late Pliocene–Early Pleistocene (4–3.6 to 1.5 Ma)

Early extension was distributed on a predominantly north-dipping fault system across a 20–30 km-wide zone over a period of 2–3 Myr starting from around 4 Ma (Figure 6.4). The area under extension may have been wider. For example, undated normal faults are documented further south (Skourtsos & Kranis, 2009). As the amount of Phase 1 strata preserved below the Gulf is unknown, we provisionally draw the northern border below the proximal southern Gulf. This margin may have been controlled by a south-dipping fault or faults, which were later buried. The early rift closed to the west. In C4 and C3, synchronous north-dipping faults define tilted blocks 4–8 km wide. In C4, these are relatively small faults with approximately the same length (10–16 km) that accommodate similar displacements (throws of 500–1000 m ; Ford *et al.*, 2013). Total Phase 1 extension in C4 was low and extension rate was slow, estimated at 0.6–1 mm (Ford *et al.*, 2013). To the east (C3), faults accommodated considerably more displacement (Rohais *et al.*, 2007a), the largest fault being the Killini Fault with an estimated throw of over 4 km. Using our revised stratigraphy, the Phase 1 extension rate in C3 is estimated as 1.5–2.3 mm/a (assuming

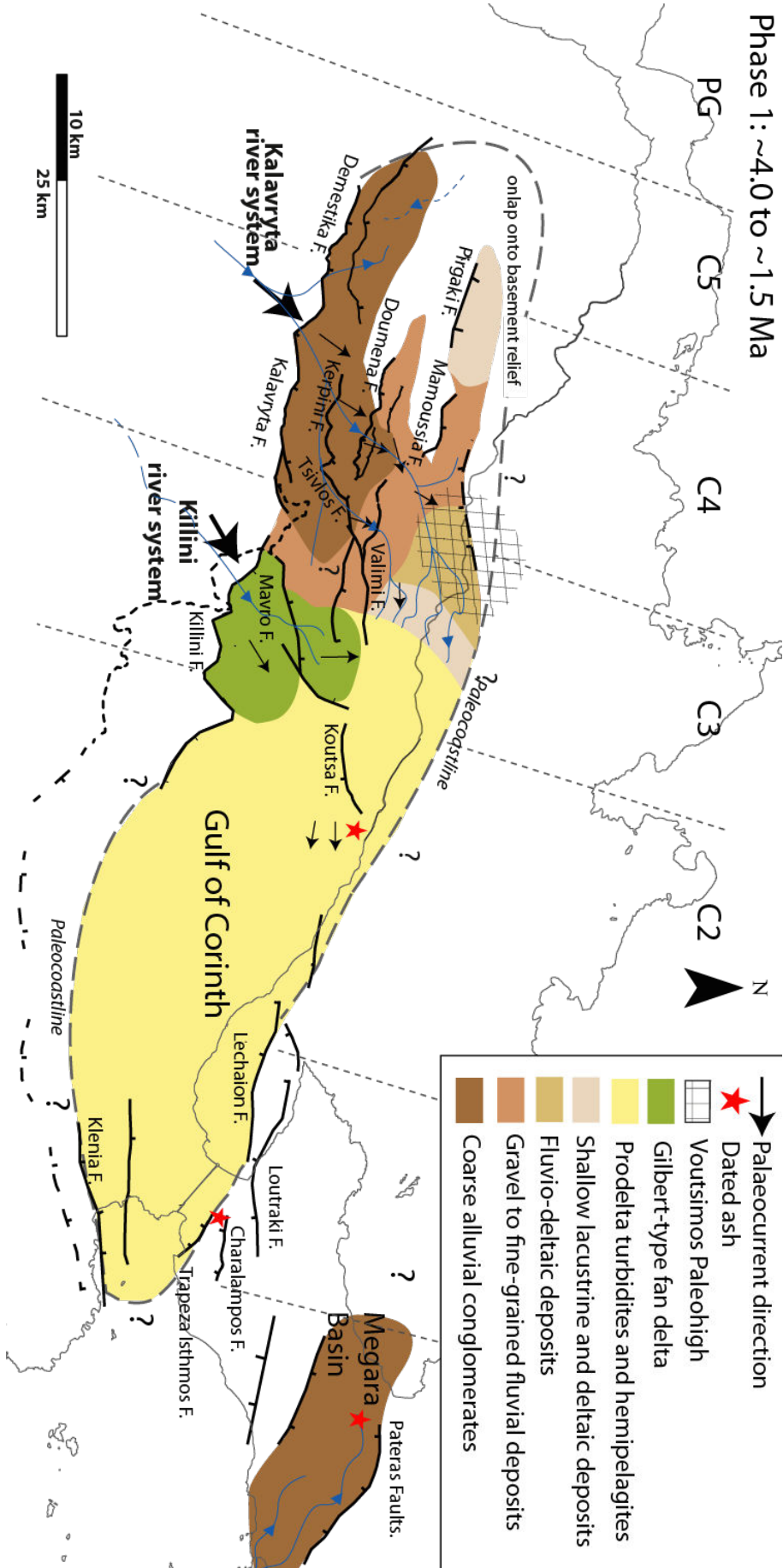


FIGURE 6.4 – Paleogeographic reconstruction of Phase 1 from ~4 to ~1.5 Ma.

rift initiation at 5–4 Ma ; [Ford *et al.*, 2013](#)).

Phase 1 is characterized by continental environments that deepen from fluvial (C4) in the west to lacustrine in the east (C3, C2) recording an overall fining eastwards. Sediments were fed into the rift from the SW by two major routing systems (Kalavryta and Killini, [Figure 6.4](#)). In C4, coarse-grained alluvial strata (1000 m thick) onlap a significant inherited relief. Sediment supply was relatively high and largely outstripped the creation of accommodation, thus burying active normal faults. Although the succession is condensed on a local palaeogeographical high between C4 and C3 (Voutsimos paleohigh, [6.4](#)), facies distribution and palaeocurrent analysis show that sediment was routed toward the NE and east. These depocentres were therefore always connected ([Rohais *et al.*, 2007b](#); [Ford *et al.*, 2013](#)) and not separated as proposed by [Ghisetti & Vezzani \(2004, 2005\)](#).

In C3, the basin very quickly became lacustrine after a first 'deepening event' at 3.2–3.0 Ma (base of the lacustrine Aiges Formation ; [Leeder *et al.*, 2012](#)). Subsequently, the Killini sediment routing system built the Killini and Mavro Gilbert delta complexes axially into the shallow lake. These delta complexes comprise stacked prograding deltas, each several tens of metres in height. The Mavro and then Killini deltas are coeval with the Valimi Formation of the Kalavryta river system. Both Kalavryta and Killini river systems evolved independently and fed the same basin ([Figure 6.4](#)).

Coarse-grained facies are mostly confined to the western part of the rift (C4). In contrast, the central and eastern rift (C3 and C2) are predominated by fine-grained basinal sediments and appear to have been sediment-starved throughout rift development. The concentration of coarse-grained alluvial conglomerates along the south and west of the early rift is interpreted as being due to the capture of well-established antecedent rivers of the Hellenide mountain belt. In the eastern lacustrine succession, published palaeocurrent data indicate that sediment supply was predominantly axial and from the west ([Leeder *et al.*, 2012](#)). Grain-size and facies distribution in the early rift were therefore controlled by : (i) the position of antecedent rivers along the southern rift margin, (ii) the rate of sediment supply from these rivers, and (iii) their interaction with evolving accommodation on the young fault system.

The onset of rifting is estimated at about 3.6 Ma in the western Corinth (C4, our study) but is older in the eastern rift (?4–5 Ma). In C2, the southern limit of the basin is highly uncertain and there is no data documenting active structures at this time. In C1, the Klenia, Loutraki and Lechaion Faults were active and marked the eastern margins of the Corinth basin ([Collier & Dart, 1991](#); [Charalampakis *et al.*, 2014](#)). We assume here that the basin was closed to the east during the Phase 1, but it possibly extended further to the south. During the Later Pliocene, the Megara Basin was infilled by an axial drainage flowing toward the NW. Equivalent sediments are likely be present in the basal offshore succession of the eastern Alkyonides Gulf, infilling preexisting basement topography ([Sakellariou *et al.*, 2007](#)).

6.3.2 Phase 2 : Early–Middle Pleistocene (1.5 to -0.7 Ma)

In the Early Pleistocene, starting at around 1.8 Ma, the southern rift margin migrated northwards in C3 and C4 by approximately 15 and 10 km, respectively (Figure 6.5). At the same time, the rift propagated west to form a new depocentre in C5. This phase of northwards and westwards fault migration (1.8–1.5 Ma) is correlated with a significant period of erosion that marks the base of the Middle Group in C4 (but not C3). New south-dipping faults were also initiated on the northern side of the rift, and played a major role in controlling a more symmetrical and deeper depocentre, largely corresponding to the present-day Gulf in C3 and C2 (Bell *et al.*, 2009; Nixon *et al.*, 2016). During this phase, the rift was 20–25 km wide in C3, and narrowed to the west to 10–15 km in C4 and C5.

Eustatic control on delta stratigraphic architecture (Backert *et al.*, 2010), local presence of limestones (Ford *et al.*, 2007), and marine Foraminifera assemblages (Rohais *et al.*, 2007b), all indicate that the main 'Corinth Basin' was at least periodically marine to brackish in character during the Early–Middle Pleistocene. The Psaromita–Aegion High separated the C5 fluvio-lacustrine depocentre from the main rift. The principal north-dipping faults along the southern rift margin were the Xylocastro–Evrostini–Valimi fault system, and the DF (Derveni Fault) in C3, the PMF in C4, and the Lakka and Panachaikon faults in C5. On the northern rift margin, principal south-dipping faults were the Galaxidi Fault in C3 (known as the East Channel Fault in; Bell *et al.*, 2008), the West Channel Fault in C4 and the Trizonia Fault in C5. In C3, the highest sediment accumulation occurred between the Galaxidi and Derveni Faults, focusing more towards the south-dipping Galaxidi Fault (Figure 6.5). The Galaxidi Fault has an estimated throw of 1.3 km and was principally active during Phase 2 (Bell *et al.*, 2009). The DF, still active today, is by far the largest fault in C3, with a total estimated throw of around 4 km (Hemelsdaël & Ford, 2016). At the same time, the Valimi–Evrostini Fault system to the south accommodated 1000 m throw during deposition of the Ilias and Evrostini deltas (Figure 6.5). The estimated extension rate in C4 doubled to 2–2.5 mm/yr during Phase 2 (Ford *et al.*, 2013). Extension may have increased to the east in C3 and C2, as reflected in the position of the main depocentre.

The northward fault migration at the beginning of Phase 2 (at about 1.8 Ma, transition Lower/Middle Groups) was preceded by a marine transgression at the top of the Lower Group (Katafugion Formation) in C4 followed by an enigmatic phase of (submarine) erosion in the PMF block (Ford *et al.*, 2007). In C4, this deepening event is recorded by a marked change from a continental fluvial environment to a gradually deepening basin where large Gilbert deltas began to build. Equivalent prodelta turbidites and hemipelagics are preserved both onshore and offshore (most probably the seismic stratigraphic unit SU1; Nixon *et al.*, 2016).

The fluvial network underwent a radical reorganization, changing from a NE-flowing network to a new system of equally spaced (6–8 km), north-flowing rivers. These powerfully erosive transverse rivers and incised the uplifting footwall area to supply the giant Gilbert deltas along the

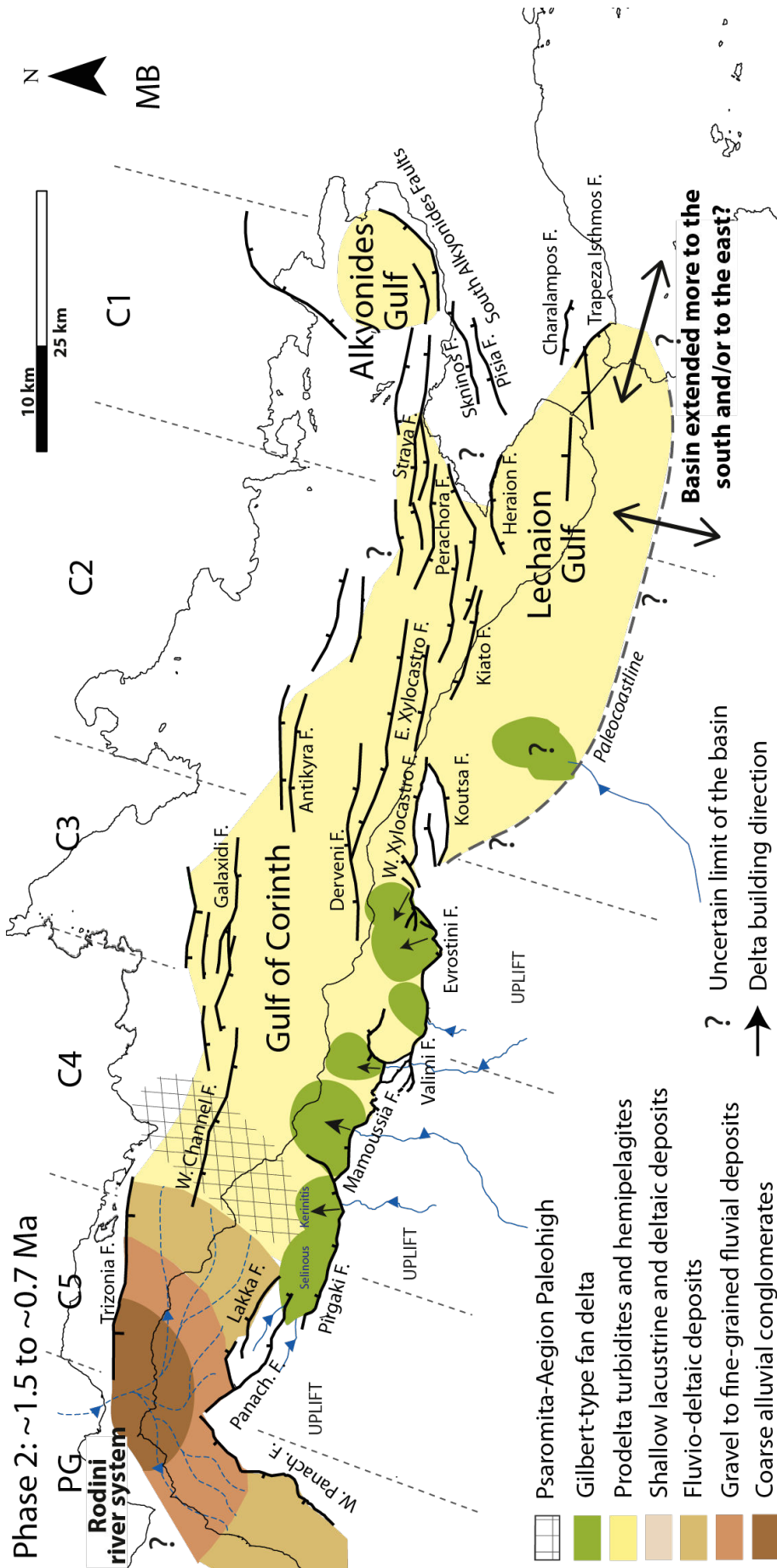


FIGURE 6.5 – Paleogeographic reconstruction of Phase 2 from ~1.5 to ~0.7 Ma.

newly formed rift margin. The combined effects of footwall uplift due to hangingwall fault migration, associated with basin deepening and increasing extension rate can explain the northward deflection of the antecedent rivers.

In C3, the deepening event is not marked by a major sedimentological change, as Gilbert deltas were already building into a lacustrine basin. However, deeper-water conditions are recorded by the distinct stratal architecture of the new Evrostini deltas, characterized by aggradation–progradation and significant foreset height (hundreds of metres). As the two Phase 2 deltas lie directly north of the Phase 1 deltas, it is reasonable to suggest that they were supplied by the same north-flowing drainage system (Rohais *et al.*, 2007a).

To the west, the new C5 depocentre was controlled by the Lakka and Panachaikon Faults to the south, and the Trizonia Fault and an unidentified fault to the north and NW (Beckers *et al.*, 2015). The lacustrine basin was supplied from the north by the Rodini fluvial system, which may also have supplied the eastern Patras rift (Palyvos *et al.*, 2008). During Phase 2, the C5 area received little or no sediment from the south. It was limited to the east by the Psaromita–Aegion High, as evidenced by a thin and incomplete succession onlapping pronounced palaeorelief, major unconformities, and local facies and thickness changes.

In C2, the southern limit of the basin is still unknown so we cannot yet establish whether there was an active structure at this time or northward migration of depocentres. Although, Gilbert-type deltas in C2 are poorly studied, they can be ascribed to Phase 2 (see forced regressive deltas in Figure 6.3). As represented in Figure 6.5, the limited accommodation required to build these deltas was possibly generated by the south-dipping Koutsia Fault. These Gilbert deltas were possibly built along an unfaulted rift margin, into a shallow lacustrine margin. The limited creation of accommodation at the basin margin would explain the strong prograding pattern of the deltas (c.f. question mark on Figure 6.5).

In the central rift (C2), minimal sedimentation is registered in the hangingwall of the Xylokastró Fault at this time (Nixon *et al.*, 2016). A number of south dipping faults was active, including the Heraion Fault in the Lechiaon Gulf, and the Perachora Fault (Charalampakis *et al.*, 2014). In the Megara basin, deformation ceased and transferred northwest to the Alkyonides Gulf between at about 2.2 Ma with initiation of north to NW dipping faults along the southern margin of the Alkyonides Gulf (Leeder *et al.*, 2008). Nixon *et al.* (2016) propose that the Alkyonides Gulf was isolated from the main Corinth basin at this time. Again, the extent of the basin to the south and to the east is uncertain. The basin may have been temporarily opened to the Aegean sea, bringing marine to brackish conditions into the gulf.

6.3.3 Phase 3 : Calabrian–Middle Ionian (0.7 to 0.4 Ma)

In the Middle Pleistocene, at around 0.7 Ma, the southern basin margin, migrated northwards (in C3 and C4) by some 5–10 km (Figure 6.6). In C3-C2, the West Xylokastró Fault was

progressively abandoned as deformation focused onto the pre-existing DF, linking eastwards with the Lykoporia and East Xylocastro Faults (Nixon *et al.*, 2016). Displacement gradually decreased on the south-dipping Galixidi and West Channel faults and was transferred onto the south dipping Eratini fault system (McNeill *et al.*, 2005; Bell *et al.*, 2008, 2009).

In C4, the PMF was abandoned as displacement transferred onto the East and West Helike fault system, which gradually propagated eastwards to link to the DF (Hemelsdaël & Ford, 2016). Deposition increased in the deep basin, but again, thinned westwards onto the Psaromita–Aegion High. The North and South Eratini Faults developed to the north of the now inactive West Channel Fault. However, these faults played a minor role in the development of the C4 depocentre. The rift in C4 had an estimated width of 10–12 km. In C5, the Lakka-Trizonia depocentre and Psaromita–Aegion High retained the same configuration as in Phase 2.

In the eastern rift (C2 and C1), north of Lechiaon Gulf, the fault system became more active and more complex, including the north-dipping Perachora and Strava faults. A graben formed with the activation of the south-dipping Domvrema Fault (Figure 6.6). The fault activity migrated northward not only along the southern margin, but also along the northern margin by around 10–15 km. However, the Alkyonides Gulf remained disconnected from the Corinth Gulf at this time (Nixon *et al.*, 2016).

In C4, major rivers continued to flow north across the uplifting footwall of the East and West Helike faults, cannibalizing their own Phase 2 deltas (Figure 6.2). Numerous small Gilbert deltas record the progressive uplift of the western PMF block that may have locally inherited a bathymetry of up to 400 m basinwards of the large Phase 2 deltas. However, where the new East Helike Fault cut across a major delta (e.g. Vouraikos and Platanos, Figure 6.2), new deltas began to build immediately into the hanging wall of the new fault. The Krathis River diverted ENE to build the new Akrata delta across the evolving relay ramp between the DF and EHF. East of Akrata, no major river supplied coarse-grained sediments into the rift. Mainly fine-grained prodelta and hemipelagic sediments were deposited here (lower SU2 of Nixon *et al.*, 2016).

While we focus on the persistence of rivers throughout the rift history, some minor flowing rivers were reversed by footwall uplift. In C3–C2, footwall uplift (south of the Xylocastro Fault) caused the river system to turn south into the Feneos endorheic basin (Rohais *et al.*, 2007a), thus terminating a major supply route (Killini). Clendenon (2009) and Brocard *et al.* (2012) suggest that rivers defeat by footwall uplift in the Corinth rift may be facilitated by the ability of rivers to partly discharge water through large karstic systems. In C2, the uplift of the southern margin is possibly related to regional uplift rather than direct footwall uplift as no faulted margin is evidenced (Figure 6.6).

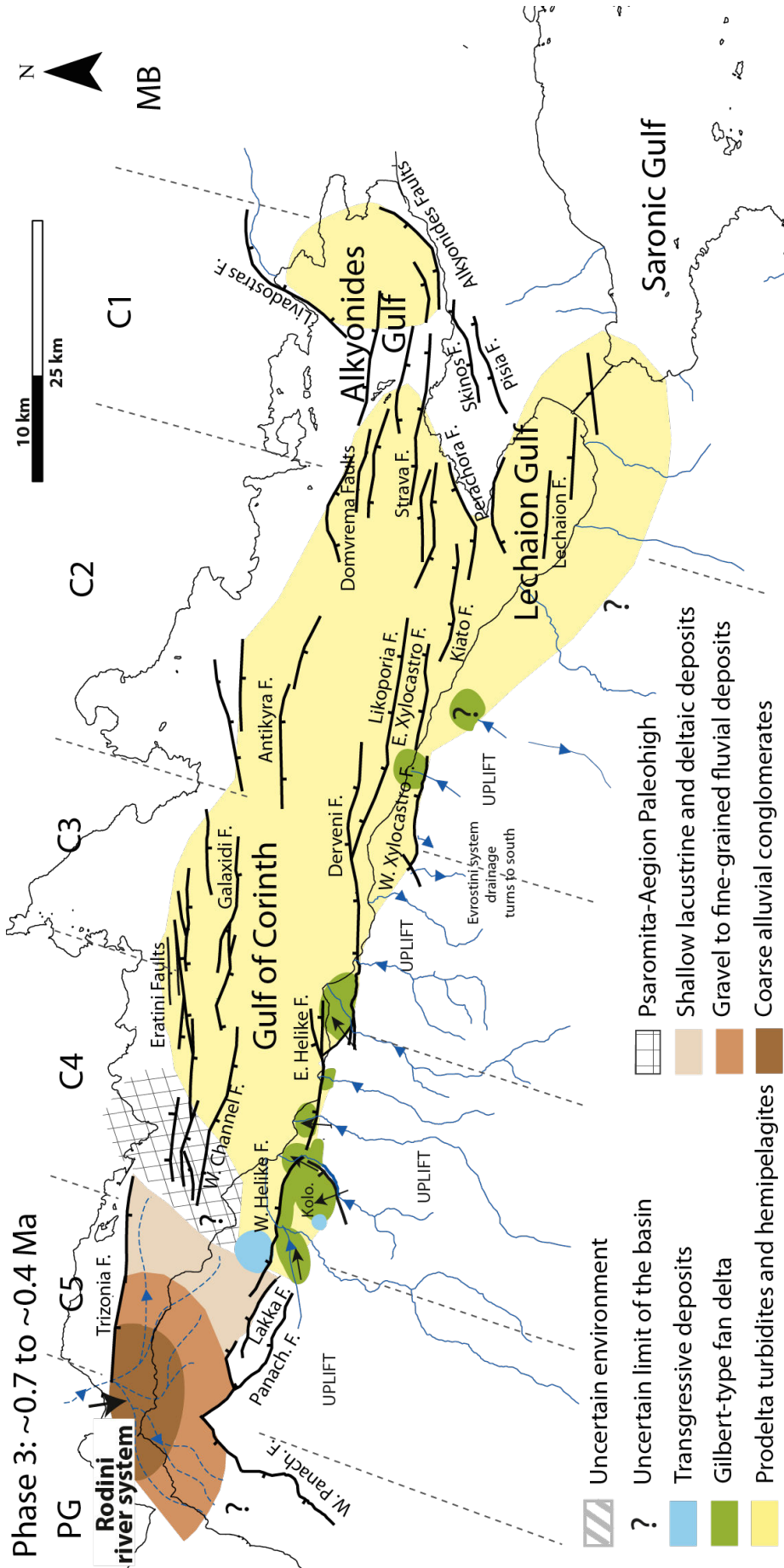


FIGURE 6.6 – Paleogeographic reconstruction of Phase 3 from ~0.7 to ~0.4 Ma. Panach. F. : Panachaikon Fault.

6.3.4 Phase 4 : Middle Ionian–present day (0.4–Present Ma)

From 400 ka onwards, nearly all sedimentation was concentrated in the Gulf and most probably consisted of predominantly fine-grained prodelta facies and hemipelagics. The eastern rift is clearly sediment-starved, with bathymetry increasing eastwards to over 800 m. In C4 and western C3, however, major rivers continued (and continue today) to flow north to build coarse-grained Gilbert-type deltas into the Gulf across basin-bounding faults.

During Phase 3 and Phase 4, from approximately 620 ka to present day, activity increased on major rift-bounding north-dipping faults (East Helike, Derveni, Lykoporia, East Xylocastro, North Kiato and Perachora faults) to create a single major depocentre in the southern Gulf (C2, C3 and eastern C4). The progressive evolution and linkage of numerous hangingwall depocentres along these faults, eventually formed a 40 km long half-graben depocentre centred in C2 (Figure 6.7). In the Alkyonides Gulf, deformation became more focussed on the north dipping East Alkyonides Fault, while the Heraion Fault continued to control deposition in the Lechaion Gulf (Nixon *et al.*, 2016). In C2, the uplift of the southern margin over the last 350 ka is well recorded by the large marine terraces (?). These terraces give a component of regional uplift of less than 0.3 mm/yr. The strong progradation of the coastal system in the Corinth Isthmus (C1) records the uplift of the central horst and sea-level variations over the last 430 ka (Collier, 1990). The basin was therefore closed the gulf to the east at this time.

While the offshore succession still thins markedly westwards in C4, owing to the persistent influence of the Psaromita-Aegion High (Ford *et al.*, 2016), the basin is now clearly connected to the C5 depocentre (Figure 6.7). The Aegion Fault is the youngest fault of the system, dated at 50–60 ka (Cornet *et al.*, 2004). The northern margin of the C5 rift also migrated north from the Trizonia Fault onto the Marathias and Nafpaktos faults (Beckers *et al.*, 2015). The Rodini river system was forced to incise headward (northward), and to build the new Mornos delta in the hangingwall of the Nafpaktos and Marathias Faults since the last ~130 ka (Figure 6.7). The westernmost Gulf is therefore controlled by the most recently initiated (youngest) faults. Unlike the main rift, it retains a relatively symmetrical fault system.

The most intense seismicity is also concentrated below the present-day Gulf in C5 (?Lambotte *et al.*, 2014). Seismicity data indicate that it is possible that the Panachaikon and Lakka faults are also active. The Rion Straits opened to the Patras Gulf for the first time at around 400 ka as a result of the initiation of the Psathopyrgos Fault. Water depth on the Rion sill is currently 60 m, indicating that this seaway would be cut off during sea-level lowstands. The transition from lacustrine to marine conditions in the Gulf at the time of the last sea level rise, at approximately 12 ka, has been well documented in cored offshore sediments (Moretti *et al.*, 2003; Sakellariou *et al.*, 2007; Campos *et al.*, 2014).

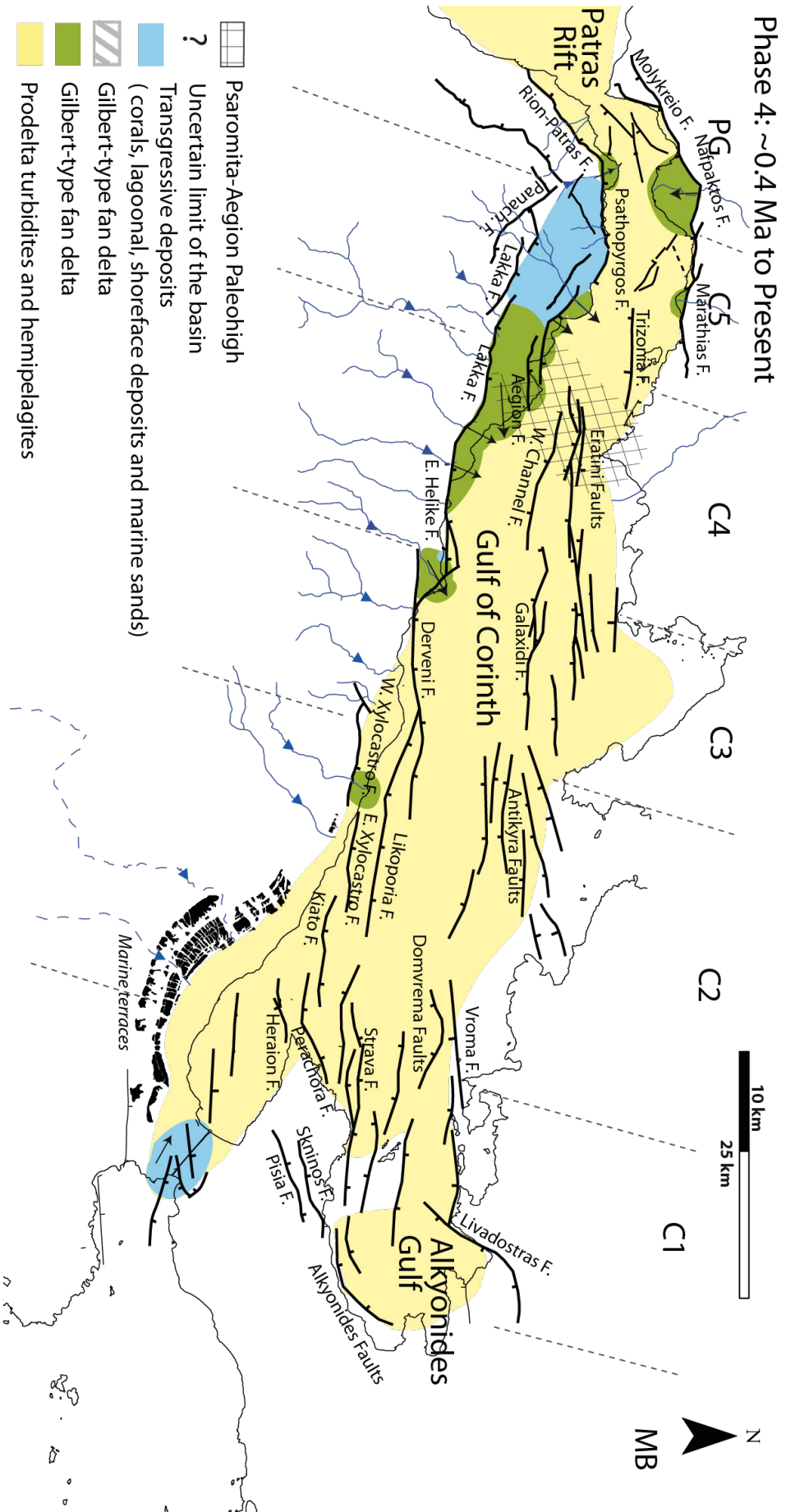


FIGURE 6.7 – Paleogeographic reconstruction of Phase 4 from ~0.4 Ma to Present.

6.4 Significance for rift basin deepening

The evolution of the Corinth rift is characterised by a strong lateral asymmetry in the volume of incoming sediments. The rift is older in the east where sediment supply was low and fine grained throughout its history. In contrast, in the west the rift was superimposed on high relief inherited from the Hellenide orogen. Here, a strong antecedent drainage supplied high volumes of coarse sediment from the onset of rifting. The erosional power of these antecedent rivers allowed northward drainage into the rift to persist throughout rift migration of the southern rift shoulder uplift. The E-W reconstruction of regional chronostratigraphy shows that basin deepening was diachronous, due to northward fault migration and lateral (mainly westward) rift propagation.

High sediment supply from the western rift can mask deepening events in some parts of the active rift. This study shows that the concepts of rift initiation and 'rift climax' should be used with caution as multiple deepening events occur and they may not be recorded basinwide. A basin deepening event does not necessarily correspond to the onset of the 'rift climax' with an acceleration of the deformation in the basin.

The concept of 'rift climax' suggests an 'abrupt' change from fluvial to lacustrine sedimentation. The resolution achieved in this study clearly shows that basin deepening is a progressive phenomenon, as demonstrated deltaic succession of the Killini river system in C3. In C4, the basin deepening at about 1.8 Ma, fluvial deposits (Ladopotamos Formation) are overlain by transgressive (lagoonal and shoreface) deposits, then followed by a major unconformity due to the drainage reorganisation (Figures 3.6 and 6.3). The apparent abruptness of the deepening event is revealed by the unconformity, which actually represents a hiatus of about 300 kyr between fault migration, drainage re-organisation and stratigraphic record.

6.5 Compilation of rivers behaviour

Antecedent river systems interact at different scales and time spans with evolving rift fault systems. Here we present a summary of different interactions observed in the Corinth Rift. We divide these interactions into two groups. Firstly the response of antecedent rivers to footwall uplift and secondly their response to fault migration.

6.5.1 Response to footwall uplift

The different interplays between rivers and growing faults are controlled by the competition between river incision and footwall uplift (Figure 6.8). They include the cases of :

- a through-going river (Figures 6.2 and 6.8A ; e.g. Vouraikos Gilbert delta),
- drainage reversal and river abandonment (Figures 6.2 and 6.8B ; e.g. the Olvios River turning south into the Feneos endorheic basin),

- and river deflection into relay zones (Figure 6.8D). Our work on the Akrata relay zone (Figure 6.2 and chapter 5) shows that river deflection and capture by relay zone occur at the scale of $10^4 - 10^5$ years, and the fault propagation and linkage occur in less than 10^6 years.
- The case of drainage reversal and deflection toward subsiding zone (Figure 6.8C) is not observed in the Corinth rift, but has been documented for example along the margin of Tanganyika lake (termed as 'backshsed drainage reentrant' by Cohen, 1991).

6.5.2 Response to fault migration

The **Kalavryta river system** represents the largest antecedent drainage system captured by the westward migrating rift. This river system evolved over about 2.0 Myr and developed over a distance of about 30 km. The through-going Kalavryta river system developed above active faults that were buried below the subsiding alluvial plain. This has been explained by long-term sediment supply by the antecedent rivers (Chapter 4). This river system was then re-organised by later northward migration of fault activity.

The **Killini River system** comprising the Killini, Mavro and Evrostini deltas was fed by a transverse drainage system recording hangingwall migration almost over 3 Myrs. Faults migrate northward and the deltas record progressive basin deepening as explained above.

The **Rodini river system** interacted with a footwall migrating fault system. Due to footwall migration of the fault system, the river abandoned its older deposits to build a new system in the footwall of the abandoned fault. This river system developed since the last 1.8 Ma and extended over about 20 km.

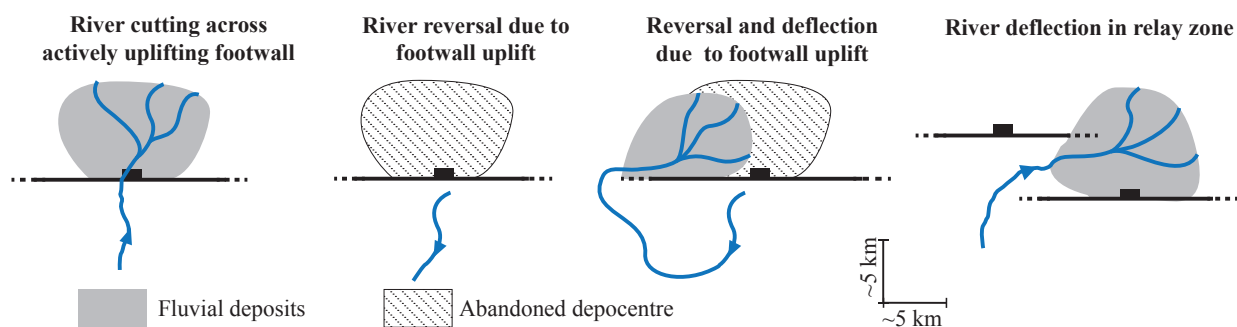


FIGURE 6.8 – Response of rivers to footwall uplift. Summary of the interactions between a pre-existing river and a growing normal fault. River cuts through an active fault when river incision rate exceeds or equals footwall uplift. Otherwise, the rivers are reversed or deflected toward topographic lows.

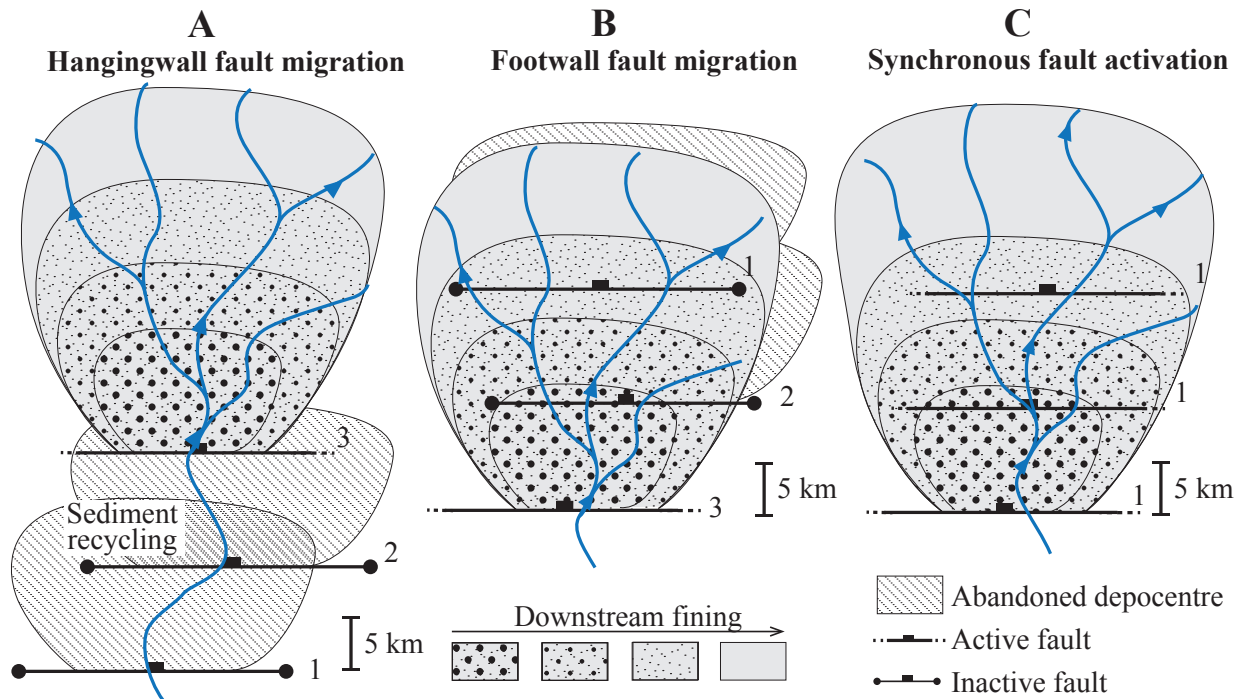


FIGURE 6.9 – Compilation of through-going river systems during the development of a normal fault array and showing different sequences of fault activation : (A) Hangingwall fault migration, (B) Footwall fault migration, (C) synchronous fault activation. Numbers 1, 2, 3 correspond to the order of fault activation. See Figure 6.10 for cross section representations of these models

6.6 Significance of through-going river systems

The Kalavryta, Killini and Rodini river systems are all through-going systems that played a primary role in the redistribution of mass and grain-size distribution in the rift. The interactions between through-going rivers and an active fault array are the main focus of this study (Figure 6.9). One of the main characteristic of through-going river systems is the sediment distribution across different active fault blocks (Figure 6.10B) and the absence (or limited evidence) of footwall-derived sediments. This characteristic significantly differs from the standard model of syn-rift infill by consequent interior drainage systems (Figure 6.10A). The cases of synchronous fault activity, hangingwall and footwall fault migrations are investigated. All present distinct facies distribution, geometries and filling history of the depocentres (Figure 6.10).

The main idea developed here is that synchronous activation of the faults enables the burial of active faults by the through-going/antecedent rivers, and thus downstream fining across different fault blocks (Figure 6.10B). Burial of the faults by the depositional system has been already documented but mainly under the influence pre-rift bathymetry (Ravnås & Steel, 1998). Our study of the Kalavryta river system suggests that burial of the active faults was possible because of pre-existing high sediment supply that continuously fed the early rift basin (chapitre 4). This highlights the role of high sediment supply and $A < S$ in the development of the normal fault

systems, as well as the positive feedback between sedimentation and tectonics (Maniatis *et al.*, 2009; Olive & Behn, 2014).

The exact conditions necessary to bury active faults by fluvial sedimentation remain to be investigated. **Does burial of active faults depend on a critical threshold in the balance between sediment supply and subsidence?** The next logical step in the understanding of this phenomenon would be the (3D ?) numerical modelling of surface processes and syn-rift infill coupled with normal fault growth. The parametrisation of sediment supply and subsidence variations within a mechanical model would help to understand the boundary conditions that control stratigraphic architectures in rift basins.

Synchronous activation and growth of the fault system (Figure 6.10A, B) follows the domino-style model (e.g. Proffett, 1977; Gans & Miller, 1983; Fedo & Miller, 1992) where both the planar faults and blocks rotate assuming uniform extension. This model is the simplest representation of a growing fault system (Schlische, 1991). Rotation of the fault blocks increases dips of strata generally between 0 and 30°, and decreases fault dips from 60° to 30° (Withjack *et al.*, 2002). This purely geometric model does not explain why new faults are created before the faults reach their lockup angle of about 30° (Collettini & Sibson, 2001).

In the cases of footwall and hangingwall fault migrations (Figure 6.10C, D), nucleation of the next fault occurs at a distance less than the width of the block when the activity of the former fault completely ceases. Moreover, the amplitude of the subsidence remains constant between the different fault activations. These simplified conceptual end-member models are used to illustrate the distinct stratigraphic patterns (Figure 6.10). The migration of fault activity is more complex and transitional in real-world systems. While a new fault is activated, the activity of the former fault starts to decrease. Thus, during hangingwall and footwall fault migrations, subsidence is distributed across several active (nascent and dying) faults over a short time window (probably from few 100's kyr to less than 1 Ma).

When faults migrate into their footwall (Figure 6.10C), inactive faults can be buried and inactive faults become progressively rotated by the subsequent fault activations. During Phase 1 several faults were activated at different times (Figure 6.11). The Prinos Fault (Figure 4.9) was active during the incipient stages of rifting and probably became inactive at about 2.8–3.0 Ma (Figure 6.11). Faulting was transferred to the south onto the Kerpini Fault, which rotated the Prinos Fault in its hangingwall. Similarly, the small rotated intra-block faults in the hangingwall in the Valimi Fault (Figures 4.9 and 3.5). This last example corresponds to distributed deformation on many small faults during the early rift phase before the larger faults take over, rather than an example of footwall fault migration. The Valimi Fault accommodated more subsidence and were active for a longer period of time (about 2.5–3.0 Ma; Figure 6.11). The newly formed Valimi depocentre unconformably overlies the early intra-block faults (Figure 3.5). This produces onlap geometries within the fanning wedge (Figure 6.10C; see also Withjack *et al.*, 2002).

When faults migrate toward their hangingwall, the stratal wedge can be cut by activation of new fault (Figure 6.10D). While onlap geometry is recorded at the contact with pre-rift rocks, toplap geometry can be generated between two 'generations' of wedges. Our simplified conceptual cross sections (Figure 6.10) are vertically exaggerated; onlap/toplap geometries are more subtle in outcrops. The geometric relationships between the fanning wedges mainly depend on the sense of the fault migration and the amplitude of the rotation before a new fault is created. Syn-rift stratigraphic patterns induced by hangingwall and footwall fault migrations are poorly investigated in present numerical experiments of normal faulting (e.g. [Ter Voorde & Cloetingh, 1996](#)) and should be the focus of future research.

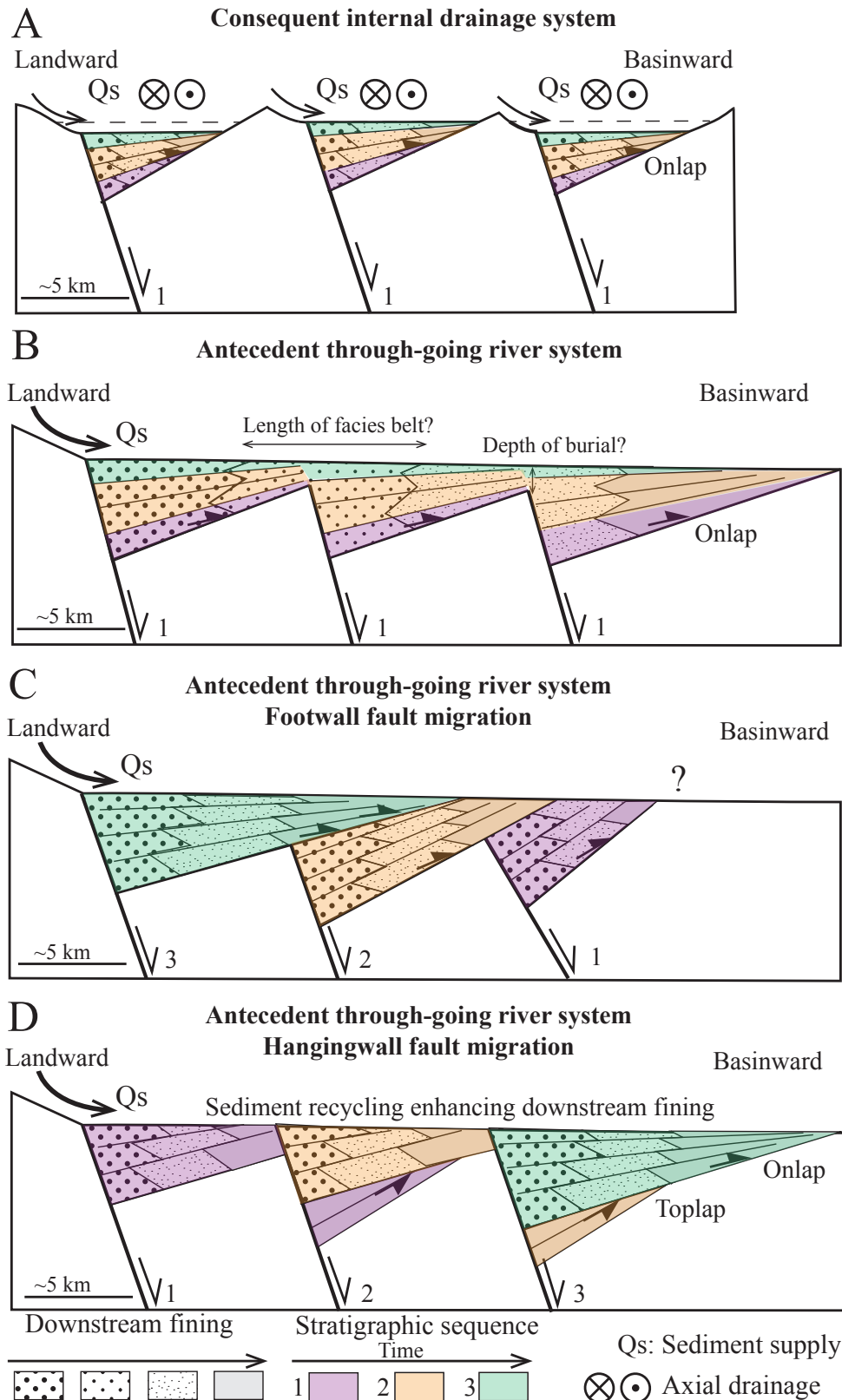


FIGURE 6.10 – Simplified transverse cross sections of three normal fault blocks with equally-spaced faults. **(A)** : Synchronous fault activation with isolated hangingwall depocentres including footwall-derived (transverse) and axial sedimentation. Individual fault blocks are characterised by internal drainage system evolving at different base levels. **(B to D)** Impact of the sequence of normal fault activation on facies distributed by an antecedent/through-going river systems. **(B)** Synchronous fault activation and burial of the faults by the depositional system ; **(C)** footwall fault migration ; **(D)** hangingwall fault migration.

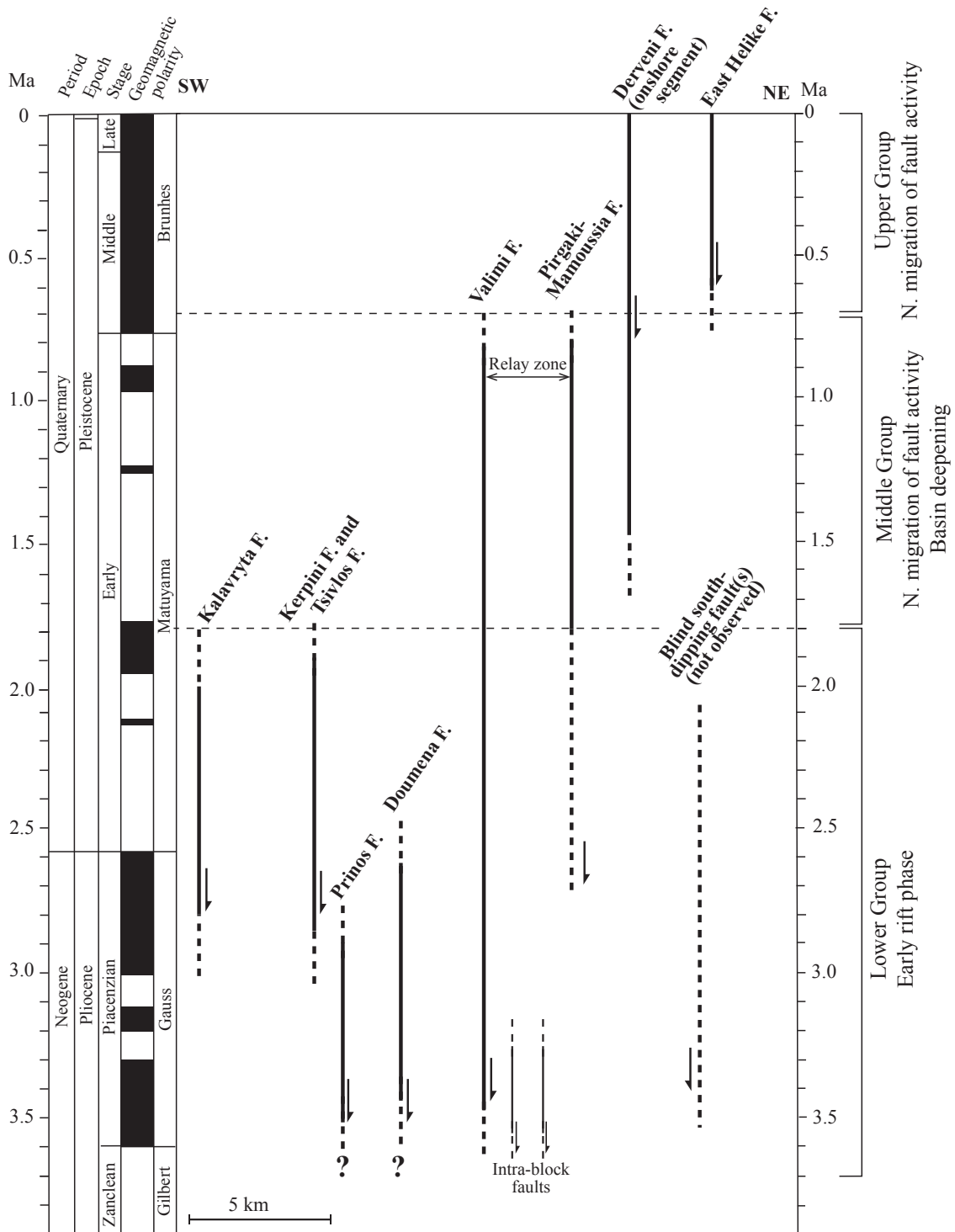


FIGURE 6.11 – Chronology of fault activation (based on the correlation model presented in chapters 3) through the rift history along a N-S transect located in the onshore part of C4 zone. Intra-blocks faults are represented in the Valimi fault blocks but they are present everywhere in the study area. Chronostratigraphy from [Gradstein et al. \(2012\)](#), magnetostratigraphy from [Lourens et al. \(2004\)](#).

Conclusions générales et perspectives

Cette thèse documente l'**enregistrement stratigraphique des rivières antécédentes** pendant les processus de croissance et de migration des failles normales. Cette thématique vise à mieux comprendre les processus tectono-sédimentaires pendant la **phase d'initiation du rifting continental**. Peu de rifts présentent l'opportunité d'étudier en détail cette phase grâce à l'enregistrement sédimentaire. De plus, le rôle des rivières antécédentes dans la distribution des faciès reste très mal connu. Dans la partie ouest de la marge sud du rift de Corinthe (Grèce), les premiers dépôts syn-rift sont exposés dans différents blocs de failles normales inactifs et soulevés. La démarche qui a été entreprise pour étudier les interactions entre les rivières antécédentes et le rifting est la suivante :

- **Acquisition de données de terrain,**
- **Datation des séries fluvio-deltaïques et lacustres à partir d'une approche pluridisciplinaire** (magnétostratigraphie, biostratigraphie, géochimie des isotopes cosmogéniques ^{26}Al et ^{10}Be),
- **Construction d'un modèle chronostratigraphique à l'initiation du rift,**
- **Implications sur les modèles tectono-stratigraphiques existants.**

Les travaux de terrain ont permis de construire une base de données cartographique importante et originale dans la partie ouest du rift de Corinthe (entre les villes d'Akrata, Diakopto et Kalavryta). La cartographie et la sédimentologie des faciès syn-rift ont permis le **découpage lithostratigraphique dans plusieurs blocs de failles**. La cartographie des unités lithostratigraphiques met non seulement en évidence des variations de faciès internes aux blocs de failles, mais aussi des variations de faciès progressives d'un bloc à un autre.

L'initiation de la rift de Corinthe dans sa partie est ("Lower Group") est caractérisée par le **développement d'un système fluvial à travers plusieurs failles normales actives** au cours du Plio-Pléistocène ("Kalavryta river system"). **La stratigraphie syn-rift peut donc être corrélée entre les blocs de failles normales**. Les dépôts syn-rift deviennent de plus en plus fins depuis un pôle fluvial proximal au sud, vers un pôle plus distal fluvio-lacustre et deltaïque au nord-est du secteur (voir chapitre 4). Les données de terrain sont couplées à des travaux de datations afin de contraindre en temps l'activité des failles en lien avec le développement de ce système fluvial. Le défi majeur est d'obtenir des **âges précis dans les dépôts alluviaux grossiers plio-quaternaires** pour quantifier les processus tectono-sédimentaires à l'initiation du rift (chapitre 3). Les processus géologiques qui l'on tente de documenter se produisent en quelques millions voire quelques centaines de milliers d'années. Cette résolution temporelle est difficile à atteindre dans les systèmes de dépôts jeunes et contrôlés par une activité tectonique rapide.

La magnéto-stratigraphie dans quatre blocs de failles normales montre peu d'inversions de polarités magnétiques (chapitre 3). Une inversion de polarité (à 2,8 Ma entre les chrons Gauss et Matuyama) peut être corrélée à l'échelle de la zone d'étude. Ces mêmes séries sédimentaires ont été étudiées pour obtenir des âges biostratigraphiques à partir des dents de micromammifères, charophytes gastéropodes. La reconnaissance de certaines espèces a permis de définir des âges minimaux ou maximaux. Malheureusement, l'analyse des isotopes cosmogéniques ^{26}Al et ^{10}Be pour la détermination d'âges d'enfouissement n'ont pas permis d'obtenir d'âges précis.

Afin de corréliser les contraintes temporelles dans les différents blocs de failles, des "lignes de temps" ont été interprétées. Ces "lignes de temps" suivent les strates et recourent plusieurs unités lithostratigraphiques, mettant ainsi en évidence la complexité de la distribution des faciès dans le bassin alluvial/fluvial. Cette exercice de corrélation a été possible grâce à la continuité de certaines "lignes de temps" dans plusieurs blocs, permettant de subdiviser la succession syn-rift du "Lower Group" en cinq stades d'évolution (chapitre 4). Les résultats de datation et la cartographie détaillée des faciès syn-rift sont donc ici complémentaires et permettent de construire un modèle chronostratigraphique entre $\sim 3,6$ et $\sim 1,8$ Ma.

Les cinq stades d'évolution montrent (chapitre 4) :

- Une première phase de **remplissage des paléoreliefs** (environ 400 m) par les dépôts fluviaux conglomératiques grossiers (entre $\sim 3,6$ et $\sim 3,5$ Ma).
- Une phase de **rétrogradation-aggradation** et le développement d'un **système fluvial distributaire** (entre $\sim 3,5$ et $\sim 3,1$ Ma) caractérisé par l'évolution radiale des faciès. Le développement d'un système distributaire est aussi démontré par les directions de paléocourants.
- Une **progradation-aggradation** continue des faciès conglomératiques pendant la suite du développement du système fluvial (entre $\sim 3,1$ et $\sim 1,8$ Ma).
- Une ouverture du rift et une **migration du système de failles normales vers le sud-ouest**.

La présence d'un système fluvial antécédent ("Kalavryta river system") à l'initiation du rift a été suggérée par :

- La présence d'un **paléorelief hérité de la chaîne hellénique** ;
- L'**enfouissement des failles**, et la quasi absence de rivières transverses conséquentes et de cônes alluviaux (incluant les dépôts gravitaires) aux pieds des failles ;
- Une entrée principale des sédiments depuis laquelle se développe le système fluvial ;
- L'**axe fluvial constant qui contrôle la distribution des faciès**. Les variations de faciès sont principalement observées le long de cet axe et ne sont pas associées à la largeur des blocs de failles. Les variations de déplacement le long des failles ne contrôlent pas

directement la distribution des faciès et correspondent donc à un paramètre de contrôle secondaire de l'architecture alluviale.

Les zones de subsidence maximales dans les dépocentres sont alignées parallèlement à l'axe fluvial antécédent. La persistance du flux sédimentaire le long de cet axe est ici capable de créer une surcharge sédimentaire, favorisant ainsi la croissance des failles. **La persistance des rivières antécédentes contrôle donc la localisation et le développement des dépocentres.**

La capacité du bassin est limitée par rapport au flux sédimentaire ($A < S$). La progradation des faciès est ici expliquée par un flux sédimentaire antécédent important plutôt que par un faible taux d'accommodation à l'initiation du rift. Le système fluvial antécédent transverse se termine à l'est où des deltas progradent en milieu lacustre peu profond.

Le modèle de corrélation a permis d'estimer un taux de sédimentation de **0.3–0,5 mm/an**. Dans le cas d'un bassin suralimenté, les sédiments sont évacués vers l'aval et seule une partie d'entre eux sont déposés et préservés. Le taux de sédimentation est donc minimal et correspond plutôt à un **taux de sédiments préservés (SPR)**. Ce dernier est ici utilisé comme un **proxi du taux d'accommodation à l'initiation du rift**.

Alors que ce système fluvial se développait à l'extrémité ouest du rift, un autre système de rivières antécédent était actif dans la partie centrale à la même période ("**Killini river system**"). Ce dernier correspond à un système deltaïque dont la subsidence est contrôlée par la migration des failles vers le nord et les variations du niveau de base. Les corrélations stratigraphiques (à l'échelle de la marge sud du rift) entre les systèmes de dépôts (fluviaux, deltaïques et turbiditiques) mettent en évidence l'ouverture et l'**approfondissement diachrone du bassin**. Ces différents systèmes de rivières antécédents ont persisté pendant 2 à 3 Ma, et ils ont subi des modifications majeures au cours des migrations successives de l'activité tectonique vers le nord ($\sim 1,8$ Ma et $\sim 0,7$ Ma). Ces migrations de l'activité des failles dans la partie ouest du rift sont associées à des épisodes d'approfondissement du bassin et à la construction de Gilbert deltas ("**Middle Group**" et "**Upper Group**").

Une autre partie de ces travaux de thèse fut consacrée à l'enregistrement sédimentaire dans une zone de relais entre deux failles bordières, au cours de la migration de l'activité des failles (Faille East Helike et faille de Derveni, chapitre 5). Les **corrélations onshore-offshore** ont permis de reconstruire l'**histoire de propagation et de connexion entre les failles normales pendant une période de 500 ka**. L'enregistrement haute résolution des processus de connexion de failles et la qualité des données présentées forment l'originalité de cette étude.

Au cours du Pléistocène moyen à supérieur, la zone de relais a capturé la rivière antécédente de Krathis qui a construit des Gilbert-deltas. Les failles de transfert obliques marquent la migration de l'activité tectonique dans la zone de relais, ainsi que la migration de la succession deltaïque vers le bassin. On a mis en évidence une connexion précoce entre les failles bordières majeures à environ 600 ka. Cependant, ces failles sont restées actives et ont continué à se propager jusqu'à

un stade final de connexion à environ 200 ka. La connexion des segments de failles en plusieurs étapes (*multiple breaching*) est ici probablement contrôlée par la présence d'une structure héritée de la chaîne hellénique. La rivière de Krathis persiste et nourrit un déposécentré majeur "offshore". Cela souligne l'interaction entre les rivières antécédentes, la formation des zones de relais et les déposécentrés en bordure de rift actif.

Alors que l'**antécédence** est considérée comme étant une anomalie du réseau hydrographique, nos travaux montrent qu'elle devrait être considérée comme une **norme dans les rifts continentaux intra-montagneux**. D'autres systèmes fluviaux dans les rifts continentaux doivent être exploités pour confirmer et développer cette idée.

Perspectives

- Le contrôle prédominant des rivières antécédentes dans la distribution des faciès suppose un flux sédimentaire important à l'initiation du rift de Corinthe (chapitre 4). Cependant, le manque de quantification du flux sédimentaire et du rapport A/S à partir des enregistrements sédimentaires limite la compréhension des contrôles de l'architecture stratigraphique. Afin de discuter plus en détail le rôle du flux sédimentaire, on pourrait envisager une étude qualitative de la granodécroissance des faciès vers l'aval ([Whittaker et al., 2011](#); [Hampson et al., 2014](#)). Cela permettrait notamment d'établir des bilans de masses sédimentaires ([Paola & Martin, 2012](#)) en fonction de la distance amont-aval et en fonction du temps.
- Une autre problématique majeure en lien avec la persistance des rivières antécédentes ("through-going river system") est l'enfouissement des failles par le système de dépôt. Les modèles numériques actuels (comme par exemple [Paola, 2000](#); [Clevis et al., 2003](#); [Armitage et al., 2011](#)) tentent de reproduire les changements de granulométrie en 2D dans un seul bloc en subsidence (20 à 50 km de large). Il serait intéressant de simuler plusieurs blocs de failles actifs (chapitre 6) et de déterminer les valeurs de flux sédimentaire à partir desquelles les faciès sont distribués à travers plusieurs blocs de failles. Cela permettrait aussi de simuler différentes architectures stratigraphiques en fonction du rapport A/S. Cependant, cette vision simplifiée en 2D sous-estime la complexité 3D de la systèmes alluviaux.
- Le système de rivières pré-rift devait transporter des sédiments vers un bassin qui est peut-être actuellement localement préservé dans la partie centrale-est du golfe de Corinthe. La base de la succession "offshore" (SU1) reste peu documentée en raison de la faible résolution des profils sismiques au delà de 1,5 s TWTT ([Taylor et al., 2011](#)). L'absence de forage profond ne permet pas de dater précisément la base de la série à l'heure actuelle. De plus, la partie en amont de ces rivières pré-rift restent inconnus. L'étude du

paysage pré-rift dans le nord du Péloponnèse pourrait donner des informations sur les dimensions des bassins versants, leurs sources, ou encore l'âge du paléorelief hérité.

- L'analyse des faciès au "Lower Group" ne montrent pas de variations lithologiques des clasts (nappe du Pinde, chapitre 4). Cependant, la composition des clasts varie à partir du "Middle Group". On note la présence de clasts de roches métamorphiques issu de la nappe des phyllade et les roches basaltiques d'origine incertaine (olistolithes emballés dans les "flysch" de la nappe du Pinde ?). La proportion des différentes lithologies de clasts pourrait être mesurées dans les unités syn-rift ("Lower, Middle, Upper Groups") afin de définir les sources sédimentaires, et pourquoi pas l'âge de la mise à l'affleurement des nappes par l'incision des rivières. Cela pourrait aussi permettre de mieux comprendre la ré-organisation du système hydrographique entre le "Lower Group" et le "Middle Group" (chapitre 6).
- Les concentrations en ^{10}Be dans les sédiments des rivières actuelles ont permis de calculer des taux d'érosion dans cinq bassins versants (Selinous, Kerenitis, Vouraikos, Krathis, Kryos) le long de la marge sud du rift de Corinthe (annexe D). Ces taux d'érosion sont compris entre 0.06 ± 0.01 mm/an et 0.26 ± 0.16 mm/an. La quantité de données est cependant insuffisante pour discuter ces taux d'érosion en lien avec le type de bassin versant (conséquent ou antécédent) ou le flux sédimentaire transporté dans le golfe actuel. Ces résultats seront valorisés par une collaboration avec d'autres chercheurs qui désirent déterminer les taux d'érosion ^{10}Be dans les bassins versants principaux de la marge sud du rift (Stephen Watkins, doctorant à l'Imperial College, Londres).
- L'étude paléomagnétique dans le bloc de Valimi (chapitre 3) a été initialement couplée à une étude palynologique dans la Formation de Valimi (données non publiées du projet de Master 2 de Maria Sekar Proborukmi en 2010). Ces données ne sont pas présentées dans cette thèse mais feront l'objet de futures collaborations au cours de la préparation des publications. Les datations palynologiques permettront d'ajuster et d'améliorer notre modèle d'âge. En plus de la datation, cette étude palynologique permettra de confronter notre modèle de corrélation et les architectures stratigraphiques avec les variations climatiques rythmées par les cycles glaciaires-interglaciaires et le développement des glaciations de l'hémisphère nord (Combourieu-Nebout, 1993).

Troisième partie

Annexes

Annexe A

Mesures et traitement des données de paléocourants

Le long de la marge sud de Corinthe, la qualité des affleurements permet généralement l'analyse banc à banc de la succession syn-rift dans les différents blocs de failles normales.. Les mesures de paléocourants sont principalement localisées le long des logs sédimentaires présentés dans le chapitre 4. D'autres sites de mesures isolées ont permis de définir des directions de paléocourants malgré un nombre de mesures N généralement moins important. Toutes les données sont regroupées par sites de mesures et sont détaillées dans le tableau ci-dessous. Les directions de paléocourant sont représentées sur la carte ci-dessous. Les paléocourants ont été mesurés à partir des objets sédimentaires suivants :

1. Des figures d'incision (flancs de chenaux ou de gouttières d'érosion) dont la direction moyenne des plans mesurés correspond à la direction du courant. Les plans subverticaux sont privilégiés mais ne représentent pas l'essentiel des données.
2. Stratifications obliques dans des rides et mégarides. La qualité des affleurements permettent uniquement d'estimer une direction du courant sur une section verticale (peu de structures 3D) . La direction de courant correspond à l'azimut moyen porté par les laminations mesurées.
3. Imbrications des clastes de type $a(t)b(i)$ qui fournissent un sens de courant (grand axe a transverse au sens du courant). La grande dispersion des plans d'imbrication (ab) nécessite un nombre important de données (au moins une dizaine) pour définir un sens de paléocourant. Ce dernier est donné par le pôle moyen des plans d'imbrication (ab) mesurés.

La grande majorité des mesures effectués sur les bases de surfaces chenalisées permet d'estimer des directions de paléocourants uniquement. Les mesures complémentaires de plans d'im-

brications permettent de définir les sens de paléocourants. Le logiciel *Stereonet* (développé par *Cornell university*) permet le traitement des mesures. Les différents plans mesurés sont restaurés de la stratification S0 avec un pendage sub-horizontale. Les séries de mesures sont traitées individuellement par site et par type d'objet sédimentaire mesurée. Pour N mesures, la direction moyenne de paléocourant est définie par le vecteur moyen \bar{x} qui s'exprime par la formule suivante :

$$\bar{x} = \arctan \left[\frac{\sum_1^N \sin\theta}{\sum_1^N \cos\theta} \right] \quad (\text{A.1})$$

avec θ , l'azimut de l'objet mesuré entre 0° et 360° . La magnitude R du vecteur moyen quantifie la dispersion des mesures et correspond à la déviation angulaire :

$$R = \sqrt{\left(\sum_1^N \sin\theta\right)^2 + \left(\sum_1^N \cos\theta\right)^2} \quad (\text{A.2})$$

La magnitude d'un vecteur, exprimée en %, est une valeur sensible à la dispersion des données :

$$L = \frac{R}{N} \cdot 100 \quad (\text{A.3})$$

Chaque vecteur moyen est caractérisé par la déviation angulaire à 2σ (95% de la distribution des données) et la magnitude du vecteur moyen, $L(\%)$. Le test statistique de Rayleigh (voir Figure A.2) permet de valider ou non la pertinence du vecteur moyen calculé. Dans un graphe représentant $L(\%)$ en fonction du nombre de mesures N est représentée la probabilité que les mesures soient uniformément distribuées ou pas entre 0° et 360° . Une probabilité $p < 0,05$ signifie une distribution non aléatoire des mesures et ces dernières peuvent alors être présentées (Curry, 1956). Les autres ne sont pas prises en compte et donc rejetées. L'utilisation du test de Rayleigh est particulièrement utile quand les vecteurs directions sont calculés à partir d'un faible nombre d'observations N .

Les directions de paléocourants sont présentées dans le chapitre 4 sous différentes formes : (i) Les diagrammes de rose regroupent de nombreuses mesures de paléocourant (parfois plusieurs centaines) dans une même unité lithostratigraphique. Les diagrammes de rose sont représentés le long de certains logs et aussi sur la carte des paléocourants. (ii) Les vecteurs de direction et le sens de paléocourants sur la carte du secteur. Chaque vecteur regroupe les mesures d'un ou plusieurs sites dans une même unité lithostratigraphique. La représentation sous forme de vecteur de direction est privilégiée quand peu de mesures sont disponibles.

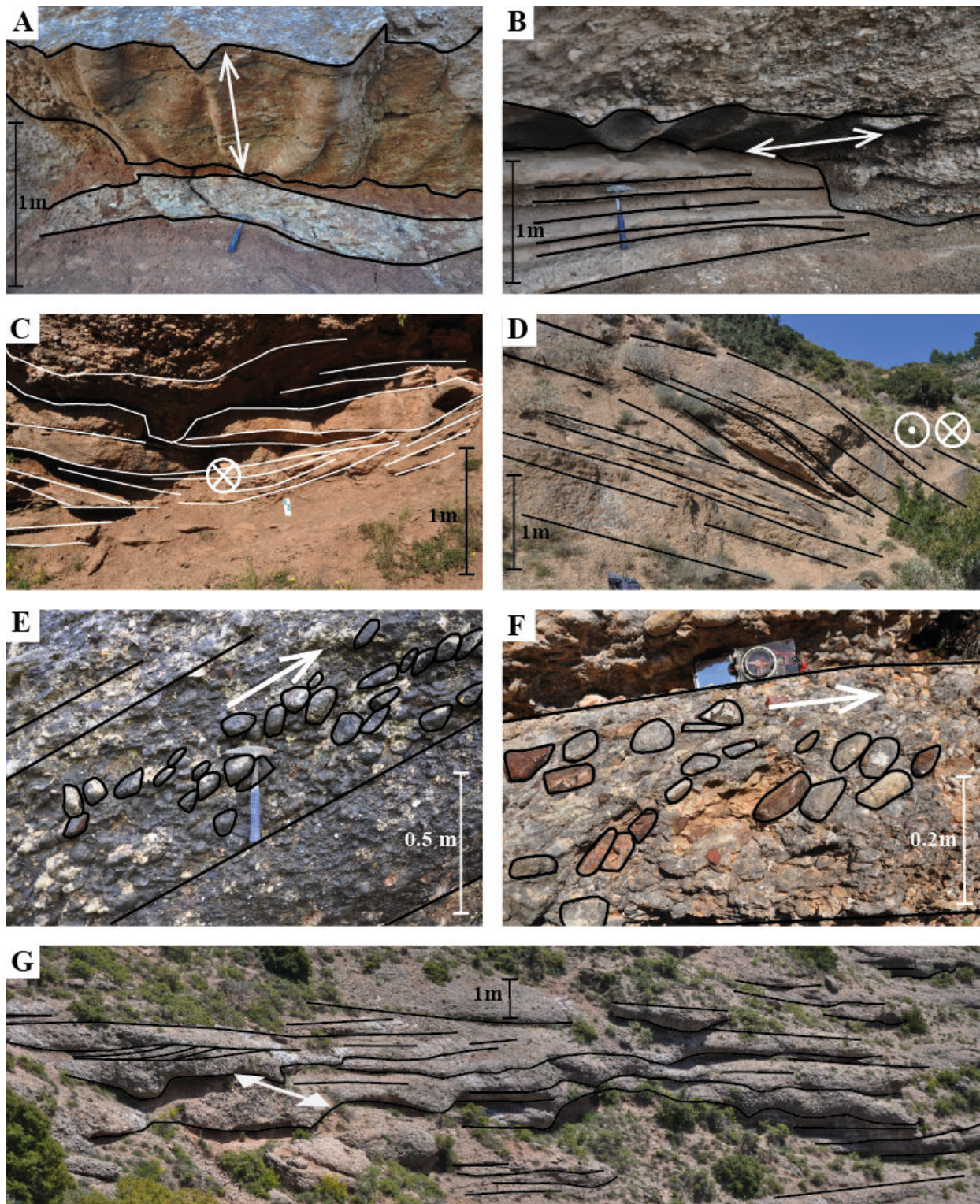


FIGURE A.1 – Quelques exemples de figures sédimentaires à partir desquelles sont mesurées les paléocourants. Les flèches indiquent la direction ou le sens de paléocourant. (A) et (B) Surface de banc érosive présentant des figures de groove ; (C) Stratifications en auges dans des bancs gréseux ; (D) Accrétion latérale de bancs conglomératiques ; (E) et (F) Bancs conglomératiques comprenant quelques alignements de clastes imbriqués ; (G) Ensembles de bancs conglomératiques présentant des surfaces érosives, chenalisées et amalgamés.

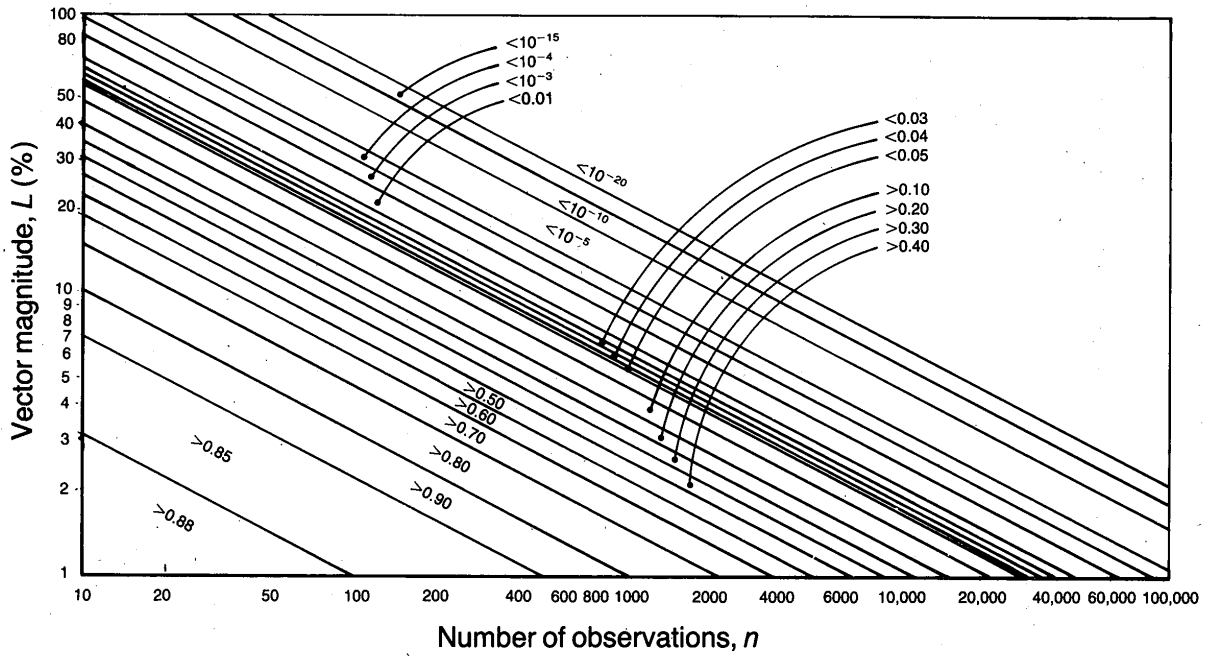
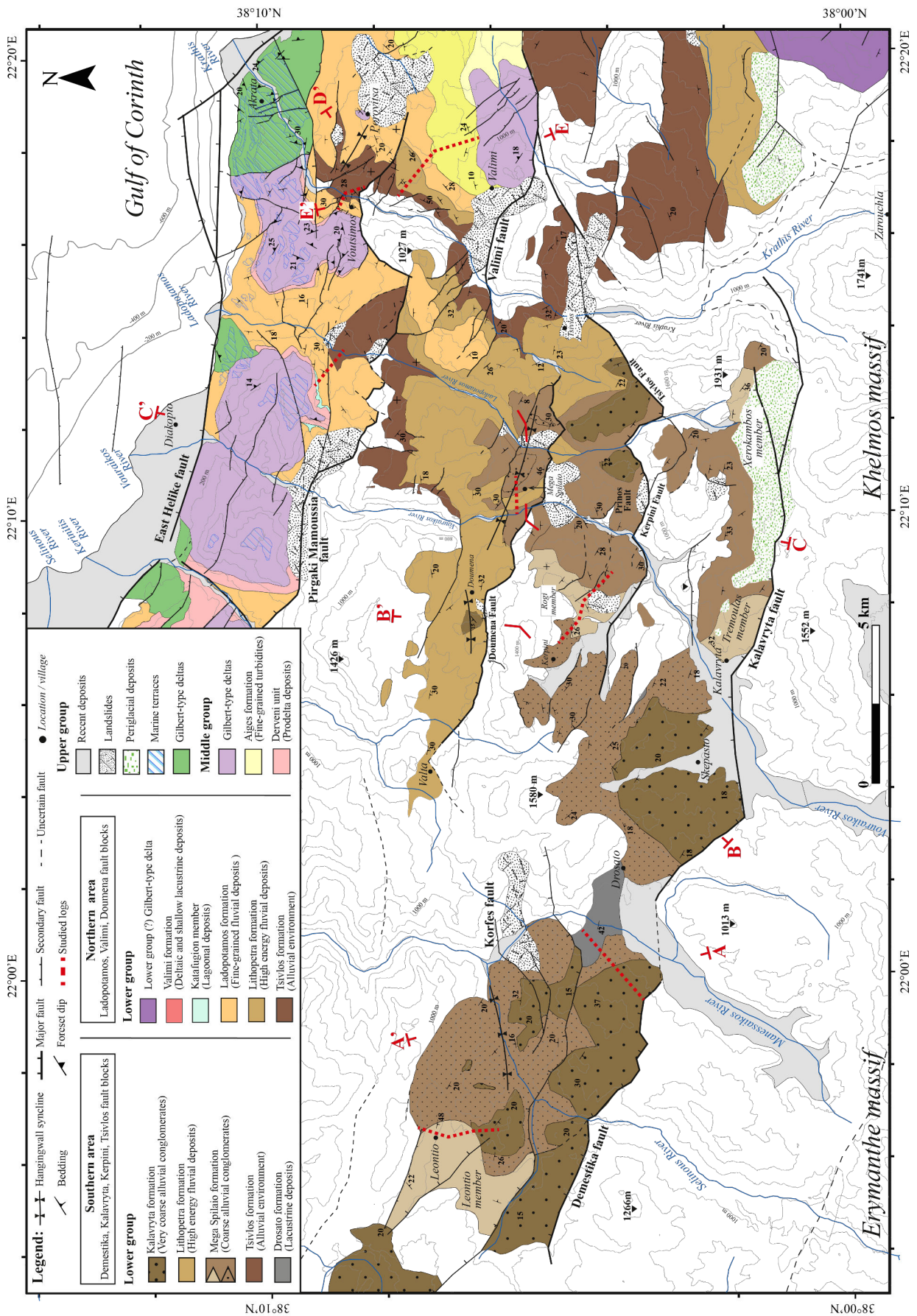


FIGURE A.2 – Test de probabilité de Rayleigh (d'après [Curry, 1956](#))



N.01.88

N.00.88

CHAPITRE A : Mesures et traitement des données de paléocourants

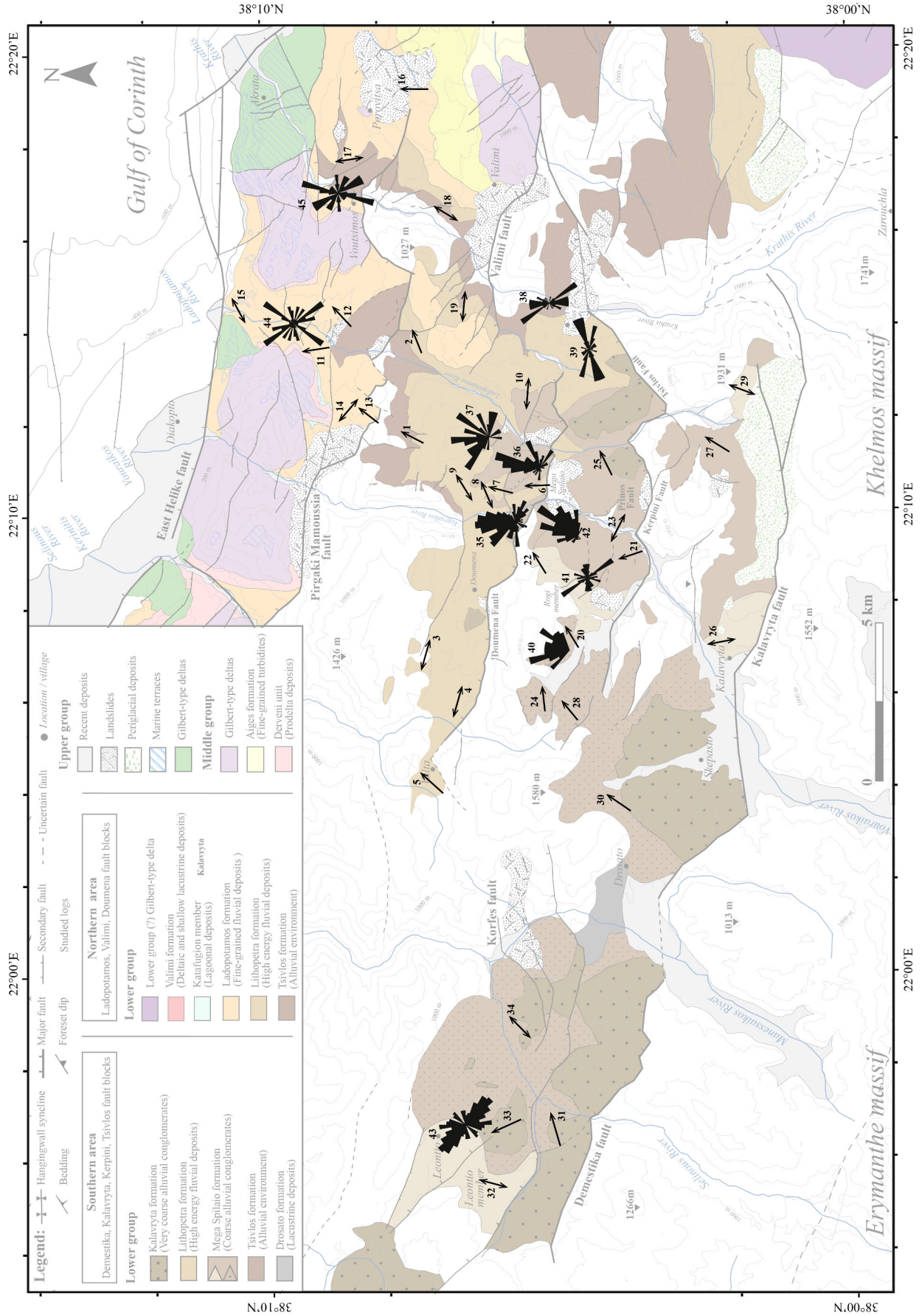


TABLE A.1 – Tableau résumant le traitement des données de paléocourants. *Palaeocurrent data are represented on a rose diagram

Label	Sedimentary figures	Type	Mean vector	<i>N</i>	Vector magnitude,%	α_{95}
1	Clast imbrications	Directional	N023	7	0.84	29
2	Clast imbrications	Directional	N249	8	0.71	38
3	Trough cross lamination	Non directional	N288	2	0.99	22
4	Trough cross lamination	Non directional	N285	3	0.99	8
5	Clast imbrications	Directional	N042	13	0.82	20
6	Flanks of channels/hollows	Non directional	N063	12	0.82	21
7	Flanks of channels/hollows	Non directional	N014	15	0.81	19
8	Flanks of channels/hollows	Non directional	N065	15	0.84	17
9	Flanks of channels/hollows	Non directional	N061	21	0.87	13
10	Flanks of channels/hollows	Non directional	N094	24	0.75	18
11	Flanks of channels/hollows	Non directional	N170	33	0.72	16
12	Clast imbrications	Directional	N046	17	0.87	14
13	Clast imbrications	Directional	N037	5	0.94	21
14	Flanks of channels/hollows	Non directional	N128	16	0.85	16
15	Flanks of channels/hollows	Non directional	N066	4	0.88	40
16	Clast imbrications	Directional	N001	4	0.65	84
17	Flanks of channels/hollows	Non directional	N172	25	0.71	19
18	Flanks of channels/hollows	Non directional	N029	28	0.61	<i>n/a</i>
19	Flanks of channels/hollows	Non directional	N096	13	0.81	21
20	Flanks of channels/hollows	Non directional	N059	21	0.80	16
21	Clast imbrications	Directional	N343	13	0.95	10
22	Clast imbrications	Directional	N058	14	0.86	6
23	Flanks of channels/hollows	Non directional	N119	9	0.74	33
24	Clast imbrications	Directional	N084	12	0.93	12
25	Clast imbrications	Directional	N063	3	0.94	37
26	Flanks of channels/hollows	Non directional	N350	8	0.83	27
27	Clast imbrications	Directional	N032	11	0.96	10
28	Clast imbrications	Directional	N050	7	0.92	19
29	Flanks of channels/hollows	Non directional	N019	14	0.73	25
30	Clast imbrications	Directional	N035	22	0.95	7
31	Clast imbrications	Directional	N074	11	0.70	27
32	Flanks of channels/hollows	Non directional	N339	16	0.65	28
33	Flanks of channels/hollows	Non directional	N337	9	0.76	31
34	Flanks of channels/hollows	Non directional	N048	11	0.81	23
35*	Clast imbrications	Directional	N004	215	0.80	5
36*	Clast imbrications	Directional	N038	83	0.80	8
37*	Clast imbrications	Directional	N358	32	0.85	11
38*	Flanks of channels/hollows	Non directional	N350	24	0.884	11
39*	Flanks of channels/hollows	Non directional	N086	36	0.82	11
40*	Clast imbrications	Directional	N012	105	0.89	5
41*	Flanks of channels/hollows	Non directional	N145	94	0.99	<i>n/a</i>
42*	Clast imbrications	Directional	N036	90	0.92	5
43*	Flanks of channels/hollows	Non directional	N315	128	<i>n/a</i>	<i>n/a</i>
44*	Flanks of channels/hollows	Non directional	N177	50	0.67	14
45*	Flanks of channels/hollows	Non directional	N155	50	0.73	18

Annexe B

Sédimentologie et paléontologie

B.1 Analyse sédimentologique détaillée des faciès syn-rift du *Lower group*

Les faciès syn-rift rencontrés dans les séries du *Lower group* sont décrits ci-dessous (en anglais). Les principales caractéristiques sédimentologiques et environnementales sont résumées dans le chapitre 4, dans les tableaux 4.1, 4.2 et 4.3. Ces faciès sont aussi illustrés sur les figures 4.4, 4.5 et 4.6. The syn-rift deposits are mainly clast-supported conglomerates with variable proportion of sand and silt. The clast provenance is the Pindos nappe and the different clast lithologies are micritic carbonates and their associated chert nodules, radiolarites, tubiditic sandstones. The presence of reworked clasts (coarse sandstone or granule conglomerate) with the same clast composition is very rare. The details of clast-counting provenance does not show significant change in proportions of the clasts composition and micritic carbonate clasts are always predominant in the study area. The major change in clast composition occurs in *Middle group* conglomerates building the Gilbert-type deltas, but is not documented in this facies analysis. For facies analysis of the *Middle Group*, see Rohais *et al.* (2007a) and Backert *et al.* (2010).

F1

Description

Lithofacies F1 is a matrix-supported breccia with clasts comprising angular pebbles to boulders clasts (up to 0.8 m). Deposits are massive with no obvious stratification, ungraded and present disorganised fabrics. Isolated large cobbles and boulders may be localised in the middle part of the plurimetre-scale beds. Locally, isolated clasts are vertical. The poorly consolidated heterometric matrix is composed of angular clast, brown silt and clay. Bed surface is planar with an unchannelised base. Internal bed structure is absent. This facies is poorly represented on the field.

Interpretation

Vertical clasts indicate a subaerial motion of sediments within a debris flow rather than a

more organised stream flow where crude orientation and more stratified facies developed (Nemec & Steel, 1984). Poor grain size sorting suggests a debris flow process with clasts floating in an abundant matrix (Hampton, 1979). This facies associated to sediment gravity flow depositional processes is volumetrically small, developed essentially as localized packages that often mantled the pre-existing bedrock topography of mountain foot zones (Fisher, 1971; Blair & McPherson, 1994).

F2

Description

Lithofacies F2 is a massive clast-supported and poorly sorted conglomerate composed of rounded pebbles to boulders and sometime subangular pebbles. Beds are very crudely stratified and bed thicknesses are not often defined (at least metre-scale beds). Beds are highly erosive and form massive plurimetric bedsets/packages. Boulders occur as isolated meter scale clasts in polymictic conglomerates or can be mixed with cobbles, aligned parallel to the bedding. In some places, only clasts alignment defines the crude stratification. The scarcity of fine-grained material preserved between beds makes the F2 lithofacies easily recognisable.

Interpretation

Massive, structureless beds are likely to be a consequence of rapid deposition ('dumping'). Nevertheless, some beds present very crudely discontinuous stratification, signs of tractive bedload transport. The characteristics of this facies are consistent with bedload transport in high flow regimes. Variations in grain-size and sorting reflect the extreme changeability of flow and transport rates (Hein, 1984; Nemec & Postma, 1993).

F3

Description

Lithofacies F3 is a massive to crudely laminated clast-supported conglomerate. Pebbles to large cobbles clasts are poorly to moderately sorted, with subangular and rounded shape. Boulders are locally present, aligned at the base of the bed. This conglomeratic lithofacies is marked by common a(t)b(i) clast imbrications where pebbles and cobbles are imbricated with their long axes aligned transverse to the paleoflow direction. Erosional features are represented by (i) scour pockets that show a regular, more or less circular "pot" shape and are locally very deep (1 m) and sharp that cutting out underlying sediments ; (ii) continuous elongate ridges with a sharply relief, developing on bed undersurfaces ; (iii) metre-scale and plurimetre-scale incisions defining basal channelised surfaces. Channel geometry and amalgamation can be documented in some places. Plurimetric to hectometric massive bedsets are composed of highly erosive plurimetric beds where interstratified fine-grained material is poorly preserved.

Interpretation

Imbricated clasts were and palaeoflow measurements are used as palaeocurrent indicator, particularly in conglomeratic facies where sedimentary structures are poorly developed. In fluvial

situations, where pebbles and cobbles are rolled on the bed, the long (a-) axis is usually transverse to flow directions, and the intermediate (b-) axis dips upstream, characterizing the imbrication (Harms *et al.*, 1975; Collinson *et al.*, 2006). Deep scour pockets result from a combination of fluid scour and the erosive action of coarser grains within the flow during a single erosional event (Miall, 1996). Here, infilling erosional relief on the bases of beds are groove casts that result from the infilling of erosional features gouged by unknown objects. This facies is interpreted as longitudinal bedform deposits (Miall, 1996) and is typical of rapid gravel sheet transport processes (Hein, 1984).

F4

Description

Lithofacies F4 is a clast-supported conglomerate. Pebbles and small cobbles clasts are poorly to moderately sorted and can be subangular to well-rounded. Bed thickness is generally up to one metre. Beds are erosive with poor lateral extension. Bed structures are mainly decimetre to metre scale oblique bedding (tabular to trough cross bedding and locally sigmoidal geometries). Normal grading and clasts imbrications are also locally observed. F4 lithofacies are included in massive conglomeratic beds successions rather than isolated in the sandy and finer-grained material.

Interpretation

Trough cross bedding indicates that these conglomerates were deposited by migrating bedforms. The so-called sigmoidal-shaped bedding is here difficult to interpret because of poorly exposed outcrops. The general macroform suggests downstream to lateral-accretion deposits. Moreover, large-scale lateral-accretion surfaces are difficult to identify because lithofacies are pebbles to small cobbles dominated. Coarse grained-size facies often obscure the continuity of the lateral accretion surfaces. The cross-cutting erosion surfaces within macroforms (meters high) should not be interpreted as true lateral accretion surfaces (i.e. epsilon cross beds) of point bar. There are no clear evidence of true internal small-scale structures displaying significant three-dimensional geometries. Here, the bars could accreted mainly downstream but with a slightly oblique direction (high current dispersal) that permit the development of lateral-diagonal geometries. So, we interpret this lithofacies as belonging to a transitional one between low sinuosity (i.e. braided river) and true high sinuosity (i.e. classic meandering river), maybe related to a wandering river morphology (Church, 1983; Billi *et al.*, 1987).

F5

Description

Lithofacies F5 is a clast-supported pebble conglomerate. Clasts are moderately to well sorted, with a subangular to rounded shape. Crude horizontal lamination is very discontinuous and beds are generally structureless. Beds thickness varies from 0.1 to 1 m. They are mostly erosive with lenticular shape. Locally, structures with general "wing shape" morphology are encountered

at the sole of beds. Some are emplaced parallel to bedding, whereas others cut vertically or obliquely through the bedding. They exhibit size scales from centimeters to decimeters.

Interpretation

The crudely developed planar horizontal lamination is reflecting varying discharge and discontinuous sedimentation (Nemec & Steel, 1984). Decimeter to meter-thickness strata implies deep channelised flow. The presence of erosion surfaces is reflecting combined effect of both entrenching and quickly lateral shifting of braided channels (Rust, 1972; Rust & Koster, 1984). The "wing-shape" structures are formed by sediment injection as clastic dykes. The orientation of this sediment disturbance evidenced that a "per descensum" mechanism is involved. Commonly, sediment injection occurs as the result of over-pressurization of buried sediment (Jolly & Lonergan, 2002; Vandromme, 2007) and represent a kind of subsurface sediment mobilization (Van Rensbergen *et al.*, 2003).

F6

Description

Lithofacies F6 is a clast-supported pebbles conglomerate composed of moderately to well-sorted clasts. Clasts are particularly well-rounded to near-spherical shape in this lithofacies. The base of the beds is erosive and sharp. Beds are less than half a meter thick, regularly stratified and are continuous over several metres. Planar horizontal lamination is generally well developed.

Interpretation

The horizontally stratified beds may have formed in shallow, low-velocity flows (Harms *et al.*, 1975) within gravel bedforms.

Sandy lithofacies

F7

Description

Lithofacies F7 is a cross-bedded granule conglomerate to coarse sandstone. Clasts or grains are angular to rounded. Aligned pebbles mark the oblique lamination locally. The metre scale beds are highly erosive with a lenticular shape. Low angle lamination can be observed in well sorted granule conglomerates.

Interpretation

The low-angle inclined cross stratification may be the result of deposition in high-energy shoreface barrier and beach system (Nemec & Steel, 1984; Ford *et al.*, 2007)

F8

Description

Lithofacies F8 is a coarse to medium sandstone. The decametric beds are non erosive and present a shap planar base surface. Beds can display planar parallel to undulated lamination and also tangential lamination in places. Beds are poorly exposed and often eroded by the overlying

conglomeratic beds.

Interpretation

Flat bedding planes reveal parallel lamination defined by slight grain-size differences. This facies is interpreted as a planar bed flow in the upper-stage phase. This facies may be deposited during a succession of single dynamic event, such as a flash flood, when flow conditions may remain in the critical stage for short periods of time. The origin of the low-relief undulating lamination can be explained by an increase in velocity of water flowing above an upper-flow regime planar bed (Collinson *et al.*, 2006). The crudely preserved oblique lamination can be assigned to weakly developed megaripples.

F9

Description

Lithofacies F9 is a medium to fine-grained, well sorted sandstone with interbedded pebble well rounded clasts. The poorly consolidated beds (up to half a metre thick) are well stratified and present a clear planar parallel lamination, often underlined by pebble lag. Bed successions form plurimetre scale (2–3 metres) clinoform gently dipping 5° to 10° and with internal erosive base. Pebbles pass laterally to sandier facies in the lower part of the dipping beds. The beige to orange colour of this lithofacies is commonly observed in bed successions.

Interpretation

Grain size associated to inclined clinoform geometry can be assigned to small-scale prograding foresets Gilbert-type fan deltas (Postma, 1990).

F10

Description

Lithofacies F10 is defined as a coarse to fine-grained poorly consolidated sandstone. Grains are well-sorted. Meter scale beds are specifically characterised by mainly oblique tangential laminations.

Interpretation

Internal oblique laminations develop due to migration of 3D bedforms. This facies occurs in association with F9 and the variable texture of sandy beds result from changing hydraulic conditions. Erosional surfaces can be produced by bedform migration or when bedform migration ceased for a long time and then re-started as the flow stage increased (Bridge, 2003; Bridge & Lunt, 2006).

F11

Description

Lithofacies F11 is a medium to fine-grained, well-sorted sandstone. Internal variations in cementation are parallel to the bedding and often observed at the top of the bed. Facies colour varies from yellow to beige and reddish. Beds are crudely stratified and horizontal parallel lami-

nation can locally be observed. Top of beds can be highly bioturbated, as a more or less irregular network. The morphology consists (i) of vertical to oblique shafts connecting horizontal tunnels (cm in diameter), (ii) typically T- to Y-shaped branching patterns.

Interpretation

The horizontal lamination is generated through subaqueous deposition at high flow velocities in the upper flow regime. Various orange to reddish colour may be due to superimposed weathering overprint, but with no pedogenesis remnants. Traces of bioturbations represent 3D burrow systems (fodinichnia to dominichnia) that are produced by *Camborygma* ichnogenus (Bromley, 1996; Buatois & Mángano, 2011; Knaust & Bromley, 2012; Hasiotis *et al.*, 2006).

F12

Description

Lithofacies F12 is a fine-grained sandstone to silt. Locally, granules and pebbles are present in variable proportions. Sometimes, they are arranged as lag deposits on erosional surfaces. Others are randomly dispersed within unstratified units. Decimetric beds are generally structureless, despite some of them are showing weak horizontal lamination locally disrupted by soft-sediment deformation. They also may contain few centimetres in diameter irregular carbonates nodules with no internal fabrics. Vertical to low inclined centimeter scale burrows are rare and poorly preserved. Mammalian skeletal elements (namely Hipparion hip) and undetermined teeth and bones fragments can be found associated with the coarsest grain size part of the lithofacies.

Interpretation

The bedding that have been subsequently deformed is assigned to water-escape events that superimposed on primary lamination. Scattered, crudely rounded carbonate nodules (i.e. glebules) indicate immature paleosol development (Retallack, 1988, 1997; Bridge, 2003).

Silt and clay lithofacies

F13

Description

Description and interpretation of this facies is mainly synthesized from previous studies (Malartre *et al.*, 2004; Ford *et al.*, 2007, 2013). Lithofacies F13 is described as a distinctive white-weathering flat- and parallel-laminated shelly siltstone/marly limestone. Calcareous silts contain abundant broken and complete bivalve and gastropod shells disposed parallel to the bedding. Interbedded fossiliferous beds are up to 10–12 cm thick. Much of the broken and intact bivalve material appears to be from a single genus, of small (<1 cm) members of the suborder Pterioida. Gastropod shells of *Theodoxus micans* are abundant and well preserved. The finely laminated calcareous silts alternate with sandier beds (few centimetres thick) of beige colour. Interstratified pebbles are locally present.

Interpretation

Mixed fine-grained clastic-carbonate system capped by well-stratified fine gravel and finally

much finer-grained sediments is interpreted as representing a protected subtidal lagoon in a microtidal regime (Flemming, 1988; Anthony *et al.*, 1996) as no peritidal or obvious marsh facies were found. The restricted diversity of the mollusc fauna plus the evidence of marine microfossils, suggests a brackish to saline coastal lagoon. The rare inter-bedded pebble gravel sheets within the lagoonal facies are likely to be storm-generated washovers or due to storm-generated flow through the barrier into the lagoon (Ford *et al.*, 2007).

F14

Description

Lithofacies F14 is a finely and regularly laminated sand to silt (few millimetre to centimetre thick). Planar horizontal lamination is highlighted by thin iron-rich laminae. Convolute laminations are locally observed. Bed surfaces can be irregular and slightly erosive. Symmetric current ripples and climbing ripples (also documented in Rohais *et al.* (2007a) are observed over few metres. No biota is documented in this lithofacies.

Interpretation

This facies registered variable current velocities. The symmetrical-rippled sandstones are inferred to record waning episodes of deposition associated with moderate-energy waves followed by periods of quiescence where silt facies can settle (Lawrence & Williams, 1987; Ford & Pyles, 2014). Shoaling waves deposited thin rippled layers after which suspension clouds deposited planar-laminated silt (Martel & Gibling, 1991). Rare planar-laminated sandstones represent deposits of high-energy flows.

F15

Description

Lithofacies F15 is a finely laminated (few millimetres), well consolidated clayed silt. Grey and light beige laminae are irregularly undulated and erosive. Differential competence of the beds (up to 15 cm thick) highlights the erosive character and their lenticular shape. Coal laminae are planar parallel.

Interpretation

This fine-grained thin-bedded facies shows generally straight parallel to undulated erosive laminations. The main distinctive feature is the intermixing of carbonaceous material in clastic fines. It represents deposition from suspension and from weak traction currents (Miall, 1996)

F16

Description

Lithofacies F16 is a poorly-consolidated clayed silt. Pedogenic overprinting is indicated by carbonates globules, orange to pale green variegated colour forming discontinuous layers and more locally drab-haloed spots. Fresh-water gastropods such as *Planorbis* and other undetermined shell debris can be present locally. There is no obvious trace of organic matter. Internal bed

structures are poor.

Interpretation

Pedogenic overprinting is indicated by the few carbonate glebules, and the variegated colours. Their low development suggests immature paleosols (Retallack, 1988, 2001). *Planorbis* is an air-breathing freshwater flat-coiled gastropod mollusk. It is common in flooding margins of lakes and large rivers within aquatic flora.

F17

Description

Lithofacies F17 is characterised by an alternance of silt and clay. Beds are few millimetres to few centimetres thick. They are separated by continuous iron rich laminae where plant overprint can be preserved. Organic matter is present in variable proportion and coal fragments or laminae are observed. Gastropod shells (*Melanopsis aff. mitzopouloisi*, *Adelina elegans*) and other undetermined shell debris are randomly distributed in silty bed or form millimetre shell beds. Silty horizontal parallel lamination can be locally disrupted by soft sediment deformation.

Interpretation

Sedimentary structures are represented by very fine horizontal to slightly wavy lamination. This facies records the episodic settling of clays from suspension in a still water environment and very low flow regimes that deposited silty laminae. Then, disturbed to contorted lamination is related to convolutes. F17 is deposited in a shallow lacustrine environment and mostly corresponds to prodelta facies as documented by Rohais *et al.* (2007a).

F18

Description

Lithofacies F18 is brown to grey silt and plastic clay. Decimeter scale beds are structureless (no clear lamination) and contain sandy grains or rare isolated small pebbles. Organic matter is variable in proportion and wood debris and root remnants can be preserved. This facies presents undetermined bioclasts. When not totally fragmented, one can recognize gastropod shells and seals, ostracods, fish teeth and bones, Rodentia teeth. In some places, there are Charophyta algae remnants (mostly gyrogonites).

Interpretation

F18 represents deposition in standing pools of water that may developed in distal settings of floodplains (floodplains ponds). Root and wood fragments evidenced a locally vegetated environment. Charophyta are a group of macrophytic green algae that live submersed and occur predominantly in shallow (few meters) oligotrophic freshwater environments of lakes and rivers (Grambast, 1974; Wray, 1977). The calcified part of the oogonium (called gyrogonite) is well preserved and can be related to two different genus also recognised in the Megara basin, east of the Corinth gulf (Soulié-Märsche, 1979). One is *Nitellopsis megarensis* (Upper Pliocene age) and the other one could be related to *Lychnothamnus sp.* (determinations by S. Sen, MNHN Paris).

F19

Description

Lithofacies 19 is a poorly to moderately consolidated silty clay. Decimetric beds have variable proportions of organic matter and contain dispersed coal fragments. No internal structure is observed and beds are locally highly bioturbated. Top bed surface show small burrows. They are mostly parallel to the bedding and show simple tubular morphological sections (less than one centimeter in diameter). Some of them seem to be bifurcated but it remains unclear if this morphology is a real dichotomic feature or due to simultaneous cross over of superimposed simple burrows.

Interpretation

This facies represents deposition from suspension in a standing body of water during a period of low velocity flow. The structureless texture indicates continuous deposition by dominated-suspension fallout. If the type bioturbation is not clear (Planolites-like morphology?), the high density burrows is representing short-term periods of quiescence within the depositional environment.

F20

Description

Lithofacies F20 is a composed of meter scale compact organic-rich beds. This distinctive multi-layered brown to black lithofacies is non consolidated and is often inter-stratified with lenticular silty beds (up to few centimeters thick). Darker levels of the beds may contain undefined wood and leave fragments. Horizontal parallel lamination is highly irregular and often disrupted by primary sediment deformation and/or compaction (dewatering?).

Interpretation

Lignites are humic organic deposits. As some plant material is recognisable, it can be assumed to soft brown coal (McCabe, 1984). The occurrence, distribution and quality of the lignite in the Kalavryta area (within the Drosato formation, c.f. chapitre 4) have been the subject of detailed petrographic and organic geochemical analysis (Papanicolaou *et al.*, 2000, 2004) in order to determine (i) the potential economic value, (ii) the coal rank and calorific parameters and (iii) the nature of plants contribution. Lignites (xylic coal) have low reflectance values ($R_r = 0,3\%$) and an amount of ash contents well over 20% (between 21.7% and 45.6%). Biomarkers indicate the presence of a large contribution from gymnosperms plants such as Pinaceae and Taxodiaceae. Palynological investigations of Neogene formations in Greece have shown that Pinaceae increased during the Late Pliocene (Papanicolaou *et al.*, 2000). The presence of Taxodiaceae gymnosperm (*Glyptostrobus sp.*) dominated the coal-forming mires during the Tertiary period in Greece (Velitzelos & Gregor, 1990; Velitzelos *et al.*, 2014). It is accustomed to high water-table levels where low-lying swamp develops (Vassio *et al.*, 2008; Killops & Killops, 2005).

B.2 Logs sédimentaires

Textures and specific lithologies

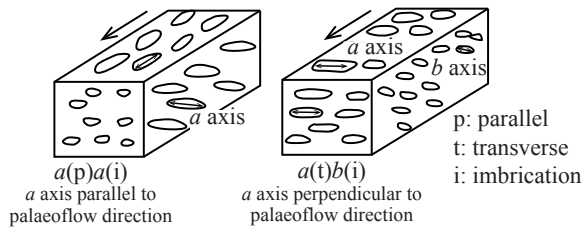
- Grain-supported conglomerate
- Matrix-supported conglomerate
- Fine grained sediments (silt and clay)
- Brown coal
- Undifferentiated pre-rift lithologies (Pindos nappe)

Palaeocurrent data

- Non-directional measurements
- Directional measurements

Clast imbrications types

from Harms *et al.*, (1975)



Grain-size classes

from Udden (1914) and Wentworth (1922)

ϕ			
-8	4 μm	Claystone fine	Clay
-6	8 μm	medium	
-2	16 μm	Siltstone coarse	
-1	32 μm	very coarse	Silt
0	63 μm	very fine	Sand
1	125 μm	fine	
2	250 μm	medium	
3	500 μm	coarse	
4	1 mm	very coarse	
5	2 mm	granules	
6	4 mm	pebbles	Conglomerate
7	64 mm	small cobbles	
	128 mm	large cobbles	
8	256 mm	boulders	

Architectural elements

- Channels amalgamation
- Channel base

Sedimentary structures

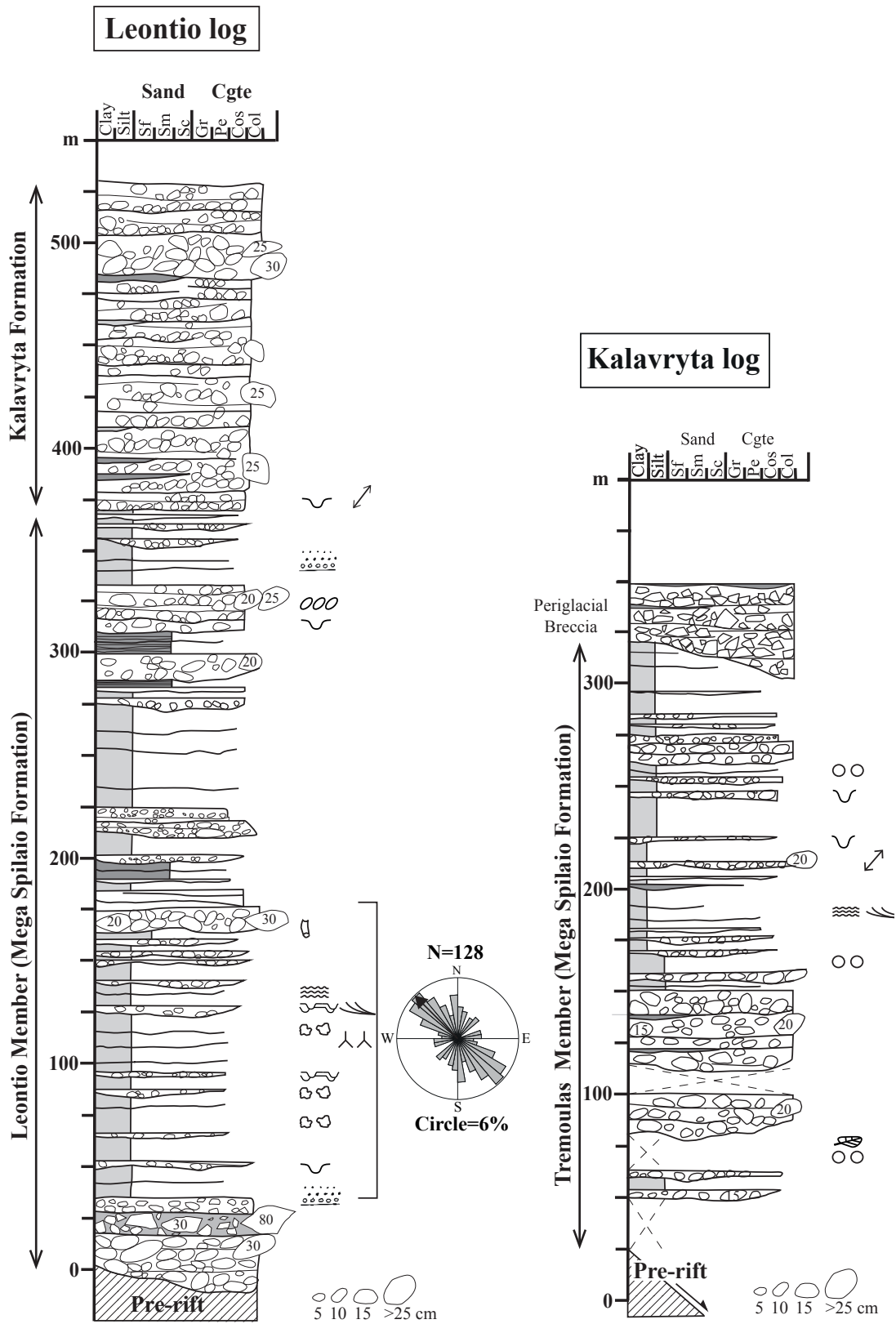
- Current ripple cross-lamination
- Climbing ripple cross-lamination
- Trough cross-lamination
- Sigmoidal cross-lamination
- Tabular cross-lamination
- Tangential cross-lamination
- Low angle lamination
- Undulated to wavy lamination
- Normal grading
- Inverse grading
- Imbricated clasts
- Load casting
- Convolute lamination
- Water-escape structure
- Clastic dyke
- Bioturbation (horizontal/vertical axis)

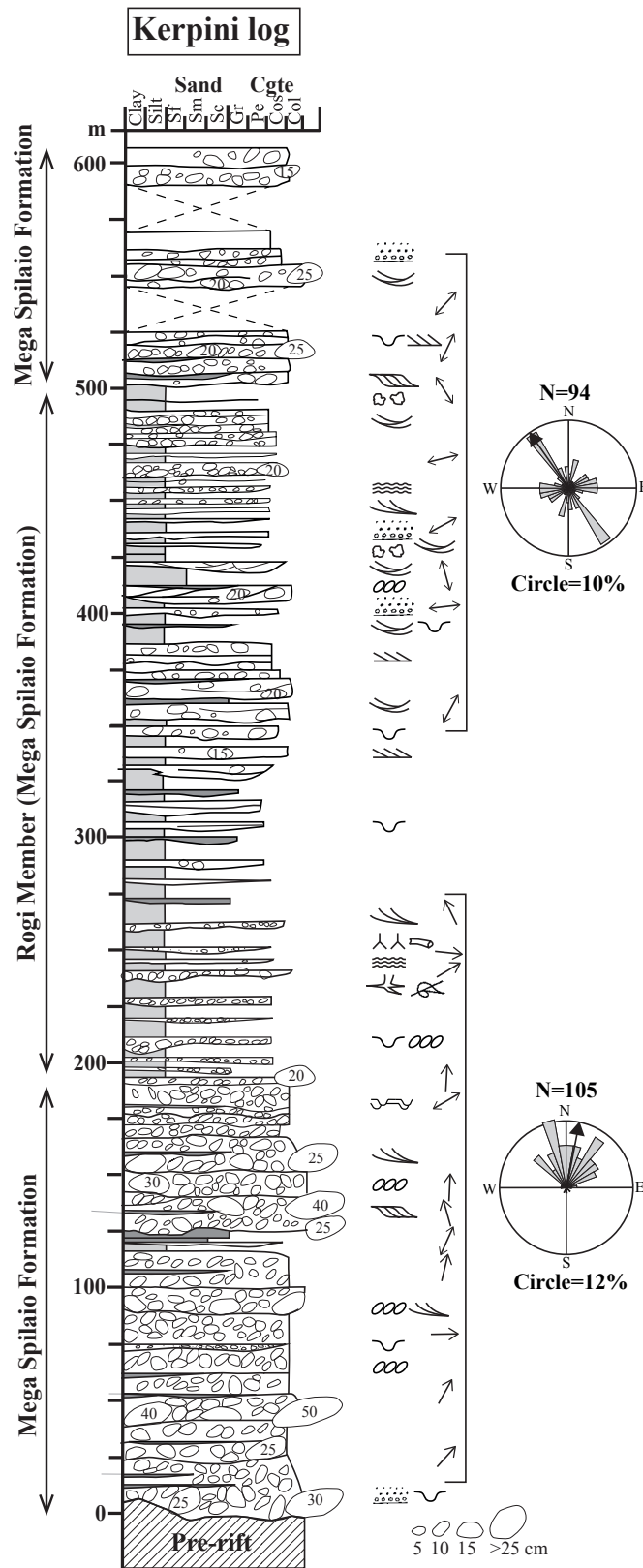
Pedogenic features and vegetation

- Roots
- Wood fragments
- Plant leaf
- Carbonate nodules

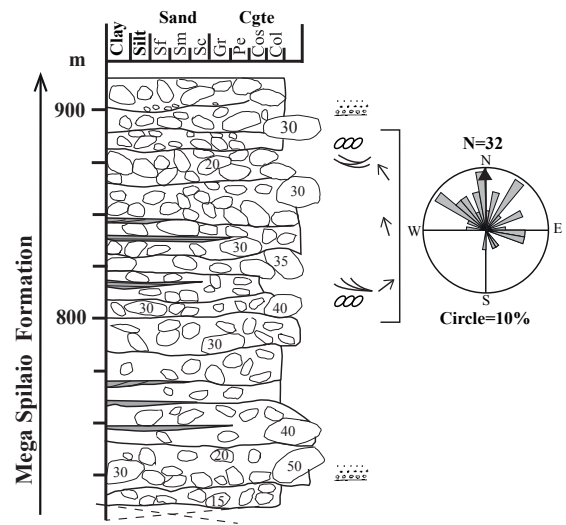
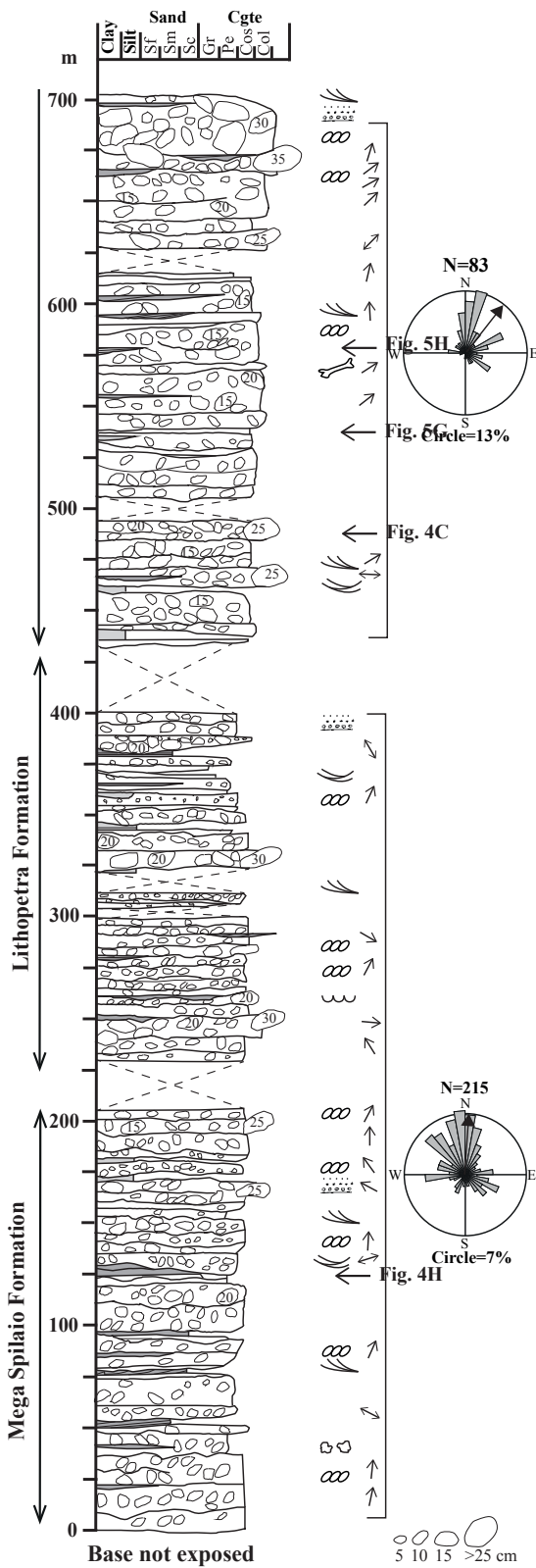
Fossils

- Gastropod
- Bioclast
- Mammal bone
- Mammal tooth
- Charophytes (green algae)

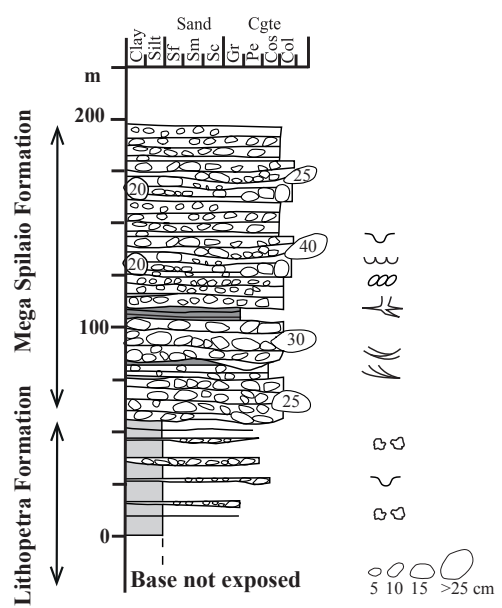


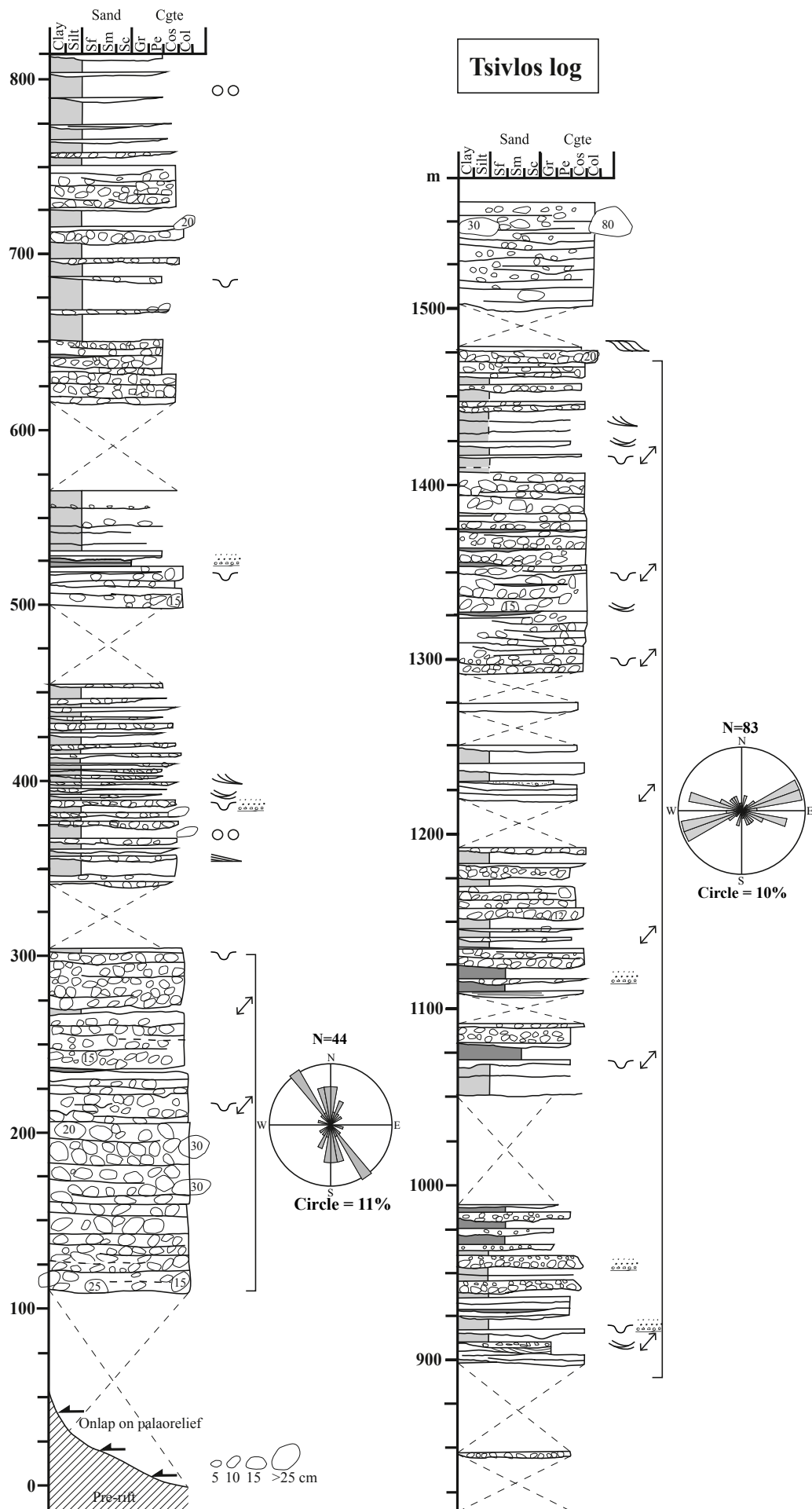


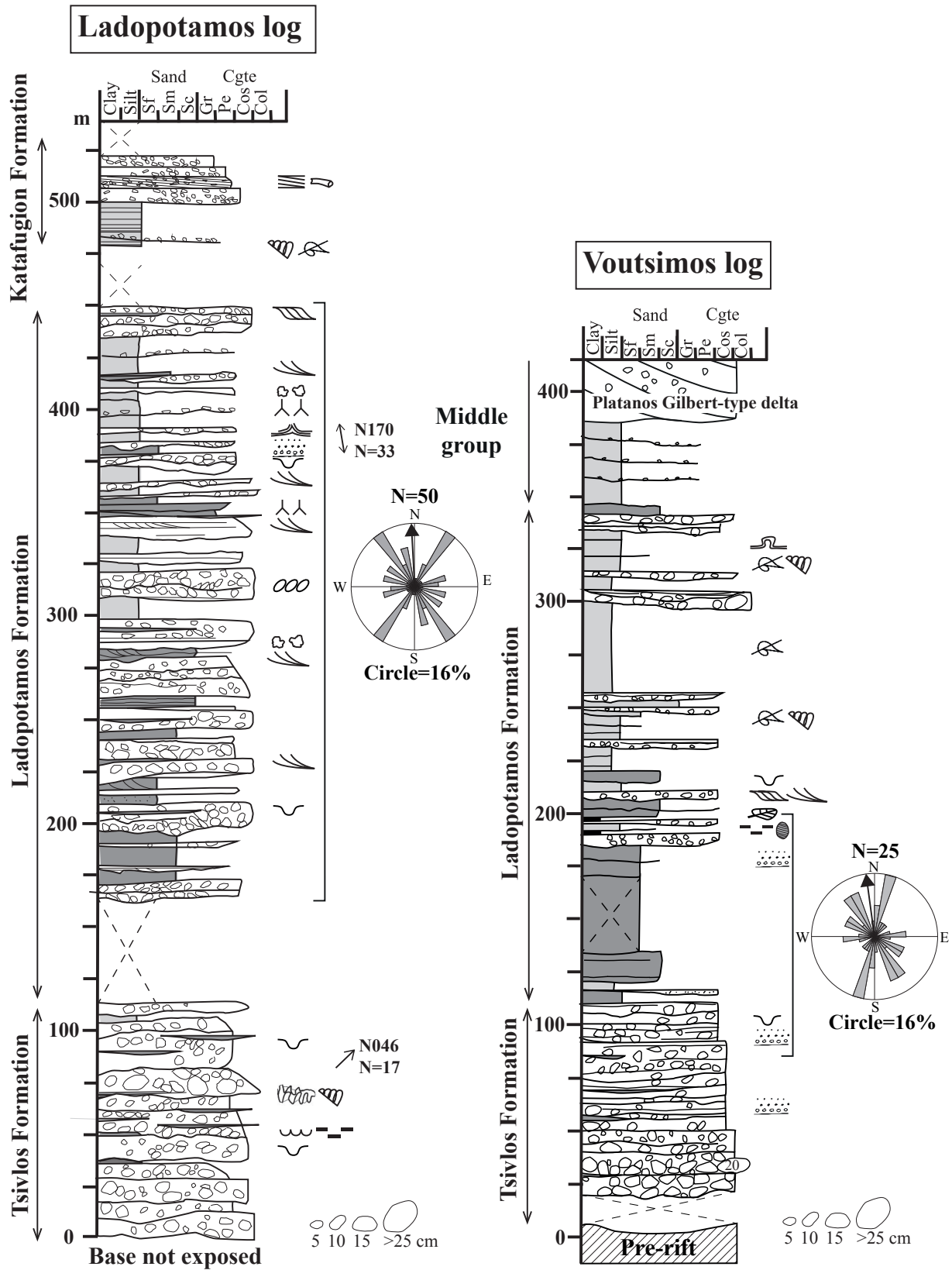
Doumena log

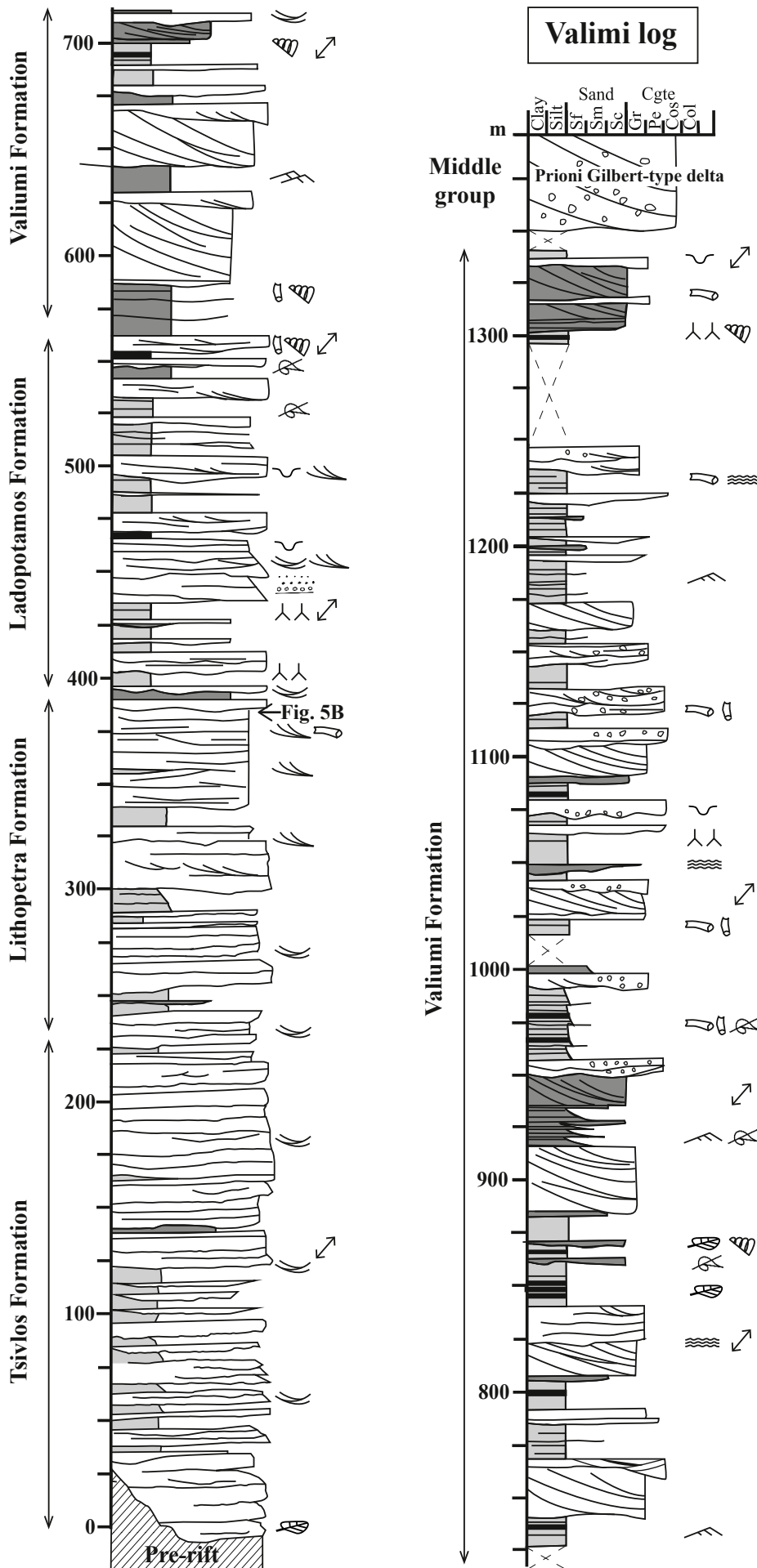


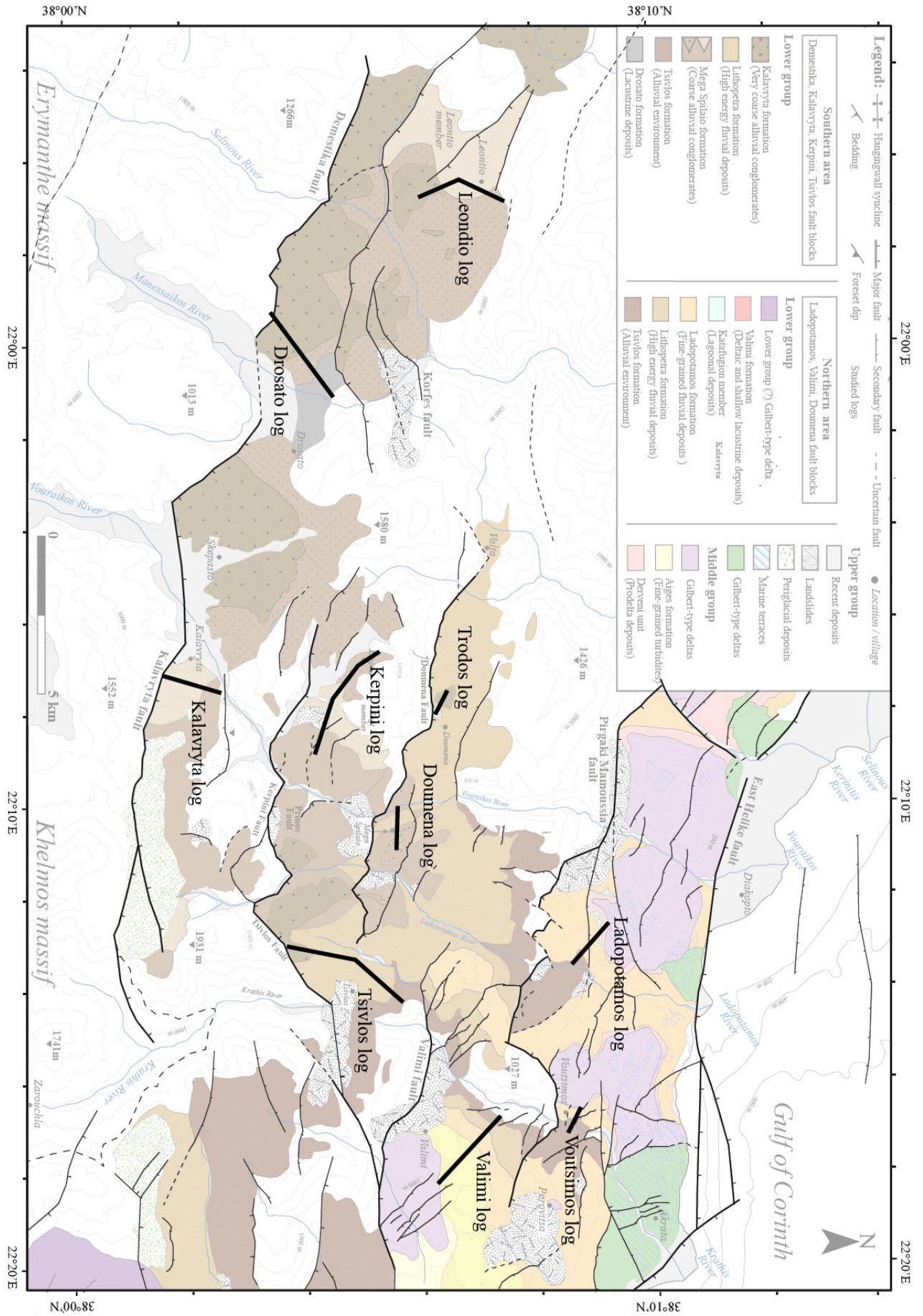
Trodos log











B.3 Algues vertes calcaires : détermination et distribution stratigraphique

Nitellopsis majoriformis (Papp, 1951)

- Figure B.1A, B et C.
- Formation de Drosato.
- Longueur entre 1,45 et 1,58 mm, largeur entre 1,28 et 1,28 mm, nombre de spires 8 ou 9.
- Cette espèce est initialement décrite dans le Miocène supérieur du bassin pannonien (Papp, 1951). Mädlér & Staeche (1979) l'ont trouvée dans une dizaine de localités en Turquie dont l'âge s'étale entre le Serravalien (Miocène moyen) et le Pléistocène. Il s'agit d'une espèce d'eau douce dont la profondeur ne dépasse pas 10 m.

Nitellopsis groupe *merianii*

- Figure B.1D, E, F et G).
- Formation de Drosato.
- 52 gyrogonites pourraient être rapportées à ce groupe. La longueur varie de 0,92 à 1,10 avec une moyenne de 9,91 mm, et la largeur varie de 0,82 à 0,91 avec une moyenne de 0,87 mm. En vue latérale les gyrogonites ont une forme de poire, l'apex est plutôt arrondi, tandis qu'à la base, l'entonnoir est petit, profond et étoilé. Les spires sont au nombre de 7 à 9, en général 8, et sont modérément convexes et arrondies. Ces caractères sont rencontrés dans de nombreux échantillons de ce groupe, depuis l'Oligocène supérieur dans toute l'Eurasie et l'Afrique du Nord.

Lychnothamnus sp. (Papp, 1951)

- Figure B.1J.
- Formation de Drosato
- Une seule gyrogonite trouvée dans cet échantillon mesure 1,02 x 0,82 mm en longueur et largeur. Le nombre de spires est de 8. Les spires sont concaves, saillantes dans les zones de suture ; la suture est simple, l'apex aplani, la base en forme d'entonnoir étoilé. Ce genre possède plusieurs espèces assez similaires les unes des autres. Avec une seule gyrogonite, il est hasardeux de déterminer l'espèce. Il est différent de *Lychnothamnus barbatus* var. *bicarinatus* décrit par Soulié-Märsche (1979) dans le Pliocène de Grèce. Ce spécimen est plus grand que *L. barbatus* (Miocène supérieur-actuel) mais présente une morphologie similaire. Mädlér & Staeche (1979) ont rapporté trois espèces similaires du genre *Amblyochara* (*A. tortonica*, *A. anatolica* et *A. concava*), et qui peuvent être rangées dans le genre *Lychnothamnus*. La forme observée dans la Formation de Drosato ressemble à *A. anatolica* en taille et en forme. Cette espèce existe depuis l'Oli-

gocène inférieur.



FIGURE B.1 – **A, B, C** : *Nitellopsis majoriformis* (Papp, 1951) found in the Drosato Formation. Lateral, apical and basal views (**A, B, C** respectively). **D, E** and **G** : *Nitellopsis*, groupe *merianii* (Braun ex Unger, 1850) found in the Drosato Formation. Lateral (**D, G**), apical (**E**) and basal views (**F**). **H** : *Chara* sp. (gender and specie not determined) found in the Drosato Formation (lateral view). **I** : Deformed gyrogonite (*Characea*) found in a lignite bed in the Ladopotamos Formation. **J** : *Lychnothamnus* sp. found in the Drosato Formation (lateral view). **K** : Teeth of voles (Rodentia) found in the Drosato Formation.

Annexe C

Isotopes cosmogéniques : âges d'enfouissement ^{26}Al et ^{10}Be

Comprendre la méthode d'âges d'enfouissement à partir des isotopes cosmogéniques ^{26}Al et ^{10}Be nécessite l'explication des généralités sur les isotopes cosmogéniques. Ces derniers sont généralement utilisés pour dater l'exposition de surfaces (érodées ou non) et déterminer des taux de dénudation dans les bassins versants. La détermination d'âges d'enfouissements permet dater des dépôts récents dont l'âge est compris entre 0,1 et 5 Ma environ. Cette technique est donc applicable aux séries alluviales plio-quadernaires du golfe de Corinthe. Les notions abordées dans cette section sont principalement issues de [Dunai \(2010\)](#) et des données récentes de la littérature.

C.1 Origine des isotopes cosmogéniques

Les isotopes cosmogéniques ou cosmonucléides sont des isotopes qui proviennent d'une cascade de réactions nucléaires dans l'atmosphère terrestre sous l'action du rayonnement cosmique (principalement composé de protons et de particules α). Le rayonnement cosmique dérive de l'explosion de supernova et sa source est extérieure au système solaire. Il est considéré comme isotrope (homogène dans toutes les directions de l'espace) mais l'intensité du flux cosmique sur Terre varie en fonction de l'altitude et de la latitude (en lien avec le champ magnétique terrestre). En considérant un champ magnétique dipolaire, le flux cosmique est perpendiculaire à l'équateur et tangentiel aux pôles terrestres. Au niveau de l'équateur, les particules cosmiques sont partiellement repoussées par le champ magnétique et le flux cosmique en surface diminue.

Le rayonnement cosmique est composé de protons (83%), de particules α , d'électrons (3%) et d'autres noyaux lourds (1%). Les rayons cosmiques de haute énergie (0,1 GeV à 10 GeV ¹) entrent dans la haute atmosphère et sont à l'origine d'une cascade de réactions nucléaires (Figure

1. Electron-volt (eV) : énergie cinétique acquise par un électron soumis à une différence de potentiel électrique d'un volt.

C.1). Ces réactions produisent des atomes plus légers et des particules secondaires composés de neutrons et de muons ² (entre 0,1 et 500 MeV). On s'intéresse au flux secondaire (auss appelé "douche secondaire") du rayonnement cosmique et à ses produits créés dans l'atmosphère. Par exemple, la collision d'un proton ou d'un neutron avec un atome d'oxygène ^{16}O peut produire des isotopes cosmogéniques atmosphériques ^{10}Be et ^{26}Al . De même, les atomes de silicium (Si) peuvent aussi engendrer les isotopes cosmogéniques atmosphériques ^{10}Be et ^{26}Al (entre autres). Toutes les réactions entre les particules cosmiques et les éléments de l'atmosphère ne sont pas développées ici (voir Gosse & Phillips, 2001; Dunai, 2010). L'ensemble des particules secondaires se propage jusqu'à la surface terrestre où est produit plus de 98% des cosmonucléides atmosphériques (Figure C.1).

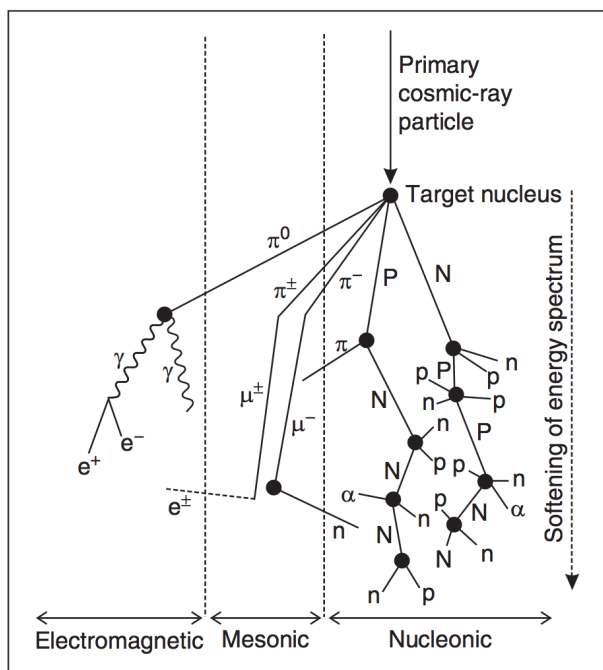


FIGURE C.1 – Le flux primaire interagit avec les particules de la haute atmosphère. La cascade réactionnelle qui en découle aboutit au flux secondaire plus bas dans l'atmosphère. Une partie de ce flux interagit avec les atomes de l'atmosphère pour former les isotopes cosmogéniques atmosphériques. Une autre partie du flux qui atteint la surface interagit avec les atomes présents dans la roche pour former les isotopes cosmogéniques produits *in situ*. Abréviations utilisées : n, neutron ; p et P, proton ; α , particule alpha ; e^- , électron ; e^+ , positon ; γ , photon rayon gamma ; π , pion ; μ , muon.

C.2 Production *in situ* des isotopes cosmogéniques

Les isotopes cosmogéniques produits *in situ* résultent de l'interaction des particules du flux cosmique secondaire avec les atomes présents dans les minéraux à la surface terrestre. En fonction de l'énergie de ces particules, les isotopes cosmogéniques (et notamment ^{26}Al et ^{10}Be) sont produits par spallation ³ ou par capture des muons (Gosse & Phillips, 2001; Dunai, 2010). Par exemple, la spallation d'un atome de ^{16}O due à l'impact d'un neutron émet un atome de ^{10}Be , 4

2. Produit secondaire du rayonnement cosmique dont la profondeur de pénétration à la surface terrestre est plus importante que celle des neutrons et responsable de la majorité de la production des cosmonucléides en profondeur.

3. Réaction nucléaire générée par l'impact des neutrons à haute énergie intervenant dans la production de nucléons. Ces derniers sont éjectés des noyaux cibles et introduits dans une cascade de réaction dans l'atmosphère ("douche secondaire").

protons, 3 neutrons. De même, la spallation d'un atome ^{28}Si due à l'impact d'un neutron émet un atome de ^{26}Al , 1 proton, 2 neutrons. Ces isotopes cosmogéniques sont piégés à l'intérieur de la maille cristalline et s'accumulent au cours du temps dans le minéral cible. On s'intéresse ici à la vitesse d'accumulation de ^{26}Al et ^{10}Be dans le quartz, minéral ubiquiste.

Le taux de production des isotopes cosmogéniques dépend de la latitude et de l'altitude du site. Comme précédemment mentionné, le paramètre de latitude est directement lié à l'intensité du champ magnétique terrestre et l'altitude traduit l'épaisseur d'atmosphère au dessus du site étudié (Lal, 1991; Stone, 2000; Lifton *et al.*, 2014). Le taux de production de référence est celui situé au niveau de la mer et à haute latitude (*SLHL, Sea Level High Latitude*). La calibration du taux de production à différents sites d'échantillonnage a fait l'objet de nombreux travaux (Balco & Rovey, 2008; Dunai, 2010; Borchers *et al.*, 2016; ?)

La majeure partie du flux secondaire est absorbée à la surface de la roche et la production *in situ* des isotopes cosmogéniques décroît exponentiellement avec la profondeur en fonction de la densité de la roche. La longueur d'atténuation correspond à la distance à partir de laquelle le flux cosmique diminue de 63%. Elle décroît en fonction de la densité croissante du matériau. La longueur d'atténuation des neutrons est comprise entre 150 et 180 g.cm^{-2} et varie avec la latitude. Pour une masse volumique de 2,7 g.cm^3 , la longueur d'atténuation est d'environ 0,6 m et moins de 1% des neutrons pénètrent le matériau après 2,5–3,0 mètres (Dunai, 2010). Quant aux muons, ils interagissent moins avec la matière et pénètrent plus profondément. La longueur d'atténuation des muons est environ un ordre de grandeur supérieure à celle des neutrons (quelques dizaines de mètres). Les longueurs d'atténuation Λ des muons rapides et des muons lents sont respectivement 510 et 260 g.cm^{-2} (Braucher *et al.*, 2011).

La production *in situ* des isotopes cosmogéniques (P) décroît exponentiellement avec la profondeur z . Elle est exprimée par l'équation C.1 (en atomes. $\text{g}^{-1}.\text{an}^{-1}$) (Lal, 1991). P_0 est le taux de production en surface exprimé en atomes. g^{-1} . La masse volumique de la roche ρ est exprimée en g.cm^3 . Les taux de production moyens par les neutrons, les muons lents et muons rapides sont définis par $P_{\text{spallation}}$, $P_{\text{muons lents}}$, $P_{\text{muons rapides}}$ en atomes. $\text{g}^{-1}.\text{an}^{-1}$ respectivement. Il en est de même pour les longueurs caractéristiques d'atténuation $\Lambda_{\text{spallation}}$, $\Lambda_{\text{muons lents}}$ et $\Lambda_{\text{muons rapides}}$ en g.cm^{-2} .

$$P(x) = P_0_{\text{spallation}} \times e^{-\left(\frac{z \cdot \rho}{\Lambda_{\text{spallation}}}\right)} + P_0_{\text{muons lents}} \times e^{-\left(\frac{z \cdot \rho}{\Lambda_{\text{muons lents}}}\right)} + P_0_{\text{muons rapides}} \times e^{-\left(\frac{z \cdot \rho}{\Lambda_{\text{muons rapides}}}\right)} \quad (\text{C.1})$$

C.3 Décroissance radioactive et production de ^{26}Al et ^{10}Be

Les isotopes cosmogéniques ^{26}Al et ^{10}Be sont radioactifs et leurs désintégrations radioactives (de type β) fait diminuer leurs concentrations au cours du temps. La décroissance radioactive

de ^{26}Al et ^{10}Be est respectivement définie par les temps de demie-vie de 0,708 Ma (Nishiizumi, 2004) et 1,387 Ma (Korschinek *et al.*, 2010; Chmeleff *et al.*, 2010). Les principales caractéristiques des isotopes cosmogéniques ^{26}Al et ^{10}Be sont rappelées dans le tableau C.1. Le taux de production en surface de ^{26}Al est cinq fois plus élevé que ^{10}Be mais ^{26}Al se désintègre deux fois plus rapidement au cours du temps que ^{26}Al .

TABLE C.1 – Principales caractéristiques des isotopes cosmogéniques ^{10}Be et ^{26}Al (SLHL). Compilation issue de (Chmeleff *et al.*, 2010; Korschinek *et al.*, 2010; Nishiizumi, 2004; Balco & Shuster, 2009; Braucher *et al.*, 2011).

Isotope cosmogénique	^{10}Be	^{26}Al
Demie-vie (Ma)	$1,387 \pm 0,139$	$0,708 \pm 0,017$
Constante de désintégration, λ (an^{-1})	$5,10 \pm 0,26 \times 10^{-7}$	$9,83 \pm 0,25 \times 10^{-7}$
Production des neutrons en surface, P (atomes. $\text{g}^{-1}.\text{an}^{-1}$)	3,900	30,030
Production des muons lents en surface, P (atomes. $\text{g}^{-1}.\text{an}^{-1}$)	0,012	0,840
Production des muons rapides en surface, P (atomes. $\text{g}^{-1}.\text{an}^{-1}$)	0,039	0,081
Minéraux cibles	Quartz	Quartz

La concentration en isotopes cosmogéniques augmente au cours du temps et dépend du taux de production P . Les isotopes cosmogéniques s'accumulent dans la roche jusqu'à ce que leur concentration atteigne un état stationnaire (courbe asymptotique) sauf pour les isotopes stables ^3He et ^{21}Ne et ^{38}Ar (Figure C.2). L'état stationnaire ou état d'équilibre est atteint lorsque la production des isotopes cosmogéniques équivaut à leurs pertes par décroissance radioactive et par dénudation. La quantité d'isotopes cosmogéniques produits *in situ* dans le minéral cible permet de déterminer le temps d'exposition aux rayonnements cosmiques. Ce temps d'exposition doit être corrigé du taux d'érosion ε car le renouvellement de la surface fait baisser la concentration en isotopes cosmogéniques.. Un fort taux d'érosion et l'état stationnaire limitent la détermination d'âge d'exposition (Figure C.3).

La concentration absolue d'une surface exposée et érodée est exprimée par la formule C.2. λ (an^{-1}) est la constante de désintégration de l'isotope radioactif, z_0 est la profondeur initiale et ε correspond au taux d'érosion. Dans le cas d'une roche exposée depuis suffisamment longtemps, à l'état stationnaire, C_{totale} ne dépend plus du temps d'exposition. On a alors le temps d'exposition $t \gg 1/(\lambda + \rho.\varepsilon)/\Lambda_i$. L'histoire géologique des sédiments échantillonnées et des minéraux les constituant est parfois complexe. Afin de fournir des âges ou des taux de processus de surface, on néglige la concentration héritée dans le minéral cible avant l'exposition de la surface. Si on suppose une concentration héritée nulle $C_{\text{inh}} = 0$, la concentration en isotopes cosmogéniques est calculée par l'équation C.3.

$$C_{\text{total}}(t, z) = C_{\text{inh}}(z)e^{-\lambda t} + \sum_i \frac{P_i(z)}{\lambda + \rho\varepsilon/\Lambda_i} \times e^{-\frac{\rho(z_0 - \varepsilon t)}{\Lambda_i}} \times (1 - e^{-(\lambda + \frac{\rho\varepsilon}{\Lambda_i})t}) \quad (\text{C.2})$$

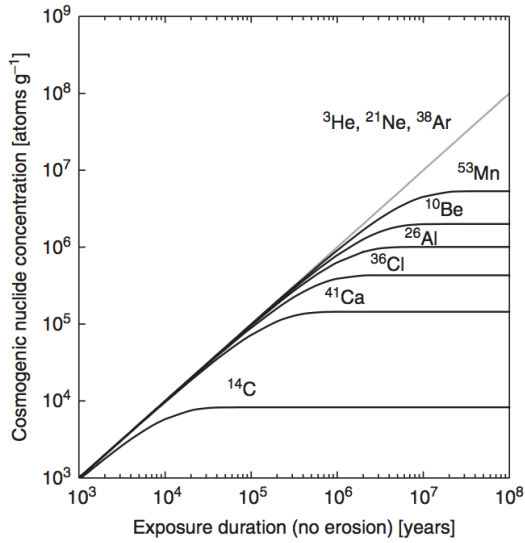


FIGURE C.2 – Influence de la décroissance radioactive sur l'accumulation des isotopes cosmogéniques au cours du temps (sans érosion). Le taux de production est ici de 1 atome.g⁻¹.a⁻¹. A part pour les isotopes stables ^3He , ^{21}Ne , ^{38}Ar , l'accumulation des isotopes cosmogéniques est saturée après 2 ou 3 demie vies (équilibre séculaire).

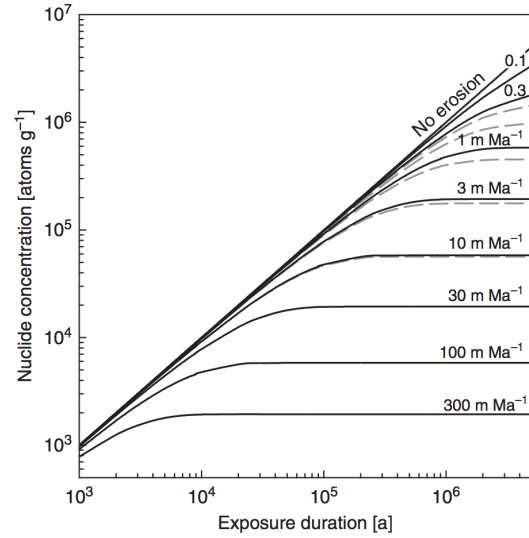


FIGURE C.3 – Influence du taux d'érosion sur l'accumulation des isotopes cosmogéniques d'une surface au temps du temps. Les courbes en trait continu correspondent aux isotopes stables et les courbes en pointillés correspondent au ^{10}Be . Dans cet exemple, le taux de production est de 1 at.gr⁻¹.a⁻¹. Le renouvellement de la surface par l'érosion fait baisser la concentration en isotopes cosmogéniques. Pour des taux d'érosion inférieurs à 10 m.Ma⁻¹, la désintégration nucléaire de ^{10}Be diminue la concentration en ^{10}Be .

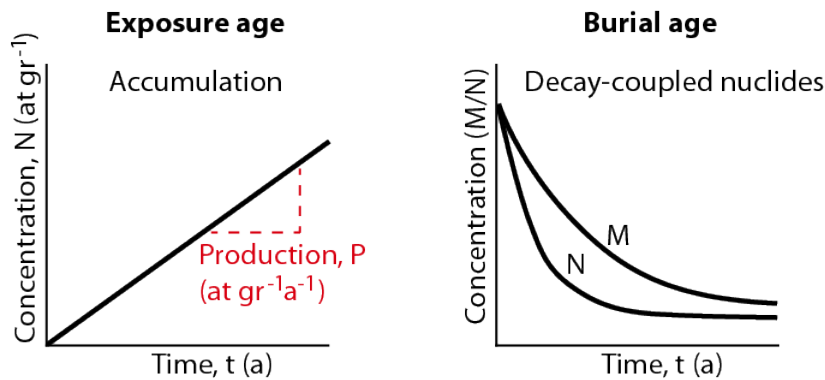


FIGURE C.4 – Modèles généraux décrivant la concentration des isotopes cosmogéniques afin de déterminer l'âge d'une roche. L'accumulation des isotopes cosmogéniques produits *in situ* dans la roche permet de déterminer un âge d'exposition (gauche). La décroissance radioactive d'un couple d'isotopes cosmogéniques permet d'estimer un âge d'enfouissement (droite).

$$C_{total}(z) = \sum_i \frac{P_i}{\lambda + \rho\varepsilon/\Lambda_i} \quad (\text{C.3})$$

Plus une surface est exposée aux rayonnements cosmiques, plus sa concentration en isotopes

cosmogéniques dans les minéraux cibles est élevée (Figure C.4). Quand le matériau est enfoui et que la surface n'est plus exposée au rayonnement cosmique, les cosmonucléides décroissent par désintégration radioactive. La décroissance radioactive d'un couple d'isotopes cosmogéniques avec des temps de demies-vies significativement différentes est exploitée pour déterminer l'âge d'enfouissement. Ce dernier correspond à l'âge depuis lequel la roche est isolée du rayonnement cosmique.

C.4 Détermination d'âge d'enfouissement à partir de ^{10}Be et ^{26}Al

Une roche exposée au rayonnement cosmique sera enrichie d'une certaine concentration en isotopes cosmogéniques ^{26}Al , ^{10}Be . Quand la roche et ses produits d'érosion sont isolés du rayonnement cosmique (sous au moins 15 mètres de sédiments), leur production cesse et leur concentration diminue par décroissance radioactive. La détermination d'âge d'enfouissement repose sur la désintégration différentielle du couple ^{10}Be - ^{26}Al . En mesurant les concentrations actuelles en ^{26}Al , ^{10}Be afin d'obtenir le rapport isotopique $^{26}\text{Al}/^{10}\text{Be}$ dans les grains de quartz, il est possible de dater le temps depuis lequel la roche a été enfouie et isolée du rayonnement cosmique (Klein *et al.*, 1986; Lal, 1991; Granger & Muzikar, 2001; Siame *et al.*, 2006). Le rapport $^{26}\text{Al}/^{10}\text{Be}$ permet de s'affranchir du taux d'érosion. Le rapport des taux de production entre ^{10}Be et ^{26}Al dans le quartz à la surface de la Terre est égal à environ 6,5 mais varie entre 6 et 8 selon les auteurs et les localités (Nishiizumi *et al.*, 1989; Goethals *et al.*, 2009; Balco & Rovey, 2008). Cette valeur correspond au rapport de production initiale R_i avant l'enfouissement. La détermination des concentrations $C_A(t)$ et $C_B(t)$ au cours du temps (équation C.3), pour les isotopes ^{26}Al et ^{10}Be respectivement, permet de calculer le rapport isotopique $^{26}\text{Al}/^{10}\text{Be}$ en surface, $R_{AB}(t)$ (équation C.4). De cette façon, on peut estimer l'âge d'enfouissement t par l'équation C.5.

$$R_{AB} = \frac{C_A(t)}{C_B(t)} = \frac{C_A(0)e^{-\lambda_A t}}{C_B(0)e^{-\lambda_B t}} = R_p \times e^{-t(\lambda_A - \lambda_B)} \quad (\text{C.4})$$

$$t = -\frac{\ln(R_{AB}/R_i)}{\lambda_A - \lambda_B} \quad (\text{C.5})$$

Un échantillon qui a été exposé en surface à l'état stationnaire puis enfoui peut être représenté dans un diagramme $^{10}\text{Be}/^{26}\text{Al}$ vs. ^{10}Be (échelle logarithmique) aussi appelé diagramme exposition-enfouissement (Klein *et al.*, 1986). La tendance des courbes est expliquée par la différence de demi-vie entre ^{26}Al et celle du ^{10}Be . La saturation (état stationnaire) des concentrations en ^{26}Al et ^{10}Be est représentée par un point invariant à l'extrémité du diagramme. Le taux de production de ^{26}Al est environ six fois plus rapide que celui de ^{10}Be , et ^{26}Al se désintègre plus

rapidement que ^{10}Be . Par conséquent, le rapport $^{26}\text{Al}/^{10}\text{Be}$ ne dépasse jamais le rapport du taux de production. Ceci implique la présence d'une "zone interdite" délimitée par les deux courbes du diagramme. Si le sédiment n'a pas été enfoui et qu'il a subi une simple histoire d'exposition et d'érosion, alors il se situe dans la "banane d'érosion constante" entre les deux courbes (Figure C.5). La courbe supérieure définit l'ensemble des valeurs observables pour une surface non érodée et d'âge quelconque. La courbe inférieure représente l'ensemble des valeurs attendues pour une surface érodée à différents taux. La position d'un échantillon sous la "banane d'érosion" dépend de son âge d'enfouissement. Si le sédiment étudié subit plusieurs épisodes d'exposition et d'enfouissement, le rapport $^{26}\text{Al}/^{10}\text{Be}$ augmente et conduit à un rajeunissement apparent. Dans ce cas, la détermination de l'âge d'enfouissement vrai n'est pas possible (Figure C.5). Afin d'utiliser les isotopes cosmogéniques comme traceur géochimique de l'âge d'enfouissement, une histoire simple d'exhumation, transport et enfouissement est supposée. Le sédiment étudié n'a pas été ré-exposé au rayonnement cosmique au cours de son histoire d'enfouissement. Bien qu'inconnue, la concentration héritée en isotopes cosmogéniques anté-enfouissement et la production post-enfouissement par les muons sont considérées comme nulles. De plus, le temps de transport par les rivières est négligeable comparé à la durée d'exhumation de la roche et n'affecte pas le rapport initial R_p (Schaller *et al.*, 2001).

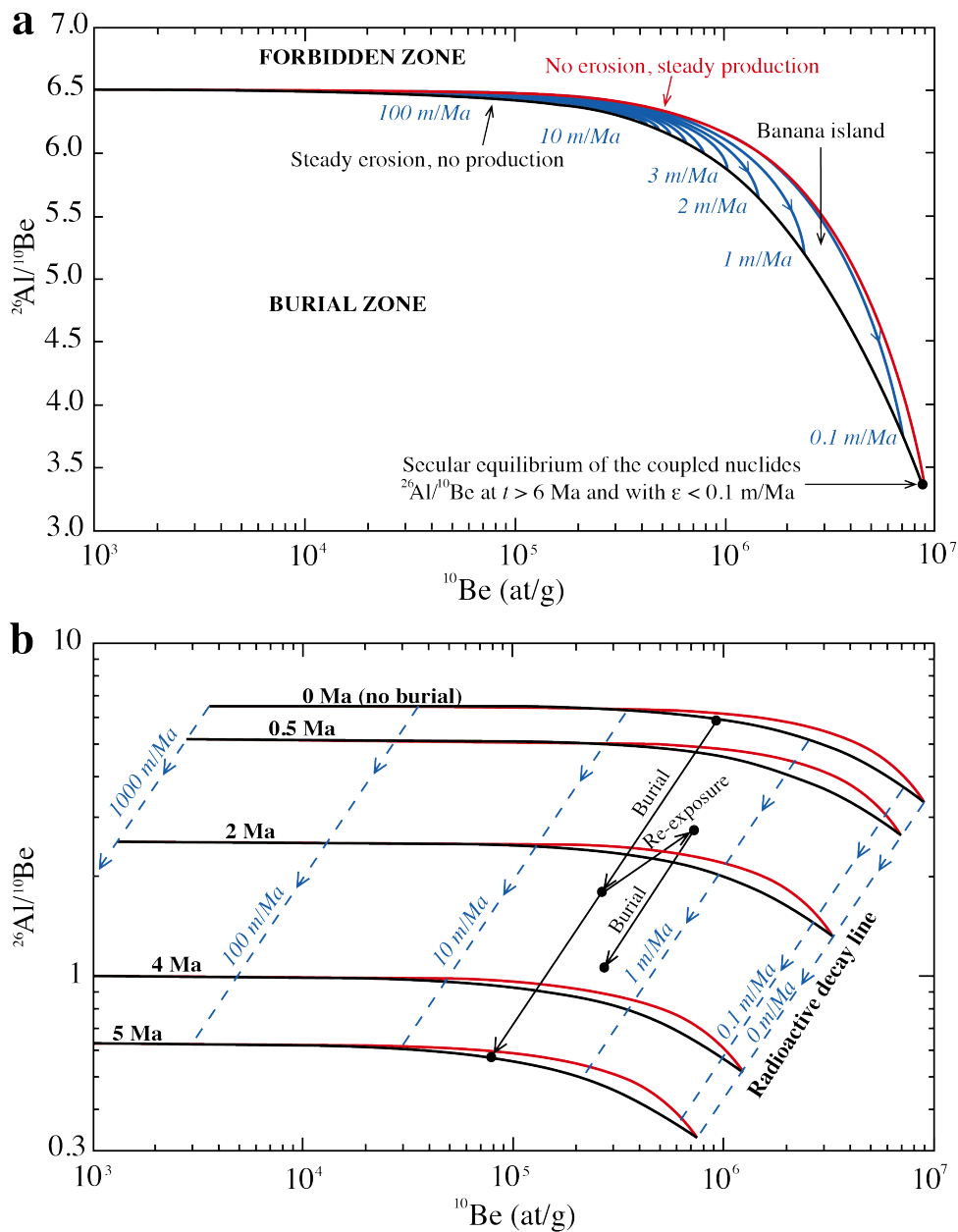


FIGURE C.5 – Diagramme $^{26}\text{Al}/^{10}\text{Be}$ vs. ^{10}Be . La courbe rouge représente le trajet isotopique d'un échantillon exposé continuellement à la surface, sans érosion. La courbe noire correspond à l'enveloppe de saturation pour différents taux d'érosion. On peut lire l'âge d'exposition le long de cette courbe. Le rapport isotopique initial $^{26}\text{Al} / ^{10}\text{Be}$ est ici de 6,5. (a) Un échantillon sans histoire d'enfouissement va se retrouver entre les deux courbes ("fenêtre d'érosion"). Les courbes en bleu représentent le trajet isotopique d'un échantillon pour différents taux d'érosion. (b) Le rapport isotopique $^{26}\text{Al} / ^{10}\text{Be}$ d'un échantillon enfoui diminue le long d'une ligne isochrone de décroissance radioactive qui dépend du taux d'érosion. L'histoire simple d'exposition-enfouissement permet la détermination de l'âge d'enfouissement. La datation de l'échantillon est erronée dans le cas d'une ré-exposition au rayonnement cosmique post-enfouissement (d'après Granger & Muzikar, 2001).

C.5 Taux de dénudation et de taux de production initial à partir des rivières actuelles

Les sédiments collectés à l'embouchure des rivières moyennent l'ensemble des concentrations en isotopes cosmogéniques provenant du matériel érodé dans un bassin versant donné. Le taux de dénudation peut donc être extrapolé à l'échelle du bassin versant à partir de l'analyse d'un ou plusieurs échantillons (Brown *et al.*, 1995; Bierman & Steig, 1996; Granger *et al.*, 1996; Schaller *et al.*, 2001; von Blanckenburg, 2005). Ceci repose sur plusieurs hypothèses : (1) les rivières actuelles sont analogues aux rivières passées (Stock *et al.*, 2004; Haeuselmann *et al.*, 2007). (2) Le taux de dénudation est constant au cours du temps. (3) Les sables échantillonnés sont représentatifs des lithologies drainées dans le bassin versant. (4) La présence de quartz est homogène à l'échelle du bassin versant. (5) Le bassin versant doit être aussi suffisamment large afin que les glissements de terrain ne diminuent pas la concentration en ^{10}Be dans la rivière échantillonnée. Si ces conditions sont rencontrées, les concentrations N en isotopes cosmogéniques ^{10}Be et ^{26}Al sont déterminées à partir de l'équation C.6. Le taux de dénudation ε est exprimé en $\text{cm}\cdot\text{an}^{-1}$. La production moyenne par les neutrons, les muons lents et les muons rapides est définie par $P_{\text{spallation}}$, $P_{\text{muons lents}}$, $P_{\text{muons rapides}}$ en $\text{atomes}\cdot\text{g}^{-1}\cdot\text{an}^{-1}$ respectivement. Il en est de même pour les longueurs d'atténuation $\Lambda_{\text{spallation}}$, $\Lambda_{\text{muons lents}}$ et $\Lambda_{\text{muons rapides}}$ exprimées en $\text{g}\cdot\text{cm}^{-2}$.

$$N = \frac{1}{\varepsilon} \times \left(\frac{P_{\text{spallation}}}{\rho/\Lambda_{\text{spallation}}} + \frac{P_{\text{muons lents}}}{\rho/\Lambda_{\text{muons lents}}} + \frac{P_{\text{muons rapides}}}{\rho/\Lambda_{\text{muons rapides}}} \right) \quad (\text{C.6})$$

Cette expression est fortement dépendante du taux de production moyen dans le bassin versant (somme de $P_{\text{spallation}}$, $P_{\text{muons lents}}$ et $P_{\text{muons rapides}}$). Pour chacun des échantillons issus de bassins versants différents, les taux de production par les neutrons, muons rapide et muons lents sont déterminés à partir du calculateur Basinga (*BASIN average cosmoGenic production and denudation rAtes*). Ce calculateur, développé au CRPG (Zumaque et al., en prép.) et utilisable sous ArcGIS, permet de calculer le taux de production locale pour ^{10}Be et ^{26}Al corrigé de l'altitude et de la latitude (Lal, 1991; Stone, 2000).

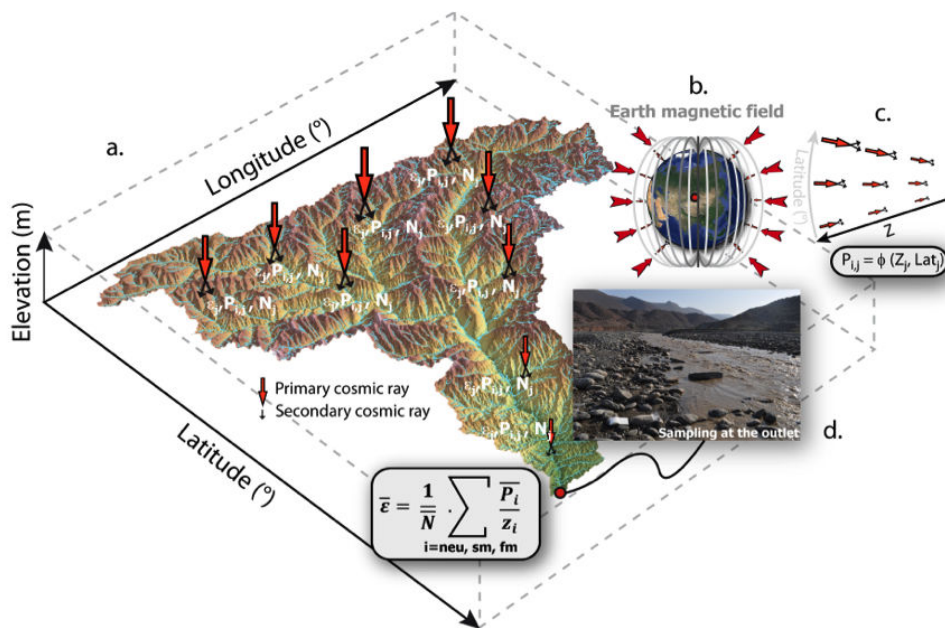


FIGURE C.6 – Modèle de calibration du taux de production des isotopes cosmogéniques en fonction de l'altitude et la latitude du site (a). Les variations spatiales et temporelles du champ magnétique terrestre (b), l'absorption atmosphérique du rayonnement cosmique (c) doivent donc être pris en compte. L'ensemble de ces variables en tous points du bassin versant permettent de déterminer le taux de dénudation moyen à partir d'un échantillon à (ou proche) de l'exutoire (d).

Annexe D

^{26}Al - ^{10}Be burial ages and interpretations

In order to provide new temporal constraints, we attempted to date the syn-rift succession using the cosmogenic isotopes ^{26}Al and ^{10}Be . This method, which dates the burial age using the ^{26}Al and ^{10}Be cosmogenic isotopes, is described below as well as the procedure to determine the ages. Unfortunately, most of the samples could not be used to determine a burial age due to high analytical uncertainty. The few ages obtained have been coupled with magnetostratigraphic dating (see chapter 3) in order to identify local polarity reversals in the syn-rift succession. We sampled quartz-bearing syn-rift sediments in the Lower, Middle and Upper Groups to determine ^{26}Al - ^{10}Be burial ages (in C3 and C4 areas ; Figure 6.1).

D.1 Theory of cosmogenic burial dating

The terrestrial cosmogenic nuclide (TCN) method relies on the fact that rocks exposed on the Earth's surface are constantly bombarded by cosmic rays from space, producing a cascade of reactions and particles, including neutrons (98.5 %) and muons (less than 1.5%), in the lower atmosphere and on the Earth's surface (Lal, 1991; Gosse & Phillips, 2001). These particles penetrate for a few meters into rocks to react with Si and O atoms present in minerals, producing the ^{10}Be and ^{26}Al cosmogenic radio-nuclides (Lal, 1988). The penetration depth is density-dependent. In the upper few meters of the Earth's crust neutron production (spallation) is dominant, whereas muogenic interactions become of increasing importance with depth (Gosse & Phillips, 2001). The rate at which these nuclides are produced depends on the flux of cosmic radiation, which varies in time and space. These variations are related to the geomagnetic field strength, latitude, altitude (i.e. thickness of the atmosphere) and also the shape of the landscape that shields areas from bombardment (Gosse & Phillips, 2001). All these factors must be considered in the determination of the cosmogenic nuclide production rates. However, if the initial erosion is high enough ($>0.01 \text{ mm yr}^{-1}$, which is the case for the northern part of the Peloponnese), the spatial variation of production rates has no effect on the initial ratio of the two cosmogenic nuclides in the samples

(here $^{26}\text{Al}/^{10}\text{Be}$ ratio).

The determination of burial ages is based on the concentration of cosmogenic isotopes ^{10}Be and ^{26}Al produced in situ in quartz grains. The radionuclides are produced before they become shielded from cosmic radiation. After production has stopped, each radionuclide will decay with respect to its half-life : 0.708 Ma for ^{26}Al (Nishiizumi, 2004) and 1.387 Ma for ^{10}Be (Korschinek *et al.*, 2010; Chmeleff *et al.*, 2010). Caves provide a near-ideal configuration for sample collection since recent exposure to cosmic rays is negligible. At a depth of 8–10 m, muons represent 1% of the surface production. Here we sampled the deepest and freshest outcrops with at least 10 m of rock overburden to minimize post-burial production. Post-burial production tends to make apparent ages younger than the actual burial ages (Figure D.1).

The accuracy of $^{26}\text{Al}/^{10}\text{Be}$ results (R_b) relies on the following assumptions : (1) The quartz from which the cosmogenic isotopes are extracted was exposed at the surface to accumulate measurable concentrations of cosmogenic radionuclides. (2) Before burial, the transport time was negligible in comparison to the time of exposure to cosmic rays during erosion. So storage within the catchment was limited. (3) Burial was rapid and deep (>10 m) to avoid cosmogenic nuclide production after deposition. Even if these conditions are fulfilled, the uncertainty of the final age also strongly depends on the detection limit and on the precision of the AMS measurement.

The concentrations of the cosmogenic nuclides ^{26}Al and ^{10}Be enable the determination of the burial age (Klein *et al.*, 1986; Lal, 1991; Granger & Muzikar, 2001; Balco & Rovey, 2008). The measured $^{26}\text{Al}/^{10}\text{Be}$ ratio (R_b) is a function of the burial time t and the initial ratio R_i (Equations D.1 and D.2). The initial concentration $N(0)$ of cosmogenic nuclides before burial of the sample of ^{26}Al and ^{10}Be is a function of the production rate P (atoms $\text{yr}^{-1} \text{gr}^{-1}$), the erosion rate ε (cm yr^{-1}), the attenuation length Λ (g cm^{-2}), the radioactive decay constants of the two radionuclides $\lambda_{^{26}\text{Al}}$ ($9.83 \pm 0.25 \times 10^{-7} \text{ yr}^{-1}$) and $\lambda_{^{10}\text{Be}}$ ($5.10 \pm 0.26 \times 10^{-7} \text{ yr}^{-1}$) and the density (here 6.500 g cm^{-3}) as given by the equation D.3.

$$t = -\frac{\ln(R_{^{26}\text{Al}/^{10}\text{Be}}/R_i)}{\lambda_{^{26}\text{Al}} - \lambda_{^{10}\text{Be}}} \quad (\text{D.1})$$

$$R_b = \frac{N_{^{26}\text{Al}}(t)}{N_{^{10}\text{Be}}(t)} = \frac{N_{^{26}\text{Al}}(0) \cdot e^{-t\lambda_{^{26}\text{Al}}}}{N_{^{10}\text{Be}}(0) \cdot e^{-t\lambda_{^{10}\text{Be}}}} = R_i \times e^{-t(\lambda_{^{26}\text{Al}} - \lambda_{^{10}\text{Be}})} \quad (\text{D.2})$$

$$N(0) = \frac{P(0)}{\lambda + \rho \cdot \varepsilon / \Lambda} \quad (\text{D.3})$$

D.2 Sample collection and analysis

All cosmogenic isotope data are presented in Table D.1. The analysis was mostly performed on amalgamated gravel clasts (AC) and sometimes on single cobble clasts (SC). Quartz-bearing

clasts originate from radiolarites (*2) and Upper Cretaceous to Eocene turbidites (*1) from the Pindos nappe. Quartz grains are rare in these lithologies. Other samples are quartzite clasts from the Phyllite-Quartzite nappe (*3). Sand samples (S) from the modern river, these samples consist predominantly of carbonate grains and quartz grains are rare.

Quartz separation followed by the isolation of pure beryllium and aluminium oxides were performed at the CRPG (Nancy, France) and at the CEREGE (Aix-en-Provence, France). Samples were first crushed and sieved. The non-magnetic fraction 200–500 μm was dissolved in a mixture of H_2SiF_6 and HCl . Quartz was then purified in three successive HF baths to remove atmospheric ^{10}Be from the quartz surfaces (Brown *et al.*, 1991; Kohl & Nishiizumi, 1992). The purified quartz was completely dissolved in HF after addition of 200 μg of a 2020 ppm Be carrier solution (with a $4 \pm 2 \times 10^{-16}$ $^{10}\text{Be}/^9\text{Be}$ ratio) and 2000 μg of a 582 ppm Al carrier. BeO and AlO samples were obtained after subsequent purification by anion exchange, cation exchange and alkaline precipitation. The resulting BeO and AlO were mixed with niobium and silver powder respectively, introduced and pressed in a copper cathode. The $^{26}\text{Al}/^{27}\text{Al}$ and $^{10}\text{Be}/^9\text{Be}$ ratios of the samples were measured at the ASTER national AMS (Accelerator Mass Spectrometer) facility (CEREGE, Aix-en-Provence, France). The measured $^{10}\text{Be}/^9\text{Be}$ ratio was measured against standard $^{10}\text{Be}/^9\text{Be}$ SRM-4325-NIS = $2.79 \pm 0.03 \times 10^{-11}$ (Nishiizumi, 2007). Three chemical blank values were used for the measured $^{10}\text{Be}/^9\text{Be}$ ratio (labelled 3, 4 and 5 in Table D.1). The blank 5 corresponds to the average blank value ($2.41 \pm 1.3 \times 10^{-15}$) obtained in 14 blank samples between 2013 and 2015 at the CRPG lab. The $^{26}\text{Al}/^{27}\text{Al}$ ratio was measured against standard $^{26}\text{Al}/^{27}\text{Al}$ SM-A1-1 ($7.401 \pm 0.064 \times 10^{-12}$) (Arnold *et al.*, 2010). Four chemical blank values were used for the measured $^{26}\text{Al}/^{27}\text{Al}$ (labelled 1, 2, 3 and 4 in Table D.1). Blank corrections represent between 2.2 and 83.6%, and between 3.3 and 78.7% of the measured $^{10}\text{Be}/^9\text{Be}$ and $^{26}\text{Al}/^{27}\text{Al}$ ratios respectively. Total concentration of ^{27}Al was measured to take into account the natural ^{27}Al that was subtracted. Natural ^9Be concentration is considered negligible.

D.3 Local production rate and determination of burial ages

Initial production rate (Equation D.3) includes production by spallation, slow muons and fast muons. The values of muonic production are taken from (Braucher *et al.*, 2011). Attenuation length of fast muons and slow muons are respectively 4320 and 1500 g cm^{-2} (Heisinger *et al.*, 2002). The concentrations of ^{26}Al and ^{10}Be in seven modern river samples and located in five different rainage basins enable us to calculate the local catchment-integrated production rates for ^{26}Al and ^{10}Be . The use of the present day rivers to determine the past production rate is correct assuming constant erosion rate and stable altitude of the rived bed. After DEM extraction of the drainage basin area upstream of the sample sites, local ^{10}Be production rates were computed using the BASINGA calculator (Zumaque *et al.*, submitted). The results of local production rate are given in Table D.2. A production ratio $P_{^{10}\text{Be}}/P_{^{26}\text{Al}}$ of 6.8 at sea level and high latitude (SLHL)

is used (Balco & Rovey, 2008). The calculated average production rate by spallation for $P_{^{26}\text{Al}}$ and $P_{^{10}\text{Be}}$ are respectively 52.8 and 4.0 atoms $\text{yr}^{-1} \text{g}^{-1}$. Using modern river samples, the average ^{10}Be production rate at the surface for fast neutrons, slow muons and fast muons are respectively 7.769, 0.016 and 0.043 atoms $\text{yr}^{-1} \text{g}^{-1}$. Average scaling factors are respectively 1.9, 1.3 and 1.1 and are used to determine the ^{26}Al production rates ($P_{\text{SLHL}} = \text{SF} \times P_{\text{local}}$) (Table D.3).

The solutions for ^{26}Al and ^{10}Be concentrations are presented on the plot, $N_{^{26}\text{Al}}(t)/N_{^{10}\text{Be}}(t)$ against $N_{^{10}\text{Be}}(t)$ (Figure D.3). Two curves delimit an "erosion island" defining the range of values that can be observed at the Earth's surface (Granger & Muzikar, 2001). The upper curve represents the range of saturation values expected on non-eroding surfaces of various ages, while the lower curve represents the range of values expected on eroding surfaces at various rates. By using the local production rate of fast neutrons, slow muons and fast muons, the plot shows an initial concentration ratio at the surface R_i of 7.3. A modern river sample with a simple exposure/erosion history is expected to be between those curves. Exposure during transportation and sediment storage is assumed negligible compared with exposure during exhumation. During burial, the $^{26}\text{Al}/^{10}\text{Be}$ ratio decreases due to radioactive decay. Buried samples with a simple burial history (no post-burial history) lie below the erosion island and the distance from the initial steady erosion curve is proportional to burial duration. More complex exhumation and burial histories will affect the final $^{26}\text{Al}/^{10}\text{Be}$ ratio, leading to the determination of a non-unique apparent (older) age (Figure D.1).

The results of ^{10}Be concentration in modern river samples enable the calculation of erosion rates in five different divides using the watershed average production rates determined from BASINGA. Two samples were analysed for the Krathis and Selinous rivers and gave similar ^{10}Be concentration and erosion rates. In the Kryos, Vouraikos and Kerenitis rivers, erosion rates were determined from the measurement of a single sample. For the different catchments, erosion rates range from $0.06 \pm 0.01 \text{ mm yr}^{-1}$ to $0.26 \pm 0.16 \text{ mm yr}^{-1}$. They are the first cosmogenic-derived erosion rates for the modern rivers of the Corinth rift. However, data are not sufficient to discuss the influence of catchment size and type of drainage (consequent or antecedent rivers) on erosion rates.

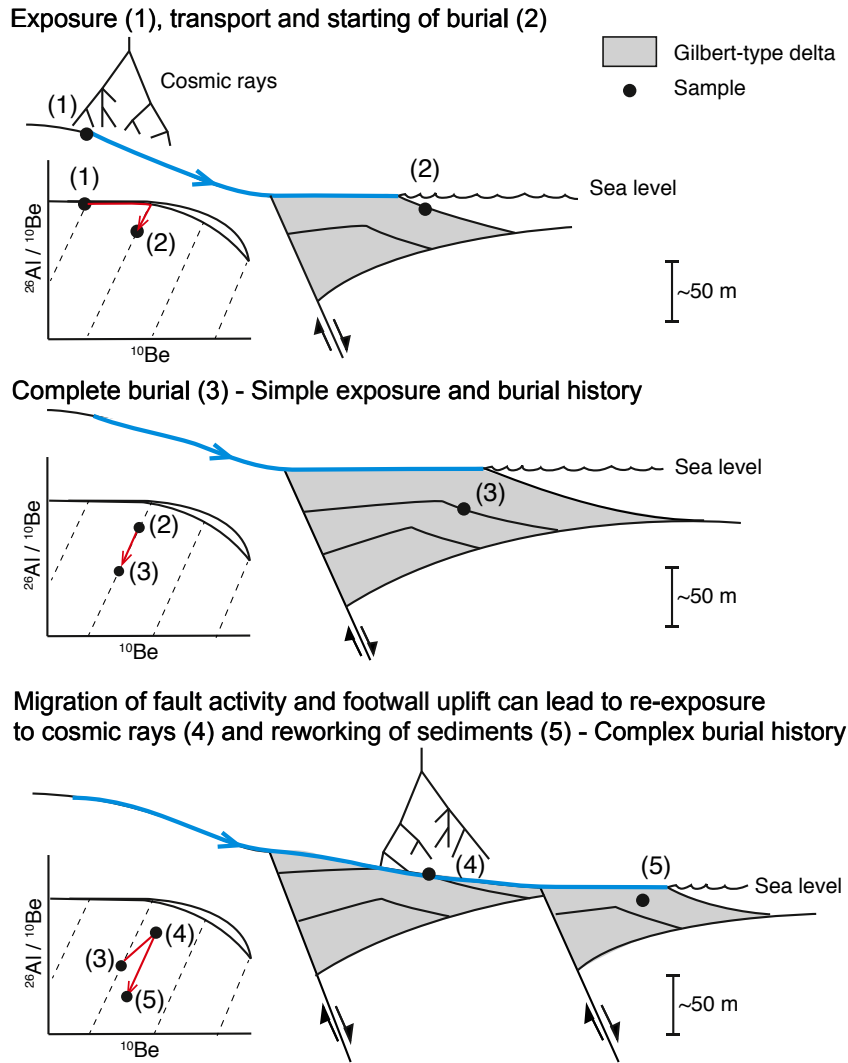


FIGURE D.1 – Application of the ^{26}Al - ^{10}Be burial dating in active rift setting. Exposure-burial diagrams $^{26}\text{Al}/^{10}\text{Be}$ v. ^{10}Be illustrate the isotopic evolution of ^{26}Al and ^{10}Be in quartz grains from exposure at the surface to syn-rift sedimentation and burial at depth. The sketches illustrate the case of the burial of syn-rift sediments during the construction of Gilbert-type fan delta along an active fault. Hangingwall fault migration and persistence of the rivers through time imply complex burial history and reworking of the syn-rift deposits.

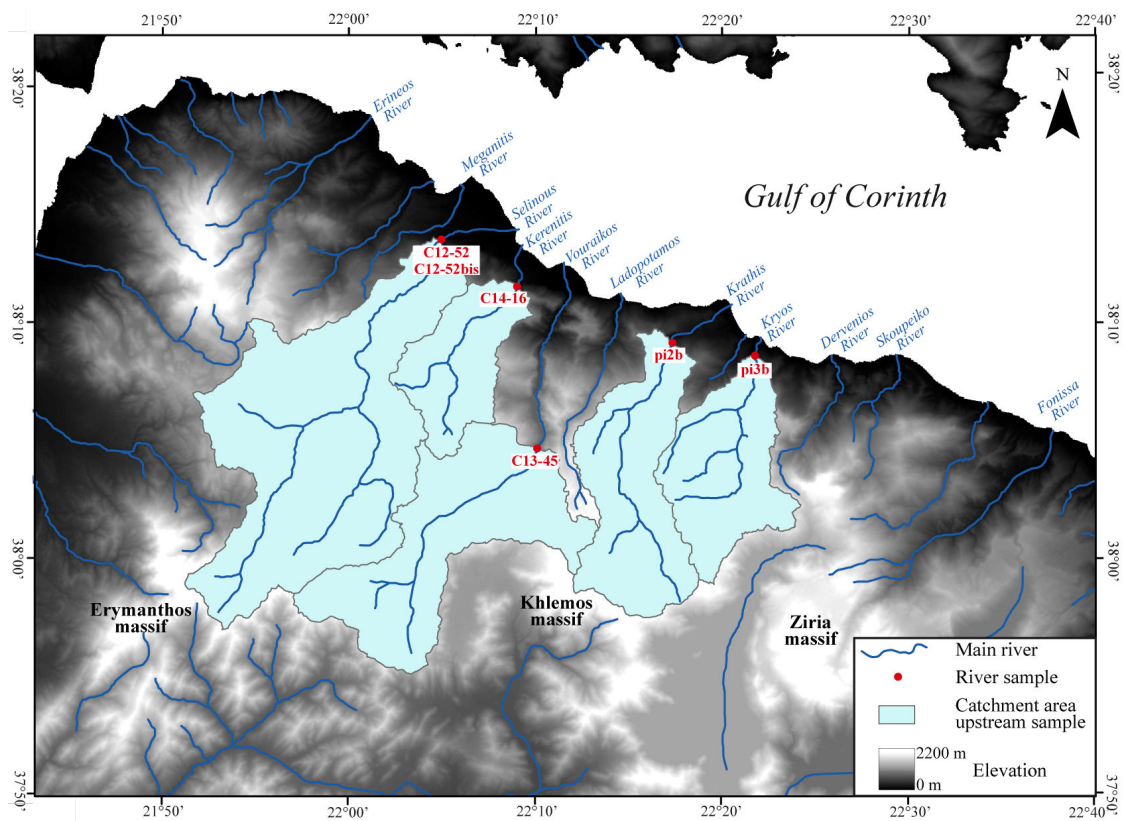


FIGURE D.2 – DEM of the northwestern part of the Peloponnese showing the main rivers. Five river samples have been collected to determine the ^{10}Be derived erosion rates (from west to east : Selinous, Kerinitis, Vouraikos, Krathis and Kryos rivers). Catchment areas are extracted upstream of these samples.

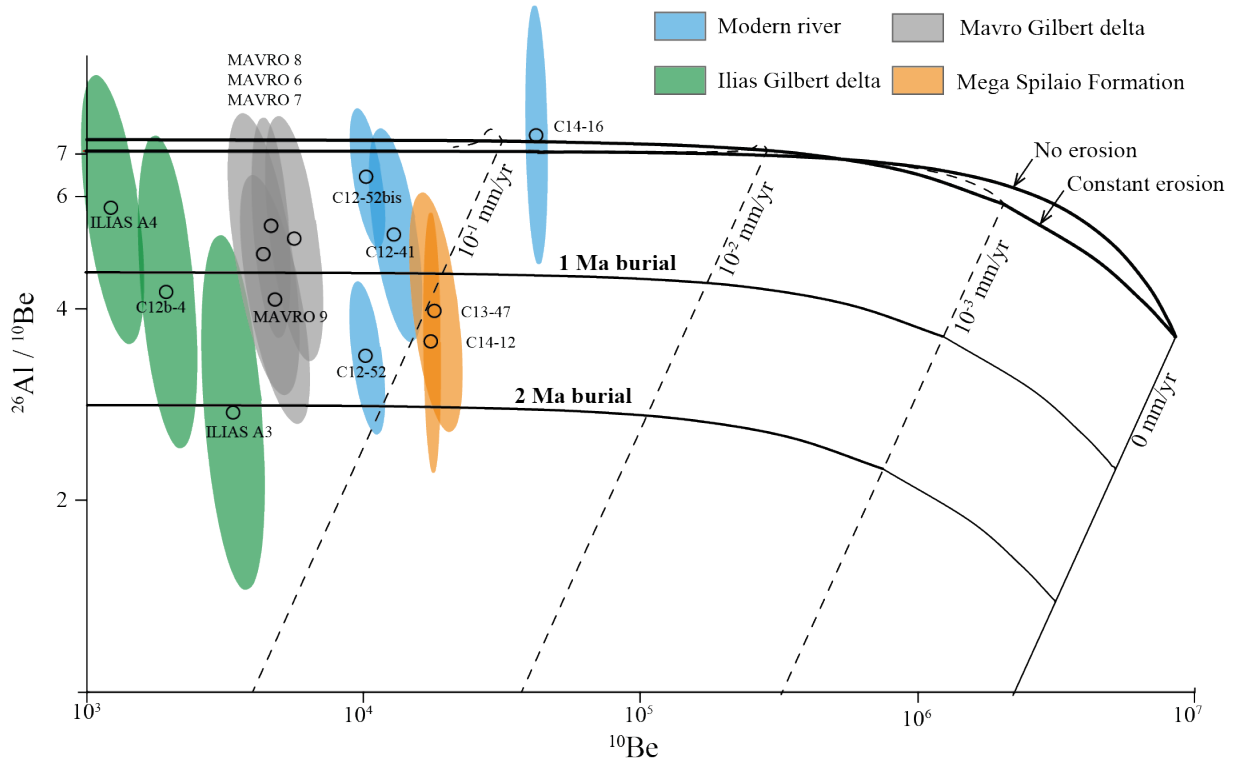


FIGURE D.3 – ^{26}Al - ^{10}Be exposure-burial plot showing the $^{26}\text{Al}/^{10}\text{Be}$ ratio and ^{10}Be concentration in different stratigraphic units. Fast neutrons and muonic productions are considered to trace the banana plot. Burial ages were calculating using an initial $^{26}\text{Al}/^{10}\text{Be}$ ratio (at the surface) of 7.3. This value is consistent with the $^{26}\text{Al}/^{10}\text{Be}$ ratio in most of the present day rivers. Erosion rate derived from four drainage basins vary from 0.06 to 0.32 mm/yr.

TABLE D.1 – Details of the cosmogenic isotope data for all analyzed samples.

	Sample	Lat (°N)	Long (°E)	Type	Quartz (g)	Blanks	Counts	$^{10}\text{Be}/^{9}\text{Be}$ $10\text{e-}14$	% unc	Counts	$^{26}\text{Al}/^{27}\text{Al}$ $10\text{e-}14$
Kryos River	pi2b	38.13650	22.35818	S	3.0	2-5	4	0.63	50 %	1	0.91
Krathis River	pi3b	38.16855	22.33005	S	5.8	5	16	1.17	25 %	-	-
	C12-41	38.15075	22.28554	S	9.6	2-5	26	1.80	21 %	11	2.82
Selinous River	C12-52	38.22200	22.08100	S	23.4	2-5	49	3.25	14 %	19	2.60
	C12-52bis	38.22200	22.08100	S	19.8	2-5	80	2.79	14 %	25	2.61
Vouraikos River	C13-45	38.07446	22.16319	SC	1.0	5	7	0.57	38 %	-	-
Kerenitis River	C14-16	38.18861	22.14836	S	26.5	2-5	120	0.74	9 %	5	1.64
Tsivlos Fm	C13b-22	38.09572	22.17111	AC*1	35.2	2-5	53	1.43	14 %	3	0.57
	C13b-30	38.08142	22.24510	AC*1	57.1	5	37	0.83	16 %	-	-
	C13b-30bis	38.08142	22.24510	AC*1	47.8	5	9	0.94	36 %	-	-
Mega Spilaio Fm	C13-5	38.15435	22.23612	AC*1	5.6	5	6	0.32	46 %	-	-
	C13-42	38.11167	22.91527	AC*1	13.4	5	44	0.77	15 %	-	-
	C13-44	38.06427	22.15568	AC*1	1.9	5	4	2.30	50 %	-	-
	C13-47	38.08684	22.17896	AC*1	4.6	1-5	32	1.35	19 %	11	0.65
	C13b-9	38.07128	22.06352	AC*3	41.9	5	13	4.48	29 %	-	-
	C14-10	38.09507	22.17089	AC*1	54.7	2-5	174	1.74	24 %	2	1.26
	C14-12	38.09009	22.20812	AC*1	65.4	2-5	200	7.56	7 %	6	5.15
Valimi Fm	V7cosA	38.12250	22.30000	AC*2	3.8	5	13	0.52	28 %	-	-
	V41cos	38.11557	22.30138	S	2.9	1-5	6	0.43	44 %	1	0.38
	V73cos	38.11252	22.30435	S	4.5	1-5	11	0.53	30 %	1	0.19
	V175cos	38.10532	22.29428	S	0.6	1-5	12	0.40	34 %	1	1.28
Mavro GD	Mavro-6	38.04243	22.38807	AC*3	5.1	3	42	0.40	15 %	10	1.10
	Mavro-7	38.04243	22.38807	AC*3	5.4	3	32	0.36	19 %	7	0.93
	Mavro-8	38.04243	22.38807	AC*3	11.9	3	60	0.62	13 %	16	2.11
	Mavro-9	38.04243	22.38807	AC*3	4.9	3	32	0.36	18 %	10	0.76
Ilias GD	Ilias-A1	38.09990	22.40650	AC*3	13.0	4	34	339	17 %	-	-
	Ilias-A2	38.09990	22.40650	AC*3	14.6	4	16	273	26 %	1	0.48
	Ilias-A3	38.09990	22.40650	AC*3	12.5	4	30	0.57	19 %	3	0.98
	Ilias-A4	38.09990	22.40650	AC*3	35.3	4	36	0.58	19 %	6	2.08
	Ilias-A4bis	38.09990	22.40650	AC*3	35.9	4	18	0.38	24 %	4	1.66
	C12b-4	38.09990	22.40650	AC*3	35.5	1	25	1.13	20 %	4	1.18
Evrostini GD	Evro-B1	38.08183	22.38365	AC*3	25.6	4	71	0.95	12 %	-	-
	Evro-B2	38.08183	22.38365	AC*3	12.4	4	35	0.57	17 %	1	2.10
	Evro-B3	38.08183	22.38365	AC*3	32.6	4	196	2.58	7 %	1	4.19
	Evro-B4	38.08183	22.38365	AC*3	43.5	4	225	4.95	7 %	-	-
	Evro-B5	38.08183	22.38365	AC*3	62.8	4	238	3.19	6 %	-	-
Kerenitis GD	C12b-3	38.16823	22.11952	SC*2	30.6	1-5	9	0.45	36 %	9	0.45
Vouraikos GD	C12-48	38.15223	22.20626	AC*3	5.9	2-5	38	0.44	50 %	3	0.29
Akrata GD	C12-43A	38.16175	22.31604	AC*3	1.3	1-5	9	0.80	33 %	4	0.52
	C12-43D	38.16175	22.31604	S	1.6	1-5	17	0.54	26 %	2	0.75
	C12-44	38.16067	22.31468	AC*3	1.9	5	7	0.23	38 %	-	-
Blanks	1	-	-	-	-	-	-	-	-	2	0.15
	2	-	-	-	-	-	-	-	-	9	0.37
	3	-	-	-	-	-	14	0.16	29 %	1	0.09
	4	-	-	-	-	-	11	0.21	32 %	2	0.09
	5	-	-	-	-	-	-	2.41	7 %	-	-

D.3 Local production rate and determination of burial ages

	Blank corrected			Blank corrected			27Al (at) 10e+19	26Al (at/g) 10e+4	± 1σ 10e+4	% unc	10Be 10e+4	± 1σ 10e+4	% unc
	% unc	10Be/9Be 10e-14	± 1σ 10e-14	% unc	26Al/27Al 10e-14	± 1σ 10e-14							
100 %	0.39	0.15	38 %	0.76	0.77	101 %	3.09	7.78	7.86	101 %	1.78	1.07	60 %
-	0.93	0.19	21 %	-	-	-	-	-	-	-	2.23	0.64	29 %
31 %	1.56	0.21	13 %	2.67	0.85	32 %	4.19	11.65	3.70	32 %	2.26	0.50	22 %
23 %	3.01	0.22	7 %	2.44	0.57	23 %	5.66	5.91	1.38	23 %	1.79	0.27	15 %
20 %	2.55	0.22	9 %	2.46	0.50	21 %	9.14	11.33	2.33	21 %	1.79	0.26	15 %
-	0.32	0.14	43 %	-	-	-	-	-	-	-	4.35	0.24	55 %
4575 %	7.12	0.23	3 %	1.35	0.63	46 %	59.95	54.40	3.19	6 %	7.33	0.69	9 %
100 %	1.19	0.20	17 %	0.20	0.24	118 %	13.26	0.75	0.89	118 %	0.93	0.16	18 %
-	0.59	0.17	29 %	-	-	-	-	-	-	-	0.27	0.08	27 %
-	0.70	0.18	26 %	-	-	-	-	-	-	-	0.39	0.16	41 %
-	0.08	0.06	76 %	-	-	-	-	-	-	-	0.19	0.33	173 %
-	0.53	0.17	31 %	-	-	-	-	-	-	-	0.53	0.15	29 %
-	0.36	0.30	84 %	-	-	-	-	-	-	-	2.06	1.55	75 %
30 %	1.11	0.20	18 %	0.50	0.19	37 %	11.45	12.37	4.62	37 %	3.17	0.70	22 %
-	4.24	0.23	5 %	-	-	-	-	-	-	-	2.68	0.78	29 %
71 %	1.49	0.21	14 %	0.89	0.64	72 %	30.12	4.92	3.55	72 %	0.73	0.19	26 %
47 %	7.32	0.23	3 %	0.48	2.26	47 %	14.70	10735	5.07	47 %	3.07	0.23	7 %
-	0.36	0.11	30 %	-	-	-	-	-	-	-	10.19	5.47	54 %
100 %	0.18	0.11	57 %	0.23	0.25	111 %	3.64	2.88	3.19	111 %	0.86	0.70	82 %
100 %	0.29	0.13	46 %	0.31	0.11	373 %	7.31	0.49	1.83	373 %	0.83	0.45	54 %
100 %	0.16	0.09	61 %	0.11	1.13	100 %	3.10	54.36	54.60	100 %	3.24	2.91	90 %
37 %	0.24	0.10	39 %	1.01	0.41	41 %	2.49	4.94	1.82	37 %	0.97	0.53	55 %
41 %	0.20	0.09	44 %	0.83	0.39	47 %	2.35	3.62	1.50	41 %	0.75	0.50	67 %
36 %	0.46	0.02	25 %	2.02	0.77	38 %	2.50	4.24	1.55	37 %	0.80	0.25	31 %
33 %	0.20	0.09	44 %	0.67	0.27	40 %	2.49	3.38	1.17	35 %	0.83	0.56	67 %
-	0.13	0.08	63 %	-	-	-	-	-	-	-	0.20	0.21	104 %
100 %	0.06	0.05	79 %	0.39	0.48	125 %	2.17	0.57	0.59	103 %	0.08	0.18	223 %
58 %	0.36	0.13	37 %	0.88	0.57	64 %	2.25	1.58	0.93	59 %	0.58	0.24	40 %
41 %	0.37	0.14	37 %	2.08	0.85	41 %	2.15	1.21	0.50	41 %	0.21	0.08	39 %
51 %	0.17	0.09	56 %	1.56	0.84	54 %	2.01	0.88	0.45	51 %	0.10	0.08	80 %
50 %	0.89	0.19	21 %	1.02	0.52	51 %	4.94	1.42	0.73	51 %	0.34	0.08	25 %
-	0.74	0.17	23 %	-	-	-	-	-	-	-	0.59	0.12	21 %
100 %	0.36	0.13	38 %	1.81	2.11	116 %	2.11	3.43	3.43	100 %	0.59	0.23	40 %
100 %	2.37	0.20	8 %	3.02	4.20	139 %	2.24	2.82	2.82	100 %	1.48	0.13	9 %
-	4.73	0.21	4 %	-	-	-	-	-	-	-	2.22	0.16	7 %
-	2.98	0.20	7 %	-	-	-	-	-	-	-	0.98	0.08	8 %
36 %	0.21	0.11	54 %	0.29	0.15	52 %	7.79	0.74	0.39	52 %	0.91	0.66	72 %
58 %	0.20	0.11	55 %	0.14	0.14	100 %	13.02	3.00	2.99	100 %	0.47	0.31	67 %
50 %	0.56	0.17	30 %	0.37	0.21	59 %	3.15	9.02	5.28	59 %	5.96	2.41	40 %
71 %	0.30	0.14	44 %	596	0.44	73 %	3.36	12.64	9.23	73 %	2.63	1.31	50 %
-	2.06	0.22	11 %	-	-	-	-	-	-	-	14.42	5.53	38 %
71 %	-	-	-	-	-	-	-	-	-	-	-	-	-
33 %	-	-	-	-	-	-	-	-	-	-	-	-	-
10 %	-	-	-	-	-	-	-	-	-	-	-	-	-
71 %	-	-	-	-	-	-	-	-	-	-	-	-	-
-	-	-	-	-	-	-	-	-	-	-	-	-	-

D.4 Burial age results

The results of 41 samples in which $^{10}\text{Be}/^9\text{Be}$ was measured are presented in Table D.1. Given uncertainties are 1σ . A $^{26}\text{Al}/^{27}\text{Al}$ ratio was detected and measured in 27 samples. ^{10}Be concentrations for all samples are on the order of 10^2 – 10^4 atoms g^{-1} of quartz, with often the same or lower order of 1σ analytical uncertainties (7–119%). ^{26}Al concentrations range from 10^3 – 10^5 atoms g^{-1} of quartz with larger uncertainties due to insufficient counts of AMS measurement. Samples with measured $^{26}\text{Al}/^{27}\text{Al}$ ratio with 100% analytical uncertainties were not used to calculate burial age and thus, only 21 samples are presented in Table D.3. Samples were excluded when one of these conditions was encountered : (1) samples plot in the forbidden zone ; (2) error bars cover the full age range of the method (3) the calculated age is not consistent with the age interval previously estimated for the Lower, Middle and Upper Groups ; (4) samples from the same site give significantly different ages (error bars do not overlap).

For example, one of the Upper Group samples from the Akrata relay zone (C12-43A) presents a burial age of 3.24 ± 1.46 Ma. However, this sample should be younger than 0.7 Ma, more specifically between 0.6 and 0.2 Ma according to [Hemelsdaël & Ford \(2016\)](#). Another example is the Middle Group sample (C12b-3) located at the base of the Kerinitis Gilbert-type delta (SU1 ; [Backert *et al.* \(2010\)](#)) that presents a burial age of 4.50 ± 1.84 Ma. However, this sample should be younger than 2.0–1.8 Ma ([Backert *et al.*, 2010](#); [Ford *et al.*, 2013](#)).

Following the criteria listed above, 28 out of 41 samples have been discarded. Only three sampled sites with a total of nine samples have been retained to give age constraints. These samples are located on the map (Figure D.4) and cross section (Figure D.5). They are also represented in the banana plot as well as the modern river samples (Figure D.2). Except for the C14-16 sample from Kerenitis River, the $^{26}\text{Al}/^{10}\text{Be}$ ratio and uncertainties of the other river samples fall into the erosion island and are thus consistent with the calculated initial concentration ratio ($Ri = 7.3$).

In the Doumena fault block, two samples collected within the Mega Spilaio Formation (see locations on Figures D.4 and D.5) give a burial age ranging from 0.4–2.5 Ma. This new constraint is considered in the correlation model of the Lower Group Kalavryta river system (Figure refmodel) in the Chapter 3.

The other burial ages are located in the Mavro and Ilias Gilbert-type deltas. Three samples collected in the foresets of the Ilias Gilbert-type delta give a maximum age of 3.5 Ma. These samples intersect in the age range 0.5–1.7 Ma, giving an average age of 1.2 Ma. Four samples collected in the uppermost alluvial fan succession of the Mavro fault block in the windgap between of the Derveni river and the Olvios catchment (Figure D.2) give a maximum age of 2.2 Ma (see locations on Figure D.4) and error bars intersect in the age interval 0.2–1.5 Ma with an average age of 0.9 Ma.

TABLE D.2 – Results of local ^{10}Be production rate P calculations with BASINGA and using the modern river samples. The average scaling factor ($P_{\text{SLHL}} = \text{SF} \times P_{\text{local}}$) were determined for fast neutrons, slow muons and rapid muons, and were then used to define a local ^{26}Al production rate based on an initial production ratio of 6.8 (at SLHL).

Sample	Lat (°N)	Long (°E)	Alt (m)	Upstream area (km ²)	P Neutrons (at/g/yr)	P Slow muons (at/g/yr)	P Fast muons (at/g/yr)	P Total (at/g/yr)	SF Neutrons	SF Slow muons	SF Fast muons	$N^{10\text{Be}}$ ($10\text{e}+4$ at/g)	Denudation rate (mm/yr)
Kryos River	38.1365	22.35818	30	110.34	7396	16	43	7454	1849	1300	1092	17.76 ± 10.66	0.26 ± 0.16
Krathis River	38.1685	22.33005	104	136.86	8852	17	44	8912	2213	1375	1126	22.32 ± 6.43	0.25 ± 0.07
C12-41	38.1507	22.28554	104	136.86	8852	17	44	8912	2213	1375	1126	22.57 ± 5	0.24 ± 0.05
Selinous River	38.2220	22.08100	62	330.92	7325	15	42	7382	1831	1233	1064	17.86 ± 2.67	0.26 ± 0.04
C12-52bis	38.2220	22.08100	62	330.92	7325	15	42	7382	1831	1233	1064	17.86 ± 2.63	0.26 ± 0.04
Vouraikos River	38.0744	22.16319	665	180.85	7343	16	43	7402	1836	1317	1103	43.49 ± 23.85	0.11 ± 0.06
Kerenitis River	38.1886	22.14836	82	79.83	7290	15	41	7346	1823	1225	1062	73.26 ± 6.89	0.06 ± 0.01
Average value	-	-	-	-	7769	16	43	7827	1942	1294	1091	-	-

TABLE D.3 – ^{26}Al - ^{10}Be concentrations and inferred burial ages. Samples labelled with * are those represented on the banana plot (Figure D.3).

	Sample	Lat (°N)	Long (°E)	Type	Quartz (g)	$^{10}\text{Be} \pm 1\sigma$ (10^{e+4})	% unc	$^{26}\text{Al}/^{10}\text{Be} \pm 1\sigma$ (10^{e+4} at/g)	% unc	Burial age (Ma)	% unc
Mega Spilatio Fm	C13-47*	38.08684	22.17896	AC-1	4.6	3.17 ± 7.04	22 %	3.91 ± 1.7	44 %	1.29 ± 0.89	69 %
	C14-10	38.09507	22.17089	AC-1	54.7	0.73 ± 1.87	26 %	6.77 ± 5.18	77 %	0.15 ± 1.58	1021 %
	C14-12*	38.09009	22.20812	AC-1	65.4	3.07 ± 2.27	7 %	3.5 ± 1.67	48 %	1.51 ± 0.98	65 %
Mavro GD	Mavro-6*	38.04243	22.38807	AC-3	5.1	0.97 ± 5.32	55 %	5.1 ± 2.41	47 %	0.74 ± 0.97	132 %
	Mavro-7*	38.04243	22.38807	AC-3	5.4	0.75 ± 5.03	67 %	4.82 ± 2.64	55 %	0.86 ± 1.13	132 %
	Mavro-8*	38.04243	22.38807	AC-3	11.9	0.8 ± 2.45	31 %	5.3 ± 2.2	42 %	0.66 ± 0.86	130 %
	Mavro-9*	38.04243	22.38807	AC-3	4.9	0.83 ± 5.57	67 %	4.09 ± 1.99	49 %	1.19 ± 1	84 %
Ilias GD	Ilias-A2	38.10102	22.40634	AC-3	14.6	0.08 ± 1.8	223 %	7.07 ± 14.92	211 %	0.06 ± 3.25	5029 %
	Ilias-A3*	38.10102	22.40634	AC-3	12.5	0.58 ± 2.36	40 %	2.71 ± 1.99	73 %	2.04 ± 1.51	74 %
	Ilias-A4*	38.10102	22.40634	AC-3	35.3	0.21 ± 0.84	39 %	5.66 ± 3.13	55 %	0.52 ± 1.14	217 %
	Ilias-A4bis	38.10102	22.40634	AC-3	35.9	0.1 ± 0.76	80 %	9.18 ± 7.89	86 %	0.47 ± 1.42	302 %
	C12b-4	38.10102	22.40634	AC-3	35.5	0.34 ± 0.84	25 %	4.2 ± 2.39	57 %	1.14 ± 1.17	103 %
Kerenitis GD	C12b-3*	38.16823	22.11952	SC-2	30.6	0.91 ± 6.57	72 %	-	89 %	4.5 ± 1.84	41 %
Vouraikos GD	C12-48	38.15223	22.20626	AC-3	5.9	0.47 ± 3.14	67 %	6.42 ± 7.8	121 %	0.26 ± 2.47	941 %
	Akrata GD	38.16175	22.31604	AC-3	1.3	5.96 ± 24.1	40 %	1.51 ± 1.08	71 %	3.24 ± 1.46	45 %
	C12-43D	38.16175	22.31604	S	1.6	2.63 ± 13.06	50 %	4.79 ± 4.27	89 %	0.86 ± 1.82	210 %
Kyros River	p12b	38.13650	22.35818	S	3.0	1.78 ± 10.66	60 %	4.38 ± 5.15	118 %	1.05 ± 2.42	230 %
Krathis River	C12-41*	38.15075	22.28554	S	9.6	2.26 ± 5	22 %	5.16 ± 2	39 %	0.71 ± 0.8	112 %
Selinous River	C12-52*	38.22200	22.08100	S	23.4	1.79 ± 2.67	15 %	3.31 ± 0.92	28 %	1.63 ± 0.57	35 %
	C12-52bis*	38.22200	22.08100	S	19.8	1.79 ± 2.63	15 %	6.35 ± 1.6	25 %	0.29 ± 0.52	181 %
Kerenitis River	C14-16*	38.18861	22.14836	S	26.5	7.33 ± 6.89	9 %	7.43 ± 0.82	11 %	0.04 ± 0.23	650 %

D.5 Significance to date the Gilbert deltas of the Killini river system

The lithostratigraphy defining the Killini river system is presented in the chapter 6 (section 6.2.2). As explained, the Mavro deltaic complex is part of the sequence of deltas (Killini, Mavro, Evrostini deltas) that became progressively younger to the north as the fault activity migrated through time (Rohais *et al.*, 2007a, 2008). In the Mavro fault block, the samples (MAVRO 6–7–8–9) are located in the upper alluvial fan succession and should record the latest construction phase of the Mavro delta. The mean burial age interval 0.2–1.5 Ma agrees with the palynological age obtained in the same area (Figure D.4). The palynological sample M04 of Rohais *et al.* (2007b) also lies in the upper alluvial fan succession of the Mavro deltaic complex and gives an age estimate of 0.7–0.82 Ma. This palynological age was used by Rohais *et al.* (2007b) to date the latest construction phase of the Mavro delta and the upper limit of the Middle Group at about 0.7 Ma. The construction of the Mavro Gilbert-type deltas during the Middle Group (1.8–1.5 to 0.7 Ma) is not consistent with the recent absolute date of Leeder *et al.* (2012) which by correlation date the base of this delta at 3.2–3.0 Ma (estimate of the central "rift climax"). The viability of the young burial ages obtained in the Mavro block with the respect to the sequence of deltas built by the Killini river system is discussed below.

Rohais *et al.* (2008) present the stratigraphic architecture of these deltas in four main sequences in different normal fault blocks. The two first sequences correspond to the Killini delta the lower Mavro delta complex and the Ilias delta. The third sequence corresponds to the upper part of the Mavro delta complex and the lower Evrostini delta. The fourth sequence is marked by the construction of the upper Evrostini delta.

The same river system fed the Killini, Mavro and Evrostini deltas. It successively cannibalised its own deltas during the northward migration of fault activity (Rohais *et al.*, 2008) The river system persisted through time and incised into the uplifted footwall to the south. The construction of these deltas was interrupted by numerous flooding events associated with major landward shifts of the shoreline. The periods of transgression (A>S) formed retrograding system tracts in the hangingwall and possibly infilled palaeovalleys in the footwalls. Periods of base level fall are recorded by a prograding-aggrading system tract in the hangingwall delta. It is therefore possible that the samples collected in the uppermost succession of the Mavro fault block (on the side of the incised windgap valley) do not date the deposition of the Mavro delta itself but rather a younger retrograding system track during the construction of the Evrostini delta. This could explain the young burial age obtained in the upper succession of the Mavro fault block and in the M04 palynology sample of Rohais *et al.* (2008) (indicated on Figure D.4). Such infill of an incised valley in the footwall of the Evrostini Fault would have possibly occurred during the last deltaic sequence (4th) of Rohais *et al.* (2008) at the end of the Middle Group around 0.7 Ma. This interpretation

is favored here, although the presence of palaeovalley infill at the sample site requires a new field examination of the site.

It is possible that the clasts sampled in the Mavro fault block were reworked from the former Killini delta to the south. This would imply a complex burial history, involving re-exposure to cosmic rays, and thus the determination of maximum burial ages (Figure D.1). Given the uncertainties related to the interpretation of the burial ages, the samples from the Mavro fault block should be used with caution as they may not directly date the deposition of the Mavro Gilbert-type delta itself. The burial ages of the Ilias delta samples are more reliable in terms of depositional age despite of their large 1σ uncertainties.

This study shows that the burial age technique cannot be easily applied in the Corinth rift. Quartz grains are rare in the syn-rift deposits and their distribution across the drainage divides is unknown. Burial ages could not be determined in most of the samples because of the large analytical uncertainties of $^{26}\text{Al}/^{27}\text{Al}$ ratio. The interactions between faulting and sedimentation are difficult to date using this technique as the buried successions were subjected to different phases of uplift and cosmic ray exposure. This is particularly true for fault-controlled successions that are uplifted and re-exposed to cosmic rays during progressive hangingwall fault migration. While the river persisted through the migrating phases of fault activity, sediment reworking was probably significant. These types of geological histories are not suitable for the determination of ^{26}Al - ^{10}Be burial ages and should be avoided.

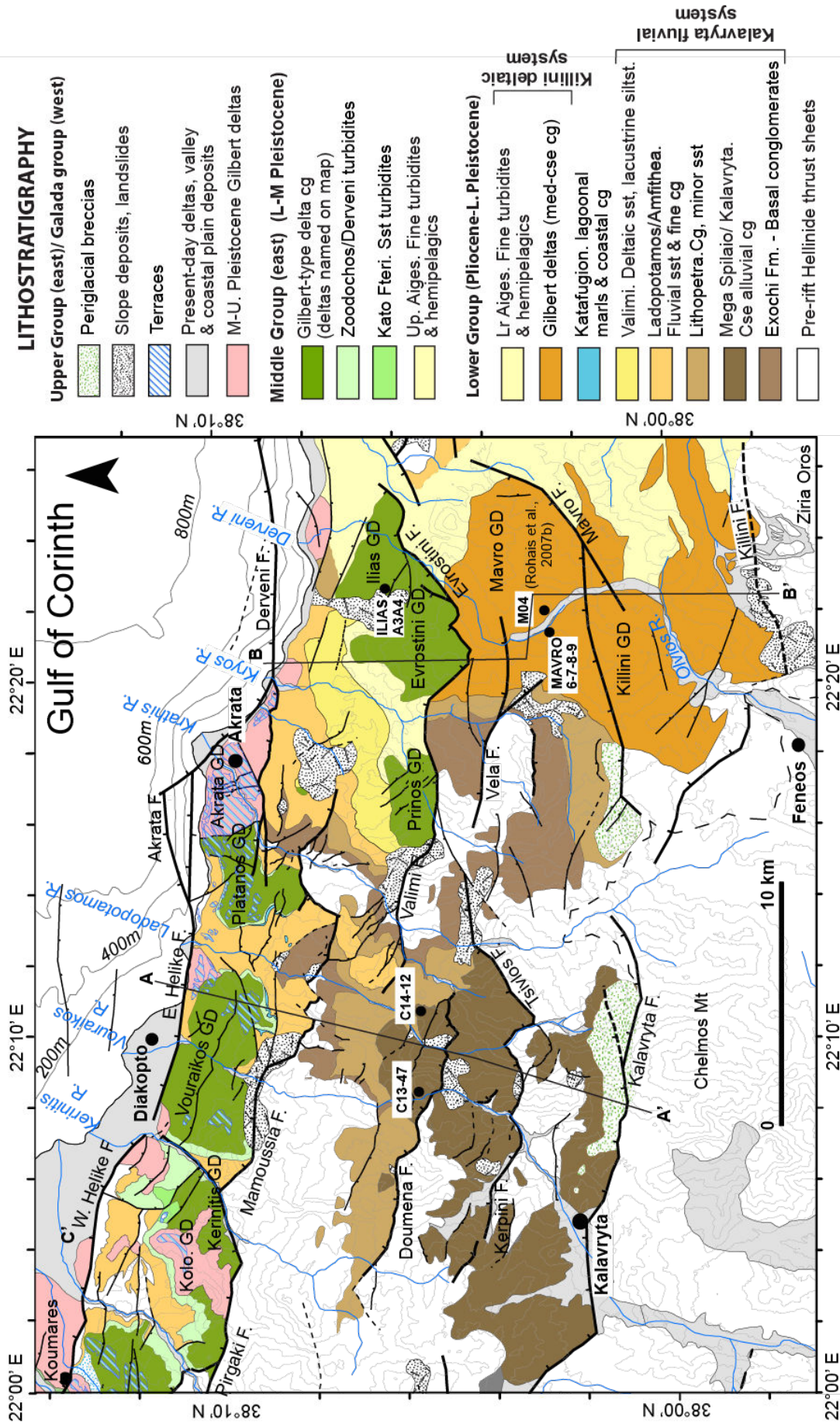


FIGURE D.4 – Geological map of southern Corinth rift margin showing the lithostratigraphy of the Kalavryta and the Killini river systems. The samples analysed for the determination of ^{26}Al - ^{10}Be burial ages are indicated.

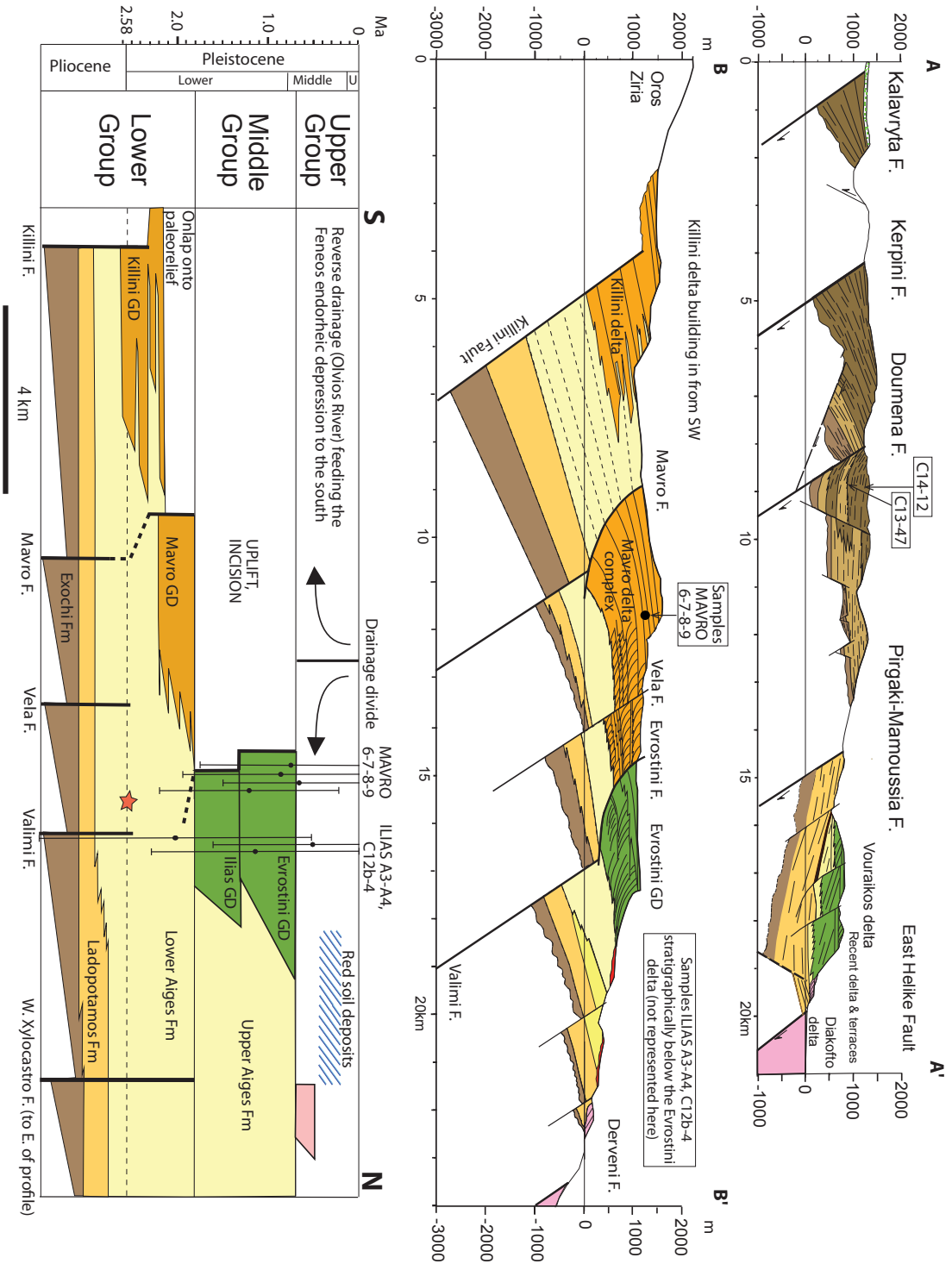


FIGURE D.5 – N-S cross sections of the southern Corinth rift margin showing the lithostratigraphy of the Kalavyta (A-A') and Killini river systems (B-B') (modified from Ford et al., in press). The chronostratigraphy along the B-B' cross section integrates the ash date of Leeder et al. (2012) (red star) and the results of ^{26}Al - ^{10}Be burial ages.

Annexe E

Palaeomagnetic rotations

In the studied sections, we calculated the virtual paleomagnetic poles (VGP) and the vertical-axis rotation with respect to Europe at 5 Ma apparent polar wander path (Besse & Courtillot, 2002). In the different thickness intervals, the palaeopole and the rotation values were calculated using the mean VGP direction (Table 3.5). The paleo-pole values do not trend toward a specific direction through time following the different thickness intervals. We only use the rotation values calculated from the mean direction per section. All declination and inclination values are transformed to normal polarity. Given uncertainties are below 9° (at 95% confidence limit). Robust palaeopoles are calculated and can be used to determine palaeomagnetic rotations during the early phase. The Valimi, Doumena and Kerpini sections present clockwise rotation of $19.2 \pm 2.6^\circ$, $22.0 \pm 3.2^\circ$ and $46.9 \pm 3.5^\circ$ respectively, while the Voutsimos section presents a mean counterclockwise rotation of $-16.7 \pm 3.2^\circ$ (Figure E.2). These rotation values are consistent with the mean declination values calculated in individual sections (Figure E.1).

Mattei *et al.* (2004) propose a counterclockwise rotation of the northern Peloponnese during the opening of the Plio-Pleistocene Corinth rift. Their mean paleomagnetic direction $D_s = 345^\circ$, $I_s = 56^\circ$, $\alpha_{95} = 7.9^\circ$ was calculated using 16 sampled sites across the southern margin (Figure E.1) and gives a counterclockwise rotation of $-15 \pm 14^\circ$ with respect to stable Eurasia. The decrease of the apparent counterclockwise rotation toward the eastern Corinth rift is explained by the location of the modern rotation pole in eastern Greece (Goldsworthy *et al.*, 2002). Geodetic data of Avallone *et al.* (2004) show that both sides of the Corinth rift behave as clockwise rotating blocks with $7.0 \pm 0.5^\circ/\text{Myr}$ and $2.8 \pm 0.8^\circ/\text{Myr}$, respectively for the northern and southern margins. The substantial difference between the palaeomagnetic rotation interpreted by Mattei *et al.* (2004) and the GPS-inferred rotation is explained by a recent reorganization of the deformation in the northern Peloponnese at the scale of one million years (Mattei *et al.*, 2004).

Apart from the Voutsimos section, the rotation and mean declination values are similar across the study area (Figure E.2). They record the clockwise rotation of the northern Peloponnese with respect to Europe during the early rift phase. Our results are consistent with the GPS-inferred clockwise rotation of the Peloponnese but are in conflict with results of Mattei *et al.* (2004),

especially in the Doumena and Kerpini sections (labelled 1 and 2 in Figure E.1). We argue that more confidence is given to our results for the following reasons. We specifically sampled the early rift sediments in different fault blocks and each mean direction is calculated using 35 to 48 samples. The sites sampled by Mattei *et al.* (2004) are randomly distributed across the basin and cover the entire rift stratigraphic evolution. Moreover, their local mean directions are calculated using 4 to 12 samples, which are significantly lower compared with our data.

Kinematic data indicate pure dip-slip displacement on the major studied faults with stretching directions mainly oriented N–S to NNE–SSW (Ford *et al.*, 2013). Rotation values cannot thus be explained by local rotation due to strike-slip components along the early Kerpini, Doumena and Valimi Faults. It reflects rather the regional rotation of the Peloponnese with respect to Europe. However, the counterclockwise rotation determined in the Voutsimos section (-17°) is not consistent with the other sections and the validity of these values is questioned here. The Voutsimos section lies within a transition zone between the Doumena and Pirgaki-Mamoussia faults. Lower Group strata have an anomalous dip toward the northwest, which has led to the proposal that they were controlled by a now, buried southeast-dipping fault. The Pirgaki-Mamoussia Fault was active during the Middle Group and may have again tilted the Lower group succession. Bedding correction is important to calculate the mean palaeomagnetic directions but, as in this case, strata may have undergone several phases of tilting around differently oriented axes. The simple rotation correction on these bedding may not have correctly restored the different phases of tilting against different faults. This could explain the different value of the mean palaeomagnetic direction obtained in the Voutsimos section. We therefore reject this value.

Our remaining palaeomagnetic directions indicate an average rotation of $+21^\circ$ to $+25^\circ$ of the northern Peloponnese with respect to a fixed Europe from about 3.6 to 1.8 Ma. This value is only valid for our study area. More data are needed to discuss variations of rotation of the whole Corinth basin in time and space. This requires careful dating of the sampled syn-rift succession to understand the history of the individual fault blocks and properly interpret the values of palaeomagnetic rotations.

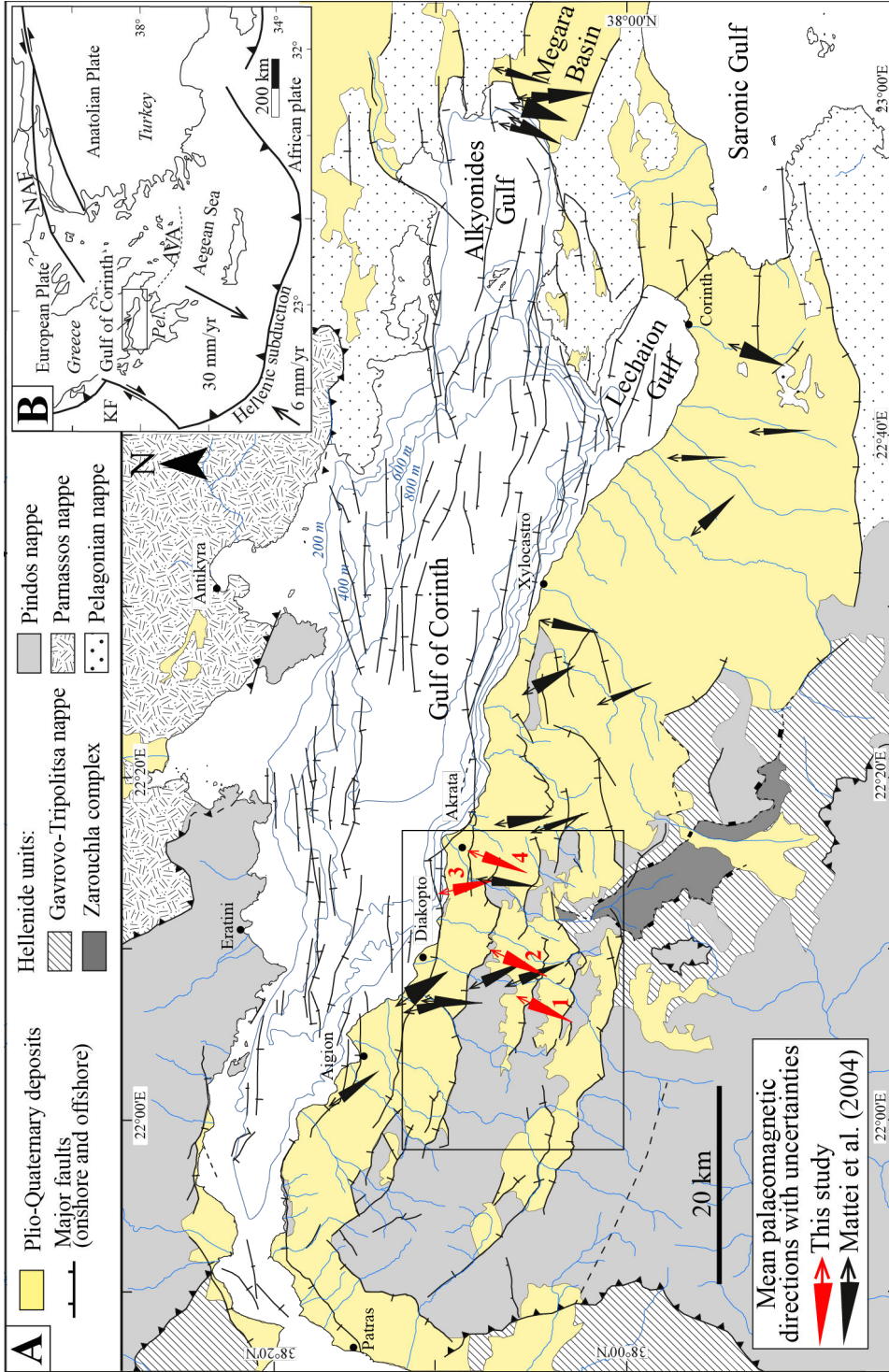


FIGURE E.1 – **A** : Geological map of the Corinth rift. The black box corresponds to the study area shown in the Figure E.1. Offshore fault traces [Beckers et al. \(2015\)](#); [Hemelsdaël & Ford \(2016\)](#); [Nixon et al. \(2016\)](#); [Rohais et al. \(2007a\)](#); [Leeder et al. \(2012\)](#). **B** Regional context of the Corinth above the active Hellenic subduction zone and lying between the Cephalonia Fault (KF) and the North Anatolian Fault (NAF). Subduction of the African plate generated the Aegean Volcanic Arc (AVA). The rift separates mainland Greece from the Peloponnes peninsula (Pel.). Tilted-corrected mean palaeomagnetic declinations in the four studied sections are compared with the values of ([Matti et al., 2004](#)) along the Corinth and Megara basins. All declination values in each section are transferred to normal polarity. **1** : Kerpini section ; **2** : Doumena section ; **3** : Voutsimos section ; **4** : Valimi section.

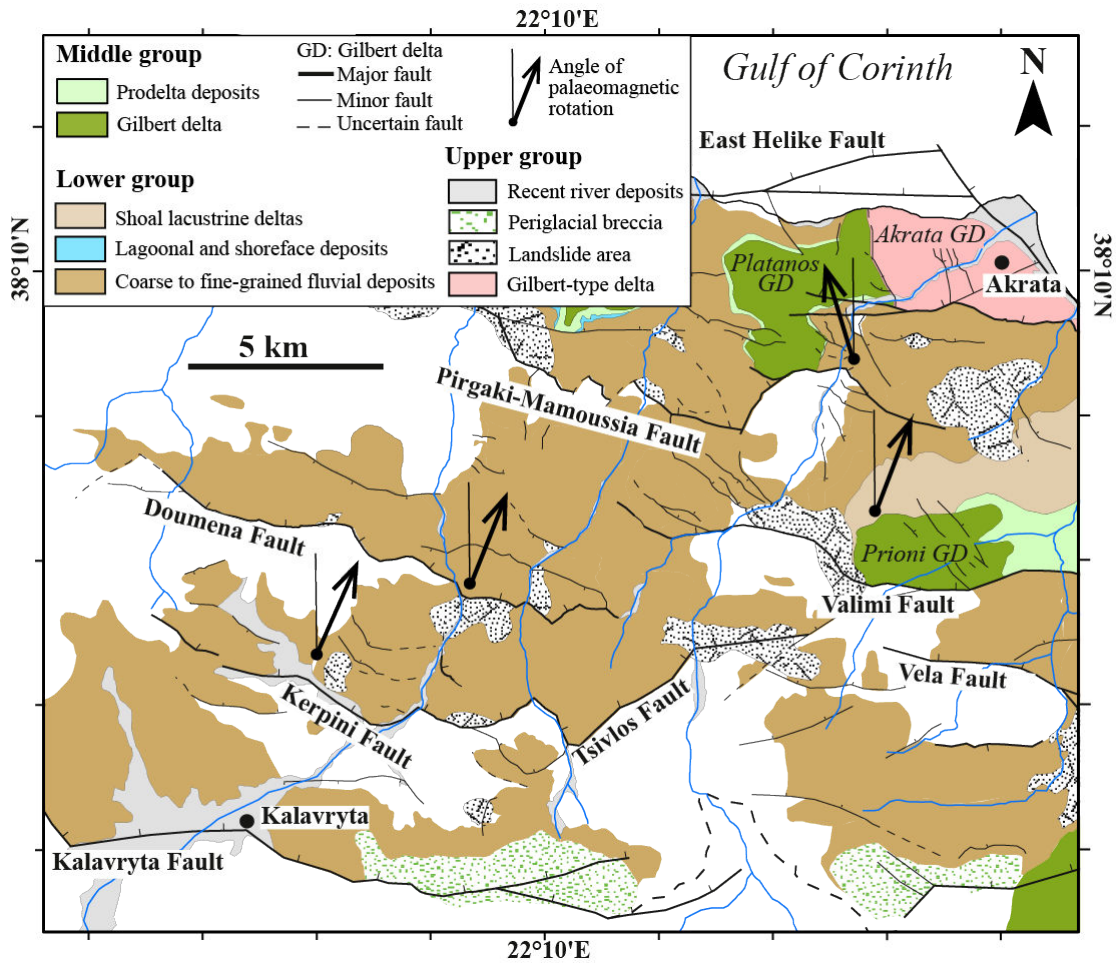


FIGURE E.2 – Simplified geological map of the study area along the southern Corinth rift showing the palaeomagnetic rotations with respect to stable Europe at 5 Ma (Besse & Courtillot, 2002).

Annexe F

Publication en second auteur

Rift migration and lateral propagation: evolution of normal faults and sediment-routing systems of the western Corinth rift (Greece)

MARY FORD^{1,2*}, ROMAIN HEMELSDAËL², MARCO MANCINI³ & NIKOLAOS PALYVOS^{4†}

¹*Université de Lorraine, ENSG, INP, rue du Doyen-Marcel-Roubault, 54501 Vandoeuvre-lès-Nancy, France*

²*CPRG, UMR 7358, 15 Rue Notre-Dame-des-Pauvres, 54501 Vandoeuvre-lès-Nancy, France*

³*CNR-IGAG, Cnr Area della Ricerca Roma 1, Via Salaria km 29,300, 00015 Monterotondo Scalo, Rome, Italy*

⁴*Department of Geography, Harokopio University, 70 El. Venizelou Street, Athens, Greece*

*Corresponding author (e-mail: mford@crpg.cnrs-nancy.fr)

Abstract: The active Corinth rift records hanging-wall migration of faulting and slip-rate acceleration. The rift initiated at approximately 5–4 Ma, and older parts are well exposed in the northern Peloponnese. A new correlation of chrono- and lithostratigraphy and structure across the onland central to westernmost rift with offshore data reveals westward rift propagation, as well as northward fault migration. Northward fault migration ended first in the east, with the stabilization of major north-dipping faults that now bound the Gulf. The basin then propagated to the WNW in two stages, each involving the initiation of a new fault that propagated east to SE to link to the stable fault system. Extension rates accelerated in distinct steps as the rift opened to the west. The youngest faults in the westernmost rift are associated with high seismicity and highest geodetic extension due to rapid fault growth and linkage at depth.

The early synrift succession infilled substantial inherited palaeo-relief. Antecedent rivers established vigorous sediment-routing systems that controlled facies distribution throughout rifting, albeit with drainage reorganization during fault-migration events. Multiple deepening events recorded in the stratigraphy can be due to lateral rift propagation. The transition from rift initiation to rift climax is, therefore, diachronous along the rift axis.

The Corinth rift is one of the fastest opening rifts in the world. It initiated in the Late Pliocene (5–4 Ma: Keraudren & Sorel 1987; Ori 1989; Doutsos & Piper 1990; Billiris *et al.* 1991; Roberts 1996; Doutsos & Kokkalas 2001; Leeder *et al.* 2008) as part of the western Aegean extension system (Le Pichon & Angelier 1979; Jolivet 2001). The older parts of the rift are now relatively inactive, and have been uplifted and exposed in a 25–30 km swathe of the northern Peloponnese (Fig. 1). Present-day extension and seismic activity are focused below the Gulf of Corinth itself (Rigo *et al.* 1996; Bernard *et al.* 2006; Lambotte *et al.* 2014), indicating that the locus of deformation has migrated northwards. Intense seismicity and microseismicity are concentrated below the westernmost Gulf (west of Aegion: Fig. 1) where the highest north–south extension rates (15–16 mm a⁻¹) have been geodetically

recorded over the last 20–25 years (Bernard *et al.* 1997, 2006; Clarke *et al.* 1998; Briole *et al.* 2000). Geodetic extension rates decrease to 11 mm a⁻¹ in the central and eastern Gulf (Clarke *et al.* 1998; Briole *et al.* 2000), where major earthquakes are less frequent than to the west (Jackson *et al.* 1982). If we extrapolate the geodetic extension rates back through the 4–5 myr of rifting history, total extension would be 50–80 km, nearly an order of magnitude greater than that estimated from surface geology by Bell *et al.* (2008: 11 km in the central rift) and Ford *et al.* (2013: 6–8 km in the western rift), and from crustal thinning by Bell *et al.* (2011: 5–13 km for the western rift and 11–21 km for the central rift). Similarly, geologically derived total extension estimates give an average extension rate over 5 myr of 1.3–2.2 mm a⁻¹, an order of magnitude less than current geodetic extension rates.

†Deceased 23 April 2012.

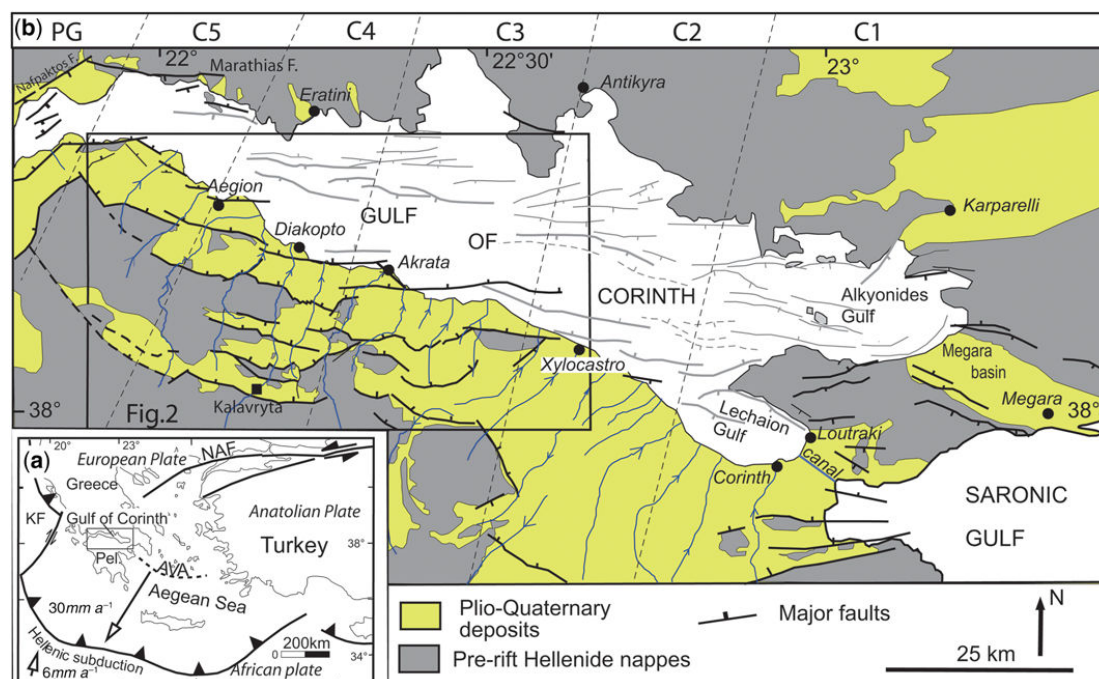


Fig. 1. (a) Tectonic map of the Aegean region showing main plates and plate boundaries, and the location of the Gulf of Corinth. Plate movement vectors are with respect to a fixed European Plate. NAF, North Anatolian Fault; KF, Kefalonia Fault; Pel., Peloponnesus peninsula; AVA, Aegean volcanic arc. (b) Tectonic map of the Corinth rift showing principal faults and the onshore distribution of Plio-Pleistocene sediments based on work of Lyon-Caen *et al.* (2004), Moretti *et al.* (2004), Bernard *et al.* (2006), Flotté *et al.* (2005), Rohais *et al.* (2007a), and Ford *et al.* (2013). Offshore faults in grey are from Nixon *et al.* (2016). Rivers of the northern Peloponnese are shown with an arrow in the direction of flow. The location of Figure 2 (study area) is boxed. For this study, the Corinth rift (onshore and offshore) is subdivided into five areas, C1–C5 (top of figure). PG is the Patras rift to the west.

Although, this comparison of geodetic and geological data must be treated with caution, it suggests that extension rate accelerated during rifting, a hypothesis that we will examine in this paper.

Evidence of northwards migration of fault activity has been noted and discussed by many authors (e.g. Dufaure 1975; Doutsos & Poulimenos 1992; Armijo *et al.* 1996; Goldsworthy & Jackson 2001; Collier & Jones 2003; De Martini *et al.* 2004; Flotté *et al.* 2005; Rohais *et al.* 2007a; Bell *et al.* 2008; Ford *et al.* 2013; Demoulin *et al.* 2015), most of whom focus on migration events since 0.7 Ma that are well expressed in the tectonic geomorphology of the northern Peloponnese.

The excellent exposures of the synrift succession in the northern Peloponnese provide the opportunity to investigate the evolution of the synrift structure and sedimentary succession: in particular, the response of sediment supply, facies distributions and depocentre connectivity to rift migration and acceleration over a period of 4–5 myr. Seismic reflection data provide clearer constraints on the structure and seismic stratigraphy of the offshore

rift (Bell *et al.* 2011; Taylor *et al.* 2011; Nixon *et al.* 2016), although the offshore succession still remains undrilled except for the upper levels representing the last 25 kyr that have been sampled by piston coring (Moretti *et al.* 2004; Lykousis *et al.* 2007a; Campos *et al.* 2013).

This paper presents a new geological map of the onshore western and central Corinth rift (65 km long), with a new coherent stratigraphy and structure integrating published work and new unpublished work. These data were used to construct a tectonostratigraphic model for the evolution of the western and central rift in order to clarify: (1) the distribution of deformation in space and time (evolution of the fault system); (2) the principal controlling factors on synrift fill, including inherited palaeo-relief and antecedent drainage systems; and (3) the sedimentary response to rift migration and strain-rate acceleration. We discuss the significance of the present-day seismicity and high geodetic strain in the context of rift migration and strain-rate acceleration, and the problems associated with the recognition of major tectonic events in the

stratigraphic record of rifts. We discuss, in particular, the relevance of deepening events in rifts.

Regional geological setting

The Aegean tectonic domain is defined by the Hellenic subduction system where the African Plate is subducting to the NNE below the European Plate at a rate of 6 mm a^{-1} (Fig. 1a) (Le Pichon & Angelier 1979, 1981; Jolivet *et al.* 1994; Gautier *et al.* 1999). Back-arc extension of over 400 km due to slab rollback created the Aegean Sea in the overriding plate from around 30 Ma (Armijo *et al.* 1996; Jolivet *et al.* 2010; van Hinsbergen & Schmid 2012). This extension was accompanied by a clockwise rotation of the Peloponnese peninsula by up to 40° – 50° (van Hinsbergen *et al.* 2007; Burchfiel 2008). At around 5 Ma, the North Anatolian Fault (NAF) started to propagate west to SW into the northern Aegean Sea (Armijo *et al.* 1996), generating a zone of transtension with deep, isolated rift zones. This coincided with the cessation of active extension in the central Aegean Sea as deformation migrated outwards to the east and west (Burchfiel 2008; Royden & Papanikolaou 2011). Geodetic studies show that north–south extension is now concentrated in the western Anatolian block, and in a broad zone between the SW tip point of the NAF and the Kefalonia Fault to the west (Fig. 1a) (Briole *et al.* 2000; McClusky *et al.* 2000; Avallone *et al.* 2004; Bernard *et al.* 2006; Nocquet 2012) wherein lie the Corinth and Evia rifts (Fig. 1).

The Corinth rift cuts obliquely across the Hellenide mountain belt, which comprises a stack of NNW–SSE-trending, west-verging thrust sheets that were progressively emplaced towards the west to WSW from Cretaceous to Miocene times (Aubouin *et al.* 1963; Dercourt 1964; Richter 1976; Fleury 1980; Doutsos *et al.* 1993, 2006; Skourlis & Doutsos 2003). The rift is underlain principally by the Pindos thrust sheet with part of the Parnassos sheet to the east, and the Gavrovo–Tripolitza sheet to the west. The Pindos thrust sheet comprises an approximately 1300 m-thick succession of Upper Triassic–Jurassic hemipelagic carbonates with minor red and green radiolarites (cherts) and Upper Cretaceous–Tertiary sandy turbidites (graywackes/flysch) (Degnan & Robertson 1998; Skourlis & Doutsos 2003). These strata have been highly deformed at sub-greenschist grade during Alpine nappe emplacement. The Pindos sheet overthrusts the carbonate-dominated Gavrovo–Tripolitza thrust sheet and the underlying Zarouchla complex, which includes the Phyllite–Quartzite unit that records Miocene high-pressure–low-temperature metamorphism (Dornsiepen *et al.* 1986; Trotet *et al.* 2006; Jolivet *et al.* 2010).

The Corinth rift

The Gulf of Corinth is an approximately 120 km-long active rift, trending $N110^\circ$, with a maximum width of 30 km, narrowing westwards to 3 km at the Rion Straits (Fig. 1b). The Gulf represents the currently active part of a rift whose Plio-Quaternary history is preserved in uplifted blocks across the northern Peloponnese (Moretti *et al.* 2003; Ghisetti & Vezzani 2004). The normal fault system is dominated by north-dipping faults both onshore and offshore with an average strike of $N105$ – 110° and dips of 42 – 64° N (Rohais *et al.* 2007a; Bell *et al.* 2008; Taylor *et al.* 2011; Ford *et al.* 2013). More than 2.5 km of synrift stratigraphy can underlie the eastern and central Gulf (McNeill *et al.* 2005; Bell *et al.* 2008, 2009, 2011; Taylor *et al.* 2011; Nixon *et al.* 2016). Onshore, the synrift succession reaches around 2.8 km in thickness. A north–south extension direction is recorded since the beginning of rifting (Roberts & Michetti 2004; Ford *et al.* 2013), corresponding to the present-day orientation of geodetic extension (Briole *et al.* 2000; Avallone *et al.* 2004; Bernard *et al.* 2006).

Moho depth, reflecting crustal thinning and derived from tomographic inversion, increases along the rift from 25–30 km in the east below the Peloponnese peninsula (and the southern Saronic Gulf; Fig. 1) to 45 km below the Rion Straits, with a particularly rapid increase in Moho depth from the central to the western Gulf (Zelt *et al.* 2005; Sachpazi *et al.* 2007). The decreasing influence of Corinth rifting on crustal thickness is also reflected in the orientation of Moho depth contours, which trend WNW–ESE (Corinth rift trend) below the eastern Gulf and changing to a NNW–SSE Hellenide trend to the west (Sachpazi *et al.* 2007). The variations in Moho depth are reflected in variations in depth to base synrift, synrift sediment thickness and fault displacement along the rift. The increase in geodetic extension rates to the west suggests that the locus of deformation has migrated west along the axis of the Gulf, and that the westernmost Gulf is the youngest part of the rift and the least extended. It is clear that the evolution of the Corinth rift is intimately related to that of the Patras rift to the west (Fig. 1), about which very little is known (Brooks & Ferentinos 1984; Ferentinos *et al.* 1985).

For the purposes of this paper, the Corinth rift is divided into five zones (C1–C5) orientated NNE–SSW, and traversing both the onshore and offshore rift (Figs 1 & 2). These are, from east to west, the Alkyonides Gulf and the Lechaion Gulf (C1), the central and eastern Gulf (C2 and C3), the west to central transition zone (C4) and the westernmost Gulf (C5). The Patras Gulf lies further to the west (Fig. 1). This paper will focus mainly on the onshore

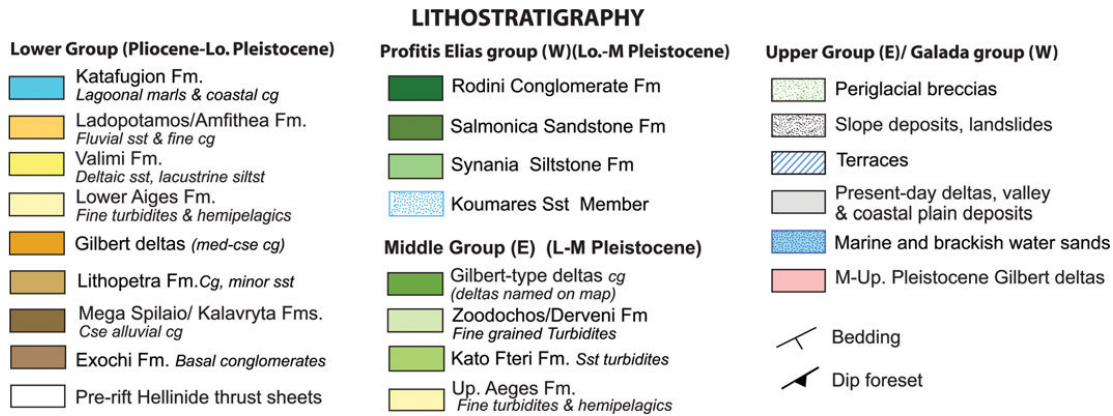


Fig. 2. Geological map of the Plio-Pleistocene Corinth rift of the northern Peloponnese from Xylocastro to Psathopyrgos. The map for the central and eastern areas (C2, C3 and C4) has been compiled from Rohais *et al.* (2007a, b), Leeder *et al.* (2012) and Ford *et al.* (2013), with several revisions detailed in the text. The western area (C5) integrates new work and that of Palyvos (2005) and Palyvos *et al.* (2010, 2013). The structure and chronostratigraphy of C4 along cross-section A–A' is presented in Figure 3, of C3 on section B–B' in Figure 4, and of C5 on sections C–C', D–D' and E–E' in Figures 5, 7 and 8, respectively. Bathymetric and topographical contours are spaced every 200 m. The red star shows the location of the dated ash layer of Leeder *et al.* (2012). Abbreviations on map and legend: A, Ano; cg, conglomerate; cse, coarse; F, Fault; Fm, Formation; E, East; GD Gilbert Delta; Lr, Lower; med, medium; M, Middle; Mt, Mountain; R, River; siltst., siltstone; sst, sandstone; Up., Upper; W, West.

areas C3–C5 where onshore geological investigations are most advanced.

Offshore Gulf of Corinth: structure and stratigraphy of the active rift

In zones C2 and C3, the Gulf is bound to the south by right-stepping en echelon, north-dipping normal faults (the Derveni, Lykopora and East Xylocastro faults: Fig. 1) that form a steep basin-margin slope. Offshore swath bathymetry data show a 9–12 km-wide, flat basin floor with water depths of 800–870 m (Fig. 2) (Alexandri *et al.* 2003; Nomikou *et al.* 2011). South-dipping normal faults delimit the depocentre to the north (the Galaxidi and West Antikyria faults: Nixon *et al.* 2016), separating it from a broad, relatively shallow-water (<400 m) platform rising gently to a deeply indented northern coastline (Fig. 1). To the east (C1), the Gulf splits into two rifts: the Alkyonides Gulf and the Lechaion Gulf (Fig. 1) (Leeder *et al.* 2005; Sakellariou *et al.* 2007; Charalampakis *et al.* 2014) with shallow water (<400 m in Nomikou *et al.* 2011; Alkyonides <200 m and <100 m in Lachaion in Taylor *et al.* 2011). A major horst forms the Perachora peninsula between these basins (Fig. 1). The Corinth Isthmus separates the Corinth Gulf from the Saronic Gulf to the east (Collier & Dart 1991). Major earthquakes occur regularly in this area: for example, in 1981 (Jackson *et al.* 1982).

To the west (Fig. 1), the active rift steps northwards by some 8 km across area C4, while

narrowing in width to 10 km. The bounding normal fault system correspondingly steps northwards. The East and West Helike faults define the active rift's southern boundary in C4, while the West and East Channel faults define its northern boundary (McNeill *et al.* 2005; Bell *et al.* 2008). The North and South Eratini faults define a small offshore horst further north.

In C5, the active rift is principally controlled by the north-dipping Neos Erineos Fault zone trending NW–SE, and comprising four short faults (Lambiri, Selianitika, Fassoulaika and Aegion) (Palyvos 2005; Palyvos *et al.* 2007) and the east–west-trending Psathopyrgos Fault, considered by many as the most seismically active fault in the rift (Bernard *et al.* 2006). These en echelon coastal faults are considerably shorter than those to the east (Beckers *et al.* 2015). The south-dipping Trizonia Fault delimits the main depocentre, while the Marathias Fault defines the northern coastline. Between these two faults lies a shallow platform. From Aegion to the Rion Straits, bathymetry shallows (over some 33 km) from 400 to 60 m.

The present-day eastern and central Gulf (C3, C2, Fig. 1) can be described as sediment-starved. Little sediment is supplied from the north as no significant rivers flow into the Gulf. Only fine-grained sediment is supplied from the south by short, consequent rivers (Fig. 1) (Seeger & Alexander 1993; Zeliidis 2000; Demoulin *et al.* 2015) and from the west along a submarine axial channel (Bell *et al.* 2008; Nomikou *et al.* 2011). In contrast, from Akrata westwards, major antecedent rivers carry coarse-grained

bedload northwards into the shallower basin, building large Gilbert-type fan deltas in the hanging walls of active faults (Ford *et al.* 2007, 2013; see later). More distal deposits comprise prodelta turbidites and hemipelagic deposits (Bell *et al.* 2008). These deltas build steep foresets (angles of repose up to 29°) that can record seismically induced gravitational mass flows (Lykousis *et al.* 2007b; Nomikou *et al.* 2011; Beckers 2015).

Recent seismic reflection studies show that the thickest offshore synrift accumulation underlies the area of flat, deep bathymetry of C2 and C3. Here a band of maximum sediment thickness (> 3 km) parallels the south coast, defining the main depocentres in the hanging walls of major north-dipping faults (Bell *et al.* 2008, 2009, 2011; Taylor *et al.* 2011; Nixon *et al.* 2016). Bell *et al.* (2009) estimate 1.3–1.9 km, thickening to 2.4 km into hanging-wall depocentres, while Taylor *et al.* (2011) estimate a thickness of over 3 km. To the east, in C1, maximum sediment thickness in the Alkyonides Gulf is estimated at 1 km (Bell *et al.* 2009; >1 km in Taylor *et al.* 2011) and >2 km in the Lechaion Gulf (Taylor *et al.* 2011; Charalampakis *et al.* 2014). To the west, the synrift succession thins rapidly to < 1 km across C4 (Bell *et al.* 2009), corresponding to a marked shallowing of top basement (estimated at 0.6–0.9 km below sea level (bsl); Beckers 2015).

The offshore synrift succession is, as yet, undrilled. Based on seismic attributes, two main units are recognized in areas C2 and C3, separated by a widespread, locally angular unconformity (Moretti *et al.* 2003; Sachpazi *et al.* 2003; McNeill *et al.* 2005; Bell *et al.* 2008; Taylor *et al.* 2011; Nixon *et al.* 2016). The lower unit SU1 (Unit B of McNeill *et al.* 2005; Bell *et al.* 2008; ‘early rift’ of Taylor *et al.* 2011; Seismic Unit 1 (SU1) of Hemelsdaël & Ford 2016) lacks clear seismic impedance contrasts and appears to be poorly stratified, while the younger unit SU2 is highly reflective, showing clear cyclical stratification (Unit A of McNeill *et al.* 2005; Bell *et al.* 2008; ‘late rift’ of Taylor *et al.* 2011; Seismic Unit 2 (SU2) of Hemelsdaël & Ford 2016). Giant piston cores (up to 30 m long) taken in the eastern C2 recovered Holocene fine-grained marine distal gravity deposits and hemipelagics (12–14 m) underlain by lacustrine varve-like muds interbedded with silt to fine sand turbidites recording a transition from lacustrine to marine conditions at around 12 ka (Lykousis *et al.* 2007a; Campos *et al.* 2013). Age estimates of the reflective SU2 are derived from correlation of its cyclical seismic stratigraphic packages with Pleistocene eustatic sea-level cycles (Stefatos *et al.* 2002; Sachpazi *et al.* 2003; Sakellariou *et al.* 2007; Bell *et al.* 2008, 2009; Taylor *et al.* 2011), although the number of packages varies depending on the study area of each paper. The age of the unconformity between SU1

and SU2 is estimated by Taylor *et al.* (2011) in the C2 area as 600 ka, and by Bell *et al.* (2008) in the C4 area as 400 ka. More recently, Nixon *et al.* (2016) reconcile these incoherencies by proposing that the basin-wide unconformity at the base of SU2 has an age of approximately 620 ka and that there is a second local unconformity within SU2 at 340 ka in the western Gulf, which is that identified by Bell *et al.* (2008). They demonstrate that SU2 thins and onlaps westwards onto the main unconformity due to the presence of a palaeohigh, as will be discussed later (here named the Psaromita–Aegion High). The synrift succession thickens again into the Trizonia depocentre west of Aegion (C5; Moretti *et al.* 2003; Lykousis *et al.* 2007b). In C5, recent work by Beckers (2015) and Beckers *et al.* (2015), on an unpublished industrial seismic line, indicates that the top basement becomes deeper again (1.6 km bsl) in the hanging wall of the Trizonia Fault before shallowing westwards toward the Mornos delta. To the SW, in the hanging wall of the Psathopyrgos Fault, the top basement is estimated to be at 1.2 km bsl (Beckers 2015).

Onshore–offshore correlations (e.g. Lykousis *et al.* 2007a; Bell *et al.* 2008, 2009; Taylor *et al.* 2011; Hemelsdaël & Ford 2016) propose that the lower offshore unit SU1 corresponds mainly to the onshore Middle Group and to the Lower Group, should it be present. The upper offshore unit SU2 would then be equivalent in time to the Upper Group onshore (Bell *et al.* 2009; Taylor *et al.* 2011; Hemelsdaël & Ford 2016). However, the ages of lithostratigraphic boundaries are probably diachronous from east to west owing to lateral propagation of rifting: a high-precision dating along a cored borehole is essential to better constrain offshore stratigraphy.

Onshore synrift stratigraphy and structure

In the northern Peloponnese, Plio-Quaternary synrift strata are exposed in a belt approximately 30 km wide (C3 and C4) that narrows abruptly to the west (C5), and broadens to the east in zones C2 and C1 (Fig. 1). In areas C3–C5, fault blocks and their synrift successions have been uplifted to elevations of over 1000 m and deeply incised by north-flowing rivers, providing excellent natural cross-sections (Fig. 2). Further east in areas C2 and C1, however, broad marine terraces mask finer-grained synrift facies in a more subdued landscape with poorer exposures. Apart from the Corinth Isthmus area (Collier 1990; Collier & Dart 1991; Dart *et al.* 1994), the synrift stratigraphy and structure of this eastern area is, as yet, not well documented. To the NE of C1, lies the Megara rift (Fig. 1) that

initiated in the Miocene and was active until the Late Pleistocene (Bentham *et al.* 1991; Leeder *et al.* 2008).

In C3 and C4, the western onshore synrift succession is divided into three informal lithostratigraphic groups named the Lower, Middle and Upper groups (Fig. 2) (Rohais *et al.* 2007a; Ford *et al.* 2013); while, in C5, the recently defined Profitis Elias and Galada groups are roughly equivalent in time to the Middle and Upper groups (Palyvos *et al.* 2013). The aim of this section is to present the structure and stratigraphy of each of these three onshore areas and to propose an along-strike regional correlation, thus covering about 70% of the onshore rift. The onshore compilation is mainly based on Ford *et al.* (2013) and Hemelsdaël *et al.* (2015) in C4, a reinterpretation of the work of Rohais *et al.* (2007a, b) in C3, and Palyvos *et al.* (2013) and unpublished work by the authors for C5. We start with the C4 area, where the lithostratigraphic groups are most clearly defined.

Area C4: Diakopto–Kalavryta

The C4 area lies between the Selinous and Krathis rivers (15–20 km wide). Various aspects of its onshore geology have been described previously (Doutsos *et al.* 1988; Doutsos & Piper 1990; Doutsos & Poulimenos 1992; Ghisetti & Vezzani 2004; Flotté *et al.* 2005; Ghisetti & Vezzani 2005), most recently in Ford *et al.* (2013). The zone is characterized by five major north-dipping faults (Kalavryta, Kerpini–Tsvilos, Doumena, Pirgaki–Mamoussia and Helike (east and west segments)) defining four onshore fault blocks, 4–7 km wide, that have been uplifted to elevations just under 1500 m (Fig. 3). The three southern blocks preserve only Lower Group strata that are well exposed along the Vouraikos Valley (Fig. 3a). The Pirgaki–Mamoussia (PM) Fault preserves Middle Group Gilbert deltas uplifted to over 800 m, while the active East and West Helike faults control subsidence of the coastal plain comprising the fluvial topsets of Gilbert-type deltas currently building into the Gulf (part of the Upper Group). The normal faults, which can each be traced from tip point to tip point, trend between N086° and N112°, except for the Tsvilos Fault which trends N067°. Fault dips are between 42° N and 64° N, and are extrapolated to 2 km depth with a planar geometry. An exception is the Prinos Fault, which is a NE-dipping fault that was abandoned and passively rotated to a low dip (10–15°) within the Kerpini fault block. Secondary south-dipping faults occur within all fault blocks, while a major south-dipping normal fault (buried) is proposed to terminate Lower Group strata to the north. Field kinematic data indicate pure dip-slip displacement recording a north–south to NNE–SSW extension.

Synrift stratal geometries include fanning dips typical of tilting fault blocks and hanging wall forced folds (the Doumena Fault). The presence of palaeo-relief renders accurate measurement of displacement across the faults difficult; heave estimates on major faults are 500–1000 m, while throw estimates are 700–1400 m (Ford *et al.* 2013).

Lower Group. In the south and SW (Kalavryta and Kerpini fault blocks), the Lower Group is characterized by a coarse conglomeratic succession (Kalavryta Formation up to 2200 m thick) deposited by alluvial fans and/or permanent gravelly rivers (Collier & Jones 2003; Ford *et al.* 2013). To the north and NE, these strata pass laterally into a finer-grained fluvial succession (the Ladopotamos Formation). Palaeocurrents record a predominantly north and NE palaeoflow in all Lower Group formations (Ford *et al.* 2013). The lower levels (including basal conglomerates) onlap onto and infill a palaeo-relief of up to 700 m inherited from the Hellenide fold and thrust belt. At the western end of the Pirgaki–Mamoussia fault block, the sand-silt dominated fluvio-lacustrine Melissa Formation (250–500 m) onlaps and infills a palaeo-relief and is laterally equivalent to the Ladopotamos Formation (Backert 2009; Backert *et al.* 2010). At the top of the succession in the PM fault block, the fine-grained Katafugion Formation records a marine transgression marking the onset of basin deepening in the C4 area (Ford *et al.* 2007, 2013), here identified as deepening event 2.

The age of the Lower Group is poorly constrained, and is assigned by most authors to the Late Pliocene (<5 Ma) and Early Pleistocene (up to 1.8 Ma) based on rare palynological dates and regional correlation arguments (Fig. 3b) (Ford *et al.* 2013). Lithostratigraphic correlations across fault blocks suggest two pulses of northwards progradation by a major antecedent river system (Fig. 3b) (Ford *et al.* 2013). The volume of sediment provided by these rivers overwhelmed the accommodation created by early faults that therefore grew below a continuous floodplain landscape traversed by high-energy gravelly rivers. These strata gradually buried the pre-existing relief, although some may have persisted to later times. A marine transgression at the end of the Lower Group is recorded only in the northern PM fault block. Further south, the top of the Lower Group is not preserved.

Middle Group. In the C4 area, the Middle Group comprises four large conglomeratic Gilbert-type fan deltas, regularly spaced (6–8 km) in the hanging wall of the PM Fault (Platanos, Vouraikos, Kerinitis and palaeo-Meganitis). Equivalent prodelta facies comprise fine sand and silt-dominated turbidites and hemi-pelagic deposits (the Derveni Formation

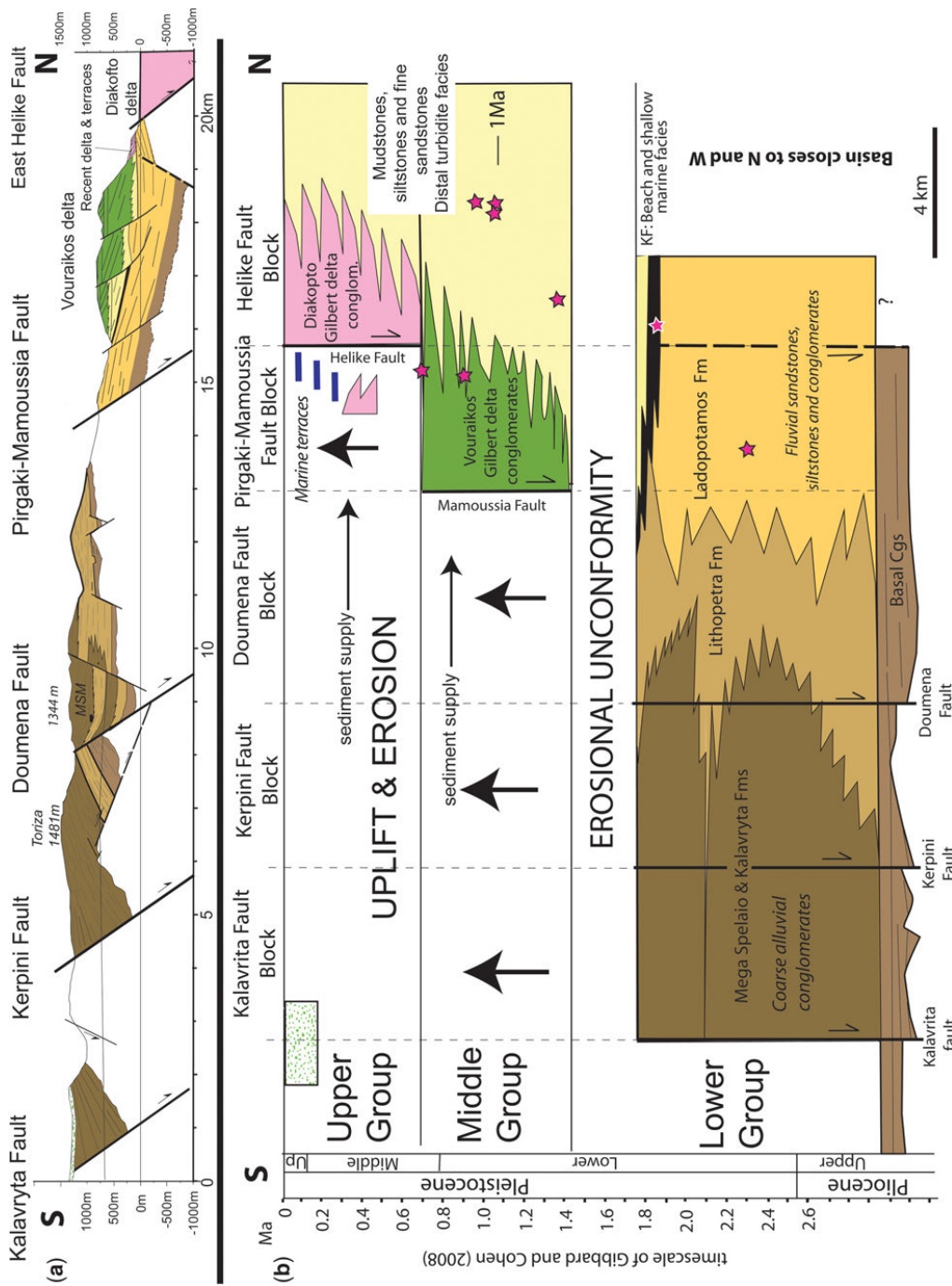


Fig. 3. Onshore area C4 stratigraphy and structure revised from Ford *et al.* (2013). **(a)** North-south cross-section located on Figure 2 (A-A'). Stratigraphic legend in Figure 2. MISM, Mega Spelαιο Monastery. **(b)** Revised chronostratigraphy along cross-section A-A' using the timescale of Gibbard & Cohen (2008). Small pink stars represent palynological dates. Note that time is not constrained below the Plio-Pleistocene boundary. KF, Katafugion Formation.

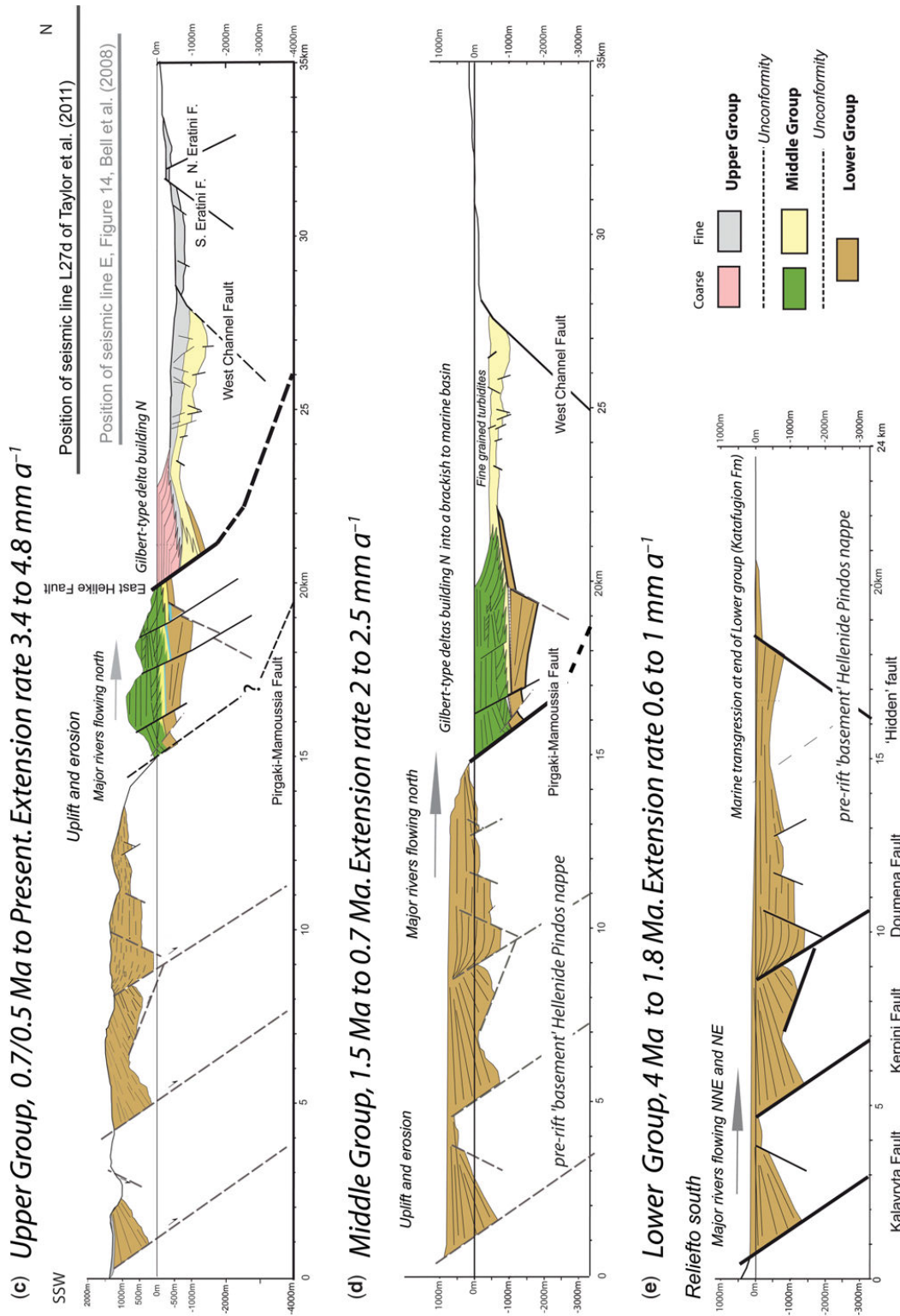


Fig. 3. (Continued) (c) Cross-section across the whole rift, integrating section A-A' with offshore seismic data (Bell et al. 2008; Taylor et al. 2011). (d) & (e) A two-step restoration of the full rift section.

of Ford *et al.* 2007; the Zoodochos Formation of Backert *et al.* 2010: up to 500 m). The exceptional cliff exposures of the Kerinitis and Vouraikos deltas (600 m) have been the focus of numerous studies, providing insight into the interactions of sedimentation, climate and tectonics in extensional settings (Ori *et al.* 1991; Dart *et al.* 1994; Zelilidis & Kontopoulos 1996; Hardy & Gawthorpe 1998; Ulicny *et al.* 2002; Malartre *et al.* 2004; Ritchie *et al.* 2004; Rohais *et al.* 2007b; Backert *et al.* 2010). These giant deltas (radii up to 4 km, thickness from 400 m to >800 m) of cobble to pebble conglomerates built northwards from point sources across the PM Fault into a deepening basin (marine/lacustrine) from Early to Middle Pleistocene. They display an overall aggradational architecture comprising stacked highstand stratal packages. Foresets show a radial organization with depositional dips of up to 28°. In contrast, the less well-studied Platanos and palaeo-Meganitis deltas lie at the eastern and western terminations of the fault block. These are thinner (<400 m), pebble to sand grade deltas with strongly progradational foreset geometries. The palaeo-Meganitis delta built to the east along a relay ramp between the western termination of the Pirgaki Fault and the Panachaikon Fault. The Platanos delta built from south to north at the eastern end of the Mamoussia Fault. The base of each delta is marked by a major erosional unconformity, each recording the incision of a palaeo-valley up to 300 m deep and 700 m wide into the underlying Lower Group strata (Ford *et al.* 2007; Backert *et al.* 2010). It is estimated by Ford *et al.* (2007) that these valleys would take around 300 kyr to erode at reasonable erosion rates. In C4, the Lower and Middle groups appear to be separated by a short-lived marine transgression (the Katafugion Formation), followed by an important period of non-deposition and erosion. The cause of this incision event(s) is enigmatic and may have been submarine (Ford *et al.* 2007). The lower Vouraikos delta displays a clear rollover geometry recording early control by listric faulting, while its upper levels record only gentle tilting into the PM Fault (Ford *et al.* 2007). The Kerinitis delta records gentle tilting into the oblique breaching fault (the Kerinitis Fault: Backert *et al.* 2010).

The age of the Middle Group in C4 is bracketed from Early to Middle Pleistocene ($1.8-0.7 \pm 0.2$ Ma; Fig. 3b) by palynological data (Malartre *et al.* 2004; Ford *et al.* 2013) and by compatibility with Upper Group marine terraces deposited in the footwall of the younger Helike Fault (see below). The Vouraikos and Kerinitis deltas record the birth, growth and death of the Pirgaki–Mamoussia Fault over an estimated period of 0.7 ± 0.2 myr (Backert *et al.* 2010; Ford *et al.* 2013). Stratal architectures record the abrupt termination of displacement on

the PM Fault, which is correlated with the initiation of the Helike Fault, some 5 km to the north.

Upper Group. From 0.7 ± 0.2 Ma onwards, the PM fault block was uplifted and incised by powerful north-flowing rivers, the same rivers that deposited the four major deltas of the Middle Group. The Meganitis, Kerinitis and Vouraikos rivers have cannibalized their Early–Middle Pleistocene deltas to build new Upper Group deltas into the Gulf in the hanging wall of the new Helike Fault (Figs 2 & 3a). Their delta-tops have merged to form the present-day, densely populated coastal plain (Fig. 1). Equivalent prodelta deposits lie offshore below the Gulf (Fig. 3a) (Bell *et al.* 2008).

Uplift of the footwall of the East and West Helike faults is recorded by flights of marine terraces and limestone notches on the range front. These have been well studied and dated to give an average uplift rate for the East Helike Fault footwall of 1.1 mm a^{-1} since at least 0.5 Ma (De Martini *et al.* 2004; McNeill & Collier 2004), increasing to $1.3-2.2 \text{ mm a}^{-1}$ during the Holocene (Stewart 1996; Stewart & Vita-Finzi 1996; Pirazzoli *et al.* 2004). Footwall uplift is also recorded by small uplifted sandy to conglomeratic Gilbert-type deltas (radii < 1 km) with erosive bases that are concentrated around the mouths of river valleys exiting the Helike Fault footwall (Fig. 2). A notably larger Upper Group delta (the Kolokotronis delta, Fig. 2) (Backert *et al.* 2010) directly overlies the Kerinitis delta (Middle Group) with a strongly erosive base, recording a more complex history. At the beginning of uplift, the Kerinitis River first incised its Middle Group delta and built a new delta into deep water toward the north, as evidenced by foresets over 300 m high (Backert *et al.* 2010). This delta was finally abandoned when the river diverted to incise along the NE-trending Kerinitis Fault to find its present bed. Finally, red soil deposits (Terra Rossa), several metres thick, cover the tops of uplifted Middle Group deltas. At the southern edge of C4, periglacial angular limestone breccias (up to 300 m thick) form an apron around the northern and eastern slopes of the Chelmos Massif (>2500 m), which shows evidence of mountain glaciers (Mastronuzzi *et al.* 1994).

Area C3: Derveni–Killini

At the western edge of C3, pre-rift lithologies are exposed in a series of inliers along the Krathis River (Fig. 2) (Ghisetti & Vezzani 2005). To the east, there are few pre-rift basement exposures in the rift, with the largest block in the footwall of the West Xylocastro Fault (Fig. 2). The C3 area is bordered to the south by the Mount Ziria pre-rift massif (2374 m), bounded by the major Killini

Fault largely buried below synrift strata (Figs 2 & 4). Synrift strata have been uplifted to elevations of 1726 m (Mavro GD: Figs 2 & 4).

In C3, the main north-dipping faults (Valimi, Vela, Mavro and Killini) accommodate higher displacement (throws of up to 4.5 km, Killini Fault: Ford *et al.* 2013) compared with those of C4. The onshore area is bound to the north by the coastal Derveni Fault (4 km throw: Fig. 2) (Hemelsdaël & Ford 2016), which passes offshore at Mavro Litharia (a small basement high in its immediate footwall). Basement-cutting faults are required to accommodate tilting of older Lower Group strata (Killini fault block tilted 25–30° S). However, both the Evrostini and Mavro faults show clear listric geometries at the surface with hanging-wall rollovers (Rohais *et al.* 2007a). We link these superficial listric faults to the basement-cutting planar faults at depth (Fig. 4a). The fine-grained synrift succession acts as a decoupling layer between the two structural levels. The Valimi Fault links to the Xylocastro Fault along a NE-trending breached relay zone (Evrostini Fault) across which the Middle Group Ilias Gilbert delta built towards the NW (Fig. 2) (Rohais *et al.* 2007a).

Lower Group. Around the village of Voutsimos (Fig. 2: northern Krathis River), the Lower Group succession is complete but very thin (Hemelsdaël & Ford 2016), indicating the presence of a palaeo-high (Voutsimos High). East of the Krathis River, the Lower Group succession thickens and fines rapidly (Rohais *et al.* 2007a, b). This fluvial succession is ubiquitous throughout C3 and further east in C2, showing an overall fining-eastward, frequently onlapping, palaeo-relief. The Exochi Formation of Rohais *et al.* (2007a) is here subdivided into basal conglomerates (redefined Exochi Formation) overlain by conglomerates and sandstones (Lithopetra Formation), both of which are replaced to the east and north by the sandstone–conglomerate succession of the Ladopotamos Formation (Hemelsdaël *et al.* 2015; named the Amfithea Formation in C2 by Leeder *et al.* 2012).

In the Valimi area, the fluvial Ladopotamos Formation (Hemelsdaël *et al.* 2015) passes eastwards first into a fluvio-deltaic succession (the Valimi Formation), containing low-height (5–50 m) delta clinoforms, and then into a fine-grained lacustrine succession with biostratigraphic evidence of frequent marine incursions (foraminifera; lower Aiges Formation of Rohais *et al.* 2007a). Palaeocurrent data for the whole succession show that sediment was sourced from the SW, west and south, with a predominant eastwards flow (Rohais *et al.* 2007a).

Revision of the Lower–Middle Group boundary. Four large Gilbert-type delta complexes are aligned

north–south over some 15 km, forming the highest relief in the C3 area (Fig. 2). Successive incision indicates that these deltas become progressively younger to the north (Killini, Mavro, Ilias and Evrostini). Rohais *et al.* (2007a) assign all four deltas and their fine-grained prodelta equivalents (upper Aiges Formation) to the Middle Group. Recently, a volcanic calc-alkaline ash layer found further east near Xylocastro (in the C2 area: red star in Fig. 2) has been dated by ^{40}Ar – ^{39}Ar single-crystal CO_2 laser fusion, yielding a precise age of 2.550 ± 0.007 Ma (Leeder *et al.* 2012). This is the first and only absolute age from the Corinth synrift succession, and, as such, its importance cannot be overemphasized. The unworked ash layer is interbedded with fine-grained turbidites and hemipelagics in the Rethio-Dendro Formation, which can be roughly correlated westwards with the Aiges Formation: however, detailed mapping of the intervening area is not yet available. Palaeocurrent data indicate that, south of the Xylocastro Fault, both the Lower Aiges Formation and the laterally equivalent Rethio-Dendro Formation were sourced from either the Killini or Mavro Gilbert delta (Rohais *et al.* 2007a; Leeder *et al.* 2012). Using sedimentation rate estimates and the occurrence of distinctive clast lithologies, Leeder *et al.* (2012) argue that the turbidites containing the ash were supplied specifically from the Mavro delta. They use this correlation to date the base of the Middle Group (taken as the base of the Killini delta following Rohais *et al.* 2007a) at 3.2–3 Ma, which is considerably older than the estimate of 1.8–1.5 Ma in the C4 area. Their discussion of the significance of rift-wide deepening events is based on this hypothesis (see the Discussion section later in this paper).

Here we propose a significantly different interpretation of the stratigraphy of the C3 area, which we believe respects all data and has very different implications for rift evolution. This revision reassigns both the Killini and Mavro deltas and their prodelta equivalents (the Lower Aiges Formation) to the Lower Group, while the Ilias and Evrostini deltas remain in the Middle Group. The arguments for this are: (1) apart from a basal fluvial unit (Amfithea Formation), Lower Group facies in the C2 and C3 areas prove that the central and eastern rift was occupied principally by a lake/marine basin for most of its history; (2) the Killini and Mavro delta complexes comprise a stacked series of strongly prograding, low-height Gilbert deltas (ranging from 10 m to some tens of metres) passing to alluvial fans to the SW and south, respectively (Fig. 4); these successive deltas clearly built into a relatively shallow body of water from a stable coarse sediment input point; (3) in contrast, the Ilias and Evrostini deltas show mainly aggrading

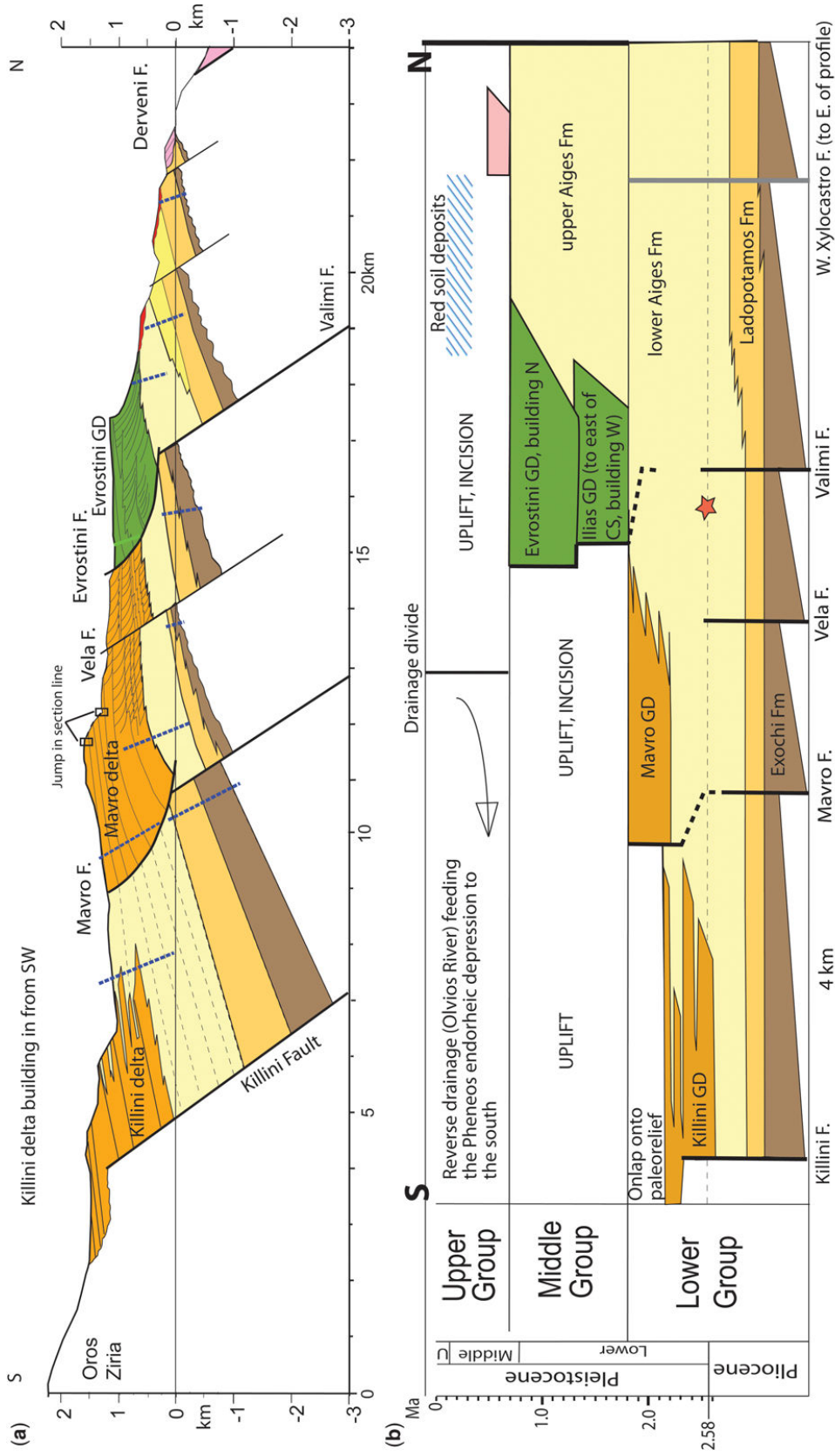


Fig. 4. Onshore area C3. **(a)** North–south cross-section (B–B' in Fig. 2) revised and completed to the south after Rohais *et al.* (2007a). **(b)** Chronostratigraphy along the B–B' cross-section revised to integrate the ash date of Leeder *et al.* (2012) (star) using the timescale of Gibbard & Cohen (2008). Dashed blue lines locate the projected sedimentary logs of Rohais *et al.* (2007a). The red star represents the projected ash layer dated at 2.55 Ma by Leeder *et al.* (2012).

stratigraphic architectures similar to those of the Vouraikos and Kerinitis deltas to the west, with large foresets (several hundreds of metres high), recording deposition into a deepening basin; and (4) the alignment of the four delta complexes and their building directions suggest a stable input point for coarse sediment, which was present since the onset of rifting. After the initial flooding/deepening event between the basal fluvial succession and the overlying lacustrine succession in C3 (here identified as deepening event 1), water depth remained relatively shallow during deposition of the Killini and Mavro delta complexes. The Ilias delta records the onset of a major deepening of the basin on the Valimi–Xylocastro fault system (here identified as deepening event 2, also recognized in C4).

Figure 4b shows our revised chronostratigraphy adapted from that of Rohais *et al.* (2007b). Our reconstruction suggests that the ash level more probably correlates with the Killini delta complex, although more precise mapping is required to constrain stratigraphic correlation.

Upper Group. The Upper Group onland in C3 is, again, composed of uplifted marine-terrace deposits, and small Gilbert-type deltas (Rohais *et al.* 2007a, b) along the coastal slopes. Periglacial slope breccias occur further inland, and red soil deposits are found on high plateaux (Fig. 4). Apart from the Krathis River, no major river flows northwards into the Gulf in C3. Wind gaps and abandoned river valleys record the reversal of the drainage system that built the Middle Group delta. This drainage system now flows southwards into the Feneos endorheic basin, and can be identified as the Olvios River (Rohais *et al.* 2007a; Demoulin *et al.* 2015).

Further west, Hemelsdaël & Ford (2016) show that after having deposited the Middle Group Platanos Gilbert delta, the Krathis River was diverted NE to deposit a strongly prograding Gilbert delta (Akrata GD: Fig. 2) along a relay ramp that developed between the eastwards-propagating East Helike Fault and the pre-existing Derveni Fault. The delta prograded along the multiply-breached relay ramp from 0.7 Ma until final breaching at 0.2 Ma. Subsequent uplift of the East Helike Fault footwall is well documented by dated marine terraces (McNeill & Collier 2004).

Area C5: The Lakka fault block

This subsection presents previously unpublished data and interpretations on the stratigraphy and structure of the onshore Lakka Fault block based on fieldwork, logging and biostratigraphic dating. We build on and integrate the work of Palyvos *et al.* (2007, 2010). The stratigraphy of the AIG10

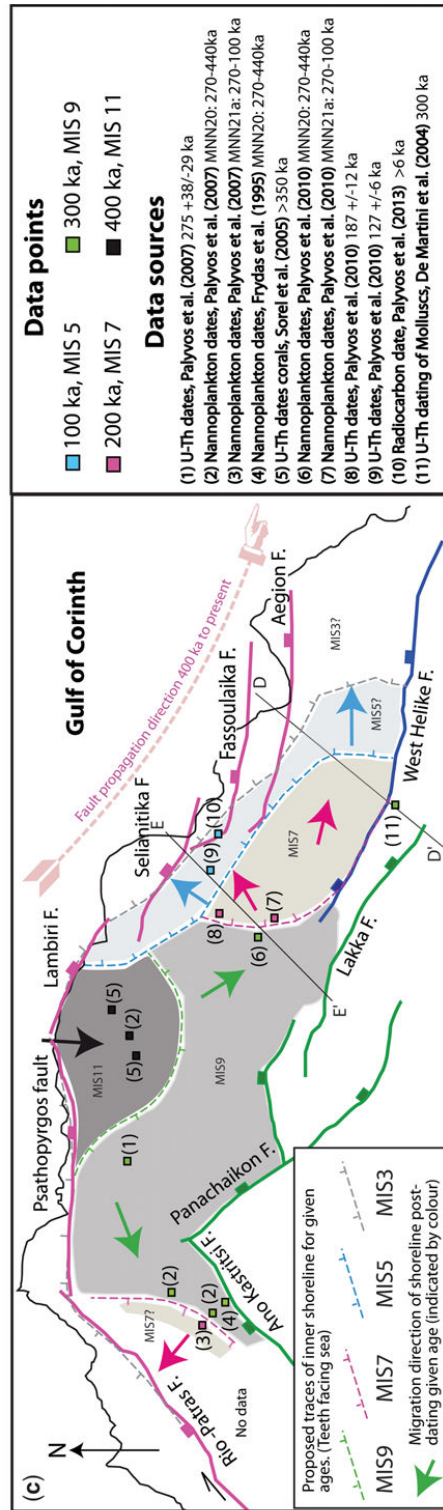
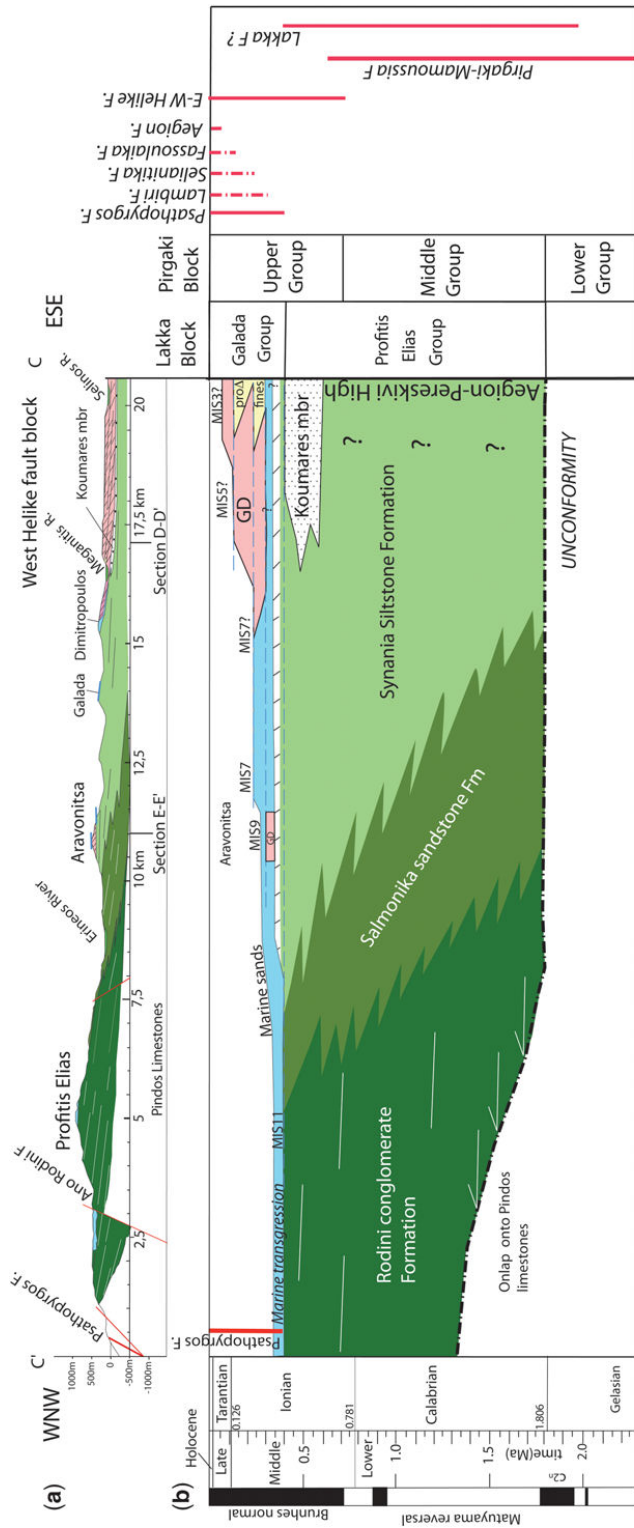
borehole is integrated for the first time into a regional stratigraphy.

Between the Rion Straits in the west and the Selinous River, synrift strata are preserved on the 7–8 km-wide Lakka fault block, and in a small outlier in the Panachaikon fault block further south (Figs 1 & 2). The active coastal fault system that limits the Lakka fault block to the north comprises the east–west Psathopyrgos Fault (with Ano Rodini Fault in its footwall) and the NW–SE-trending Neos Erineos fault system, which includes four east–west, right-stepping en echelon faults (Palyvos 2005; Palyvos *et al.* 2010). These are the Lambiri (with the Ziria Fault in its footwall), Selianitika, Fassoulaika and Aegion faults (Fig. 2). The Lakka fault block terminates to the west against the NE–SW-trending dextral normal Rion–Patras fault zone (Fig. 1).

Throw on the Aegion Fault has been constrained to 150–185 m in the AIG10 borehole that intersects the fault at 760 m bsl (Guernet *et al.* 2003; Cornet *et al.* 2004; Lemeille *et al.* 2004; Apostolidis *et al.* 2006). Displacement on the other four faults is difficult to constrain due to the lack of control on depth to basement both offshore and onshore. However, recent work by Beckers (2015) and Beckers *et al.* (2015) on an unpublished seismic line provides an estimate of the combined throw on the Psathopyrgos and Ano Rodini faults of 1400–1600 m, including 745 m of footwall uplift. A progressive eastwards decrease in elevation in the footwall of coastal faults is noted by Palyvos *et al.* (2007), who estimate a dip of 2.3° E on the topographical surface of the Lakka fault block from 745 m at the peak of Profitis Elias to sea level at Aegion (Fig. 5a). We propose that this footwall relief reflects a progressive decrease in displacement on the coastal faults from west to east. Throws can thus be roughly estimated as 1100 m on Lambiri-Zeria, 800 m on Selianitika and 500 m on Fassoulaika. The age of these faults is discussed below.

The synrift succession of the Lakka fault block is estimated to have a maximum thickness of 1.4 km, although the depth to the base is poorly constrained (Fig. 5a). It is divided into two informal groups: the Profitis Elias Group and the younger Galada Group (Palyvos *et al.* 2010, 2013). Building on the work of Palyvos *et al.* (2010), these stratigraphic units and their structure are described in some detail here for the first time.

Profitis Elias Group. The Profitis Elias Group consists of three formations: the Rodini Conglomerate Formation, the Salmoniko Sandstone Formation and the Synania Siltstone Formation (including the Koumares Member), which are all laterally equivalent and record an overall fining to the east across the Lakka fault block (Figs 2 & 5a) (Palyvos *et al.*



2010, 2013). The entire succession is tilted south against the Lakka Fault by up to 35° (Fig. 6a), and is cut by many second-order oblique and north-dipping faults (Figs 5, 7 & 8).

The Profitis Elias Group is dated as Early–Middle Pleistocene based on the presence of a very rich freshwater to oligohaline mollusc assemblage in the Synania Formation and Koumares Member, with *Didacna spratti* (Fuchs), *Monodacna tenue* (Fuchs), *Dreissena polymorpha* (Pallas), *Unio cf. crassus*, *Theodoxus patrae* (Esu & Girotti), *T. micans* (Gaudy & Fischer), *Viviparus Melanoides elegans*, *Melanopsis mitzopoulosi*, *Hydrobia attica*, *Pyrgula incisa*, *Valvata graeca* (Fuchs) and *Adelina elegans* (Fuchs). The reader is referred to Esu & Girotti (2015), and references therein, for further details on the local mollusc assemblage.

The Rodini Conglomerate Formation (<600 m thick) forms the Profitis Elias Massif (Fig. 2), west of the Erineos River. It is composed predominantly of brown-reddish to grey, coarse conglomerates up to boulder grade, poorly sorted, both matrix and clast supported, and normally or inversely graded limestone and chert clasts of the Pindos thrust sheet dominate, with a sandy–silty matrix. Lenses of trough cross-bedded sandstones of the same composition locally including some grains of quartz, muscovite, feldspar and rare red, clay-rich, palaeosols are found interlayered within the conglomerates. Conglomerates and sands are organized into metre-scale, laterally persistent tabular or channelized bodies with basal erosive scours (Fig. 6b), vertically stacked to form a multistorey wedge showing southwards and eastwards thinning. Beds present gentle to moderate southwards dips. Imbricated clasts and erosive features record SW-, south- and SE-directed palaeocurrents. Locally, the formation overlies onto a palaeo-relief formed by pre-rift Pindos limestones in the immediate footwall of the Psathopyrgos Fault. Conglomerates are here interpreted as gravity-flow deposits (the Gmm, Gmg, Gci and Gcm lithofacies of Miall 1996), and referred to as debris and hyper-concentrated flows, while sands are interpreted as traction current deposits. Preliminary facies analysis indicate that the Rodini Conglomerate Formation was deposited by an alluvial fan and

braided river system, most probably sourced from the north. It passes laterally into the Salmoniko Formation to the east.

The Salmoniko Formation (<250 m thick) comprises tabular bodies of poorly lithified yellow-beige, cross-bedded and planar-bedded fine sandstones and silty sandstones, alternating with lenticular (ribbon-like structures) and tabular beds of granule- to pebble-grade conglomerates (metre scale) and dark grey clayey hydromorphic palaeosols (histosol) (Fig. 6c). The formation represents distal alluvial-fan and fluvial environments, with sands and silts interpreted as floodplain deposits (North & Davidson 2012), while pebble and granule conglomerates represent hyper-concentrated flow deposits filling small distributary channels. Histosols are found on top of metre-scale small sandy–silty sequences recording phases of marshy inundation.

Along the eastern side of the Erineos River (Fig. 2), isolated fluvio-deltaic sands and pebble conglomerates interfinger with the Synania Formation and prograde both eastwards (Fig. 5) and southwards (Fig. 8). A small inlier of sandstones and conglomerates at Nerantzies (Figs 2 & 5) is assigned to this formation.

The Synania Formation (<400 m thick) is a lacustrine unit composed of planar bedded, greenish-grey siltstones and very fine sandstones, interbedded with cross-laminated fine sandstones, decimetre-scale thick lignite horizons, and white thinly laminated calcareous mudstone and marlstone (Fig. 6d). The formation gradually passes to finer massive facies eastwards. The laminated calcareous mudstones and marlstones are rich in charophyte stems and lacustrine molluscs, and are interpreted as laminites (Gierlowski-Kordesch 2010). They are organized into decametre-thick tabular bodies, used as local marker beds, regularly alternating with siltstone and fine sandstones of a distal prodelta environment. The formation has a rich freshwater to oligohaline mollusc assemblage that is typical of the Early Pleistocene basins of Greece described earlier (Gillet 1963; Fuchs 1877; Fernandez-Gonzalez *et al.* 1994; Frydas *et al.* 1995; Koskeridou & Ioakim 2009; Esu & Girotti

Fig. 5. (a) WNW–ESE longitudinal section C–C' along the Lakka and West Helike fault blocks (section line located in Fig. 2). The key to stratigraphic units is shown in Figure 2. The intersections with cross-sections D–D' and E–E' are shown. (b) Chronostratigraphic model along the section C–C' showing the distribution in time and space of the Profitis Elias and Galada groups. The timescale is that of Gibbard & Cohen (2008). To the east, major uncertainty is associated with the presence of a long-lived palaeogeographical high (Aegion–Psaromita High). MIS 5 and MIS 3 terraces can only be suggested as no reliable data exist in this area. Estimated periods of activity on various faults are shown to the right. (c) Compilation map of dated Galada Group deposits across the Lakka fault block and environs with main faults. Data sources are given to the right of the map. These data are used to construct a model of shoreline regression since 400 ka, which is interpreted as due to footwall uplift in the SE-propagating coastal fault system (see the text for discussion). The position of sections E–E' (Fig. 7) and D–D' (Fig. 8) are shown. Fault colours indicate the age of fault initiation and correspond to those in Figures 10–13.



Fig. 6 The Lakka fault block. (a) NE–SW-orientated panoramic view from Profitis Elias Massif to the Aravonitsa Hill in the foreground (SW on the right). Gravels and sands of the Galada Group (GG) Aravonitsa Formation (AF) overlie with angular unconformity (dashed line) the 30° S-tilted lacustrine deposits of the Profitis Elias Group (PEF) Synania Formation (SyF). The N110°-trending Lidoriki Fault is a synthetic normal fault of the main Lakka Fault (see also Fig. 8) and cuts the Synania Formation (arrows indicate the downthrown block). The Pindos Unit (P) is in the background. (b) Along strike, west–east-orientated view of the Rodini Conglomerate Formation (west is on the left, and progradation is directed to the viewer) close to Ano Kastritsi: massive conglomerates (cg), cross-bedded sandstones (sb). (c) NE–SW-orientated outcrop of the Salmmonika Formation north of Neo Salmmonika (SW is on the right): south-tilted channel pebble conglomerates (pb) interbedded with overbank silty sandstones and siltstones (ssb) and histosol (h).

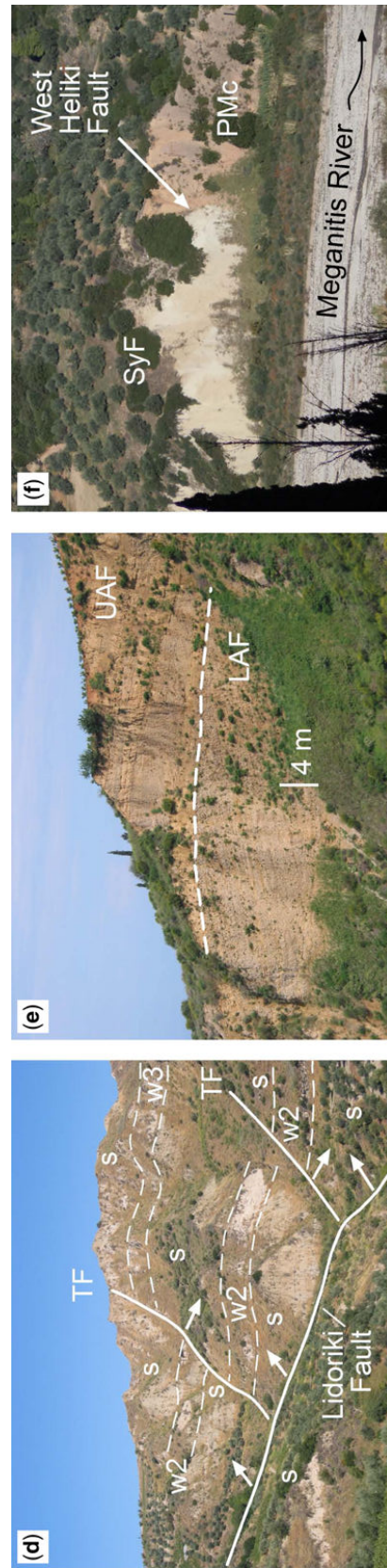


Fig. 6. (Continued) (d) Lacustrine Synania Formation cropping out north of Aravonitsa (the outcrop is west–east orientated, with west on the left, and 170 m high). Open lacustrine, white calcareous laminated mudstones (w2 and w3 marker beds) alternate with distal prodelta silt and sand (s). The hanging-wall block of the Lidoriki Fault is dissected by small north–south-trending transverse faults (TF); arrows indicate the downthrown blocks. (e) Galada Group. North–south-orientated outcrop of Gilbert-type fan delta gravels of the Lower Aravonitsa Formation (LAF) unconformably overlain (dashed line) by nearshore marine sandstones and pebble conglomerates of the Upper Aravonitsa Formation (UAF), at Aravonitsa (south on the right). The succession is tilted south. (f) SW–NE-orientated outcrop on the left bank of the Meganitis River, close to Koumares (SW on the left). The West Heliki Fault (N110° trending, NE60° dipping) separates the Synania Formation (SyF), in its footwall block, from the younger palaeo-Meganitis conglomerates (PMc; Galada Group).

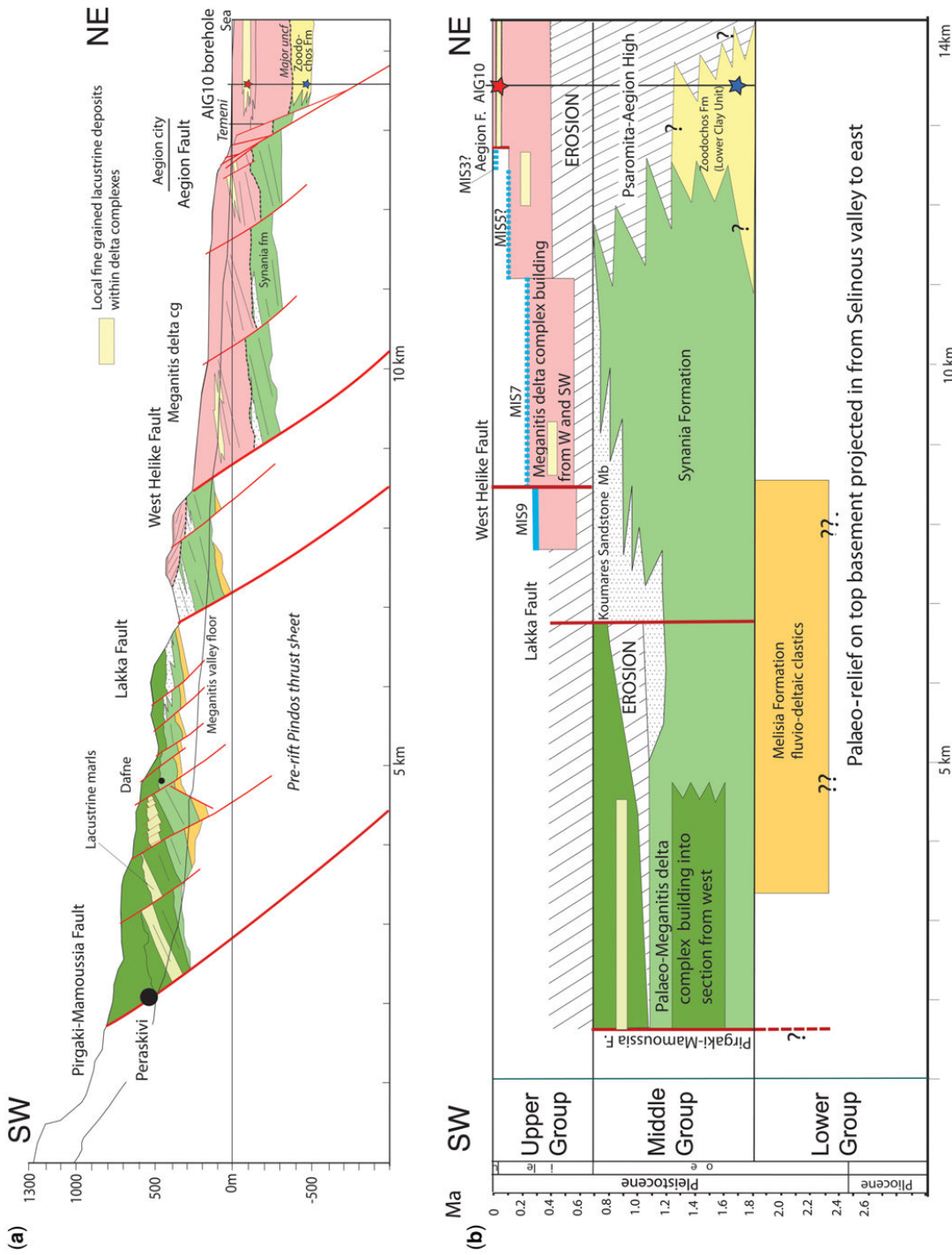


Fig. 7. (a) NNE-SSW cross-section D-D' from the Aegion borehole in the north to the village of Peraskivi to the south on the Pirgaki Fault. The trace of the section line and the key to stratigraphic units are given in Figure 2. (b) Chronostratigraphy along the D-D' cross-section. The timescale is that of Gibbard & Cohen (2008). In the AIG10 borehole, published ages are 11.5 ka at 65 m (Lemeille *et al.* 2004), 35.3 ka at 103 m (red star: Guernet *et al.* 2003) and 1.7 Ma in the Lower Clay Unit at 420 m (blue star: Lemeille *et al.* 2004).

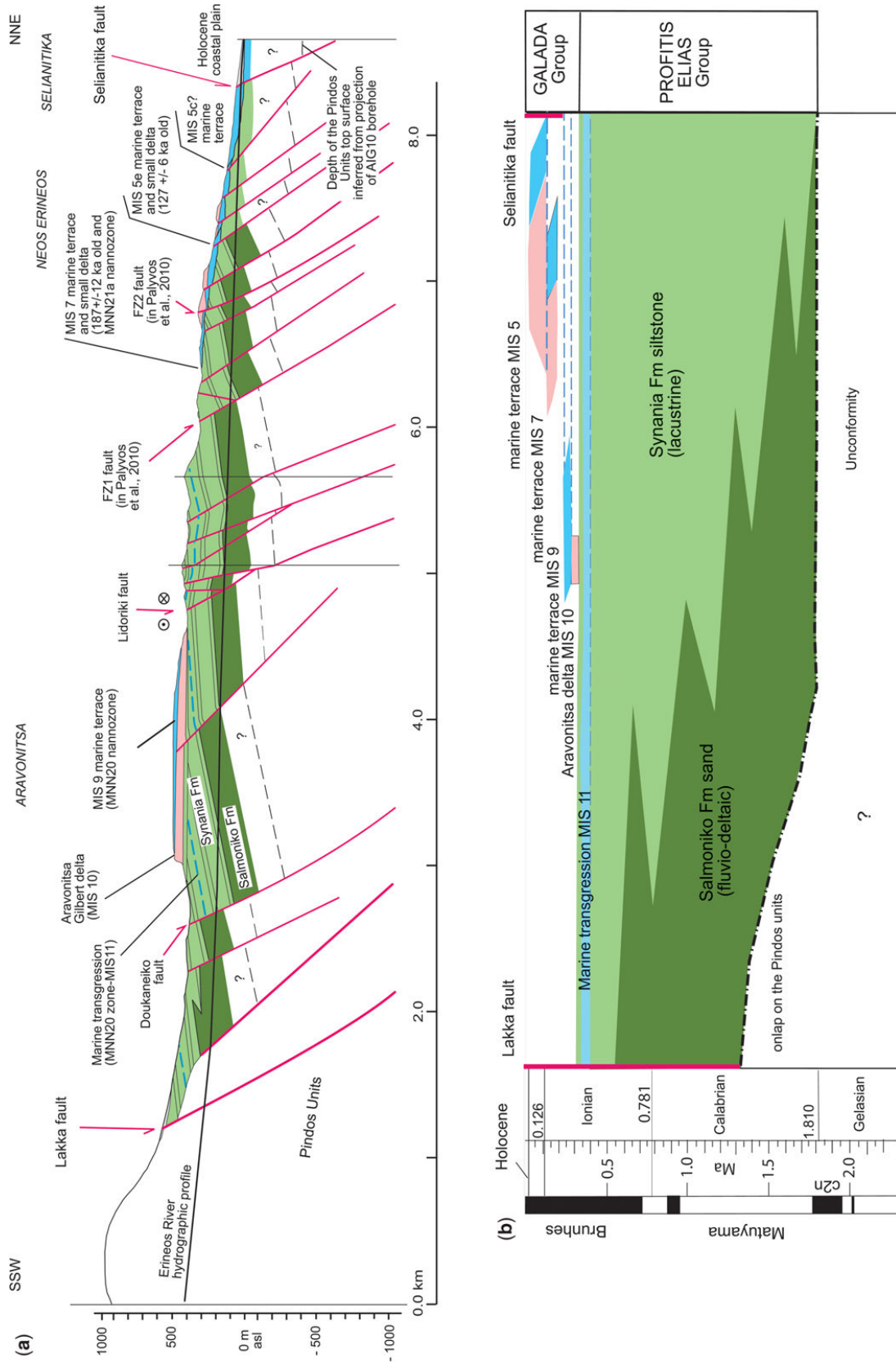


Fig. 8. (a) NNE-SSW cross-section through the western Lakka fault block (C5) from Aravonitsa to Selianitika (E-E'), located on Fig. 2. (b) Corresponding chronostratigraphy revised from Palyvos *et al.* (2010) using the timescale of Gibbard & Cohen (2008). The stratigraphic key in Figure 2.

2015). In the upper portions of the formation, brackish-water layers are present. Palyvos *et al.* (2010) tentatively attributed a fully marine intercalation at Aravonitsa (Fig. 2) to marine isotope stage (MIS) 11 (420–400 ka). The Synania Formation thins to the east of the Meganitis river valley, and its upper levels pass laterally into shallow-marine to brackish-water fine sands and pebbly sands of the Koumares Member (<100 m thick) with abundant *Mytilus* sp.

The Synania Formation is correlated laterally with the Zoodochos Formation further to the east (Backert *et al.* 2010). Rapid changes in facies associated with thinning and onlapping onto outcropping pre-rift lithologies in the Selinous Valley (Backert *et al.* 2010) strongly suggest that there was a persistent palaeogeographical high orientated roughly north–south, extending south from Aegion to Peraskivi along the section represented in Figure 7. Offshore seismic data also indicate that this feature extends northwards across the Gulf to the Psaromita Peninsula on the north shore (Psaromita–Aegion high).

Galada Group. The Galada Group unconformably overlies all formations of the Profitis Elias Group, often with angular discordance (Fig. 6a). It comprises variable lithologies including cool-water carbonate marine terraces, Gilbert-type delta conglomerates, and shallow-marine to brackish-water sands and silts. As a whole, the Galada Group records discontinuous marine–brackish–lacustrine sedimentation due to the interplay of eustatic sea-level fluctuations and tectonics during the progressive uplift of the Lakka fault block from around 400 ka (Palyvos *et al.* 2010). Its depositional history records the tectonic evolution of the coastal fault system.

To the west, a succession of fine sands, silts and marls of the Galada Group overlie the Rodini Conglomerate Formation at the top of the Profitis Elias Massif (peak 745 m). These strata have mixed marine, lacustrine and brackish characteristics, and contain the highest and oldest dated marine layer of the Galada Group. Using diatom assemblages, Frydas (1989, 1991) dated this layer as Middle Pleistocene (biozone MNN20: 270–440 ka). Palyvos *et al.* (2007) argued that this marine level could be correlated to the MIS 11 marine incursion (*c.* 400 ka). Uplift began soon after, thus dating the first opening of the Rion Straits as due to the onset of activity on the Pspathopyrgos Fault.

Moving east, the south-dipping Synania Formation strata below the Aravonitsa Plateau (500 m altitude; Fig. 2) contain a marine level dated as MIS 11 (MNN20: Palyvos *et al.* 2010). This tilted succession is unconformably overlain by a 70 m-high Gilbert delta building north (Lower Aravonitsa

Formation; Galada Group: dated as MIS10), which is, in turn, overlain by shallow-marine sands and pebbly sands of the Upper Aravonitsa Formation (Figs 2 & 6e) (Palyvos *et al.* 2010). The sands of the Upper Aravonitsa Formation have yielded a rich marine macrofauna (corals) dated at 283 ± 40 ka by the U–Th method (MIS 8.5–9: Palyvos *et al.* 2010).

To the east again, shallow-marine sands, often reaching 10–20 m in thickness and tilted gently east, cap many hillcrests (Fig. 2). Just to the west of the Meganitis river valley, these sands are strongly incised by conglomerates of the Meganitis Gilbert delta that dip gently eastwards across the hanging wall of the West Helike Fault (Fig. 6f). Figure 7 shows a cross-section from Aegion to the village of Peraskivi, integrating the 1000 m-deep AIG10 borehole in the hanging wall of the Aegion Fault (Cornet *et al.* 2004). The marine Lower Clay Units (110 m thick) at the base of the synrift succession in the AEG10 borehole is dated as Early Pleistocene (Lemeille *et al.* 2004) and is thus equivalent in age to the Synania and Zoodochos formations. The overlying fluvial conglomerates and sands (400 m thick) are placed in the Galada Group, and have a strongly erosive base that has been given an estimated age of 400 ka (Lemeille *et al.* 2004).

On a north–south profile from Aravonitsa to Selianitika (Fig. 8a, b), Palyvos *et al.* (2010) presented reliable chronological constraints on terraces using nannoflora in silty levels, and U–Th dating of corals and syndepositional calcite encrustations. Each terrace corresponds to a single high-order eustatic cycle (IV and V) in which transgressive and sea-level highstand sands are preserved (MIS 9, 7, 5 and 1). In general, terraces are well defined but are only partly preserved, often cut by minor faults (Fig. 8). These dated terraces record the northwards migration of footwall uplift over a distance of just over 3 km since around 300 ka. The cross-section (Fig. 8a) shows the marked tilting of the Profitis Elias Group below the untilted Galada units of the Aravonitsa plateau.

Finally, all dated terraces and marine sediments preserved above the Profitis Elias Group in the Lakka fault block are compiled on the map in Figure 5c. The uncertainty associated with some of these ages, in particular the U–Th dating of corals, is discussed by Palyvos *et al.* (2007, 2010). A clear pattern emerges, however, of oldest marine sediments preserved on the highest relief (Profitis Elias, 745 m: Frydas *et al.* 1995) with younger ages radiating away from this massif to the SW and SE. The northwards-younging trend seen on the Aravonitsa–Selianitika section (Fig. 8) is also integrated into this model, showing shorelines gradually migrating to the ESE (and possibly west) and

also, more locally, to the north in the footwalls of the coastal faults. This pattern can be explained by migrating footwall uplift on the coastal fault system with the initiation of the Psathopyrgos Fault around 400 ka, followed by a gradual propagation of the coastal fault system to the SE, with the Aegion Fault being the youngest segment initiated around 50–70 ka (Micarelli 2003; Cornet *et al.* 2004; Lemeille *et al.* 2004).

The Lakka fault block contains no known strata equivalent to the Lower Group: however, a fine-grained fluvial succession is preserved further south in the hanging wall of the eastern Panachaikon fault block. This unit correlates laterally to the Melisia Formation (Lower Group) of the Pirgaki–Mamoussia fault block (Backert *et al.* 2010; Fig. 2). With its upper boundary at 400 ka, the Early–Middle Pleistocene Profitis Elias Group is laterally equivalent to the Middle Group and to part of the Upper Group further east. However, direct correlation is obscured by the presence of the Aegion–Psaromita palaeohigh. The Lakka Fault was active during deposition of the Profitis Elias Group, although no sediment appears to have been supplied from its footwall during this time. Instead, its footwall area appears to have drained eastwards across the relay zone between the Panachaikon and Pirgaki faults to feed the palaeo-Meganitis delta complex building to the east and NE. The small north-building Aravonitsa Gilbert delta, dated at 400–300 ka (Palyvos *et al.* 2010), records the first coarse sediment supplied from the Lakka footwall (possibly by the proto-Erineos River). The Lakka and Panachaikon faults were active until about this time, when the new fault system initiated to the NW (Psathopyrgos Fault) and then propagated eastwards.

Evolution of the central and western rift

Using the data presented above, we here reconstruct the evolution of the western and central rift in four phases. Figure 9 presents an along-strike chronostratigraphic model correlating onshore areas C5–C3. For this purpose, the northwards-migrating depocentres are all projected onto a single plain. Figures 10–13 represent palaeogeographical reconstructions of the evolution of the western and central Corinth rift. Offshore data on fault geometries and ages, and seismic stratigraphy were derived from McNeill *et al.* (2005), Bell *et al.* (2008, 2009) Taylor *et al.* (2011) and Nixon *et al.* (2016).

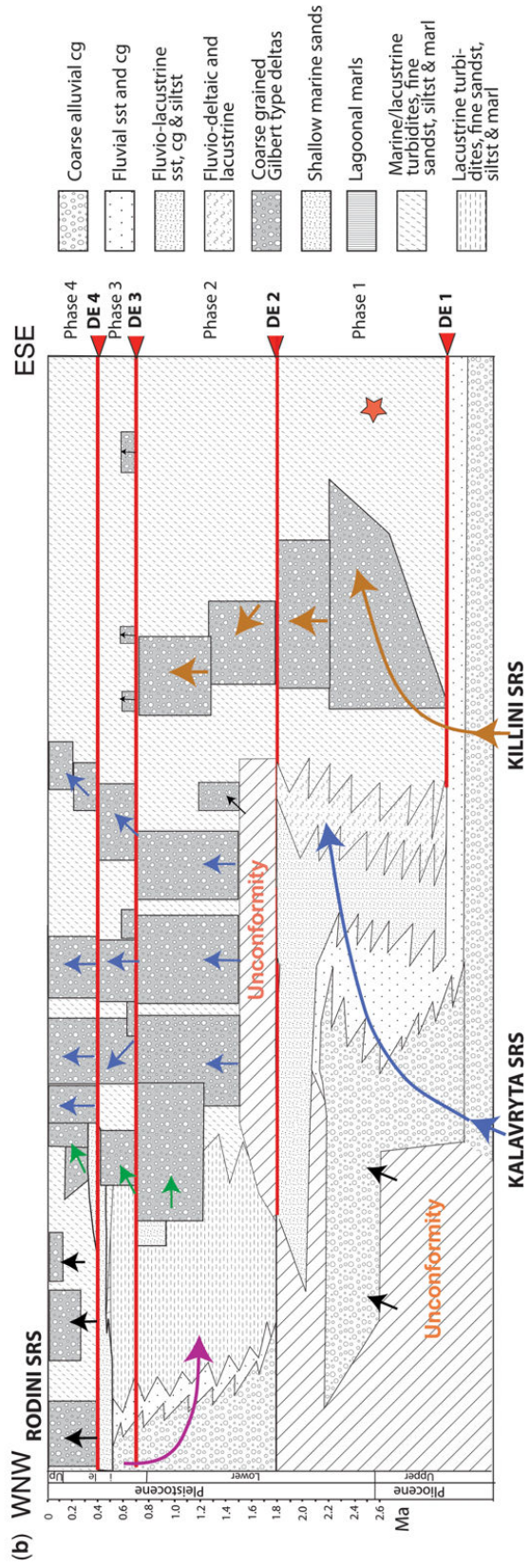
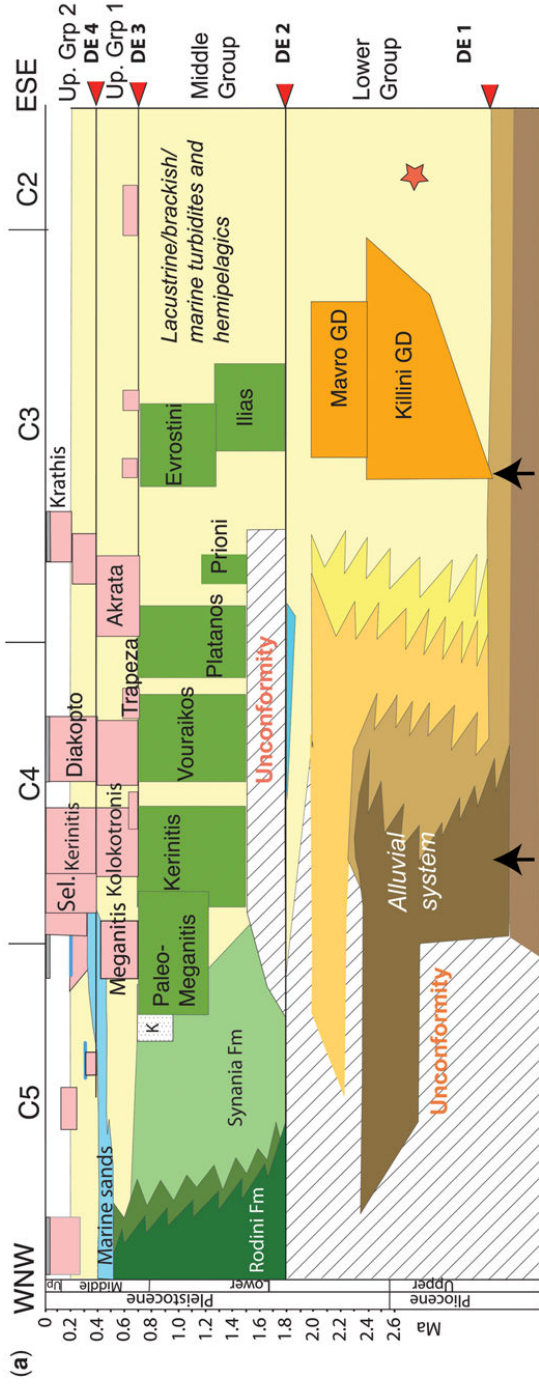
Phase 1: Late Pliocene–Early Pleistocene (5–4 to 1.8 Ma)

Early extension was distributed on a predominantly north-dipping fault system across a 20–30 km-wide

zone over a period of 2–3 myr starting from around 4 Ma. The area under extension may have been wider. For example, undated normal faults are documented further south (Skourtsos & Kranis 2009). As the amount of Phase 1 strata preserved below the Gulf is unknown, we provisionally draw the northern border below the proximal southern Gulf (Fig. 10). This margin may have been controlled by a south-dipping fault or faults, which were later buried. The early rift closed to the west (Fig. 10). In C4 and C3, synchronous north-dipping faults define tilted blocks 4–8 km wide. In C4 (Fig. 3), these are relatively small faults with approximately the same length (10–16 km) that accommodate similar displacements (throws of 500–1000 m: Ford *et al.* 2013). Total Phase 1 extension in C4 (section A–A') was low and extension rate was slow, estimated at 0.6–1 mm a⁻¹ (Fig. 3e) (Ford *et al.* 2013). To the east (C3) faults accommodated considerably more displacement (Rohais *et al.* 2007a; Ford *et al.* 2013), the largest fault being the Killini Fault with an estimated throw of over 4 km (Fig. 4a). Using our revised stratigraphy, the Phase 1 extension rate in C3 (Fig. 4a) is estimated as 1.5–2.3 mm a⁻¹ (assuming rift initiation at 5–4 Ma). Faults in the lacustrine succession to the east (C2 and C1: Fig. 10) are, as yet, poorly known.

Phase 1 is characterized by continental environments that deepen from fluvial (C4) in the west to lacustrine in the east (C3, C2) recording an overall fining eastwards (Fig. 10b). Coarse-grained sediment was fed into the rift from the SW by two major routing systems (Kalavryta and Killini: Fig. 10). In C4, coarse-grained alluvial strata (> 1000 m thick) onlap a significant inherited relief. Sediment supply was high and largely outstripped the creation of accommodation, thus burying active normal faults. Although the succession is condensed on a local palaeogeographical high between C4 and C3 (Vougsimos, Fig. 2), facies and palaeocurrent analysis show that sediment was routed from C4 to C3. These depocentres were therefore always connected (Rohais *et al.* 2007b; Ford *et al.* 2013) and not separated as proposed by Ghisetti & Vezani (2005).

In C3, the basin very quickly became lacustrine after a 'deepening event' at 3.2–3.0 Ma (DE1; base of the lacustrine Aiges Formation: Leeder *et al.* 2012). Subsequently, the Killini sediment-routing system built the Killini and Mavro Gilbert delta complexes axially into the shallow lake (Figs 9 & 10) comprising stacked, prograding deltas, each several tens of metres in height (Fig. 4). The concentration of coarse-grained alluvial conglomerates along the south and west of the early rift is interpreted as being due to the capture of well-established antecedent rivers of the Hellenide orogen (Ford *et al.* 2013; Hemelsdaël *et al.* 2015). In the



eastern lacustrine succession, published palaeo-current data indicate that sediment supply was predominantly axial and from the west (Leeder *et al.* 2012). Grain-size and facies distribution in the early rift (Fig. 9) were therefore controlled by: (1) the position of captured antecedent rivers along the southern rift margin; (2) the rate of sediment supply from these rivers; and (3) their interaction with evolving accommodation on the young fault system.

Phase 2: Early–Middle Pleistocene (1.8–0.7 Ma)

In the Early Pleistocene, starting at around 1.8 Ma, the southern rift margin migrated northwards in C3 and C4 by approximately 15 and 10 km, respectively. At the same time, the rift propagated west to form a new depocentre in C5. This phase of northwards and westwards fault migration (1.8–1.5 Ma) is correlated with a significant period of erosion that marks the base of the Middle Group in C4 (but not C3: Figs 9 & 11). New south-dipping faults were also initiated on the northern side of the rift (Fig. 11), and played a major role in controlling a more symmetrical and deeper depocentre, largely corresponding to the present-day Gulf in C3 and C2 (Bell *et al.* 2009; Nixon *et al.* 2016). The new rift was 20–25 km wide in C3, and narrowed to the west to 10–15 km in C4 and C5. Eustatic control on delta stratigraphic architecture (Backert *et al.* 2010), the local presence of limestones with corals (Ford *et al.* 2007) and marine Foraminifera assemblages (see Rohais *et al.* 2007b for a summary) all indicate that the main Corinth Basin was predominantly at least periodically marine to brackish in character during the Early–Middle Pleistocene. The Psaromita–Aegion High separated the C5 fluvio-lacustrine depocentre from the main rift (Fig. 11).

The principal north-dipping faults along the southern rift margin were the Xylocastro–Evrostini–Valimi fault zone, and the Derveni Fault in C3, the Pirgaki–Mamoussia Fault in C4, and the Lakka and Panachaikon faults in C5. On the northern rift margin, principal south-dipping faults were the Galaxidi Fault in C3 (also known as the East Channel Fault: e.g. Bell *et al.* 2008), the West Channel Fault in C4 and the Trizonia Fault in C5

(Fig. 11). In C3, the highest sediment accumulation occurred between the Galaxidi and Derveni faults, focusing more towards the south-dipping Galaxidi Fault. The Galaxidi Fault has an estimated throw of 1.3 km and was principally active during Phase 2 (Bell *et al.* 2009). The Derveni Fault, still active today, is by far the largest fault in C3, with a total estimated throw of around 4 km (Hemelsdaël & Ford 2016), a quarter of which occurred during Phase 2 (Nixon *et al.* 2016). At the same time, the pre-existing Valimi–Evrostini Fault to the south accommodated >1000 m throw during deposition of the Ilias and Evrostini deltas (Fig. 4a). The estimated extension rate in C4 doubled to 2–2.5 mm a⁻¹ during Phase 2 (Fig. 3d) (Ford *et al.* 2013). Extension may have increased to the east in C3 and C2, as reflected in the position of the main depocentre.

The northwards fault migration over a period of some 300 kyr at the beginning of Phase 2 was associated, first, with a marine transgression at the top of the Lower Group (Katafugion Formation) in C4, followed by an enigmatic phase of (submarine) erosion (Ford *et al.* 2007) (Fig. 9). The fluvial network underwent a radical reorganization, changing from an east- to NE-flowing network to a new system of equally spaced (6–8 km), north-flowing rivers (Fig. 11). These rivers reworked Phase 1 sediments that were uplifted further south. Their coarse bedload provided high erosional capacity that allowed the rivers to cut across uplifting footwalls (Cowie *et al.* 2006).

In area C4, the deepening event (DE2) is recorded by a marked change from a continental fluvial environment to a deeper basin in the hanging wall of the Pirgaki–Mamoussia Fault. Large Gilbert deltas began to build into the ever-deepening basin supplied by new north-flowing rivers (Figs 9 & 11). Equivalent prodelta turbidites and hemipelagics are preserved both onshore (the Derveni and Zoodochos formations) and offshore (most probably the seismic stratigraphic unit SU1: Nixon *et al.* 2016). In area C3, the deepening event is not marked by a major sedimentological change, as Gilbert deltas were already building into a lacustrine basin. However, deeper-water conditions are recorded by the distinct stratal architecture of the Ilias and Evrostini deltas, characterized by aggradation–progradation and significant foreset

Fig. 9. WNW–ESE Wheeler diagram of synrift chronostratigraphy correlating areas C2–C5 along the northern Peloponnese. In (a) lithostratigraphic colour codes in Figure 2. K, Koumares Formation. In (b) facies distributions and sediment-routing systems are represented. Four deepening events are identified (DE1–DE4) to the right of the figure. The timescale is that of Gibbard & Cohen (2008). The three major sediment-routing systems (SRS) feeding into the rift are shown (Rodini in purple, Kalavryta in blue and Killini in orange). Green arrows represent the Meganitis systems draining off the Panachaikon and Lakka blocks. Other sediment-supply routes are more local and short-lived (black arrows). The red star represents the ash layer dated at 2.55 Ma by Leeder *et al.* (2012). Sel., Selinous.

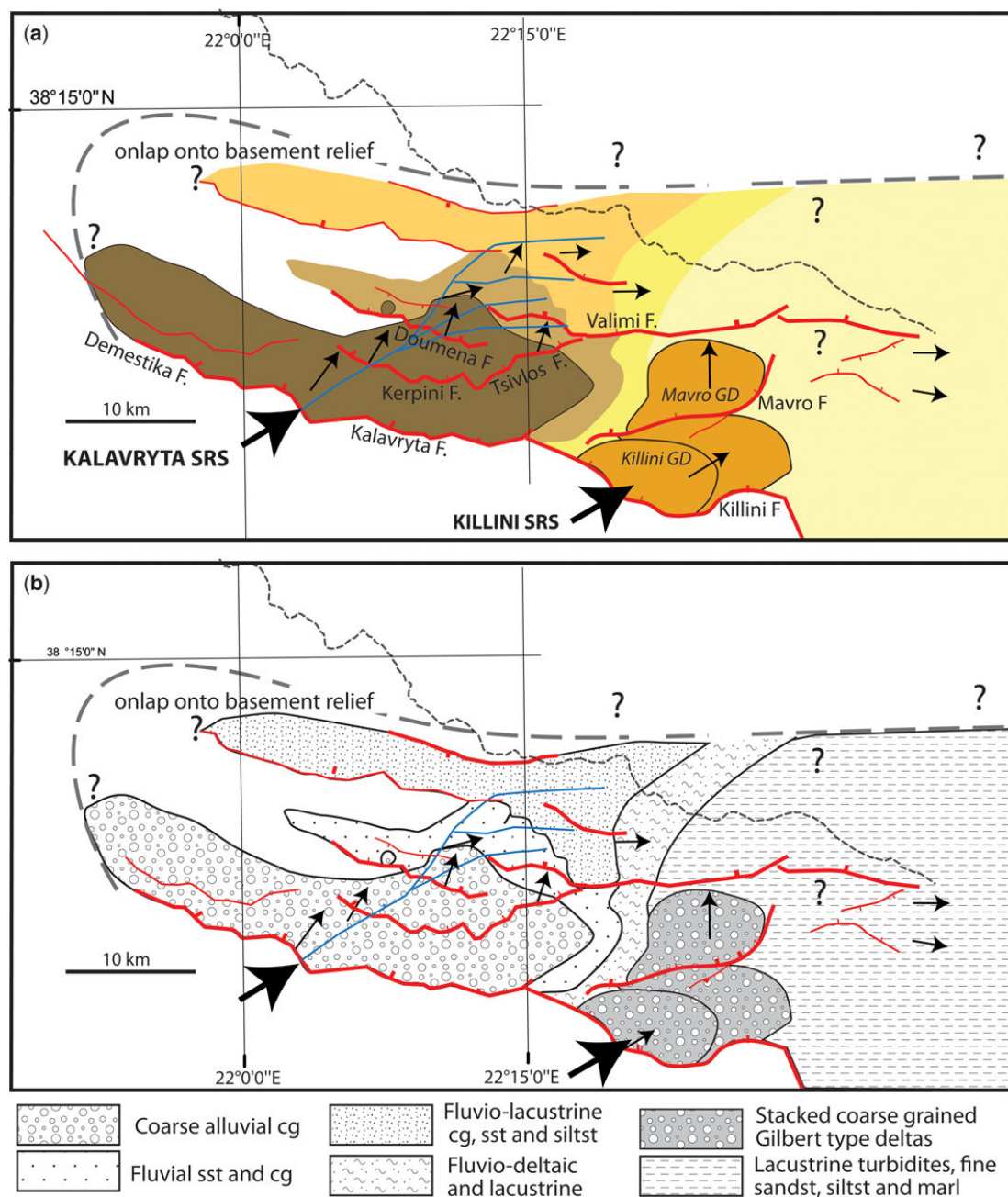


Fig. 10. (a) Phase 1 (Pliocene–Early Pleistocene) rift model showing deposition of the Lower Group. Colours correspond to stratigraphic units in Figures 2 and 8. The northern basin margin is very poorly constrained. Small black arrows summarize the palaeocurrent data of Rohais *et al.* (2007a) and Leeder *et al.* (2012). Large black arrows indicate the two main captured antecedent drainage systems (SRS, sediment-routing systems). (b) Facies distributions during Phase 1 with the main sediment-routing systems.

height (hundreds of metres). As the two Phase 2 deltas lie directly north of the Phase 1 deltas, it is reasonable to suggest that they were supplied by the same north-flowing drainage system (Rohais *et al.* 2007a).

To the west, the new C5 depocentre was controlled by the Lakka and Panachaikon faults to the south, and the Trizonia Fault and an unidentified fault to the north and NW (Beckers 2015; Beckers *et al.* 2015). The lacustrine basin was supplied

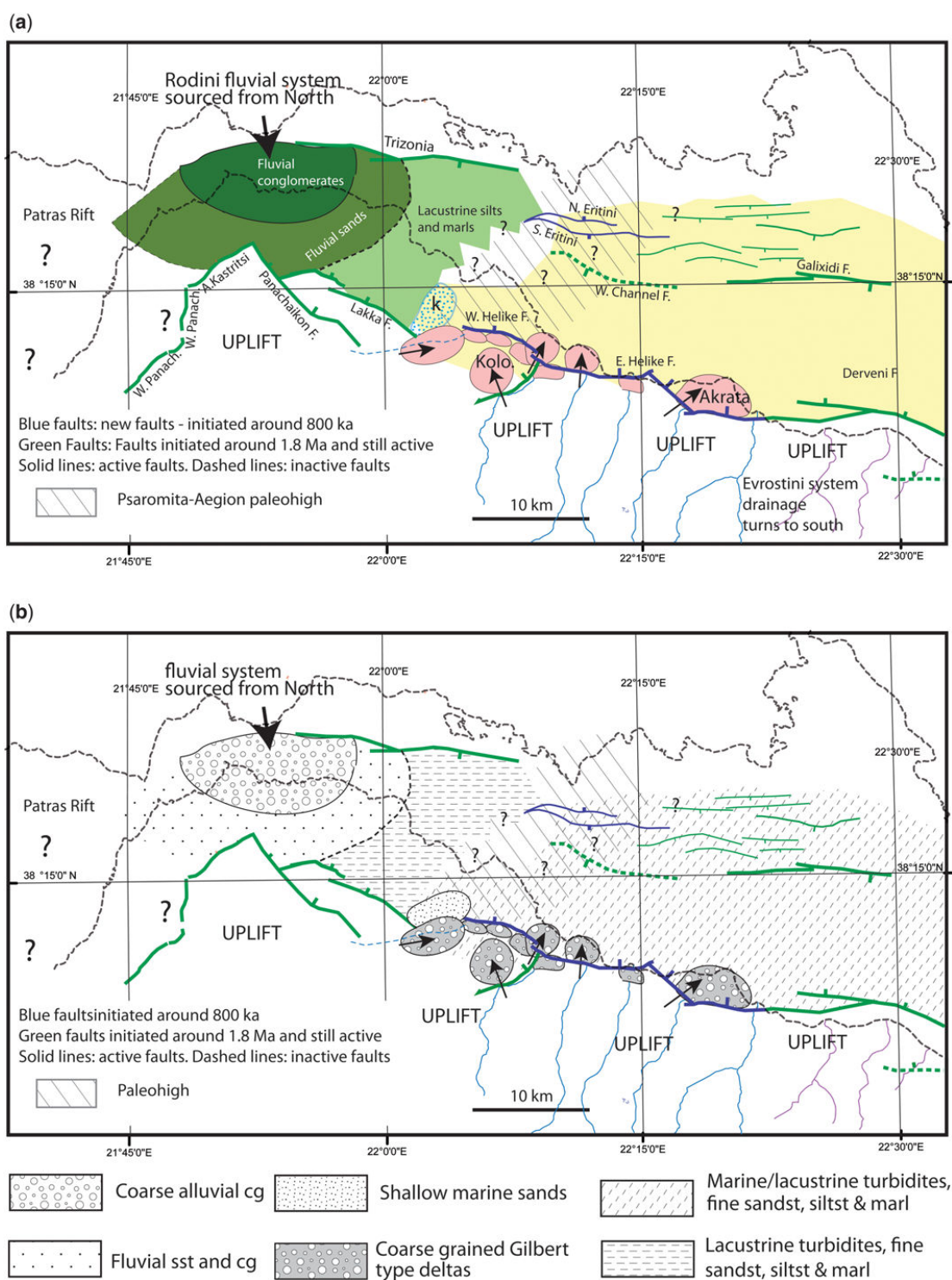


Fig. 12. Reconstruction of the Phase 3 rift (Calabrian–Middle Ionian, 0.8–0.4 Ma) showing that northwards migration of fault activity occurred only in C4 onto new blue faults. New deltas formed in the hanging wall of the new faults. Inactive faults are shown as dashed lines; active faults have solid traces. In zones C3 and C5, no change occurs. Colours correspond to the stratigraphy in Figures 2 and 8. Consequent rivers are shown in purple, while antecedent rivers are in blue. Kolo, Kolokotronis Gilbert delta (Backert *et al.* 2010); k, Koumares Member. (b) Facies distributions during Phase 3. Black arrows indicate delta building directions.

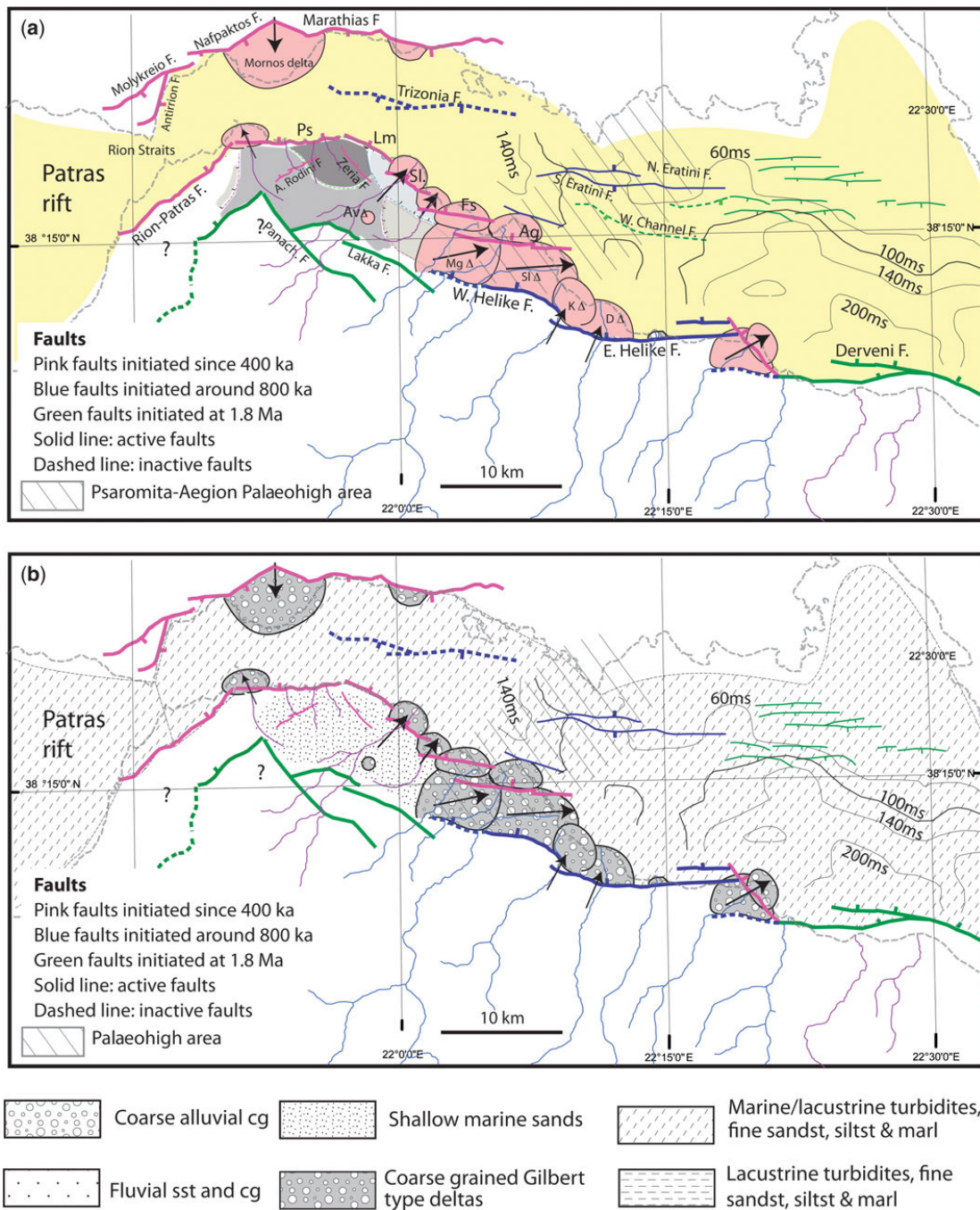


Fig. 13. (a) Phase 4 reconstruction (Middle Ionian–present day, 0.4 Ma–0) showing northwards rift migration only in the west (C5), with the initiation of the north-dipping Psathopyrgos (Ps) and Neos Erineos fault systems (Lambiri (Lm), Selianitika (Sl), Fassoulaika (Fs) and Aegion (Ag) faults) and new antithetic faults on the north coast (Marathias and Nafpaktos). The Rion Straits opened at approximately 400 ka due to the initiation of the Ps Fault. To the east in C4 and C3, the main rift remained static with accelerating subsidence concentrated along the southern margin faults. Colours correspond to the stratigraphy in Figures 2 and 8 (deltas are Av, Aravonitsa; Mg, Meganitis; Sl, Selinous; K, Kerinitis; D, Diakopto) with black arrows indicating palaeoflow. Migrating shorelines (Fig. 5c) record the progressive uplift in the footwall of the Neos Erineos fault system (toothed lines: green, 400 ka; pink, 300 ka; blue, 200 ka). Active offshore faults and selected isochores for offshore vertical sediment thickness in milliseconds two-way travel time (TWTT; fine black lines) for the period 135 ka to 0 are taken from Nixon *et al.* (2016). (b) Facies distribution in the rift during Phase 4. Black arrows indicate delta building directions.

from the north by the Rodini fluvial system, which may also have supplied the eastern Patras rift (Fig. 11) (Palyvos *et al.* 2007). During Phase 2, the C5 area received little or no sediment from the south. It was limited to the east by the Psaromita–Aegion High, as evidenced by a thin and incomplete succession onlapping pronounced palaeo-relief, major unconformities (e.g. in the AIG10 borehole), and local facies and thickness changes (the Koumares Member). Marine incursions into the depocentre probably came from the east during high sea levels.

Phase 3: Calabrian–Middle Ionian (0.7–0.4 Ma)

In the Middle Pleistocene, at around 0.7 ± 0.2 Ma, the southern basin margin, again, migrated northwards in C3 and C4 by some 5–10 km (Fig. 12). In C3, the West Xylocastro Fault was abandoned as deformation focused onto the pre-existing Derveni Fault, which became the principal focus of extension, linking eastwards with the Lykopora and East Xylocastro faults (Nixon *et al.* 2016). Displacement gradually decreased on south-dipping faults (Galixidi and West Channel). The main C3 depocentre narrowed to around 12 km, as the northern boundary did not migrate, although minor south-dipping faults developed in the footwall of the Galixidi Fault. Mainly fine-grained prodelta and hemipelagic sediments were deposited here (lower SU2 of Nixon *et al.* 2016).

In C4, the Pirkaki–Mamoussia Fault was abandoned as displacement transferred onto the East and West Helike fault system, which gradually propagated eastwards to link to the Derveni Fault (Fig. 12) (Hemelsdaël & Ford 2016). Deposition increased in the deep basin (lower SU2), but still thinned westwards onto the Psaromita–Aegion High. The North and South Eratini faults developed to the north of the now inactive West Channel Fault. However, these faults played a minor role in the development of the C4 depocentre. The rift in C4 has an estimated width of 10–12 km. In C5, the Lakka–Trizonia depocentre and Psaromita–Aegion High retained the same configuration as in Phase 2.

In C4, major rivers continued to flow north across the uplifting footwall of the East and West Helike faults, cannibalizing their own Phase 2 deltas. Numerous small Gilbert deltas record the progressive uplift of the western PM block that may have locally inherited a bathymetry of up to 400 m basinwards of the large Phase 2 deltas. However, where the new East Helike Fault cut across a major delta (e.g. Vouraikos and Platanos), new deltas began to build immediately into the hanging wall of the new fault. The Krathis River diverted ENE to build the new Akrata delta across the evolving relay ramp between the Derveni and East Helike faults. In

C3, however, footwall uplift caused the Evrostini river system to turn south into the Feneos endorheic basin (Rohais *et al.* 2007a), thus terminating a major supply route (Killini) into the rift. East of Akrata, no major river supplied coarse-grained sediment into the rift.

Phase 4: Middle Ionian–present day (0.4–0.0 Ma)

During Phase 3 and Phase 4, from approximately 620 ka to present day, activity increased on major north-dipping faults (Derveni–Lykopora, East Xylocastro and North Kiato) to create a single major depocentre in the southern Gulf (C2, C3 and eastern C4). By constructing detailed isochore maps in six steps, Nixon *et al.* (2016) document the progressive evolution and linkage of numerous hanging-wall depocentres along the these faults, which eventually (from around 130 ka) formed a 40 km long half-graben depocentre centred in C2 (isochores from Nixon *et al.* 2016 on Fig. 13). While the succession still thins markedly westwards in C4, owing to the persistent influence of the Psaromita–Aegion High, the basin is now clearly connected to the C5 depocentre.

In C5, fault activity migrated, again, onto the east–west Psathopyrgos Fault at approximately 400 ka, which then propagated east-southeastwards to form the Neos Erineos fault system (Fig. 13). The Aegion Fault is the youngest fault of the system, dated at 50–60 ka (Cornet *et al.* 2004). The northern margin of the C5 rift also migrated north from the Trizonia Fault onto the Marathias and Nafpaktos faults (Beckers *et al.* 2015), which are clearly major faults, although, as yet, not well documented. The westernmost Gulf is controlled by the most recently initiated (youngest) faults. Unlike the main rift, it retains a relatively symmetrical fault system. Highest geodetic extension rates occur here, increasing from 13 mm a^{-1} around Aegion to 16 mm a^{-1} near Lambiri (Lambotte *et al.* 2014). The most intense seismicity is also concentrated below the present-day Gulf in C5 (Bernard *et al.* 2006; Lambotte *et al.* 2014). Seismic data indicate that it is possible that the Panachaikon and Lakka faults may also still be active.

The Rion Straits opened to the Mediterranean for the first time at around 400 ka as a result of the initiation of the Psathopyrgos Fault. Water depth on the sill is currently 60 m, indicating that this sea-way would be cut off during sea-level lowstands. The transition from lacustrine to marine conditions in the Gulf at the time of the last sea-level rise, at approximately 12 ka, has been well documented in cored offshore sediment (Moretti *et al.* 2003; Sakellariou *et al.* 2007; Campos *et al.* 2013). The well-stratified nature of the SU2 seismic

stratigraphic succession, consisting of highly reflective bands alternating with transparent bands, is attributed to alternating marine and lacustrine conditions (Bell *et al.* 2008; Taylor *et al.* 2011; Nixon *et al.* 2016).

From 400 ka onwards, nearly all sedimentation was concentrated in the Gulf and most probably consisted of predominantly fine-grained prodelta facies and hemipelagics. The eastern rift is clearly sediment-starved, with bathymetry increasing eastwards to over 800 m. In C4 and western C3, however, major rivers continued (and continue today) to flow north to build coarse-grained Gilbert-type deltas into the Gulf across basin-bounding faults. In C2 and C3, younger, less powerful consequent rivers fed the rift: several rivers were turned south by rapid uplift starting at the beginning of Phase 3 (Demoulin *et al.* 2015). In C5, Galada Group deposits record progressive footwall uplift associated with the eastwards propagation of the Neos Erineos fault system (Figs 5, 7 & 8). The resulting eastwards tilting of the Lakka fault block, and passage from uplift to subsidence along the relay ramp between the Neos Erineos and Helike fault systems, is clearly seen in the deviation and building directions of the youngest Gilbert deltas (Selinous and Meganitis: Fig. 13).

Demoulin *et al.* (2015) presented a morphometric analysis of the 10 largest catchments of the north Peloponnese margin. The authors used a wide range of metrics to study the fluvial landscape in order to clarify the timing, location and intensity of uplift episodes along the 100 km-long rift margin. Their results clarified the episodic nature of rift shoulder uplift and they identified three distinct episodes of increasing uplift rate that correspond to major phases of rift migration identified in this study. They propose that the youngest event, with an uplift rate of $2\text{--}5\text{ mm a}^{-1}$, propagated from east to west over the last 20–10 ka and can be related to the location of high seismicity in the westernmost rift. Their intermediate episode is dated at 0.35–0.45 Ma and occurred only in the centre of the rift margin (C4, C3 and C2). We suggest that this may correspond to the transition from Phase 3 to Phase 4 rather than to their proposed transition from Phase 2 to Phase 3. Demoulin *et al.* (2015) proposed that their oldest uplift event may correlate with the transition from Phase 1 to Phase 2.

Interactions of sediment-routing system with the migrating rift

Western Corinth rift stratigraphy records a range of interactions between the river systems and the migrating and evolving rift (Allen 2008). On the largest scale, we identify three major long-lived

sediment-routing systems that supplied coarse sediment into the basin, each with a different history (Fig. 9) depending on its interaction with the migrating fault activity. The high volume of coarse sediment supplied by these rivers from the earliest phase indicates that they were not consequent rivers but, rather, antecedent rivers of the Hellenide mountain belt that were captured by the young rift.

- The Killini River fed an axial drainage system, recording hanging-wall migration over at least 3 myr. It reacted to each fault-migration event by building a new Gilbert delta, while incising and cannibalizing its older delta(s) to the south. The river system first built the stacked prograding Killini and Mavro Gilbert delta systems into a shallow lacustrine depocentre over at least 2 myr (Phase 1: Fig. 10). The Killini delta system built mainly eastwards, while the Mavro delta system built northwards above a listric fault. During Phase 2 (Fig. 11), the river system continued to flow northwards, cannibalizing its own deltas to build, first, the Ilias delta toward the NW across a relay zone, and then the Evrostini delta towards the north above a listric fault. Some time after 0.7 Ma, the river was finally defeated by a major uplift event, turning south to flow into the Feneos endorheic basin (Figs 2 & 12), abruptly ending sediment supply into the Corinth rift.
- The Kalavryta river system represents, by far, the largest antecedent drainage system captured by the westwards migrating rift (Fig. 9). The river(s) flowed north and NE into the western termination of the early rift and then turned east to become a longitudinal axial drainage system that built low-height deltas into a shallow lacustrine basin (Fig. 10), much like those seen today in Lake Turkana, Lake Albert and Lake Rukwa in the East African rift system. When the rift migrated west and north in the Early Pleistocene (between Phases 1 and 2), this drainage system was again captured and diverted north, reorganizing into equally spaced rivers, each carrying a coarse bedload (Figs 9 & 11). These powerfully erosive transverse rivers incised the uplifting footwall area, and built the giant Gilbert deltas into the new depocentre. When the rift margin, again, migrated north (Phase 2 to Phase 3 transition: Fig. 12), the rivers were able to continue flowing north, cannibalizing their Phase 2 deltas to build new deltas into the present-day Gulf. They continue to flow into the Gulf today, and represent the principal source of coarse clastic sediment (Fig. 13). When possible, the rivers exploited relay ramps (e.g. Kerinitis and Akrata), but their incision power allowed them to cut across the faults at any point.

- The Rodini river system interacted with a footwall-migrating fault system. In other words, due to footwall migration of the fault system, the river abandoned its older deposits to build a new system in the footwall of the abandoned fault. During Phases 2 and 3, the river supplied the C5 Profitis Elias Group across south-dipping faults and effectively defined the western end of the rift (Figs 11 & 12). When the rift migrated northwards (Phase 4), the river was forced to retreat north, and established the new Mornos delta in the hanging wall of the Nafpaktos and Marathias faults (Fig. 13), which it continues to supply today.

Overall, these three inherited sediment-routing systems have played a primary role in the redistribution of mass in the rift and, thus, in the final grain-size distribution, with coarse-grained facies confined to the western rift where they have been constantly reworked by the Killini and Kalavryta routing systems due to fault migration. In contrast, the eastern rift appears to have been sediment-starved throughout rift development.

Smaller, more local, interactions of rivers with the growing and migrating fault system are numerous in this rift, and include interactions with relay ramps of various scales, consequent drainage on various scales, diversion and abandonment of rivers on various scales due to fault linkage, migration and footwall uplift (Allen 2008). The duration of a river's history in this active rift can vary from very short (some thousands of years) to several millions of years, the longest-lived being those that predate the initiation of the rift itself.

Discussion

Rift migration and lateral propagation

From its inception, the Corinth rift was controlled mainly by north-dipping faults. Although south-dipping faults may have played a significant role during the immature stages of rifting, they become secondary to the major basin-controlling faults once these are established, as seen in areas C2 and C3. In the western C4 area, the south-dipping South Eratini Fault is still an important structure. Figure 14 summarizes the northwards and westwards migration of the major basin-bounding faults of the western rift over 4 myr. The last fault migration in C3 was at 1.8–1.5 Ma, in C4 at 0.7 ± 0.2 Ma and in C5 at 400 ka, demonstrating that the age of initiation of the faults controlling the southern margin of the active rift becomes progressively younger towards the west (Fig. 14). The rift is therefore opening towards the west rather than towards the east, as proposed by Leeder *et al.* (2008, 2012).

The zones C3–C5 contain fault systems of decreasing maturity, with the most mature faults in C3 and the most immature faults in C5. This is reflected in a progressively older and thicker synrift fill towards the east. However, this simple prediction is complicated by the presence of the Psaromita–Aegion basement high between C4 and C5 that was probably inherited from the Hellenide fold and thrust belt. The main basin-controlling fault in C2 and C3 (Derveni–Lykopora–East Xylocastro) became stable during Phase 2 and has been accumulating slip since then. Our reconstructions suggest that the westwards propagation of this major fault zone occurred in several steps, each involving the initiation of a new fault some way to the west and north. This new fault then proceeded to propagate towards the east or SE and to eventually link with the major fault. Thus, the West and East Helike faults initiated at 0.7 ± 0.2 Ma, and propagated eastwards to hard link to the Derveni Fault at around 200 ka (Hemelsdaël & Ford 2016). The initiation of the Psathopyrgos Fault further NW at 0.4 Ma and its current propagation SE along the Neos Erineos fault system can be seen as the same process in action. These two stages in westwards fault propagation overlap in time.

Such lateral propagation of a rift is a natural process related to the progressive accumulation of strain over time (Cowie *et al.* 2007). As well as the westwards rift propagation in the Corinth rift, there is also a clear component of northwards fault migration. The combination of these two phenomena is probably responsible for the consistent right-stepping arrangement of active faults along the southern margin of the Gulf (Figs 1 & 14). When seen on a north–south cross-section, fault migration appears to have occurred in discrete events, rather than as a continuous process. The exact timing and duration of all these events are not yet well constrained. We can say, however, that the oldest migration event in C4 between Phases 1 and 2 lasted around 300 kyr. Many authors have observed that fault migration was associated with major uplift events in the northern Peloponnese. A recent study by Demoulin *et al.* (2015) demonstrated that quantitative morphometric analysis of the tectonic landscape may be used to extract the distribution and timing of these uplift events that correspond well with the model presented here. This promising new technique may lead to a more detailed understanding of the fault-migration history of the rift margin.

The large-scale geodynamic cause of northwards rift migration has been widely discussed and many models proposed, including orogenic collapse, slab rollback and back-arc extension, and propagation of the North Anatolian Fault. These models will not be discussed here and the interested reader is referred to publications (Westaway 2002; Leeder

CORINTH RIFT EVOLUTION

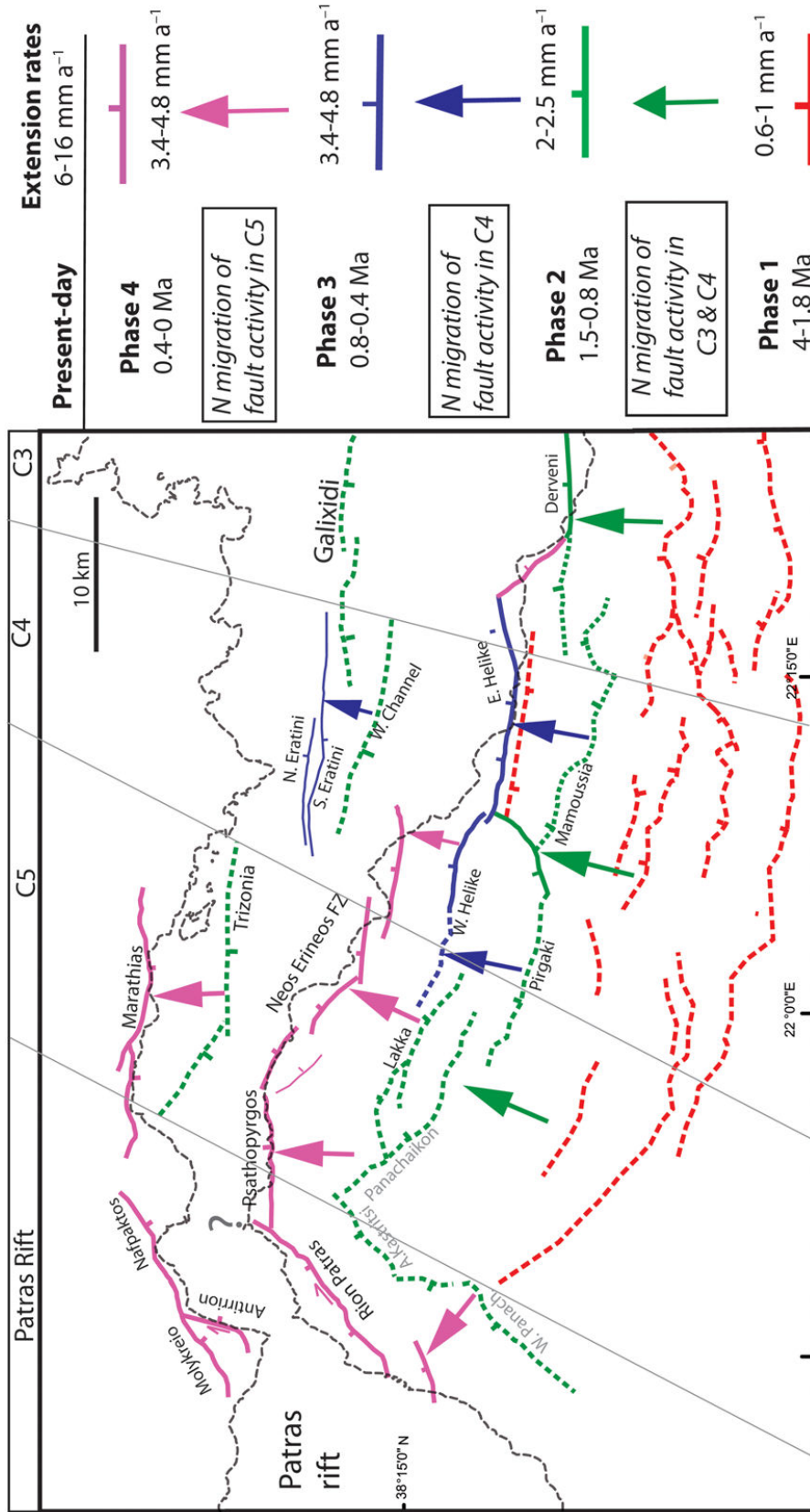


Fig. 14. Summary of rift migration through time based on data in Figures 10–13. Solid lines indicate active faults; dashed lines indicate inactive faults. Fault colour codes indicate the age of initiation of the fault, shown on the right of the figure where a summary of rifting phases is given with an estimated extension rate for each phase (from Ford *et al.* 2013). Dextral displacement on the Rion–Patras and Antirion faults is based on Beckers *et al.* (2015).

et al. 2008, 2012; Jolivet *et al.* 2010; Royden & Papanikolaou 2011) and references therein.

Placing present-day seismicity and geodetic extension rates in the context of full rift evolution

Our reconstructions show that current zone of high seismicity and highest geodetic extension rates in the westernmost rift (C5: Lyon-Caen *et al.* 2004) corresponds to the youngest part of the rift due to the progressive northwards and westwards migration of the fault system. Estimates of the extension rate along the cross-section A–A' (Fig. 3) (Ford *et al.* 2013) show that rift migration was also associated with an increase in extension rate through time. As new faults were generated for each stage, it follows that strain-rate acceleration is unrelated to fault linkage but, rather, to larger-scale regional plate-tectonic processes (Ford *et al.* 2013). The estimate of extension for Phases 3 and 4 of 3.4–4.8 mm a⁻¹ does not, however, approach the current geodetic extension rate of 12–13 mm a⁻¹ for the same area (Briole *et al.* 2000; Avallone *et al.* 2004). The initiation of these very high geodetic extension rates along the whole rift may be linked: (a) to a transient acceleration within a seismic cycle (Bernard *et al.* 2006); or (b) to a longer-term external tectonic forcing; for example, due to the lateral propagation of the North Anatolian Fault at depth.

GPS studies have shown that the deformation gradient is localized offshore in a 10 km-wide zone (Briole *et al.* 2000; Avallone *et al.* 2004) and deformation, therefore, is most probably concentrated on the very young north-dipping faults along the southern rift margin. Seismicity is extremely high in C5 because the faults are very young (400 ka to 50–60 ka) and in the process of linking at depth. The microseismic layer at depth may represent an incipient detachment, as proposed by Lambotte *et al.* (2014).

Significance of deepening events

In this paper, we have demonstrated that the western end of the Corinth rift migrated not only northwards but also westwards throughout its evolution. Would such a rift record a single major rift climax event, or would the standard phases of rift evolution – namely, rift initiation followed by rift climax (e.g. Gupta *et al.* 1998; Cowie *et al.* 2007) – be diachronous along the rift axis? Rift initiation is typified by slow subsidence due to distributed deformation across a young network of isolated growing faults (Gupta *et al.* 1998). Early rift fill is typically continental in character (fluvial, shallow lake, shallow marine: Prosser 1993; Lambiase & Bosworth 1995).

Rift climax is marked by a distinct acceleration in fault displacement due to the development of a fully linked fault system onto which deformation is focused. Subsidence rate increases, leading to a deepening of depositional environments. Major deepening events in the stratigraphic record of many rifts are therefore interpreted as recording the transition from rift initiation to rift climax.

In the western Corinth rift, four deepening events are identified (Fig. 9) and here we discuss their relevance for local and regional tectonic history. Deepening event 1 (DE1) was identified by Leeder *et al.* (2012) in area C2 and dated as 3.2–3 Ma. They interpreted this event as recording the main Corinth rift climax, correlating it with a similar deepening event to the east. Sedimentologically, this event is characterized by a transition from fluvial to shallow-lacustrine environments (Fig. 9) and we suggest that it probably represents a minor event in area C2. In addition, the event cannot be recognized to the west (in C4), where, at this stage, the rift fill was fluvial in character.

The transition to deeper environments in area C4 (DE2: Fig. 9) occurred in the Early Pleistocene (beginning of Phase 2). In area C4, this second deepening event is recorded in the change from fluvial to deltaic deposition associated with the reorganization of the drainage system. In area C3, delta stratigraphic architecture changed markedly to reflect deepening water (higher foresets, aggradation-dominated). In area C2, the signature of this deepening event is, as yet, unidentified in the monotonous turbidite succession.

Deepening event 3 is recognized in C4 and C5 around the 700 ka is related to the initiation of the East and West Helike faults in C4. Deepening event 4 occurred at approximately 400 ka (between Phases 3 and 4: DE4, Fig. 9) with the initiation of the Psathopyrgos Fault in the westernmost rift (C5), leading to the opening of the Rion Straits. Again, such events are difficult to identify in deeper-water successions, such as those further east. To summarize, area C5 records only two deepening events, C4 records three deepening events and C3 (and C2) records four deepening events (Fig. 9). We have shown that the major linkage and stabilization of the controlling fault network in the centre of the rift occurred at the beginning of Phase 2 associated with deepening event 2 (see also Nixon *et al.* 2016), suggesting that this may be considered as the rift climax transition, while the western rift (C5) remains in the initiation phase.

This study demonstrates that the concepts of rift initiation and rift climax should be used with caution when interpreting rift stratigraphy. Migrating and laterally propagating rifts will record multiple deepening events, which may be quite subtle and difficult to recognize in older, deeper parts of the rift.

Deepening events, therefore, need to be correlated across a basin and linked with local fault-growth history in order to appreciate their relevance in full rift evolution.

Conclusions

This paper presents new data of the westernmost onland section of the Corinth rift (Lakka fault block), and proposes the first complete correlation of the chrono- and lithostratigraphy and structure of the onland central to western Corinth rift. By correlating with offshore basin data, we have built a model of the westwards propagation and northwards migration of the rift since the Late Pliocene. The main points of rift evolution and behaviour can be separated into two packages regarding fault evolution and basin-fill evolution.

Evolution of the fault system

- The rift was controlled by a predominantly asymmetrical, north-dipping fault system. In each zone, south-dipping faults were mainly active during early stages of the fault-system development.
- Four phases of subsidence are separated by distinct northwards (hanging wall) and westwards fault-migration events (see Figs 9 & 14 for a summary).
- Rates of extension across the rift accelerated in distinct steps during rifting, probably due to external tectonic processes.
- Fault migration ended in the east with the stabilization of the major basin-bounding fault system. The age of initiation of this main basin-bounding fault system then becomes younger to the west.
- The major basin-bounding fault system propagated westwards in two stages (during phases 3 and 4). Each stage involves the initiation of a new fault segment to the north and west, which subsequently propagated east or SE to link to the main fault system. These two propagation stages overlap in time. There are no strike-slip faults between rift segments.
- The youngest faults in the westernmost rift are associated with high seismicity and high geotectonic extension, probably due to their rapid growth and linkage at depth.

Basin-fill evolution

- Antecedent rivers played a major role in establishing vigorous sediment-routing systems from rift inception. Their influence on facies distributions endured throughout rift history. In particular, powerfully erosive rivers in the western

rift constantly reworked their deposits to supply coarse sediment. In contrast, the eastern rift appears to have been sediment-starved since rift initiation.

- The rift was superimposed on significant palaeorelief inherited from the Hellenide mountain belt, that influenced sediment routing, facies distributions and connectivity between depocentres in the early stages of rifting;
- A major reorganization of sediment-routing systems (creation of consequent rivers, capture or defeat of older rivers) occurred during fault-migration events.
- The stratigraphy of a migrating rift can record multiple deepening events. The concepts of rift initiation and rift climax should, therefore, be used with caution.

This paper is dedicated to our colleague Nikolaos Palyvos, whose energy and enthusiasm we sadly miss. Nikos worked on the geomorphology, structure and stratigraphy of the Lakka fault block and Patras area. This work forms part of the SISCOR project funded by the French Agence Nationale de Recherche and led by Pascal Bernard, who we thank for his insight and encouragement. R. Hemelsdaël was financed by a doctoral bursary from the French Ministry of National Education, Higher Education and Research. We thank Rebecca Bell and Christian Beck and editor Conrad Childs for their constructive reviews and support. We thank our colleagues and students for many discussions in the field, in particular Ed Williams and Rob Gawthorpe. Marco Mancini wishes to thank Daniela Pantosti and Paolo Marco De Martini (INGV, Rome) for introducing him to the Corinth rift geology. CRPG Publication Number 2439.

References

- ALEXANDRI, N., NOMIKOU, P., BALLAS, D., LYKOUSIS, V. & SAKELLARIOU, D. 2003. Swath bathymetry map of Corinth Gulf. *Geophysical Research Abstracts*, **5** (EGS), 14268.
- ALLEN, P.A. 2008. Time scales of tectonic landscapes and their sediment routing systems. In: GALLAGHER, K., JONES, S.J. & WAINWRIGHT, J. (eds) *Landscape Evolution: Denudation, Climate and Tectonics over Different Time and Space Scales*. Geological Society, London, Special Publications, **296**, 7–28, <http://doi.org/10.1144/SP296.2>
- APOSTOLIDIS, P.I., RAPTAKIS, D.G., PANDI, K.K., MANAKOU, M.V. & PITILAKIS, K.D. 2006. Definition of subsoil structure and preliminary ground response in Aigion city (Greece) using microtremor and earthquakes. *Soil Dynamics and Earthquake Engineering*, **26**, 922–940, <http://doi.org/10.1016/j.soildyn.2006.02.001>
- ARMIJO, R., MEYER, B., KING, G.C.P., RIGO, A. & PAPANASTASSIOU, D. 1996. Quaternary evolution of the Corinth rift and its implications for the late Cenozoic evolution of the Aegean. *Geophysical Journal International*, **126**, 11–53.

- AUBOUIN, J., BRUNN, J.H., CELET, P., DERCOURT, J., GODFRIAUX, I. & MERCIER, J. 1963. *Esquisse de la Géologie de la Grèce. Fallot Memorial Volume*. Société Géologique de France, Paris, 583–610.
- AVALLONE, A., BRIOLE, P. ET AL. 2004. Analysis of eleven years of deformation measured by GPS in the Corinth Rift Laboratory area. *Comptes Rendus Geoscience*, **336**, 301–311, <http://doi.org/10.1016/j.crte.2003.12.007>
- BACKERT, N. 2009. *Interaction tectonique–sédimentation dans Le Rift de Corinthe, Grèce. Architecture stratigraphique et sédimentologie du Gilbert Delta de Kerinitis*. PhD memoir, Institut Polytechnique de Lorraine, France.
- BACKERT, N., FORD, M. & MALARTRE, F. 2010. Architecture and sedimentology of the Kerinitis Gilbert-type fan delta, Corinth Rift, Greece. *Sedimentology*, **57**, 543–586.
- BECKERS, A. 2015. *Late Quaternary sedimentation in the western tip of the Gulf of Corinth*. PhD thesis, University of Liège, Belgium.
- BECKERS, A., HUBBERT-FERRARI, A., BECK, C., BODEUX, S., TRIPANAS, E. & DE BATIST, M. 2015. Active faulting at the western top of the Gulf of Corinth, Greece, from high-resolution seismic data. *Marine Geology*, **360**, 1–84.
- BELL, R.E., MCNEILL, L., BULL, J.M. & HENSTOCK, T.J. 2008. Evolution of the offshore western Gulf of Corinth. *Geological Society of America Bulletin*, **120**, 156–178.
- BELL, R.E., MCNEILL, L., BULL, J.M., HENSTOCK, T.J., COLLIER, R.E.L. & LEEDER, M.R. 2009. Fault architecture, basin structure and evolution of the Gulf of Corinth Rift, central Greece. *Basin Research*, **21**, 824–855, <http://doi.org/10.1111/j.1365-2117.2009.00401.x>
- BELL, R.E., MCNEILL, L.C., HENSTOCK, T.J. & BULL, J.M. 2011. Comparing extension on multiple time and depth scales in the Corinth Rift, Central Greece. *Geophysical Journal International*, **186**, 463–470, <http://doi.org/10.1111/j.1365-246X.2011.05077.x>
- BENTHAM, P., COLLIER, R.E., GAWTHORPE, R.L., LEEDER, R. & STARK, C. 1991. Tectono-sedimentary development of an extensional basin: the Neogene Megara Basin, Greece. *Journal of the Geological Society, London*, **148**, 923–934, <http://doi.org/10.1144/gsjgs.148.5.0923>
- BERNARD, P., MEYER, B. ET AL. 1997. The Ms = 6.2 June 15, 1995 Aigiopn earthquake (Greece): evidence for low-angle normal faulting in the Corinth rift. *Journal of Seismology*, **1**, 131–150.
- BERNARD, P., LYON-CAEN, H. ET AL. 2006. Seismicity, deformation and seismic hazard in the western rift of Corinth: new insights from the Corinth Rift Laboratory (CRL). *Tectonophysics*, **426**, 7–30, <http://doi.org/10.1016/j.tecto.2006.02.012>
- BILLIRIS, H., PARADISSIS, D. ET AL. 1991. Geodetic determination of tectonic deformation in central Greece from 1900 to 1988. *Nature*, **350**, 124–129.
- BRIOLE, P., RIGO, A. ET AL. 2000. Active deformation of the Corinth rift, Greece: results from repeated Global Positioning System surveys between 1990 and 1995. *Journal of Geophysical Research: Solid Earth*, **105**, 25,605–25,625.
- BROOKS, M. & FERENTINOS, G. 1984. Tectonics and sedimentation in the Gulf of Corinth and the Zakynos and Kefallinia channels, western Greece. *Tectonophysics*, **101**, 25–54.
- BURCHFIEL, B.C. 2008. The Aegean: a natural laboratory for tectonics. In: *Donald D. Harrington Symposium on the Geology of the Aegean. IOP Conference Series: Earth and Environmental Science*, **2**, 012001, <http://iopscience.iop.org/article/10.1088/1755-1307/2/1/012001>
- CAMPOS, C., BECK, C., CROUZET, C., CARRILLO, E., VAN WELDEN, A. & TRIPANAS, E. 2013. Late Quaternary paleoseismic sedimentary archive from deep central Gulf of Corinth: time distribution of inferred earthquake-induced layers. *Annals of Geophysics*, **56**, S0670, <http://doi.org/10.4401/ag-6226>
- CHARALAMPAKIS, M., LYKOUSIS, V., SAKELLARIOU, D., PAPTODOROU, G. & FERENTINOS, G. 2014. The tectono-sedimentary evolution of the Lechaion Gulf, the southeastern branch of the Corinth graben, Greece. *Marine Geology*, **351**, 58–75.
- CLARKE, P., DAVIES, R. ET AL. 1998. Crustal strain in Central Greece from repeated GPS measurements in the interval 1989–1997. *Geophysical Journal International*, **135**, 195–214.
- COLLIER, R. & JONES, G. 2003. Rift sequences of the southern margin of the Gulf of Corinth (Greece) as exploration/production analogs. Paper presented at the AAPG International Conference, Barcelona, Spain, 21–24 September 2003.
- COLLIER, R.E.L. 1990. Eustatic and tectonic controls upon Quaternary coastal sedimentation in the Corinth Basin, Greece. *Journal of the Geological Society, London*, **147**, 301–314, <http://doi.org/10.1144/gsjgs.147.2.0301>
- COLLIER, R.E.L. & DART, C.J. 1991. Neogene to Quaternary rifting, sedimentation and uplift in the Corinth Basin, Greece. *Journal of the Geological Society, London*, **148**, 1049–1065, <http://doi.org/10.1144/gsjgs.148.6.1049>
- CORNET, F., DOAN, M.L., MORETTI, I. & BORM, G. 2004. Drilling through the active Aigion Fault: the AIG10 well observatory. *Comptes Rendus de l'Académie des Sciences*, **336**, 395–406.
- COWIE, P.A., ATTAL, M., TUCKER, G.E., WHITTAKER, A.C., NAYLOR, M., GANAS, A. & ROBERTS, G.P. 2006. Investigating the surface process response to fault interaction and linkage using a numerical modelling approach. *Basin Research*, **18**, 231–266, <http://doi.org/10.1111/j.1365-2117.2006.00298.x>
- COWIE, P.A., ROBERTS, G.P. & MORTIMER, E. 2007. Strain localization within fault arrays over timescales of 100–107 years. In: HANDY, M.R., HIRTH, G. & HOVIUS, N. (eds) *Tectonic Faults. Agents of Change on a Dynamic Earth*. MIT Press, Cambridge, MA, 47–75.
- DART, C.J., COLLIER, R.E.L., GAWTHORPE, R.L., KELLER, J.V.A. & NICHOLS, G. 1994. Sequence stratigraphic of (?)Pliocene-Quaternary synrift, Gilbert-type fan deltas, northern Peloponnesos, Greece. *Marine and Petroleum Geology*, **11**, 545–560.
- DEGNAN, P.J. & ROBERTSON, A.H.F. 1998. Mesozoic-early Tertiary passive margin of the Pindos Ocean (NW Peloponnesos, Greece). *Sedimentary Geology*, **117**, 33–70.

- DE MARTINI, P.M., PANTOSTI, D., PALYVOS, N., LEMEILLE, F., MCNEILL, L.C. & COLLIER, R.E.L. 2004. Slip rates of the Aigion and Eliki Faults from uplifted marine terraces, Corinth Gulf, Greece. *Comptes Rendus Geoscience*, **336**, 325–334, <http://doi.org/10.1016/j.crte.2003.12.006>
- DEMOULIN, A., BECKERS, A. & HUBERT-FERRARI, A. 2015. Patterns of Quaternary uplift of the Corinth rift southern border (N Peloponnese, Greece) revealed by fluvial landscape morphometry. *Geomorphology*, **246**, 188–204.
- DERCOURT, J. 1964. *Contribution à l'étude géologique du Secteur du Péloponnèse Septentrional*. PhD thesis, Université de Paris.
- DORNSIEPEN, U., GEROLYMATOS, E. & JACOBSHAGEN, V. 1986. Die Phyllit–Quartzit-Serie im Fenster von Feneos (Nord-Peloponnes). *IGME Geological and Geophysical Research*, Special Issue, 99–105.
- DOUTSOS, T. & KOKKALAS, S. 2001. Stress and deformation patterns in the Aegean region. *Journal of Structural Geology*, **23**, 455–472.
- DOUTSOS, T. & PIPER, D.J.W. 1990. Listric faulting, sedimentation, and morphological evolution of the Quaternary eastern Corinth rift, Greece: first stages of continental rifting. *Geological Society of America Bulletin*, **102**, 812–829.
- DOUTSOS, T. & POULIMENOS, G. 1992. Geometry and kinematics of active faults and their seismotectonic significance in the western Corinth-Patras rift (Greece). *Journal of Structural Geology*, **14**, 689–699.
- DOUTSOS, T., KONTOPOULOS, N. & POULIMENOS, G. 1988. The Corinth-Patras rift as the initial stage of continental fragmentation behind an active island arc (Greece). *Basin Research*, **1**, 177–190.
- DOUTSOS, T., PIPER, G., BORONKAY, K. & KOUKOUVELAS, I.K. 1993. Kinematics of the Central Hellenides. *Tectonics*, **12**, 936–953.
- DOUTSOS, T., KOUKOUVELAS, I.K. & XYPOLIAS, P. 2006. A new orogenic model for the External Hellenides. In: ROBERTSON, A.H.F. & MOUNTRAKIS, D. (eds) *Tectonic Development of the Eastern Mediterranean Region*. Geological Society, London, Special Publications, **260**, 507–520, <http://doi.org/10.1144/GSL.SP.2006.260.01.21>
- DUFAURE, J.J. 1975. *Le Relief Du Péloponnèse*. Thesis, Paris IV.
- ESU, D. & GIROTTI, O. 2015. The late Early Pleistocene non-marine molluscan fauna from the Synania Formation (Achaia, Greece), with description of nine new species. *Archiv für Molluskenkunde*, **114**, 65–81.
- FERENTINOS, G., BROOKS, M. & DOUTSOS, T. 1985. Quaternary tectonics in the Gulf of Patras, Western Greece. *Journal of Structural Geology*, **7**, 713–717.
- FERNANDEZ-GONZALEZ, M., FRYDAS, D., GUERNET, C. & MATHIEU, R. 1994. Foraminifères et Ostracodes du Plio-Pléistocène de la région de Patras (Grèce). Intérêt stratigraphique et paléogéographique. *Revista Española de micropaleontología*, **1**, 89–107.
- FLEURY, J. 1980. *Les zones de Gavrovo-Tripolitza et du Pindos (Grèce continentale et Peloponnese du Nord). Evolution d'une plateforme et d'un bassin dans leur cadre alpin*. Memoire de la Société géologique du Nord, **1**.
- FLOTTÉ, N., SOREL, D., MÜLLER, C. & TENSI, J. 2005. Along strike changes in the structural evolution over a brittle detachment fault: example of the Pleistocene Corinth–Patras rift (Greece). *Tectonophysics*, **403**, 77–94, <http://doi.org/10.1016/j.tecto.2005.03.015>
- FORD, M., WILLIAMS, E.A., MALARTRE, F. & POPESCU, S.-M. 2007. Stratigraphic architecture, sedimentology and structure of the Vouraikos Gilbert-type fan delta, Gulf of Corinth, Greece. In: NICHOLS, G., WILLIAMS, E.A. & PAOLA, C. (eds) *Sedimentary Processes, Environments and Basins*. International Association of Sedimentologists, Special Publications, **38**, 49–90.
- FORD, M., ROHAIS, S., WILLIAMS, E.A., BOURLANGE, S., JOUSSELIN, D., BACKERT, N. & MALARTRE, F. 2013. Tectonosedimentary evolution of the western Corinth rift (Central Greece). *Basin Research*, **25**, 3–25.
- FRYDAS, D. 1989. Biostratigraphische Untersuchungen aus dem Neogen der NW und W Peloponnes, Griechenland. *Neues Jahrbuch für Geologie und Paläontologie Monatshefte*, **6**, 321–344.
- FRYDAS, D. 1991. Paläontologische und stratigraphische untersuchungen der diatomen des Pleistozäns des N-Peloponnes, Griechenland. In: *Proceedings of the 5th Congress*, May 1990, Thessoloniki. *Bulletin of the Geological Society of Greece*, **XXV**(2), 499–513.
- FRYDAS, D., KONTOPOULOS, N., STAMATOPOULOS, L., GUERNET, C. & VOLTAGGIO, M. 1995. Middle-Late Pleistocene sediments in the northwestern Peloponnese, Greece. A combined study of biostratigraphical, radiochronological and sedimentological results. *Berliner Geowissenschaftliche Abhandlungen*, **E16**, 589–605.
- FUCHS, T. 1877. Studien über die jüngeren Tertiärbildungen Griechenlands. *Denkschriften der Kaiserlichen Akademie der Wissenschaften. Mathematisch–Naturwissenschaftliche Classe*, **37**, 1–42.
- GAUTIER, P., BRUN, J.P., MORICEAU, R., SOKOUTIS, D., MARTINOD, J. & JOLIVET, L. 1999. Timing kinematics and cause of the Aegean extension: a scenario based on a comparison with simple analogue experiments. *Tectonophysics*, **315**, 31–72.
- GHISETTI, F. & VEZZANI, L. 2004. Plio-Pleistocene sedimentation and fault segmentation in the Gulf of Corinth (Greece) controlled by inherited structural fabric. *Comptes Rendus Geosciences*, **336**, 243–249.
- GHISETTI, F. & VEZZANI, L. 2005. Inherited structural controls on normal fault architecture in the Gulf of Corinth (Greece). *Tectonics*, **24**, TC4016, <http://doi.org/10.1029/2004TC001696>
- GIBBARD, P. & COHEN, K.M. 2008. The global chronostratigraphical correlation table for the last 2.7 million years. *Episodes*, **31**, 243–247.
- GIERLOWSKI-KORDESCH, E.H. 2010. Lacustrine carbonates. In: ALONSO-ZARZA, A.M. & TANNER, L.H. (eds) *Carbonates in Continental Settings: Facies, Environments and Processes*. Developments in Sedimentology, **61**. Elsevier, Amsterdam, 1–101.
- GILLET, S. 1963. Nouvelles données sur le gisement villafranchien de Néa-Corinthos. *Praktika tis Akademias Athinon*, **38**, 400–419.
- GOLDSWORTHY, M. & JACKSON, J. 2001. Migration of activity within normal fault systems: examples from the Quaternary of mainland Greece. *Journal of*

- Structural Geology*, **23**, 489–506, [http://doi.org/10.1016/S0191-8141\(00\)00121-8](http://doi.org/10.1016/S0191-8141(00)00121-8)
- GUERNET, C., LEMEILLE, F., SOREL, D., BOURDILLON, C., BERGE-THIERRY, C. & MANAKOU, M. 2003. Les Ostracodes et le Quaternaire d'Aigion (Golfe de Corinthe, Grèce) [Ostracodes and Quaternary from Aigion (Gulf of Corinth, Greece)]. *Revue de micropaléontologie*, **46**, 73–93, [http://doi.org/10.1016/S0035-1598\(03\)00013-8](http://doi.org/10.1016/S0035-1598(03)00013-8)
- GUPTA, S., COWIE, P., DAWERS, N. & UNDERHILL, J. 1998. A mechanism to explain rift-basin subsidence and stratigraphic patterns through fault-array evolution. *Geology*, **26**, 595–598.
- HARDY, S. & GAWTHORPE, R.L. 1998. Effects of variations in fault slip rate on sequence stratigraphy in fan deltas: insights from numerical modelling. *Geology*, **26**, 911–914.
- HEMELSDAËL, R. & FORD, M. 2016. Relay zone evolution: a history of repeated fault propagation and linkage, central Corinth rift, Greece. *Basin Research*, **28**, 34–56, <http://doi.org/10.1111/bre.12101>
- HEMELSDAËL, R., FORD, M., MALARTRE, F., GAWTHORPE, R., CHARREAU, J. & SEN, S. 2015. Rivers and rifting: evolution of a fluvial system during rift initiation, central Corinth rift (Greece). AAPG Search and Discovery Article 30419. AAPG Annual Convention and Exhibition, 31 May–3 June 2015, Denver, CO.
- JACKSON, J.A., GAGNEPAIN, J., HOUSEMAN, G., KING, G.C.P., PAPADIMITRIOU, P., SOUFLERIS, C. & VIRIEUX, J. 1982. Seismicity, normal faulting and the geomorphological development of the Gulf of Corinth (Greece): the Corinth earthquakes of February and March 1981. *Earth and Planetary Science Letters*, **57**, 377–397.
- JOLIVET, L. 2001. A comparison of geodetic and finite strain pattern in the Aegean, geodynamic implications. *Earth and Planetary Science Letters*, **187**, 95–104.
- JOLIVET, L., BRUN, J.P., GAUTIER, P., LALLEMEANT, S. & PATRIAT, M. 1994. 3D kinematics of extension in the Aegean region from the early Miocene to the present, insights from the ductile crust. *Bulletin de la Societe Geologique de France*, **165**, 195–209.
- JOLIVET, L., LABROUSSE, L. ET AL. 2010. Rifting and shallow-dipping detachments, clues from the Corinth Rift and the Aegean. *Tectonophysics*, **483**, 287–304, <http://doi.org/10.1016/j.tecto.2009.11.001>
- KERAUDREN, B. & SOREL, D. 1987. The terraces of Corinth (Greece): a detailed record of eustatic sea level variations during the last 500 000 years. *Marine Geology*, **77**, 99–107.
- KOSKERIDOU, E. & IOAKIM, C. 2009. An Early Pleistocene mollusc fauna with Ponto-Caspian elements, in intra Hellenic Basin of Atalanti, Arkitisa Region (Central Greece). In: *9th Panhellenic Symposium Oceanography & Fisheries, 2009 – Proceedings*. HCMR Publications **1**, 96–101.
- LAMBIASE, J.J. & BOSWORTH, W. 1995. Structural controls on sedimentation in continental rifts. In: LAMBIASE, J.J. (ed.) *Hydrocarbon Habitat in Rift Basins*. Geological Society, London, Special Publications, **80**, 117–144, <http://doi.org/10.1144/GSL.SP.1995.080.01.06>
- LAMBOTTE, S., LYON-CAEN, H. ET AL. 2014. Reassessment of the rifting process in the Western Corinth Rift from relocated seismicity. *Geophysical Journal International*, **197**, 1822–1844, <http://doi.org/10.1093/gji/ggu096>
- LEEDER, M.R., PORTMAN, C. ET AL. 2005. Normal faulting and crustal deformation, Alkyonides Gulf and Perachora peninsula, eastern Gulf of Corinth rift, Greece. *Journal of the Geological Society, London*, **162**, 549–561, <http://doi.org/10.1144/0016-764904-075>
- LEEDER, M.R., MACK, G.H., BRASIER, A.T., PARRISH, R.R., MCINTOSH, W.C., ANDREWS, J. & DUERMEIJER, C.E. 2008. Late-Pliocene timing of Corinth (Greece) rift-margin fault migration. *Earth and Planetary Science Letters*, **274**, 132–141, <http://doi.org/10.1016/j.epsl.2008.07.006>
- LEEDER, M.R., MARK, D.F. ET AL. 2012. A ‘Great Deepening’: chronology of rift climax, Corinth rift, Greece. *Geology*, **40**, 999–1002, <http://doi.org/10.1130/G33360.1>
- LEMEILLE, F., CHATOUPIS, F. ET AL. 2004. Recent syn-rift deposits in the hangingwall of the Aigion Fault (Gulf of Corinth, Greece). *Comptes Rendus Geoscience*, **336**, 425–434.
- LE PICHON, X. & ANGELIER, J. 1979. The Hellenic arc and trench system: a key to the neotectonic evolution of the eastern Mediterranean area. *Tectonophysics*, **60**, 1–42.
- LE PICHON, X. & ANGELIER, J. 1981. The Aegean Sea. *Philosophical Transactions of the Royal Society of London*, **A300**, 357–372.
- LYKOUSIS, V., SAKELLARIOU, D., MORETTI, I. & KABERI, H. 2007a. Late Quaternary basin evolution of the Gulf of Corinth: sequence stratigraphy, sedimentation, fault-slip and subsidence rates. *Tectonophysics*, **440**, 29–51, <http://doi.org/10.1016/j.tecto.2006.11.007>
- LYKOUSIS, V., SAKELLARIOU, D. ET AL. 2007b. Sediment failure processes in active grabens: the western Gulf of Corinth (Greece). In: LYKOUSIS, V., SAKELLARIOU, D. & LOCAT, J. (eds) *Submarine Mass Movements and Their Consequences*. Advances in Natural and Technological Hazards Research, **27**. Springer, Dordrecht, 297–305, http://doi.org/10.1007/978-1-4020-6512-5_31
- LYON-CAEN, H., PAPADIMITRIOU, P., DESCHAMPS, A., BERNARD, P., MAKROPOULOS, K., PACCHIANI, F. & PATAU, G. 2004. First results of the CRLN seismic network in the western Corinth Rift: evidence for old-fault reactivation. *Comptes Rendus Geoscience*, **336**, 343–351, <http://doi.org/10.1016/j.crte.2003.12.004>
- MALARTRE, F., FORD, M. & WILLIAMS, E.A. 2004. Preliminary biostratigraphy and 3D geometry of the Vouraikos Gilbert-type fan delta, Gulf of Corinth, Greece. *Comptes Rendus Geoscience*, **336**, 269–280, <http://doi.org/10.1016/j.crte.2003.11.016>
- MASTRONUZZI, G., SANSONO, P. & STAMATOPOULOS, L. 1994. The glacial landforms of the Peloponnisos (Greece). *Rivista geografica Italiana*, **101**, 77–86.
- MCCLUSKY, S., BALASSANIAN, S. ET AL. 2000. Global Positioning System constraints on plate kinematics and dynamics in Caucasus and the eastern Mediterranean. *Journal of Geophysical Research*, **105**, 5695–5719.
- MCNEILL, L.C. & COLLIER, R.E.L. 2004. Uplift and slip rates of the eastern Eliko fault segment, Gulf

- of Corinth, Greece, inferred from Holocene and Pleistocene terraces 1. *Journal of the Geological Society, London*, **161**, 81–92, <http://doi.org/10.1144/0016-764903-029>
- MCNEILL, L.C., COTTERILL, C.J. *ET AL.* 2005. Active faulting within the offshore western Gulf of Corinth, Greece: implications for model of continental rift deformation. *Geology*, **33**, 241–244.
- MIALL, A.D. 1996. *The Geology of Fluvial Deposits. Sedimentary Facies, Basin Analysis, and Petroleum Geology*. Springer, Berlin.
- MICARELLI, L. 2003. Structural properties of rift-related normal faults: the case study of the Gulf of Corinth, Greece. *Journal of Geodynamics*, **36**, 275–303, [http://doi.org/10.1016/S0264-3707\(03\)00051-6](http://doi.org/10.1016/S0264-3707(03)00051-6)
- MORETTI, I., SAKELLARIOU, D., LYKOUSIS, V. & MICARELLI, L. 2003. The Gulf of Corinth: an active half graben? *Journal of Geodynamics*, 1–18, [http://doi.org/10.1016/S0264-3707\(03\)00053-X](http://doi.org/10.1016/S0264-3707(03)00053-X)
- MORETTI, I., LYKOUSIS, V., SAKELLARIOU, D., REYNAUD, J.Y., BENZIANE, B. & PRINZHOFFER, A. 2004. Sedimentation and subsidence rate in the Gulf of Corinth: what we learn from the *Marion Dufresnés* long-piston coring. *Comptes Rendus Geoscience*, **336**, 291–299, <http://doi.org/10.1016/j.crte.2003.11.011>
- NIXON, C.W., MCNEILL, L.C. *ET AL.* 2016. Rapid spatiotemporal variations in rift structure during development of the Corinth Rift, central Greece. *Tectonics*, **35**, first published online May 24, 2016, <http://doi.org/10.1002/2015TC004026>
- NOCQUET, J.M., 2012. Present-day kinematics of the Mediterranean: a comprehensive overview of GPS results. *Tectonophysics*, **579**, 220–242.
- NOMIKOU, P., ALEXANDRI, M., LYKOUSIS, V., SAKELLARIOU, D. & BALLAS, D. 2011. Swath bathymetry and morphological slope analysis of the Corinth Gulf. In: GRÜTZNER, C. PÉREZ-LÓPEZ, R. FERNANDEZ STEEGER, T. PAPANIKOLAOU, I. REICHERTER, K. SILVA, P.G. & VÖTT, A. (eds) *Earthquake Geology and Archaeology: Science, Society and Critical Facilities*. 2nd INQUA-IGCP-567 International Workshop on Active Tectonics, Earthquake Geology, Archeology and Engineering, 19–24 September 2011, Corinth, Greece, 155–158.
- NORTH, C.P. & DAVIDSON, S.K. 2012. Unconfined alluvial flow processes: recognition and interpretation of their deposits, and the significance for palaeogeographic reconstruction. *Earth-Science Reviews*, **111**, 199–223.
- ORI, G.G. 1989. Geological history of the extensional basin of the Gulf of Corinth (?Miocene–Pleistocene), Greece. *Geology*, **17**, 918–921.
- ORI, G.G., ROVERI, M. & NICHOLS, G. 1991. Architectural patterns in large-scale Gilbert-type delta complexes, Pleistocene, Gulf of Corinth, Greece. In: MIALL, A.D. & TYLER, N. (eds) *The Three-Dimensional Facies Architecture of Terrigenous Clastic Sediments and Its Implications for Hydrocarbon Discovery and Recovery*. Concepts in Sedimentology and Paleontology, **3**. Society for Sedimentary Geology (SEPM), 207–216.
- PALYVOS, N. 2005. The Aigion–Neos Erineos coastal normal fault system (western Corinth Gulf Rift, Greece): geomorphological signature, recent earthquake history, and evolution. *Journal of Geophysical Research*, **110**, B09302, <http://doi.org/10.1029/2004JB003165>
- PALYVOS, N., SOREL, D. *ET AL.* 2007. Review and new data on uplift rates at the W termination of the Corinth Rift and the NE Rion graben area (Achaia, NW Peloponnese). In: *Proceedings of the 11th International Congress*, May 2007, Athens. *Bulletin of the Geological Society of Greece*, **40**, 412–424.
- PALYVOS, N., MANCINI, M., SOREL, D., LEMEILLE, F., PANTOSTI, D. & JULIA, R. 2010. Geomorphological, stratigraphic and geochronological evidence of fast Pleistocene coastal uplift in the westernmost part of the Corinth Gulf Rift (Greece). *Geological Journal*, **45**, 78–104, <http://doi.org/10.1002/gj.1171>
- PALYVOS, N., FORD, M., MANCINI, M., ESU, D., GIROTTI, O. & URBAN, B. 2013. Western closure of the Corinth Rift: stratigraphy and structure of the Lakka fault block. *Geophysical Research Abstracts*, **15**, EGU2013-5360.
- PIRAZZOLI, P.A., STIROS, S.C., FONTUGNE, M. & ARNOLD, M. 2004. Holocene and Quaternary uplift in the central part of the southern coast of the Corinth Gulf (Greece). *Marine Geology*, **212**, 35–44.
- PROSSER, S. 1993. Rift-related linked depositional systems and their seismic expression. In: WILLIAMS, G.D. & DOBB, A. (eds) *Tectonics and Seismic Sequence Stratigraphy*. Geological Society, London, Special Publications, **71**, 35–66, <http://doi.org/10.1144/GSL.SP.1993.071.01.03>
- RICHTER, D. 1976. Das Flysch-Stadium der Helleniden—Ein Überblick. *Zeitung deutsche der Geologische Gesellschaft*, **127**, 96–128.
- RIGO, A., LYON-CAEN, H. *ET AL.* 1996. A microseismic study in the western part of the gulf of Corinth (Greece) implication for large-scale normal faulting mechanisms. *Geophysical Journal International*, **126**, 663–688.
- RITCHIE, B.D., GAWTHORPE, R.L. & HARDY, S. 2004. Three-dimensional numerical modelling of delta depositional sequences 2: influence of local controls. *Journal of Sedimentary Research*, **74**, 221–238.
- ROBERTS, G.P. 1996. Non-characteristic normal faulting surface ruptures from the Gulf of Corinth Greece. *Journal of Geophysical Research*, **101**, 25,255–25,267.
- ROBERTS, G.P. & MICHETTI, A.M. 2004. Spatial and temporal variations in growth rates along active normal fault systems: an example from The Lazio-Abruzzo Apennines, central Italy. *Journal of Structural Geology*, **26**, 339–376.
- ROHAIS, S., ESCHARD, R., FORD, M., GUILLOCHEAU, F. & MORETTI, I. 2007a. Stratigraphic architecture of the Plio-Pleistocene infill of the Corinth Rift: implications for its structural evolution. *Tectonophysics*, **440**, 5–28.
- ROHAIS, S., JOANNIN, S., COLIN, J.P., SUC, J.P., GUILLOCHEAU, F. & ESCHARD, R. 2007b. Age and environmental evolution of the syn-rift fill of the southern coast of the Gulf of Corinth (Akrata-Derveni region, Greece). *Bulletin de la Société Géologique de France*, **178**, 231–243.
- ROYDEN, L.H. & PAPANIKOLAOU, D.J. 2011. Slab segmentation, late Cenozoic disruption of the Hellenic arc. *Geochemistry, Geophysics Geosystems*, **12**, <http://doi.org/10.1029/2010GC003280>
- SACHPAZI, M., CLÉMENT, C., LAIGLE, M., HIRN, A. & ROUSSOS, N. 2003. Rift structure, evolution, and earthquakes in the Gulf of Corinth, from reflection seismic

- images. *Earth and Planetary Science Letters*, **216**, 243–257, [http://doi.org/10.1016/S0012-821X\(03\)00503-X](http://doi.org/10.1016/S0012-821X(03)00503-X)
- SACHPAZI, M., GALVÉ, A. ET AL. 2007. Moho topography under central Greece and its compensation by Pn time-terms for the accurate location of hypocenters: the example of the Gulf of Corinth 1995 Aigion earthquake. *Tectonophysics*, **440**, 53–65, <http://doi.org/10.1016/j.tecto.2007.01.009>
- SAKELLARIOU, D., LYKOUSIS, V. ET AL. 2007. Faulting, seismic-stratigraphic architecture and Late Quaternary evolution of the Gulf of Alkyonides Basin, East Gulf of Corinth, Central Greece. *Basin Research*, **19**, 273–295, <http://doi.org/10.1111/j.1365-2117.2007.00322.x>
- SEGER, M.J. & ALEXANDER, J. 1993. Distribution of Plio-Pleistocene and modern coarse grained deltas south of the Gulf of Corinth, Greece. In: FROSTICK, L. & STEEL, R. (eds) *Tectonic Controls and Signatures in Sedimentary Successions*. International Association of Sedimentologists, Special Publications, **20**, 37–48.
- SKOURLIS, K. & DOUTSOS, T. 2003. The Pindos fold and thrust belt (Greece): inversion kinematics of a passive continental margin. *International Journal of Earth Sciences*, **92**, 891–903.
- SKOURTSOS, E. & KRANIS, H. 2009. Structure and evolution of the western Corinth Rift, through new field data from the Northern Peloponnesus. In: RING, U. & WERNICKE, B. (eds) *Extending a Continent: Architecture, Rheology and Heat Budget*. Geological Society, London, Special Publications, **321**, 119–138, <http://doi.org/10.1144/SP321.6>
- SOREL, D., PANTOSTI, D., LEMEILLE, F., PALYVOS, N. & DE-MARTINI, P.-M. 2005. The step-over between the Eliki and Aigion fault systems: slip transfer and present rates of activity. Report for CNRS project GDR Corinth No. 234.
- STEFATOS, A., PAPATHEODOROU, G., FERENTINOS, G. & LEEDER, M. & COLLIER, R. 2002. Seismic reflection imaging of active offshore faults in the Gulf of Corinth: their seismotectonic significance. *Basin Research*, **14**, 487–502.
- STEWART, I. & VITA-FINZI, C. 1996. Coastal uplift on active normal faults: the Eliki fault, Greece. *Geophysical Research Letters*, **23**, 1853–1856.
- STEWART, S.A. 1996. Influence of detachment layer thickness on style of thin-skinned shortening. *Journal of Structural Geology*, **18**, 1271–1274.
- TAYLOR, B., WEISS, J.R., GOODLIFFE, A.M., SACHPAZI, M., LAIGLE, M. & HIRN, A. 2011. The structures, stratigraphy and evolution of the Gulf of Corinth rift, Greece. *Geophysical Journal International*, **185**, 1189–1219, <http://doi.org/10.1111/j.1365-246X.2011.05014.x>
- TROTET, F., GOFFÉ, B., VIDAL, O. & JOLIVET, L. 2006. Evidence of retrograde Mg-carpholite in the phyllite-quartzite nappe of the Peloponnese from thermobarometric modelisation – geodynamic implications. *Geodynamica Acta*, **19**, 323–343.
- ULICNY, D., NICHOLS, G. & WALTHAM, D. 2002. Role of initial depth at basin margins in sequence architecture: field examples and computer models. *Basin Research*, **14**, 347–360.
- VAN HINSBERGEN, D.J.J. & SCHMID, S.M. 2012. Map view restoration of Aegean-West Anatolian accretion and extension since the Eocene. *Tectonics*, **31**, TC5005, <http://doi.org/10.1029/2012TC003132>
- VAN HINSBERGEN, D.J.J., KRIJGSMAN, W., LANGEREIS, C.G., CORNÉE, J.J., DUERMEIJER, C.E. & VAN VUGT, N. 2007. Discrete Plio-Pleistocene phases of tilting and counterclockwise rotation in the southeastern Aegean arc (Rhodos, Greece): early Pliocene formation of the south Aegean left-lateral strike-slip system. *Journal of the Geological Society, London*, **164**, 1133–1144, <http://doi.org/10.1144/0016-76492006-061>
- WESTAWAY, R. 2002. The Quaternary evolution of the Gulf of Corinth, central Greece: coupling between surface processes and flow in the lower continental crust. *Tectonophysics*, **348**, 269–318.
- ZELILIDIS, A. 2000. Drainage evolution in a rifted basin, Corinth graben, Greece. *Geomorphology*, **35**, 69–85.
- ZELILIDIS, A. & KONTOPOULOS, N. 1996. Significance of fan deltas without toe-sets within rift and piggy-back basins: examples from the Corinth graben and the Meso-hellenic trough, Central Greece. *Sedimentology*, **43**, 253–262.
- ZELT, B.C., TAYLOR, B., SACHPAZI, M. & HIRN, A. 2005. Crustal velocity and Moho structure beneath the Gulf of Corinth, Greece. *Geophysical Journal International*, **162**, 257–268, <http://doi.org/10.1111/j.1365-246X.2005.02640.x>

Table des figures

1.1	Modèle d'extension lithosphérique en considérant les comportements rhéologiques fragile de la croûte supérieure et ductile dans le manteau supérieur, ainsi que les processus de surface.	27
1.2	Variations de la longueur des failles bordières dans différents rifts continentaux .	28
1.3	Déplacement maximal en fonction de la longueur des failles (Kim & Sanderson, 2005)	29
1.4	Schéma simplifié illustrant le modèle de croissance des failles isolées (a-b) et le modèle de failles à longueur constante (c-e).	30
1.5	Résultat de simulations numériques montrant le rejet vertical des failles α , β et γ (A) et le nombre de failles actives (B) au cours de l'évolution d'un réseau de failles.	31
1.6	Modèle d'évolution d'un réseau de failles normales en surface issu des résultats de simulations numériques de Cowie (1998).	32
1.7	Résultats des modèles analogiques (argiles) reproduisant la direction des structures de rifts en lien avec l'obliquité des structures héritées.	33
1.8	Rôle des structures héritées dans la croissance d'un réseau de failles.	34
1.9	Résultat de simulations numériques de l'étirement crustal à partir de trois failles normales activées simultanément.	35
1.10	Flexure et déplacement associés à l'activité d'une faille normale (coupe transverse) montrant la distribution du soulèvement dans le mur et de la subsidence dans le toit (d'après Allen & Allen, 2013).	36
1.11	Système de drainage transverse et construction des cônes alluviaux en fonction du gradient de déplacement le long d'une faille normale.	37
1.12	Résultats du modèle tectonique couplé au modèle d'évolution des reliefs CASCADE montrant l'évolution du taux de productivité du bassin versant (volume de sédiments/aire du bassin versant), du flux sédimentaire (Q_s) et du rejet vertical des failles en fonction du temps	38
1.13	Principaux paramètres de contrôle de l'architecture stratigraphique des systèmes alluviaux et fluviaux.	38
1.14	Représentation schématique 2D du flux sédimentaire depuis les zones en soulèvement et du remplissage dans un bassin en subsidence.	40

TABLE DES FIGURES

1.15 Flux sédimentaire et préservation des dépôts dans les bassins. Les aires des rectangles représentent les volumes de sédiments distribués depuis la source jusqu'aux différents dépo-centres. FW : "footwall" ; HW : "hangingwall" ; AX : "axial" (d'après Leeder <i>et al.</i> , 1991).	42
1.16 Vue aérienne d'un système axial de rivières ("Big Lost River", Idaho, Etats-Unis) recoupant les rivières distributaires des cônes alluviaux transverses aux failles normales actives (d'après Leeder & Mack, 2001).	43
1.17 Vue aérienne (Google Earth) de l'extrémité nord du lac Turkana (Kenya) alimenté par un système fluvial axial (carte extraite de Vétel <i>et al.</i> , 2005).	44
1.18 (A) Bloc diagramme illustrant les systèmes de rivières transverse ("platform margin drainage") et axiales ("axial margin drainage") dans les différents demi-grabens du lac Tanganyika. (B) Réseau hydrographique du lac Tanganyika montrant les principales sources de sédiments entrants dans le bassin (d'après Tiercelin <i>et al.</i> , 1992; Cohen, 1991).	44
1.19 Modèle conceptuel de demi-graben illustrant (A) un système de drainage interne, transverse et (B) un système de drainage axial/longitudinal (d'après Leeder & Gawthorpe, 1987).	45
1.20 Surimposition et antécédence en contexte compressif (d'après Coque, 1977).	45
1.21 Représentation des différentes échelles spatiales et des types d'unités sédimentaires observées dans l'enregistrement sédimentaires des systèmes fluviaux.	47
1.22 Modèle architectural d'une succession fluviale enregistrant un cycle de variation du niveau de base de troisième ordre.	48
1.23 Coupe transverse à l'axe fluvial illustrant schématiquement l'architecture stratigraphique dans le cas d'un système distributaire non confiné (A) et d'un système confiné (Pisel, 2015).	49
1.24 Vue aérienne (Google Earth) du fan Okavango (Botswana) (McCarthy, 2002).	50
1.25 Modèle 2D de la stratigraphie alluviale d'une rivière axiale (modèle LAB) dans un demi-graben (modifié d'après Alexander & Leeder, 1987).	51
1.26 Résultat des modélisations expérimentales de l'architecture fluviale d'amont en aval.	52
1.27 Modèle conceptuel de l'évolution tectono-sédimentaire des rifts en milieu continental	56
1.28 Reconstitution paléogéographique du système fluvial "Guarda Velta", bassin cambrien de Camaqua au sud du Brésil.	57
2.1 Carte géologique du rift de Corinthe et des structures helléniques majeures	61
2.2 Coupe N-S à l'ouest du rift de Corinthe passant par Aigion et illustrant l'ensemble de la sismicité sous le golfe.	62
2.3 Carte tectonique de la région méditerranéenne (centrale et orientale)	62
2.4 Carte de la région égéenne montrant les limites des microplaques	64

2.5	Carte et coupes simplifiées des nappes helléniques dans la région du golfe de Corinthe	66
2.6	Schéma simplifié de l'empilement des nappes helléniques externes et lithostratigraphie de la nappe de Pinde-Olonos observée le long de la marge sud du rift de Corinthe.	68
2.7	Carte tectonique générale de la Méditerranée orientale.	70
2.8	Reconstruction paléogéographique de la région égéenne à -5 Ma.	71
2.9	Migration de la déformation au cours de l'extension égéenne depuis le Miocène.	72
2.10	Carte simplifiée du domaine égéen et des structures extensives majeures à la fin du Miocène et depuis la fin du Pliocène.	73
2.11	Location de la zone d'amincissement crustale maximale à l'est du rift de Corinthe.	75
2.12	Deux coupes N-S de la marge sud du rift de Corinthe suivant le modèle de détachement et le modèle de rotation des blocs.	76
2.13	Exemples de profils sismiques (EW0108 <i>Multichannel seismic</i> , campagne géophysique Maurice Ewing 2001) convertis en profondeur.	77
2.14	Coupe schématique N-S présentant la sismicité et la géométrie des failles proposée par Sorel (2000).	77
2.15	Coupe N-S de la partie ouest du rift de Corinthe illustrant les essaims de sismicité récents de 1991, 2001, 2007 et 2013	78
2.16	Coupe simplifiée illustrant la présence d'un flux de matériel crustal vers le sud, sous le Péloponnèse (Westaway, 2002).	78
2.17	Bloc diagramme 3D illustrant le développement de la marge sud du rift de Corinthe et des dépocentres associés (d'après Nixon <i>et al.</i> , 2016).	81
2.18	Carte géologique simplifiée de la marge sud du golfe de Corinthe illustrant les rivières principales	82
3.1	Geological map of the Corinth rift	90
3.2	Geological map of the study area.	91
3.3	Interpretation of syn-rift succession in the central Doumena fault block	95
3.4	Interpretation of syn-rift succession in the western Kerpini fault block	96
3.5	Interpretation of syn-rift succession in the northern Valimi fault block and photo of the upper part of the Voutsimos logged section along the Krathis River valley.	97
3.6	Interpretation of syn-rift succession in the Pirgaki-Mamoussia fault block exposed along the Lapodotamos River valley	98
3.7	Thermomagnetic curves (temperature v. magnetic susceptibility) in four representative samples	101
3.8	Isothermal remanent acquisition curves for six representative samples	102
3.10	Representative demagnetization diagrams and stereographic projections (tilt corrected)	105

TABLE DES FIGURES

3.11	Magnetostratigraphic columns for the four studied section	114
3.13	Correlation models of the Kalavryta river system across a series of normal faults .	119
3.14	Correlation between thickness of the paleomagnetic sections and the polarity reference scale (Lourens <i>et al.</i> , 2004)	120
4.1	Simplified map of the Gulf of Corinth and general syn-rift stratigraphy	128
4.2	Logged sections in the southern fault blocks	139
4.3	Logged sections in the northern fault blocks	140
4.4	Conglomeratic lithofacies.	141
4.5	Sandy lithofacies.	142
4.6	Fine-grained (silt to clay) lithofacies.	143
4.7	Main alluvial-fluvial architectures observed in the conglomeratic facies associations	144
4.8	Geological map of the study area.	145
4.9	Cross-sections showing the details of the Lower Group stratigraphy across the different fault blocks	146
4.10	Correlation model of the Lower Group across a series of normal fault by combining magnetostratigraphy results and biostratigraphic ages	150
4.11	Interpretation of pseudo-timelines with respect to the main lithostratigraphic markers and age constraints.	153
4.12	Chronostratigraphic scheme of Lower Group depositional fluvial system	154
4.13	Fence diagrams along strike of the hangingwall depocentres showing the different timelines and evolutionary phases	158
4.14	Palaeogeographic reconstructions describing the main tectono-sedimentary features for the five evolutionary phases	161
5.1	Schematic map view of the development of a relay ramp according to the coherent fault model and the isolated fault model.	173
5.2	Geological map of the Gulf of Corinth rift.	176
5.3	Stratigraphic correlation between offshore and onshore domains in the Central rift basin.	177
5.4	Map of the Akrata relay zone including onshore and offshore domains.	179
5.5	Gocad view (from NE) of the Derveni-Krathis-East Helike fault system along the southern Corinth rift border.	180
5.6	Un-interpreted and interpreted complete seismic lines L14.	182
5.7	Onshore-offshore cross-sections transverse to the relay zone.	183
5.8	Upper group displacement profile plotted along the East Helike-Derveni fault system.	185
5.9	Cross-section of the Akrata relay zone.	190
5.10	Krathis valley between Kalamias and Akrata looking N.	191

5.11	Akrata Gilbert-type delta seen from the Akrata village, along the Krathis River.	192
5.12	Palaeogeographic maps of the Akrata relay zone evolution.	194
5.13	Correction schemes for <i>Cladocora coespitosa</i>	199
6.1	Tectonic map of the Corinth rift showing principal faults and the onshore distribution.	203
6.2	Geological map of the Plio-Pleistocene Corinth rift of the northern Peloponnese	204
6.3	Synthetic regional chronostratigraphy along the southern Corinth rift margin.	210
6.4	Paleogeographic reconstruction of Phase 1 from ~4 to ~1.5 Ma.	212
6.5	Paleogeographic reconstruction of Phase 2 from ~1.5 to ~0.7 Ma.	215
6.6	Paleogeographic reconstruction of Phase 3 from ~0.7 to ~0.4 Ma. Panach. F. : Panachaikon Fault.	217
6.8	Response of rivers to footwall uplift.	222
6.9	Compilation of through-going river systems during the development of a normal fault array and showing different sequences of fault activation.	223
6.10	Simplified transverse cross sections of three normal fault blocks with equally-spaced faults.	226
6.11	Chronology of fault activation thought the rift history along a N-S transect located in the onshore part of C4 zone	227
A.1	Quelques exemples de figures sédimentaires à partir desquelles sont mesurées les paléocourants.	237
A.2	Test de probabilité de Rayleigh (d'après Curray, 1956)	238
B.1	Photos MEB des algues vertes calcaires et d'une dent de rongeur	262
C.1	Les rayons cosmiques primaires (principalement des protons) entrent dans la haute atmosphère à l'origine d'une série de réactions nucléaires secondaires (Dunai, 2010).	264
C.2	Influence de la décroissance radioactive sur l'accumulation des isotopes cosmogéniques au cours du temps (sans érosion)	267
C.3	Influence du taux d'érosion sur l'accumulation des isotopes cosmogéniques d'une surface au temps du temps	267
C.4	Modèles généraux décrivant la concentration des isotopes cosmogéniques afin de déterminer l'âge d'une roche.	267
C.5	Diagramme $^{26}\text{Al}/^{10}\text{Be}$ vs. ^{10}Be	270
C.6	Modèle de calibration du taux de production des isotopes cosmogéniques en fonction de l'altitude et la latitude du site	272
D.1	Application of the ^{26}Al - ^{10}Be burial dating in active rift setting.	277
D.2	DEM of the northwestern part of the Peloponnese showing the main rivers.	278

TABLE DES FIGURES

D.3	^{26}Al - ^{10}Be exposure-burial plot showing the $^{26}\text{Al}/^{10}\text{Be}$ ratio and ^{10}Be concentration in different stratigraphic units.	279
D.4	Geological map of southern Corinth rift margin showing the lithostratigraphy of the Kalavryta and the Killini river systems.	287
D.5	N-S cross sections of the southern Corinth rift margin showing the lithostratigraphy of the Kalavryta (A-A') and Killini river systems (B-B')	288
E.1	Geological map of the Corinth rift	291

Quatrième partie

Bibliographie

Bibliographie

- ACOCELLA, V., MORVILLO, P. & FUNICIELLO, R. 2005 What controls relay ramps and transfer faults within rift zones ? Insights from analogue models. *Journal of Structural Geology* **27** (3), 397–408.
- ALEXANDER, J. & LEEDER, M. R. 1987 Active Tectonic Control on Alluvial Architecture. *Recent Developments in Fluvial Sedimentology* (ed. M. A. Etheridge, R. M. Flores & M. D. Harvey), pp. 243–252. Society of Economic Paleontologists and Mineralogists, Special Publication 39.
- ALLEMAND, P., BRUN, J.-P., DAVY, P. & VAN DEN DRIESSCHE, J. 1989 Symétrie et asymétrie des rifts et mécanismes d'amincissement de la lithosphère. *Bulletin de la Société géologique de France* **3** (5), 445–451.
- ALLEN, J. 1978 Studies in fluvial sedimentation : an exploratory quantitative model for the architecture of avulsion-controlled alluvial suites. *Sedimentary Geology* **21** (2), 129–147.
- ALLEN, J. R. L. 1983 Studies in fluvial sedimentation : bars, bar-complexes and sandstone sheets (low-sinuosity braided streams) in the Brownstones (L. Devonian), Welsh Borders. *Sedimentary Geology* **33** (4), 237–293.
- ALLEN, P. A. 1998 Sediment supply from landslide dominated catchments : implications for basin margin fans. *Basin Research* **10** (1), 19–35.
- ALLEN, P. A. 2008 Time scales of tectonic landscapes and their sediment routing systems. *Landscape Evolution : Denudation, Climate and Tectonics Over Different Time and Space Scales* (ed. K. Gallagher, S. J. Jones & J. Wainwright), pp. 7–28. Geological Society, London, Special Publications 296.
- ALLEN, P. A. & ALLEN, J. R. 2013 *Basin analysis : Principles and application to petroleum play assessment*, 3rd edn. John Wiley & Sons.
- ALLEN, P. A., ARMITAGE, J. J., CARTER, A., DULLER, R. A., MICHAEL, N. A., SINCLAIR, H. D., WHITCHURCH, A. L. & WHITTAKER, A. C. 2013 The Qs problem : Sediment volumetric balance of proximal foreland basin systems. *Sedimentology* **60** (1), 102–130.
- ALLEN, P. A. & DENSMORE, A. L. 2000 Sediment flux from an uplifting fault block. *Basin Research* **12** (3-4), 367–380.
- ALLEN, P. A. & HELLER, P. L. 2012 Dispersal and preservation of tectonically generated alluvial gravels in sedimentary basins. *Tectonics of Sedimentary Basins : Recent Advances* (ed. C. J. Busby & A. Azor Pérez), pp. 111–130. Blackwell Publishing Ltd.
- ALVAREZ 1999 Drainage on evolving fold-thrust belts : a study of transverse canyons in the Apennines. *Basin Research* **11** (3), 267–284.
- ANDERS, M. H., SPIEGELMAN, M., RODGERS, D. W. & HAGSTRUM, J. T. 1993 The growth of fault-bounded tilt blocks. *Tectonics* **12** (6), 1451–1459.

BIBLIOGRAPHIE

- ANTHONY, E. J., LANG, J. & OYEDE, L. M. 1996 Sedimentation in a tropical, microtidal, wave dominated coastal plain estuary. *Sedimentology* **43** (4), 665–675.
- ARGUS, D. F., GORDON, R. G., DEMETS, C. & STEIN, S. 1989 Closure of the Africa-Eurasia-North America Plate motion circuit and tectonics of the Gloria Fault. *Journal of Geophysical Research* **94** (B5), 5585.
- ARMIJO, R., MEYER, B., HUBERT, A. & BARKA, A. 1999 Westward propagation of the North Anatolian fault into the northern Aegean : Timing and kinematics. *Geology* **27** (3), 267–270.
- ARMIJO, R., MEYER, B., KING, G. C. P., RIGO, A. & PAPANASTASSIOU, D. 1996 Quaternary evolution of the Corinth Rift and its implications for the Late Cenozoic evolution of the Aegean. *Geophysical Journal International* **126** (1), 11–53.
- ARMIJO, R., MEYER, B., NAVARRO, S., KING, G. & BARKA, A. 2002 Asymmetric slip partitioning in the Sea of Marmara pull-apart : a clue to propagation processes of the North Anatolian Fault? *Terra Nova* **14** (2), 80–86.
- ARMITAGE, J. J., DULLER, R. A., WHITTAKER, A. C. & ALLEN, P. A. 2011 Transformation of tectonic and climatic signals from source to sedimentary archive. *Nature Geoscience* **4** (4), 231–235.
- ARMITAGE, J. J., DUNKLEY JONES, T., DULLER, R. A., WHITTAKER, A. C. & ALLEN, P. A. 2013 Temporal buffering of climate-driven sediment flux cycles by transient catchment response. *Earth and Planetary Science Letters* **369-370**, 200–210.
- ARNOLD, M., MERCHEL, S., BOURLÈS, D. L., BRAUCHER, R., BENEDETTI, L., FINKEL, R. C., AUMAÎTRE, G., GOTTDANG, A. & KLEIN, M. 2010 The French accelerator mass spectrometry facility ASTER : Improved performance and developments. *Nuclear Instruments and Methods in Physics Research Section B : Beam Interactions with Materials and Atoms* **268** (11–12), 1954–1959.
- ATHMER, W., GROENENBERG, R. M., LUTHI, S. M., DONSELAAR, M. E., SOKOUTIS, D. & WILLINGSHOFER, E. 2010 Relay ramps as pathways for turbidity currents : a study combining analogue sandbox experiments and numerical flow simulations. *Sedimentology* **57** (3), 806–823.
- ATHMER, W. & LUTHI, S. M. 2011 The effect of relay ramps on sediment routes and deposition : A review. *Sedimentary Geology* **242** (1-4), 1–17.
- ATTAL, M. & LAVÉ, J. 2009 Pebble abrasion during fluvial transport : Experimental results and implications for the evolution of the sediment load along rivers. *Journal of Geophysical Research* **114** (F4), F04023.
- AUBOUIN, J. 1959 Contribution à l'étude géologique de la Grèce septentrionale : les confins de l'Épire et de la Thessalie. *Annales Géologiques des Pays Helléniques* **10**, 1–525.
- AUBOUIN, J., BRUNN, J., CELET, P., DERCOURT, J., GODFRIAUX, I. & MERCIER, J. 1963 Esquisse de la géologie de la Grèce. *Livre à la Mémoire du Professeur Paul Fallot*, pp. 583–610. Société Géologique de France.
- AUBOUIN, J. & DERCOURT, J. 1965 Sur la géologie de l'Égée : regard sur la Crète (Grèce). *Bulletin de la Société géologique de France* **7** (1), 787–821.
- AVALLONE, A., BRIOLE, P., AGATZA-BALODIMOU, A. M., BILLIRIS, H., CHARADE, O., MITSAKAKI, C., NERCESSIAN, A., PAPAIZISSI, K., PARADISSIS, D. & VEIS, G. 2004 Analysis of eleven years of deformation measured by GPS in the Corinth Rift Laboratory area. *Comptes Rendus Geoscience* **336** (4-5), 301–311.

- BACKERT, N., FORD, M. & MALARTRE, F. 2010 Architecture and sedimentology of the Kerinitis Gilbert-type fan delta, Corinth Rift, Greece. *Sedimentology* **57** (2), 543–586.
- BALCO, G. & ROVEY, C. W. 2008 An isochron method for cosmogenic-nuclide dating of buried soils and sediments. *American Journal of Science* **308** (10), 1083–1114.
- BALCO, G. & SHUSTER, D. L. 2009 ^{26}Al – ^{10}Be – ^{21}Ne burial dating. *Earth and Planetary Science Letters* **286** (3–4), 570–575.
- BALLATO, P. & STRECKER, M. R. 2014 Assessing tectonic and climatic causal mechanisms in foreland-basin stratal architecture : insights from the Alborz Mountains, northern Iran. *Earth Surface Processes and Landforms* **39** (1), 110–125.
- BANDEL, K. 2001 The history of Theodoxus and Neritina connected with description and systematic evaluation of related Neritimorpha (Gastropoda). *Mitteilungen aus dem Geologisch-Paläontologischen Institut der Universität Hamburg* **85**, 65–164.
- BANKS, N. L., BARDWELL, K. A. & MUSIWA, S. 1995 Karoo Rift basins of the Luangwa Valley, Zambia. *Hydrocarbon Habitat in Rift Basins* (ed. J. Lambiase), pp. 285–295. Geological Society, London, Special Publications 80.
- BARNDT, J., JOHNSON, N., JOHNSON, G., OPDYKE, N., LINDSAY, E., PILBEAM, D. & TAHIRKHELI, R. 1978 The magnetic polarity stratigraphy and age of the Siwalik group near Dhok Pathan village, Potwar Plateau, Pakistan. *Earth and Planetary Science Letters* **41** (3), 355–364.
- BASTESSEN, E., BRAATHEN, A., NØTTVEIT, H., GABRIELSEN, R. H. & SKAR, T. 2009 Extensional fault cores in micritic carbonate – Case studies from the Gulf of Corinth, Greece. *Journal of Structural Geology* **31** (4), 403–420.
- BECKERS, A., HUBERT-FERRARI, A., BECK, C., BODEUX, S., TRIPSANAS, E., SAKELLARIOU, D. & DE BATIST, M. 2015 Active faulting at the western tip of the Gulf of Corinth, Greece, from high-resolution seismic data. *Marine Geology* **360** (1), 55–69.
- BEHN, M. D., LIN, J. & ZUBER, M. T. 2002 A continuum mechanics model for normal faulting using a strain-rate softening rheology : implications for thermal and rheological controls on continental and oceanic rifting. *Earth and Planetary Science Letters* **202** (3–4), 725–740.
- BEHRENSMEYER, A. K. 1987 Miocene fluvial facies and vertebrate taphonomy in northern Pakistan. *Recent developments in fluvial sedimentology* (ed. F. G. Etheridge, R. M. Flores & M. D. Harvey), pp. 169–176. Society of Economic Paleontologists and Mineralogists, Special Publication 39.
- BEHRENSMEYER, A. K. 1988 Vertebrate preservation in fluvial channels. *Palaeogeography, Palaeoclimatology, Palaeoecology* **63** (1), 183–199.
- BELL, R. E., MCNEILL, L., BULL, J. M. & HENSTOCK, T. J. 2008 Evolution of the offshore western Gulf of Corinth. *Geological Society of America Bulletin* **120** (1–2), 156–178.
- BELL, R. E., MCNEILL, L., BULL, J. M., HENSTOCK, T. J., COLLIER, R. & LEEDER, M. R. 2009 Fault architecture, basin structure and evolution of the Gulf of Corinth Rift, central Greece. *Basin Research* **21** (6), 824–855.
- BELL, R. E., MCNEILL, L., HENSTOCK, T. J. & BULL, J. M. 2011 Comparing extension on multiple time and depth scales in the Corinth Rift, Central Greece. *Geophysical Journal International* **186** (2), 463–470.

BIBLIOGRAPHIE

- BELLAHSEN, N. & DANIEL, J. M. 2005 Fault reactivation control on normal fault growth : an experimental study. *Journal of Structural Geology* **27** (4), 769–780.
- BENTHAM, P., COLLIER, R. E., GAWTHORPE, R. L., LEEDER, R. & STARK, C. 1991 Tectono-sedimentary development of an extensional basin : the Neogene Megara Basin, Greece. *Journal of the Geological Society* **148** (5), 923–934.
- BERNARD, P., BRIOLE, P., MEYER, B., GOMEZ, J., TIBERI, C., BERGE, C., CATTIN, R., HATZFELD, D., LACHET, C., LEBRUN, B., DESCHAMPS, A., COURBOULEX, F., LARROQUE, C., RIGO, A., MASSONNET, D., PAPADIMITRIOU, P., KASSARAS, J., DIAGOURTAS, D., MAKROPOULOS, K., VEIS, G., PAPAIZI, E., MITSAKAKI, C., KARAKOSTAS, V. & PAPADIMITRIOU, E. 1997 The Ms=6.2, June 15, 1995 Aigion earthquake (Greece) : evidence for low angle normal faulting in the Corinth rift P. *Journal of Seismology* **1** (2), 131–150.
- BERNARD, P., LYON-CAEN, H., BRIOLE, P., DESCHAMPS, A. & BOUDIN, F. 2006 Seismicity , deformation and seismic hazard in the western rift of Corinth : New insights from the Corinth Rift Laboratory (CRL). *Tectonophysics* **426** (1), 7–30.
- BERTINI, A. 2010 Pliocene to Pleistocene palynoflora and vegetation in Italy : State of the art. *Quaternary International* **225** (1), 5–24.
- BESSE, J. & COURTILLOT, V. 2002 Apparent and true polar wander and the geometry of the geomagnetic field over the last 200 Myr. *Journal of Geophysical Research : Solid Earth* **107** (B11), 2300.
- BHATTACHARYA, J. 2011 Practical problems in the application of the sequence stratigraphic method and key surfaces : integrating observations from ancient fluvial-deltaic wedges with Quaternary and modeling studies. *Sedimentology* **58** (1), 120–169.
- BIALAS, R. W. & BUCK, W. R. 2009 How sediment promotes narrow rifting : Application to the Gulf of California. *Tectonics* **28** (4), TC4014.
- BIERMAN, P. & STEIG, E. J. 1996 Estimating rates of denudation using cosmogenic isotope abundances in sediment. *Earth surface processes and landforms* **21** (2), 125–139.
- BILLI, P., MAGI, M. & SAGRI, M. 1987 Coarse-grained low-sinuosity river deposits : example from Plio-Pleistocene Valdarno Basin, Italy. *Recent developments in fluvial sedimentology* (ed. F. Ethridge, R. Flores & M. Harney), pp. 197–203. Society of Economic Paleontologists and Mineralogists, Special Publication 39.
- BILLIRIS, H., PARADISSIS, D., VEIS, G., ENGLAND, P., FEATHERSTONE, W., PARSONS, B., CROSS, P., RANDES, P., RAYSON, M., SELLERS, P., ASHKENAZI, V., DAVISON, M., JACKSON, J. & AMBRASEYS, N. 1991 Geodetic determination of tectonic deformation in central Greece from 1900 to 1988. *Nature* **350**, 124–129.
- BLAIR, T. C. & BILODEAU, W. L. 1988 Development of tectonic cyclothems in rift, pull-apart, and foreland basins : Sedimentary response to episodic tectonism. *Geology* **16** (6), 517–520.
- BLAIR, T. C. & MCPHERSON, J. G. 1994 Alluvial fans and their natural distinction from rivers based on morphology, hydraulic processes, sedimentary processes, and facies assemblages. *Journal of sedimentary research* **64** (3), 450–489.
- VON BLANCKENBURG, F. 2005 The control mechanisms of erosion and weathering at basin scale from cosmogenic nuclides in river sediment. *Earth and Planetary Science Letters* **237** (3-4), 462–479.

- BLUM, M., MARTIN, J., MILLIKEN, K. & GARVIN, M. 2013 Paleovalley systems : Insights from Quaternary analogs and experiments. *Earth-Science Reviews* **116**, 128–169.
- BLUM, M. D. & TÖRNQVIST, T. E. 2000 Fluvial responses to climate and sea-level change : a review and look forward. *Sedimentology* **47** (1), 2–48.
- BOHACS, K. M., CARROLL, A. R., NEAL, J. E. & MANKIEWICZ, P. J. 2000 Lake-Basin Type, Source Potential, and Hydrocarbon Character : an Integrated Sequence-Stratigraphic–Geochemical Framework. *Lake basins through space and time* (ed. E. H. Gierlowski-Kordesch & K. R. Kelts), pp. 3–34. American Association of Petroleum Geologists, Studies in Geology 46.
- BORCHERS, B., MARRERO, S., BALCO, G., CAFFEE, M., GOEHRING, B., LIFTON, N., NISHIZUMI, K., PHILLIPS, F., SCHAEFER, J. & STONE, J. 2016 Geological calibration of spallation production rates in the CRONUS-Earth project. *Quaternary Geochronology* **31**, 188–198.
- BRAUCHER, R., MERCHEL, S., BORGOMANO, J. & BOURLÈS, D. 2011 Production of cosmogenic radionuclides at great depth : A multi element approach. *Earth and Planetary Science Letters* **309** (1-2), 1–9.
- BRAUN, J. & SAMBRIDGE, M. 1997 Modelling landscape evolution on geological time scales : a new method based on irregular spatial discretization. *Basin Research* **9** (1), 27–52.
- BRAYSHAW, A. C. 1984 Characteristics and origin of cluster bedforms in coarse-grained alluvial channels. *Sedimentology of Gravels and Conglomerates* (ed. E. H. Koster & R. Steel), pp. 77–85. Canadian Society of Petroleum Geologists, Memoir 10.
- BRIDGE, J. S. 1993 The interaction between channel geometry, water flow, sediment transport and deposition in braided rivers. *Braided Rivers* (ed. J. L. Best & C. S. Bristow), pp. 13–71. Geological Society, London, Special Publications 75.
- BRIDGE, J. S. 2003 *Rivers and floodplains : forms, processes, and sedimentary record*. Blackwell Publishing.
- BRIDGE, J. S. & LEEDER, M. 1979 A simulation model of alluvial stratigraphy. *Sedimentology* **26** (5), 617–644.
- BRIDGE, J. S. & LUNT, I. A. 2006 Depositional models of braided rivers. *Braided Rivers, Processes, Deposits, Ecology and Management* (ed. G. H. Sambrook, Smith, J. L. Best & C. S. Bristow), pp. 11–50. International Association of Sedimentologists, Special Publication 36.
- BRIDGE, J. S. & MACKEY, S. D. 1993 A Revised Alluvial Stratigraphy Model. *Alluvial Sedimentation* (ed. M. Marzo & C. Puigdefábregas), pp. 317–336. IAS Special Publications 17.
- BRIOLE, P., RIGO, A., LYON-CAEN, H., RUEGG, J., PAPAZISSI, K., MITSAKAKI, C., BALODIMOU, A., VEIS, G., HATZFELD, D. & DESCHAMPS, A. 2000 Active deformation of the Corinth rift Greece' Results from repeated Global Positioning System surveys between 1990 and 1995. *Journal of Geophysical Research* **105** (B11), 25 605–25 625.
- BROCARD, G., WILLENBRING, J., SUSKI, B., AUDRA, P., AUTHEMAYOU, C., COSENZA-MURALLES, B., MORAN-ICAL, S., DEMORY, F., ROCHETTE, P., VENNEMANN, T., HOLLIGER, K. & TEYSSIER, C. 2012 Rate and processes of river network rearrangement during incipient faulting : The case of the Cahabon River, Guatemala. *American Journal of Science* **312** (5), 449–507.
- BROMLEY, R. G. 1996 *Trace fossils : Biology, taphonomy and applications*. Taylor & Francis.

BIBLIOGRAPHIE

- BROWN, E. T., EDMOND, J. M., RAISBECK, G. M., YIOU, F., KURZ, M. D. & BROOK, E. J. 1991 Examination of surface exposure ages of Antarctic moraines using in situ produced ^{10}Be and ^{26}Al . *Geochimica et Cosmochimica Acta* **55** (8), 2269–2283.
- BROWN, E. T., STALLARD, R. F., LARSEN, M. C., RAISBECK, G. M. & YIOU, F. 1995 Denudation rates determined from the accumulation of in situ-produced ^{10}Be in the Luquillo experimental forest, Puerto Rico. *Earth and Planetary Science Letters* **129** (1-4), 193–202.
- BRUN, J. & BESLIER, M. 1996 Mantle exhumation at passive margins. *Earth and Planetary Science Letters* **142** (1-2), 161–173.
- BRUN, J.-P. 1999 Narrow rifts versus wide rifts : inferences for the mechanics of rifting from laboratory experiments. *Philosophical Transactions of the Royal Society A : Mathematical, Physical and Engineering Sciences* **357** (1753), 695–712.
- BRUN, J.-P. & CHOUKROUNE, P. 1983 Normal faulting, block tilting, and décollement in a stretched crust. *Tectonics* **2** (4), 345–356.
- BRUNE, S., HEINE, C., PÉREZ-GUSSINYÉ, M. & SOBOLEV, S. V. 2014 Rift migration explains continental margin asymmetry and crustal hyper-extension. *Nature Communications* **5**, 4014.
- BRYANT, M., FALK, P. & PAOLA, C. 1995 Experimental study of avulsion frequency and rate of deposition. *Geology* **23** (4), 365.
- BUATOIS, L. A. & MÁNGANO, M. G. 2011 *Ichnology : Organism-substrate interactions in space and time*. Cambridge University Press.
- BUEHLER, H. A., WEISSMANN, G. S., SCUDERI, L. A. & HARTLEY, A. J. 2011 Spatial and Temporal Evolution of an Avulsion on the Taquari River Distributive Fluvial System from Satellite Image Analysis. *Journal of Sedimentary Research* **81** (8), 630–640.
- BURBANK, D. W., BECK, R. A., RAYNOLDS, R. G. H., HOBBS, R. & TAHIRKHELI, R. 1988 Thrusting and gravel progradation in foreland basins : A test of post-thrusting gravel dispersal. *Geology* **16** (12), 1143–1146.
- BUROV, E. & CLOETINGH, S. 1997 Erosion and rift dynamics : new thermomechanical aspects of post-rift evolution of extensional basins. *Earth and Planetary Science Letters* **150** (1), 7–26.
- BUROV, E., FRANCOIS, T., YAMATO, P. & WOLF, S. 2014 Mechanisms of continental subduction and exhumation of HP and UHP rocks. *Gondwana Research* **25** (2), 464–493.
- BUROV, E. B. & DIAMENT, M. 1995 The effective elastic thickness (T_e) of continental lithosphere : What does it really mean ? *Journal of Geophysical Research* **100** (B3), 3905.
- BUSSOLOTTO, M., BENEDICTO, A., MOEN-MAUREL, L. & INVERNIZZI, C. 2015 Fault deformation mechanisms and fault rocks in micritic limestones : Examples from Corinth rift normal faults. *Journal of Structural Geology* **77**, 191–212.
- CAIN, S. A. & MOUNTNEY, N. P. 2009 Spatial and temporal evolution of a terminal fluvial fan system : the Permian Organ Rock Formation, South-east Utah, USA. *Sedimentology* **56** (6), 1774–1800.
- CAMERON, A. R., KALKREUTH, W. D. & KOUKOUZAS, C. 1984 The petrology of Greek brown coals. *International journal of coal geology* **4** (3), 173–207.

- CAMPOS, C., BECK, C., CROUZET, C., CARRILLO, E., VAN WELDEN, A. & TRIPSANAS, E. 2014 Late Quaternary paleoseismic sedimentary archive from deep central Gulf of Corinth : time distribution of inferred earthquake-induced layers. *Annals of Geophysics* **56** (6), S0670.
- CARROLL, A. R. & BOHACS, K. M. 1999 Stratigraphic classification of ancient lakes : Balancing tectonic and climatic controls. *Geology* **27** (2), 99.
- CARTWRIGHT, J. A., TRUDGILL, B. D. & MANSFIELD, C. S. 1995 Fault growth by segment linkage : an explanation for scatter in maximum displacement and trace length data from the Canyonlands Grabens of SE Utah. *Journal of Structural Geology* **17** (9), 1319–1326.
- CASTELLTORT, S. & SIMPSON, G. 2006 River spacing and drainage network growth in widening mountain ranges. *Basin Research* **18** (3), 267–276.
- CATUNEANU, O. 2006 *Principles of sequence stratigraphy*. Elsevier Ed.
- CHARALAMPAKIS, M., LYKOUSIS, V., SAKELLARIOU, D., PAPTAEODOROU, G. & FERENTINOS, G. 2014 The tectono-sedimentary evolution of the Lechaion Gulf, the south eastern branch of the Corinth graben, Greece. *Marine Geology* **351**, 58–75.
- CHARREAU, J., AVOUAC, J.-P., CHEN, Y., DOMINGUEZ, S. & GILDER, S. 2008 Miocene to present kinematics of fault-bend folding across the Huerguosi anticline, northern Tianshan (China), derived from structural, seismic, and magnetostratigraphic data. *Geology* **36** (11), 871.
- CHENG, H., EDWARDS, R., HOFF, J., GALLUP, C., RICHARDS, D. & ASMEROM, Y. 2000 The half-lives of uranium-234 and thorium-230. *Chemical Geology* **169** (1-2), 17–33.
- CHÉRY, J. 2001 Core complex mechanics : From the Gulf of Corinth to the Snake Range. *Geology* **29** (5), 439–442.
- CHILDS, C., NICOL, A., WALSH, J. J. & WATTERSON, J. 2003 The growth and propagation of synsedimentary faults. *Journal of Structural Geology* **25** (4), 633–648.
- CHILDS, C., WATTERSON, J. & WALSH, J. J. 1995 Fault overlap zones within developing normal fault systems. *Journal of the Geological Society* **152** (3), 535–549.
- CHMELEFF, J., VON BLANCKENBURG, F., KOSSERT, K. & JAKOB, D. 2010 Determination of the ^{10}Be half-life by multicollector ICP-MS and liquid scintillation counting. *Nuclear Instruments and Methods in Physics Research Section B : Beam Interactions with Materials and Atoms* **268** (2), 192–199.
- CHURCH, M. 1983 Pattern of instability in a wandering gravel bed channel. *Modern and ancient fluvial systems* (ed. J. D. Collinson & J. Lewin), pp. 169–180. International Association of Sedimentologists, Special Publication 6.
- CLARKE, P. J., DAVIES, R. R., ENGLAND, P. C., PARSONS, B., BILLIRIS, H., PARADISSIS, D., VEIS, G., CROSS, P. A., DENYS, P. H., ASHKENAZI, V., BINGLEY, R., KAHLE, H.-G., MULLER, M.-V. & BRIOLE, P. 1998 Crustal strain in central Greece from repeated GPS measurements in the interval 1989–1997. *Geophysical Journal International* **135** (1), 195–214.
- CLÉMENT, C., SACHPAZI, M., CHARVIS, P., GRAINDORGE, D., LAIGLE, M., HIRN, A. & ZAFIROPOULOS, G. 2004 Reflection–refraction seismics in the Gulf of Corinth : hints at deep structure and control of the deep marine basin. *Tectonophysics* **391** (1-4), 97–108.
- CLENDENON, C. 2009 Karst hydrology in ancient myths from Arcadia and Argolis, Greece. *Acta Carsologica* **1** (146), 38.

BIBLIOGRAPHIE

- CLEVIS, Q., DE BOER, P. & WACHTER, M. 2003 Numerical modelling of drainage basin evolution and three-dimensional alluvial fan stratigraphy. *Sedimentary Geology* **163** (1-2), 85–110.
- CLIFTON, A. E., SCHLISCHE, R. W., WITHJACK, M. O. & ACKERMANN, R. V. 2000 Influence of rift obliquity on fault-population systematics : results of experimental clay models. *Journal of Structural Geology* **22** (10), 1491–1509.
- CLOETINGH, S., VAN WEES, J., VAN DER BEEK, P. & SPADINI, G. 1995 Role of pre-rift rheology in kinematics of extensional basin formation : constraints from thermomechanical models of Mediterranean and intracratonic basins. *Marine and Petroleum Geology* **12** (8), 793–807.
- COGNÉ, J. P. 2003 PaleoMac : A Macintosh™ application for treating paleomagnetic data and making plate reconstructions. *Geochemistry, Geophysics, Geosystems* **4** (1), 509–520.
- COHEN, A. S. 1991 Tectono-stratigraphic model for sedimentation in Lake Tanganyika, Africa. *Lacustrine basin exploration : Case studies and modern analogs* (ed. B. Katz), , vol. 50, pp. 137–150. American Association of Petroleum Geologists, Memoir 50.
- COHEN, H. A., DART, C. J., AKYUZ, H. S. & BARKA, A. 1995 Syn-rift sedimentation and structural development of the Gediz and Buyuk Menderes graben, western Turkey. *Journal of the Geological Society* **152** (4), 629–638.
- COLLETTINI, C. & SIBSON, R. H. 2001 Normal faults, normal friction ? *Geology* **29** (10), 927–930.
- COLLIER, R. & DART, C. 1991 Neogene to Quaternary rifting, sedimentation and uplift in the Corinth Basin, Greece. *Journal of the Geological Society, London* **148**, 1049–1065.
- COLLIER, R., LEEDER, M. R., ROWE, P. J. & ATKINSON, T. C. 1992 Rates of tectonic uplift in the Corinth and Megara Basins, central Greece. *Tectonics* **11** (6), 1159–1167.
- COLLIER, R. E. 1988 Sedimentary facies evolution in continental fault-bounded basins formed by crustal extension : the Corinth Basin, Greece. PhD thesis, University of Leeds.
- COLLIER, R. E. L. 1990 Eustatic and tectonic controls upon Quaternary coastal sedimentation in the Corinth Basin, Greece. *Journal of the Geological Society* **147** (2), 301–314.
- COLLINSON, J., MOUNTNEY, N. & THOMPSON, D. 2006 *Sedimentary structures*. Terra Publishing.
- COLOMBERA, L., MOUNTNEY, N. P. & MCCAFFREY, W. D. 2013 A quantitative approach to fluvial facies models : Methods and example results. *Sedimentology* **60**, 1526–1558.
- COLOMBERA, L., MOUNTNEY, N. P. & MCCAFFREY, W. D. 2015 A meta-study of relationships between fluvial channel-body stacking pattern and aggradation rate : Implications for sequence stratigraphy. *Geology* **43** (4), 283–286.
- COMBOURIEU-NEBOUT, N. 1993 Vegetation Response to Upper Pliocene Glacial/Interglacial Cyclicity in the Central Mediterranean. *Quaternary Research* **40** (2), 228–236.
- CONNALLY, J., CHILDS, C. & WALSH, J. J. 2014 Contrasting origins of breached relay zone geometries. *Journal of Structural Geology* **58** (0), 59–68.
- COQUE, R. 1977 *Géomorphologie*. Armand Colin Ed.
- CORNET, F. H., DOAN, M. L., MORETTI, I. & BORM, G. 2004 Drilling through the active Aigion Fault : the AIG10 well observatory. *Comptes Rendus Geoscience* **336** (4-5), 395–406.

- COWIE, P. 1998 A healing–reloading feedback control on the growth rate of seismogenic faults. *Journal of Structural Geology* **20** (8), 1075–1087.
- COWIE, P., ATTAL, M., TUCKER, G., WHITTAKER, A. C., NAYLOR, M., GANAS, A. & ROBERTS, G. P. 2006 Investigating the surface process response to fault interaction and linkage using a numerical modelling approach. *Basin Research* **18** (3), 231–266.
- COWIE, P., UNDERHILL, J., BEHN, M., LIN, J. & GILL, C. 2005 Spatio-temporal evolution of strain accumulation derived from multi-scale observations of Late Jurassic rifting in the northern North Sea : A critical test of models for lithospheric extension. *Earth and Planetary Science Letters* **234** (3-4), 401–419.
- COWIE, P. A., GUPTA, S. & DAWERS, N. H. 2000 Implications of fault array evolution for synrift depo-centre development : insights from a numerical fault growth model. *Basin Research* **12** (3-4), 241–261.
- COWIE, P. A., ROBERTS, G. P. & MORTIMER, E. 2007 Strain localization within fault arrays over timescales of 1–10 000 000 years. *Tectonic faults : Agents of change on a dynamic Earth : Dahlem Workshop Report* (ed. M. R. Handy, G. Hirth & N. Hovius), pp. 47–77. MIT Press, Cambridge, MA.
- COWIE, P. A. & SCHOLZ, C. H. 1992 Displacement-length scaling relationship for faults : data synthesis and discussion. *Journal of Structural Geology* **14** (10), 1149–1156.
- COWIE, P. A., SORNETTE, D. & VANNESTE, C. 1995 Multifractal scaling properties of a growing fault population. *Geophysical Journal International* **122** (2), 457–469.
- COWIE, P. A., VANNESTE, C. & SORNETTE, D. 1993 Statistical physics model for the spatiotemporal evolution of faults. *Journal of Geophysical Research : Solid Earth* **98** (B12), 21809–21821.
- CRIDER, J. G. & PEACOCK, D. 2004 Initiation of brittle faults in the upper crust : a review of field observations. *Journal of Structural Geology* **26** (4), 691–707.
- CRIDER, J. G. & POLLARD, D. D. 1998 Fault linkage : Three-dimensional mechanical interaction faults. *Journal of Geophysical Research* **103** (B10), 24 373–24 391.
- CROSSLEY, R. 1984 Basin Analysis : Principles and Applications Controls of sedimentation in the Malawi rift valley, Central Africa. *Sedimentary Geology* **40** (1), 33–50.
- CURRAY, J. 1956 The analysis of two dimensional orientation data. *Journal of Geology* **64** (1), 117–131.
- CURRIE, B. S. 1997 Sequence stratigraphy of nonmarine Jurassic–Cretaceous rocks, central Cordilleran foreland-basin system. *Geological Society of America Bulletin* **109** (9), 1206–1222.
- DALRYMPLE, M., PROSSER, J. & WILLIAMS, B. 1998 A dynamic systems approach to the regional controls on deposition and architecture of alluvial sequences, illustrated in the Staffjord Formation (United Kingdom, Northern North Sea). *Relative Role of Eustasy Climate and Tectonism in Continental Rock* (ed. K. Shanley & P. McCabe), pp. 65–81. Society of Economic Paleontologists and Mineralogists, Special Publication 59.
- DALRYMPLE, R. W. & ZAITLIN, B. A. 1994 High-resolution sequence stratigraphy of a complex, incised valley succession, Cobequid Bay - Salmon River estuary, Bay of Fundy, Canada. *Sedimentology* **41** (6), 1069–1091.
- DART, C. J., COLLIER, R. E., GAWTHORPE, R. L., KELLER, J. V. & NICHOLS, G. 1994 Sequence stratigraphy of (?)Pliocene-Quaternary synrift, Gilbert-type fan deltas, northern Peloponnesos, Greece. *Marine and Petroleum Geology* **11** (5), 545–560.

BIBLIOGRAPHIE

- DAVIDSON, S. K., HARTLEY, A. J., WEISSMANN, G. S., NICHOLS, G. J. & SCUDERI, L. A. 2013 Geomorphic elements on modern distributive fluvial systems. *Geomorphology* **180-181**, 82–95.
- DAVIES, R., ENGLAND, P., PARSONS, B., BILLIRIS, H., PARADISSIS, D. & VEIS, G. 1997 Geodetic strain of Greece in the interval 1892–1992. *Journal of Geophysical Research : Solid Earth* **102** (B11), 24571–24588.
- DAVIES, S. J., DAWERS, N. H., MCLEOD, A. E. & UNDERHILL, J. R. 2000 The structural and sedimentological evolution of early synrift succession : The Middle Jurassic Tarbert formation, North Sea. *Basin Research* **12** (3-4), 343–365.
- DAWERS, N. H. & ANDERS, M. H. 1995 Displacement-length scaling and fault linkage. *Journal of Structural Geology* **17** (5), 607–614.
- DAWERS, N. H., ANDERS, M. H. & SCHOLZ, C. H. 1993 Growth of normal faults : Displacement-length scaling. *Geology* **21** (12), 1107.
- DAY, R., FULLER, M. & SCHMIDT, V. 1977 Hysteresis properties of titanomagnetites : Grain-size and compositional dependence. *Physics of the Earth and Planetary Interiors* **13** (4), 260–267.
- DE MARTINI, P. M., PANTOSTI, D., PALYVOS, N., LEMEILLE, F., MCNEILL, L. & COLLIER, R. 2004 Slip rates of the Aigion and Eliki Faults from uplifted marine terraces, Corinth Gulf, Greece. *Comptes Rendus Geoscience* **336** (4-5), 325–334.
- DE WEVER, P. 1975 Etude géologique des séries apparaissant en fenêtre sous l'allochtone pindique (série de Tripolitza et série épimétamorphique de Zaroukla) Péloponnèse septentrional, Grèce. Thèse de 3ème cycle, Université de Lille.
- DECELLES, P. G. & CAVAZZA, W. 1999 A comparison of fluvial megafans in the Cordilleran (Upper Cretaceous) and modern Himalayan foreland basin systems. *Geological Society of America Bulletin* **111** (9), 1315–1334.
- DEGNAN, P. J. & ROBERTSON, A. H. F. 1998 Mesozoic-early Tertiary passive margin evolution of the Pindos ocean (NW Peloponnese, Greece). *Sedimentary Geology* **117** (1–2), 33–70.
- DEMOULIN, A., BECKERS, A. & HUBERT-FERRARI, A. 2015 Patterns of Quaternary uplift of the Corinth rift southern border (N Peloponnese, Greece) revealed by fluvial landscape morphometry. *Geomorphology* **246** (1), 188–204.
- DENSMORE, A. L., DAWERS, N. H., GUPTA, S. & GUIDON, R. 2005 What sets topographic relief in extensional footwalls ? *Geology* **33** (6), 453.
- DENSMORE, A. L., DAWERS ; NANCYE, H., SANJEEV, G., ALLEN, P. A. & GILPIN, R. 2003 Landscape evolution at extensional relay zones. *Journal of Geophysical Research* **108** (B5), 2273.
- DENSMORE, A. L., ELLIS, M. A. & ANDERSON, R. S. 1998 Landsliding and the evolution of normal fault-bounded mountains. *Journal of Geophysical Research : Solid Earth*. **103** (B7), 15203–15219.
- DENSMORE, A. L., GUPTA, S., ALLEN, P. A. & DAWERS, N. H. 2007 Transient landscapes at fault tips. *Journal of Geophysical Research* **112** (F3), F03S08.
- DERCOURT, J. 1964 Contribution à l'étude géologique d'un secteur du Péloponnèse septentrional. PhD thesis, Faculté des Sciences de l'Université de Paris.

- DERCOURT, J., FLAMENT, J. M., FLEURY, J. J. & MEILLIEZ, F. 1973 Stratigraphie des couches situées sous les radiolarites de la zone du Pinde-Olonos (Grèce) : le Trias supérieur et le Jurassique inférieur. *Annales Géologiques des Pays Helléniques* **25** (1), 397–406.
- DERRUAU, M. 1965 *Précis de géomorphologie*. Masson & Cie Ed.
- DERRUAU, M. 2010 *Les formes du relief terrestre*. Armand Colin Ed.
- DEWEY, J. F., SENGÖR, A. & CELİL, M. 1979 Aegean and surrounding regions : Complex multiplate and continuum tectonics in a convergent zone. *Geological Society of America Bulletin* **90** (1), 84–92.
- DIESSEL, C. 1992 *Coal-bearing depositional systems*. Springer.
- DOUTSOS, T. & KOKKALAS, S. 2001 Stress and deformation patterns in the Aegean region. *Journal of Structural Geology* **23** (2-3), 455–472.
- DOUTSOS, T., KONTOPOULOS, N. & POULIMENOS, G. 1988 The Corinth-Patras rift as the initial stage of continental fragmentation behind an active island arc (Greece). *Basin Research* **1** (3), 177–190.
- DOUTSOS, T. & PIPER, D. J. W. 1990 Listric faulting, sedimentation, and morphological evolution of the Quaternary eastern Corinth rift, Greece : First stages of continental rifting. *Geological Society of America Bulletin* **102** (6), 812–829.
- DOUTSOS, T. & POULIMENOS, G. 1992 Geometry and kinematics of active faults and their seismotectonic significance in the western Corinth-Patras rift (Greece). *Journal of Structural Geology* **14** (6), 689–699.
- DUBILLE, M. & LAVÉ, J. 2015 Rapid grain size coarsening at sandstone/conglomerate transition : similar expression in Himalayan modern rivers and Pliocene molasse deposits. *Basin Research* **27** (1), 26–42.
- DUFAURE, J. 1975 Le relief du Péloponnèse. PhD thesis, Université Paris IV, France.
- DUFAURE, J.-J., BOUSQUET, B. & PECHOUX, P.-Y. 1979 Contributions de la geomorphologie a la connaissance du Quaternaire continental grec, en relation avec les etudes de neotectonique. *Revue Géologique Dynamique et de Géographie Physique* **21**, 29–40.
- DUFFY, O. B., BROCKLEHURST, S. H., GAWTHORPE, R. L., LEEDER, M. R. & FINCH, E. 2015 Controls on landscape and drainage evolution in regions of distributed normal faulting : Perachora Peninsula, Corinth Rift, Central Greece. *Basin Research* **27** (4), 473–494.
- DULLER, R. A., WHITTAKER, A. C., FEDELE, J. J., WHITCHURCH, A. L., SPRINGETT, J., SMITHELLS, R., FORDYCE, S. & ALLEN, P. A. 2010 From grain size to tectonics. *Journal of Geophysical Research : Earth Surface* **115**, F03022.
- DUNAI, T. J. 2010 *Cosmogenic Nuclides : Principles, Concepts and Applications in the Earth Surface Sciences*. Cambridge University Press.
- DUNLOP, D. J. & ÖZDEMİR, Ö. 2001 *Rock magnetism : fundamentals and frontiers*. Cambridge university press.
- DUTTON, C. E. 1882 The physical geology of the Grand Cañon district. *Second Annual Report of the United States Geological Survey 1880–81*, pp. 49–166. US Government Printing Office.
- EBINGER, C. J., JACKSON, J. A., FOSTER, A. N. & HAYWARD, N. J. 1999 Extensional basin geometry and the elastic lithosphere. *Philosophical Transactions of the Royal Society A : Mathematical, Physical and Engineering Sciences* **357** (1753), 741–765.

BIBLIOGRAPHIE

- ELIET, P. & GAWTHORPE, R. 1995 Drainage development and sediment supply within rifts, examples from the Sperchios basin, central Greece. *Journal of the Geological Society* **152** (5), 883–893.
- ELLIS, DENSMORE & ANDERSON 1999 Development of mountainous topography in the Basin Ranges, USA. *Basin Research* **11** (1), 21–41.
- EMERY, D. & MYERS, K. J. 1996 *Sequence stratigraphy*. Blackwell Science.
- ETHRIDGE, F. G., WOOD, L. J. & SCHUMM, S. A. 1998 Cyclic variables controlling fluvial sequence development : problems and perspectives. *Relative Role of Eustasy Climate and Tectonism in Continental Rock* (ed. K. Shanley & P. McCabe), pp. 17–29. SEPM Special Publication 59.
- FACCENNA, C., JOLIVET, L., PIROMALLO, C. & MORELLI, A. 2003 Subduction and the depth of convection in the Mediterranean mantle. *Journal of Geophysical Research : Solid Earth* **108** (B2), 2099.
- FANG, X., YAN, M., VAN DER VOO, R., REA, D. K., SONG, C., PARÉS, J. M., GAO, J., NIE, J. & DAI, S. 2005 Late Cenozoic deformation and uplift of the NE Tibetan Plateau : Evidence from high-resolution magnetostratigraphy of the Guide Basin, Qinghai Province, China. *Geological Society of America Bulletin* **117** (9), 1208–1225.
- FEDELE, J. J. & PAOLA, C. 2007 Similarity solutions for fluvial sediment fining by selective deposition. *Journal of Geophysical Research* **112** (F2), F02038.
- FEDO, C. M. & MILLER, J. G. 1992 Evolution of a Miocene half-graben basin, Colorado River extensional corridor, southeastern California. *Geological Society of America Bulletin* **104** (4), 481–493.
- FERRILL, D. A. & MORRIS, A. P. 2001 Displacement gradient and deformation in normal fault systems. *Journal of Structural Geology* **23** (4), 619–638.
- FISHER, J. A., KRAPF, C. B. E., LANG, S. C., NICHOLS, G. J. & PAYENBERG, T. H. D. 2008 Sedimentology and architecture of the Douglas Creek terminal splay, Lake Eyre, central Australia. *Sedimentology* **55** (6), 1915–1930.
- FISHER, R. 1953 Dispersion on a Sphere. *Proceedings of the Royal Society A : Mathematical, Physical and Engineering Sciences* **217** (1130), 295–305.
- FISHER, R. V. 1971 Features of coarse-grained, high-concentration fluids and their deposits. *Journal of Sedimentary Research* **41** (1), 916–927.
- FLEMMING, B. W. 1988 Process and pattern of sediment mixing in a microtidal coastal lagoon along the west coast of South Africa. *Tide-influenced sedimentary environments and facies*. (ed. P. L. de Boer, A. Van Gelder & S. Nio), pp. 257–288. Reidel Dordrecht.
- FLEURY, J. J. 1980 Evolution d'une plateforme et d'un bassin dans leur cadre alpin : les zones de Gavrovo-Tripolitze et du Pinde-Olonos. *Société Géologique du Nord, Spécial Publication 4*, , vol. 1, p. 473.
- FLOTTÉ, N., SOREL, D., MÜLLER, C. & TENSI, J. 2005 Along strike changes in the structural evolution over a brittle detachment fault : Example of the Pleistocene Corinth–Patras rift (Greece). *Tectonophysics* **403** (1-4), 77–94.
- FORD, G. L. & PYLES, D. R. 2014 A hierarchical approach for evaluating fluvial systems : Architectural analysis and sequential evolution of the high net-sand content, middle Wasatch Formation, Uinta Basin, Utah. *American Association of Petroleum Geologists Bulletin* **98** (7), 1273–1304.

- FORD, M., HEMELSDAËL, R., MANCINI, M. & PALYVOS, N. 2016 Rift migration and lateral propagation : evolution of normal faults and sediment-routing systems of the western Corinth rift (Greece). *The Geometry and Growth of Normal Faults* (ed. C. Childs, R. E. Holdsworth & C.-L. Jackson). Geological Society, London, Special Publications 439.
- FORD, M., ROHAIS, S., WILLIAMS, E. A., BOURLANGE, S., JOUSSELIN, D., BACKERT, N. & MALARTRE, F. 2013 Tectono sedimentary evolution of the western Corinth rift (Central Greece). *Basin Research* **25** (1), 3–25.
- FORD, M., WILLIAMS, E. A., MALARTRE, F. & POPESCU, S. 2007 Stratigraphic architecture, sedimentology and structure of the Vouraikos Gilbert-type fan delta, Gulf of Corinth, Greece. *Sedimentary processes, environments and basins : A tribute to Peter Friend* (ed. E. Williams, G. Nichols & C. Paola), pp. 49–90. International Association of Sedimentologists, Special Publication 38.
- FOSSEN, H. & ROTEVATN, A. 2016 Fault linkage and relay structures in extensional settings—A review. *Earth-Science Reviews* **154**, 14–28.
- FOSTER, A. N. & JACKSON, J. A. 1998 Source parameters of large African earthquakes : implications for crustal rheology and regional kinematics. *Geophysical Journal International* **134** (2), 422–448.
- VON FREYBERG, B. 1973 Geologie des Isthmus von Korinth. *Junge and Sohn, Universitäts-Buchdruckerei, Erlangen* **95**.
- FRIEDMANN, S. J. & BURBANK, D. W. 1995 Rift basins and supradetachment basins : intracontinental extensional end-members. *Basin Research* **7** (2), 109–127.
- FROSTICK, L. E. & REID, I. 1987 Tectonic control of desert sediments in rift basins ancient and modern. *Desert Sediments : Ancient and Modern* (ed. L. E. Frostick & I. Reid), pp. 53–68. Geological Society, London, Special Publications 35.
- FYTIKAS, M., INNOCENTI, F., MANETTI, P., MAZZUOLI, R. & PECCERILLO, A. 1984 Tertiary to Quaternary evolution of volcanism in the Aegean region. *The Geological Evolution of the Eastern Mediterranean* (ed. J. E. Dixon & A. H. F. Robertson), pp. 687–699. Geological Society, London, Special Publications 17.
- FYTROLAKIS, N. 1971 Die bis heute unbekanntes paläozoischen Schichten Südöstlich von Kalamata. *Bulletin of the Geological Society of Greece* **8**, 70–81.
- GANS, P. B. & MILLER, E. L. 1983 The Snake Range Décollement. *Tectonics* **2** (3), 239–263.
- GAWTHORPE, R. L. & HURST, J. M. 1993 Transfer zones in extensional basins : their structural style and influence on drainage development and stratigraphy. *Journal of the Geological Society* **150** (6), 1137–1152.
- GAWTHORPE, R. L., JACKSON, C., YOUNG, M. J., SHARP, I. R., MOUSTAFA, A. R. & LEPPARD, C. W. 2003 Normal fault growth, displacement localisation and the evolution of normal fault populations : the Hammam Faraun fault block, Suez rift, Egypt. *Journal of Structural Geology* **25** (6), 883–895.
- GAWTHORPE, R. L. & LEEDER, M. R. 2000 Tectono-sedimentary evolution of active extensional basins. *Basin Research* **12** (3-4), 195–218.
- GEDDES, A. 1960 The Alluvial Morphology of the Indo-Gangetic Plain : Its Mapping and Geographical Significance. *Transactions and Papers (Institute of British Geographers)* **28**, 253–276.

BIBLIOGRAPHIE

- GHISSETTI, F. & VEZZANI, L. 2004 Plio–Pleistocene sedimentation and fault segmentation in the Gulf of Corinth (Greece) controlled by inherited structural fabric. *Comptes Rendus Geoscience* **336** (4-5), 243–249.
- GHISSETTI, F. & VEZZANI, L. 2005 Inherited structural controls on normal fault architecture in the Gulf of Corinth (Greece). *Tectonics* **24**, TC4016.
- GIBA, M., WALSH, J. & NICOL, A. 2012 Segmentation and growth of an obliquely reactivated normal fault. *Journal of Structural Geology* **39**, 253–267.
- GIBSON, J., WALSH, J. & WATTERSON, J. 1989 Modelling of bed contours and cross-sections adjacent to planar normal faults. *Journal of Structural Geology* **11** (3), 317–328.
- GILES, P. T., WHITEHOUSE, B. M. & KARYMBALIS, E. 2016 Interactions between alluvial fans and axial rivers in Yukon, Canada and Alaska, USA. *Geology and Geomorphology of Alluvial and Fluvial Fans : Terrestrial and Planetary Perspectives* (ed. D. Ventra & L. E. Clarke). Geological Society, London, Special Publications 440.
- GILLET, S. 1963 Nouvelles données sur le gisement villafranchien de Néa-Corinthos. *Praktika Akadimias Athinon* **40**, 400–419.
- GLOPPEN, T. G. & STEEL, R. 1981 The Deposits, Internal Structure and Geometry in Six Alluvial Fan-Fan Delta Bodies (Devonian-Norway). A Study in the Significance of Bedding Sequence in Conglomerates. *Recent and ancient nonmarine depositional environments, models for exploration* (ed. F. Ethridge & R. Flores), pp. 49–69. Society of Economic Paleontologists and Mineralogists, Special Publication 39.
- GOBO, K., GHINASSI, M., NEMEC, W. & SJURSEN, E. 2014 Development of an incised valley-fill at an evolving rift margin : Pleistocene eustasy and tectonics on the southern side of the Gulf of Corinth, Greece. *Sedimentology* p. in press.
- GOETHALS, M., HETZEL, R., NIEDERMANN, S., WITTMANN, H., FENTON, C., KUBIK, P., CHRISTL, M. & VON BLANCKENBURG, F. 2009 An improved experimental determination of cosmogenic $^{10}\text{Be}/^{21}\text{Ne}$ and $^{26}\text{Al}/^{21}\text{Ne}$ production ratios in quartz. *Earth and Planetary Science Letters* **284** (1-2), 187–198.
- GOLDSWORTHY, M. & JACKSON, J. 2001 Migration of activity within normal fault systems : examples from the Quaternary of mainland Greece. *Journal of Structural Geology* **23** (2-3), 489–506.
- GOLDSWORTHY, M., JACKSON, J. & HAINES, J. 2002 The continuity of active fault systems in Greece. *Geophysical Journal International* **148** (3), 596–618.
- GOSSE, J. C. & PHILLIPS, F. M. 2001 Terrestrial in situ cosmogenic nuclides : theory and application. *Quaternary Science Reviews* **20** (14), 1475–1560.
- GRADSTEIN, F. M., OGG, J. G., SCHMITZ, M. D. & OGG, G. M. 2012 *The geologic time scale 2012*. Elsevier, Oxford.
- GRAMBAST, L. J. 1974 Phylogeny of the Charophyta. *Taxon* pp. 463–481.
- GRANGER, D. E., KIRCHNER, J. W. & FINKEL, R. 1996 Spatially averaged long-term erosion rates measured from in situ-produced cosmogenic nuclides in alluvial sediment. *The Journal of Geology* **104**, 249–257.

- GRANGER, D. E., KIRCHNER, J. W. & FINKEL, R. C. 1997 Quaternary downcutting rate of the New River, Virginia, measured from differential decay of cosmogenic ^{26}Al and ^{10}Be in cave-deposited alluvium. *Geology* **25** (2), 107–110.
- GRANGER, D. E. & MUZIKAR, P. F. 2001 Dating sediment burial with in situ-produced cosmogenic nuclides : theory, techniques, and limitations. *Earth and Planetary Science Letters* **188** (1-2), 269–281.
- GRIFFITHS, P. S. 1980 Box-fault systems and ramps : atypical associations of structures from the eastern shoulder of the Kenya Rift. *Geological Magazine* **117** (6), 579–586.
- GUPTA, S. 1997 Himalayan drainage patterns and the origin of fluvial megafans in the Ganges foreland basin. *Geology* **25** (1), 11–14.
- GUPTA, S. & COWIE, P. A. 2000 Processes and controls in the stratigraphic development of extensional basins. *Basin Research* **12**, 185–194.
- GUPTA, S., COWIE, P. A., DAWERS, N. H. & UNDERHILL, J. R. 1998 A mechanism to explain rift-basin subsidence and stratigraphic patterns through fault-array evolution. *Geology* **26** (7), 595–598.
- GUPTA, S., UNDERHILL, J. R., SHARP, I. R. & GAWTHORPE, R. L. 1999 Role of fault interactions in controlling synrift sediment dispersal patterns : Miocene, Abu Alaqa Group, Suez Rift, Sinai, Egypt. *Basin Research* **11**, 167–189.
- HACK, J. T. 1957 Studies of longitudinal stream profiles in Virginia and Maryland. *U.S. Geological Survey Professional Paper 294B* pp. 1–97.
- HAEUSELMANN, P., GRANGER, D. E., JEANNIN, P.-Y. & LAURITZEN, S.-E. 2007 Abrupt glacial valley incision at 0.8 Ma dated from cave deposits in Switzerland. *Geology* **35** (2), 143–146.
- HAJEK, E. A., HELLER, P. L. & SCHUR, E. L. 2012 Field test of autogenic control on alluvial stratigraphy (Ferris Formation, Upper Cretaceous-Paleogene, Wyoming). *Geological Society of America Bulletin* **124** (11-12), 1898–1912.
- HAJEK, E. A., HELLER, P. L. & SHEETS, B. A. 2010 Significance of channel-belt clustering in alluvial basins. *Geology* **38** (6), 535–538.
- HAMPSON, G. J., DULLER, R. A., PETTER, A. L., ROBINSON, R. A. J. & ALLEN, P. A. 2014 Mass-Balance Constraints On Stratigraphic Interpretation of Linked Alluvial-Coastal-Shelfal Deposits From Source To Sink : Example From Cretaceous Western Interior Basin, Utah and Colorado, U.S.A. *Journal of Sedimentary Research* **84** (11), 935–960.
- HAMPTON, M. A. 1979 Buoyancy in debris flows. *Journal of Sedimentary Research* **49** (3), 753–758.
- HARMS, J., SOUTHARD, J., SPEARING, D. & WALKER, R. 1975 *Depositional environments as interpreted from primary sedimentary structures and stratification sequences*.
- HARTLEY, A. J., WEISSMANN, G. S., NICHOLS, G. J. & SCUDERI, L. A. 2010a Fluvial form in modern continental sedimentary basins : Distributive fluvial systems : REPLY. *Geology* **38** (12), 231.
- HARTLEY, A. J., WEISSMANN, G. S., NICHOLS, G. J. & WARWICK, G. L. 2010b Large Distributive Fluvial Systems : Characteristics, Distribution, and Controls on Development. *Journal of Sedimentary Research* **80** (2), 167–183.
- HARVEY, A. M. 1984 Debris flows and fluvial deposits in Spanish Quaternary alluvial fans : implications for fan morphology. *Sedimentology of gravels and conglomerates* (ed. E. H. Koster & R. J. Steel), pp. 123–132. Canadian Society of Petroleum Geologists, Memoir 10.

BIBLIOGRAPHIE

- HASIOTIS, T., CHARALAMPAKIS, M., STEFATOS, A., PAPTAEODOROU, G. & FERENTINOS, G. 2006 Fan delta development and processes offshore a seasonal river in a seismically active region, NW Gulf of Corinth. *Geo-Marine Letters* **26** (4), 199–211.
- HATZFELD, D., KARAKOSTAS, V., ZIAZIA, M., KASSARAS, I., PAPADIMITRIOU, E., MAKROPOULOS, K., VOULGARIS, N. & PAPAIOANNOU, C. 2000 Microseismicity and faulting geometry in the Gulf of Corinth (Greece). *Geophysical Journal International* **141** (2), 438–456.
- HATZFELD, D., KEMENTZETZIDOU, D., KARAKOSTAS, V., ZIAZIA, M., NOTHARD, S., DIAGOURTAS, D., DESCHAMPS, A., KARAKAISIS, G., PAPADIMITRIOU, P., SCORDILIS, M., SMITH, R., VOULGARIS, N., KIRATZI, S., MAKROPOULOS, M., BOUIN, M. P. & BERNARD, P. 1996 The Galaxidi Earthquake of 18 November 1992 : A possible asperity within the normal fault system of the Gulf of Corinth (Greece). *Bulletin of the Seismological Society of America* **86** (6), 1987–1991.
- HAYDEN, F. V. 1862 Some remarks in regard to the period of elevation of those ranges of the Rocky Mountains near the sources of the Missouri River and its tributaries. *American Journal of Science* **s2-33** (99), 305–313.
- HAYWARD, N. J. & EBINGER, C. J. 1996 Variations in the along axis segmentation of the Afar Rift system. *Tectonics* **15** (2), 244–257.
- HEIN, F. J. 1984 Deep-sea and fluvial braided channel conglomerates : a comparison of two case studies. *Sedimentology of gravels and conglomerates* (ed. E. H. Koster & R. J. Steel), pp. 33–50. Canadian Society of Petroleum Geologists, Memoir 10.
- HEISINGER, B., LAL, D., JULL, A., KUBIK, P., IVY-OCHS, S., KNIE, K. & NOLTE, E. 2002 Production of selected cosmogenic radionuclides by muons : 2. Capture of negative muons. *Earth and Planetary Science Letters* **200** (3-4), 357–369.
- HELLER, P. L., ANGEVINE, C. L., WINSLOW, N. S. & PAOLA, C. 1988 Two-phase stratigraphic model of foreland-basin sequences. *Geology* **16** (6), 501–504.
- HELLER, P. L. & PAOLA, C. 1996 Downstream changes in alluvial architecture ; an exploration of controls on channel-stacking patterns. *Journal of Sedimentary Research* **66** (2), 297–306.
- HEMELSDAËL, R. & FORD, M. 2016 Relay zone evolution : a history of repeated fault propagation and linkage, central Corinth rift, Greece. *Basin Research* **28** (1), 34–56.
- HERBERT, T. D., NG, G. & CLEVELAND PETERSON, L. 2015 Evolution of Mediterranean sea surface temperatures 3.5–1.5 Ma : Regional and hemispheric influences. *Earth and Planetary Science Letters* **409**, 307–318.
- HICKSON, T. A., SHEETS, B. A., PAOLA, C. & KELBERER, M. 2005 Experimental Test of Tectonic Controls on Three-Dimensional Alluvial Facies Architecture. *Journal of Sedimentary Research* **75** (4), 710–722.
- VAN HINSBERGEN, D. J. J., HAFKENSCHIED, E., SPAKMAN, W., MEULENKAMP, J. & WORTEL, R. 2005 Nappe stacking resulting from subduction of oceanic and continental lithosphere below Greece. *Geological Society of America* **33** (4), 325–328.
- VAN HINSBERGEN, D. J. J. & SCHMID, S. M. 2012 Map view restoration of Aegean–West Anatolian accretion and extension since the Eocene. *Tectonics* **31** (5), TC5005.
- HOEY, T. B. & BLUCK, B. J. 1999 Identifying the controls over downstream fining of river gravels. *Journal of Sedimentary Research* **69**, 40–50.

- HOLZ, M., TROCCOLI, E. & VIEIRA, M. 2014 Sequence Stratigraphy of Continental Rift Basins I : A Conceptual Discussion of Discrepant Models. *STRATI 2013* (ed. R. Rocha), pp. 9–13. Springer International Publishing.
- HOPPER, J. R. & BUCK, W. R. 1996 The effect of lower crustal flow on continental extension and passive margin formation. *Journal of Geophysical Research : Solid Earth (1978–2012)* **101** (B9), 20175–20194.
- HORTON, B. K. & DECELLES, P. G. 2001 Modern and ancient fluvial megafans in the foreland basin system of the central Andes, southern Bolivia : implications for drainage network evolution in fold-thrust belts. *Basin Research* **13** (1), 43–63.
- HOUGHTON, S. L., ROBERTS, G. P., PAPANIKOLAOU, I. D., MCARTHUR, J. M. & GILMOUR, M. A. 2003 New 234U-230Th coral dates from the western Gulf of Corinth : Implications for extensional tectonics. *Geophysical Research Letters* **30** (19), 2013.
- HOVIUS, N. 1996 Regular spacing of drainage outlets from linear mountain belts. *Basin Research* **8** (1), 29–44.
- HUBERT-FERRARI, A., SUPPE, J., GONZALEZ-MIERES, R. & WANG, X. 2007 Mechanisms of active folding of the landscape (southern Tian Shan, China). *Journal of Geophysical Research* **112** (B3), B03S09.
- HUERTA, P., ARMENTEROS, I. & SILVA, P. G. 2011 Large-scale architecture in non-marine basins : The response to the interplay between accommodation space and sediment supply. *Sedimentology* **58** (7), 1716–1736.
- HUGGINS, P., WATTERSON, J., WALSH, J. & CHILDS, C. 1995 Relay zone geometry and displacement transfer between normal faults recorded in coal-mine plans. *Journal of Structural Geology* **17** (12), 1741–1755.
- HUISMANS, R. S. 2003 Symmetric and asymmetric lithospheric extension : Relative effects of frictional-plastic and viscous strain softening. *Journal of Geophysical Research* **108** (B10), 2496.
- HUISMANS, R. S. & BEAUMONT, C. 2007 Roles of lithospheric strain softening and heterogeneity in determining the geometry of rifts and continental margins. *Imaging, Mapping and Modelling Continental Lithosphere Extension and Breakup* (ed. G. D. Karner, G. Manatschal & L. M. Pinheiro), pp. 111–138. Geological Society, London, Special Publications 282.
- HUS, R., ACOCELLA, V., FUNICIELLO, R. & DEBATIST, M. 2005 Sandbox models of relay ramp structure and evolution. *Journal of Structural Geology* **27**, 459–473.
- JACKSON, C. A. L., GAWTHORPE, R. L. & SHARP, I. R. 2006 Style and sequence of deformation during extensional fault-propagation folding : examples from the Hammam Faraun and El-Qaa fault blocks, Suez Rift, Egypt. *Journal of Structural Geology* **28** (3), 519–535.
- JACKSON, J. & MCKENZIE, D. 1983 The geometrical evolution of normal fault systems. *Journal of Structural Geology* **5** (5), 471–482.
- JACKSON, J. & MCKENZIE, D. 1984 Active tectonics of the Alpine—Himalayan Belt between western Turkey and Pakistan. *Geophysical Journal International* **77** (1), 185–264.
- JACKSON, J. & MCKENZIE, D. 1988 The relationship between plate motions and seismic moment tensors, and the rates of active deformation in the Mediterranean and Middle East. *Geophysical Journal International* **93** (1), 45–73.

BIBLIOGRAPHIE

- JACKSON, J., NORRIS, R. & YOUNGSON, J. 1996 The structural evolution of active fault and fold systems in central Otago, New Zealand : evidence revealed by drainage patterns. *Journal of Structural Geology* **18** (2-3), 217–234.
- JACKSON, J. & WHITE, N. 1989 Normal faulting in the upper continental crust : observations from regions of active extension. *Journal of Structural Geology* **11** (1-2), 15–36.
- JACKSON, J. A., GAGNEPAIN, J., HOUSEMAN, G., KING, G. C. P., PAPADIMITRIOU, P., SOUFLERIS, C. & VIRIEUX, J. 1982 Seismicity, normal faulting, and the geomorphological development of the Gulf of Corinth (Greece) : the Corinth earthquakes of February and March 1981. *Earth and Planetary Science Letters* **57**, 377–397.
- JACOBSHAGEN, V. 1987 *Geologie von Griechenland*. Berlin : Gebruder Borntraeger.
- JACOBSHAGEN, V., DÜRR, S., KOCKEL, F., KOPP, K. O., KOWALCZYK, G., BERCKHEMER, H. & BÜTTNER, D. 1978 Structure and geodynamic evolution of the Aegean region. *Alps, Apennines, Hellenides* (ed. H. Closs, D. Roeder & K. Schmidt), pp. 537–654. Nägele and Obermiller, Stuttgart.
- JERVEY, M. T. 1988 Quantitative geological modelling of siliclastic rock sequences and their seismic expression. *Sea-Level Changes : An Integrated Approach* (ed. C. K. Wilgus, B. S. Hastings, C. G. S. C. Kendall, H. W. Posamentier, C. A. Ross & J. C. Van Wagoner), pp. 47–69. Society of Economic Paleontology and Mineralogy, Special Publication 42.
- JOHANNESSEN, P. N. & ANDSBJERG, J. 1993 Middle to Late Jurassic basin evolution and sandstone reservoir distribution in the Danish Central Trough. *Petroleum Geology of Northwest Europe : Proceedings of the 4th Conference*, pp. 271–283. Geological Society of London.
- JOHANNESSEN, P. N., DYBKJAER, K. & RASMUSSEN, E. S. 1996 Sequence stratigraphy of Upper Jurassic reservoir sandstones in the northern part of the Danish Central Trough, North Sea. *Marine and Petroleum Geology* **13** (7), 755–770.
- JOHNSON, N. M., OPDYKE, N. D. & LINDSAY, E. H. 1975 Magnetic Polarity Stratigraphy of Pliocene-Pleistocene Terrestrial Deposits and Vertebrate Faunas, San Pedro Valley, Arizona. *Geological Society of America Bulletin* **86** (1), 5–12.
- JOLIVET, L. 2001 A comparison of geodetic and finite strain pattern in the Aegean, geodynamic implications. *Earth and Planetary Science Letters* **187** (1-2), 95–104.
- JOLIVET, L. & BRUN, J.-P. 2008 Cenozoic geodynamic evolution of the Aegean. *International Journal of Earth Sciences* **99** (1), 109–138.
- JOLIVET, L., DANIEL, J., TRUFFERT, C. & GOFFÉ, B. 1994 Exhumation of deep crustal metamorphic rocks and crustal extension in arc and back-arc regions. *Lithos* **33** (1-3), 3–30.
- JOLIVET, L. & FACCENNA, C. 2000 Mediterranean extension and the Africa-Eurasia collision. *Tectonics* **19** (6), 1095–1106.
- JOLIVET, L., FACCENNA, C., HUET, B., LABROUSSE, L., LE POURHIET, L., LACOMBE, O., LECOMTE, E., BUROV, E., DENÈLE, Y., BRUN, J.-P., PHILIPPON, M., PAUL, A., SALAÜN, G., KARABULUT, H., PIROMALLO, C., MONIÉ, P., GUEYDAN, F., OKAY, A. I., OBERHÄNSLI, R., POURTEAU, A., AUGIER, R., GADENNE, L. & DRIUSSI, O. 2013 Aegean tectonics : Strain localisation, slab tearing and trench retreat. *Tectonophysics* **597–598**, 1–33.

- JOLIVET, L., FAMIN, V., MEHL, C., PARRA, T., AUBOURG, C., HÉBERT, R. & PHILIPPOT, P. 2004 Progressive strain localisation, boudinage and extensional metamorphic complexes, the Aegean Sea Case, in Whitney DL, Teyssier C. and Siddoway CS, Gneiss domes in orogeny : Boulder, Colorado. *Geological Society of America Special Paper* **380**, 185–210.
- JOLIVET, L., LABROUSSE, L., AGARD, P., LACOMBE, O., BAILLY, V., LECOMTE, E., MOUTHEREAU, F. & MEHL, C. 2010 Rifting and shallow-dipping detachments, clues from the Corinth Rift and the Aegean. *Tectonophysics* **483** (3-4), 287–304.
- JOLIVET, L. & PATRIAT, M. 1999 Ductile extension and the formation of the Aegean Sea. *Geological Society, London, Special Publications* **156** (1), 427–456.
- JOLLY, R. J. H. & LONERGAN, L. 2002 Mechanisms and controls on the formation of sand intrusions. *Journal of the Geological Society* **159** (5), 605–617.
- KAPETANIDIS, V., DESCHAMPS, A., PAPADIMITRIOU, P., MATRULLO, E., KARAKONSTANTIS, A., BOZIOELOS, G., KAVIRIS, G., SERPETSIDAKI, A., LYON-CAEN, H., VOULGARIS, N., BERNARD, P., SOKOS, E. & MAKROPOULOS, K. 2015 The 2013 earthquake swarm in Helike, Greece : seismic activity at the root of old normal faults. *Geophysical Journal International* **202** (3), 2044–2073.
- KELLY, S. B. & OLSEN, H. 1993 Terminal fans - a review with reference to Devonian examples. *Sedimentary Geology* **85** (1-4), 339–374.
- KERAUDREN, B. 1975 Essai de stratigraphie et de paleogeographie du Plio-Pleistocene egeen. *Bulletin de la Societe Geologique de France* **S7-XVII** (6), 1110–1120.
- KERAUDREN, B. 1979 Le Plio-Pléistocène marin et oligohalin en Grèce : stratigraphie et paléogéographie. *Revue de Géologie Dynamique et de Géographie Physique* **21** (1), 17–28.
- KERAUDREN, B. & SOREL, D. 1987 The terraces of Corinth (Greece) — A detailed record of eustatic sea-level variations during the last 500,000 years. *Marine Geology* **77** (1–2), 99–107.
- KILLOPS, S. & KILLOPS, V. 2005 *Introduction to Organic Geochemistry*. Blackwell Publishing.
- KIM, W., CONNELL, S. D., STEEL, E., SMITH, G. A. & PAOLA, C. 2011 Mass-balance control on the interaction of axial and transverse channel systems. *Geology* **39** (7), 611–614.
- KIM, W. & PAOLA, C. 2007 Long-period cyclic sedimentation with constant tectonic forcing in an experimental relay ramp. *Geology* **35** (4), 331–334.
- KIM, Y.-S. & SANDERSON, D. J. 2005 The relationship between displacement and length of faults : a review. *Earth-Science Reviews* **68** (3-4), 317–334.
- KIM, Y.-S. & SANDERSON, D. J. 2010 Inferred fluid flow through fault damage zones based on the observation of stalactites in carbonate caves. *Journal of Structural Geology* **32** (9), 1305–1316.
- KIRSCHVINK, J. L. 1980 The least-squares line and plane and the analysis of palaeomagnetic data. *Geophysical Journal International* **62** (3), 699–718.
- KLEIN, J., GIEGENGACK, R., MIDDLETON, R., SHARMA, P. T., UNDERWOOD, J. R. & WEEKS, R. A. 1986 Revealing histories of exposure using in situ produced ²⁶Al and ¹⁰Be in Libyan desert glass. *Radiocarbon* **28** (2A), 547–555.
- KNAUST, D. & BROMLEY, R. G. 2012 *Trace fossils as indicators of sedimentary environments*. Elsevier.

BIBLIOGRAPHIE

- KOHL, C. & NISHIZUMI, K. 1992 Chemical isolation of quartz for measurement of in-situ -produced cosmogenic nuclides. *Geochimica et Cosmochimica Acta* **56** (9), 3583–3587.
- KOOI, H. & BEAUMONT, C. 1994 Escarpment evolution on high-elevation rifted margins : Insights derived from a surface processes model that combines diffusion, advection, and reaction. *Journal of Geophysical Research : Solid Earth* **99** (B6), 12191–12209.
- KOPP, J. & KIM, W. 2015 The effect of lateral tectonic tilting on fluviodeltaic surficial and stratal asymmetries : experiment and theory. *Basin Research* **27** (4), 517–530.
- KORSCHINEK, G., BERGMAIER, A., FAESTERMANN, T., GERSTMANN, U., KNIE, K., RUGEL, G., WALLNER, A., DILLMANN, I., DOLLINGER, G., VON GOSTOMSKI, C. L., KOSSERT, K., MAITI, M., POUTIVTSEV, M. & REMMERT, A. 2010 A new value for the half-life of ^{10}Be by Heavy-Ion Elastic Recoil Detection and liquid scintillation counting. *Nuclear Instruments and Methods in Physics Research Section B : Beam Interactions with Materials and Atoms* **268** (2), 187–191.
- KOSKERIDOU, E. & IOAKIN, C. 2009 An early Pleistocene mollusc fauna with Pono-Caspian elements in intra-Hellenic Basin of Atlanti, Arkitsa region (Central Greece). *9th Symposium on Oceanography and Fisheries*, pp. 96–101.
- KOSTER, E. H. 1987 Vertebrate taphonomy applied to the analysis of ancient fluvial systems. *Recent Developments in Fluvial Sedimentology* (ed. F. G. Ethridge, R. M. Flores & M. D. Havey), pp. 159–168. SEPM Special Publication 39.
- KOUKOZAS, C. N. 1978 Greek coal : Potential, exploration and future. *Minutes of Technical Chamber of Greece* **3**, 158–166.
- KRAUS, M. J. 2002 Basin-Scale Changes in Floodplain Paleosols : Implications for Interpreting Alluvial Architecture. *Journal of Sedimentary Research* **72** (4), 500–509.
- KREUSER, T., WOPFNER, H., KAAYA, C. Z., MARKWORT, S., SEMKIWA, P. M. & ASLANDIS, P. 1990 Depositional evolution of Permo-Triassic Karoo basins in Tanzania with reference to their economic potential. *Journal of African Earth Sciences (and the Middle East)* **10**, 151–167.
- KRUSE, S. E., LIU, Z. J., NAAR, D. F. & DUNCAN, R. A. 1997 Effective elastic thickness of the lithosphere along the Easter Seamount Chain **102** (B12), 27305–27317.
- KU, T.-L. & LIANG, Z.-C. 1984 The dating of impure carbonates with decay-series isotopes. *Nuclear Instruments and Methods in Physics Research* **223** (2–3), 563–571.
- KUMAR, R. 1993 Coalescence megafan : multistorey sandstone complex of the late-orogenic (Mio-Pliocene) sub-Himalayan belt, Dehra Dun, India. *Sedimentary Geology* **85** (1-4), 327–337.
- LAL, D. 1988 In situ-produced cosmogenic isotopes in terrestrial rocks. *Annual Review of Earth and Planetary Sciences* **16**, 355–388.
- LAL, D. 1991 Cosmic ray labeling of erosion surfaces : in situ nuclide production rates and erosion models. *Earth and Planetary Science Letters* **104** (2–4), 424–439.
- LALLEMANT, S. 1984 La transversale nord-maniote : étude géologique et aéromagnétique d'une structure transverse à l'arc égéen externe. PhD thesis, Thèse de troisième cycle, Université Pierre et Marie Curie, Paris, France.

- LAMBIASE, J. & BOSWORTH, W. 1995 Structural controls on sedimentation in continental rifts. *Hydrocarbon Habitat in Rift Basins* (ed. J. Lambiase), pp. 117–144. Geological Society, London, Special Publications 80.
- LAMBIASE, J. J. 1990 A Model for Tectonic Control of Lacustrine Stratigraphic Sequences in Continental Rift Basins. *Lacustrine basin exploration : case studies and modern analogs* (ed. B. J. Katz), pp. 265–276. American Association of Petroleum Geologists, Memoir 50.
- LAMBOTTE, S., LYON-CAEN, H., BERNARD, P., DESCHAMPS, A., PATAU, G., NERCESSIAN, A., PACCHIANI, F., BOUROUIS, S., DRILLEAU, M. & ADAMOVA, P. 2014 Reassessment of the rifting process in the Western Corinth Rift from relocated seismicity. *Geophysical Journal International* **197**, 1822–1844.
- LAVIER, L. L. & STECKLER, M. S. 1997 The effect of sedimentary cover on the flexural strength of continental lithosphere. *Nature* **389** (6650), 476–479.
- LAWRENCE, D. A. & WILLIAMS, B. P. J. 1987 Evolution of drainage systems in response to Acadian deformation : the Devonian Battery Point Formation, eastern Canada. *Recent developments in fluvial sedimentology* (ed. F. G. Ethridge, R. M. Flores & M. D. Harvey), pp. 287–300. SEPM Special Publication 39.
- LE PICHON, X. & ANGELIER, J. 1979 The Hellenic arc and trench system : a key to the neotectonic evolution of the eastern Mediterranean area. *Tectonophysics* **60**, 1–42.
- LE PICHON, X. & ANGELIER, J. 1981 The Aegean Sea. *Philosophical Transactions of the Royal Society of London* **300**, 357–372.
- LE PICHON, X., CHAMOT-ROOKE, N., LALLEMANT, S., NOOMEN, R. & VEIS, G. 1995 Geodetic determination of the kinematics of central Greece with respect to Europe : Implications for eastern Mediterranean tectonics. *Journal of Geophysical Research : Solid Earth* **100**, 12675–12690.
- LE PICHON, X., CHAMOT-ROOKE, N., RANGIN, C. & SENGÖR, A. M. C. 2003 The North Anatolian fault in the Sea of Marmara. *Journal of Geophysical Research : Solid Earth* **108** (B4), 2149.
- LE PICHON, X., LALLEMANT, S., CHAMOT-ROOKE, N., LEMEUR, D. & PASCAL, G. 2002 The Mediterranean Ridge backstop and the Hellenic nappes. *Marine Geology* **186** (1-2), 111–125.
- LE POURHIET, L., BUROV, E. & MORETTI, I. 2003 Initial crustal thickness geometry controls on the extension in a back arc domain : Case of the Gulf of Corinth. *Tectonics* **22** (4), n/a–n/a.
- LE POURHIET, L., BUROV, E. & MORETTI, I. 2004 Rifting through a stack of inhomogeneous thrusts (the dipping pie concept). *Tectonics* **23** (4), TC4005.
- LE POURHIET, L., MATTIONI, L. & MORETTI, I. 2006 3D modelling of rifting through a pre-existing stack of nappes in the Gulf of Corinth (Greece) : a mixed analogue/numerical approach. *Geological Society, London, Special Publications* (ed. S. J. H. Buiter & G. Schreurs), pp. 233–252. Geological Society, London, Special Publications 253.
- LEEDER, M. & MACK, G. 2007 Basin-fill incision, Rio Grande and Gulf of Corinth rifts : Convergent response to climatic and tectonic drivers. *Sedimentary Processes, Environments and Basins : A Tribute to Peter Friend* (ed. G. Nichols, E. Williams & C. Paola), pp. 9–27. International Association of Sedimentologists, Special Publication 38.

BIBLIOGRAPHIE

- LEEDER, M., MACK, G., BRASIER, A., PARRISH, R., MCINTOSH, W., ANDREWS, J. & DUERMEIJER, C. 2008 Late-Pliocene timing of Corinth (Greece) rift-margin fault migration. *Earth and Planetary Science Letters* **274** (1-2), 132–141.
- LEEDER, M., SEGER, M. J. & STARK, C. P. 1991 Sedimentation and tectonic geomorphology adjacent to major active and inactive normal faults, southern Greece. *Journal of the Geological Society* **148** (2), 331–343.
- LEEDER, M. R. 1978 A quantitative stratigraphic model for alluvium, with special reference to channel deposit density and interconnectedness. *Fluvial sedimentology* (ed. A. Miall), pp. 587–596. Canadian Society of Petroleum Geology, Calgary, Memoir 5.
- LEEDER, M. R. 1993 Tectonic controls upon drainage basin development, river channel migration and alluvial architecture : implications for hydrocarbon reservoir development and characterization. *Characterization of fluvial and aeolian reservoirs* (ed. C. P. North & D. J. Prosser), pp. 7–22. Geological Society, London, Special Publications 73.
- LEEDER, M. R. & ALEXANDER, J. 1987 The origin and tectonic significance of asymmetrical meanderbelts. *Sedimentology* **34** (2), 217–226.
- LEEDER, M. R. & GAWTHORPE, R. L. 1987 Sedimentary models for extensional tilt-block/half-graben basins. *Continental Extensional Tectonics* (ed. M. P. Coward, J. F. Dewey & P. L. Hancock), pp. 139–152. Geological Society, London, Special Publications 28.
- LEEDER, M. R. & MACK, G. H. 2001 Lateral erosion ('toe-cutting') of alluvial fans by axial rivers : implications for basin analysis and architecture. *Journal of the Geological Society* **158** (6), 885–893.
- LEEDER, M. R., MACK, G. H., PEAKALL, J. & SALYARDS, S. L. 1996 First quantitative test of alluvial stratigraphic models : Southern Rio Grande rift, New Mexico. *Geology* **24** (1), 87–90.
- LEEDER, M. R., MARK, D. F., GAWTHORPE, R. L., KRANIS, H., LOVELESS, S., PEDENTCHOUK, N., SKOURTSOS, E., TURNER, J., ANDREWS, J. E. & STAMATAKIS, M. 2012 A "Great Deepening" : Chronology of rift climax, Corinth rift, Greece. *Geology* **40** (11), 999–1002.
- LEEDER, M. R., MCNEILL, L., COLLIER, R., PORTMAN, C., ROWE, P., ANDREWS, J. & GAWTHORPE, R. 2003 Corinth rift margin uplift : New evidence from Late Quaternary marine shorelines. *Geophysical Research Letters* **30** (12), 1611.
- LEGARRETA, L. 1998 Anatomy of hinterland depositional sequences : Upper Cretaceous fluvial strata, Neuquen Basin, west-central Argentina. *Relative Role of Eustasy, Climate and Tectonism in Continental Rocks* (ed. K. W. Shanley & P. J. McCabe), pp. 83–92. Society of Economic Paleontology and Mineralogy, Special Publication 59.
- LEIER, A. L., DECELLES, P. G. & PELLETIER, J. D. 2005 Mountains, monsoons, and megafans. *Geology* **33** (4), 289.
- LI, Y., JIA, D., PLESCH, A., HUBBARD, J., SHAW, J. H. & WANG, M. 2013 3-D geomechanical restoration and paleomagnetic analysis of fault-related folds : An example from the Yanjinggou anticline, southern Sichuan Basin. *Journal of Structural Geology* **54**, 199–214.
- LIFTON, N., SATO, T. & DUNAI, T. J. 2014 Scaling in situ cosmogenic nuclide production rates using analytical approximations to atmospheric cosmic-ray fluxes. *Earth and Planetary Science Letters* **386**, 149–160.

- LINDSAY, E. H., BUTLER, R. F. & JOHNSON, N. M. 1981 Magnetic polarity zonation and biostratigraphy of Late Cretaceous and Paleocene continental deposits, San Juan Basin, New Mexico. *American Journal of Science* **281** (4), 390–435.
- LISTER, G. S. & DAVIS, G. A. 1989 The origin of metamorphic core complexes and detachment faults formed during Tertiary continental extension in the northern Colorado River region, U.S.A. *Journal of Structural Geology* **11** (1–2), 65–94.
- LONG, J. J. & IMBER, J. 2012 Strain compatibility and fault linkage in relay zones on normal faults. *Journal of Structural Geology* **36**, 16–26.
- LONGHITANO, S. G. 2008 Sedimentary facies and sequence stratigraphy of coarse-grained Gilbert-type deltas within the Pliocene thrust-top Potenza Basin (Southern Apennines, Italy). *Sedimentary Geology* **210** (3), 87–110.
- LOURENS, L., HILGEN, F., SHACKLETON, N., LASKAR, J. & WILSON, D. 2004 The Neogene Period. A *Geological Time Scale* (ed. F. Gradstein, J. Ogg & A. Smith), pp. 409–440. Cambridge University Press.
- LYKOUSIS, V., SAKELLARIOU, D., MORETTI, I. & KABERI, H. 2007 Late Quaternary basin evolution of the Gulf of Corinth : Sequence stratigraphy, sedimentation, fault-slip and subsidence rates. *Tectonophysics* **440** (1–4), 29–51.
- LYKOUSIS, V., SAKELLARIOU, D. & PAPANIKOLAOU, D. 1998 Sequence stratigraphy in the northern margin of the Gulf of Corinth : implications to upper Quaternary basin evolution. *Bulletin of the Geological Society of Greece* **32** (2), 157–165.
- LYON-CAEN, H., PAPADIMITRIOU, P., DESCHAMPS, A., BERNARD, P., MAKROPOULOS, K., PACCHIANI, F. & PATAU, G. 2004 First results of the CRLN seismic network in the western Corinth Rift : evidence for old-fault reactivation. *Comptes Rendus Geoscience* **336** (4–5), 343–351.
- MACK, G. H. 2002 Temporal and spatial variability of alluvial-fan and axial-fluvial sedimentation in the Plio-Pleistocene Palomas half graben, southern Rio Grande rift, New Mexico, USA. *Sedimentation in continental rifts* (ed. G. Ashley), pp. 539–545. Society of Economic Paleontology and Mineralogy, Special Publication 73.
- MACK, G. H. & LEEDER, M. R. 1999 Climatic and tectonic controls on alluvial-fan and axial-fluvial sedimentation in the Plio-Pleistocene Palomas half graben, southern Rio Grande Rift. *Journal of Sedimentary Research* **69** (3), 635–652.
- MACK, G. H., SALYARDS, S. L. & JAMES, W. C. 1993 Magnetostratigraphy of the Plio-Pleistocene Camp Rice and Palomas Formations in the Rio Grande rift of the southern New Mexico. *American Journal of Science* **293**, 49–77.
- MACK, G. H. & SEAGER, W. R. 1990 Tectonic control on facies distribution of the Camp Rice and Palomas Formations (Pliocene-Pleistocene) in the southern Rio Grande rift. *Geological Society of America Bulletin* **102** (1), 45–53.
- MACKEY, S. D. & BRIDGE, J. S. 1995 Three-dimensional model of alluvial stratigraphy : theory and application. *Journal of Sedimentary Research* **65** (1), 7–31.
- MÄDLER, K. & STAECHE, U. 1979 Fossile Charophyten aus dem Känozoikum (Tertiär und Quartär) der Türkei. (Känozoikum und Braunkohlender Türkei, 19). *Geologisches Jahrbuch* **33** (B), 82–157.
- MAKRIS, J. 1978 The crust and upper mantle of the Aegean region from deep seismic soundings. *Tectonophysics* **46** (3–4), 269–284.

BIBLIOGRAPHIE

- MALARTRE, F., FORD, M. & WILLIAMS, E. A. 2004 Preliminary biostratigraphy and 3D geometry of the Vouraikos Gilbert-type fan delta, Gulf of Corinth, Greece. *Comptes Rendus Geoscience* **336** (4-5), 269–280.
- MANIATIS, G., KURFESS, D., HAMPEL, A. & HEIDBACH, O. 2009 Slip acceleration on normal faults due to erosion and sedimentation — Results from a new three-dimensional numerical model coupling tectonics and landscape evolution. *Earth and Planetary Science Letters* **284** (3-4), 570–582.
- MANIGHETTI, I., KING, G. & GAUDEMER, Y. 2001 Slip accumulation and lateral propagation of active normal faults in Afar. *Journal of Geophysical Research* **106** (B7), 13,667–13,696.
- MANSFIELD, C. & CARTWRIGHT, J. 2001 Fault growth by linkage : observations and implications from analogue models. *Journal of Structural Geology* **23** (5), 745–763.
- MARR, J. G., SWENSON, J. B., PAOLA, C. & VOLLER, V. R. 2000 A two diffusion model of fluvial stratigraphy in closed depositional basins. *Basin Research* **12** (3 4), 381–398.
- MARTEL, A. T. & GIBLING, M. R. 1991 Wave-dominated lacustrine facies and tectonically controlled cyclicity in the Lower Carboniferous Horton Bluff Formation, Nova Scotia, Canada. *Lacustrine Facies Analysis* (ed. L. Anadon & K. Kelts), pp. 223–243. International Association of Sedimentologists, Special Publication 13.
- MARTHALER, M. 2001 *Le Cervin est-il africain ?*. LEP Ed.
- MARTINS-NETO, M. & CATUNEANU, O. 2010 Rift sequence stratigraphy. *Marine and Petroleum Geology* **27** (1), 247–253.
- MARZO, M., NIJMAN, W. & PUIGDEFABREGAS, C. 1988 Architecture of the Castissent fluvial sheet sandstones, Eocene, south Pyrenees, Spain. *Sedimentology* **35** (5), 719–738.
- MATTEI, M., D'AGOSTINO, N., ZANANIRI, I., KONDOPOULOU, D., PAVLIDES, S. & SPATHARAS, V. 2004 Tectonic evolution of fault-bounded continental blocks : Comparison of paleomagnetic and GPS data in the Corinth and Megara basins (Greece). *Journal of Geophysical Research : Solid Earth* **109** (B2), B02106.
- MAZZANTI, R. & TREVISAN, L. 1978 Evoluzione della rete idrografica nell'Appennino centro-settentrionale. *Geografia Fisica e Dinamica Quaternaria* **1** (8), 55–62.
- MCCABE, P. J. 1984 Depositional environments of coal and coal bearing strata. *Sedimentology of coal and coal-bearing sequences* (ed. R. A. Rahmani & R. M. Flores), pp. 13–42. International Association of Sedimentologists, Special Publications 7.
- MCCARTHY, T. S. 2002 The Okavango Delta—semiarid alluvial-fan sedimentation related to incipient rifting. *Sedimentation in continental rifts* (ed. S. Renaut & G. Ashley), pp. 179–193. SEPM Special Publication 73.
- MCCCLUSKY, S., BALASSANIAN, S., BARKA, A., DEMIR, C., ERGINTAV, S., GEORGIEV, I., GURKAN, O., HAMBURGER, M., HURST, K., KAHLE, H., KASTENS, K., KEKELIDZE, G., KING, R., KOTZEV, V., LENK, O., MAHMOUD, S., MISHIN, A., NADARIYA, M., OUZOUNIS, A., PARADISSIS, D., PETER, Y., PRILEPIN, M., REILINGER, R., SANLI, I., SEEGER, H., TEALEB, A., TOKSÖZ, M. N. & VEIS, G. 2000 Global Positioning System constraints on plate kinematics and dynamics in the eastern Mediterranean and Caucasus. *Journal of Geophysical Research : Solid Earth* **105** (B3), 5695–5719.
- MCELHINNY, M. W. 1964 Statistical significance of the fold test in palaeomagnetism. *Geophysical Journal International* **8** (3), 338–340.

- MCFADDEN, P. L. 1990 A new fold test for palaeomagnetic studies. *Geophysical Journal International* **103** (1), 163–169.
- MCKENZIE, D. 1972 Active tectonics of the Mediterranean region. *Geophysical Journal International* **30** (2), 109–185.
- MCKENZIE, D. 1978a Active tectonics of the Alpine-Himalayan belt : the Aegean Sea and surrounding regions. *Geophysical Journal International* **55** (1), 217–254.
- MCKENZIE, D. 1978b Some remarks on the formation of sedimentary basins. *Earth and Planetary Science Letters* **40**, 25–32.
- MCKENZIE, D. & JACKSON, J. 1983 The relationship between strain rates, crustal thickening, palaeomagnetism, finite strain and fault movements within a deforming zone. *Earth and Planetary Science Letters* **65** (1), 182–202.
- MCLEOD, A. E., DAWERS, N. H. & UNDERHILL, J. R. 2000 The propagation and linkage of normal faults : insights from the Strathspey-Brent-Statfjord fault array, northern North Sea. *Basin Research* **12**, 263–284.
- MCMURRAY, L. S. & GAWTHORPE, R. L. 2000 Along-strike variability of forced regressive deposits : late Quaternary, northern Peloponnesos, Greece. *Geological Society, London, Special Publications* **172** (1), 363–377.
- MCNEILL, L. & COLLIER, R. 2004 Uplift and slip rates of the eastern Eliki fault segment, Gulf of Corinth, Greece, inferred from Holocene and Pleistocene terraces. *Journal of the Geological Society* **161** (1), 81–92.
- MCNEILL, L., COTTERILL, C., HENSTOCK, T., BULL, J., STEFATOS, A., COLLIER, R., PAPANTHEODEROU, G., FERENTINOS, G. & HICKS, S. 2005 Active faulting within the offshore western Gulf of Corinth, Greece : Implications for models of continental rift deformation. *Geology* **33** (4), 241.
- MEDICI, G., BOULESTEIX, K., MOUNTNEY, N. P., WEST, L. J. & ODLING, N. E. 2015 Palaeoenvironment of braided fluvial systems in different tectonic realms of the Triassic Sherwood Sandstone Group, UK. *Sedimentary Geology* **329** (1), 188–210.
- MEDLICOTT, H. B. 1864 On the geological structure and relations of the southern portion of the Himalayan range between the rivers Ganges and Ravee. *Memoir of the Geological Survey of India* **3** (2), 1–206.
- MELCHOR, R. N. 2007 Changing lake dynamics and sequence stratigraphy of synrift lacustrine strata in a half-graben : an example from the Triassic Ischigualasto–Villa Unión Basin, Argentina. *Sedimentology* **54** (6), 1417–1446.
- MELIS, N. S., BROOKS, M. & PEARCE, R. G. 1989 A microearthquake study in the Gulf of Patras region, western Greece, and its seismotectonic interpretation. *Geophysical Journal International* **98** (3), 515–524.
- MEULENKAMP, J. E., WORTEL, M. J. R., VAN WAMEL, W. A., SPAKMAN, W. & HOOGERDUYN STRATING, E. 1988 On the Hellenic subduction zone and the geodynamic evolution of Crete since the late Middle Miocene. *Tectonophysics* **146** (1–4), 203–215.
- MEULENKAMP, J. E., VAN DER ZWAAN, G. J. & VAN WAMEL, W. A. 1994 On late Miocene to recent vertical motions in the Cretan segment of the Hellenic arc. *Tectonophysics* **234** (1–2), 53–72.

BIBLIOGRAPHIE

- MEYER, V., NICOL, A., CHILDS, C., WALSH, J. & WATTERSON, J. 2002 Progressive localisation of strain during the evolution of a normal fault population. *Journal of Structural Geology* **24** (1), 1215–1231.
- MIALL 2013 *Fluvial depositional systems*. Springer Ed.
- MIALL, A. D. 1996 *The geology of fluvial deposits : Sedimentary facies, basin analysis and Petroleum Geology*. Springer Verlag Berlin.
- MIALL, A. D. 2010 *The geology of stratigraphic sequences*. Springer Ed.
- MOHAMMED, M., PATON, D., COLLIER, R. E. L., HODGSON, N. & NEGONGA, M. 2016 Interaction of crustal heterogeneity and lithospheric processes in determining passive margin architecture on the southern Namibian margin. *Petroleum Geoscience of the West Africa Margin* (ed. T. Sabato Ceraldi, R. A. Hodgkinson & G. Backe). Geological Society, London, Special Publications 438.
- MORETTI, I., SAKELLARIOU, D., LYKOUSIS, V. & MICARELLI, L. 2003 The Gulf of Corinth : an active half graben ? *Journal of Geodynamics* **36** (1-2), 323–340.
- MOREWOOD, N. C. & ROBERTS, G. P. 1999 Lateral propagation of the surface trace of the South Alkyonides normal fault segment, central Greece : its impact on models of fault growth and displacement–length relationships. *Journal of Structural Geology* **21** (6), 635–652.
- MORGAN, P., SEAGER, W. R. & GOLOMBEK, M. P. 1986 Cenozoic thermal, mechanical and tectonic evolution of the Rio Grande Rift. *Journal of Geophysical Research* **91** (B6), 6263.
- MORLEY, C. 1994 Interaction of deep and shallow processes in the evolution of the Kenya rift. *Tectonophysics* **236** (1-4), 81–91.
- MORLEY, C. K. 1989 Extension, detachments, and sedimentation in continental rifts (with particular reference to East Africa). *Tectonics* **8** (6), 1175–1192.
- MORLEY, C. K. 1999 How successful are analogue models in addressing the influence of pre-existing fabrics on rift structure ? *Journal of Structural Geology* **21** (8-9), 1267–1274.
- MORLEY, C. K. 2002 Evolution of large normal faults : Evidence from seismic reflection data. *American Association of Petroleum Geologists Bulletin* **6** (6), 961–978.
- MORLEY, C. K., NELSON, R., PLATTON, T. & MUNN, S. 1990 Transfer zones in the East African rift system and their relevance to hydrocarbon exploration in rifts. *The American Association of Petroleum Geologists Bulletin* **74** (8), 1234–1253.
- MORLEY, C. K. & WONGANAN, N. 2000 Normal fault displacement characteristics, with particular reference to synthetic transfer zones, Mae Moh mine, northern Thailand. *Basin Research* **12** (1), 307–327.
- MOUYARIS, N., PAPASTAMATIOU, D. & VITA-FINZI, C. 1992 The Helice Fault ? *Terra Nova* **4** (1), 124–128.
- MURAOKA, H. & KAMATA, H. 1983 Displacement distribution along minor fault traces. *Journal of Structural Geology* **5** (5), 483–495.
- MUTTO, T. & STEEL, R. J. 2000 The accommodation concept in sequence stratigraphy : some dimensional problems and possible redefinition. *Sedimentary Geology* **130**, 1–10.

- NEMEC, W. & POSTMA, G. 1993 Quaternary alluvial fans in southwestern Crete : sedimentation processes and geomorphic evolution. *Alluvial sedimentation* (ed. M. Marzo & C. Puigdefabregas), pp. 235–276. International Association of Sedimentologists, Special Publication 17.
- NEMEC, W. & STEEL, R. 1984 Alluvial and coastal conglomerates their significant features and some comments on gravelly mass-flow deposits. *Sedimentology of gravels and conglomerates* (ed. E. Koster & R. Steel), pp. 1–32. Canadian Society of Petroleum Geologists.
- NEWELL, A. J., TVERDOKHLEBOV, V. P. & BENTON, M. J. 1999 Interplay of tectonics and climate on a transverse fluvial system, Upper Permian, Southern Uralian Foreland Basin, Russia. *Sedimentary Geology* **127** (1-2), 11–29.
- NICHOLS, G. & WATCHORN, F. 1998 Climatic and geomorphic controls on rift sedimentation : Oligo-Miocene syn-rift facies in the Gulf of Aden, Yemen. *Marine and Petroleum Geology* **15** (6), 505–518.
- NICHOLS, G. J. & FISHER, J. A. 2007 Processes, facies and architecture of fluvial distributary system deposits. *Sedimentary Geology* **195** (1-2), 75–90.
- NICOL, A., WALSH, J., VILLAMOR, P., SEEBECK, H. & BERRYMAN, K. 2010 Normal fault interactions, paleoearthquakes and growth in an active rift. *Journal of Structural Geology* **32** (8), 1101–1113.
- NICOL, A., WATTERSON, J., WALSH, J. J., CHILDS, C. & GROUP, F. A. 1996 The shapes, major axis orientations and displacement patterns of fault surfaces. *Journal of Structural Geology* **18** (5), 235–248.
- NISHIZUMI, K. 2004 Preparation of ²⁶Al AMS standards. *Nuclear Instruments and Methods in Physics Research Section B : Beam Interactions with Materials and Atoms* **223-224** (1), 388–392.
- NISHIZUMI, K. 2007 Absolute calibration of ¹⁰Be AMS standards. *Nuclear Instruments and Methods in Physics Research Section B : Beam Interactions with Materials and Atoms* **258** (2), 403–413.
- NISHIZUMI, K., WINTERER, E. L., KOHL, C. P., KLEIN, J., MIDDLETON, R., LAL, D. & ARNOLD, J. R. 1989 Cosmic ray production rates of ¹⁰Be and ²⁶Al in quartz from glacially polished rocks. *Journal of Geophysical Research* **94** (B12), 17907.
- NIXON, C. W., MCNEILL, L. C., BULL, J. M., BELL, R. E., GAWTHORPE, R. L., HENSTOCK, T. J., CHRISTODOULOU, D., FORD, M., TAYLOR, B., SAKELLARIOU, D., FERENTINOS, G., PAPANATHANASSIOU, G., LEEDER, M. R., COLLIER, R. E., GOODLIFFE, A. M., SACHPAZI, M. & KRANIS, H. 2016 Rapid spatio-temporal variations in rift structure during development of the Corinth Rift, central Greece. *Tectonics* **35**, 1225–1248.
- NYST, M. & THATCHER, W. 2004 New constraints on the active tectonic deformation of the Aegean. *Journal of Geophysical Research* **109** (1), B11406.
- OBERLANDER, T. M. 1985 Origin of drainage transverse to structures in orogens. *Tectonic Geomorphology : The Binghamton Symposia in Geomorphology : International Series, 15* (ed. M. Morisawa & J. T. Hack), pp. 155–182. Allen and Unwin, London.
- OLIVE, J.-A. & BEHN, M. D. 2014 Rapid rotation of normal faults due to flexural stresses : An explanation for the global distribution of normal fault dips. *Journal of Geophysical Research : Solid Earth* **119** (4), 3722–3739.
- OLIVE, J.-A., BEHN, M. D. & MALATESTA, L. C. 2014 Modes of extensional faulting controlled by surface processes. *Geophysical Research Letters* **41** (19), 6725–6733.
- OLLIER, C. & PAIN, C. 2000 *The origin of mountains*. Taylor & Francis Ed.

BIBLIOGRAPHIE

- OLSEN, T., STEEL, R., HOGSETH, K., SKAR, T. & ROE, S.-L. 1995 Sequential architecture in a fluvial succession : sequence stratigraphy in the Upper Cretaceous Mesaverde Group, Price Canyon, Utah. *Journal of Sedimentary Research* **65** (2), 265–280.
- ORI, G. G. 1989 Geologic history of the extensional basin of the Gulf of Corinth (?Miocene-Pleistocene), Greece. *Geology* **17** (10), 918–921.
- PACCHIANI, F. & LYON-CAEN, H. 2010 Geometry and spatio-temporal evolution of the 2001 Agios Ioanis earthquake swarm (Corinth Rift, Greece). *Geophysical Journal International* **180** (1), 59–72.
- PAIM, P. S. G. 1995 Alluvial Palaeogeography of the Guaritas Depositional Sequence of Southern Brazil. *Sedimentary Facies Analysis – A Tribute to the Research and Teaching of Harold G. Reading* (ed. A. Plint), pp. 3–16. International Association of Sedimentologists, Special Publication 22.
- PALYVOS, N., LEMEILLE, F., SOREL, D., PANTOSTI, D. & PAVLOPOULOS, K. 2008 Geomorphic and biological indicators of paleoseismicity and Holocene uplift rate at a coastal normal fault footwall (western Corinth Gulf, Greece). *Geomorphology* **96** (1-2), 16–38.
- PALYVOS, N., MANCINI, M., SOREL, D., LEMEILLE, F., PANTOSTI, D., JULIA, R., TRIANTAPHYLLOU, M. & DE MARTINI, P.-M. 2010 Geomorphological, stratigraphic and geochronological evidence of fast Pleistocene coastal uplift in the westernmost part of the Corinth Gulf Rift (Greece). *Geological Journal* **45** (1), 78–104.
- PALYVOS, N., PANTOSTI, D., DE MARTINI, P. M., LEMEILLE, F., SOREL, D. & PAVLOPOULOS, K. 2005 The Aigion-Neos Erineos coastal normal fault system (western Corinth Gulf Rift, Greece) : Geomorphological signature, recent earthquake history, and evolution. *Journal of Geophysical Research : Solid Earth* **110** (B9).
- PAOLA, C. 2000 Quantitative models of sedimentary basin filling. *Sedimentology* **47** (1), 121–178.
- PAOLA, C., HELLER, P. L. & ANGEVINE, C. L. 1992 The large-scale dynamics of grain-size variation in alluvial basins, 1 : Theory. *Basin Research* **4** (2), 73–90.
- PAOLA, C. & MARTIN, J. M. 2012 Mass-Balance Effects In Depositional Systems. *Journal of Sedimentary Research* **82** (6), 435–450.
- PAPANICOLAOU, C., DEHMER, J. & FOWLER, M. 2000 Petrological and organic geochemical characteristics of coal samples from Florina, Lava, Moschopotamos and Kalavryta coal fields, Greece. *International Journal of Coal Geology* **44** (3-4), 267–292.
- PAPANICOLAOU, C., KOTIS, T., FOSCOLOS, A. & GOODARZI, F. 2004 Coals of Greece : a review of properties, uses and future perspectives. *International Journal of Coal Geology* **58** (3), 147–169.
- PAPANIKOLAOU, D. 1993 Geotectonic evolution of the Aegean. *Bulletin of the Geological Society of Greece* **27** (1), 33–48.
- PAPANIKOLAOU, D., GOULIOTIS, L. & TRIANTAPHYLLOU, M. 2009 The Itea-Amfissa detachment : a pre-Corinth rift Miocene extensional structure in central Greece. *Geological Society, London, Special Publications* **311** (1), 293–310.
- PAPANIKOLAOU, D. J. & ROYDEN, L. H. 2007 Disruption of the Hellenic arc : Late Miocene extensional detachment faults and steep Pliocene-Quaternary normal faults-Or what happened at Corinth ? *Tectonics* **26** (5), TC5003.

- PAPATHEODOROU, G. & FERENTINOS, G. 1993 Sedimentation processes and basin infilling depositional architecture in an active asymmetric graben : Strava graben, Gulf of Corinth, Greece. *Basin Research* **5** (4), 235–253.
- PAPAZACHOS, B. C. & COMNINAKIS, P. E. 1971 Geophysical and tectonic features of the Aegean Arc. *Journal of Geophysical Research* **76** (35), 8517–8533.
- PAPP, A. 1951 Das Pannon des Wiener Beckens. *Mitteilungen der Geologischen Gesellschaft Wien* **39-41**, 99–193.
- PARKER, G. 1991 Selective Sorting and Abrasion of River Gravel. I : Theory. *Journal of Hydraulic Engineering* **117** (2), 131–147.
- PATON, D. A. & UNDERHILL, J. R. 2004 Role of crustal anisotropy in modifying the structural and sedimentological evolution of extensional basins : the Gamtoos Basin, South Africa. *Basin Research* **16** (3), 339–359.
- PATTON, T. L., MOUSTAFA, A. R., NELSON, R. A. & ABDINE, S. A. 1994 Tectonic evolution and structural setting of the Suez Rift. *Interior rift basins* (ed. S. Landon), pp. 9–55. American Association of Petroleum Geologists, Memoir 59.
- PE-PIPER, G. & PIPER, D. J. W. 1984 Tectonic setting of the Mesozoic Pindos basin of the Peloponnese, Greece. *Geological Society, London, Special Publications* **17** (1), 563–567.
- PEACOCK, D. & PAR, E. A. 2002 Active relay ramps and normal fault propagation on Kilauea Volcano , Hawaii. *Journal of Structural Geology* **24** (4), 729–742.
- PEACOCK, D. & SANDERSON, D. 1994 Geometry and development of relay ramps in normal fault systems. *AAPG Bulletin* **78** (2), 147–165.
- PEACOCK, D. C. P. 1991 Displacements and segment linkage in strike-slip fault zones. *Journal of Structural Geology* **13** (9), 1025–1035.
- PEACOCK, D. C. P. & SANDERSON, D. J. 1996 Effects of propagation rate on displacement variations along faults. *Journal of Structural Geology* **18** (2–3), 311–320.
- PEAKALL, J., LEEDER, M., BEST, J. & ASHWORTH, P. 2000 River response to lateral ground tilting : a synthesis and some implications for the modelling of alluvial architecture in extensional basins. *Basin Research* **12** (3-4), 413–424.
- PEIZHEN, Z., MOLNAR, P. & DOWNS, W. R. 2001 Increased sedimentation rates and grain sizes 2–4 Myr ago due to the influence of climate change on erosion rates. *Nature* **410** (6831), 891–897.
- PÉROUSE, E., CHAMOT-ROOKE, N., RABAUTE, A., BRIOLE, P., JOUANNE, F., GEORGIEV, I. & DIMITROV, D. 2012 Bridging onshore and offshore present-day kinematics of central and eastern Mediterranean : Implications for crustal dynamics and mantle flow. *Geochemistry, Geophysics, Geosystems* **13** (9), Q09013.
- PIPER, D. J. W. 2006 Sedimentology and tectonic setting of the Pindos Flysch of the Peloponnese, Greece. *Tectonic Development of the eastern Mediterranean Region* (ed. A. H. F. Robertson & D. Mountrakis), pp. 493–505. Geological Society, London, Special Publications 260.
- PIRAZZOLI, P., STIROS, S., FONTUGNE, M. & ARNOLD, M. 2004 Holocene and Quaternary uplift in the central part of the southern coast of the Corinth Gulf (Greece). *Marine Geology* **212** (1-4), 35–44.

BIBLIOGRAPHIE

- PIROMALLO, C. & MORELLI, A. 2003 P wave tomography of the mantle under the Alpine-Mediterranean area. *Journal of Geophysical Research* **108** (B2), 2065.
- PISEL, J. 2015 Multi-scale stratigraphic and statistical analysis of allogenic and autogenic controls on fluvial systems. PhD thesis, Colorado School of Mines.
- PLATT, N. H. & WRIGHT, V. P. 1991 Lacustrine carbonates : facies models, facies distributions and hydrocarbon aspects. *Lacustrine Facies Analysis* (ed. P. Anadon, L. Cabrera & K. Kelts), pp. 57–74. International Association of Sedimentologists, Special Publication 13.
- POPOV, V. V. 2001 Late Pliocene voles (Mammalia : Arvicolidae) from Varshets (North Bulgaria). *Acta zoologica cracoviensia* **44** (2), 143–172.
- POSAMENTIER, H. & ALLEN, G. 1999 *Siliciclastic sequence stratigraphy : concepts and applications, Concepts in Sedimentology and Paleontology*. Society of Economic Paleontologists and Mineralogists, Special Publication 7.
- POSAMENTIER, H., JERVEY, M. & VAIL, P. 1988 Eustatic control on clastic deposition I - conceptual framework. *Sea-Level Changes : An Integrated Approach* (ed. C. Wilgus, B. Hastings, H. Posamentier, J. Van Wagoner, C. Ross & C. Kendall), pp. 109–124. Society of Economic Paleontologists and Mineralogists, Special Publication 42.
- POSAMENTIER, H. W. 2001 Lowstand alluvial bypass systems : incised vs. unincised. *American Association of Petroleum Geologists Bulletin* **85** (10), 1771–1793.
- POSAMENTIER, H. W. & VAIL, P. R. 1988 Eustatic control on clastic sedimentation II-sequence and systems tract models. *Sea Level Changes : An Integrated Approach* (ed. C. Wilgus, B. Hastings, C. Ross, H. Posamentier, J. van Wagoner & C. S. C. Kendall), pp. 125–154. Society of Economic Paleontologists and Mineralogists, Special Publication 42.
- POSTMA, G. 1990 Depositional architecture and facies of river and fan deltas : a synthesis. *Coarse-grained deltas* (ed. A. Colella & D. B. Prior), pp. 13–28. International Association of Sedimentologists, Special Publication 10.
- POULIMENOS, G., ZELILIDIS, A., KONTOPOULOS, N. & DOUTSOS, T. 1993 Geometry of trapezoidal fan deltas and their relationship to extensional faulting along the southwestern active margins of the Corinth rift, Greece. *Basin Research* **5** (3), 179–192.
- POWELL, J. W. 1875 *Exploration of the Colorado River of the West and its Tributaries*. Government Printing Office, Washington, DC.
- PROFFETT, J. M. 1977 Cenozoic geology of the Yerington district, Nevada, and implications for the nature and origin of Basin and Range faulting. *Geological Society of America Bulletin* **88** (2), 247–266.
- PROSSER, S. 1993 Rift-related linked depositional systems and their seismic expression. *Tectonics and Seismic Sequence Stratigraphy* (ed. G. Williams & A. Dobb), pp. 35–66. Geological Society, London, Special Publications 71.
- RAFFI, I., BACKMAN, J., FORNACIARI, E., PÄLIKE, H., RIO, D., LOURENS, L. & HILGEN, F. 2006 A review of calcareous nannofossil astrobiochronology encompassing the past 25 million years. *Quaternary Science Reviews* **25** (23–24), 3113–3137.
- RANERO, C. R. & PÉREZ-GUSSINYÉ, M. 2010 Sequential faulting explains the asymmetry and extension discrepancy of conjugate margins. *Nature* **468** (7321), 294–299.

- RAVNÅS, R. & STEEL, R. J. 1998 Architecture of marine rift-basin successions. *American Association of Petroleum Geologists Bulletin* **82** (1), 110–146.
- REILINGER, R., MCCLUSKY, S., PARADISSIS, D., ERGINTAV, S. & VERNANT, P. 2010 Geodetic constraints on the tectonic evolution of the Aegean region and strain accumulation along the Hellenic subduction zone. *Tectonophysics* **488** (1-4), 22–30.
- REILINGER, R., MCCLUSKY, S., VERNANT, P., LAWRENCE, S., ERGINTAV, S., ÇAKMAK, R., ÖZENER, H., KADIROV, F., GULIEV, I., STEPANYAN, R., NADARIYA, M., HAHUBIA, G., MAHMOUD, S., K., S., ARRAJEHI, A., DEMITRIS, P., AL-AYDRUS, A., PRILEPIN, M., TAMARA, G., EVREN, E., DMITROTSIA, A., FILIKOV, S., GOMEZ, G., AL-GHAZZI, R. & KARAM, G. 2006 GPS constraints on continental deformation in the Africa-Arabia-Eurasia continental collision zone and implications for the dynamics of plate interactions. *Journal of Geophysical Research* **111**, B05411.
- RESTALLACK, G. J. 1988 Field recognition of paleosols. *Geological Society of America Special Papers* **216**, 1–20.
- RESTALLACK, G. J. 1997 *Colour guide to paleosols*. John Wiley & Sons Ltd.
- RESTALLACK, G. J. 2001 *Soils of the past : an introduction to paleopedology*. Blackwell Science.
- RIGO, A., LYON-CAEN, H., ARMIJO, R., DESCHAMPS, A., HATZFELD, D., MAKROPOULOS, K., PAPADIMITRIOU, P. & KASSARAS, I. 1996 A microseismic study in the western part of the Gulf of Corinth (Greece) : implications for large-scale normal faulting mechanisms. *Geophysical Journal International* **126** (3), 663–688.
- RIVELINE, J., BERGER, J.-P., FEIST, M., MARTIN-CLOSAS, C., SCHUDACK, M. & SOULIE-MAERSCHE, I. 1996 European Mesozoic-Cenozoic charophyte biozonation. *Bulletin de la Société géologique de France* **167**, 453–468.
- ROBERTS, A. M., YIELDING, G., KUSZNIR, N. J., WALKER, I. & DORN-LOPEZ, D. 1993 Mesozoic extension in the North Sea : constraints from flexural backstripping, forward modelling and fault populations. *Petroleum Geology of Northwest Europe : Proceedings of the 4th Conference*, pp. 1123–1136. Geological Society of London.
- ROBERTS, G. P. 1996 Variation in fault-slip directions along active and segmented normal fault systems. *Journal of Structural Geology* **18** (6), 835–845.
- ROBERTSON, A. H. F., DIXON, J. E., BROWN, S., COLLINS, A., MORRIS, A., PICKETT, E., SHARP, I. & USTAOMER, T. 1996 Alternative tectonic models for the Late Palaeozoic-Early Tertiary development of Tethys in the Eastern Mediterranean region. *Geological Society, London, Special Publications* **105** (1), 239–263.
- ROHAIS, S., BONNET, S. & ESCHARD, R. 2012 Sedimentary record of tectonic and climatic erosional perturbations in an experimental coupled catchment-fan system. *Basin Research* **24** (2), 198–212.
- ROHAIS, S., ESCHARD, R., FORD, M., GUILLOCHEAU, F. & MORETTI, I. 2007a Stratigraphic architecture of the Plio-Pleistocene infill of the Corinth Rift : Implications for its structural evolution. *Tectonophysics* **440** (1-4), 5–28.
- ROHAIS, S., ESCHARD, R. & GUILLOCHEAU, F. 2008 Depositional model and stratigraphic architecture of rift climax Gilbert-type fan deltas (Gulf of Corinth, Greece). *Sedimentary Geology* **210** (3-4), 132–145.

BIBLIOGRAPHIE

- ROHAIS, S., JOANNIN, S., COLIN, J.-P., SUC, J.-P., GUILLOCHEAU, F. & ESCHARD, R. 2007b Age and environmental evolution of the syn-rift fill of the southern coast of the Gulf of Corinth (Akrata-Derveni region, Greece). *Bulletin de la Société géologique de France* **178** (3), 231–243.
- ROSENDAHL, B. R. 1987 Architecture of continental rifts with special reference to East Africa. *Annual Review of Earth and Planetary Sciences* **15** (1), 445.
- ROYDEN, L. H. & PAPANIKOLAOU, D. J. 2011 Slab segmentation and late Cenozoic disruption of the Hellenic arc. *Geochemistry Geophysics Geosystems* **12** (3), Q03010.
- RUST, B. R. 1972 Structure and process in a braided river. *Sedimentology* **18** (3-4), 221–245.
- RUST, B. R. & KOSTER, E. H. 1984 Coarse alluvial deposits. *Facies models* (ed. R. Walker), pp. 53–69. Geoscience Canada Reprint Series 1.
- SACHPAZI, M., CLÉMENT, C., LAIGLE, M., HIRN, A. & ROUSSOS, N. 2003 Rift structure, evolution, and earthquakes in the Gulf of Corinth, from reflection seismic images. *Earth and Planetary Science Letter* **216** (3), 243–257.
- SACHPAZI, M., GALVÉ, A., LAIGLE, M., HIRN, A., SOKOS, E., SERPETSIDAKI, A., MARTHELOT, J.-M., PI ALPERIN, J., ZELT, B. & TAYLOR, B. 2007 Moho topography under central Greece and its compensation by Pn time-terms for the accurate location of hypocenters : The example of the Gulf of Corinth 1995 Aigion earthquake. *Tectonophysics* **440** (1-4), 53–65.
- SAINT-CARLIER, D., CHARREAU, J., LAVÉ, J., BLARD, P.-H., DOMINGUEZ, S., AVOUAC, J.-P., WANG, S. & ASTER TEAM 2016 Major temporal variations in shortening rate absorbed along a large active fold of the southeastern Tianshan piedmont (China). *Earth and Planetary Science Letters* **434** (1), 333–348.
- SAKELLARIOU, D., LYKOUSIS, V., ALEXANDRI, S., KABERI, H., ROUSAKIS, G., NOMIKOU, P., GEORGIIOU, P. & BALLAS, D. 2007 Faulting, seismic-stratigraphic architecture and Late Quaternary evolution of the Gulf of Alkyonides Basin-East Gulf of Corinth, Central Greece. *Basin Research* **19** (2), 273–295.
- SALA, B. & MASINI, F. 2007 Late Pliocene and Pleistocene small mammal chronology in the Italian peninsula. *Quaternary International* **160** (1), 4–16.
- SANTOS, M. G. M., ALMEIDA, R. P., GODINHO, L. P. S., MARCONATO, A. & MOUNTNEY, N. P. 2014 Distinct styles of fluvial deposition in a Cambrian rift basin. *Sedimentology* **61** (4), 881–914.
- SCHALLER, M., VON BLANCKENBURG, F., HOVIUS, N. & KUBIK, P. 2001 Large-scale erosion rates from in situ-produced cosmogenic nuclides in European river sediments. *Earth and Planetary Science Letters* **188** (3-4), 441–458.
- SCHLAGENHAUF, A., MANIGHETTI, I., MALAVIEILLE, J. & DOMINGUEZ, S. 2008 Incremental growth of normal faults : Insights from a laser-equipped analog experiment. *Earth and Planetary Science Letters* **273** (3–4), 299–311.
- SCHLISCHE, R. W. 1991 Half-graben basin filling models : new constraints on continental extensional basin development. *Basin Research* **3** (3), 123–141.
- SCHLISCHE, R. W. & ANDERS, M. H. 1996 Stratigraphic effects and tectonic implications of the growth of normal faults and extensional basins. *Reconstructing the History of Basin and Range Extension Using Sedimentology and Stratigraphy* (ed. K. Beratan), pp. 183–203. Geological Society of America Special Publication 303.

- SCHLISCHE, R. W. & OLSEN, P. E. 1990 Quantitative filling model for continental extensional basins with applications to early Mesozoic rifts of eastern North America. *The Journal of Geology* **98** (2), 135–155.
- SCHLISCHE, R. W. & WITHJACK, M. O. 2009 Origin of fault domains and fault-domain boundaries (transfer zones and accommodation zones) in extensional provinces : Result of random nucleation and self-organized fault growth. *Journal of Structural Geology* **31** (9), 910–925.
- SCHOLZ, C. H. 1988 The brittle-plastic transition and the depth of seismic faulting. *Geologische Rundschau* **77** (1), 319–328.
- SCHOLZ, C. H. & CONTRERAS, J. C. 1998 Mechanics of continental rift architecture. *Geology* **26** (11), 967.
- SCHUMM, S. A., DUMONT, J. F. & HOLBROOK, J. M. 2000 *Active tectonics and alluvial rivers*. Cambridge University Press.
- SCHWARCZ, H. P. & LATHAM, A. G. 1989 Dirty calcites 1. Uranium-series dating of contaminated calcite using leachates alone. *Chemical Geology : Isotope Geoscience section* **80** (1), 35–43.
- SEIDEL, E., KREUZER, H. & HARRE, W. 1982 A late Oligocene/early Miocene high pressure belt in the external Hellenides. *Geologisches Jahrbuch E* **23**, 165–206.
- SHANLEY, K. W. & MCCABE, P. J. 1993 Alluvial architecture in a sequence stratigraphic framework : a case history from the Upper Cretaceous of southern Utah, USA. *Quantitative Modeling of Clastic Hydrocarbon Reservoirs and Outcrop Analogues, Special Publication* **15**, 21–55.
- SHANLEY, K. W. & MCCABE, P. J. 1994 Perspectives on the sequence stratigraphy of continental strata. *American Association of Petroleum Geologists Bulletin* **78** (4), 544–568.
- SHEETS, B. A., HICKSON, T. A. & PAOLA, C. 2002 Assembling the stratigraphic record : Depositional patterns and time-scales in an experimental alluvial basin. *Basin Research* **14** (3), 287–301.
- SIAME, L., BOURLÈS, D. L. & BROWN, E. T. 2006 *In Situ-Produced Cosmogenic Nuclides and Quantification of Geological Processes*. Macmillan Publishers Limited. All rights reserved.
- SIDDALL, M., ROHLING, E. J., ALMOGI-LABIN, A., HEMLEBEN, C., MEISCHNER, M., SCHMELZER, I. & SMEED, D. A. 2003 Sea-level fluctuations during the last glacial cycle. *Nature* **423**, 853–858.
- SIMPSON, G. 2004 Role of river incision in enhancing deformation. *Geology* **32** (4), 341.
- SINGH, H., PARKASH, B. & GOHAIN, K. 1993 Facies analysis of the Kosi megafan deposits. *Sedimentary Geology* **85** (1-4), 87–113.
- SINHA, R. & FRIEND, P. 1994 River systems and their sediment flux, Indo-Gangetic plains, Northern Bihar, India. *Sedimentology* **41** (4), 825–845.
- SKOURTSOS, E. & KRANIS, H. 2009 Structure and evolution of the western Corinth Rift, through new field data from the Northern Peloponnesus. *Geological Society, London, Special Publications* **321** (1), 119–138.
- SOLIVA, R., BENEDICTO, A., SCHULTZ, R., MAERTEN, L. & MICARELLI, L. 2008 Displacement and interaction of normal fault segments branched at depth : Implications for fault growth and potential earthquake rupture size. *Journal of Structural Geology* **30** (10), 1288–1299.

BIBLIOGRAPHIE

- SOREL, D. 2000 A Pleistocene and still-active detachment fault and the origin of the Corinth-Patras rift, Greece. *Geology* **28** (1), 83–86.
- SOULIÉ-MÄRSCHÉ, I. 1979 Charophytes fossiles des formations pliocènes de l’Isthme de Megara (Grèce). *Annales Géologiques des Pays Helléniques Tome hors série fasc. 4*, 1127–1136.
- SPROVIERI, R., DI STEFANO, E., HOWELL, M., DI SAKAMOTO, T., DI STEFANO, A. & MARINO, M. 1998 Integrated calcareous plankton biostratigraphy and cyclostratigraphy at site 964. *Proceedings of the Ocean Drilling Program, Scientific Results 160* (ed. A. Robertson, K.-C. Emeris, C. Ritcher & C. Camerlenghi), pp. 155–165.
- STAMPFLI, G. M. & BOREL, G. D. 2004 The TRANSMED Transects in Space and Time : Constraints on the Paleotectonic Evolution of the Mediterranean Domain. *The TRANSMED Atlas. The Mediterranean Region from Crust to Mantle*, pp. 53–80. Berlin, Heidelberg : Springer Berlin Heidelberg.
- STANISTREET, I. G. & MCCARTHY, T. S. 1993 The Okavango Fan and the classification of subaerial fan systems. *Sedimentary Geology* **85** (1), 115–133.
- STEFATOS, A., PAPTAEODOROU, G., FERENTINOS, G., LEEDER, M. & COLLIER, R. 2002 Seismic reflection imaging of active offshore faults in the Gulf of Corinth : their seismotectonic significance. *Basin Research* **14** (4), 487–502.
- STEVANOVIC, P. M. 1963 Beitrag zur Kenntnis der pontischen Molluskenfauna aus Griechenland und ihre stratigraphische Bedeutung. *Académie Serbe des Sciences et des Arts* **32**, 73–93.
- STEWART, I. S. 1996 Holocene uplift and paleoseismicity on the Eliki fault, western Gulf of Corinth, Greece. *Annals of Geophysics* **39** (3), 575–588.
- STEWART, I. S. & VITA-FINZI, C. 1996 Coastal uplift on active normal faults : The Eliki Fault, Greece. *Geophysical Research Letters* **23** (14), 1853–1856.
- STOCK, G. M., ANDERSON, R. S. & FINKEL, R. C. 2004 Pace of landscape evolution in the Sierra Nevada, California, revealed by cosmogenic dating of cave sediments. *Geology* **32** (3), 193–196.
- STONE, J. O. 2000 Air pressure and cosmogenic isotope production. *Journal of Geophysical Research* **105**, 23753–23759.
- STRAHLER, A. N. 1945 Hypothesis of stream development in the folded appalachians of Pennsylvania. *Geological Society of America Bulletin* **56** (1), 45–88.
- STRAUB, K. M., PAOLA, C., KIM, W. & SHEETS, B. 2013 Experimental Investigation of Sediment-Dominated Vs. Tectonics-Dominated Sediment Transport Systems In Subsiding Basins. *Journal of Sedimentary Research* **83** (12), 1162–1180.
- STRAUB, K. M., PAOLA, C., KIM, W. & SHEETS, B. 2014 Experimental Investigation of Sediment-Dominated Vs. Tectonics-Dominated Sediment Transport Systems In Subsiding Basins. *Journal of Sedimentary Research* **83** (12), 1162–1180.
- STRONG, N. & PAOLA, C. 2008 Valleys That Never Were : Time Surfaces Versus Stratigraphic Surfaces. *Journal of Sedimentary Research* **78** (8), 579–593.
- STRONG, N., SHEETS, B. A., HICKSON, T. A. & PAOLA, C. 2005 A mass-balance framework for quantifying downstream changes in fluvial architecture. *Fluvial Sedimentology VII* (ed. M. Blum, S. Marriott & S. Leclair), pp. 243–253. International Association of Sedimentologists, Special Publication 35.

- SURLYK, F. 1978 Submarine fan sedimentation along fault scarps on tilted fault blocks (Jurassic-Cretaceous boundary, East Greenland). *Bulletin Grønlands Geologiske Undersøgelse* **128** (1), 108.
- SYMEONIDIS, N., THEOTHOROU, G., SCHUTT, H. & VELITZELOS, E. 1987 Paleontological and stratigraphic observations in the area of Achaia and Etoloakarnania W-Greece. *Annales Géologiques des Pays Helléniques* **38**, 317–353.
- TALLING, P. J., STEWART, M. D., STARK, C. P., GUPTA, S. & VINCENT, S. J. 1997 Regular spacing of drainage outlets from linear fault blocks. *Basin Research* **9** (4), 275–302.
- TAUXE, L., MULLENDER, T. A. T. & PICK, T. 1996 Potbellies, wasp waists, and superparamagnetism in magnetic hysteresis. *Journal of Geophysical Research : Solid Earth (1978–2012)* **101** (B1), 571–583.
- TAYLOR, B., WEISS, J. R., GOODLIFFE, A. M., SACHPAZI, M., LAIGLE, M. & HIRN, A. 2011 The structures, stratigraphy and evolution of the Gulf of Corinth rift, Greece. *Geophysical Journal International* **185** (3), 1189–1219.
- TAYMAZ, T., JACKSON, J. & MCKENZIE, D. 1991 Active tectonics of the north and central Aegean Sea. *Geophysical Journal International* **106** (2), 433–490.
- TER VOORDE, M. & CLOETINGH, S. 1996 Numerical modelling of extension in faulted crust : effects of localized and regional deformation on basin stratigraphy. *Modern Developments in Structural Interpretation, Validation and Modelling* (ed. P. G. Buchanan & D. A. Nieuwland), pp. 283–296. Geological Society, London, Special Publications 99.
- THEODOROPOULOS, D. 1968 Stratigraphic und Tectonik des Isthmus von Megara. *Erlanger Geologische Abhandlungen* **73**.
- THEYE, T., SEIDEL, E. & VIDAL, O. 1992 Carpholite, sudoite and chloritoid in low-grade high-pressure metapelites from Crete and the Peloponnese. *European Journal of Mineralogy* **4** (3), 487–507.
- THIÉBAULT, F. & TRIBOULET, C. 1984 Alpine metamorphism and deformation in phyllites nappes (external Hellenides, southern Peloponnese, Greece) : Geodynamic implications. *The Journal of Geology* **92** (2), 185–199.
- TIBERI, C., DIAMENT, M., LYON CAEN, H. & KING, T. 2001 Moho topography beneath the Corinth Rift area (Greece) from inversion of gravity data. *Geophysical Journal International* **145** (3), 797–808.
- TIBERI, C., LYON-CAEN, H., HATZFELD, D., ACHAUER, U., KARAGIANNI, E., KIRATZI, A., LOUVARI, E., PANAGIOTOPOULOS, D., KASSARAS, I., KAVIRIS, G., MAKROPOULOS, K. & PAPADIMITRIOU, P. 2000 Crustal and upper mantle structure beneath the Corinth rift (Greece) from a teleseismic tomography study. *Journal of Geophysical Research : Solid Earth* **105** (B12), 28159–28171.
- TIERCELIN, J.-J., SOREGHAN, M., COHEN, A. S., LEZZAR, K.-E. & BOUROULLEC, J.-L. 1992 Sedimentation in large rift lakes : example from the Middle Pleistocene—Modern deposits of the Tanganyika Trough, East African Rift System. *Bulletin des centres de Recherche Exploration et Production d'Elf Aquitaine* **16**, 83–111.
- TROTET, F., GOFFE, B., VIDAL, O. & JOLIVET, L. 2006 Evidence of retrograde Mg-carpholite in the Phyllite-Quartzite nappe of Peloponnese from thermobarometric modelisation - geodynamic implications. *Geodinamica Acta* **19** (5), 323–343.
- TRUDGILL, B. D. 2002 Structural controls on drainage development in the Canyonlands grabens of southeast Utah. *American Association of Petroleum Geologists Bulletin* **86** (6), 1095–1112.

BIBLIOGRAPHIE

- TRUDGILL, B. D. & CARTWRIGHT, J. 1994 Relay-ramp forms and normal-fault linkages, Canyonlands National Park, Utah. *Geological Society of America Bulletin* **106** (9), 1143–1157.
- TSELENTIS, G.-A. & MAKROPOULOS, K. 1986 Rates of crustal deformation on in the Gulf of Corinth (central greece) as determined from seismicity. *Tectonophysics* **124** (1-2), 55–66.
- TUCKER, G. E. & SLINGERLAND, R. L. 1994 Erosional dynamics, flexural isostasy, and long-lived escarpments : A numerical modeling study. *Journal of Geophysical Research : Solid Earth* **99** (B6), 12229–12243.
- TWIDALE, C. 2004 River patterns and their meaning. *Earth-Science Reviews* **67** (3-4), 159–218.
- VAN RENSBERGEN, P., HILLIS, R. R., MALTMAN, A. J. & MORLEY, C. K. 2003 Subsurface sediment mobilization : introduction. *Geological Society, London, Special Publications* **216** (1), 1–8.
- VAN WAGONER, J. C., MITCHUM, R. M., CAMPION, K. M. & RAHMANIAN, V. D. 1990 Siliciclastic sequence stratigraphy in well logs, cores, and outcrops : concepts for high-resolution correlation of time and facies. *American Association of Petroleum Geologists, Methods in Exploration Series*, 7, p. 55. American Association of Petroleum Geologists, Special Volumes.
- VAN WAGONER, J. C., POSAMENTIER, H., MITCHUM, R., VAIL, P., SARG, J., LOUTIT, T. & HARDENBOL, J. 1988 An overview of the fundamentals of sequence stratigraphy and key definitions. *Sea Level Changes : An Integrated Approach* (ed. C. K. Wilgus, H. Posamentier, C. A. Ross & K. C. G. St), pp. 39–45. Society of Economic Paleontologists and Mineralogists, Special Publication 42.
- VANDROMME, R. 2007 Approche des mécanismes de l'injection sableuse per descensum. PhD thesis, Thèse Ecole Mines Paris, France.
- VASILATOS, C., VLACHOU-TSIPOURA, M. & STAMATAKIS, M. G. 2010 On the occurrence of a volcanic ash layer in the Xylocastro area, North Peloponnesus, Greece : Mineralogy and geochemistry. *Bulletin of the Geological Society of Greece* **43** (5), 2773–2785.
- VASSIO, E., MARTINETTO, E., DOLEZYCH, M. & VAN DER BURGH, J. 2008 Wood anatomy of the *Glyptostrobus europaeus* “whole-plant” from a Pliocene fossil forest of Italy. *Review of Palaeobotany and Palynology* **151** (3), 81–89.
- VELITZELOS, D., BOUCHAL, J. M. & DENK, T. 2014 Review of the Cenozoic floras and vegetation of Greece. *Review of Palaeobotany and Palynology* **204**, 56–117.
- VELITZELOS, E. & GREGOR, H.-J. 1990 Some aspects of the Neogene floral history in Greece. *Review of Palaeobotany and Palynology* **62** (3), 291–307.
- VÉTEL, W., LE GALL, B. & JOHNSON, T. C. 2004 Recent tectonics in the Turkana Rift (North Kenya) : an integrated approach from drainage network, satellite imagery and reflection seismic analyses. *Basin Research* **16** (2), 165–181.
- VÉTEL, W., LE GALL, B. & WALSH, J. J. 2005 Geometry and growth of an inner rift fault pattern : the Kino Sogo Fault Belt, Turkana Rift (North Kenya). *Journal of Structural Geology* **27** (12), 2204–2222.
- WALKER, R. & JAMES, N. 1992 *Facies model : response to sea level change*. Geological Association of Canada.
- WALSH, J., BAILEY, W., CHILDS, C., NICOL, A. & BONSON, C. 2003 Formation of segmented normal faults : a 3-D perspective. *Journal of Structural Geology* **25** (8), 1251–1262.

- WALSH, J., NICOL, A. & CHILDS, C. 2002 An alternative model for the growth of faults. *Journal of Structural Geology* **24** (11), 1669–1675.
- WALSH, J., WATTERSON, J., BAILEY, W. & CHILDS, C. 1999 Fault relays, bends and branch-lines. *Journal of Structural Geology* **21** (8-9), 1019–1026.
- WALSH, J. J. & WATTERSON, J. 1988 Analysis of the relationship between displacements and dimensions of faults. *Journal of Structural Geology* **10** (3), 239–247.
- WALSH, J. J. & WATTERSON, J. 1991 Geometric and kinematic coherence and scale effects in normal fault systems. *The geometry of normal faults* (ed. A. Roberts, G. Yielding & B. Freeman), pp. 193–206. Geological Society, London, Special Publications 56.
- WEISS, J. R. 2004 A geophysical investigation of the gulf of Corinth, Greece. PhD thesis, University of Hawaii.
- WEISSEL, J. K. & KARNER, G. D. 1989 Flexural uplift of rift flanks due to mechanical unloading of the lithosphere during extension. *Journal of Geophysical Research* **94** (B10), 13919–13950.
- WEISSMANN, G., HARTLEY, A., NICHOLS, G., SCUDERI, L., OLSON, M., BUEHLER, H. & BANTEAH, R. 2010 Fluvial form in modern continental sedimentary basins : Distributive fluvial systems. *Geology* **38** (1), 39–42.
- WERNICKE, B. & BURCHFIEL, B. 1982 Modes of extensional tectonics. *Journal of Structural Geology* **4** (2), 105–115.
- WESTAWAY, R. 2002 The Quaternary evolution of the Gulf of Corinth, central Greece : coupling between surface processes and flow in the lower continental crust. *Tectonophysics* **348** (4), 269–318.
- WESTAWAY, R. 2007 Improved modelling of the Quaternary evolution of the Gulf of Corinth, incorporating erosion and sedimentation coupled by lower-crustal flow. *Tectonophysics* **440** (1-4), 67–84.
- WHEELER 1964 Base level, lithosphere surface and time-stratigraphy. *Geological Society of America Bulletin* **75** (1), 599–610.
- WHIPPLE, K. & MEADE, B. 2006 Orogen response to changes in climatic and tectonic forcing. *Earth and Planetary Science Letters* **243** (1-2), 218–228.
- WHIPPLE, K. X. & TRAYLER, C. R. 1996 Tectonic control of fan size : the importance of spatially variable subsidence rates. *Basin Research* **8** (3), 351–366.
- WHITTAKER, A. C., ATTAL, M. & ALLEN, P. A. 2010 Characterising the origin, nature and fate of sediment exported from catchments perturbed by active tectonics. *Basin Research* **22** (6), 809–828.
- WHITTAKER, A. C., DULLER, R. A., SPRINGETT, J., SMITHELLS, R. A., WHITCHURCH, A. L. & ALLEN, P. A. 2011 Decoding downstream trends in stratigraphic grain size as a function of tectonic subsidence and sediment supply. *Geological Society of America Bulletin* **123** (7-8), 1363–1382.
- WILLIAMS, E. A. 2000 Flexural cantilever models of extensional subsidence in the Munster Basin (SW Ireland) and Old Red Sandstone fluvial dispersal systems. *New Perspectives on the Old Red Sandstone* (ed. P. F. Friend & B. P. J. Williams), pp. 239–268. Geological Society, London, Special Publications 180.
- WILLIAMS, G. E. 1971 Flood deposits of the sand bed ephemeral streams of central Australia. *Sedimentology* **17** (1 2), 1–40.

BIBLIOGRAPHIE

- WITHJACK, M. O. & JAMISON, W. R. 1986 Deformation produced by oblique rifting. *Tectonophysics* **126** (2-4), 99–124.
- WITHJACK, M. O., SCHLISCHE, R. W. & OLSEN, P. E. 2002 Rift-basin structure and its influence on sedimentary systems. *Sedimentation in Continental rifts* (ed. S. Renaut & G. Ashley), pp. 57–81. Society of Economic Paleontologists and Mineralogists, Special Publication 73.
- WOOD, J. M., THOMAS, R. G. & VISSER, J. 1988 Fluvial processes and vertebrate taphonomy : the upper cretaceous Judith River formation, south-central dinosaur Provincial Park, Alberta, Canada. *Palaeogeography, Palaeoclimatology, Palaeoecology* **66** (1), 127–143.
- WRAY, J. L. 1977 Calcareous algae. *Developments in Paleontology and Stratigraphy* 4, p. 185. Elsevier.
- WRIGHT, V. P. & MARRIOTT, S. B. 1993 The sequence stratigraphy of fluvial depositional systems : the role of floodplain sediment storage. *Sedimentary Geology* **86** (3–4), 203–210.
- YARNOLD, J. C. & LOMBARD, J. P. 1989 A facies model for large rock-avalanche deposits formed in dry climates. *Conglomerates in Basin Analysis* (ed. L. Colburn, P. Abbott & J. Minch), pp. 9–32. Society of Economic Paleontologists and Mineralogists, Pacific Section Symposium Book 62.
- YOUNG, M. J., GAWTHORPE, R. L. & HARDY, S. 2001 Growth and linkage of a segmented normal fault zone ; the Late Jurassic Murchison-Stratjord North Fault, northern North Sea. *Journal of Structural Geology* **23** (12), 1933–1952.
- ZELILIDIS, A. 2000 Drainage evolution in a rifted basin, Corinth graben, Greece. *Geomorphology* **35** (1), 69–85.
- ZELILIDIS, A., PIPER, D. & KONTOPOULOS, N. 2002 Sedimentation and basin evolution of the Oligocene–Miocene Mesohellenic basin, Greece. *American Association of Petroleum Geologists Bulletin* **86** (1), 161–182.
- ZELT, B. C., TAYLOR, B., WEISS, J. R., GOODLIFFE, A. M., SACHPAZI, M. & HIRN, A. 2004 Streamer tomography velocity models for the Gulf of Corinth and Gulf of Itea, Greece. *Geophysical Journal International* **159** (1), 333–346.
- ZHENG, H., POWELL, C. M., AN, Z., ZHOU, J. & DONG, G. 2000 Pliocene uplift of the northern Tibetan Plateau. *Geology* **28** (8), 715.
- ZIJDERVELD, J. D. A. 1967 AC demagnetization of rocks : analysis of results. *Methods in paleomagnetism* (ed. D. Collinson, K. Creer & S. Runcorn), pp. 254–286. Elsevier, Amsterdam, Netherlands.